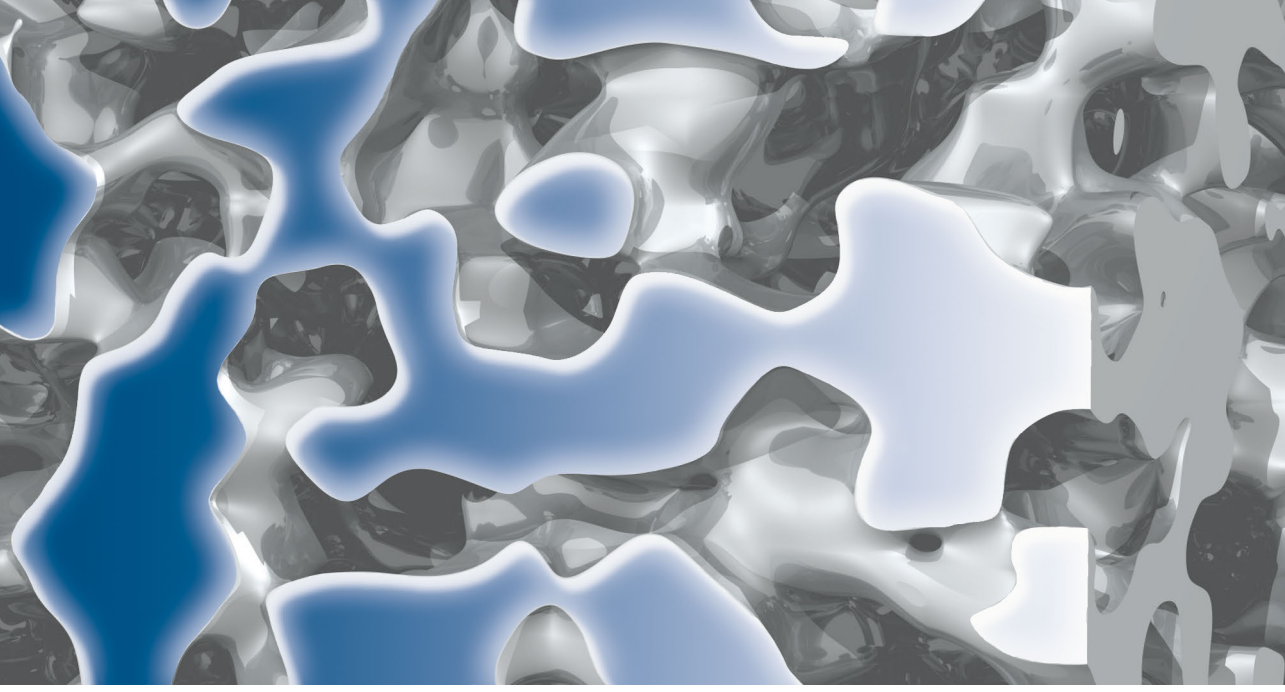

FAU Forschungen, Reihe B, Medizin, Naturwissenschaft, Technik 10

Michael Andreas Klatt

Morphometry of random spatial structures in physics

FAU UNIVERSITY PRESS

Michael Andreas Klatt

Morphometry of random spatial structures in physics

FAU Forschungen, Reihe B
Medizin, Naturwissenschaft, Technik
Band 10

Herausgeber der Reihe:
Wissenschaftlicher Beirat der FAU University Press

Michael Andreas Klatt

Morphometry of random spatial structures in physics

Erlangen
FAU University Press
2016

Bibliografische Information der Deutschen Nationalbibliothek:
Die Deutsche Nationalbibliothek verzeichnet diese Publikation in der Deutschen Nationalbibliografie; detaillierte bibliografische Daten sind im Internet über http://dnb.d-nb.de abrufbar.

Das Werk, einschließlich seiner Teile, ist urheberrechtlich geschützt.
Die Rechte an allen Inhalten liegen bei ihren jeweiligen Autoren.
Sie sind nutzbar unter der Creative Commons Lizenz BY-NC-ND.

Der vollständige Inhalt des Buchs ist als PDF über den OPUS Server der Friedrich-Alexander-Universität Erlangen-Nürnberg abrufbar:
https://opus4.kobv.de/opus4-fau/home

Verlag und Auslieferung:

FAU University Press, Universitätsstraße 4, 91054 Erlangen

Druck: docupoint GmbH

ISBN: 978-3-944057-77-4 (Druckausgabe)
eISBN: 978-3-944057-78-1 (Online-Ausgabe)
ISSN: 2198-8102

Morphometry of random spatial structures in physics

Morphometrie von zufälligen räumlichen Strukturen in der Physik

Der Naturwissenschaftlichen Fakultät
der Friedrich-Alexander-Universität Erlangen-Nürnberg

zur

Erlangung des Doktorgrades Dr. rer. nat.

vorgelegt von

Michael Andreas Klatt
aus Nürnberg

Als Dissertation genehmigt

von der Naturwissenschaftlichen Fakultät
der Friedrich-Alexander-Universität Erlangen-Nürnberg

Tag der mündlichen Prüfung:	17. 02. 2016
Vorsitzender des Promotionsorgans:	Prof. Dr. Jörn Wilms
Gutachter:	Prof. Dr. Klaus Mecke
	Prof. Dr. Hanno Sahlmann
	Prof. Dr. Salvatore Torquato

Abstract

From the large-scale structure of the universe to pasta shapes in nuclear matter: random or disordered spatial structures appear ubiquitously on nearly all length scales in very different physical, chemical, or biological systems as well as in food industry, geology, medicine, astronomy or cosmology. The shapes vary from cellular structures, packings of grains, or point processes to random fields. In systems with complex structure, there is a close interconnection of physics and geometry, and physical insight is often best achieved by a rigorous characterization of the structure. Because physics is a quantitative science, these relations can only be understood by a quantitative shape analysis. However, the structure of disordered systems is a remarkably incoherent concept; in order to characterize all of these complex shapes with the same measures, advanced mathematical tools are needed, i.e., versatile, sensitive, and robust measures of structure. Aiming for both rigorous mathematical foundation and relevance to the application, I use integral geometric measures for a sensitive and comprehensive morphometric analysis. These measures extend the notion of volume and surface area to scalar and tensorial morphometric measures, the so-called Minkowski functionals and tensors.

In this thesis, I use and extend these integral geometric measures to characterize the structures of a variety of systems on very different length scales ranging from nuclear matter over condensed and soft matter to gamma-ray astronomy, including both simulations and experimental data as well as analytic calculations for common and important models of stochastic geometry. The shapes of interest range from maximally disordered configurations to systems forming spontaneously regular structures. The same shape descriptors are applied to all of these systems, providing physical insight via a characterization of the complex geometry. A special emphasis is on the extension of the morphometric analysis to higher moments of the structure distributions or even to the full probability distributions as well as to anisotropic random spatial structures. In the latter case, I use tensorial shape descriptors to characterize the anisotropy, where I also investigate the information content of higher-rank tensors.

I thoroughly characterize the anisotropy of common models of porous media, overlapping grains and Gaussian random fields. I compare anisotropy measures w.r.t. their sensitivity and show how the Minkowski tensors resolve the disadvantages of a common measure of anisotropy. Explicit formulas for the mean values of the anisotropy measures are derived and compared to simulations. For the Minkowski functionals of overlapping grains, I also study the covariance structure and a central limit theorem. For the Gaussian random field, the tensors of higher rank are shown to contain additional anisotropy information as compared to the

tensor of rank two. However, surprisingly, the latter is nevertheless sufficient to estimate all model parameters that are necessary to determine the mean values of the Minkowski tensors of arbitrary rank which characterize the interfacial anisotropy of the level sets of the Gaussian random field. This relation could be used to test for non-Gaussianities in anisotropic random fields. The results on the models are important for applications, e.g., to estimate parameters, for null hypothesis tests, or to adjust the model to experimental data, and the results provide fundamental insights, e.g., how geometric and topological characteristics either depend on the specific system parameters or when they instead exhibit a universal behavior.

The models of overlapping grains with preferred orientation are then used to study the topology of system spanning clusters, so-called percolating clusters; especially the dependence of their topology on the anisotropy of the system. Their topology can, e.g., be connected to transport properties. The percolation threshold, i.e., the volume fraction at which such a percolating cluster appears, depends on the anisotropy of the system. However, interestingly, even the most anisotropic model simultaneously percolates in all directions. In other words, the percolation threshold is isotropic, which is linked to the uniqueness of the percolating cluster. The Minkowski functionals allow for explicit estimates of the threshold.

To analyze both the local and the global structure of cellular systems, I extend an analysis which uses local cell characteristics by introducing global correlation functions. I find for tessellations with qualitatively nearly indistinguishable local structure distributions a significantly different global structure, which here arises from disordered hyperuniformity, which can be considered to be a new state of matter. Moreover, I show that the here defined Minkowski correlation functions are supreme to standard two-point correlation functions in that they incorporate higher n-point information which could be used, e.g., for sensitive hypothesis tests to distinguish models of galaxy distributions.

Even on an extremely small length scale, I use the Minkowski functionals to characterize and classify simulated exotic states of nuclear matter, so-called nuclear pasta, which is expected to appear, e.g., in supernova explosions. Interestingly, among these pasta shapes a spontaneously formed gyroid is identified, a special minimal surface which also appears many orders of magnitudes larger in biology, making this the discovery of the smallest reported gyroid found in dynamical simulations and demonstrating the universal principles of shape formation. The binding energy of the pasta matter seems to be closely related to the Minkowski functionals, but anisotropic deformations, which can be quantified by Minkowski tensors, seem to be irrelevant.

Finally, I use the Minkowski functionals for a sensitive morphometric data analysis in gamma-astronomy: via a combination of different geometric measures

more information can be taken out of the same data without the need to assume prior knowledge about potential sources. I improve the method, especially the correction of detector effects and via detailed simulations to test the significance of structural deviations. Most importantly, I derive an accurate estimate of the distribution of background structure jointly characterized by all Minkowski functionals for large scan windows. Thus, I am able to gain an increase in sensitivity for the morphometric analysis: in the same data formerly undetected sources can eventually be detected. I then apply the method also to H.E.S.S. sky maps. Moreover, I present an alternative approach using a less precise knowledge of the background structure, for which I show how the joint characterization by all three Minkowski functionals increases the sensitivity to detect inhomogeneities in examples where there is no excess in the total number of counts.

In conclusion, the Minkowski functionals and tensors allow for an intuitive and versatile morphometric analysis that can sensitively and comprehensively characterize the geometry of very different complex structures on nearly all length scales providing physical insight.

Zusammenfassung

Von der Großraumstruktur des Universums bis hin zu Pasta Formen in der nuklearen Materie: auf beinahe allen Längenskalen tauchen zufällige oder ungeordnete räumliche Strukturen auf; sie erscheinen in sehr unterschiedlichen physikalischen, chemischen oder biologischen Systemen und auch in der Nahrungsmittelindustrie, in der Geologie, in der Medizin, in der Astronomie oder in der Kosmologie. Ihre Erscheinung und ihre Form variieren dabei von zellulären Strukturen, zufälligen Körnerpackungen oder Punktprozessen bis hin zu Zufallsfeldern. In Systemen mit komplexer Struktur gibt es enge Beziehungen zwischen ihren physikalischen und geometrischen Eigenschaften. Einen Einblick in das physikalische Verhalten kann man oft am Besten durch eine rigorose Strukturbeschreibung gewinnen. Da Physik eine quantitative Wissenschaft ist, kann man diese Beziehungen auch nur mit Hilfe einer quantitativen Analyse der Form verstehen. Allerdings ist die Struktur von ungeordneten Systemen ein außergewöhnlich uneinheitliches Konzept. Um all diese komplexen Formen mit den selben Maßen zu beschreiben, werden fortschrittliche mathematische Methoden und Techniken benötigt. Diese sollten vielseitige, sensitive und robuste Maße zur Strukturbeschreibung sein. Dabei strebe ich sowohl nach einer rigorosen mathematischen Fundierung als auch nach Relevanz für unterschiedliche Anwendungen. Dazu verwende ich integralgeometrische Maße, die so genannten Minkowski Funktionale und Tensoren, für eine sensitive, kompakte und umfassende morphometrische Analyse, welche die Begriffe von Volumen und Oberfläche erweitern zu skalaren und tensoriellen morphometrischen Maßen.

In dieser Arbeit verwende ich diese integralgeometrischen Maße und entwickle sie fort um die Struktur dieser vielfältigen Systeme zu beschreiben in verschiedensten Längenskalen, die von nuklearer Materie über kondensierte und weiche Materie bis zur Gammaastronomie reichen. Dies schließt sowohl Simulationen als auch experimentelle Daten ein, ebenso wie analytische Rechnungen für wichtige und weit verbreitete Modelle der stochastischen Geometrie. Die betrachteten Strukturen reichen von maximal ungeordneten Konfigurationen bis zu Systemen welche spontan reguläre Strukturen bilden. Ich wende dieselben Formmaße auf all diese Systeme an um physikalische Einsichten durch eine Charakterisierung dieser komplexen Geometrien zu erlangen. Eine besondere Betonung lege ich dabei auf die Erweiterung der morphometrischen Analyse zu höheren Momenten der Strukturbeschreibung oder sogar zur vollen Wahrscheinlichkeitsverteilung, sowie auf die Anwendung auf anisotrope zufällige räumliche Strukturen. Für letztere verwende ich tensorielle Formmaße um die Anisotropie zu charakterisieren, dabei untersuche ich besonders den Informationsgehalt der Tensoren höheren Ranges.

Ich beschreibe gründlich die Anisotropie von üblichen Modellen für poröse Medien, überlappende Körner und Gaußsche Zufallsfelder. Ich vergleiche Aniso-

tropiemaße in Hinsicht auf ihre Sensitivität und zeige wie die Minkowski Tensoren die Nachteile eines weitverbreiteten Anisotropiemaßes auflösen. Explizite Formeln für die Erwartungswerte der Anisotropiemaße werden hergeleitet und mit Simulationen verglichen. Für die Minkowski Funktionale von überlappenden Körnern untersuche ich auch die Kovarianzstruktur und einen Zentralen Grenzwertsatz. Für Gaußsche Zufallsfeld wird gezeigt, dass Tensoren höheren Ranges zusätzliche Anisotropieinformationen enthalten im Vergleich zum Tensor zweiten Ranges. Allerdings ist der letztere trotzdem überraschender Weise ausreichend, um alle Parameter schätzen zu können, die notwendig sind um die Mittelwerte aller Minkowski Tensoren beliebigen Ranges zu schätzen welche die Anisotropie der Höhenlinien des Gaußschen Zufallsfeldes beschreiben. Diese Beziehung kann für einen Test auf Nicht-Gaußsches Verhalten in anisotropen Zufallsfeldern genutzt werden. Die Ergebnisse sind wichtig für Anwendungen, z.B. Parameterschätzungen, Nullhypothesentests oder um Modelle an experimentelle Daten anzupassen und sie ermöglichen auch grundlegende Einsichten, z.B. wie geometrische und topologische Größen entweder von spezifischen Systemparametern abhängen oder wann sie stattdessen universelles Verhalten aufweisen.

Die Modelle überlappender Körner mit bevorzugter Ausrichtung nutze ich anschließend um die Topologie von systemüberspannenden Clustern, sogenannten perkolierenden Clustern, zu untersuchen. Insbesondere studiere ich die Abhängigkeit ihrer Topologie von der Anisotropie des Systems. Ihre Topologie kann z.B. in Bezug gesetzt werden zu Transporteigenschaften. Die Perkolationsschwelle, d.h. der Volumenbruchteil bei dem solch ein perkolierender Cluster erscheint, hängt von der Anisotropie des Systems ab. Allerdings perkoliert interessanter Weise sogar das am stärksten anisotrope System gleichzeitig in alle Richtungen. Mit anderen Worten: die Perkolationsschwelle ist isotrop, was mit der Eindeutigkeit des perkolierenden Clusters zusammenhängt. Mit Hilfe der Minkowski Funktionale können explizite Schätzer für den Schwellwert angegeben werden.

Um sowohl die lokale als auch die globale Struktur von zellulären Systemen zu untersuchen, erweitere ich eine Analyse mit lokalen Zellcharakeristika indem ich globale Korrelationsfunktionen einführe. Für Tessellierungen, mit qualitativ ununterscheidbarer Verteilung in der lokalen Struktur, entdecke ich eine deutlich verschiedene globale Struktur, welche hier von so genannter ungeordneter extremer Gleichförmigkeit herrührt. Diese kann als ein neuer Zustand der Materie verstanden werden. Darüber hinaus zeige ich, dass die hier definierten Minkowski Korrelationsfunktionen einer üblichen Zweipunktkorrelationsfunktion überlegen sind, indem sie höhere n-Punkt Informationen enthalten, was z.B. für sensitive Hypothesentests zur Unterscheidung von Modellen der Galaxienverteilung eingesetzt werden könnte.

Sogar auf extrem kleinen Längenskalen verwende ich die Minkowski Funktionale, um simulierte exotische Zustände der nuklearen Materie, der so genannten Pasta Formen, zu charakterisieren und zu klassifizieren. Es wird angenommen, dass diese Pasta Formen z.B. in Supernovae auftreten. Interessanterweise kann unter diesen Pasta Formen ein sich spontan bildender Gyroid identifiziert werden, eine besondere Minimalfläche welche auch um viele Größenordnungen größer in der Biologie auftaucht; dies ist die Entdeckung des kleinsten Gyroids in dynamischen Simulationen, was die universellen Prinzipien der Strukturbildung veranschaulicht. Die Bindungsenergie der Pasta Materie steht anscheinend in enger Beziehung zu den Minkowski Funktionalen, aber anisotrope Deformationen, welche durch die Minkowski Tensoren quantifiziert werden, scheinen keinen Einfluss zu haben.

Schließlich verwende ich die Minkowski Funktionale für eine sensitive morphometrische Datenanalyse in der Gammaastronomie: durch die Kombination verschiedener geometrischer Maße kann mehr Information aus den selben Daten entnommen werden ohne Anfangsannahmen über mögliche Quellen. Ich verbessere die Methode, insbesondere den Ausgleich von Detektoreffekten und durch ausführliche Simulationen um die Signifikanz von strukturellen Abweichungen zu testen. Am bedeutsamsten ist, dass ich eine präzise Schätzung für die Verteilung der Hintergrundstruktur, welche durch alle Minkowski Funktionale gemeinsam beschrieben wird, für große Suchfenster ermittle. Dadurch kann ich für die morphometrische Analyse eine Steigerung der Sensitivität erreichen: ehemals unentdeckte Quellen können nun eventuell in denselben Daten nachgewiesen werden. Anschließend, wende ich diese Methode auf H.E.S.S. Himmelskarten an. Darüber hinaus stelle ich einen alternativen Zugang vor, der ein weniger genaues Wissen über die Hintergrundstruktur verwendet. Auch für diese Methode zeige ich für Beispiele ohne Überschuss in der Gesamtzahl der Ereignisse, wie die gemeinsame Charakterisierung durch alle Minkowski Funktionale die Sensitivität zum Nachweis von Inhomogenitäten steigert.

In Kürze zusammengefasst, die Minkowski Funktionale und Tensoren ermöglichen eine intuitive und vielseitige morphometrische Analyse welche sensitiv, kompakt und umfassend die Geometrie sehr verschiedener komplexer Strukturen auf fast allen Längenskalen beschreibt, was physikalische Einsichten ermöglicht.

Overview

Because of the large extent of this work, I provide in the following pages an overview of the important results and show how the same morphometric approach using Minkowski functionals and Minkowski tensors provides both geometric and physical insights to the very different systems considered here. A special emphasis of the structure characterization is put on anisotropy and higher-rank tensors as well as determining higher moments or even full probability distributions of the Minkowski functionals.

Chapter 2: Minkowski tensors of anisotropic random fields

The Minkowski functionals and tensors are used to quantify the shape, especially the anisotropy, of two important models for porous media, the Boolean model and the Gaussian random field, both in simulations and in analytic calculations. The disadvantages of the mean intercept length (MIL) tensor, for which a common approach is in general ill-defined, are resolved by the Minkowski tensors. Besides the expectations, also the variances and covariances of the Minkowski functionals are studied for differently anisotropic Boolean models as well as the universal behavior of their rescaled probability distribution. For the Gaussian random field, a relation among the tensors of different rank allows estimating all higher-rank tensors if only the second-rank tensor is known.

- A parametric orientation biased Boolean model is introduced with possible degrees of anisotropy ranging from perfect isotropy to alignment, see Fig. 2.2.

- An explicit formula of the MIL of anisotropic Boolean models with fixed grain shape is derived, see Eq. (2.19), and compared against simulations.

    - The global average of the MIL can be expressed by single grain characteristics, the volume and the size of the perpendicular projection, see Fig. 2.4 and Eq. (2.11).

    - The MIL separates in an intensity dependent and an orientation dependent factor; see Figs. 2.10 or 2.11, respectively.

    - The MIL figure of Boolean models is in general not an ellipse, see Figs. 2.3, 2.9, and 2.14 and Eq. (2.23).

    - The definition of the MIL via a fit of an ellipse is ill-defined.

- ◇ Further deficiencies of the MIL analysis are discussed, including the need for higher-rank tensors, implicit symmetry assumptions, the limitation to interfacial anisotropy, and even systems with an obviously anisotropic interface can appear perfectly isotropic w.r.t. the MIL; see Figs. 2.12 and 2.14.

- ◇ Improving the MIL analysis leads to the more general framework of the Minkowski tensors, see Eqs. (2.27)–(2.28).

- ◇ The irreducible representation of Minkowski tensors in two dimensions is discussed, and the circular Minkowski tensors are defined, see Eq. (2.30).

- ◇ Scalar anisotropy indices of arbitrary rank are defined, see Eq. (2.31).

- ◇ For the indices of second and fourth rank, explicit expressions are provided given Minkowski tensors in the Cartesian representation, see Eqs. (2.32) and (2.33).

- ◇ The Minkowski tensors in Cartesian representation can be derived from the irreducible representation, see Eq. (2.34), and for the second-rank tensor the explicit formula for the inverse problem is given in Eq. (2.35).

- ◇ It is shown how the Minkowski tensors resolve the disadvantages of the MIL analysis, see Figs. 2.14 and 2.15.

- ◇ Minkowski tensor densities are defined, see Eq. (2.36), and explicit formulas presented for general anisotropic Boolean models, see Eq. (2.39), and for the exemplary parametric Boolean models, see Eq. (2.40), expressing the global average by single grain characteristics. (For convenience and where the meaning is obvious from the context, I sometimes simplify the notation in the text and use only the terms “Minkowski functionals or tensors” when referring to their densities.)

- ◇ They are compared against numerical simulations, see Figs. 2.16–2.18, and Figs. 2.20 and 2.21 for the Euler characteristic of anisotropic Boolean models.

- ◇ Bias-free estimators of the model parameters are defined and tested in a simulation study, see Eqs. (2.44) and (2.45) and Fig. 2.19.

- ◇ The variance-covariance structure of the Minkowski functionals of the Boolean model with rectangles is estimated from simulations in finite boxes and compared to analytic formulas of the asymptotic covariances, see Eqs. (2.49)–(2.51) and Fig. 2.22. They are in excellent agreement.

- ◇ For some Boolean models with rectangles, qualitatively new behavior can be observed compared to the covariances of Minkowski functionals of overlapping discs, e.g., additional anticorrelations, see Fig. 2.22.
- ◇ In contrast to the mean values of area and perimeter which are independent of the grain shape, their variances and their covariance are nonuniversal, see Fig. 2.23.
- ◇ Empirical probability density functions of the Minkowski functionals of differently anisotropic Boolean models are already for relatively small observation windows well approximated by Gaussian distributions, see Fig. 2.24.
- ◇ Detailed simulation studies small systematic deviations of the rescaled probability distributions of the Minkowski functionals from a Gaussian distribution due to finite size effects, see Fig. 2.25.
- ◇ At small intensities, these rescaled probability distributions of the Minkowski functionals for different Boolean models still collapse within error bars to the rescaled probability distribution of the number of grains hitting the observation window, see Fig. 2.25.
- ◇ For a comparison of the empirical cumulative distribution functions to analytic bounds, see Eq. (2.52) and Figs. 2.26 and 2.27.
- ◇ An outlook to Minkowski maps of inhomogeneous Boolean models is presented, see Fig. 2.28.
- ◇ For homogeneous random fields, the volume Minkowski tensors $W_0^{a,0}$ do not contain additional geometrical information compared to the volume fraction, see Eq. (2.54).
- ◇ For sufficiently smooth, homogeneous random fields, the global average of the translation invariant Minkowski tensors can be expressed by a local average, see Eq. (2.56).
- ◇ The density of the first order Minkowski functional for level sets of differently anisotropic Gaussian random fields change by a prefactor, see Eq. (2.62) and Fig. 2.30.
- ◇ The normal vector on the excursion set is antiparallel to the gradient, see Eq. (2.63).
- ◇ For (sufficiently smooth) Gaussian random fields, the interfacial Minkowski tensor densities of odd rank vanish on average, see Eq. (2.65).

- ◇ Integral formulas are given for the interfacial Minkowski tensor densities of arbitrary rank of level sets of (sufficiently smooth) Gaussian random fields in arbitrary dimension, see Eq. (2.66).
- ◇ Explicit formulas are given for the second and fourth rank tensors in two dimensions, see Eqs. (2.67) and (2.68) and Fig. 2.31.
- ◇ Scalar anisotropy indices independent of the threshold, e.g., see Eq. (2.69), are compared; the higher-rank tensors contain for Gaussian random fields nonredundant anisotropy information, see Fig. 2.32.
- ◇ The global average of the extended Gaussian image of a homogeneous random field can be expressed by a local average, see Eq. (2.70).
- ◇ An explicit formula for the extended Gaussian image density of level sets of homogeneous Gaussian random fields in arbitrary dimensions is given in Eq. (2.71), see Fig. 2.33, which contains the information of all interfacial Minkowski tensor densities, see Eq. (2.72).
- ◇ The extended Gaussian image density does not depend on the complete covariance function of the Gaussian random field, but only on the covariance matrix of the gradient at the origin, see Eq. (2.71).
- ◇ Therefore, the extended Gaussian image density can robustly and accurately be estimated based on the second-rank tensor density alone, see Figs. 2.33 and 2.34.
- ◇ Higher-rank tensors contain additional information, but they can nevertheless be determined for a homogeneous Gaussian random field from the second-rank tensor alone. This could be used for a test of non-Gaussianities in anisotropic random fields, see page 104.
- ◇ An extension of the Minkowski tensors to gray-scale images are defined, see Eq. (2.77) and (2.78).
- ◇ They are calculated for a blurred rectangle, for which the anisotropy is accurately estimated, see Fig. 2.35 and Eq. (2.79).

Chapter 3: Anisotropic continuum percolation

The Minkowski functionals, especially the Euler characteristic, are used to study anisotropic continuum percolation, which is connected to transport properties. For isotropic Boolean models, a universal scaling of the topology of the percolation

cluster is studied. For anisotropic Boolean models, the isotropy of the percolation threshold is discussed as well as how the value depends on the anisotropy of the system. Explicit approximations and bounds are discussed and compared to simulation results.

- ◇ A universal scaling of the Euler characteristic of the percolating void cluster, see Fig. 3.1, is investigated in simulations, see Fig. 3.2.
- ◇ Percolation in finite samples of anisotropic Boolean models is studied in simulations by determining the connectivity, which is found to be different in x- or y-direction, see Fig. 3.4.
- ◇ Effective percolation thresholds are defined via fitting an error function to the connectivity, see Eqs. (3.1) and (3.2).
- ◇ The finite size scaling of the effective percolation thresholds is considered separately in x- and y-direction, see Eq. (3.3).
- ◇ They are extrapolated to an infinite systems size, see Fig.3.6, where they are found to be isotropic within statistical significance, see Table 3.1.
- ◇ The isotropy of the percolation threshold can be explained by the uniqueness of the percolating cluster, see Fig. 3.5.
- ◇ The isotropic percolation thresholds are estimated for differently anisotropic Boolean models by a simultaneous fit of the finite size scaling in x- and y-direction, see Eqs. (3.4)–(3.5), Table 3.1, and Fig. 3.7.
- ◇ Explicit formulas for different approximations of the percolation threshold are discussed and compared to the simulation results.
  - ○ Using the percolation thresholds of squares with different orientation distributions as empirical parameters, the excluded area approximation is in relatively good agreement with the percolation thresholds of the rectangles, see Fig. 3.9.
  - ○ For these Boolean models with rectangles, the excluded area approximation seems to be an upper bound if the empirical parameters of overlapping squares following the same orientation distribution are used, see Fig. 3.9.
  - ○ The zero of the Euler characteristic as a function of the intensity is for the Boolean models studied here empirically confirmed to serve as a simple and explicit lower bound on the percolation threshold without using any empirical parameters, see Fig. 3.10.

- For the models studied here, this geometrical approach accurately approximates the dependence of the critical intensity on the aspect ratio, i.e., the difference of the critical intensity of a rectangle compared to that of a square with the same orientation distribution, see Fig. 3.11.
- The extremum points of the asymptotic variances and covariances of the Minkowski functionals are compared to the critical intensities for four differently anisotropic Boolean models with rectangles, see Figs. 3.12 and 3.13.
- Some extremum points are in surprisingly good agreement, e.g., the minimum point of the covariance of area and Euler characteristic is suggested as a candidate for an approximation of the critical intensity without using any empirical parameters, see Figs. 3.12 and 3.13.

Chapter 4: Minkowski correlation functions of random tessellations

The Minkowski functionals and Minkowski correlation functions characterize the structure of point processes and corresponding tessellations. While the probability distributions of the local shape measures are qualitatively similar for physically very different processes, the here defined Minkowski correlation and probability distribution functions quantify the global structural difference, coming from the different state of matter, the hyperuniformity. Also, the Minkowski correlation functions can distinguish point processes with identical pair-correlation functions.

- Local distributions, i.e., empirical probability density functions of Minkowski functionals of single cells, are determined for the Poisson point process, an equilibrium hard-sphere liquid, and for maximally random jammed (MRJ) sphere packings, see Table 4.1 and Figs. 4.2 and 4.3.
- Local distributions are qualitatively similar for distinctly different processes, see Fig. 4.2.
- Small but significant deviations from a generalized gamma distribution are found for the jammed sphere packings, see page 150.
- Joint distributions of Minkowski functionals are determined, see Table 4.1 and Fig. 4.3.
- A map of anisotropy is created for a variety of tessellations and particle processes, see Fig. 4.4.
- Global correlation functions of Minkowski functionals, see Eq. (4.2), and cell-cell probability density functions, see Eq. (4.3), are defined.

- They are analytically calculated for a one-dimensional Poisson point process, see Eqs. (4.7) and (4.8) and Fig. 4.5.

- They are numerically determined for the three-dimensional Poisson point process, see Fig. 4.6, the equilibrium hard-sphere liquid, see Fig. 4.7(a), and the MRJ sphere packing, see Fig. 4.7(b).

- In contrast to the local distributions, the global distributions distinctly quantify the structural difference between these processes, especially revealing strong anticorrelations in the hyperuniform MRJ packings.

- The cell-cell probability distributions allow for a detailed global structure characterization, see Figs. 4.14–4.15.

- The Minkowski correlation functions contain visibly more information than the standard two-point correlation function because Minkowski functionals contain multipoint information.

    - A two-dimensional line-segment process modeling the distribution of galaxies is simulated as well as a Gauss-Poisson process, see Fig. 4.16.
    - For both point processes, the Voronoi diagrams are constructed, see Fig. 4.16.
    - While they have the same pair correlation function, see Eq. (4.14), their Minkowski correlation functions are distinctly different, see Fig. 4.17.
    - Also the empirical distribution functions of the Minkowski functionals of a single cell exhibit slight, but statistically significant deviations, see Fig. 4.18.

- Mixed correlation functions, which correlate different Minkowski functionals, are defined, see Eq. (4.9).

- They approximately agree very well with the arithmetic average of the single Minkowski functional correlation functions, see Eq. (4.10) and Figs. 4.8–4.10.

- This approximation corresponds to a nearly vanishing correlation of the difference of rescaled Minkowski functionals, see Eq. (4.12) Fig. 4.11.

- The surface area-surface area correlation function $C_{11}(r)$ is approximately equal to the volume-integrated mean curvature correlation function $C_{02}(r)$, see Fig. 4.13.

Chapter 5: Shape indices for nuclear matter

The Minkowski functionals and tensors accurately characterize the shape of exotic states of nuclear matter, the "nuclear pasta", which is simulated by collaborators from the University of Frankfurt. The distribution of the Euler characteristics reveals a great variety of spontaneously emerging random labyrinths at these small length scales. We find a structure already known from soft-matter systems at the nanometer scale, the gyroid. As a first step to understand the connection between geometry and physics, the binding energies are found to mainly depend on the scalar Minkowski functionals, i.e., volume, surface area, and curvature, but it is rather independent of deformations detected by the Minkowski tensors.

- ◇ Minkowski functionals and tensors characterize the structure of the spontaneously emerging pasta shapes, see Fig. 5.2.
    - ○ Structural relationships are established between pasta shapes and their complementary bubble states.
    - ○ Strong distortions and fluctuations are found, e.g., Minkowski tensors detect strong anisotropies, but the preferred orientation is random.
    - ○ The coexistence of pasta shapes is detected by the Minkowski functionals as a function of the threshold, see Fig. 5.2(c).
- ◇ The proton and neutron densities are equivalently distributed, see page 191.
- ◇ Unique identification and classification of pasta shapes (in small simulation boxes) is possible using only the signs of integrated mean curvature and of the Euler characteristic, see Fig. 5.4 and Table 5.1.
- ◇ Static calculations find isomeric gyroid and primitive pasta structures, see Fig. 5.6.
- ◇ The Minkowski functionals of pasta shapes and primitive and gyroid surfaces of constant mean curvature are compared and found to be in good agreement, see Tables 5.2 and 5.3, but deformations are detected by Minkowski tensors.
- ◇ Spontaneously emerging random labyrinthine pasta shapes are discussed, see Fig. 5.8.
- ◇ Distribution of the topology of these networks is quantified by the Euler characteristic, see Fig. 5.9.
- ◇ Discovery of the smallest reported gyroid found in dynamical simulations: spontaneously forming gyroidal pasta shapes are identified, see Fig. 5.10.

- ◇ Minkowski functionals and tensors characterize the shape of gyroid and primitive structures, see Fig. 5.11.
- ◇ Strong deformations and anisotropies are detected, but with a random preferred orientation, see Fig. 5.11(c).
- ◇ Cooled gyroids get even more anisotropic, but the scalar Minkowski functionals converge to those of the static calculations, which implies that energies depend primarily on the Minkowski functionals and is rather insensitive to deformations, see page 203.

Chapter 6: Minkowski sky maps in gamma-ray astronomy

The Minkowski functionals quantify the structure of gamma-ray sky maps. They allow for source detection including additional geometrical information without any prior knowledge about the source. Accurate estimates of the joint probability distribution of the Minkowski functionals are derived. By such a refined structure characterization formerly undetected sources can be detected.

- ◇ A refined morphometric analysis is presented.
  - ◦ The gamma-ray count maps are thresholded, and the structure of the black and white images are quantified by the Minkowski functionals as a function of the threshold, see Fig. 6.1.
  - ◦ A look-up table allows for a fast computation of the Minkowski functionals, see Table 6.1.
  - ◦ Different boundary conditions are discussed, see page 212.
  - ◦ The global null hypothesis test is defined based on the distribution of Minkowski functionals, see Fig. 6.2, from which the compatibility with the background structure follows, see Eq. (6.2).
  - ◦ The deviation strength, see Eq. 6.3, quantifies the significance of a structural deviation for each threshold, see Fig. 6.3.
  - ◦ Local structure deviations are detected by the Minkowski sky maps, i.e., by restricting the global null hypothesis test to a scan window, see Fig. 6.4 and Fig. 6.5 for an exemplary application to a simulated test pattern.
- ◇ Applying a marching square algorithm instead of using a pixelated black and white image is shown to have no measurable effect for small scan window sizes, see Fig. 6.6.

- ◇ A trial correction due to the repeated null hypothesis tests at different thresholds is derived.
  - ○ Assuming independent trials with the number of trials equal to the number of thresholds provides a conservative estimate, see Eq. (6.4), which is shown to be close, see Fig. 6.7(a), even for a constant upper bound on the number of thresholds, see Fig. 6.7(b).
  - ○ The difference between the trial factors for simple (only area A) or joint (area A , perimeter P, and Euler characteristic χ) structure characterization is found to be negligible, see Fig. 6.8.
- ◇ A local detector acceptance correction is introduced (see Fig. 6.9 for an exemplary spatially varying detector acceptance) which significantly reduces the suppression of source signals and can thus allow for a huge increase in sensitivity for the detection of sources distributed over the whole sky map, see Fig. 6.10.
- ◇ An accurate estimate of the joint probability distribution of all Minkowski functionals is derived for large scan windows, extending the analysis from 7×7 to 15×15 observation windows, i.e., from $5.6 \cdot 10^{14}$ to $5.4 \cdot 10^{67}$ total number of possible b/w images.
  - ○ The density of states (DoS) must be determined, i.e., the number of configurations with a given macrostate, i.e., area A, perimeter P, and Euler characteristic χ, see Eq. (6.5).
  - ○ Reliable estimates for both macrostates with a DoS $O(10^{64})$ or $O(1)$ are achieved by combining the Wang-Landau algorithm with analytic knowledge of the number of states with a given area, see page 231.
    1. The configuration space is reduced (up to two orders of magnitude smaller number of macrostates), and the algorithm converges much faster.
    2. Less memory is needed allowing for optimizations that decrease the computation time by at least one order of magnitude.
    3. A parallelization is possible for different areas A.
    4. The probability distribution is perfectly normalized, see Eq. (6.6).
    5. For either small or larger values of the area A, the DoS can be determined analytically.
  - ○ The reliability of the estimates is tested by saturation of error analyses, see Fig. 6.11.

- The relative statistical error of the DoS estimates is $O(10^{-3})$, the relative error of the deviation strength is even some orders of magnitude smaller, see page 6.5.2.
- Four-dimensional plots of the DoS of area, perimeter, and Euler characteristic visualize the complex distribution and reveal bounds on the possible values of the Minkowski functionals; it seems to converge quickly for large scan windows, which would allow for accurate estimates of extremely large observation windows, see Fig. 6.12.

◇ An increase in sensitivity of the morphometric analysis via this joint structure characterization for large scan windows is confirmed.

- For a simulated test pattern consisting of differently strong and differently large sources, sources which lead to no significant fluctuations in the simple deviation strength are detected by the joint deviation strength, which is shown both for a single count map and for averages over many simulations, see Fig. 6.13.
- In a systematic analysis, the simple and joint deviation strengths of differently shaped sources are compared, see Fig. 6.14.
  1. For a point source within a single pixel, they are identical because there is no complex structure to be quantified.
  2. For a constant offset, the joint deviation strength slightly favors more the null hypothesis than the simple deviation strength, because the additional structural information is in agreement with the background structure.
  3. For a Gaussian shaped source, the joint distribution leads to a huge increase in sensitivity because it takes more information out of the same data.
- This heuristic explanation is confirmed in a detailed discussion of the probability distributions and the compatibility w.r.t. either only A or both A and P, see Fig. 6.15.

◇ The deviation strengths of different thresholds are combined in an alternative test statistic, see Eq. (6.8).

- Instead of the maximum of the deviation strength, the sum of the deviation strengths over all thresholds is used, see Eq. (6.7).
- The empirical complementary cumulative distribution function is determined, see Fig. 6.16.

  - Figure 6.18 demonstrates the increase in sensitivity for diffuse radiation or extended sources.

◇ The morphometric analysis is then compared to a standard null hypothesis test in gamma-ray astronomy.

  - The morphometric analysis follows a completely different ansatz and a comparison of the two methods depends both on the shape of the source and on the experimental details, like the binning or the accuracy of the estimate of the background intensity.
  - The morphometric analysis depends less on the size of the scan window and can detect both rather extended and pointlike sources using the same scan window size, compare Figs. 6.13 and 6.19.
  - As an example, a source like a dotted pattern is simulated where only low statistics are available. The morphometric analysis is for the vast majority of samples more sensitive than the counting method for all scan window sizes; even if there is no significant excess in the total number of counts, the source can still be detected because of the additional structural information, see Fig. 6.20.

◇ The morphometric analysis is applied to real data from the H.E.S.S. experiment

  - First, to the supernova remnant RX J1713.7−3946, see Fig. 6.21.
  - To demonstrate the detection of very weak sources, the statistics is artificially reduced by postselection and Monte Carlo observations, see Fig. 6.22, which demonstrates the increase in sensitivity of the morphometric analysis by the improvements of this thesis.
  - Similarly, the extended region of gamma-ray emission in the galactic center ridge is analyzed, and for the artificially reduced statistics, a strong increase in sensitivity is demonstrated, see Fig. 6.23.

◇ The variance-covariance structure of the Minkowski functionals is calculated analytically and compared against simulation results, see Eqs. (6.12)–(6.13) and Fig. 6.24.

◇ The deviation of the Minkowski functionals from their mean values weighted by the covariances are defined as new test statistics, see Eqs. (6.14) and (6.15).

- ◇ Their empirical cumulative distribution function is determined, see Fig. 6.25 and Eqs. (6.16) and (6.17), and a new null hypothesis test is defined, see Eq. (6.18).
- ◇ The joint characterization by all three Minkowski functionals increases the sensitivity to detect inhomogeneities in cases where there is no excess of the total number of counts, see Fig. 6.26 and Table 6.2.

Publications

Parts of this work are direct quotes from joint publications:

G. E. Schröder-Turk, W. Mickel, S. C. Kapfer, M. A. Klatt, F. M. Schaller, M. J. F. Hoffmann, N. Kleppmann, P. Armstrong, A. Inayat, D. Hug, M. Reichelsdorfer, W. Peukert, W. Schwieger, and K. Mecke. Minkowski Tensor Shape Analysis of Cellular, Granular and Porous Structures. *Adv. Mater.*, 23(22–23):2535, 2011

M. A. Klatt, D. Göring, C. Stegmann, and K. Mecke. Shape analysis of counts maps. *AIP Conf. Proc.*, 1505(1):737, 2012

B. Schuetrumpf, M. A. Klatt, K. Iida, J. A. Maruhn, K. Mecke, and P.-G. Reinhard. Time-Dependent Hartree-Fock Approach to Nuclear Pasta at Finite Temperature. *J. Phys.: Conf. Ser.*, 426(1):012009, 2013

B. Schuetrumpf, M. A. Klatt, K. Iida, J. Maruhn, K. Mecke, and P.-G. Reinhard. Time-dependent Hartree-Fock approach to nuclear "pasta" at finite temperature. *Phys. Rev. C*, 87:055805, 2013

D. Göring, M. A. Klatt, C. Stegmann, and K. Mecke. Morphometric analysis in gamma-ray astronomy using Minkowski functionals. *Astron. Astrophys.*, 555:A38, 2013

M. A. Klatt, T. Ichikawa, K. Iida, N. Itagaki, J. A. Maruhn, K. Matsuyanagi, K. Mecke, S. Ohkubo, P.-G. Reinhard, and B. Schuetrumpf. Exotic cluster structures in the mean-field theory. *J. Phys.: Conf. Ser.*, 445(1):012036, 2013

J. Hörrmann, D. Hug, M. A. Klatt, and K. Mecke. Minkowski tensor density formulas for Boolean models. *Adv. Appl. Math.*, 55(0): 48, 2014

B. Schuetrumpf, M. A. Klatt, K. Iida, G. E. Schröder-Turk, J. A. Maruhn, K. Mecke, and P.-G. Reinhard. Minimal surfaces in nuclear pasta with the time-dependent Hartree-Fock approach. *Proceedings of Science*, Bormio2014:032, 2014

M. A. Klatt and S. Torquato. Characterization of maximally random jammed sphere packings: Voronoi correlation functions. *Phys. Rev. E*, 90:052120, 2014

B. Schuetrumpf, M. A. Klatt, K. Iida, G. E. Schröder-Turk, J. A. Maruhn, K. Mecke, and P.-G. Reinhard. Appearance of the single gyroid network phase in "nuclear pasta" matter. *Phys. Rev. C*, 91: 025801, 2015

Contents

Chapter 1

Random spatial structures

Random and disordered spatial structures occur ubiquitously in nature and on nearly all length scales ranging from particle physics to cosmology. Figure 1.1 illustrates some of this variety showing disordered spatial systems from nuclear matter to the large-scale structure of the universe: the cosmic microwave background, the large-scale structure of the universe, a galaxy cluster, geostatistical data from a reservoir of natural gas, foam, trabecular bone, porous structure in food influencing its taste, heterogeneous and composite materials, cell packings, atom clusters at temperatures above the melting point, and labyrinthine nuclear matter. There are complex structures at even smaller length scales, e.g., the topological charge density in lattice quantum chromodynamics simulations which has features smaller than 1 fm [87].

Because of the ubiquity of such random or disordered structures on nearly all length-scales, a morphological analysis can be beneficial for very different fields as demonstrated by numerous morphological studies in physics [305, 307, 408, 460], chemistry [184, 185, 247], biology [54, 61, 224], engineering [124, 134, 256, 392], material sciences [179, 449, 483, 519], geology [241, 344, 345], medicine [75, 257, 347, 350], astronomy [5], cosmology [4, 67, 363], or in food industry [11, 117, 133, 517].

Understanding physics by understanding geometry Obviously not all physical systems are dominated by geometry. However, in systems with complex structure, there is a close interconnection of physics and geometry, and physical insight is often best achieved by a rigorous characterization of the structure; for example, to understand the principles of structure formation where the intricate structure results from physical processes [213, 356, 361, 420], or when the physical principles are of geometric nature, e.g., packing problems that can exhibit inter-

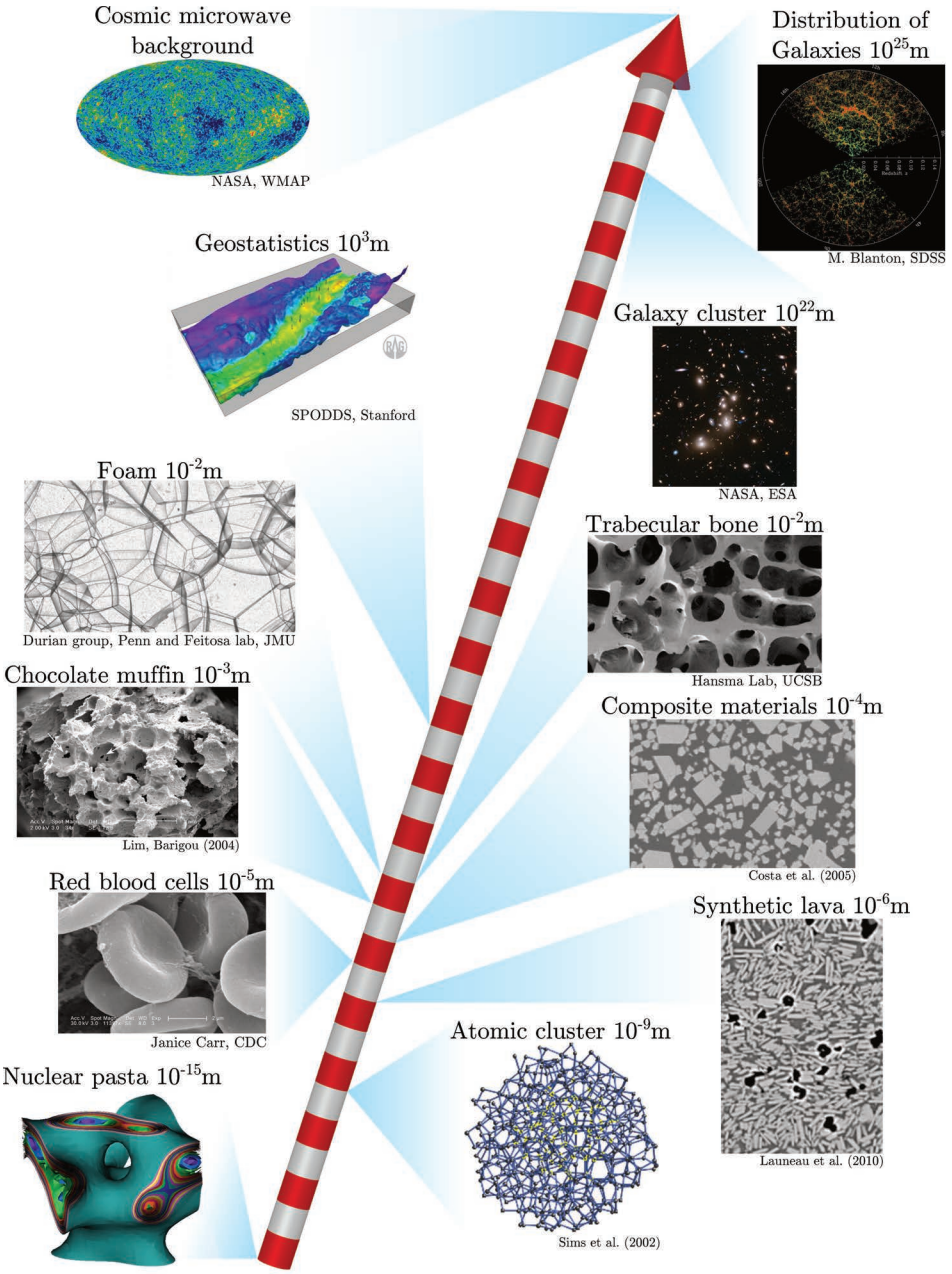

Figure 1.1: From exotic states in nuclear matter to the large-scale structure of the universe: random and disordered spatial structures appear ubiquitously on nearly all length scales in very different physical, chemical, or biological systems as well as in food industry, geology, medicine, astronomy or cosmology. For the image sources, see Ref. [2].

esting phase transitions [181, 182, 197, 382]. The physical properties of systems with complex spatial structure can dramatically differ from those of the bulk material; examples where the geometry of the microstructure dominates the physical properties are anomalous transport in porous materials close to the percolation threshold [439], optimization of composite materials [66, 389], or photonic crystals in butterfly wing scales [495]. The physics of these systems cannot be understood without understanding the geometry, and an analysis of the geometry can provide fundamental insights independent of the specific physical, chemical, or biological details [132]. Therefore, a "quantitative morphology", here called morphometry, is an essential step for physical investigation.

A prominent example, where geometric investigation holds the key to understanding a physical process, are the thermal fluctuations in the cosmic microwave background, which is thermal radiation emitted "shortly" after the Big Bang and the oldest light in our universe. In the model of inflation [363], quantum fluctuations during the inflation of the universe would lead to a description of the thermal fluctuations by a Gaussian random field, i.e., a random function for which the functional values are Gaussian distributed[1] and which is uniquely characterized by its mean value and its covariance function [486]. Therefore, the geometric investigation of the existence of non-Gaussian features provides a test of this hypothesis and could possibly discriminate different cosmological models [55, 170] and even imply new physics beyond the standard model. Therefore, there is very active research on whether these fluctuations exhibit non-Gaussianity or not [130, 491, 494].

Another example from medicine is the diagnosis of osteoporosis, which is one of the most common bone diseases. The trabecular, or spongy, bone structure inside human bones is a complex filamentous network [107], see Fig. 1.2(a). It leads to a flexible yet strong bone. Because the bone experiences a preferred mechanical load direction, the trabecular bone is anisotropic. The elasticity and the tensile strength strongly depends on the microstructure. However, osteoporosis causes not only a loss of bone material but also a deterioration of the microarchitecture; see Fig. 1.2(b). Its anisotropy changes due to the disease. Sensitive anisotropy indices, which capture and quantify these structural changes, are therefore needed for a refined diagnosis of osteoporosis [125]. The aim is an improved fracture risk evaluation via an in-vivo study of the trabecular bone structure [487].

The microstructure of random heterogeneous materials has a length scale much smaller than the size of the macroscopic sample, but much larger than the molecular dimensions. Materials consisting of mainly the same chemical compounds can have completely different physical properties because of a different microstructure,

[1] Even each collection of functional values at different positions are multivariate Gaussian distributed.

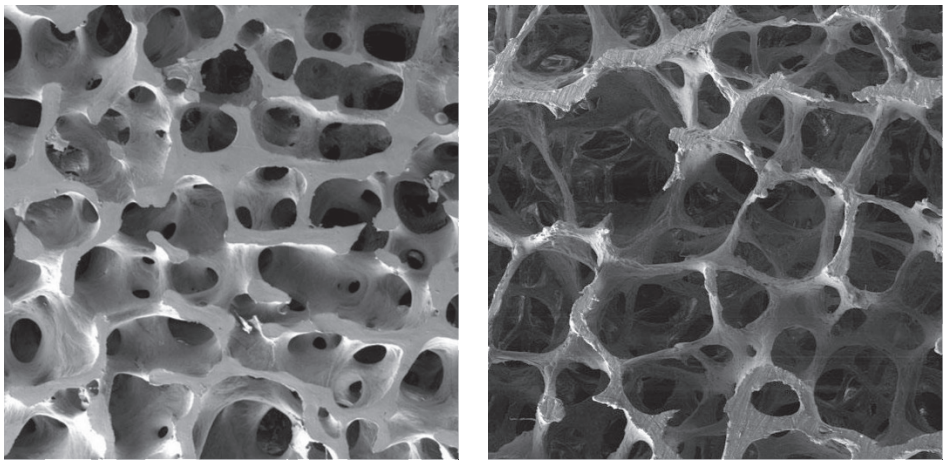

(a) (b)

Figure 1.2: Scanning electron microscopy image of trabecular bone (a) of a young male human bone and (b) of an elderly bone of a woman suffering from osteoporosis. Image courtesy of Hansma lab, USCB [183].

for example, depending on whether or not the pore-space is connected and spanning the whole system. A central aim of material science is to have exquisite knowledge of structure/property relations, e.g., predicting mechanical properties from the microstructure of a heterogeneous materials [459, 460], in order to design materials with the desired properties [258, 330, 427]. A characterization of the microstructure allows to derive rigorous bounds on the effective physical properties [458], e.g., for the mechanical, thermal, or electric properties or the permeability [378, 464]. Understanding the flow through a porous medium (see Fig. 1.3) is, e.g., of utmost importance for the oil industry [393]. This problem is linked to the question whether or not there is a connected path spanning the whole medium, whether the liquid can flow through the porous medium [211, 212]. Percolation theory discusses the interesting finding that in many models and materials such a connected path appears almost sure at a fixed volume fraction of the pore space, the so-called percolation threshold [24, 165, 313]. Another prominent example is that for particle ensembles with pairwise additive central forces, e.g., an equilibrium hard-sphere liquid. The latter is a many-body system in thermal equilibrium that consists of non-overlapping spheres. Although there are no other interactions besides the hard-core repulsion, an equilibrium hard-sphere liquid can exhibit a surprisingly complex behavior [460]. For such systems, the pair-correlation function $g_2(r)$ can be related to thermodynamic properties, like the pressure [180, 460].

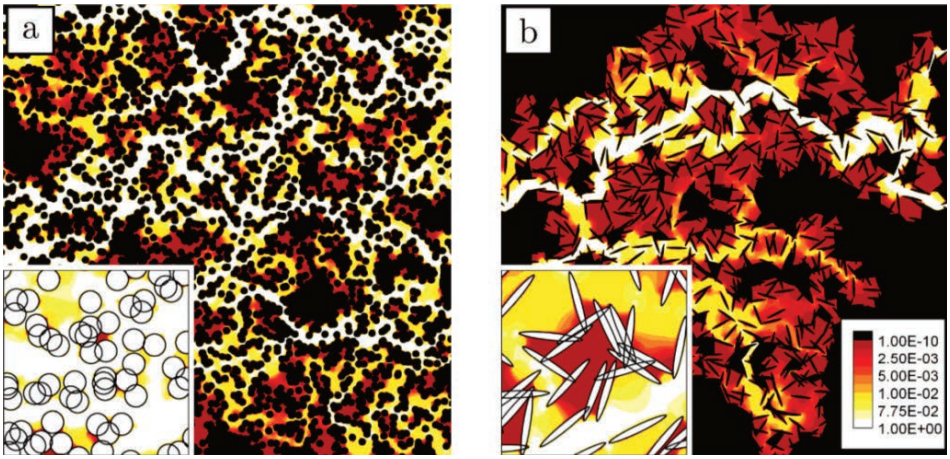

Figure 1.3: Laminar flow through a porous medium: the color plots show simulated velocity fields in the pore space of either overlapping (a) spheres or (b) overlapping ellipses, the unit is $\mu m/s$; the permeability can be related to the geometry and topology of the disordered structure [58, 402, 460]. Image reproduced from Ref. [402], copyright by the American Physical Society.

A detailed understanding of the geometry and the physical properties of complex spatial structures allows to design new materials to solve technical problems. Complex periodic nanostructures can, e.g., be used for modern optical devices, e.g., a chiral beamsplitter [479]. Sometimes random media can be advantageous to regular structures even in man-made materials for applications. For example, in contrast to periodic or quasiperiodic solids, disordered materials can be isotropic. Thus, they can allow for complete band gaps that block all directions [142, 286] as well as cavities and waveguide architectures unattainable in photonic crystals [143]. Therefore, a thorough understanding of a hidden long-range order is needed, the so-called hyperuniformity: although disordered like a fluid at short length scales, the material is homogeneous like a crystal on large length scales [467].

The randomness in physical systems can arise for purely statistical reasons like in many porous materials or in dry foam[2], or because of geometrical constraints which inhibit a crystal arrangement [224], or it corresponds to very fundamental questions about inherent randomness, e.g., in the cosmic microwave background [363].

Shape descriptors and quantitative image analysis Modern imaging techniques, like confocal microscopy [357], electron or X-ray tomography [206], or high-resolution magnetic resonance imaging [86], can resolve fine structural

[2] Foam in the limit of vanishing liquid content.

details and call for sensitive real space measures of shape, which capture complex features hidden to the naked eye. For a diagnosis based on high resolution magnetic resonance imaging often a quantitative image analysis is needed, e.g., for statistical hypothesis tests [93, 257] or to predict physical properties [75, 497], like the elasticity, by a characterization of the complex microstructure [74, 426].

While crystallography provides a thorough description of crystalline phases, e.g., see Ref. [163], a complete characterization of disordered shapes remains elusive, mainly because of the extreme variety of physical systems and the types of random or disordered structures. For a specific system, the physically most relevant shape descriptors depend both on which system and which property is considered. For example, thermodynamic properties such as the pressure of particle ensembles with pairwise additive central forces can, as mentioned above, explicitly be related to the pair-correlation function g_2 [180, 460]. However, in many cases such a supporting theory and thus the physically relevant shape index is not known. Then, a shape descriptors should unfold the essential geometrical information; therefore, efficient and accurate structure characteristics are needed to quantify the shape and capture the important structural features.

Often, the two-point correlation function is applied to systems not because it is physically justified, but mainly because it is a well-understood shape descriptor; it is related to the structure factor, and it was thus accessible via scattering experiments even before high resolution real space images became available. However, the two-point correlation function contains, e.g., only limited information of connectedness [460], and a generalization to multipoint correlation functions is computationally very expensive [289, 325, 525]. Alternative versatile morphometric methods based on comprehensive shape descriptors are needed.

So far, many solutions are explicitly designed for specific systems or specific geometrical features [232], like the mean intercept length [186, 483, 512], star-volumes [240, 347, 492], bond-orientational order parameters [444], or wavelet analyses [473, 498]; for example, the mean intercept length (MIL) tensor, which is a common measure of the anisotropy of trabecular bone [512], is restricted to interfacial anisotropy [347].

To better understand the influence of structure on such a variety of physical systems and to find the structural connection between seemingly unrelated concepts, a more versatile morphometric analysis is needed, i.e., a more general and systematic approach to shape characterization with both solid mathematical foundation and relevance to the application. The examples in Figure 1.1 are not only very different w.r.t. their physical properties, but also the "types" of disordered structures exhibit a remarkable variety: the temperature fluctuations in the cosmic microwave background can be described by a continuous field, the large-scale structure of

the universe can be modeled by single points, the foam is a cellular structure, the trabecular bone is a network, the composite material consists of overlapping grains, and the red cells form packings of extended particles. Because the structure of disordered systems is such a remarkably incoherent and far-reaching concept, advanced mathematical tools are needed to both model and characterize these complex shapes. They must be sensitive and robust measures of structure which can effectively be applied to all of the systems mentioned above.

Minkowski functionals and stochastic geometry How to comprehensively measure the shape of a disordered material? An intuitive approach is to follow the law of parsimony and start with simple and fundamental shape measures. Can an intuitive extension of these measures allow for a comprehensive and probably even complete structure characterization? Given some spatial structure, we can describe its geometry very simply by its volume or surface area. If these integrals over the volume or surface are slightly extended by introducing local weights, other shape measures can be derived, e.g., the mean width of a convex domain or a topological index. The so-called Minkowski functionals[3] and Minkowski tensors[4] from integral geometry are such intuitive geometric functionals that extend the notion of volume and surface area to scalar and tensorial morphometric measures [303, 396, 400, 408]. In d dimensions, there are $d + 1$ Minkowski functionals, and corresponding to each functional Minkowski tensors of arbitrary rank can be defined. Surprisingly, it turns out that they allow under certain conditions a complete characterization of additive geometrical properties: the Minkowski functionals for scalar [172–174] and the Minkowski tensors for tensorial properties [27, 28], see also Refs. [242, 400].

The Minkowski functionals and tensors are robust, versatile, and sensitive shape measures that, e.g., quantify both connectivity and shape, in other words, topology and geometry. They are efficient numerical tools and they have already been successfully applied to a variety of biological [54, 61] and physical systems [305, 307] on all length scales from nuclear physics [413, 416], over condensed and soft matter [181, 234, 516], to cosmology [104, 127, 151, 238, 399] as well as to pattern analysis [59, 288, 304]. In contrast to the ad-hoc solutions, the Minkowski tensors allow for a comprehensive[5] and systematic approach to quantify various aspects of structural anisotropy [408]. In two dimensions, the Minkowski functionals of a

[3] Other names are valuations, quermaßintegrals, intrinsic volumes, or Hadwiger measures.

[4] The Minkowski tensors are also called tensor valuations.

[5] As indicated above, they provide a complete characterization of additive structural properties: they span the space of all translational covariant, conditional continuous, and additive measures of convex bodies [27, 28].

compact body K correspond to its area, its perimeter, and its Euler characteristic[6]. In three dimensions, the Minkowski functionals correspond to the volume, the surface area, the integrated mean curvature[7], and the Euler characteristic[8].

The disordered systems exhibit both interesting geometrical and statistical properties. Stochastic geometry combines these concepts. It studies random spatial patterns [400, 448]. It introduces random measures and also models that can accurately approximate the variety of real physical systems. The diversity of these models is indicated in Fig. 1.4, which shows a packing of hard spheres, overlapping cuboids, two different cellular tessellations of space, a point process, and a continuous random field.

For such diverse systems in nature and models in mathematics, the natural question arises: is there a universal approach to structure characterization in the sense that it sensitively extracts morphometric information and indeed provides new insights to all of these systems? This thesis sets out to investigate the usefulness of using the Minkowski functionals and tensors from integral geometry and the concepts from stochastic geometry as such a versatile approach. I improve or define new shape descriptors and evaluate them both analytically and numerically for important models and apply them to a variety of physical systems. This work aims for both a rigorous mathematical foundation and the application to physical systems (both in simulation and in experiment), spanning from mathematics to theoretical and experimental physics as well as from nuclear physics over soft matter to gamma-ray astronomy.

Random spatial structures in physics The aim is to model and characterize random or disordered spatial structures in physics. Therefore, new mathematical concepts are introduced, developed, and applied to interesting physical problems; thus, this approach should be both beneficial for mathematics and physics. The Minkowski functionals and tensors as versatile shape descriptors characterize the structure of very different systems. Thus, this thesis in particular shows

[6] The Euler characteristic is a topological constant. For a compact domain K in two dimensions, it can be expressed by the number of components minus the number of holes. It can be defined for sufficiently smooth bodies by a surface integral over the curvature, the Gauss-Bonnet theorem relates the geometry of compact manifolds to their topology.

[7] The integrated mean curvature of a domain K is the integral over its surface weighted by the arithmetic mean of the principle curvatures. It vanishes trivially for a flat surface with no curvature at all, but also for a minimal surface where the two principle curvatures at every point have the same absolute value but opposite signs. For a convex body K, it is also proportional to the mean width, i.e., the mean distance between two parallel planes touching K [400].

[8] In three dimensions, the Euler characteristic of a compact domain K can be expressed by the number of components minus the number of rings plus the number of cavities, respectively (the so-called Betti-numbers).

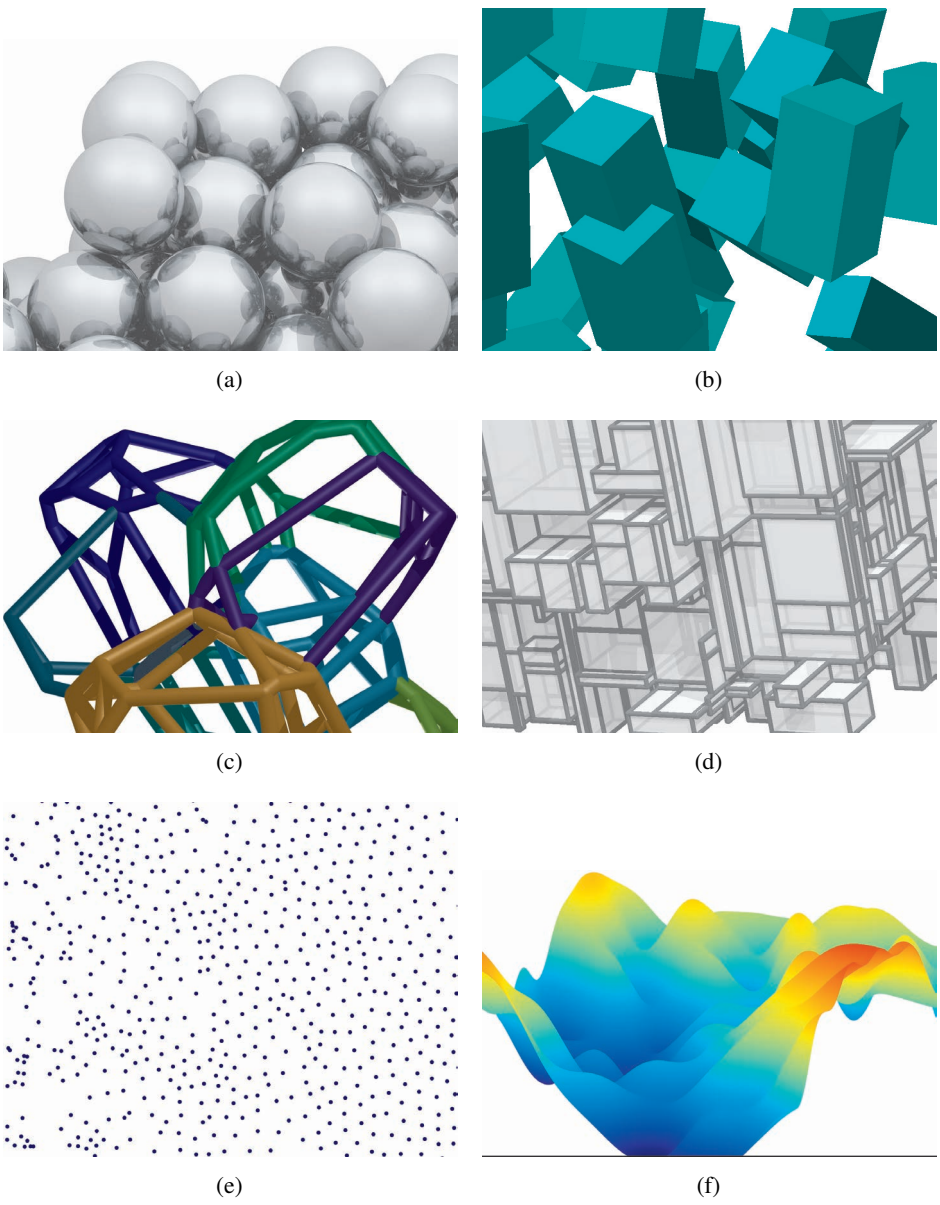

(a) (b)

(c) (d)

(e) (f)

Figure 1.4: A collection of models from stochastic geometry: (a) a packing of hard spheres; (b) Boolean model with noninteracting cuboids with an orientation bias; (c) a Poisson-Voronoi tessellation (starting from uncorrelated points, each cell contains all points closer to its center than to any other point); (d) an iteration stable (STIT) tessellation, a model for subsequent cell division; the tessellation is simulated by Claudia Redenbach; (e) an inhomogeneous point process; (f) a continuous random field.

how different topics in stochastic geometry are interrelated: tensor valuations[9], tessellations [10] and hard-core particle systems[11], Boolean models[12], random fields[13], percolation[14], image analysis and spatial statistics.

Moreover, these topics also relate seemingly unrelated physical systems, for example, the eye of a chicken [224] and the large-scale structure of the universe [363, 368]: these systems are disordered and can be statistically isotropic like liquids, but there is a hidden long-range order that suppresses density fluctuations on large length scales like for crystals; such an intermediate state of matter between crystals and liquids is called hyperuniform [467]. I study the global structure of a hyperuniform system in Chapter 4 and compare it to that of classical liquids. Structure formation also relates nonrandom seemingly unrelated systems like the scales of a butterfly wing and metastable exotic states of nuclear matter, see Chapter 5 and also Fig. 1.8.

Throughout this thesis,

1. the same shape descriptors are applied to a great variety of systems on very different length scales,

2. physical insight is provided via the characterization of the complex geometry,

3. the analysis of the geometric functionals is extended to higher moments of the structure distributions or even to the full probability distributions,

4. a special emphasis is on anisotropic random spatial structures, for which the anisotropy is characterized by tensorial shape descriptors and the information content of higher-rank tensors is investigated,

5. different "types of disorder" are characterized, for example, inhomogeneities, anisotropic deformations, or maximally disordered systems.

Both local and global structure characteristics are defined, developed and applied to important common models like the Gaussian random field [8], Boolean

[9] A valuation is a real function φ on the space of convex bodies that is additive, i.e., $\varphi(A \cup B) = \varphi(A) + \varphi(B) - \varphi(A \cap B)$. A continuous valuation can be extended to be defined on unions of convex bodies. A tensor valuation is a tensor-valued valuation.

[10] Tilings that divide the space into cells with no overlaps and no gaps.

[11] Many body systems with grains that cannot penetrate each other but no other interaction.

[12] The Boolean model is the union of noninteracting grains distributed randomly in space, see Fig. 1.4(b); their shapes and orientations are drawn from the so-called grain distribution. It is a common model for porous media.

[13] A random field is a function where the functional values are random variables.

[14] A connected component that spanns the whole system is called a percolating cluster. Percolation is a critical phenomenon.

models [299], hard-sphere packings [460], or the Poisson point process[15] [448], but also to exotic states of matter (pasta matter) [413, 416] or to state-of-the-art experimental data in gamma-ray astronomy [18]. They allow, e.g., for a prediction of physical quantities, a classification of states, or a morphometric data analysis. For the simulated and experimental data, the morphometric analysis is applied to pixelated, voxelated, or triangulated data and also to exact representations (up to numerical precision).

Many shape analyses concentrate only on the expected value of a geometric functional, i.e., only on the first moment of its probability distribution. Evaluating higher moments is a complex problem in both analytic and numeric calculations [448]. This thesis tackles this challenge and extracts the higher moments and even the full probability distributions of Minkowski functionals in various systems and shows what can be learned from this additional information. For a Poisson random field, e.g., the probability distribution is determined with high accuracy and used for detecting gamma-ray sources. While very often homogeneity is assumed, and there are many detailed studies of homogeneous systems, I here investigate in detail inhomogeneous random fields and the structural difference to a homogeneous Poisson noise, in order to detect and localize the inhomogeneities.

Also anisotropy is often neglected for simplicity, but both many man-made or natural materials are actually anisotropic, e.g., the trabecular bone—see Fig. 1.2—where the anisotropy corresponds to a preferred axial loading and a quantification of anisotropy allows for a refined diagnosis of osteoporosis. So, here a special emphasis is on sensitive tensor-valued shape measures that are needed to detect and quantify anisotropy. Besides its importance for application, a thorough anisotropy analysis can also reveal more fundamental insights to the relation between geometry and topology or between geometry and physics, e.g., detect deformations which do or do not influence the physical properties.

Minkowski tensors of anisotropic random fields

The Minkowski tensors, as well as the standard MIL measure, quantify the anisotropy of common models of porous media. The different anisotropy measures are compared w.r.t. their sensitivity. The global averages are calculated analytically and related to local characteristics. In both analytic and numeric calculations, I determine also higher moments and probability distributions of the Minkowski tensors, which is important for an adequate modeling of porous media as well as for a quantitative image analysis.

[15] Noninteracting points are placed randomly in space such that for a finite set the number of points within this set is Poisson distributed with a mean value proportional to the volume of that set.

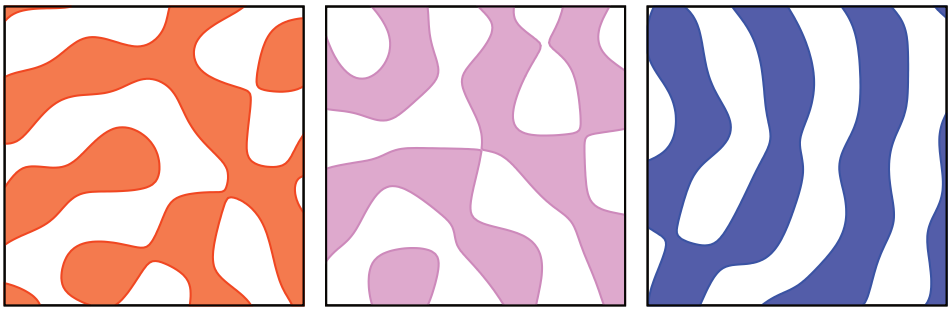

(a) (b) (c)

Figure 1.5: Level sets of differently anisotropic Gaussian random fields, i.e., the set of all points for which the Gaussian distributed random functional value exceeds a given threshold: (a) an isotropic model, (b) a slightly preferred orientation of the interface along the vertical direction, (c) a strongly anisotropic model.

The Boolean model (see Fig. 1.4(b)), and the Gaussian random field (see Fig. 1.5) are important and common models for porous media. In Chapter 2, I characterize the structure of these anisotropic models for porous media.

A standard measure of anisotropy in trabecular bone is the so-called mean intercept length (MIL) tensor [186, 512]. I calculate the MIL both analytically and numerically for anisotropic Boolean models, i.e., overlapping grains with an orientation bias. I show that the MIL tensor can appear perfectly isotropic for structures that are obviously anisotropic and the common approach can sometimes be even ill-defined. In this sense, the MIL tensor is actually not a tensor. Moreover, I show its inherent insensitivity for anisotropy of higher rank.

Instead, I suggest the Minkowski tensors from integral geometry for a comprehensive and systematic approach to quantify various aspects of structural anisotropy. Minkowski tensors are defined for arbitrary rank, which is needed to detect, e.g., anisotropy in systems with cubic symmetry. Usually, Minkowski tensors are given in a Cartesian representation. In order, to extract higher-order anisotropy which is not contained in Minkowski tensors of lower rank, an irreducible representation is presented, the circular Minkowski tensors[16]. I show how the Minkowski tensors resolve the disadvantages of the MIL analysis, e.g., the Minkowski tensors clearly detect anisotropy for systems which appear isotropic w.r.t. the common MIL analysis.

Explicit formulas can be derived for mean values of Minkowski tensors of overlapping grains[17]. I compare the analytic results against simulations, and a

[16] Similar to the definition of the spherical Minkowski tensors for three dimensions in Ref. [232].

[17] For convenience and where the meaning is obvious from the context, I sometimes simplify the

sensitive estimator of the degree of anisotropy is introduced. For Boolean models with either aligned or randomly oriented rectangles, I also study the variances and covariances of the Minkowski functionals. Compared to a Boolean model with discs [210], I find in part qualitatively new behavior, e.g., an additional regime with anticorrelations. I even study the full probability distributions of the Minkowski functionals. If the Minkowski functionals are suitably normalized, they satisfy a central limit theorem [210]. In other words, in the limit of an infinitely large observation window the cumulative distribution function of the Minkowski functionals converges to that of a normal distribution. In my simulation study, I find that already for relatively small observation windows the empirical probability density functions of the rescaled Minkowski functionals are well approximated by Gaussian distributions. In detailed simulations at a small intensity in a finite observation window, I find statistically significant deviations from the Gaussian distribution. However, the rescaled probability distributions still collapse to a master curve that agrees within error bars with the rescaled probability distribution of the number of grains hitting the observation window. Hypothesis tests could be defined that use the Minkowski functionals to decide for a given grain distribution whether or not a random two-phase medium can be modeled by overlapping grains of a certain type.

Also for level sets of anisotropic[18] Gaussian random fields, the expectations of the Minkowski tensors are calculated analytically, and the explicit formulas are compared to simulation results. Surprisingly, I find that although tensors of higher rank contain additional anisotropy information compared to the tensor of rank two, the second-rank tensor is sufficient to estimate the model parameters which are necessary to determine the mean values of all Minkowski tensors of arbitrary rank which characterize the interfacial anisotropy of the level sets of Gaussian random fields. Based on this relation among the mean Minkowski tensors a null hypothesis test for non-Gaussianities in anisotropic random fields could be defined.

Many morphometric techniques like the two-point correlation function, the pore size distribution function, the mean intercept length, or the Minkowski analysis can only analyze black and white images. However, often the experimental data consists of gray-scale values. A common method is to choose an appropriate

notation in the text and use only the terms “Minkowski functionals” or “Minkowski tensors” when referring to their densities, that is, the mean values of the Minkowski functionals or tensors divided by the size of the observation window in the limit of an infinitely large observation window.

[18] Be aware of the different use of the term “anisotropy” in stochastic geometry or in cosmology: here, anisotropy refers to a preferred orientation in the correlation function of the Gaussian random field; in cosmology, the thermal fluctuations of the cosmic microwave background as a random function on the unit sphere are sometimes referred to as anisotropies, because the radiation differs for different directions of the detector.

threshold and turn the intensity data into black and white data. However, this thresholding is not robust against inhomogeneous detector effects like a position dependent point spread function in X-ray tomography. Therefore, a generalization of Minkowski functionals and tensors to gray-scale random fields would be a promising tool for the application to experimental data. I define an intuitive generalization of the Minkowski tensors, apply it to a simple example, and thus demonstrate in a proof-of-principle how it reconstructs the anisotropy of a blurred image.

Anisotropic continuum percolation

The Minkowski functionals, especially the Euler characteristic serving as a topology index, allow to predict properties of anisotropic continuum percolation, i.e., the geometric phase transition describing the appearance of a system spanning cluster of connected components. They are used to study both the geometry and topology of the percolating cluster as well as how the geometry and topology of the Boolean model depend on each other.

Therefore, I further study the anisotropic Boolean model. The Boolean model is also an important model systems for continuum percolation. Below a critical occupied volume fraction no infinite, i.e., system-spanning, cluster exists. However, above this threshold there is (almost sure) an unbounded cluster, called percolating cluster, see Fig. 1.6. This geometric phase transition at the percolation threshold is important, e.g., for flow through porous medium, elasticity or conductivity of heterogeneous materials, gelation and polymerization, hopping conductivity, galaxy formation, or immunological systems [84, 394, 417, 460, 522].

In the isotropic case, a topological ansatz, which can be connected to transport properties and the permeability, is investigated. Darcy's law allows to treat the tortuous microstructure like a homogeneous material with an effective permeability [110, 510]. However, this effective permeability depends on the complex microstructure. Flow is only possible through the percolating cluster and vanishes at the percolation threshold. In experiments, a universal scaling of the permeability and the scaling of geometrical and topological measures has been found [402]. Starting from this as a motivation, a universal relation between the topology of the percolating void cluster (quantified by the Euler characteristic) and the rescaled porosity is studied in extensive simulations for isotropic Boolean models.

In detail, I investigate anisotropic continuum percolation both in finite systems and in the thermodynamic limit. In a finite system, a Boolean model with elongated particles with an orientation bias first percolates in the preferred direction, then in the other direction, like depicted in Fig. 1.6. However, as already known for other anisotropic percolation models, I show that this difference vanishes in the limit of

Figure 1.6: A percolating cluster of connected components spans the whole system and connects opposite edges; for an infinite system percolation is a geometrical phase transition.

infinite system size. Even the most anisotropic model simultaneously percolates in all directions, i.e., the percolation threshold is isotropic. I discuss how this is related to the uniqueness of the percolating cluster.

The value of the percolation threshold, however, depends on the anisotropy of the system. Percolation thresholds are determined in extensive simulations for a collection of anisotropic Boolean models. Because of the huge numerical effort, efficient approximations for the percolation thresholds are needed.

For the anisotropic Boolean models, I compare the well-known so-called excluded area approximation [52], for which I discuss an explicit expression, to the numerical estimates. The approximation is in relatively good agreement, but uses an empirical parameter, namely the percolation threshold of a similar system. In contrast to this, based on the first and second moments of the Minkowski functionals, bounds and approximations on the percolation thresholds have been suggested which do not need any empirical parameters. I discuss explicit formulas for these bounds and compare them to the numerical results. For the systems studied here, I find that the zero of the Euler characteristic captures the qualitative behavior very well. In other words, it provides an accurate approximation of the difference of the critical intensity of a rectangle compared to that of a square with the same orientation distribution. If an empirical parameter is used similar to the excluded area approximation, an improved approximation for the models studied here can be derived from the zero of the Euler characteristic. Moreover, I discuss and propose candidates for close bounds and approximations of the percolation threshold which are based on the variances and covariances of the Minkowski functionals.

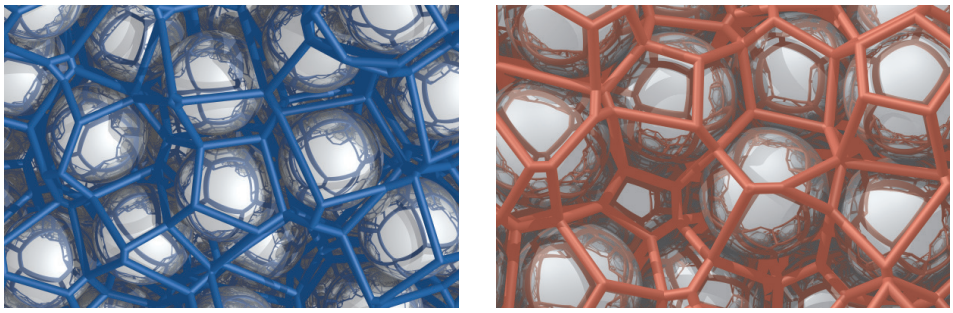

(a) (b)

Figure 1.7: Disordered hard-sphere packings and the corresponding Voronoi diagrams, i.e., to each sphere a cell is assigned containing the points closer to this sphere than to any other sphere for (a) an equilibrium hard-sphere liquid and (b) a jammed, i.e., mechanically stable, hard-sphere packing. While the local structure appears qualitative similar, their global structure differs distinctly (see Chapter 4).

Minkowski correlation functions of random tessellations

Can you tell the generating process from the shape of the single cells? The answer is actually no: the local structure distributions of very different physical systems can be qualitatively very similar. To analyze the global structure also of cellular systems, the local analysis based on single cell characteristics is extended by introducing global correlation functions of Minkowski functionals, which find for tessellations with qualitatively very similar local structure a distinctly different global structure, which is also linked to the so-called disordered hyperuniformity, i.e., at short ranges one of the systems is disordered like a liquid and at large length scales it is homogeneous like a crystal. Moreover, these Minkowski correlation functions can distinguish systems with equal standard two-point correlation functions.

A particle process like the uncorrelated Poisson point process or the Boolean model can be naturally related to a cellular structure via the Voronoi tessellation: to each particle a cell is assigned containing all points closer to this than to any other particle; this can be related to the concept of free-volume and is an important method for analyzing the structures of many-particle systems [353]. Packings of frictionless monodisperse hard spheres in three dimensions serve as a simple, yet effective tool for modeling the complex behavior of such diverse many-particle systems as crystals, colloids, liquids, glasses, heterogeneous materials, and biological systems [95, 152, 180, 460].

A local structure characterization quantifies the shape of a single cell. How sensitive are such local descriptors? The Minkowski functionals robustly quantify

their geometry, e.g., in contrast to discontinuous measures like the number of faces or the number of edges. However, if only the Minkowski functionals of single cells are used, physically important processes with distinct structural differences like a equilibrium hard-sphere liquid or jammed sphere packings, which are depicted together with their Voronoi diagrams in Fig. 1.7, cannot be distinguished qualitatively. In this sense, the local structure of a typical Voronoi cell is qualitatively the same.

More sensitive global characteristics are needed to examine the correlations of shape in a tessellation. Therefore, I define global cell-cell correlation and probability density functionals and evaluate them for the Poisson point process, the equilibrium sphere packings and for jammed sphere packings. More precisely, I investigate the maximally random among all mechanically stable packings. It has the interesting geometric property of hyperuniformity, i.e., although disordered at short length scales like a fluid, the system is homogeneous like a crystal on large length scales [467]. This hyperuniformity leads to strong anticorrelations in the cell-cell correlation functions and thus indeed to a distinct structural difference in the global structure, where the local structure is qualitatively indistinguishable. I also investigate global cross-correlations among different Minkowski functionals and find approximative relations between them which arise from the vanishing of correlations of deviations.

The Minkowski functionals contain multipoint information, i.e., more than two-point information. In other words, the Minkowski correlation functions contain visibly more information than the standard pair-correlation function, in that it can distinctly distinguish point patterns with the same pair-correlation function. Here, I analyze a model system for galaxy distributions and show how its global Voronoi structure differs from that of a simple clustering process with the same pair-correlation function.

Shape indices for nuclear matter

Even on extremely small length scales, I apply the Minkowski functionals and tensors to characterize and classify simulated exotic states of nuclear matter, so-called nuclear pasta [377], which are expected to appear, e.g., in supernova explosions. The simulations are carried out by our collaborators at Frankfurt University. The neutrino transport during and after a supernova-explosion is greatly affected by the state of nuclear matter at this high nuclear density. Thus, the pasta states are important to understand, e.g., the production of heavy elements.

At small nuclear densities, the nuclei can be considered as deformed balls, but at very high densities new exotic states of nuclear matter emerge, e.g., rods, slabs, tubes, or bubbles [187, 358, 377, 503]. We analyze the structure of these complex

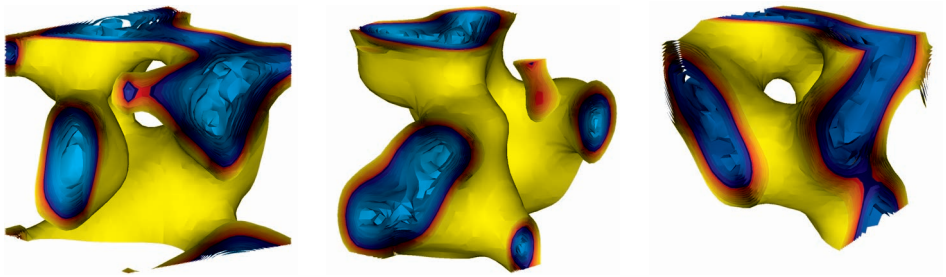

(a) (b) (c)

Figure 1.8: Spontaneously formed nuclear pasta, i.e., exotic states of nuclear matter at very high nuclear densities: (a) and (b) intricate and apparently disordered labyrinthine pasta shapes, (c) among them a complex, yet well-ordered structure can be found, a so-called gyroid-like network; it is a structure, e.g., also found orders of magnitude larger in butterfly wing scales [317]; time-dependent Hartree-Fock calculations in the unit cube with periodic boundary conditions (data from Ref. [416], see also Chapter 6).

pasta shapes derived from static calculations. Distortions are quantified by the Minkowski tensors, and a classification of the stable pasta shapes is presented that is based only on the signs of integrated mean curvature and Euler characteristic.

In dynamical simulations, we observe the spontaneous formation of intricate nuclear labyrinths, see Fig. 1.8[19]. The distribution of the Euler characteristic reveals a variety of complex topologies. The Euler characteristic here also aids to identify among apparently disordered networks a complex but well ordered labyrinth with the same topology as a well-known regular network-like labyrinth bounded by a minimal surface, the so-called gyroid, see Fig. 1.8(c). The gyroid has become a house-hold name in soft materials with order on the nanometer scale, for example in the nanoporous photonic crystals of some green butterfly wing scales [317, 397, 409]. So, surprisingly, the nuclear pasta and butterfly scales can be united by the same spatial microstructure. While we find that the nuclear matter spontaneously exhibits the same geometries as soft-matter systems at the nanometer scale, the length scale of nuclear matter, which is a few femtometers, is radically different from soft-matter systems. Therefore, our finding of the pasta gyroid is the discovery of the smallest reported gyroid found in dynamical simulations. The static calculations reveal that the gyroid is an isomeric state.

We find that the binding energy is rather independent from anisotropic deformations quantified by Minkowski tensors, but the energy is strongly related to the scalar Minkowski functionals, which is a first step to understand in these systems the connection between their geometry and binding energies.

[19] Figure 1.8, as well as Figures 5.1, 5.2, 5.9, and 6.12, were created using the program VisIt [99].

Minkowski sky maps in gamma-ray astronomy

Finally, I use the Minkowski functionals for a morphometric data analysis in gamma-ray astronomy: by characterizing the shape of a noisy sky-map more information can be taken out of the same data without assuming prior knowledge about the source. The latter can then be detected via significant deviations from the background structure. I derive an accurate estimate of the distribution of the background structure, which is simultaneously characterized by all Minkowski functionals. Such a refined structure characterization can detect formerly undetected sources.

For example, the remnants of supernovae, i.e., material ejected by the explosion of the red giant, can be strong gamma-ray sources [18]. The detection and observation of these sources provides insights to physics at extremely high energies about 1 TeV and is a fast developing branch of astroparticle physics [6, 191]. However, the detection of gamma rays at these very high energies is experimentally very complicated and only limited data is available; see Fig. 1.9(c). Therefore, a sensitive data analysis is needed. On the one hand, the common counting methods only use the total number of detected events and neglect all spatial information encoded in the sky maps [273]. On the other hand, likelihood fits of complex models to the gamma-ray sources are not only extremely time-consuming, but the outcome strongly depends on the goodness of the model.

Therefore, we have developed an alternative approach: the morphometric analysis in gamma-ray astronomy using Minkowski functionals. The idea is to quantify the structure of the background using the Minkowski functionals as versatile shape measures. A null hypothesis test then detects any significant structural deviation from the background noise; no a priori knowledge about the source is needed, but still additional structural information is taken into account. The counts map, i.e., the number of events in each bin of the sky map, is first turned into a black and white image via thresholding. For each threshold the structure is quantified by the Minkowski functionals. The null hypothesis is that there are only background signals, which means the number of counts in the pixels are mutually independent and Poisson distributed. Then, the compatibility with the background structure is determined. A null hypothesis test is performed to check whether there is a significant structural deviation from that of the homogeneous Poisson random field.

Although we have developed this new method especially for gamma-ray source detection, it is a general morphometric hypothesis test which is applicable to other spatial data like medical data sets, e.g., in tumor recognition, for geo-spatial data and raster data in earth science, or for image and video analysis. More generally speaking, this project distinguishes the structure of inhomogeneous random fields from homogeneous ones.

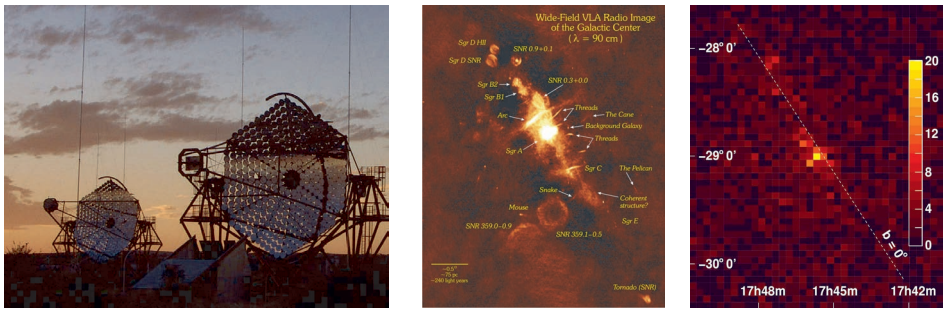

(a) (b) (c)

Figure 1.9: Sky maps: (a) two H.E.S.S. Cherenkov telescopes in Namibia; image reproduced from Ref. [189]; (b) a high resolution, panoramic radio image of the center ridge of our Galaxy; image courtesy of NRAO/AUI and N.E. Kassim, Naval Research Laboratory [343]; (c) a corresponding gamma-ray sky map obtained by two H.E.S.S. telescopes during commissioning; image reproduced from Ref. [189]; for better data and a detailed analysis of the gamma rays from the galactic center ridge see, e.g., Ref. [17]; for an analysis of the galactic center ridge using the morphometric analysis which is presented here, see Ref. [243].

The concept of the morphometric analysis in gamma-ray astronomy is revised. In detailed numerical studies, I confirm the efficiency of this approach and derive a conservative yet close correction of repeated trials, which is needed to validate the claimed significance of a signal. Moreover, real H.E.S.S. sky-maps are distorted by detector effects. I develop an improved local correction, by which the sensitivity of the morphometric analysis in the application to real data is significantly increased. I discuss further advantages of the morphometric analysis, e.g., that it is rather independent of the scan window size. The morphometric analysis can detect sources of very different extensions with the same scan window size. Moreover, the advantage of additional structural information should be most effective for short observation times and low statistics, i.e., when it is most needed.

For a thorough structure characterization the joint probability distribution of all three Minkowski functionals is needed, i.e., the probability density for detecting simultaneously specific values of area A, perimeter P, or Euler characteristic χ. Gaining such a detailed knowledge about the background structure distribution provides the increased sensitivity of the test detecting structural deviations. However, it is therefore also the main difficulty of this approach, especially because a high accuracy is needed in order to distinguish a statistical fluctuation, e.g., appearing with a probability 10^{-5}, from a significant structural distortion.

One the one hand, a small observation window does not contain rich structural information. On the other hand, the calculation of the joint probability distribution

of all Minkowski functionals for larger Poisson fields is analytically practically impossible [161]. Also simple Monte Carlo simulations have so far failed to provide sufficiently accurate numerical estimates. I achieve an accurate estimate of the probability distribution for extremely unlikely events by combining analytic knowledge of the structure distributions with a very efficient algorithm from statistical physics for estimating density of states, the so-called Wang-Landau algorithm [499, 500]. Thereby, I accurately estimate for a given set of Minkowski functionals the number of possible b/w images ranging from the order of magnitude $O(1)$ to $O(10^{64})$.

Knowing the joint distribution of all Minkowski functionals, I can indeed show that there is an increase in sensitivity via an improved structure characterization compared to a simple characterization by only the area if there is a structured source within the scan window. Formerly undetected sources can now be detected by analyzing the same data with all three Minkowski functionals, which is shown both for a single count map and for averages over many simulations. I also evaluate more systematically the dependency of this change in sensitivity on the shape of the source for true point sources, constant offsets, or a nontrivially shaped gamma-ray source. A new test statistic is introduced which combines different thresholds leading, e.g., to a better detection of diffuse radiation. The morphometric analysis is then compared to a standard null hypothesis test in gamma-ray astronomy. The comparison depends both on the shape of the source and on the experimental details. An example is discussed for which there is no significant excess in the total number of counts, but the source can still be detected because of the additional structural information.

The technique is also applied to real data from the H.E.S.S. experiment, a Cherenkov telescope array in Namibia, see Fig. 1.9(a). The increase in sensitivity of the morphometric analysis by the improvements of this thesis is demonstrated for very weak sources, for which the statistics is artificially reduced by postselection and Monte Carlo observations.

Finally, a different approach to a morphometric data analysis is presented that is based on the variance-covariance structure of the Minkowski functionals. Using a less accurate description of the background structure, this approach is even more versatile and can in principle be easily applied to other random fields. It is robust to a limited knowledge of the background shape. The variance-covariance structure of the Minkowski functionals of a Poisson field is derived analytically. I determine the empirical cumulative distribution function of our test statistic and show how the joint characterization by all three Minkowski functionals increases the sensitivity to detect inhomogeneities again in cases where there is no excess in the total number of counts.

Morphometry of random spatial structures

The rich variety of random spatial structures from nuclear physics to gamma-ray astronomy and from various fields of research is here characterized by a versatile morphometric approach using for all of these very different physical systems the same shape descriptors, the Minkowski functionals and tensors. I show how these integral geometric measures robustly and comprehensively characterize the various disordered structures and thus provide physical insight into systems dominated by their complex structures, from predicting the percolation threshold over estimating and adjusting model parameters to source detection. I especially focus on the quantification of the anisotropy, e.g., that while the value of the percolation threshold depends on the anisotropy of the system, even the most anisotropic model simultaneously percolates in all directions. Moreover, I unfold the morphometrical information of higher moments of the shape measures or of even their full probability distributions, e.g., a accurate knowledge of the structure distribution allows for an improved hypothesis test.

Because of the vast literature in very different fields of research each with different names and nomenclature[20], I cannot provide a complete review of the literature but only a basic overview that links different topics and communities.

This thesis demonstrates the benefits of combining the knowledge of different fields, especially mathematics and physics, e.g., integral geometry and nuclear physics (for an accurate classification and description of pasta matter) or methods from statistical physics and gamma-ray astronomy (for an improved data-analysis).

The different physical systems and the unifying problem of random or disordered structures provide ample interesting phenomena and observations that call for both a comprehensive overview and detailed studies and investigations. Such a vast field can obviously not be concluded in a single work. In this thesis, I want to contribute to this field by further developing a robust and versatile morphometric approach, applying it to gain insight into the specific systems, but also to learn about unifying principles or common features and observations about the "structure of disorder."

[20] This thesis uses terms and notations as they are common in physics, which can sometimes be in conflict with their usage in other fields. For example, a "probability distribution" (which is here basically the same as "probability distribution function") is in contrast to mathematics literature a non-cumulative distribution function. Another example is that "measure" is often not used in the strict mathematical sense. It can refer to some "shape descriptor", some "metric", or a "geometrical property." Moreover, I use different notations for mean values: $\langle\cdot\rangle$, $\bar{\cdot}$, or $\mathbb{E}[\cdot]$.

Chapter 2

Minkowski tensors of anisotropic random fields[1]

Models are indispensable tools for both a statistical analysis and fundamental insights of random spatial systems [217]: not only for simulation of random processes, but also because the theoretical form can help understanding and interpreting the disordered structures as well as the behavior of the morphometric measures. For example, the models can help estimating possible statistical fluctuations [217]. In applications, a detailed knowledge of the structure of the models is important, e.g., to estimate parameters [204], for hypothesis tests [93, 130, 257], or to adjust the model to experimental data [34, 35]. More fundamental insights are how global averages can be expressed by local characteristics only [507] or how the topology changes for increasing anisotropy. Last but not least, structure-property relations, which relate the shape of the microstructure to physical properties like the elasticity, need sensitive measures of structure. What are suitable fabric tensors to quantify, e.g., the shape of anisotropic heterogeneous materials? The mean intercept length (MIL) is a common characteristic of anisotropy in porous media [483], e.g., in medical physics to analyze trabecular bone [512].

First, I compare the MIL as a measure of anisotropy to the Minkowski tensors from integral geometry and show how the latter resolves the disadvantages of the former. Then, I use the Minkowski tensors to analyze the structure of two common models for porous media.

[1] The results of this chapter were derived in collaboration with Klaus Mecke, Julia Hörrmann (see Ref. [203]), Daniel Hug, Max Hörmann (see Ref. [199]), Günter Last, Maria Schlecht, Gerd E. Schröder-Turk, and Matthias Schulte. Parts of it are direct quotes from our publications Refs. [204, 408]. Some of the figures in this chapter are reproduced from Ref. [204] with permission from Elsevier.

The structures referred to in this chapter are two-phase random media, i.e., they can be described by indicator functions with only two possible functional values, e.g., zero or one. Two different ways to derive such a random structure are considered: first, overlapping grains distributed randomly in space or second, level sets of random real valued functions. In the first case, the indicator function denotes whether a point is covered by a grain or whether it is part of the remaining void. In the second case, the indicator function distinguishes whether the functional value of the random function at the point is larger (or equal) than some given threshold or whether it is smaller than the threshold. In the end of the chapter, I give an outlook how the structure characterization discussed here could be generalized to intensity profiles, meaning gray-scale images.

As an introduction[2], the well-known Boolean model and Gaussian random field are shortly presented and discussed in Section 2.1. For each, a special parametric model is defined which can be used for simulations of differently anisotropic systems. Still as an introduction, the importance of fabric tensors to characterize complex microstructure is shortly discussed in Section 2.2, especially the common MIL analysis as a prominent example.

In Section 2.3, the MIL of Boolean models is discussed and the shortcomings of the MIL analysis revealed. The MIL of Boolean models is already known analytically. I nevertheless provide in Section 2.3.1 another concise analytic derivation and discussion of the MIL of Boolean models in order to provide especially for applied scientists an easier insight into which information is contained in the MIL. The analytic results are compared to simulation results in Section 2.3.2. The standard approach assumes that the polar plot of the MIL is an ellipse and thus defines a tensorial measure called the fabric tensor [186]. The results for anisotropic Boolean models reveal fundamental shortcomings of this common MIL analysis, see Sections 2.3.3–2.3.5. I find that the polar plot of the MIL of a porous medium is in general not an ellipse and hence not represented by a tensorial quantity of second rank, which is contrary to the common understanding that for a large collection of grains the MIL figure averages to an ellipse. The standard MIL tensor defined by a least-square fit of an ellipse is, strictly speaking, ill-defined and not a tensor. Moreover, I demonstrate that obviously anisotropic Boolean models can appear perfectly isotropic in the MIL analysis. In Section 2.3.6, I show how an improvement of the definition of the MIL tensor can lead to the more general family of Minkowski tensors.

In Section 2.4, the Minkowski tensors from integral geometry are compared to the MIL analysis. First, their well-known definition and properties are presented and discussed, see Section 2.4.1, especially their irreducible representation in the

[2] Because this chapter is especially long, I here provide a more detailed outline.

planar case, see Section 2.4.2. Then, I show their advantages over the MIL analysis both from a practical and a fundamental point of view. The Minkowski tensors allow for a thorough, comprehensive, and systematic approach to quantify various aspects of structural anisotropy. I demonstrate that the Minkowski tensors are more sensitive, in the sense, that they can quantify anisotropy in systems which appear isotropic to the MIL analysis, see Section 2.4.3. They are used in the following to characterize first the structure of Boolean models and then of level sets of Gaussian random field.

In Section 2.5, the Minkowski tensors of Boolean models are analyzed. After repeating the well-known results for the mean values of the scalar Minkowski functionals (suitably rescaled for growing observation windows) in Section 2.5.2, the corresponding results for the Minkowski tensors are presented in Section 2.5.2. In Section 2.5.3, the analytic results are compared to simulations of nonisotropic Boolean models. Moreover, I demonstrate how the model parameters can be estimated sensitively and bias free if the Minkowski tensors of the Boolean model are measured. In Sections 2.5.4 and 2.5.5, I study for Boolean models with either aligned or randomly oriented rectangles the covariances and probability distributions of the Minkowski functionals and find both universal and nonuniversal behavior. In Section 2.5.6, bounds on the cumulative distribution function are discussed, and in Section 2.5.7, a short outlook to inhomogeneous Boolean models is given.

In Section 2.6, the mean Minkowski tensors of level sets of Gaussian random fields are analyzed. In Sections 2.6.1–2.6.3, the relation between global and local averages of Minkowski tensors of level sets of homogeneous and sufficiently smooth random fields, the probability distribution of the gradient of a Gaussian random field at the origin, and the well-known mean values of the Minkowski functionals of the level sets of a Gaussian random field are discussed. In Section 2.6.4, this is generalized to corresponding mean values of Minkowski tensors that quantify the distribution of the normals on the level sets. Again, explicit formulas are compared against numerical simulations. Using the irreducible representation of the Minkowski tensors in Section 2.6.5, the tensor of rank four is shown to include additional anisotropy information compared to the second-rank tensor. Nevertheless, if the random field is known to be Gaussian, they can be robustly and accurately predicted from the second-rank tensor only. This is because the anisotropy of Gaussian random fields does not depend on the entire correlation function, but only on a single second-rank tensor, see Section 2.6.6. In other words, if the random field is a Gaussian random field, all tensors of arbitrary rank are determined by the second-rank tensor. This relation could be used for a null hypothesis test to detect non-Gaussianities in anisotropic random fields.

Finally in Section 2.7, I give, as mentioned above, an outlook how the Minkowski tensors can be generalized to gray-scale images. As an example, it is applied to a blurred rectangle.

2.1 Orientation biased random fields

An ideal random field captures the essential features of the complex behavior of physical systems, but it should depend only on a limited number of parameters, which are both physically meaningful and which can be determined in experiments [486].

Two common and important random fields for applications to very different physical systems are the Boolean model, a two-phase random medium built by noninteracting grains, and the Gaussian random field, spatially correlated normal distributed random variables. In many disordered systems, either one description or the other are physically well justified [69, 149, 158, 293, 418, 432, 501]. While the definition of these models is relatively simple, they are very versatile models that can be accurately adjusted to physical systems [35, 432, 460].

In this section, I give a short overview of these models in general, and I present specific parametrized models that allow an analysis of different degrees of anisotropy. The analytic calculations in this chapter are often valid for general Boolean models or general Gaussian random fields, but the specific models are used for a comparison to simulation results.

2.1.1 The Boolean model

Many random spatial structures can be viewed as a system of overlapping pores and many composite materials are actually formed by overlapping grains. In other words, a porous medium can often be well modeled by noninteracting grains with random shape or orientation [34, 35], this is called the Boolean model [299].

The Boolean model is a popular model to study heterogeneous materials [447, 460], for example, ceramic powders [385], wood composites [501], sedimentary rock [293, 418], fractured materials, hydrating cement-based materials [149], biometrical data [310], inhomogeneous distributions of galaxies [238], or in the estimation of percolation thresholds [309, 311]. Either the solid phase or the pore space of a porous medium can be modeled by the Boolean model: for example, the pore space of bread [73] or the solid phase in sintered ceramic composites [385].

The construction of any Boolean model starts with a random point pattern: noninteracting, i.e., uncorrelated points, are placed randomly in space; see Fig. 2.1. The number of points in a finite observation window is a Poisson distributed

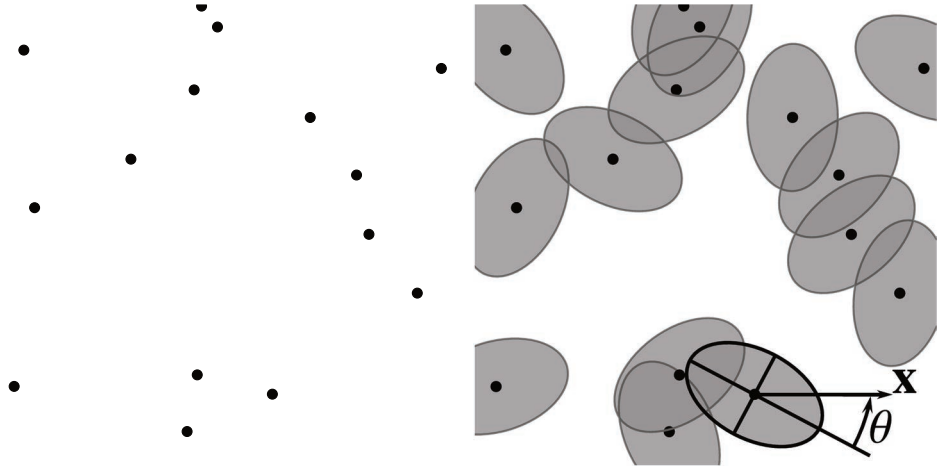

Figure 2.1: The construction of the Boolean model: first, uncorrelated points are placed in the plane (left); then, a grain is assigned to each of these points (right). Here, the grains are ellipses with a fixed aspect ratio, but a random orientation. In two dimensions, the orientation can be characterized by the angle θ between the main axis of the grain and the x-axis of the system. The angle θ is drawn from a probability distribution $\mathcal{P}$. The Boolean model will only be isotropic if the orientation distribution $\mathcal{P}(\theta)$ is uniform on $(-\pi/2, \pi/2]$; otherwise the model will be anisotropic.

random number. The expected number of points per unit square is the intensity or number density ρ.

Then, each point is decorated with a grain, e.g., a rectangle in Fig. 2.2 or an ellipse in Fig. 2.1. Both the shape and the orientation of the grain can be random, i.e., drawn from a probability distribution. For example, the aspect ratio, size, or orientation of the ellipse could vary; in Fig. 2.1 the shape is fixed, but the orientation is random with an orientation bias towards the x-axis. Different Boolean models can be created by choosing different grain distributions. I consider here only homogeneous Boolean models[3], i.e., the distribution does not depend on the position of the grain.

The distribution of the grains stores the local information of the Boolean model, i.e., the characteristics of a single grain. The Boolean model Z is defined as the union of all grains. The space is subdivided into two phases: first, the grain phase which is formed by the union of the grains, the so-called covered or occupied phase; second, the complement which is not covered by the grains, the so-called void phase.

If the orientations are randomly and isotropically distributed, the Boolean model will also be isotropic. However, if the single grains have an anisotropic

[3] Also called stationary Boolean models.

shape and their orientation distribution is biased towards an axis, the resulting model will be anisotropic. A disordered material can be reconstructed by choosing appropriate distributions of grain shape and orientation [241], which provides accurate models, e.g., w.r.t. the elasticity and the transport properties of the model [34, 35], or accurate predictions of how thermodynamic quantities depend on the shape of the microstructure [248].

The volume fraction (or area fraction in 2 D) of the void phase is $\phi_{void} = \mathrm{e}^{-\rho\bar{V}} \in [0,1]$ with $\bar{V}$ the mean volume (or mean area in 2 D) of a single particle (or the average particle volume in case of particles with a random size); then, the occupied volume fraction is $\phi_{cov} = 1 - \mathrm{e}^{-\rho\bar{V}}$, which is also called porosity and denoted simply by ϕ. If the porosity converges to unity $\phi \to 1$, the whole space is covered with grains. In the dilute limit, i.e., if the expected number of grains per unit area vanishes, also the porosity tends to zero $\phi \to 0$. Note that a dependence on the intensity is equivalent to the dependence on the porosity.

Parametric orientation biased Boolean models

As a very general class of two-dimensional anisotropic heterogeneous materials, we introduced [204, 408] a model with overlapping grains (either rectangles or ellipses) where both the aspect ratio, i.e., the elongation of the particles, and the standard deviation of the orientation distribution, i.e., its anisotropy, can be varied.

The anisotropic orientation distribution of the grains is depicted in Fig. 2.2. The angle θ between the main axis of the grain and the x-axis follows a cosine distribution

$$\mathcal{P}(\theta) = Z_\alpha \, \cos^\alpha(\theta) \tag{2.1}$$

with $Z_\alpha = \Gamma(1+\alpha/2)/(\sqrt{\pi}\,\Gamma(1/2+\alpha/2))$ with $\theta \in (-\pi/2, \pi/2]$; see Fig. 2.2. The anisotropy is varied by choosing the parameter α: $\alpha = 0$ produces to a uniform, i.e., isotropic, distribution, and $\alpha = \infty$ leads to a δ-distribution, i.e., all grains are aligned along the x-axis. For a more general characterization of the anisotropy distribution, I parametrize it sometimes by the standard deviation σ of the orientation probability density function $\mathcal{P}(\theta)$, which is an invertible function of the parameter α:

$$\sigma^2 = \int_{-\frac{\pi}{2}}^{\frac{\pi}{2}} \mathrm{d}\theta \; \theta^2 \, \mathcal{P}(\theta) \; .$$

$\sigma = 0$ corresponds to perfect alignment of the major axes with the x-axis and $\sigma = \pi/\sqrt{12} \approx 0.91$ to an isotropic, i.e., uniform orientation distribution.

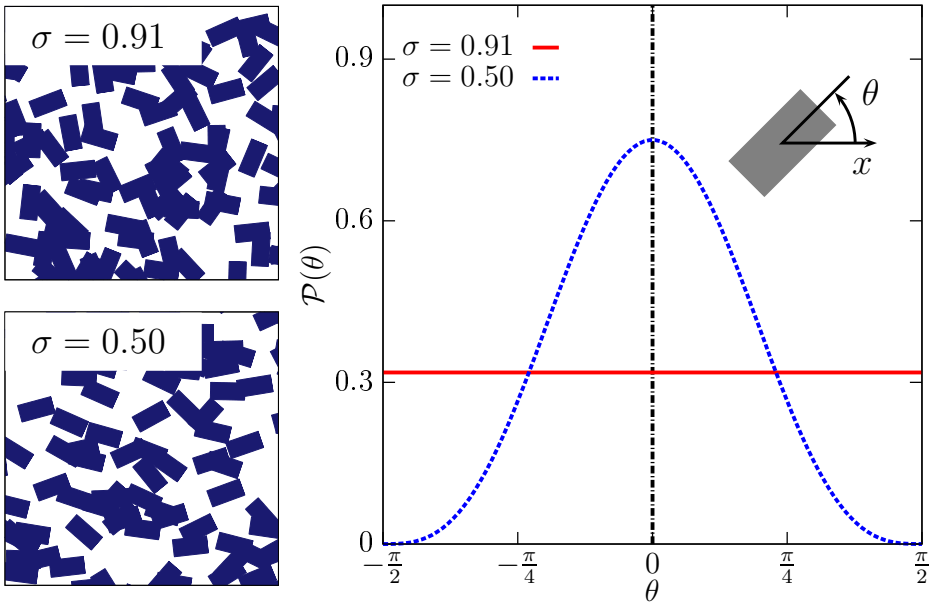

Figure 2.2: Anisotropic Boolean models: the angle θ between the main axis of the grain and the x-axis characterizes the orientation of the single grain. On the right-hand side, three differently anisotropic probability distribution $\mathcal{P}(\theta)$ are plotted: an isotropic, i.e., uniform distribution with standard deviation $\sigma = \pi/\sqrt{12} \approx 0.91$, a distribution with preferred direction $\theta = 0$ and a standard deviation $\sigma = 0.50$, and $\delta(\theta)$ for perfect alignment with the x-axis. On the left-hand side, two samples of Boolean models either isotropic (top) or with orientation bias (bottom) are depicted.

2.1.2 The Gaussian random field

In contrast to the Boolean model which only takes on binary values, covered or not covered, the Gaussian random field assigns to each position $\mathbf{r} \in \mathbb{R}^d$ a real-valued random variable, i.e., a realization is a function $g(\mathbf{r}) \in \mathbb{R}$ [8, 486]. Note, however, that also the Gaussian random field can be used to model two-phase media simply by thresholding, e.g., considering the set of all points $\mathbf{r}$ for which $g(\mathbf{r}) > 0$.

The defining property of the Gaussian random field is that for each $n \in \mathbb{N}$ and for each $\mathbf{r}_1, \dots \mathbf{r}_n \in \mathbb{R}^d$ the random vector $(g(\mathbf{r}_1), \dots g(\mathbf{r}_n))$ is a Gaussian random vector. A Gaussian random variable is determined by its mean value and its covariance, similarly the Gaussian random field is determined by its mean value and covariance functions:

$$\mu(\mathbf{r}) = \mathbb{E}[g(\mathbf{r})]$$
$$\mathrm{Cov}(\mathbf{r}_1, \mathbf{r}_2) = \mathbb{E}[(g(\mathbf{r}_1) - \mu(\mathbf{r}_1))(g(\mathbf{r}_2) - \mu(\mathbf{r}_2))] \,.$$

For stationary (i.e., homogeneous) Gaussian random fields, which are considered here, the mean value is a constant μ, in other words, it does not depend on the

position $\mathbf{r}$. I am interested in the structure of level sets, i.e., the set of all points for which the functional value is above a threshold ρ. A constant mean value only results in an offset in the threshold ρ, and without loss of generality I choose $\mu \equiv 0$.

Moreover, for stationary Gaussian random fields the covariance function only depends on the difference of $\mathbf{r}_1$ and $\mathbf{r}_2$: $\mathrm{Cov}(\mathbf{r}_1, \mathbf{r}_2) = \mathrm{Cov}(0, \mathbf{r}_2 - \mathbf{r}_1) =: \mathrm{Cov}(\mathbf{r}_2 - \mathbf{r}_1)$. For isotropic Gaussian random fields, the covariance function actually only depends on the radial distance $\|\mathbf{r}_2 - \mathbf{r}_1\|$. However, for anisotropic random fields, it is a function of both distance and direction.

The utmost importance of the Gaussian random fields arises from the central limit theorem, a superposition of many identically and independently distributed random fields can be well approximated by a Gaussian random field. It is also a popular model, because on the one hand, it is a rather simple model which only depends on the covariance function, on the other hand, it is a very versatile model which can be adjusted to physical systems by choosing an appropriate covariance function[4].

The Gaussian random field model can be defined in real space [e.g. 159, 199] by

$$\mathbb{P}[g] \propto \mathrm{e}^{-\mathcal{H}(g)} \quad \text{with} \quad \mathcal{H}(g) = \iint_{\mathbb{R}^d} \mathrm{d}^d\mathbf{r}_1 \mathrm{d}^d\mathbf{r}_2 \; g(\mathbf{r}_1) \mathrm{Cov}^{-1}(\mathbf{r}_1, \mathbf{r}_2) g(\mathbf{r}_2) \; .$$

Following for example Mantz et al. [288], the Fourier modes

$$\tilde{g}(\mathbf{q}) = \int_{\mathbb{R}^d} \mathrm{d}^d\mathbf{r} \; g(\mathbf{r}) \cdot \mathrm{e}^{-i\mathbf{q}\mathbf{r}}$$

decouple for different wave vectors $\mathbf{q}$ for homogeneous Gaussian random fields and the Gaussian random field model can conveniently be defined by

$$\mathbb{P}[\tilde{g}(\mathbf{q})] = \frac{1}{\pi\tilde{\sigma}^2(\mathbf{q})} \mathrm{e}^{-|\tilde{g}(\mathbf{q})|^2/\tilde{\sigma}^2(\mathbf{q})} \; ,$$

using the Fourier transform of the covariance function

$$\tilde{\sigma}^2(\mathbf{q}) = \int_{\mathbb{R}^d} \mathrm{d}^d\mathbf{r} \; \mathrm{Cov}(\mathbf{r}) \cdot \mathrm{e}^{-i\mathbf{q}\mathbf{r}} \; .$$

The representation in Fourier modes allows for stationary Gaussian random fields to define an integration measure

$$\int \mathcal{D}g \cdot = \prod_{\mathbf{q} \in \mathbb{R}^d/2} \int_{-\infty}^{\infty} \mathrm{d}(\mathrm{Re}(\tilde{g}(\mathbf{q}))) \int_{-\infty}^{\infty} \mathrm{d}(\mathrm{Im}(\tilde{g}(\mathbf{q}))) \; \mathbb{P}[\tilde{g}(\mathbf{q})] \cdot \; ,$$

[4] The covariance function must be positive definite.

where the product runs over a (discretized) half space of wave vectors $\mathbf{q} \in \mathbb{R}^d/2$, where only a half space is needed, because the Gaussian random field is real valued and $\tilde{g}(-\mathbf{q}) = \tilde{g}^*(\mathbf{q})$, see also the spectral representation of random fields, e.g., in Ref. [10].

This integration measure allows to straightforwardly calculate for a functional $\mathcal{M}[g(\mathbf{r})]$ of the random field $g(\mathbf{r})$ the expectation

$$\langle \mathcal{M} \rangle = \int \mathcal{D}g \; \mathcal{M}[g(\mathbf{r})]$$

and the probability density that the functional takes on a value m_0

$$f_{\mathcal{M}}(m_0) = \int \mathcal{D}g \; \delta(m_0 - \mathcal{M}[g(\mathbf{r})]) \tag{2.2}$$

using the Dirac δ-distribution.

The structure of the level sets of the isotropic Gaussian random field quantified by geometric functionals is intensively studied, and some insights could be gained [e.g. 8, 10, 288, 457]. Considerably less studies have been devoted to the anisotropic Gaussian random fields, which are needed to model anisotropic porous media [77] or for stochastic partial differential equations including the stochastic heat and wave equations, see also Ref. [518] and references therein.

Anisotropic Gaussian random fields are also important for nonisotropic quantum systems [484], modeling sea-waves [485], or reflection and diffraction models [437]. The anisotropy is also connected to vortices in the random field [146].

The Gaussian random wave model

The Gaussian random wave model [69] is an exemplary class of Gaussian random fields especially important in physics. For example, Gaussian random waves solve the time-independent Helmholtz wave equation [116] and are physically well-justified models for chaotic quantum systems [45, 484]. Moreover, they are connected to optical speckle patterns [157, 158].

The basic idea is simply to superimpose plane waves with random phases and random orientation of the wave vector. At each position $\mathbf{r}$, the functional values of the random waves are independently and identically distributed random variables. Because of the central limit theorem, the superposition is approximately a Gaussian random wave for a large number N_w of random waves.

$$g(\mathbf{r}) = \sqrt{\frac{2}{N_w}} \sum_{i=1}^{N_w} \cos(\mathbf{k}_i \cdot \mathbf{r} + \eta_i) \; , \tag{2.3}$$

where the random phases η_i are uniformly distributed on $[0, 2\pi)$ and $\|\mathbf{k}_i\| \equiv 1$. The distribution of the orientation of $\mathbf{k}_i$ on the unit sphere defines the anisotropy of the system, i.e., either isotropic for a uniform distribution on $\mathbb{S}^{d-1}$ or anisotropic for an orientation bias. In the two-dimensional simulations of the Gaussian random field below, I parametrize the orientation by the angle θ_i between $\mathbf{k}_i$ and the x-axis and use $\mathcal{P}(\theta_i)$ from Eq. (2.1) and Fig. 2.2 as an orientation distribution, where the varying degree of anisotropy is quantified by the standard deviation σ_θ of the distribution. The number of random waves is chosen to be $N_w = 100$.

The Fourier transform of the covariance function $\tilde{\sigma}^2(\mathbf{q})$ is according to the Wiener-Khinchin theorem given by the mean of the power density spectrum $S(q)$. The latter can be calculated for a single cosine function $a\cos(\mathbf{k}\cdot\mathbf{r})$ in the limit of an infinite system size as the absolute square of the Fourier transform which is restricted to the observation window and divided by the size of the observation window, which yields, see Ref. [204],

$$S(q) = a^2\pi^2(\delta(\mathbf{q}+\mathbf{k}) + \delta(\mathbf{q}-\mathbf{k})) \ .$$

$\tilde{\sigma}^2(\mathbf{q})$ is in the limit of infinitely many random waves thus given by

$$\tilde{\sigma}^2(\mathbf{q}) = 2\pi^2\langle \lim_{N_w\to\infty} \frac{1}{N_w}\sum_{i=1}^{N_w}(\delta(\mathbf{q}+\mathbf{k}) + \delta(\mathbf{q}-\mathbf{k}))\rangle \ . \tag{2.4}$$

From the choice of the distribution of the wave vectors, i.e., $\|\mathbf{k}_i\| \equiv 1$ and θ_i drawn from $\mathcal{P}(\theta_i)$, follows the Fourier transform of the covariance function

$$\tilde{\sigma}^2(\mathbf{q}) = 2\pi^2 \cdot \delta(\|\mathbf{q}\| - 1) \cdot Z_\alpha \,|\cos(\theta)|^\alpha \ ,$$

where $\theta \in [-\pi, \pi)$ is the angle between q and the x-axis; note that in contrast to the orientation distribution from Eq. (2.1), $Z_\alpha\,|\cos(\theta)|^\alpha$ is defined for all directions, and it is normalized to two, because every wave $\mathbf{k}$ contributes in both directions $\mathbf{k}$ and $-\mathbf{k}$ in Eq. (2.4).

2.2 Fabric tensors

Fabric tensors characterize the complex microstructure in both natural and man-made materials [483], e.g., in geology [344, 345], granular matter [229, 346], foams [207, 250], rough surfaces [136], solids with cracks [227, 424], and trabecular bone [218, 347, 350]. The aim is to gain physical insights via a better understanding of the geometrical properties, e.g., relate the mechanical properties of the material to its microstructure [344–346, 460, 528]. In medicine, an especially important example is to predict the mechanical stability or elasticity of

trabecular or cancellous bone by analyzing its complex structure [383, 508, 509]; see Fig. 1.2.

Scalar measures, i.e., rotation and translation invariant quantities like the volume fraction of the material or the area of the interface, can accurately describe isotropic media. However, for anisotropic heterogeneous materials, like trabecular bone, the so-called fabric tensors are needed to both determine the preferred orientations and the strength of the anisotropy.

For a better understanding of tensorial physical properties, such as elasticity tensors, via a geometrical analysis, sensitive tensorial shape measures are needed. These should be both robust against noise in experiments and sensitive to allow for an accurate characterization of the anisotropy. Which fabric tensors are appropriate?

One of the first measures of anisotropy has been the so-called mean intercept length (MIL) tensor, by now a common approach to quantify the anisotropy of composite materials [107, 347].

The MIL analysis is applied in metallography [106, 179, 449], geology [228, 262, 263], mineralogy [241], food science [117, 133, 275, 364, 517], and biomechanics [107, 395]. Especially in medicine, it has become a standard tool to characterize the structure of bone [32, 97, 218, 240, 512], which can be used for a diagnosis and a better understanding of the effects of osteoporosis [102, 196, 252]; compare Figs. 1.2(a) and 1.2(b). The MIL fabric tensor has been used to relate the microstructure to the elasticity or compliance of the material to predict the mechanical properties [108, 164, 194, 195, 226, 350, 477, 478].

To analyze a heterogeneous medium, parallel test lines are drawn through the sample intersecting with the interface between the two phases; see Fig. 2.3. An intercept is an isolated segment within one phase. The MIL $\bar{L}$ is the mean length of these intercepts [483]; to be more precisely, the mean length of typical intercept in the Palm sense [e.g. 448]. If the MIL varies with the orientation of the test lines, the medium has an anisotropic distribution of the interface. The orientation of a test line is either described by a unit vector $\mathbf{u}$ along the test line or by the angle ω between the test lines and the x-axis of the system. Usually, the polar diagram of the MIL $\bar{L}(\omega)$ is plotted[5], i.e., the MIL for each orientation, where a deviation from a circle implies interfacial anisotropy; see Fig. 2.3.

In 1974, Whitehouse examined the structure of trabecular bone [512] and found empirically that the polar diagram of the MIL $\bar{L}(\omega)$ is similar to an ellipse. The standard MIL analysis fits an ellipse to the MIL figure which can then be

[5] For application of the MIL analysis to digital images see Refs. [218, 240, 262, 263].

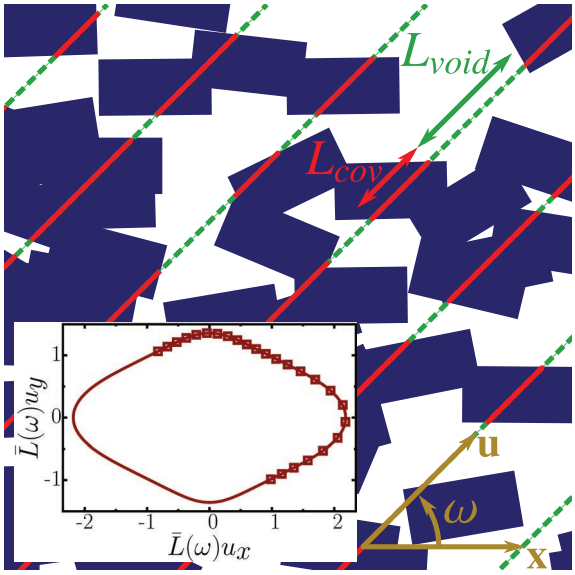

Figure 2.3: The mean intercept length (MIL) is the mean length of the intercepts of test lines lying either within the void or the covered phase of the Boolean model: $\bar{L} = (\bar{L}_{cov} + \bar{L}_{void})/2$. The MIL is a function of the angle ω between the test line and the x-axis and usually plotted in a polar diagram (inset); see Fig. 2.9(a) for more details. In general, the MIL figure is not an ellipse.

represented by a tensor [186]

$$\bar{L}^{-2}(\omega) = \mathbf{u}^t \mathbf{M} \mathbf{u} \tag{2.5}$$

with $\mathbf{u} = (\cos(\omega), \sin(\omega))^t$. The second-rank tensor $\mathbf{M}$ is positive definite, so there exists exactly one positive definite square root, which is indicated by $\sqrt{\mathbf{M}}$ in the following. The MIL tensor is then often also defined by [107]

$$\mathbf{H} = \left(\sqrt{\mathbf{M}}\right)^{-1} . \tag{2.6}$$

To gain insight into the orientation dependence of the MIL and to test this assumption, I calculate in this thesis both analytically and numerically the MIL of anisotropic Boolean models. I find that the MIL figure is in general not an ellipse, and the MIL tensor is, strictly speaking, not a tensor; see Fig. 2.3. A fit of an ellipse to the MIL figure would induce an unknown systematic error and, e.g., strongly depend on the sampling of the test lines.

I analytically derive the MIL, discuss its orientation and intensity dependence, and show that the MIL is in general significantly different from an ellipse (see Eq. (2.23) and Figs. 2.3, 2.9(b), and 2.14). Below, I also show and discuss further disadvantages of the MIL as an anisotropy measure:

1. standard line or intersection counting techniques to determine the MIL are time-consuming, sensitive to noise, and depend on variations in the implementation [327, 430],

2. higher than second-rank tensors are sometimes needed to characterize the anisotropy and predict, e.g., mechanical properties [227, 424],

3. the MIL analysis implicitly assumes an additional two-fold rotation axis in the heterogeneous material [512],

4. the MIL analysis is limited to interfacial anisotropy [327, 347, 349],

5. even systems with an obvious anisotropy in the interface can appear perfectly isotropic w.r.t. the MIL; see Figs. 2.12 and 2.14.

While the MIL analysis was among the first measures of anisotropy and is today a standard tool for characterizing anisotropy in medical bone morphology, its inherent drawbacks call for a more sensitive and especially systematic approach to shape quantification.

I show how a correction of the ill-definition of the MIL analysis naturally leads to using instead the much more general family of Minkowski tensors from integral geometry [396, 400].

The Minkowski tensors are sensitive, robust, and comprehensive shape measures, and in particular, they allow for a systematic shape analysis w.r.t. different geometrical aspects, like volume or interface. They can be interpreted as moment tensors of the volume or interface distributions and have already been successfully applied to many physical systems as sensitive measures of anisotropy [406, 408]. Free software is available; see Section 2.4.3.

2.3 Mean intercept length of Boolean models

To determine the MIL of a Boolean model, parallel test lines are drawn through the sample, as described above, see Fig. 2.3. The length of the intercepts of the test line within the void or covered phase are denoted by L_{void} or L_{cov}, respectively.

The MIL is the mean length of these intercepts

$$\bar{L} = \frac{\bar{L}_{void} + \bar{L}_{cov}}{2} , \tag{2.7}$$

which is equal to the length of the test line divided by the number of intercepts [107, 347]. Another common normalization [263, 327] is $\bar{L} = \bar{L}_{void} + \bar{L}_{cov}$, which corresponds to always combining an intercept in the covered phase with the following intercept in the void phase or, in other words, counting the intersections only if the line leaves the covered phase and enters the void phase or vice versa.

The MIL of isotropic Boolean models is intensively studied and well known, e.g., see Refs. [178, 386, 460]. For convex grains, it is simply a function of the

porosity, the intensity, and the mean perimeter or surface area of a single grain, or more general, it is related to the specific surface of an isotropic two-phase medium [460]. Also for anisotropic and rather general Boolean models, the MIL has been derived, e.g., see Refs. [178, 321, 322]. The distribution of the length of a typical intercept can be related to problems from queuing theory [454], or to the linear contact distribution [448], which is also called lineal path function [460], see also Ref. [209].

In my calculations, I provide another concise analytic derivation and discussion of the MIL of Boolean models in order to provide especially for applied scientists an easier insight into which information is contained in the MIL. I especially focus on the functional form of the MIL as a function of the orientation of the test lines and check the widespread assumption that a large number of objects not all parallel to each other produce on average an elliptic global MIL figure [263]. Therefore, I also compare explicit formulas for the parametric Boolean model from Section 2.1.1 to simulation results.

I analytically calculate the MIL of Boolean models in any dimension d. Often the MIL analysis is applied to planar sections [186, 347], but modern tomography also provides three-dimensional data, of which the MIL can directly be estimated for all orientations on the unit sphere [240, 275]. The numerical simulations are performed in two dimensions. Here, I derive the MIL for anisotropic Boolean models using convex grains with a fixed shape, but differently anisotropic orientation distributions. However, the calculations could easily be generalized to arbitrary grain distributions.

2.3.1 Analytic calculation for anisotropic Boolean models

In order to calculate the MIL, I need a more formal definition of the Boolean model. The random point pattern, i.e., uncorrelated points placed randomly in space, is formally defined as a Poisson point process in d-dimensional Euclidean space $\mathbb{R}^d$ of intensity ρ. To each point $\mathbf{r}_i \in \mathbb{R}^d$ in the point pattern a convex grain $K(\mathbf{r}_i)$ is attached. I want to study the geometric properties of the Boolean model, i.e., their union

$$\mathcal{B} := \bigcup_i K(\mathbf{r}_i) \ .$$

Whereas the point pattern and thus the position of the grains is homogeneously distributed, I allow for an arbitrarily anisotropic orientation distribution $\mathcal{P}(\Omega)$ of K_i, where Ω denotes all necessary angles to fix orientation of K_i. In 2 D, Ω is simply the angle θ between the main axis of the grain and the x-axis; in 3 D, Ω is the polar and azimuthal angle of the direction of the main axis. If $\mathcal{P}(\Omega)$ is a uniform distribution, the Boolean model is said to be isotropic, but if the orientation

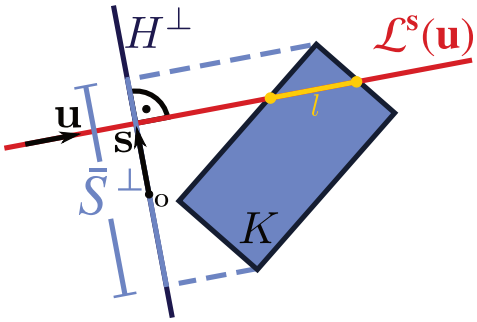

Figure 2.4: A single grain K is intersected by a line $\mathcal{L}^{\mathbf{s}}$ along the direction $\mathbf{u}$. The length of the intercept (endpoints marked by dots; colored yellow) is l. The position of the line is described by the perpendicular distance vector $\mathbf{s}$ to the origin $\mathbf{O}$. The line $H^\perp$ is the line perpendicular to $\mathcal{L}^{\mathbf{s}}$ which contains the origin $\mathbf{O}$. The set K is projected (dashed lines; colored blue) onto this one-dimensional hyperplane; the projection is denoted by $K^\perp_{\mathbf{u}}$.

distribution is in the extreme case a δ-distribution, the grains will be perfectly aligned. Any other degree of orientation bias can be adjusted by choosing $\mathcal{P}(\Omega)$.

The MIL is determined by drawing one-dimensional test lines. Their orientation can be parametrized by a unit vector $\mathbf{u}$ along the line and their position by the perpendicular distance vector $\mathbf{s} \perp \mathbf{u}$ to the origin $\mathbf{O} \in \mathbb{R}^d$. Here, I denote such a test line by $\mathcal{L}^{\mathbf{s}}(\mathbf{u})$; see Fig. 2.4.

A test line will intersect a given grain K if and only if it intersects the projection of the grain onto a hyperplane perpendicular to the test line—see Fig. 2.6—simply by definition of a projection: a line between the projection $\mathbf{p_z}$ and the original point $\mathbf{z}$ in K must be perpendicular to the hyperplane, i.e., a line in direction $\mathbf{u}$. In 2 D, the hyperplane is simply a line perpendicular to the test line; in 3 D, it is a two-dimensional plane perpendicular to the test line. The $(d-1)$-dimensional hyperplane which contains the origin and is perpendicular to $\mathcal{L}^{\mathbf{s}}(\mathbf{u})$ is denoted by $H^\perp(\mathbf{u})$ and the perpendicular projection of the grain K by $K^\perp_{\mathbf{u}}$; see Fig. 2.4.

Single grain characteristics

Before I derive the global average for the union of all grains, I first need to derive the average characteristics of a single grain K. The simplest geometric property is its volume $V[K]$ or short V; in 2 D this is the area of the grain K; in arbitrary dimension this is the Lebesgue measure.

The length of an intercept $L[K \cap \mathcal{L}^{\mathbf{s}}(\mathbf{u})]$, i.e., the length of the intersection of K with the test line $\mathcal{L}^{\mathbf{s}}(\mathbf{u})$, depends on the position $\mathbf{s}$ of the test line. If a random line with orientation $\mathbf{u}$ is drawn through the sample such that it intersects the grain K, i.e., all such $\mathbf{s}$ are equally probable, then the probability density function of the length l of an intercept is proportional to the integral over all points $\mathbf{s}$ on the hyperplane $H^\perp$ for which $L[K \cap \mathcal{L}^{\mathbf{s}}(\mathbf{u})]$ is equal to l:

$$P_{\mathbf{u}}[l; K] \propto \int_{H^\perp} \mathrm{d}\mathbf{s}\ \delta\left(l - L[K \cap \mathcal{L}^{\mathbf{s}}(\mathbf{u})]\right) \tag{2.8}$$

for $0 < l \leq l_{max}(\mathbf{u})$, where l_{max} is an upper bound of the intercept length, the length of the projection of K onto the line $\mathcal{L}^{\mathbf{s}}(\mathbf{u})$. Note that the length $l_{max}(\mathbf{u})$ is only a function of the orientation of the test lines, but does not depend on their position $\mathbf{s}$.

Because I here consider only test lines which intersect the grain K, the normalization constant[6] in Eq. (2.8) is given by the integral over such test lines, i.e., over all positions $\mathbf{s}$ for which $L[K \cap \mathcal{L}^{\mathbf{s}}(\mathbf{u})] > 0$. As discussed above this is by definition equal to an integral over the perpendicular projection $K^{\perp}_{\mathbf{u}}$. I denote by $S^{\perp}[\mathbf{u}; K]$ the size of the perpendicular projection $K^{\perp}_{\mathbf{u}}$: in 2 D this is its length; in 3 D, it is the area of the projection; and in arbitrary dimension d, it is proportional to the so-called intrinsic volume [400] V_{d-1} of $K^{\perp}_{\mathbf{u}}$.

The distribution of the intercept length l in a single grain K with lines along $\mathbf{u}$ is thus given by

$$P_{\mathbf{u}}[l; K] = \frac{1}{S^{\perp}[\mathbf{u}; K]} \int_{H^{\perp}} \mathrm{d}\mathbf{s}\ \delta\left(l - L[K \cap \mathcal{L}^{\mathbf{s}}(\mathbf{u})]\right) \ . \tag{2.9}$$

Now, I can calculate the mean length $L^{\parallel}[\mathbf{u}; K]$ of an intercept in a single grain K. By exchanging the order of integration and applying iterated Fubini's theorem[7], I derive

$$\begin{aligned} L^{\parallel}[\mathbf{u}; K] &= \int_0^{l_{max}} dl\ P_{\mathbf{u}}[l; K] \cdot l \\ &= \frac{1}{S^{\perp}[\mathbf{u}; K]} \int_{H^{\perp}} \mathrm{d}\mathbf{s}\ L[K \cap \mathcal{L}^{\mathbf{s}}(\mathbf{u})] \\ &= \frac{V[K]}{S^{\perp}[\mathbf{u}; K]} \ . \end{aligned} \tag{2.10}$$

Figure 2.5 gives an intuitive explanation for this formula.

So far, I have considered a grain K with a fixed orientation, for which I have defined the size $S^{\perp}[\mathbf{u}; K]$ of the perpendicular projection $K^{\perp}_{\mathbf{u}}$ and derived the mean length of intercepts $L^{\parallel}[\mathbf{u}; K]$.

By construction, these quantities depend on the relative orientation between the grain K and the direction $\mathbf{u}$ of the test lines[8]. The grains are randomly oriented following the distribution $\mathcal{P}(\Omega)$. I therefore define the orientational averages of

[6] A normalization of the distribution of the intercept lengths l is needed such that $\int_0^{l_{max}} dl\ P_{\mathbf{u}}[l; K] = 1$.

[7] The integral over the projection weighted by the length of the intercept is equal to the volume $V[K]$ of the grain K.

[8] In contrast to scalar measures like the volume.

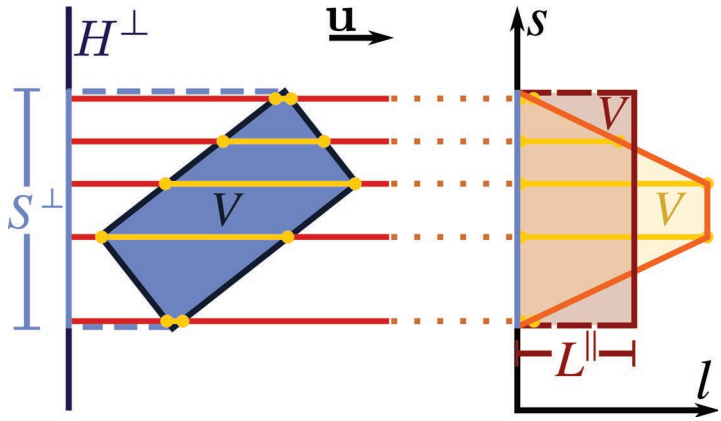

Figure 2.5: Intuitive explanation of Eq. (2.10): a grain K with area V is projected onto the plane $H^\perp$ perpendicular to the unit vector $\mathbf{u}$; the size of the projection is $S^\perp$. Test lines in direction of $\mathbf{u}$ intersect the grain (yellow bars in figure on left-hand side). The length l of these intercepts varies with the position s of the test lines (orange line in figure on right-hand side). $L^\parallel$ is the average of this length, i.e., the integral of the curve $l(s)$ divided by the size of the projection $S^\perp$. The area enclosed by this curve is the area V of the grain, because the line segments were moved to the s-axis but did not change their length; therefore, $L^\parallel = V/S^\perp$. An alternative geometric construction follows the rule that the area below the red line indicating $L^\parallel$ must be the same as below $l(s)$, i.e., $L^\parallel \cdot S^\perp = V$.

the perpendicular projection and the mean length of intercepts:

$$\bar{S}^\perp[\mathbf{u}] = \int_{\mathbb{S}^{d-1}} \mathrm{d}\Omega\, \mathcal{P}(\Omega)\; S^\perp[\mathbf{u}; K]\;, \tag{2.11}$$

$$\begin{aligned} \bar{L}^\parallel[\mathbf{u}] &= \int_{\mathbb{S}^{d-1}} \mathrm{d}\Omega\, \mathcal{P}(\Omega)\; L^\parallel[\mathbf{u}; K] \\ &= V \int_{\mathbb{S}^{d-1}} \mathrm{d}\Omega\, \mathcal{P}(\Omega) \frac{1}{S^\perp[\mathbf{u}; K]} \neq \frac{V}{\bar{S}^\perp[\mathbf{u}]}\;. \end{aligned} \tag{2.12}$$

While for a fixed grain the mean length of an intercept $L^\parallel[\mathbf{u}; K]$ is proportional to the inverse of the size of the perpendicular projection $S^\perp[\mathbf{u}; K]$, this does not hold for the orientational averages of a single grain, which is important in following calculation.

In the isotropic case, the average size of the perpendicular projection of a convex grain $\bar{S}^\perp$ is proportional to its surface area $S[K]$ (or perimeter in two dimensions) [400].

Induced one-dimensional Boolean model

In the previous section, I have derived the average characteristics of a single grain K. Now, I determine the mean intercept length for the union of all grains $\mathcal{B}$, that

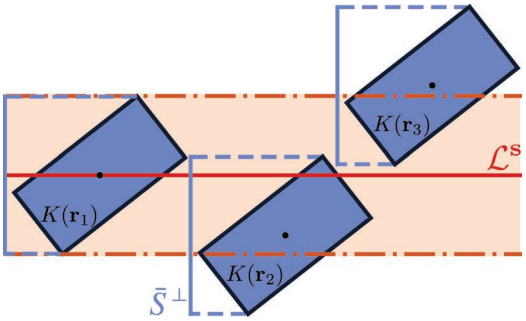

Figure 2.6: The test line $\mathcal{L}^{\mathbf{s}}$ intersects the grains $K(\mathbf{r}_1)$ and $K(\mathbf{r}_2)$ but not grain $K(\mathbf{r}_3)$. Accordingly, the perpendicular projections $K_{\mathbf{u}}^{\perp}$ of the first two grains intersect the line $\mathcal{L}^{\mathbf{s}}$ in contrast to the projection of $K(\mathbf{r}_3)$. Therefore, the grain K with fixed orientation intersects the line if and only if its center (marked by a dot) lies within the highlighted band (between the dash-dotted lines; colored orange). The width of the band is by definition equivalent to the size $S^{\perp}[\mathbf{u}; K]$ of the perpendicular projection.

is, the Boolean model. I intersect the one-dimensional test line $\mathcal{L}^{\mathbf{s}}(\mathbf{u})$ with the d-dimensional realization of the Boolean model $\mathcal{B} = \bigcup_i K(\mathbf{r}_i)$:

$$\mathcal{B}_{\mathbf{u}}^{(1)} := \mathcal{L}^{\mathbf{s}}(\mathbf{u}) \cap \mathcal{B} \ .$$

In contrast to the previous section which considered only a single grain, here a collection of many particles with different orientations is analyzed. The union of intercepts $\mathcal{B}_{\mathbf{u}}^{(1)}$ is again a Boolean model in one-dimension [299]: random intersections with single grains are distributed along the test line; they are overlapping and form clusters; their unions are the final intercepts of the test line with the Boolean model; see Fig. 2.7.

Notice the two different types of intercepts: first, the intersections of the test line with a single grain K, which I call "segment" (marked by $*$ in Fig. 2.7). They can be seen as the one-dimensional grains in the one-dimensional Boolean model with varying length $L[K \cap \mathcal{L}^{\mathbf{s}}(\mathbf{u})]$. Second, an intercept in the grain phase of the Boolean model formed by the union of a cluster of segments (marked by $\star$ in Fig. 2.7). Be reminded that their length is denoted by L_{cov}. L_{void} is the length of the void intercepts in the one-dimensional model along the test line $\mathcal{L}^{\mathbf{s}}(\mathbf{u})$. Their average intercept lengths directly determine the MIL $\bar{L}$, which I want to derive.

However, I first need to determine the intensity of the segments in the one-dimensional Boolean model and the distribution of their length.

The intensity $\rho_{\mathbf{u}}^{(1)}$ of the one-dimensional Boolean model $\mathcal{B}_{\mathbf{u}}^{(1)}$ is the average number of segments per unit length. The probability for a grain to intersect the line depends on the orientation of the grain. Therefore, the average number of intercepts varies for different orientations.

I first determine the intensity $\rho_{\mathbf{u}}^{(1)}[K]$ for a fixed grain K, i.e., the average number of segments per unit length if all grains are decorated with a grain K with the same orientation; see Fig. 2.6. As discussed above, only those grains intersect the line for which the projection intersects the line. From Fig. 2.6 can be seen

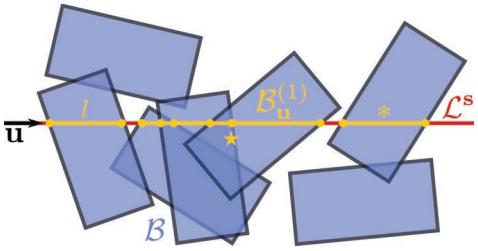

Figure 2.7: The section of a test line $\mathcal{L}^{\mathbf{s}}(\mathbf{u})$ with the Boolean model $\mathcal{B}$ is again a one-dimensional Boolean model $\mathcal{B}_{\mathbf{u}}^{(1)}$. The intercepts of the single rectangles are highlighted (colored yellow), their endpoints are marked by a dot. They overlap like the original two-dimensional grains (colored blue).

that this is equivalent to the condition that the center of a grain falls in a region which extends parallel to the line and which has a width equal to the size of the perpendicular projection. The average number of grains in such a region with length t parallel to the line is $\rho \cdot S^{\perp} \cdot t$ by definition of the intensity ρ, and the average number of intersections per unit length is therefore

$$\rho_{\mathbf{u}}^{(1)}[K] = \rho S^{\perp}[\mathbf{u}; K] \; . \tag{2.13}$$

If the grain orientation is not fixed, but their orientations are distributed according to $\mathcal{P}(\Omega)$, the intensity $\rho_{\mathbf{u}}^{(1)}$ of the one-dimensional Boolean model is simply the orientational average of Eq. (2.13):

$$\rho_{\mathbf{u}}^{(1)} = \int_{\mathbb{S}^{d-1}} \mathrm{d}\Omega \, \mathcal{P}(\Omega) \; \rho_{\mathbf{u}}^{(1)}[K] = \rho \bar{S}^{\perp}[\mathbf{u}] \; . \tag{2.14}$$

Obviously, not only the length of the intercepts L_{cov} varies, but also the length $L[K \cap \mathcal{L}^{\mathbf{s}}(\mathbf{u})]$ of the segments, i.e., the one-dimensional grains. What is the probability density function $P_{\mathbf{u}}^{(1)}[l]$ of the length l of such a segment?

Only if the grains have a fixed orientation, the length l of a segment follows the probability density function $P_{\mathbf{u}}^{(1)}[l] = P_{\mathbf{u}}[l; K]$ given by Eq. (2.9). However, if the orientation of the grains is drawn from a nontrivial distribution $\mathcal{P}(\Omega)$, the density function will be different from only an orientational average of $P_{\mathbf{u}}[l; K]$. In the previous section, I have considered a given grain K and determined the average length of intersections with lines hitting the grain. Here, the line is given and I ask for the distribution of the lengths of the intersections with all grains hitting the line. This distribution is different because grains with different orientations are differently probable to hit the line. The distribution must be weighted by the fraction $\rho_{\mathbf{u}}^{(1)}[K]/\rho_{\mathbf{u}}^{(1)}$ of grains K with orientation Ω among all grains intersecting the line; see Eqs. (2.13) and (2.14).

$$\begin{aligned} P_{\mathbf{u}}^{(1)}[l] &= \int_{\mathbb{S}^{d-1}} \mathrm{d}\Omega \, \mathcal{P}(\Omega) \cdot \frac{\rho_{\mathbf{u}}^{(1)}[K]}{\rho_{\mathbf{u}}^{(1)}} \cdot P_{\mathbf{u}}[l; K] \\ &= \frac{1}{\bar{S}^{\perp}[\mathbf{u}]} \int_{\mathbb{S}^{d-1}} \mathrm{d}\Omega \, \mathcal{P}(\Omega) \int_{H^{\perp}} \mathrm{d}\mathbf{s} \; \delta \left(l - L[K \cap \mathcal{L}^{\mathbf{s}}(\mathbf{u})] \right) \end{aligned}$$

Therefore, also the mean length of a segment $\bar{L}^{(1)}[\mathbf{u}]$, i.e., of the intersection of a grain with the line is different from the mean length of an intercept of a line with a grain $\bar{L}^{\parallel}[\mathbf{u}]$ given by Eq. (2.12). Similar to the calculation in Eq. (2.10), I get

$$\begin{aligned}\bar{L}^{(1)}[\mathbf{u}] &:= \int_0^\infty dl\ P_{\mathbf{u}}^{(1)}[l] \cdot l \\ &= \frac{1}{\bar{S}^{\perp}[\mathbf{u}]} \int_{\mathbb{S}^{d-1}} \mathrm{d}\Omega\ \mathcal{P}(\Omega) \int_{H^{\perp}} \mathrm{d}\mathbf{s}\ L[K \cap \mathcal{L}^{\mathbf{s}}(\mathbf{u})] \\ &= \frac{V}{\bar{S}^{\perp}[\mathbf{u}]}\ .\end{aligned} \tag{2.15}$$

Note that the mean length of a segment $\bar{L}^{(1)}[\mathbf{u}]$ is different from the single grain characteristic $\bar{L}^{\parallel}[\mathbf{u}]$, i.e., the mean length of a segment conditional on the fact that the line hits the grain.

This difference $\bar{L}^{\parallel}[\mathbf{u}] \neq \bar{L}^{(1)}[\mathbf{u}]$ can be illustrated by a simple example of rectangles with only two possible orientations: with equal probability a rectangle is either oriented along (↔) or perpendicular (↕) to $\mathbf{x}$, see Fig. 2.8; the side lengths of a rectangle are $a = 2p$ or $b = 2q$. Then, for a test line along $\mathbf{x}$ the mean size of the projection $\bar{S}^{\perp} = {}^{(a+b)}/_{2}$ is by coincidence equal to the mean length $\bar{L}^{\parallel}$ of an intercept conditional on the line hitting the grain in Eq. (2.12). However, the probability to hit the test line is larger for the vertically (↕) than for the horizontally (↔) aligned grains. According to Eq. (2.15) the mean length of a segment is therefore

$$\bar{L}^{(1)}[\mathbf{u}] = \frac{2ab}{a+b} = \frac{2}{\frac{1}{a} + \frac{1}{b}}\ ,$$

which is the harmonic mean of the side lengths and smaller than the arithmetic mean $\bar{L}^{\parallel} = {}^{(a+b)}/_{2}$.

I recall that for a fixed grain K the mean intercept length $L^{\parallel}[\mathbf{u}; K]$ is the volume of the grain divided by the size of the perpendicular projection $S^{\perp}[\mathbf{u}; K]$, see Eq. (2.10), but this does not hold for the orientational averages $\bar{L}^{\parallel}[\mathbf{u}]$ and $\bar{S}^{\perp}[\mathbf{u}]$; see Eq. (2.12). Instead, the volume divided by the average size of the perpendicular projection is equal to the mean length of a segment $\bar{L}^{(1)}[\mathbf{u}]$. Below it is shown that the MIL is therefore not a function of $\bar{L}^{\parallel}[\mathbf{u}]$, but of the average size of the perpendicular projection $\bar{S}^{\perp}[\mathbf{u}]$.

In other words, I must not average over the mean length of an intercept with a grain $L^{\parallel}[\mathbf{u}; K]$, but I must instead average over its inverse ${}^{S^{\perp}[\mathbf{u};K]}/_{V}$ to derive the inverse of the mean length of a segment $\bar{L}^{(1)}[\mathbf{u}]^{-1} = \frac{\bar{S}^{\perp}[\mathbf{u}]}{V} \neq (\bar{L}^{\parallel}[\mathbf{u}])^{-1}$.

The average length of a segment $\bar{L}^{(1)}[\mathbf{u}]$ can also be seen as the average size of the one-dimensional grains in $\mathcal{B}_{\mathbf{u}}^{(1)}$. Together with its intensity $\rho_{\mathbf{u}}^{(1)}$ from Eq. (2.14), I can now calculate directly the void probability of the one-dimensional Boolean

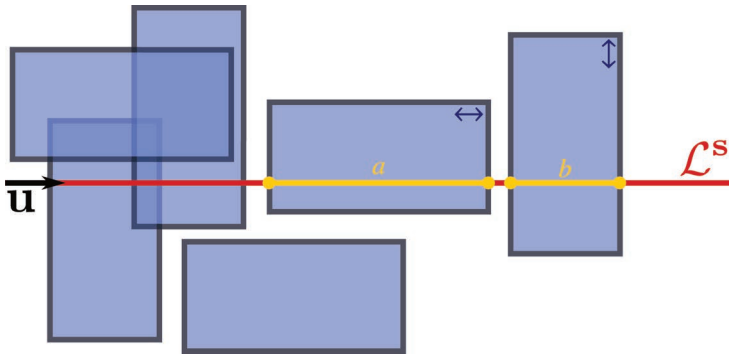

Figure 2.8: Illustration to explain the difference between the mean length of a segment $\bar{L}^{(1)}[\mathbf{u}]$, see Eq. (2.15). It includes the probability for a grain to hit the line $\mathcal{L}^{\mathbf{s}}(\mathbf{u})$, and the mean length of an intercept of a single grain with the test line conditional on the line hitting the grain: $\bar{L}^{\parallel} = (a+b)/2$, see Eq. (2.12). With equal probability a rectangle is either oriented along (↔) or perpendicular (↕) to $\mathbf{u}$. However, a vertically aligned rectangle (with a smaller segment length) is more likely to hit the line. Therefore, the mean length of a segment $\bar{L}^{(1)}[\mathbf{u}] = 2/(1/a+1/b)$ is smaller than $\bar{L}^{\parallel}$.

model, i.e., the probability that a random point on the test line $\mathcal{L}^{\mathbf{s}}$ is not covered by any grain. It equals the fraction of length of the void phase, which is, as mentioned above, well known [448] to be $\mathrm{e}^{-\rho_{\mathbf{u}}^{(1)}\bar{L}^{(1)}[\mathbf{u}]}$. Inserting Eqs. (2.14) and (2.15), I see that, as expected, this is equal to the volume fraction of the void phase $\phi_{void} = \mathrm{e}^{-\rho V}$ in the d-dimensional Boolean model.

A crucial step in the calculation of the MIL is the use of another well-known formula [448] for one-dimensional Boolean models, the complementary cumulative distribution function of the void intercepts L_{void} (see Fig. 2.3), i.e., the probability to find voids v larger than L_{void} given the one-dimensional intensity $\rho_{\mathbf{u}}^{(1)}$,

$$\mathrm{Prob}[v > L_{void}] = \mathrm{e}^{-\rho_{\mathbf{u}}^{(1)} L_{void}} \ .$$

The probability density function of the void intercepts L_{void}, i.e., the distribution of the length of the intercepts of the test lines with the void phase, is then simply the negative of the derivative w.r.t. L_{void}:

$$\mathcal{P}_{void}(L_{void}) = \rho_{\mathbf{u}}^{(1)} \cdot \mathrm{e}^{-\rho_{\mathbf{u}}^{(1)} L_{void}}$$

with the normalization $\int_0^\infty \mathrm{d}L_{void}\, \mathcal{P}_{void}(L_{void}) = 1$. Knowing the probability density function of the lengths of the void intercepts finally allows us to determine

the mean length of the void intercepts

$$\begin{aligned}\bar{L}_{void} &= \int_0^\infty \mathrm{d}L_{void}\, \mathcal{P}_{void}(L_{void}) \cdot L_{void} \\ &= \int_0^\infty \mathrm{d}L_{void}\, \mathrm{e}^{-\rho_{\mathbf{u}}^{(1)} L_{void}} \cdot \rho_{\mathbf{u}}^{(1)} L_{void} \\ &= \frac{1}{\rho_{\mathbf{u}}^{(1)}} \int_0^\infty \mathrm{d}z\, \mathrm{e}^{-z} \cdot z = \frac{1}{\rho_{\mathbf{u}}^{(1)}} \,.\end{aligned} \tag{2.16}$$

The mean void length is the inverse of the one-dimensional intensity.

The calculation of the mean length of the void intercepts $\bar{L}_{void}$ is the first part in calculating the total mean intercept length $\mathcal{L}$, which is the average of the mean void length $\bar{L}_{void}$ and the mean length of the intercepts in the grain phase $\bar{L}_{cov}$; see Eq. (2.7).

The distribution of the covered length L_{cov} is much more difficult to calculate explicitly. It is the length between two void regions and consists of many overlapping segments of different length $L[K \cap \mathcal{L}^{\mathbf{s}}(\mathbf{u})]$. If, however, the line $\mathcal{L}^{\mathbf{s}}$ is interpreted as a time axis and the beginning of a segment $K \cap \mathcal{L}^{\mathbf{s}}(\mathbf{u})$ as the arrival of a customer with a job of length $L[K \cap \mathcal{L}^{\mathbf{s}}(\mathbf{u})]$, the one-dimensional Boolean model can be described as a queue [448], where the customers arrive independently of each other and there are infinitely many servers, i.e., no customer has to wait. Queuing theory calls such a system a $M/G/\infty$-queue. Then, the mean covered length L_{cov} can be interpreted as the mean busy time of the server, which is well known in queuing theory [425, 436, 453, 454].

However, because I am here only interested in the mean covered length and not in its distribution, I can in the following express the MIL $\bar{L}$ from Eq. (2.7) by properties of the void phase only, by applying the so-called formula of the mean, and thus explicitly derive the MIL with methods from stochastic geometry.

MIL of anisotropic homogeneous Boolean models

The area fraction ϕ_{void} of the void phase, i.e., the ratio of the area of the void phase and the sum of the areas of void and occupied phase, is equal to the ratio of the length of the intercepts in the void phase and the total length of the test lines, i.e., the sum of the intercepts in both phases [483]. Because every intercept in the void phase is followed by one in the covered phase, the number of intercepts is equal; therefore, the area fraction ϕ_{void} is equal to the ratio of the mean length of the intercepts in the void phase $\bar{L}_{void}$ and the sum of the mean lengths of the

intercepts in both phases $\bar{L}_{void} + \bar{L}_{void}$:

$$\phi_{void} = \frac{\bar{L}_{void}}{\bar{L}_{void} + \bar{L}_{cov}} \ .$$

Inserting the definition of the MIL $\bar{L} = (\bar{L}_{void} + \bar{L}_{cov})/2$ provides a simple relation between the mean void length given in Eq. (2.16) and the MIL [483, 512]:

$$\bar{L} = \frac{\bar{L}_{void}}{2\phi_{void}} \ . \tag{2.17}$$

The area fraction of the void phase in a Boolean model with the volume of a single grain V is well known to be

$$\phi_{void} = \mathrm{e}^{-\rho V} \ . \tag{2.18}$$

Inserting Eqs. (2.14), (2.16), and (2.18) in Eq. (2.17), I find the mean intercept length as a function of the orientation of the test lines along $\mathbf{u}$ for a homogeneous Boolean model with fixed grain shape but arbitrary orientation distribution:

$$\begin{aligned} \bar{L}(\mathbf{u}) &= \frac{\bar{L}_{void}}{2} \cdot \mathrm{e}^{\rho V} = \frac{1}{2\rho_{\mathbf{u}}^{(1)}} \cdot \mathrm{e}^{\rho V} \\ &= \frac{1}{2\rho \bar{S}^{\perp}[\mathbf{u}]} \cdot \mathrm{e}^{\rho V} \\ &= \underbrace{\frac{V}{\bar{S}^{\perp}[\mathbf{u}]}}_{\substack{\text{orientation} \\ \text{dependent}}} \cdot \underbrace{\frac{\mathrm{e}^{\rho V}}{2\rho V}}_{\substack{\text{intensity} \\ \text{dependent}}} \ . \end{aligned} \tag{2.19}$$

Interestingly, the orientational dependence on $\mathbf{u}$ is solely given by the mean length of an intersection of a grain with a given test line

$$\bar{L}^{(1)}[\mathbf{u}] = \frac{V}{\bar{S}^{\perp}[\mathbf{u}]} \tag{2.20}$$

which is the volume V of the grain divided by the orientational average $\bar{S}^{\perp}[\mathbf{u}]$ of the size of the perpendicular projection; see Eqs. (2.11) and (2.15). It is independent of the intensity or area fraction ϕ. The formula for the MIL of Boolean models separates in an orientation and an intensity-dependent factor. The orientation dependent factor includes the volume of the particle so that the unit of $\bar{L}^{(1)}$ is length, like for the MIL $\bar{L}$, while the intensity-dependent factor is a prefactor without unit.

Note that the mean intercept length $\bar{L}^{\parallel}[\mathbf{u}]$ of a single grain from Eq. (2.12) does not enter the expression, as predicted above, because it does not take the probability to hit a line into account. To calculate the MIL, one must therefore not determine the average of $L^{\parallel}[\mathbf{u}; K]$, but of its inverse; see Eq. (2.10).

The complete anisotropy information of the MIL analysis is contained in the single grain characteristic $\bar{S}^{\perp}$ as a function of the orientation of the test lines.

This also means that measuring the global average of the MIL of the union of all grains for all orientations provides access to the average shape of a single grain, in the sense, that it allows us to determine the average size $\bar{S}^{\perp}$ of the projection of a single grain as a function of the orientation of the test lines up to a proportionality constant. If a porous medium is, e.g., built up by the successive addition of inclusions, this single grain characteristic allows for a better understanding of the formation of this porous medium, because the average shape of such an inclusion can be approximated. Moreover, this allows to adjust the Boolean model to the experiment by choosing an appropriate grain distribution.

Equation 2.19 expresses the MIL of the Boolean model, i.e., the union of the grains, by single grains characteristics V and $\bar{S}^{\perp}[\mathbf{u}]$ and the intensity of the particle process, see Section 2.3.1. I thus relate the local to the global properties of the Boolean model.

In the plane, the projected length of a fixed grain K is given by

$$S^{\perp}[\mathbf{u}; K] = |\mathbf{u}^{\perp} \cdot \mathbf{r}^{(1)}(\varphi) - \mathbf{u}^{\perp} \cdot \mathbf{r}^{(2)}(\varphi)| \,, \tag{2.21}$$

where $\mathbf{u}^{\perp}$ is the vector perpendicular to $\mathbf{u}$, and $\mathbf{r}^{(i)}(\varphi) \in \partial K$ are the points on the boundary of K which are projected on the boundary of $K_{\mathbf{u}}^{\perp} \subset H^{\perp}(\mathbf{u})$; in other words, $\mathbf{r}^{(i)}(\varphi)$ are the extrema of $\mathbf{u}^{\perp} \cdot \mathbf{r}(\varphi)$ for all $\mathbf{r}(\varphi) \in \partial K$. For polygons these points are identical to the corners of the polygon. $S^{\perp}[\mathbf{u}; K]$ in Eq. (2.21) then needs to be averaged according to the orientation distribution $\mathcal{P}$ of the grain K to determine $\bar{S}^{\perp}[\mathbf{u}]$. Its inverse inserted in Eq. (2.19) provides an explicit formula for the MIL of the anisotropic Boolean model.

In the following sections, I evaluate the MIL explicitly as a function of the orientation of the test lines the parametric Boolean model with ellipses and rectangles with an orientation bias from Section 2.1.1 and compare the results to numerical estimates.

2.3.2 Monte Carlo sampling

To simulate a sample of a Boolean model, first the number of particles inside the simulation box has to be determined. It is a random number following the Poisson distribution. Its mean value equals the mean number of particles, i.e., the intensity ρ times the size of the simulation box. The particles are then randomly distributed

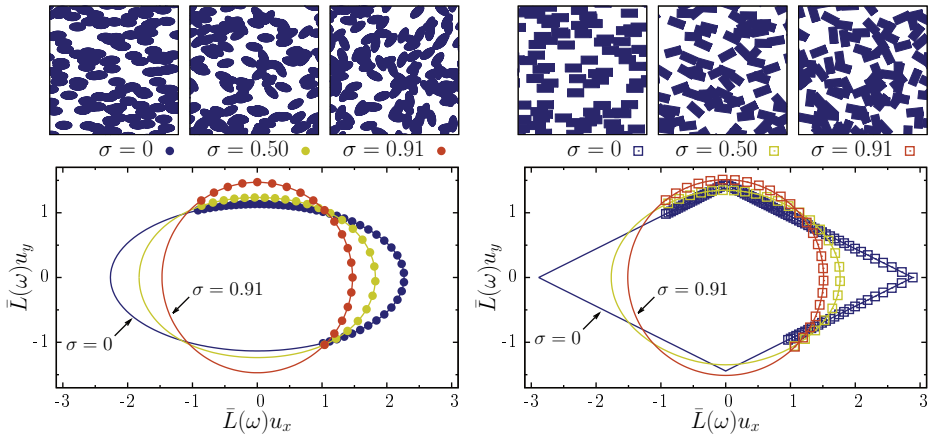

Figure 2.9: Polar plots of the MIL of Boolean models with either (a) ellipses or (b) rectangles for three differently anisotropic samples. The anisotropy is characterized by the standard deviation σ of the orientation distribution: $\sigma = 0$ corresponds to perfect alignment and $\sigma = 0.91$ to an isotropic system. The lines depict the analytic curves given by Eq. (2.19) using Eqs. (2.1)–(2.24). Samples of according Boolean models are shown above; the mean volume fraction is $\phi = 0.5$. Even for a Boolean model with ellipses, the MIL figure for $\sigma = 0.50$ is not an ellipse, although it looks similar to an ellipse (b). The polar plot of the MIL for aligned rectangles is a rhombus (b) and a least square fit of an ellipse to the data is obviously not justified.

inside the quadratic simulation box using periodic boundary conditions. I simulate differently anisotropic[9] Boolean models with either ellipses or rectangles with semiaxes lengths $p = 1$ and $q = 1/2$. The linear size of the simulation box is $50p$.

The Boolean model is then intersected with parallel test lines with constant spacing for different angles ω between the test lines and the x-axis; see Fig. 2.3. The number of intersections within the unit square are counted; the total length of the test lines is divided by the number of intersections; averaging over many samples provides the MIL $\bar{L}$ from Eq. (2.7).

2.3.3 The MIL tensor of a Boolean model is not a tensor

The analytic calculation of the MIL for Boolean models with rectangles or ellipses as a function of the orientation ω of the test lines (see Fig. 2.3) according to Eq. (2.19) is straightforward: the length of the perpendicular projection is for a

[9] The anisotropy parameter is either $\alpha = 0$ ($\sigma = 0.91$), $\alpha = 3$ ($\sigma = 0.50$), or $\alpha = \infty$ ($\sigma = 0$).

single ellipse E or rectangle R with orientation θ given by

$$S^{\perp}[\omega; \text{ellipse}] = 2\sqrt{p^2 \sin^2(\omega-\theta) + q^2 \cos^2(\omega-\theta)} \tag{2.22}$$

$$S^{\perp}[\omega; \text{rectangle}] = 2\left(p \sin|\omega-\theta| + q \cos|\omega-\theta|\right) , \tag{2.23}$$

respectively. The average over the orientation distribution is

$$\bar{S}^{\perp}[\omega] = \int_{-\pi/2}^{\pi/2} \mathrm{d}\theta \, \mathcal{P}(\theta) \cdot S^{\perp}[\omega; K] \, . \tag{2.24}$$

For $\sigma = 0$ ($\alpha = \infty$) the orientation distribution $\mathcal{P}(\theta)$ is a δ-distribution and $\bar{S}^{\perp}[\omega]$ is equal to $S^{\perp}[\omega; K]$ with $\theta = 0$. For $\sigma = \pi/\sqrt{12}$ ($\alpha = 0$) the integral over the isotropic orientation distribution can be solved explicitly; for rectangles, $\bar{S}^{\perp}[\omega] = \frac{4}{\pi}(p+q)$ and for ellipses, $\bar{S}^{\perp}[\omega] = \frac{4}{\pi} pE[1 - q^2/p^2]$ with $E[m] = \int_0^{\pi/2} \mathrm{d}\varphi \, \sqrt{1 - m \sin^2\varphi}$ the complete elliptic integral of the second kind.

Inserting Eq. (2.24) and the area of an ellipse ($V[E] = \pi pq$) or a rectangle ($V[E] = 4pq$) in Eq. (2.19) provides the MIL $\bar{L}(\mathbf{u})$.

Usually, in a MIL anisotropy analysis the polar plot of the MIL $\bar{L}(\mathbf{u})$ is assumed to be an ellipse (or an ellipsoid in three dimensions) [107, 186, 195, 221, 512]. The polar representation $r(\omega)$ of an ellipse with the origin at the center of the ellipse is

$$r(\omega) = \frac{1}{\sqrt{b^{-2} \sin^2\omega + a^{-2} \cos^2\omega}} \tag{2.25}$$

with semiaxes a and b; see also Eq. (2.5). If the MIL polar plot was an ellipse, the functional form of $\bar{L}(\mathbf{u})$ would be of the form in Eq. (2.25).

From Eqs. (2.22)–(2.24) I find that an anisotropic polar diagram of the inverse of the MIL can only be an ellipse for aligned overlapping ellipses. For other anisotropic Boolean models, the polar figure is distinctly different.

Figure 2.9(a) is a polar diagram of the MIL of the Boolean model with ellipses. The MIL is computed for perfectly aligned ellipses $\sigma = 0$, for partially aligned ellipses $\sigma = 0.50$ and for an isotropic system $\sigma = 0.91$. For each system a sample of a Boolean model is depicted above the polar plot. The analytic curves (lines) are compared to the numerical estimates (dots; the error bars are smaller than the point size). Because the polar plot of the MIL is by definition point symmetric w.r.t. the origin [512], the numerical data is shown only for $\omega = [-\pi/4, 3\pi/4]$. The numerical data is in perfect agreement with the analytic formula. Only in the special case of aligned ellipses, the polar diagram of the MIL is indeed an ellipse. If the ellipses are only partially aligned ($\sigma = 0.50$), the polar diagram is only similar to an ellipse, but for a Boolean model with ellipses the deviation of the MIL figure from an ellipse is only small.

However, the deviations become obvious for nonelliptical grain shapes[10]. Figure 2.9(b) is the same polar diagram for rectangles; see also the inset of Fig. 2.3, which shows the MIL figure of rectangles following an orientation distribution with standard deviation $\sigma = 0.22$. Again the numerical data is in perfect agreement with the analytic formula. If the rectangles are aligned, the polar diagram is a rhombus, and also for weaker alignment the MIL figure is distinctly different from an ellipse. Another example of a nonelliptical polar plot is shown in Figure 2.14 in Section 2.4.3; parabola shaped grains with fixed orientation lead to an even nonconvex MIL figure. For the Boolean model, Eq. (2.5) does not hold, and a least square fit of an ellipse to the data is not justified, unknown systematic errors would be induced[11]. The MIL tensor is actually not a tensor.

This contradicts a common assumption that a large number of objects not all parallel to each other produce on average an elliptic global MIL figure [263]. The latter turns out to be not only sensitive to the degree of alignment, but also to the shape of the individual grains, as discussed above in Section 2.3.1.

Luo et al. already derived that for a planar N-net system the polar plot of the MIL is a convex polygon [280]. I have shown here that for a realistic model of porous media [34, 241, 262, 385, 460] the MIL figure is far from being an ellipse.

A similar analysis of further stochastic models for bone geometries (such as level sets of random fields) or indeed an analysis of high-resolution tomography data is needed to shed light on the tensorial or nontensorial nature of the MIL for realistic bone structures. There are first indications, for example, Ketcham and Ryan [240] reported statistically significant deviations from an ellipsoidal shape in experimental measurements of the MIL of trabecular bone.

The fabric tensor based on a least-square fit is ill defined and suffers from an unknown systematic error[12]. Only the analysis of the MIL as a function of the orientation of the test lines is well-defined. The following sections discuss its characterization of the Boolean model, revealing inherent drawbacks of the MIL analysis, calling for an alternative approach to sensitively measure anisotropy.

2.3.4 Intensity dependence and anisotropy index

The main purpose of the MIL analysis is to quantify relative variations of the MIL with orientations $\mathbf{u}$ of the test lines, but also the absolute size of the intercept lengths

[10] For example, also cancellous bone is often model by plates and rods [190, 328, 360]

[11] Because the MIL figure is not an ellipse, Equation (2.5) does no longer hold as well. The polar plot of $\bar{L}^{-2}(\omega)$ deviates from the characteristic dumbbell shape. A fit of the quadratic form $\mathbf{u}^t\mathbf{M}\mathbf{u}$ also leads to an unknown systematic error.

[12] There is a well-defined alternative choice of a MIL fabric tensor, namely the covariance tensor of the MIL figure. However, this approach naturally leads to a replacement by the more general class of Minkowski tensors, as I show in Section 2.3.6.

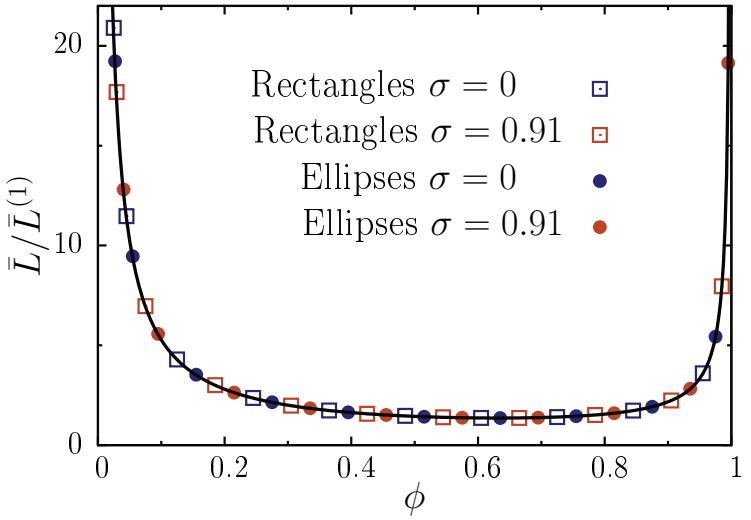

Figure 2.10: MIL $\bar{L}$ as a function of the occupied area fraction ϕ: the orientation and intensity dependence factorize. If the MIL is normalized by its orientation dependent factor $\bar{L}_0$, which is given by Eq. (2.20), it gets independent of the grain distribution. The solid line shows the analytic curve from Eq. (2.26). It is compared to the numerical estimates for both Boolean models with ellipses (dots) and with rectangles (squares) with aspect ratio 1/2 for test lines in x-direction. In each case isotropic samples $\sigma = 0.91$ (orange) and Boolean models with aligned grains $\sigma = 0$ (blue) are simulated. The error bars are smaller than point size, and the numerical estimates are in perfect agreement with the analytic curve. The intensity dependence of MIL is the same for all homogeneous Boolean models.

is interesting for relating structure to the mechanical properties [122, 164, 460] or in the reconstruction of two-phase random media [222, 521]. As I have shown in Eq. (2.19) in Section 2.3.1, the intensity dependence and the orientation dependence of the MIL factorize for Boolean models. The MIL normalized by the orientation dependent factor is a function of the occupied area fraction ϕ only and independent of the grain distribution, i.e., the explicit Boolean model:

$$\frac{\bar{L}}{\bar{L}^{(1)}} = \frac{\mathrm{e}^{\rho V}}{2\rho V} = -\frac{1}{2(1-\phi)\ln(1-\phi)} \,. \tag{2.26}$$

Figure 2.10 plots this normalized MIL $\frac{\bar{L}}{\bar{L}^{(1)}}$ as a function of the occupied area fraction ϕ and compares the analytic curve to the numerical estimate. Also the simulated results show the perfect agreement for isotropic or aligned Boolean models with either ellipses or rectangles. As expected, the MIL diverges for both vanishing void porosity ϕ_{void} ($L_{void} \to 0$ and $L_{cov} \to \infty$) and vanishing occupied area fraction ϕ_{cov} ($L_{void} \to \infty$ and $L_{cov} \to 0$).

Because of the separation in an orientation and an intensity-dependent factor

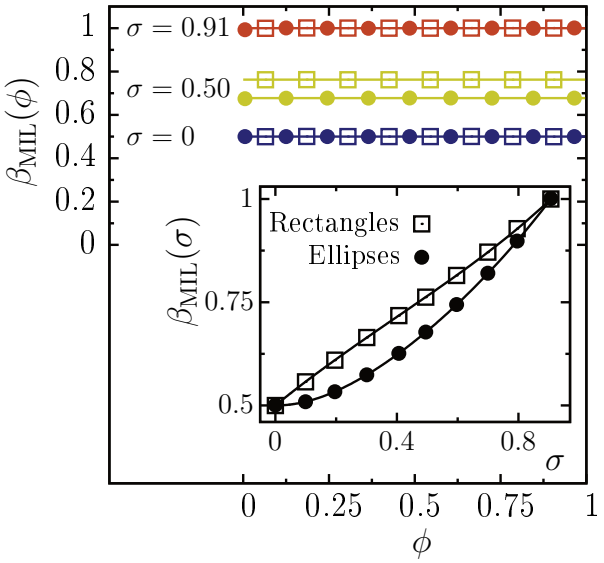

Figure 2.11: The ratio β_{MIL} of the MIL in x- and in y-direction as a function of the occupied area fraction ϕ for differently anisotropic systems. The anisotropy is characterized by the standard deviation σ of the orientation distribution; see Fig. 2.9(a). The lines depict the analytic curves, and circles and squares represent Boolean models with ellipses or rectangles with aspect ratio 1/2. Because of the separation in an orientation and an intensity-dependent factor the ratio β_{MIL} is constant for all porosities ϕ. The inset shows β_{MIL} as a function of the anisotropy σ. It cannot distinguish overlapping rectangles from ellipses if they are aligned ($\sigma = 0$).

in Eq. (2.19), the ratio of the MIL in y- and in x-direction, which is the preferred direction of the orientation distribution function $\mathcal{P}(\theta)$, is independent of the intensity and thus of the occupied area fraction ϕ; the factor from Eq. (2.26) cancels out. This ratio $\beta_{\mathrm{MIL}} := \bar{L}(\pi/2)/\bar{L}(0)$ is, therefore, a measure of the inherent anisotropy of the grain distribution. This is shown and compared to the simulation results in Fig. 2.11. In the case of aligned ellipses, where the MIL figure is an ellipse, this ratio is equivalent to various definitions of the degree of anisotropy (DA); common definitions [32, 97, 164, 218, 240, 275, 350] are $\beta_{\mathrm{MIL}} = 1/\mathrm{DA}$ or $\mathrm{DA} = 1 - \beta$. This index quantifies an interfacial anisotropy of the system determined by both the aspect ratio of the grains and the orientation distribution function $\mathcal{P}(\theta)$. $\beta_{\mathrm{MIL}} = 0$ corresponds to perfect anisotropy, i.e., an effectively one-dimensional heterogeneous material in y-direction, simply a stacking of layers (or lines) in x-direction with varying height; therefore, $\bar{L}(0) \to \infty$. $\beta_{\mathrm{MIL}} = 1$ corresponds to an isotropic model w.r.t. the MIL analysis.

However, the MIL analysis is insensitive, in the sense, that a Boolean model can appear perfectly isotropic in the MIL analysis, although the system is obviously anisotropic, as discussed below. Already Figure 2.11 shows that the index β_{MIL} cannot, for example, distinguish the anisotropy of ellipses or rectangles (with semiaxes q and p) with a fixed orientation ($\sigma = 0$); in both cases, $\beta_{\mathrm{MIL}} = p/q$.

In Section 2.4.3, I even present a Boolean model with an anisotropic interface, but with a perfectly isotropic MIL anisotropy index β_{MIL}; see Figure 2.14.

2.3.5 Deficiencies of anisotropy characterization using the MIL analysis

Apart from the standard MIL fabric tensor being ill-defined, I have found in Section 2.3.4 that it appears to be a rather insensitive structure measure. In this section, I look in detail at the possibilities and disadvantages of the MIL approach in general.

First, it might be insufficient to consider only a second-rank tensor, like in Eq. (2.5), the material is assumed to be orthotropic [186, 512]. However, for some materials higher-rank tensors are needed to characterize the anisotropy[13] and predict, e.g., mechanical properties [227, 424].

Even if higher-order tensors were used for representing the MIL figure, the MIL considers only the orientation $\mathbf{u}$ of the test lines and does not distinguish the directions $\mathbf{u}$ or $-\mathbf{u}$, an additional two-fold rotation axis is assumed [512], which is equivalent to considering only even rank tensors.

A fundamental restriction of the MIL figure is its limitation to interfacial anisotropy. A structure may appear perfectly isotropic w.r.t. its boundary, while being, e.g., obviously anisotropic w.r.t. its "mass distribution" meaning the spatial arrangement of its interior [327, 347, 349]. The MIL analysis does not allow for a systematic analysis of anisotropy w.r.t. different geometrical properties.

Moreover, even in detecting interfacial anisotropy, the MIL analysis is insensitive. Not only, that the anisotropy index β_{MIL} defined above cannot distinguish aligned rectangles from aligned ellipses, but obviously anisotropic systems can appear perfectly isotropic w.r.t. the MIL analysis, e.g., for a Boolean model with aligned Reuleaux triangles or any other curve of constant width; other famous

[13] Following the work of Kanatani [229] but generalizing the concept to nonnormalized functions $f(\mathbf{u})$, I here shortly present a general approach to characterize directional data, i.e., a polar function $f(\mathbf{u})$, by arbitrary rank fabric tensors: the function $f(\mathbf{u})$ is approximated by dumbbell-shaped polynomials $\mathbf{F} : \mathbf{u}^k := \sum_{i_1,\dots i_k=1}^{k} F_{i_1,\dots i_k} u_{i_1} \dots u_{i_k}$. For rank $k = 2$ the polynomial is $\mathbf{F} : \mathbf{u}^2 = \mathbf{u}^t \mathbf{F} \mathbf{u}$, i.e., the same as in Eq. (2.5) for $\bar{L}^{-2}$. A least square fit of the expansion to the empirical distribution minimizes $\int_{\mathbb{S}^{d-1}} \mathrm{d}\mathbf{u}\, [\mathbf{F} : \mathbf{u}^k - f(\mathbf{u})]^2$, i.e., an isotropic distribution of test lines is assumed.

However, then all tensors $\mathbf{F}$ of any rank k are needed in order to perform a statistical model selection, e.g., a likelihood-ratio test, to choose the appropriate model for the data. This might be impractical for applications, but I can derive a connection between these least-square fits and the moment tensors of $f(\mathbf{u})$: $N_{i_1 \dots i_k} = \langle u_{i_1} \dots u_{i_k} \rangle = \int_{\mathbb{S}^{d-1}} \mathrm{d}\mathbf{u}\, f(\mathbf{u}) \cdot u_{i_1} \dots u_{i_k}$. For example, for a point symmetric function $f(\mathbf{u})$, the second-moment tensor is equivalent to the covariance tensor. The fabric tensor $\mathbf{F}$ is proportional to $\mathbf{N} - \frac{1}{5}\mathrm{tr}(\mathbf{N})\,\mathbf{1}$ in three dimensions or to $\mathbf{N} - \frac{1}{4}\mathrm{tr}(\mathbf{N})\,\mathbf{1}$ in two dimensions (with $\mathbf{1}$ the identity or unit tensor).

In contrast to the least-square fits, which need the assumption of a model and are unjustified without the model selection, the moment tensors are a well-defined alternative; see Section 2.3.6.

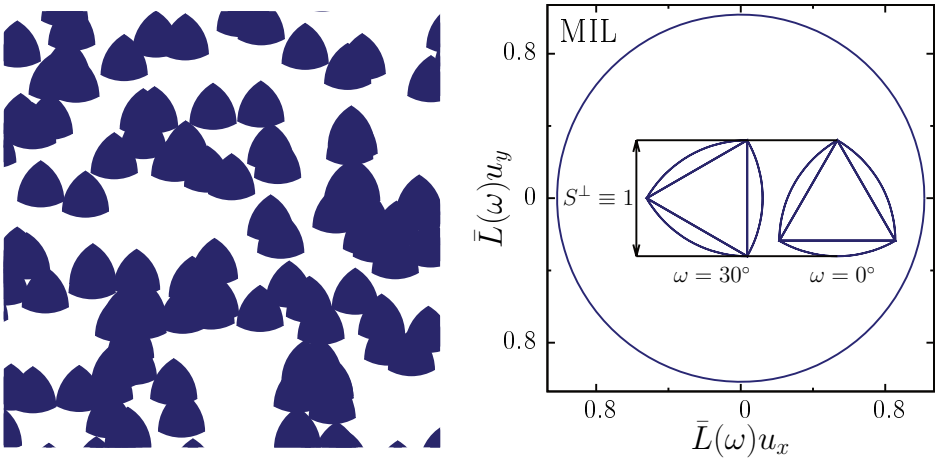

(a) (b)

Figure 2.12: Insensitivity of the MIL analysis for a Boolean model with aligned Reuleaux triangles: (a) an obviously anisotropic sample produces (b) a circle in the MIL figure, i.e., appears perfectly isotropic, because the Reuleaux triangle has a constant width, i.e., the projected length $S^\perp$ is independent of the angle ω between the test lines and the fixed orientation of the Reuleaux triangle. From Eq. (2.19) follows that the MIL is a constant $\bar{L}(\omega) = \text{const}$.

examples are the British twenty and fifty pence coins. Figure 2.12(a) shows a Boolean model with aligned Reuleaux triangles. A Reuleaux triangle is bounded by three circular arcs whose sides are the sides of an equilateral triangle. Constant width means that the length $S^\perp$ of its perpendicular projection is independent of the angle ω between the test lines and the fixed orientation of the Reuleaux triangle. From Eq. (2.19) then follows that the MIL is a constant and the MIL figure a circle, see Fig. 2.12(b). The Boolean model with aligned grains appears perfectly isotropic in the MIL analysis.

Furthermore from a practical point of view, standard line or intersection counting techniques to determine the MIL are time-consuming, sensitive to noise [327]. Moreover, variations in the implementation can significantly affect the results [430]. The lineal approach very strongly depends on the distribution of orientations ω of test lines. Even for the natural choice of uniform orientation sampling, i.e., constant spacing between the orientations ω, the principal directions can vary significantly if a relatively low number of test lines is used[14] [240].

[14] Ketcham and Ryan [240] pointed out that a bias can be avoided by using uniform orientation sampling with many test lines.

2.3.6 Generalized intercept anisotropy measures

Several extensions of the MIL tensor [263, 327] and various alternative lineal measures [218, 240, 347, 349, 350, 395] have been proposed. However, they do not offer a systematic approach to characterize different geometric aspects. A porous medium can, for example, be isotropic w.r.t. the volume but anisotropic w.r.t. the interfacial distribution or vice versa [408].

I derive here how an approach to correct and improve the MIL analysis naturally leads to replacing it by a far more general framework, family of the Minkowski tensors.

While a least-square fit of an ellipse to the MIL figure is in general not justified[15] and the resulting MIL tensor, therefore, ill-defined, the covariance is an alternative, well-defined fabric tensor[16] [327]

$$\mathbf{Cov}(\bar{L} \cdot \mathbf{u}) = \int_{\mathbb{S}^{d-1}} \mathrm{d}\mathbf{u}\ \bar{L}^2\, \mathbf{u} \otimes \mathbf{u} \tag{2.27}$$

with $\mathbf{u} \otimes \mathbf{u}$ the tensor product of the normal vectors which is represented by a matrix with $n_i \cdot n_j$ as the entry in row i and column j. Note that the average over $\mathbf{u}$ of $\bar{L} \cdot \mathbf{u}$ vanishes because of the point symmetry of $\bar{L}(\mathbf{u})$ w.r.t. the origin[17].

The definition of the covariance tensor avoids the systematic errors of an inappropriate least-square fit but suffers from larger statistical fluctuations [240]. A more robust geometrical measure is needed which should also resolve the drawbacks discussed in Section 2.3.5.

The MIL is proportional to the average of the inverse of the number of intersections m of the test lines with the interface between covered and void phase

$$\bar{L} = \left\langle \frac{\mathcal{L}}{m} \right\rangle \propto \left\langle \frac{1}{m} \right\rangle$$

with $\mathcal{L}$ the total length of the test lines. The MIL analysis can be described as the covariance tensor $\mathbf{Cov}(\langle \frac{1}{m} \rangle \cdot \mathbf{u})$.

A natural replacement is to consider instead of the mean of the inverse $\langle 1/m \rangle$, the average of the number of intersections m directly, i.e., calculate the covariance tensor of $\langle m \rangle$.

---

[15] Neither a fit of $\mathbf{u}^t \mathbf{F} \mathbf{u}$ to $\bar{L}^{-2}(\mathbf{u})$.

[16] The covariance tensor is closely related to the orientation matrix [141, 240], but depending on the convention a different normalization might be applied.

[17] In the Boolean model with aligned ellipses, where the MIL figure is an ellipse, the covariance tensor is proportional to the MIL fabric tensor $\mathbf{Cov}(\bar{L} \cdot \mathbf{u}) = {}^{2\pi}/_{\mathrm{tr}(\sqrt{\mathbf{M}})}\, \mathbf{H}$ with $\mathbf{M}$ and $\mathbf{H}$ defined in Eqs. (2.5) and (2.6). See also Section 2.3.5 about a relation between moment tensors and a least-square fit of dumbbell-shaped polynomials of arbitrary order combined with a model selection.

Note that this is not simply the inverse of $\langle 1/m \rangle$, because the mean of the inverse is strictly greater than the inverse of the mean (except if m is fixed, i.e., not a random number)

$$\left\langle \frac{1}{m} \right\rangle > \frac{1}{\langle m \rangle} , \tag{2.28}$$

which follows from Jensen's inequality. The standard estimator of $\langle m \rangle$ is the arithmetic mean, and for $\langle 1/m \rangle$ it is the inverse of the harmonic mean.

While this replacement seems to be a small step, it is actually a giant leap from an integral geometric point of view. In contrast to the average of the inverse, the expected number of intersections is an additive quantity[18], and the powerful theorem by Alesker[19] [27, 28] can be applied: the $\mathbf{Cov}(\langle m \rangle \cdot \mathbf{u})$ can be expressed by Minkowski tensors. The change from a single rather insensitive measure $\mathbf{Cov}(\langle \frac{1}{m} \rangle \cdot \mathbf{u})$ to the additive alternative opens up the broad generalization to the whole family of Minkowski tensors, versatile and powerful shape descriptors from integral geometry [400]. They can provide a systematic approach to structure characterization and anisotropy quantification [406, 408].

Note that there are also several other common structure tensors which are closely related to the Minkowski tensors and which can easily be generalized to become a Minkowski tensor [229, 230, 344, 345], which would then allow taking advantage of the rich mathematical background and powerful theorems about Minkowski tensors as well as of the ready-to-use implementation.

2.4 Minkowski tensors as metrics of anisotropy and orientation

The scalar Minkowski functionals and their generalization, the Minkowski tensors, are defined as volume or surface integrals and thus allow for an intuitive characterization of random structure. They are related, for example, to tensors of inertia or characterize the distribution of the normal vectors on the boundary of the heterogeneous material.

The Minkowski tensors allow for a systematic and sensitive anisotropy analysis of different geometrical aspects, like volume, surface, or curvature. They are defined in both two and three dimensions for arbitrary rank and need no assumptions about the heterogeneous material or its symmetry.

[18] For two disjoint systems with average number of intersections $\langle m_1 \rangle$ and $\langle m_2 \rangle$, the expected total number of intersections is simply $\langle m_1 + m_2 \rangle = \langle m_1 \rangle + \langle m_2 \rangle$

[19] The theorem by Alesker basically states that any continuous, additive and motion-covariant tensor-valued functional on convex bodies can be expressed by a linear combination of Minkowski tensors (multiplied with appropriate unit tensors).

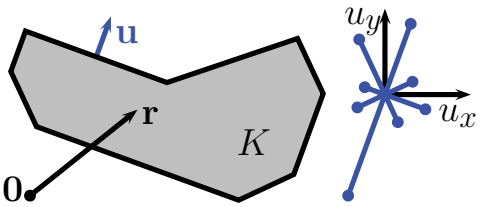

Figure 2.13: The Minkowski tensors of a domain K are tensorial shape measures that are defined as volume and surface integrals. On the left-hand side, a position vector $\mathbf{r}$ in K and a normal vector $\mathbf{u}$ at the boundary ∂K are depicted. Their tensor products are used in the integrals in Tables 2.1 and 2.2. On the right-hand side, the distribution of the normal vectors of domain K is shown; $W_1^{0,2}$ is proportional to the according covariance tensor.

Integral geometry allows for a rigorous mathematical foundation of the Minkowski tensors but offers also important insights for applications. The Minkowski functionals or tensors are proportional to the so-called intrinsic volumes or tensor valuations, which are more commonly used in mathematics literature [400].

2.4.1 Definition and applications

The Minkowski functionals are integrals over either a domain K or its surface ∂K (see Fig. 2.13) probably weighted with its curvature. For two and three dimensions, they are listed in Tables 2.1 and 2.2. There is an intuitive interpretation of the Minkowski functionals: in two dimensions, they correspond to the area, the perimeter, and the Euler characteristic[20] and in three dimensions the volume, the surface area, the integrated mean curvature, and the Euler characteristic[21]. The latter is a topological constant, i.e., it is a measure of connectivity. For example for a domain K in two dimensions, more precisely for a set $K \subset \mathbb{R}^2$ that is a union of finitely many convex bodies, the Euler characteristic equals the number of components minus the number of holes; accordingly, in three dimensions, it is equal to the number of components minus the number of tunnels and plus the number of spherical cavities.

These scalar measures are naturally generalized to the Minkowski tensors by including an integral over the tensor products of the position vector $\mathbf{r}$ and the surface normal vector $\mathbf{n}$; see Tables 2.1 and 2.2 and Fig. 2.13. The mutually linear independent Minkowski tensors are also summarized in Tables 2.1 and 2.2 for two or three dimensions, respectively. Different normalizations are used in different fields of research. In this thesis, I use for the Minkowski functionals W_ν and tensors $W_\nu^{r,s}$ a normalization such that W_0 is the area (or volume) and W_1 is the perimeter (or surface area) in two (or three dimensions). The normalizations of the Minkowski tensors are then defined accordingly. The normalizations in two or three dimensions are given in Tables 2.1 or 2.2, respectively.

[20] Strictly speaking, a functional proportional to the Euler characteristic.
[21] Again, up to a proportionality constant.

Functionals	Tensors	
Area	Moment solid	
$W_0 = \int_K \mathrm{d}A$	$W_0^{2,0} = \int_K \mathrm{d}A\ \mathbf{r}^k$	
Perimeter	Moment hollow	Normal dist.
$W_1 = \int_{\partial K} \mathrm{d}l$	$W_1^{2,0} = \int_{\partial K} \mathrm{d}l\ \mathbf{r}^k$	$W_1^{0,2} = \int_{\partial K} \mathrm{d}l\ \mathbf{n}^k$
Euler charact.	Moment vertices	
$W_2 = \int_{\partial K} \mathrm{d}l\ \kappa$	$W_2^{2,0} = \int_{\partial K} \mathrm{d}l\ \kappa\ \mathbf{r}^k$	

Table 2.1: Definition of the Minkowski functionals and tensors of rank k in two dimensions evaluated for a domain K, where κ is the local curvature on ∂K, $\mathbf{r}$ are the position vectors in K, and $\mathbf{n}$ are the normal vectors on the boundary ∂K; see also Fig. 2.13. $\mathbf{r}^k = \bigotimes_{i=1}^k \mathbf{r} = (r_{i_1} \dots r_{i_k})_{i_1 \dots i_k}$ (or $\mathbf{n}^k = \bigotimes_{i=1}^k \mathbf{n}$) is the tensor product; for $k = 2$, for example, $\mathbf{r}^2 = \mathbf{r} \otimes \mathbf{r}$ is represented by a matrix with $r_i \cdot r_j$ as the entry in row i and column j. W_0 is the area, W_1 the perimeter, and $W_2 = 2\pi\chi$ is proportional to the Euler characteristic χ.

In d-dimensional Euclidean space, the Minkowski functionals can be defined by the Steiner formula[22] [400]: for a convex body K, i.e., a compact, convex subset of $\mathbb{R}^d$, the volume W_0 of the parallel body[23] K_ϵ is given by

$$W_0(K_\epsilon) = W_0(K) + \frac{1}{d} \sum_{\nu=1}^{d} \epsilon^\nu \cdot \binom{d}{\nu} \cdot W_\nu(K) \ .$$

The Minkowski functionals can intuitively be generalized to non-convex bodies by using their additivity [400]. By this choice of normalization, the zeroth order Minkowski functional of a d-dimensional unit ball $B^d = \{x \in \mathbb{R}^d \mid \|x\| \leq 1\}$ is equal to its volume $W_0(B^d) =: \kappa_d$, and the higher-order Minkowski functionals are equal to its surface area $W_\nu(B^d) = d\kappa_d$ ($d \geq \nu \geq 1$). As mentioned above, in mathematics literature the intrinsic volumes V_ν are more commonly used than the Minkowski functionals, but only differ by a proportionality constant

$$\begin{aligned} V_d(K) &:= W_0(K) \ , \\ V_\nu(K) &:= \frac{1}{d \cdot \kappa_{d-\nu}} \cdot \binom{d}{\nu} \cdot W_{d-\nu}(K) \quad \text{for } d-1 \geq \nu \geq 0 \ . \end{aligned}$$

The Minkowski tensors of a convex body K in the d-dimensional Euclidean space can be defined using the so-called support measures $\Lambda_\nu(K; \cdot)$, which can

[22] Be aware that in d dimensions the normalization of the Minkowski functionals W_ν with $\nu > 0$ which I have chosen here is by a factor d larger than the normalization of the Minkowski functionals W_i in Ref. [400].

[23] The parallel body K_ϵ is the set of all points x for which there is a point y in K such that the distance between x and y is smaller or equal to ϵ [400].

Functionals	Tensors	
Volume	Moment solid	
$W_0 = \int_K \mathrm{d}V$	$W_0^{2,0} = \int_K \mathrm{d}V\ \mathbf{r}^k$	
Surface area	Moment hollow	Normal dist.
$W_1 = \int_{\partial K} \mathrm{d}A$	$W_1^{2,0} = \int_{\partial K} \mathrm{d}A\ \mathbf{r}^k$	$W_1^{0,2} = \int_{\partial K} \mathrm{d}A\ \mathbf{n}^k$
Mean curvature	Moment wireframe	Curvature dist.
$W_2 = \int_{\partial K} \mathrm{d}A\ \frac{\kappa_1+\kappa_2}{2}$	$W_2^{2,0} = \int_{\partial K} \mathrm{d}A\ \frac{\kappa_1+\kappa_2}{2}\ \mathbf{r}^k$	$W_2^{0,2} = \int_{\partial K} \mathrm{d}A\ \frac{\kappa_1+\kappa_2}{2}\ \mathbf{n}^k$
Euler charact.	Moment vertices	
$W_3 = \int_{\partial K} \mathrm{d}A\ \kappa_1\kappa_2$	$W_3^{2,0} = \int_{\partial K} \mathrm{d}A\ \kappa_1\kappa_2\ \mathbf{r}^k$	

Table 2.2: Definition of the Minkowski functionals and tensors of rank k in three dimensions evaluated for a domain K, where κ_1 and κ_2 are the principle curvatures on ∂K, $\mathbf{r}$ are the position vectors in K, and $\mathbf{n}$ the normal vectors on the boundary ∂K; see also Fig. 2.13. $\mathbf{r}^k = \bigotimes_{i=1}^k \mathbf{r} = (r_{i_1} \dots r_{i_k})_{i_1 \dots i_k}$ (or $\mathbf{n}^k = \bigotimes_{i=1}^k \mathbf{n}$) is the tensor product; for $k = 2$, for example, $\mathbf{r}^2 = \mathbf{r} \otimes \mathbf{r}$ is represented by a matrix with $r_i \cdot r_j$ as the entry in row i and column j. W_0 is the volume, W_1 the surface area, W_2 the integrated mean curvature, and $W_3 = 4\pi\chi$ is proportional to the Euler characteristic χ.

in turn be defined by a local Steiner formula and are thus related to the intrinsic volumes $V_\nu = \Lambda_\nu(K; \mathbb{R}^d \times \mathbb{S}^{d-1})$ [400]. Like the scalar functionals, the tensors can be generalized to non-convex bodies by using their additivity [400]. For consistency with the Minkowski functionals, I use for $\nu \geq 1$ a different normalization $\Omega_\nu(K; \cdot) := \frac{d \cdot \kappa_{d-\nu}}{\binom{d}{\nu}} \Lambda_{d-\nu}(K; \cdot)$. The Minkowski tensors are then defined as [303, 400]

$$W_0^{r,0}(K) := \int_K \mathbf{x}^r \, \mathrm{d}^d \mathbf{x} \,,$$
$$W_\nu^{r,s}(K) := \int_{\mathbb{R}^d \times \mathbb{S}^{d-1}} \mathbf{x}^r \mathbf{u}^s \, \Omega_\nu(K; \mathrm{d}(\mathbf{x}, \mathbf{u})) \quad \text{for } d \geq \nu \geq 1 \,,$$

where $\mathbf{x}^r$ or $\mathbf{u}^s$ are symmetric tensor products. Note that in most parts of this thesis, the definitions for two and three dimensions in Tables 2.1 or 2.2 are sufficient.

The Minkowski tensors can intuitively be interpreted. The tensors using the position vector are closely related to tensors of inertia where the mass is located in the region of integration and probably weighted by the curvature. $W_0^{2,0}$ contains the information of the tensor of inertia of the solid object, $W_1^{2,0}$ of a hollow object where the mass is located in the shell. For the example of polytopes in three dimensions, $W_2^{2,0}$ and $W_3^{2,0}$ are related to the tensor of inertia if the mass is distributed on the edges or vertices but weighted with the opening angles. The Minkowski tensor $W_1^{2,0}$ is proportional to the moment or covariance tensor of the distribution of

normal vectors[24], see Fig. 2.13; $W_2^{0,2}$ is proportional to the according moment tensor weighted by the curvature distribution. In contrast to the tensors that are related to the tensors of inertia, the moment tensors of the normal distributions are translation invariant.

The Minkowski functionals and tensors are robust, efficient, and versatile structure measures, which have already been successfully applied to pattern analysis [59, 288, 304] and to physical [305, 307] and biological systems [54, 61] on all length scales from nuclear physics [413, 416], over condensed and soft matter [181, 234, 516], to cosmology [104, 127, 151, 238, 399].

The Euler characteristic is already widely applied in medical physics to characterize the connectivity of trabecular bone [164, 169, 347, 348], and Räth et al. [376] have also used the other Minkowski functionals to characterize the structure of trabecular bone, see also Refs. [75, 426]. However, while the scalar functionals are rotation invariant, the Minkowski tensors provide anisotropy indices explicitly designed to quantify anisotropy [319, 406, 408], in a more robust fashion than the MIL analysis.

Minkowski tensors are defined for both two and three dimensions[25], and rotational integral geometry provides local stereological estimators of Minkowski tensors and relations for Minkowski tensors of planar sections [44, 489, 490].

The Minkowski functionals have already been used to adjust a Boolean model to an experimental structure, resulting in an excellent match of the mechanical and transport properties [34, 35]. A comprehensive introduction to the Minkowski tensors as anisotropy indices and exemplary applications can be found in Refs. [406, 408]. In Section 2.4.3, I show how these powerful shape characteristics resolve the drawbacks of the MIL analysis pointed out above.

2.4.2 Circular Minkowski tensors

While the Cartesian representation of the Minkowski tensors in Tables 2.1 and 2.2 is both intuitive and easy to compute, it is inefficient for higher-rank tensors, which are especially needed to quantify higher-order anisotropy [232], e.g., the anisotropy of a cube. Not only is it difficult to define rotational invariants, i.e., a degree of anisotropy, but even or uneven rank tensors also contain all Minkowski tensors of lower even or uneven rank, respectively: $(W_\nu^{0,s})_{i_1\dots i_s} = \sum_{j=1}^{d} (W_\nu^{0,s+2})_{i_1\dots i_s jj}$, e.g., $W_1 = \mathrm{tr}(W_1^{0,2})$. Therefore, the Minkowski tensors must be decomposed into irreducible tensors w.r.t. the rotation group $\mathrm{SO}(d)$, see Ref. [229] for a discussion

[24] $W_1^{2,0}$ is equal to the covariance tensor, because the mean value, i.e., $W_1^{0,1} = \int_{\partial K} \mathrm{d}A\, \mathbf{n}$, vanishes for closed bodies due to the envelope theorem [175].

[25] Minkowski tensors are actually defined for any dimension d.

of irreducible representations of moment tensors of the directional distributions. Alesker et al. [29] provide a general theory for such an irreducible decomposition of the space of translational-invariant and continuous valuations. Kapfer [232] presents an explicit irreducible representation and rotational invariants of Minkowski tensors for three dimensions, the "spherical Minkowski tensors"; see also Ref. [320]. Here, I discuss the two-dimensional case, for which I define in collaboration with Sebastian Kapfer the "circular Minkowski tensors". Note that this is also equivalent to the definition of the harmonic intrinsic volumes defined in Ref. [203] for any dimension d.

In two dimensions, for the irreducible representations of the translation invariant interfacial tensors $W_1^{0,s}$, I can here provide a rather intuitive approach. As already mentioned above, these tensors $W_1^{0,s}(K)$ can be interpreted as the moment tensors of the distribution of the normal vectors on the interface of the domain K. Following Schröder-Turk et al. [406], the Cartesian tensor $W_1^{0,s}(K)$ can be expressed via

$$\begin{aligned} W_1^{0,s}(K) &= \int_{\partial K} \mathrm{d}\mathbf{r}\, \mathbf{n}^s(\mathbf{r}) = \int_{\partial K} \mathrm{d}\mathbf{r} \int_{\mathbb{S}^1} \mathrm{d}\mathbf{u}\, \delta(\mathbf{n}(\mathbf{r}) - \mathbf{u})\, \mathbf{u}^s \\ &= \int_{\mathbb{S}^1} \mathrm{d}\mathbf{u}\, \mathbf{u}^s \int_{\partial K} \mathrm{d}\mathbf{r}\, \delta(\mathbf{n}(\mathbf{r}) - \mathbf{u}) = \int_{\mathbb{S}^1} \mathrm{d}\mathbf{u}\, \mathbf{u}^s E(\mathbf{u}) \,, \end{aligned} \tag{2.29}$$

where

$$E(\mathbf{u}) := \int_{\partial K} \mathrm{d}\mathbf{r}\, \delta(\mathbf{n}(\mathbf{r}) - \mathbf{u})$$

is proportional to the distribution of the normal vectors, i.e., the probability density function on the unit circle that describes the frequency with which the interface points into a given direction. However, in contrast to the probability density function, this $E(\mathbf{u})$ is in general not normalized, but the integral over the unit circle yields by definition the perimeter of the domain K

$$\int_{\mathbb{S}^1} \mathrm{d}\mathbf{u}\, E(\mathbf{u}) = W_1 \,.$$

Because of the mapping of normals onto the unit circle which is weighted by the surface measure[26], $E(\mathbf{u})$ is also called the extended Gaussian image of K [200, 450], which is closely related to the so-called surface area measure [400].

As above, the direction $\mathbf{u} \in \mathbb{S}^1$ can be identified by the angle ω between the x-axis and $\mathbf{u}$. $E(\omega)$ is a periodic function on $[0, 2\pi)$ and can thus be expressed by

[26] For polygons, this corresponds to the edge-lengths as weights of the according normal directions.

a Fourier series

$$E(\omega) = \sum_{k=-\infty}^{\infty} \mathcal{E}_k \cdot \mathrm{e}^{ik\omega} \ . \tag{2.30}$$

Because the $\mathrm{e}^{ik\omega}$ with $k \in \mathbb{Z}$ are the irreducible representations of SO(2), the Fourier coefficients $\mathcal{E}_k$ of the extended Gaussian image are the irreducible representations of the translation invariant interfacial tensors $W_1^{0,s}$. Therefore, the $\mathcal{E}_k$ are here called the circular Minkowski tensors: for a rotation of K by an angle α

$$\begin{aligned} E(\omega) &\longrightarrow E(\omega - \alpha) \ , \\ \mathcal{E}_k &\longrightarrow \mathrm{e}^{-ik\alpha} \mathcal{E}_k \ . \end{aligned}$$

Note that $\mathcal{E}_{-k} = \mathcal{E}_k^*$. The phase of the complex number $\mathcal{E}_k$ contains information about the preferred direction while the absolute value is a scalar index that contains anisotropy information for $|k| > 1$.

Because of the normalization, the zeroth coefficient is proportional to the perimeter $\mathcal{E}_0 = {}^{W_1}/_{2\pi}$. For $|k| > 1$, I define the anisotropy indices

$$a_k := \frac{|\mathcal{E}_k|}{\mathcal{E}_0} \ , \tag{2.31}$$

which are unit free. Because $E(\omega)$ is up to a prefactor a probability distribution, i.e., $E(\omega) > 0$, $|\mathcal{E}_k| < \mathcal{E}_0$ and thus $0 < a_k < 1$. However, in contrast to the index $\beta_1^{0,2}$, $a_k = 0$ corresponds to isotropy and $a_k = 1$ indicates interfacial anisotropy. Instead, $q_k := 1 - a_k$ can be used as anisotropy index for a better comparison to both $\beta_1^{0,2}$ and β_{MIL}. The anisotropy index a_2 can be expressed by the eigenvalues δ_1 and δ_2 of the Minkowski tensor $W_1^{0,2}$

$$a_2 = \frac{|\delta_1 - \delta_2|}{W_1} = \frac{|\delta_1 - \delta_2|}{\delta_1 + \delta_2} \ . \tag{2.32}$$

or the fourth rank index a_4 can be expressed by the components of the Minkowski tensor $W_1^{0,4}$. If for convenience the coordinate axes are assumed to coincide with the main axes of the system, i.e., the eigenvectors of $W_1^{0,2}$,

$$\begin{aligned} a_4 &= \frac{|(W_1^{0,4})_{xxxx} + (W_1^{0,4})_{yyyy} - 6(W_1^{0,4})_{xxyy}|}{W_1} \\ &= \frac{|(W_1^{0,4})_{xxxx} + (W_1^{0,4})_{yyyy} - 6(W_1^{0,4})_{xxyy}|}{(W_1^{0,4})_{xxxx} + (W_1^{0,4})_{yyyy} + 2(W_1^{0,4})_{xxyy}} \ . \end{aligned} \tag{2.33}$$

These equalities can be shown by expressing the Cartesian Minkowski tensors by the circular Minkowski tensors

$$\begin{aligned} W_1^{0,s} &= \int_{\mathbb{S}^1} \mathrm{d}\mathbf{u}\, \mathbf{u}^s E(\mathbf{u}) = \sum_{k=-\infty}^{\infty} \mathcal{E}_k \int_{\mathbb{S}^1} \mathrm{d}\mathbf{u}\, \mathbf{u}^s \mathrm{e}^{ik\omega} \\ &= \sum_{k=-s}^{s} \mathcal{E}_k \int_{\mathbb{S}^1} \mathrm{d}\mathbf{u}\, \mathbf{u}^s \mathrm{e}^{ik\omega} \,, \end{aligned} \tag{2.34}$$

because all summands with $|k| > s$ vanish due to the vanishing the Fourier components of $\mathbf{u}^s$. Note that these Fourier coefficients of $\mathbf{u}^s$ are independent of the domain K and, e.g., for $s = 2$ given by

$$\int_{\mathbb{S}^1} \mathrm{d}\mathbf{u}\, \mathbf{u}^2 \mathrm{e}^{ik\omega} = \begin{cases} \pi \cdot \mathbf{1} & \text{if } k = 0 \,, \\ \frac{\pi}{2} \cdot (\sigma_3 + i\sigma_1) & \text{if } k = 2 \,, \\ \frac{\pi}{2} \cdot (\sigma_3 - i\sigma_1) & \text{if } k = -2 \,, \\ \mathbf{0} & \text{else} \,, \end{cases}$$

where $\mathbf{1}$ is the unit tensor, $\mathbf{0}$ is the zero tensor, and σ_j are Pauli matrices with $\sigma_3 = \begin{pmatrix} 1 & 0 \\ 0 & -1 \end{pmatrix}$ and $\sigma_1 = \begin{pmatrix} 0 & 1 \\ 1 & 0 \end{pmatrix}$. Thus, $W_1^{0,2}$ can be expressed by $\mathcal{E}_0$, $\mathcal{E}_1$, and $\mathcal{E}_2$. These equations can also be used to derive the circular Minkowski tensors from the Cartesian Minkowski tensors, for example, from Eq. (2.34)

$$\begin{aligned} W_1^{0,s} &= \mathcal{E}_0 \cdot \pi \cdot \mathbf{1} + \mathcal{E}_2 \cdot \frac{\pi}{2} \cdot (\sigma_3 + i\sigma_1) + \mathcal{E}_{-2} \cdot \frac{\pi}{2} \cdot (\sigma_3 - i\sigma_1) \\ &= \mathcal{E}_0 \cdot \pi \cdot \mathbf{1} + \mathrm{Re}(\mathcal{E}_2) \cdot \pi \cdot \sigma_3 - \mathrm{Im}(\mathcal{E}_2) \cdot \pi \cdot \sigma_1 \end{aligned}$$

follows

$$\begin{aligned} \mathcal{E}_0 &= \frac{1}{2\pi} \cdot \left((W_1^{0,2})_{xx} + (W_1^{0,2})_{yy} \right) = \frac{W_1}{2\pi} \,, \\ \mathrm{Re}(\mathcal{E}_2) &= \frac{1}{2\pi} \cdot \left((W_1^{0,2})_{xx} - (W_1^{0,2})_{yy} \right) \,, \\ \mathrm{Im}(\mathcal{E}_2) &= -\frac{1}{\pi} \cdot (W_1^{0,2})_{xy} \,. \end{aligned} \tag{2.35}$$

2.4.3 Sensitive measures of anisotropy

In contrast to the line or intersection counting techniques for the MIL analysis which are very sensitive to noise, the Minkowski tensors are defined as volume and surface integrals, which are robust against noise[27].

[27] The Minkowski tensors are additive and conditional continuous, i.e., continuous on convex bodies. Therefore, small convex fluctuations due to noise do not greatly affect the outcome.

Because of the additivity, the Minkowski tensors can be computed by summing up local contributions listed in a look-up table [162, 288, 304]. Such an algorithm scales linearly with the system size, i.e., its computation time is of the order $O(N_p)$ with N_p the number of pixels, while for standard implementations of the MIL analysis the computation time is of the order $O(N_{\mathcal{L}} \cdot p)$ with $N_{\mathcal{L}}$ the number of test lines [327]. Free software for the Minkowski tensors based on fast linear-time algorithms are available for both two and three dimensions and for both pixelated and triangulated data[28].

A simple yet very efficient linear-time algorithm to calculate the Minkowski functionals or tensors of pixelated black and white images uses look-up tables: the look-up table lists for all 16 possible configurations of a 2×2 scan window its Minkowski functional or tensor[29]. The scan window is iterated over the whole image and the sum of the according entries in the look-up table yields the Minkowski functional or tensor element. More detailed explanations and the look-up tables for two dimensions are given in Section 6.1.2 and Appendix B.

Tables 2.1 and 2.2 show how the family of Minkowski tensors allows for a systematic analysis of anisotropy w.r.t. volume, surface, or curvature. While the sample might be isotropic w.r.t. one of the measures, the Minkowski tensors can still detect the anisotropy w.r.t. another quantity [408]. An exemplary system which is isotropic w.r.t. the MIL tensor can simply be constructed by placing discs as voids in the plane [327, 347] because the MIL analysis can only detected interfacial anisotropy. However, the sample might be anisotropic w.r.t. its mass-distribution. This anisotropy can be quantified, e.g., by the volume Minkowski tensor $W_0^{2,0}$, which is related to the tensor of inertia.

I have introduced the anisotropy index β_{MIL} similar to previously defined indices for the Minkowski tensors [408]. For example, $\beta_1^{0,2}$ is the ratio of the minimal to the maximal eigenvalue of $W_1^{0,2}$. Figure 2.14 compares the two anisotropy indices for different Boolean models[30].

[28] The free software PAPAYA and KARAMBOLA for two or three dimensions, respectively, is available at http://www.theorie1.physik.fau.de/research/software.html Exemplary analyses of different systems are also presented there.

[29] More precisely, to avoid overlap the functional value of only the region between the centers of the four pixels is assigned in the look-up table.

[30] If the main axes of the system are known or there are two axes of special interest, we have shown in Ref. [408] that it is better to use the diagonal entries in the matrix for an accordingly oriented coordinate system instead of the eigenvalues. By this way, a systematic underestimation of $\beta_1^{0,2}$ in isotropic systems is avoided: because of statistical fluctuations, a finite sample is anisotropic $\beta_1^{0,2} < 1$ even in an isotropic system, leading to an anisotropic and thus biased average $\langle \beta_1^{0,2} \rangle < 1$. The analysis of the eigenvalues does not take into account that the randomly preferred direction in an isotropic system is uniformly distributed, in contrast to the ratio of the diagonal elements of the matrix $\beta_1^{*0,2} \in [0, \infty)$; therefore, $\langle \beta_1^{*0,2} \rangle = 1$.

In Ref. [204], we have analytically derived for the Boolean model the expectations of the translation invariant Minkowski tensors, e.g., of $W_1^{0,2}$, which is presented below in Section 2.5. In the limit of infinite system size, the expectation of the Minkowski tensor $\overline{W}_1^{0,2}$ of the Boolean model (if rescaled by the size of the observation window) is proportional to the average Minkowski tensor $\overline{W}_1^{0,2}(K)$ of a single grain K. In other words, the anisotropy information is contained in the single grain characteristic $\overline{W}_1^{0,2}(K)$.

The Minkowski anisotropy index $\beta_1^{0,2}$ only coincides with β_{MIL} for aligned rectangles, for which both are equal to the aspect ratio. For ellipses with aspect ratio 1/2 and a varying bias in the orientation distribution they provide slightly different degrees of anisotropy. Therefore, in contrast to β_{MIL}, the Minkowski index $\beta_1^{0,2}$ does discriminate a Boolean model with ellipses with a fixed orientation from aligned overlapping rectangles or rhombuses with the same aspect ratio.

The higher sensitivity of the Minkowski analysis can, for example, be demonstrated by a Boolean model with parabola-shaped grains, which is depicted at the top of the right-hand side in Fig. 2.14. The boundary of such a grain is formed by two parabolas, $y = 1 - x^2$ and $y = x^2 - 1$ for $x \in [-1, 1]$ (for a grain centered at the origin). A parabola is not symmetric in x and y. Therefore, the interface of the grains and thus of the Boolean model is anisotropic in x- and in y-direction. This is also visualized in Fig. 2.14 by green normal vectors at the boundary. However, the MIL is the same for test lines along $\mathbf{x}$ and $\mathbf{y}$: $\bar{L}(\mathbf{x}) = \bar{L}(\mathbf{y})$, because the lengths of the projections along these lines are the same, which can be seen in the polar MIL plot at the bottom of the right-hand side of Fig. 2.14; therefore, $\beta_{\mathrm{MIL}} = 1$, the MIL anisotropy index indicates perfect interfacial anisotropy. However, the index of the second-rank Minkowski tensor $W_1^{0,2}$ captures the interfacial anisotropy: $\beta_1^{0,2} < 1$ ($\triangle$).

In contrast to the MIL analysis, no assumption about the heterogeneous material or its symmetry is needed, because the Minkowski tensors can be defined for arbitrary rank k. For example, a tensor of rank four is needed to distinguish cubic from spherical symmetry, i.e., characterize the anisotropy of a Boolean model with aligned cubes. With tensors of uneven rank also directed anisotropy can be quantified distinguishing $\mathbf{n}$ from $-\mathbf{n}$.

Moreover, the higher-rank tensors allow for a very sensitive and comprehensive[31] characterization of anisotropy. In the previous section 2.3, I showed that the MIL figure is a circle for Boolean models with grains of constant width even if

[31] Alesker's completeness theorem [27, 28] ensures that the Minkowski tensors provide a comprehensive shape analysis. They capture all structural information in the following sense: all tensor valuations that are defined on unions of convex sets, additive, and at least continuous on convex sets can be expressed by a linear combination of Minkowski tensors.

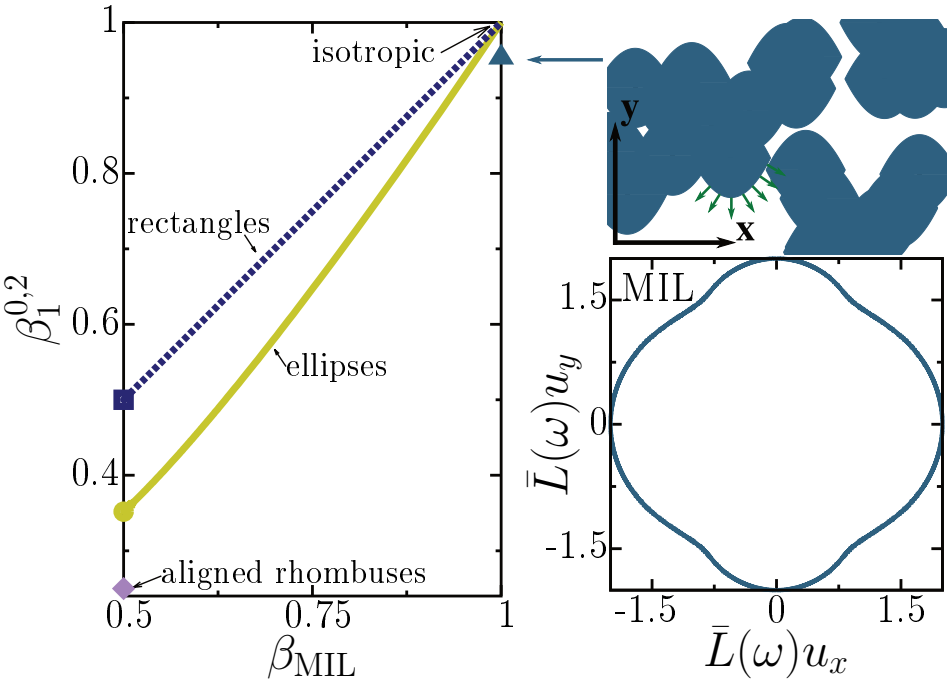

Figure 2.14: Comparison of the Minkowski tensor anisotropy index $\beta_1^{0,2}$ to the MIL degree of anisotropy β_{MIL} for different Boolean models: aligned rectangles with varying aspect ratio (dashed blue line), ellipses with aspect ratio 1/2 but varying bias in the orientation distribution (solid line colored yellow), the marks correspond to particles with fixed orientations, rectangles (□), ellipses (○), rhombuses (⋄), and parabola shaped grains (△). The latter appear perfectly isotropic w.r.t. β_{MIL}, but the Minkowski index $\beta_1^{0,2}$ detects the interfacial anisotropy. A sample of a Boolean model with the parabola shaped grains is depicted at the top of the right-hand side; at the bottom, the polar MIL diagram is depicted with $\bar{L}(0) = \bar{L}(\pi/2)$. It is obviously not an ellipse.

the system is obviously anisotropic. For example, a Boolean model with aligned Reuleaux triangles appears perfectly isotropic w.r.t. the MIL, see Fig. 2.12. This insensitivity of the MIL analysis is also demonstrated in Fig. 2.15: the MIL anisotropy index β_{MIL} is shown to be constant unity for both isotropic and anisotropic systems. It cannot distinguish the aligned grains from the randomly oriented ones.

Because of the threefold symmetry of the grains, the system appears isotropic for any second-rank tensor. Therefore, also the index $\beta_1^{0,2}$ of the Minkowski tensor $W_1^{0,2}$ is constant to unity. For the MIL, all of its tensor representations of arbitrary rank appear perfectly isotropic because the MIL figure is a perfect circle. In contrast to this, the Minkowski tensor $W_1^{0,3}$ of rank three is sensitive to the anisotropy and discriminates the isotropic Boolean model from that with aligned grains. The irreducible representation of the third-rank Minkowski tensor $W_1^{0,3}$

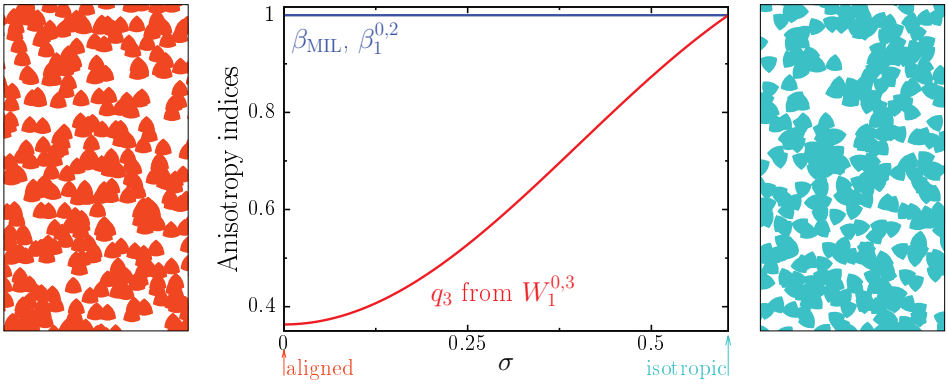

Figure 2.15: Anisotropy indices for overlapping Reuleaux triangles with differently anisotropic orientation distributions. The anisotropy is parametrized by the standard deviation σ of the distribution; $\sigma = 0$ corresponds to perfect alignment and $\sigma = \pi/3\sqrt{3} \approx 0.60$ to random orientations. Because the MIL figure is a perfect circle (see Fig. 2.12), not only the index $\beta_{\mathrm{MIL}} \equiv 1$ is perfectly isotropic, but any arbitrary rank representation. While the index $\beta_1^{0,2}$ of the second-rank Minkowski tensor $W_1^{0,2}$ is also constant unity, the tensor $W_1^{0,3}$ of rank three is sensitive to the interfacial anisotropy. The corresponding anisotropy index q_3 is plotted as a function of the standard deviation σ. $q_3 < 1$ detects the anisotropy of the systems with partially aligned Reuleaux triangles. Samples of anisotropic or isotropic Boolean models with Reuleaux triangles are depicted on the left- or right-hand side, respectively.

provides the scalar anisotropy index q_3 defined in Section 2.4.2. If the system is isotropic, $W_1^{0,3}$ vanishes and the anisotropy index is equal to unity $q_3 = 1$, but if $q_3 < 1$, the system is anisotropic.

Figure 2.15 compares the MIL anisotropy index β_{MIL} to those of the Minkowski tensors, $\beta_1^{0,2}$ for $W_1^{0,2}$ and q_3 for $W_1^{0,3}$ of overlapping Reuleaux triangles with differently anisotropic orientation distributions. In contrast to the two-fold symmetric ellipses and rectangles, where the orientation distribution of the angle θ is defined on $(-\pi/2, \pi/2]$ (see Section 2.1.1), the Reuleaux triangles are three-fold symmetric and the probability distribution of the orientation θ can be restricted to $(-\pi/3, \pi/3]$. A uniform distribution on $(-\pi/3, \pi/3]$ produces a perfectly isotropic Boolean model. As anisotropic orientation distributions, I here choose uniform distributions on intervals $(-\alpha, \alpha]$ with parameter $|\alpha| \leq \pi/3$ to adjust the anisotropy, which is then characterized by the standard deviation σ of the orientation distribution: $\alpha = \pi/3$ or $\sigma = \pi/3\sqrt{3} \approx 0.60$ corresponds to isotropy and $\alpha = 0$, i.e., $\sigma = 0$, to perfect alignment. In contrast to the perfectly isotropic MIL analysis, the Minkowski tensor anisotropy index q_3 characterizes the interfacial anisotropy for the Boolean models with orientation bias; for $\sigma = 0$ the index is $q_3 = 1 - 2/\pi \approx 0.36$.

Throughout my thesis, I use the Minkowski tensors to characterize anisotropy,

and I show that they are versatile, powerful, and comprehensive shape measures, which provide new insights into the shape of random spatial structures. In the next section, I study in detail the Minkowski tensors of Boolean models.

2.5 Minkowski functionals and tensors of Boolean models[32]

The Minkowski functionals and tensors of a finite observation window O depend on both its size and shape—see Ref. [204] for explicit expressions. Moreover, because the Boolean model Z is unbounded, the matrix entries of the Minkowski tensor $W_\nu^{0,s}$ diverge for infinitely large observation windows. Therefore, a Minkowski tensor density $\overline{w}_\nu^{0,s}$ is defined for the Boolean model

$$\overline{w}_\nu^{0,s}(Z) := \lim_{r\to\infty} \frac{\mathbb{E}[W_\nu^{0,s}(Z \cap rO)]}{W_0(rO)} , \tag{2.36}$$

i.e., the Minkowski tensor is divided by the size of the observation window in the limit of an infinitely large window. Note that this corresponds to a combined spatial and probabilistic averaging. This definition is independent of the shape of the observation window [204].

The Minkowski tensor densities are global characteristics of the union of the overlapping particles. Therefore, they can be estimated from observations, i.e., from samples of Boolean models; in contrast to the local characteristics, e.g., the volume or anisotropy, of single particles which are not directly measurable from the Boolean model, i.e., the union of the grains.

To describe these single-particle properties, we define the Minkowski tensor density for the particle process X, which is the collection of all single particles. In other words, instead of taking their union, each particle is considered separately.

$$\overline{w}_\nu^{0,s}(X) := \gamma \int_{\mathcal{K}_0} W_\nu^{0,s}(K)\, \mathbb{Q}(\mathrm{d}K) , \tag{2.37}$$

i.e., the number density γ times the average tensor of a single grain K, where $\mathbb{Q}$ is the distribution of the grain shape and $\mathcal{K}_0$ is the set of all convex bodies in $\mathbb{R}^d$.

The aim is to express the global tensor densities from Eq. (2.36) by the local particle densities from Eq. (2.37).

[32] This section is in large parts a direct quotation of a joint publication, Ref. [204], with Julia Hörrmann, Daniel Hug, and Klaus Mecke, who derived explicit formulas for the Minkowski tensors of Boolean models, which I verified against numeric simulations.

2.5.1 Minkowski functional densities

For the Minkowski functionals, such a relation is well known. Weil [507, Cor. 7.5] proved such density formulas for the scalar intrinsic volumes of stationary Boolean model Z in arbitrary dimension d. The expectations for the planar case in physics notation are

$$\begin{aligned}
\overline{w}_0(Z) &= 1 - \mathrm{e}^{-\overline{w}_0(X)} \,, \\
\overline{w}_1(Z) &= \overline{w}_1(X)\mathrm{e}^{-\overline{w}_0(X)} \,, \\
\overline{w}_2(Z) &= \left(\overline{w}_2(X) - \pi \cdot \overline{V}^0_{1,1}(X,X)\right) \mathrm{e}^{-\overline{w}_0(X)} \,,
\end{aligned} \tag{2.38}$$

where $\overline{V}^0_{1,1}(X,X)$ is a mixed density related to a mixed functional [400]. The latter has an intuitive geometrical interpretation, which is used in Section 3.3.1: for two bodies K and Q, the sum of ${V^0}_{1,1}(K,Q)$ and the areas of the single grains is equal to the so-called excluded area. The latter is the area of the region of all center positions of the second particle Q for which Q intersects K [355].

Note that $\overline{w}_0(Z)$, i.e., the mean area occupied by the grains divided by the size of the observation window in the limit of infinite system size, is by definition the occupied area fraction ϕ, which is already mentioned in Section 2.1.1. Similarly, $\overline{w}_1(Z)$ is more commonly known as the specific surface area.

For convenience, I also define the Euler characteristic density $\overline{\chi}(Z) := \overline{w}_2(Z)/2\pi$. The Euler characteristic density depends on the orientation distribution of the grains. If there is an orientation bias, the topology of the medium changes from that of the isotropic system. In contrast to $\overline{\chi}(Z)$, the occupied area fraction $\overline{w}_0(Z)$ and the specific surface area $\overline{w}_1(Z)$ are invariant under changes of the orientation distribution. In this sense, they exhibit a universal behavior. In Section 2.5.3, I present and discuss a simulation study of the Euler characteristic density of differently anisotropic Boolean models.

2.5.2 Surface tensor density

For Minkowski tensors, we generalize these density formulas in Ref. [204]. In this thesis, only the results for $\overline{w}_1^{0,s}(Z)$ are needed; it is here called the surface tensor density. The global average can be expressed by the local particle densities

$$\overline{w}_1^{0,s}(Z) = \overline{w}_1^{0,s}(X) \cdot \mathrm{e}^{-\overline{w}_0(X)} \,. \tag{2.39}$$

For example, for the second-rank ($s = 2$) tensor density of the parametric class of planar Boolean models from Section 2.1.1, the explicit result is given by

$$\overline{w}_1^{0,2}(Z) = \frac{\gamma \cdot \mathrm{e}^{-\overline{w}_0(X)}}{\alpha + 2} \begin{pmatrix} (\alpha+1)\left(W_1^{0,2}(G)\right)_{1,1} + \left(W_1^{0,2}(G)\right)_{2,2} & \alpha\left(W_1^{0,2}(G)\right)_{1,2} \\ \alpha\left(W_1^{0,2}(G)\right)_{1,2} & \left(W_1^{0,2}(G)\right)_{1,1} + (\alpha+1)\left(W_1^{0,2}(G)\right)_{2,2} \end{pmatrix}, \tag{2.40}$$

where G is the original grain, e.g., an ellipse or rectangle.

The Minkowski tensor densities of isotropic standard random sets are as expected just multiples of the densities of the Minkowski functionals. Note that for homogeneous Boolean models the tensors corresponding to the Euler characteristic do not provide additional information; a heuristic explanation is that there is no "anisotropic topology".

Because of the relations between global and local characteristics, the parameters α (anisotropy) and γ (intensity) of the parametric Boolean model can be expressed by the global characteristics occupied area fraction $\overline{w}_0(Z)$ and surface tensor density $\overline{w}_1^{0,2}(Z)$.

The occupied area fraction $\overline{w}_0(Z) = 1 - \mathrm{e}^{-\overline{w}_0(X)} = 1 - \mathrm{e}^{-\gamma W_0(G)}$ from Eq. (2.38) can be solved for the number density γ

$$\gamma = -\frac{\ln\left(1 - \overline{w}_0(Z)\right)}{W_0(G)}\,, \tag{2.41}$$

and from Eq. (2.40) follows

$$\alpha = \frac{\gamma\left(\left(W_1^{0,2}(G)\right)_{1,1} + \left(W_1^{0,2}(G)\right)_{2,2}\right) - 2\,\mathrm{e}^{\gamma W_0(G)}\left(\overline{w}_1^{0,2}(Z)\right)_{1,1}}{\mathrm{e}^{\gamma W_0(G)}\left(\overline{w}_1^{0,2}(Z)\right)_{1,1} - \gamma\left(W_1^{0,2}(G)\right)_{1,1}} \tag{2.42}$$

if $\left(W_1^{0,2}(G)\right)_{1,1} \neq \left(W_1^{0,2}(G)\right)_{2,2}$. Without the latter assumption the denominator in Eq. (2.42) is equal to zero by Eq. (2.40).

In Section 2.5.3, I use Eqs. (2.41) and (2.42) to define estimators for the intensity γ and the orientation parameter α and test their performance in a simulation study.

2.5.3 Simulations of nonisotropic Boolean models

In this subsection, the parametric Boolean model Z from Section 2.1.1 is simulated within the unit square with the base grain G being an ellipse or a rectangle with its main axis parallel to the first coordinate axis. The number of grains with their center located in the unit square is Poisson distributed with parameter γ.

The coordinates of the grain centers are random numbers uniformly distributed on the unit square. The ellipses are triangulated with 30 points[33]. The boundary conditions are periodic. The Computational Geometry Algorithms Library (CGAL) [1] computes the union of the triangulated grains. The program PAPAYA then calculates the Minkowski tensors and the Euler characteristic of the triangulated Boolean model [406].

The length of the main semiaxis of an ellipse is $p = 1/20$; the length of the minor semiaxis varies from $q = 1/80$ to $1/20$. For rectangles, larger systems are accessible[34] with a length of the main semiaxis $p = 1/100$ and of the minor semiaxis from $q = 1/400$ to $1/100$.

Surface tensor density $\overline{w}_1^{0,2}(Z)$

The elements of the tensor density $\overline{w}_1^{0,2}(Z)$ of Boolean models with ellipses or rectangles as functions of the expected occupied area fraction ϕ are plotted for different $\alpha \in [0, \infty]$ in Figs. 2.16 and 2.17, respectively. The error bars are smaller than point size. The curves depict the analytic function

$$\phi \mapsto \overline{w}_1^{0,2}(Z) = (1 - \phi) \cdot \overline{w}_1^{0,2}(X)\,, \tag{2.43}$$

which follows from Eq. (2.39); note that the intensity γ can be expressed by the occupied volume fraction using Eq. (2.41). The numeric and analytic values are in excellent agreement. Because I consider base grains that are symmetric with respect to both coordinate axes, $W_1^{0,2}(G)$ has diagonal form. Due to Eq. (2.40), this property carries over to $\overline{w}_1^{0,2}(Z)$. If the base grain G is a circle or a square, then $W_1^{0,2}(G)$ is proportional to the unit matrix, and from Eq. (2.40) the same follows for $\overline{w}_1^{0,2}(Z)$.

Figure 2.18 shows for a Boolean model with ellipses the difference of the diagonal elements of the tensor density $\overline{w}_1^{0,2}(Z)$ as a function of the orientation parameter α, again for different aspect ratios q/p. With an increasing α, the probability density function f_α of the random angle θ is more and more concentrated around 0 and the difference in the diagonal elements increases, obviously except for circles. All simulations were performed at expected occupied area fraction $\phi = 1/3$.

[33] The simulation is continuous; there is no discretization, which would lead to strong pixelation errors even if the resolution was high.

[34] In other words, the grains are smaller w.r.t. the observation window, i.e., there are more grains within the simulation box.

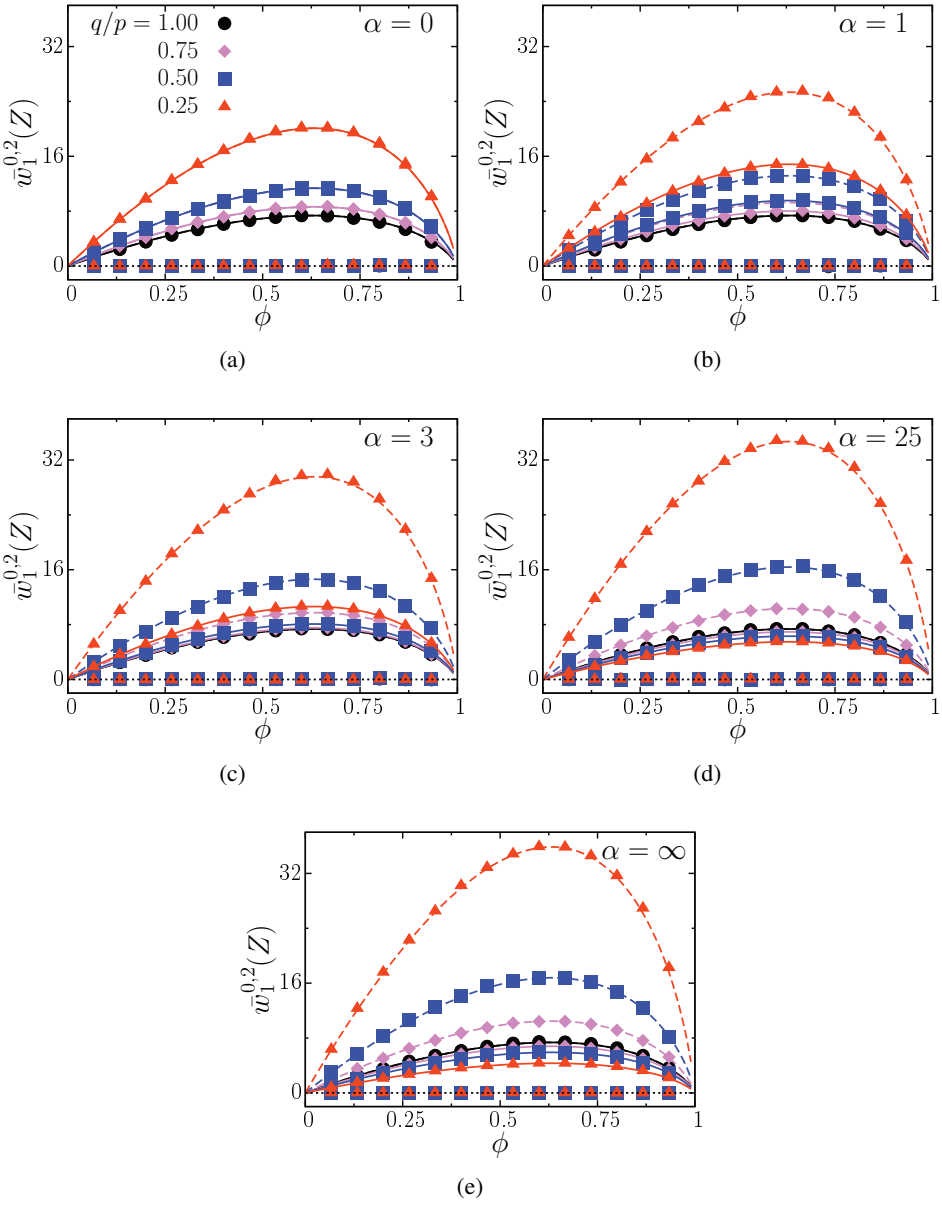

Figure 2.16: Minkowski tensor density $\overline{w}_1^{0,2}(Z)$ for the Boolean model with ellipses as a function of the expected occupied area fraction ϕ for varying aspect ratio q/p. The numerical values (represented by small symbols) are compared with the analytic function from Eq. (2.43); $\left(\overline{w}_1^{0,2}\right)_{1,1}$: dashed line; $\left(\overline{w}_1^{0,2}\right)_{2,2}$: solid line; $\left(\overline{w}_1^{0,2}\right)_{1,2}$: dotted line; (a)–(e) represent differently anisotropic orientation distributions.

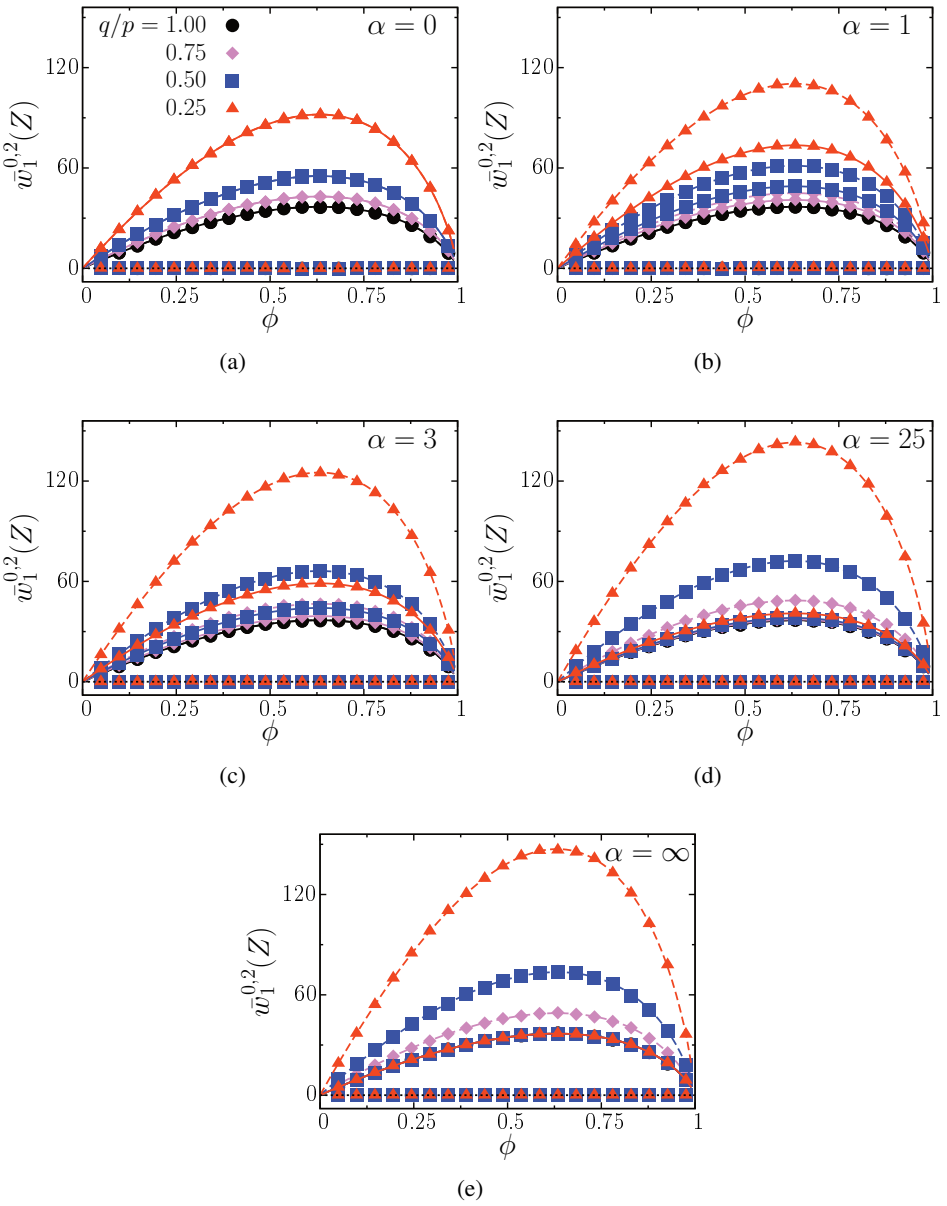

Figure 2.17: Minkowski tensor density $\overline{w}_1^{0,2}(Z)$ for the Boolean model with rectangles. For details, see Fig. 2.16.

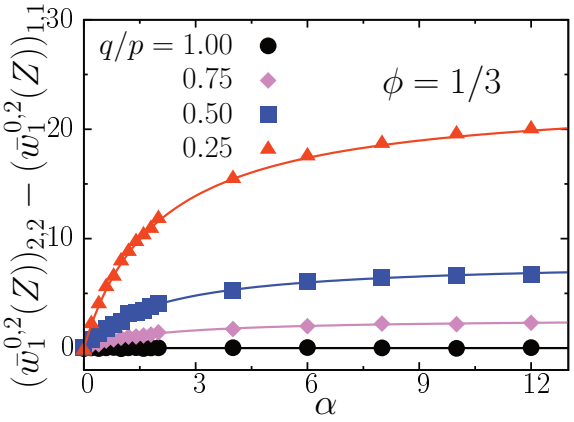

Figure 2.18: Difference of the eigenvalues of the tensor density $\overline{w}_1^{0,2}(Z)$ as a function of the orientation parameter α for different aspect ratios q/p of the ellipses. The expected occupied area fraction for the simulation was chosen to be $\phi = 1/3$. The lines show the analytic functions, which follow similarly as in Eq. (2.43).

Estimation of model parameters

If we obtain from a sample of a Boolean model an estimate $\hat{w}_1^{0,2}(Z)$ of the tensor density $\overline{w}_1^{0,2}(Z)$ and an estimate $\hat{\phi}$ of the expected occupied area fraction ϕ, Equations (2.44) and (2.45) allow an estimate of both the intensity γ and the orientation parameter α. Equations (2.41) and (2.42) lead to the estimators

$$\hat{\gamma} = -\frac{\ln\left(1-\hat{\phi}\right)}{W_0(G)} \tag{2.44}$$

and

$$\hat{\alpha} = \frac{\hat{\gamma}\left(\left(W_1^{0,2}(G)\right)_{1,1} + \left(W_1^{0,2}(G)\right)_{2,2}\right) - 2\mathrm{e}^{\hat{\gamma}W_0(G)}\left(\hat{w}_1^{0,2}(Z)\right)_{1,1}}{\mathrm{e}^{\hat{\gamma}W_0(G)}\left(\hat{w}_1^{0,2}(Z)\right)_{1,1} - \hat{\gamma}\left(W_1^{0,2}(G)\right)_{1,1}}. \tag{2.45}$$

Here, we assume that we have a priori knowledge of the base grain G. Estimating the grain distribution from empirical data is a general problem. A method of intensity can be used to estimate at least the mean value of the Minkowski functionals of the grains [34]. In our model, we assume that all particles have the same shape. Although this assumption is restrictive, it is relevant for applications. In Ref. [402], for instance, an experimental realization of a Boolean model with ellipses of fixed axes lengths is used to study flow and permeability in a two-dimensional porous medium.

In the simulations, the intensity was chosen to be $\gamma = \ln(15/14) \approx 0.06899$. For a base grain G with $(W_1^{0,2}(G))_{1,1} = (W_1^{0,2}(G))_{2,2}$, which is called isotropic with respect to the tensor density $\overline{w}_1^{0,2}$, the estimate of α is highly unstable, since then the denominator in Eq. (2.42) is equal to zero, as follows from Eq. (2.40). In

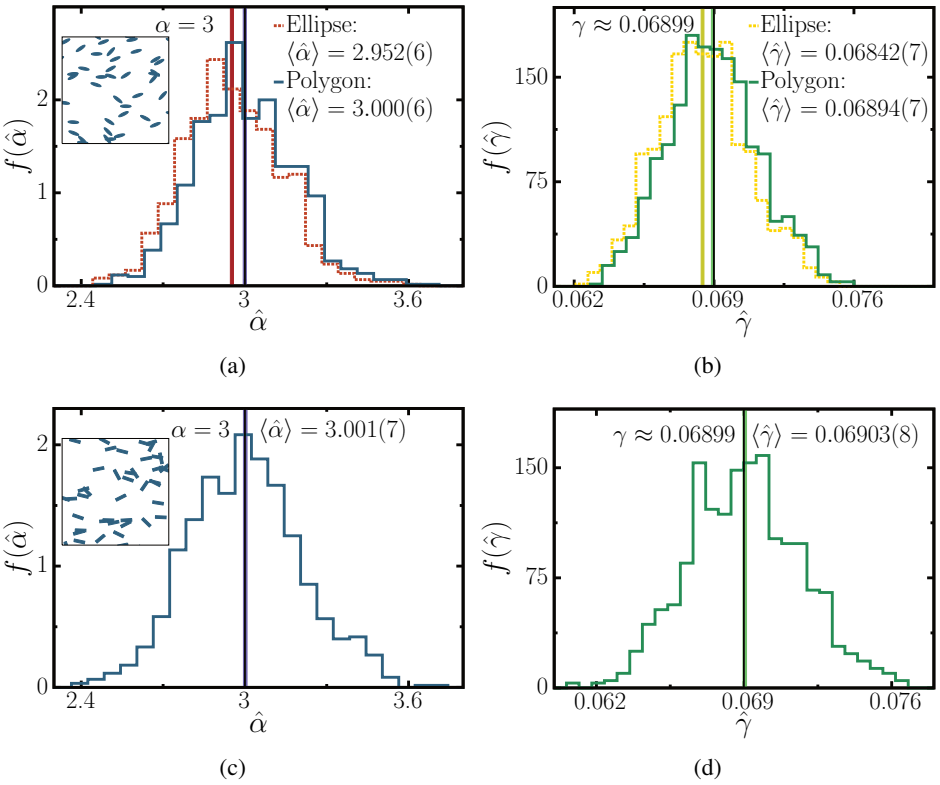

Figure 2.19: Histograms of the estimates of orientation parameter α and intensity γ for the specific choice $W_0(G) = 1$; (a) and (b) for ellipses; (c) and (d) for rectangles. The black lines depict the true values of the parameters that are to be estimated. The broad colored lines show the 1σ band of the mean of the estimate. For (a) and (b) the parameters were estimated both with the grain characteristics of an ellipse (dotted lines) and of the polygon that was actually used for the simulation (solid line). The insets in (a) and (c) illustrate samples of the Boolean models.

particular, we have to exclude spherical particles, but for example, to reconstruct sandstone with Boolean models, nonspherical particles are essential [34]. Clearly, for $\alpha \to \infty$, also the estimate of α diverges. Note the inherent disadvantage of the here applied method of moments: for small samples, estimates outside the admissible parameter space can occur, i.e., $\hat{\alpha} \leq -1$. However, with the large observation windows used for the simulations above only admissible values for α appeared.

Figure 2.19 depicts histograms of the estimates of the orientation parameter α and the intensity γ for Boolean models with ellipses in (a) and (b) or with rectangles in (c) and (d), respectively; both with an aspect ratio $q/p = 1/4$ of the grains; the

unit of the area is defined by a single grain G. To avoid finite size effects and thus systematic errors, large observation windows with $L = 100\,p$ both for rectangles and for ellipses were chosen. Because of the large observation windows, 1000 samples yield an accurate estimate of γ and α. In each plot, the black line depicts the true value of the parameter that is to be estimated. The mean of the distribution of the estimates and the error of the mean are computed via bootstrapping; the 1σ band of the mean is also shown as a broad colored line.

Both the estimation of the intensity and the orientation parameter of the Boolean model with rectangles in Figs. 2.19 (c) and (d) appear to be unbiased. The original parameters can be retained with high statistical precision. However, for smaller system sizes, finite size effects may lead to a significant bias. For the simulation of the Boolean model with ellipses in Figs. 2.19 (a) and (b), a polygon with 30 vertices approximates an ellipse; the relative error in the area is 0.7 % and in $(W_1^{0,2}(G))_{1,1}$ only 0.2 %. Nevertheless, when the parameters of the Boolean model were estimated using the single grain characteristics of an ellipse, the mean was eight standard deviations away from the true value. However, when the grain characteristics of the polygon were used, the estimator was bias-free within statistical significance. The method can be used as a very sensitive way of assessing the parameters of the system.

Euler characteristic density $\overline{\chi}(Z)$

Figures 2.20 and 2.21 show the Euler characteristic density $\overline{\chi}(Z)$ of anisotropic Boolean models with ellipses or rectangles, respectively. The Euler characteristic density $\overline{\chi}(Z)$, which is normalized with the intensity γ, is plotted as a function of the expected occupied area fraction ϕ. The Euler characteristic density $\overline{\chi}$ was computed for the same samples that were used for Figures 2.16 and 2.17. The error bars are again smaller than point size. The curves depict the analytic function

$$\phi \mapsto \overline{\chi}(Z)/\gamma = (1-\phi)[1 + \frac{W_0(G)}{2\ln(1-\phi)}\overline{V}^0_{1,1}(X,X)], \tag{2.46}$$

which follows from Eq. (2.38); note that the intensity γ can be expressed by the occupied volume fraction using Eq. (2.41).

In the case that the base grain is a rectangle, the mixed density $\overline{V}^0_{1,1}(X,X)$ can be calculated for given α using the representation of the mixed Minkowski tensors for polytopes, see Ref. [204], which leads to the formula

$$V^0_{1,1}(R, \vartheta(\theta)R) = (a^2+b^2)|\sin\theta| + 2ab|\cos\theta|, \quad \theta \in [0, 2\pi], \tag{2.47}$$

where R is a rectangle with side lengths $a, b > 0$. In the case that the base grain is an ellipse, the boundary needs to be parametrized, and a numerical integration is carried out.

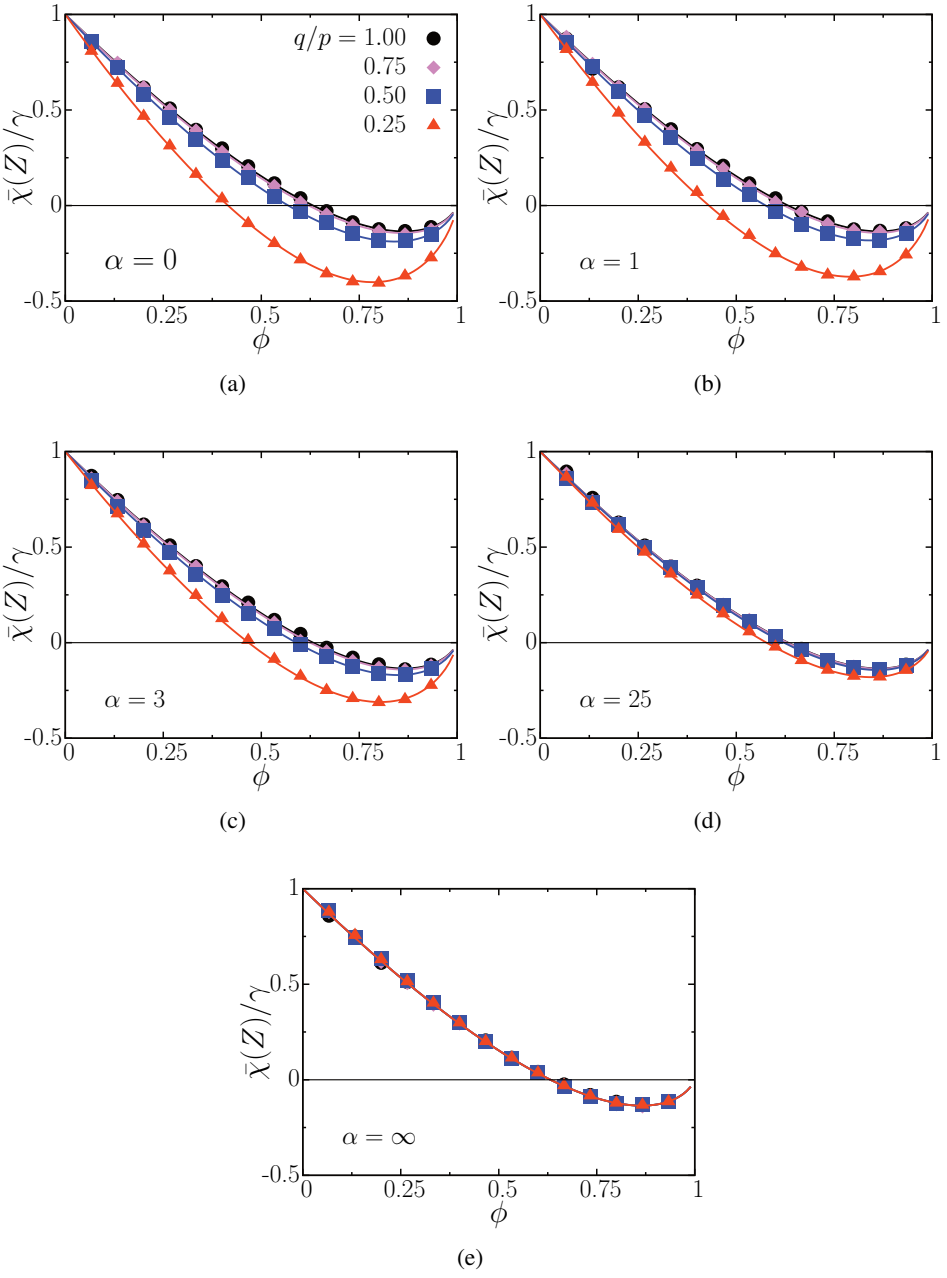

Figure 2.20: Euler characteristic density $\overline{\chi}(Z)$ normalized with the intensity γ for the Boolean model with ellipses as a function of the expected occupied area fraction ϕ for varying aspect ratio q/p. The numerical values are compared with the analytic functions from Eq. (2.46). (a)–(e) represent differently anisotropic orientation distributions.

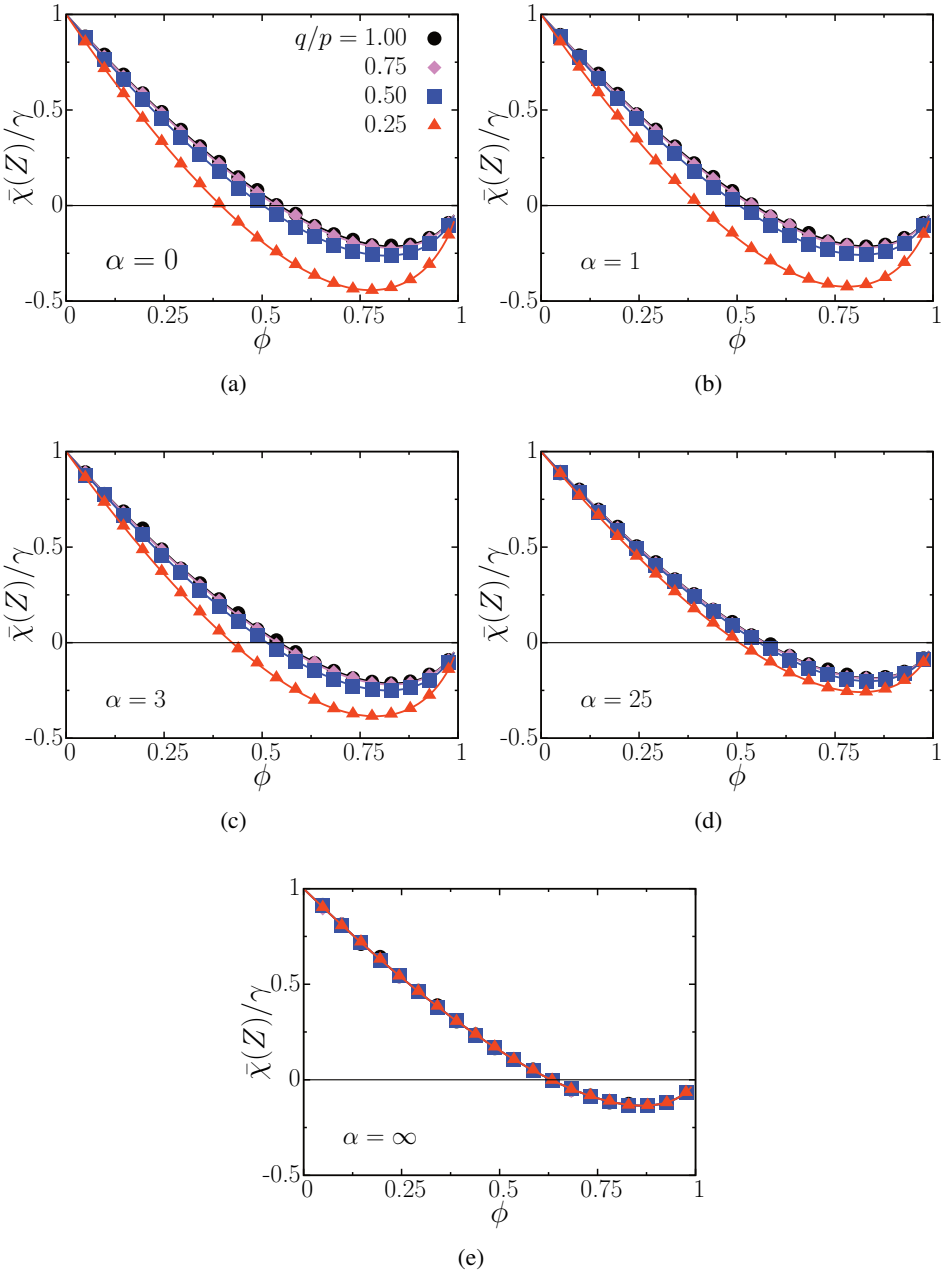

Figure 2.21: Euler characteristic density $\overline{\chi}(Z)$ normalized with the intensity γ for the Boolean model with rectangles; the lines show the analytic function from Eq. (2.46). For details, see Fig. 2.20.

The values obtained from simulations, and the analytic values are in excellent agreement. The Euler characteristic for aligned grains is independent of the aspect ratio, because in this case a change in the aspect ratio is simply an elongation of the system in one direction, in other words, an affine transformation that does not change the topology.

2.5.4 Nonuniversal variances and covariances of the Minkowski functionals

A better understanding of the structure of a random field is gained by identifying which properties are universal and which are system dependent. These (non-)universalities are interesting both from a theoretical point of view and for applications, e.g., how the geometry is related to the universal behavior of physical properties, or for estimates of the percolation threshold, see Chapter 3.

Some Minkowski functional densities exhibit a universal behavior, as discussed in Section 2.5.1. For example, the expected area fraction is independent of the grain distribution. It only depends on the intensity γ of the particle process; see Eq. 2.38. The same holds for the perimeter of the Boolean model divided by the perimeter of a single grain. In contrast to the area and the perimeter densities, the mean Euler characteristic density does depend on the orientation distribution, see Figs. 2.20 and 2.21. Only in the special case of perfectly aligned grains is the Euler characteristic density independent of the aspect ratio of the grains, see Figs. 2.20(e) and 2.21(e). In this case, a change of the aspect ratio only corresponds to a stretching of the Boolean model and does not change the topology.

Do the second moments of the Minkowski functionals also exhibit universal behavior like the first moments? The variances and covariances obviously depend on the system size. However, the asymptotic behavior of the covariances between the Minkowski functionals can be rescaled and evaluated in the limit of a convex observation window O with diverging inradius $r(O)$ such that it is independent of O. Hug *et al.* [210] defined the asymptotic covariance between the Minkowski functionals W_μ and W_ν of a Boolean model Z[35]

$$\sigma_{W_\mu W_\nu} = \lim_{r(O)\to\infty} \frac{\mathrm{Cov}(W_\mu(Z\cap O), W_\nu(Z\cap O))}{W_0(O)} \,. \tag{2.48}$$

The authors analytically derived integral formulas both for the covariances of the Minkowski functionals of stationary Boolean models in finite observation

[35] Be aware of the different notation in physics and mathematics literature. Here, I denote the asymptotic covariance between the Minkowski functionals W_μ and W_ν by $\sigma_{W_\mu W_\nu}$, which is proportional to $\sigma_{(d-\mu)(d-\nu)}$ in Ref. [210].

windows and for the asymptotic covariances[36]. For isotropic Boolean models, they found explicit expressions for the asymptotic covariances in terms of suitable moments of local curvature measures.

The formulas for the asymptotic covariances include complex integration over the grain distribution. Here, the variances and covariances are explicitly calculated, discussed, and compared for differently anisotropic Boolean models. I compare numeric evaluations of analytic formulas to simulation results. I also estimate the covariances for models for which there are currently no explicit formulas available, and address the questions: what can we learn about the qualitative behavior of the variances and covariances for differently anisotropic Boolean models? How does it differ from those of the Boolean model with discs? The covariances that include the Euler characteristic are also especially interesting for heuristic estimates of percolation thresholds, see Section 3.3.3.

Based on the general results in Ref. [210], Daniel Hug and Matthias Schulte derived for the special case of Boolean models Z of aligned rectangles with side lengths a and b explicit expressions for the variance of the area $\sigma_{W_0W_0}$, the covariance between the area and the perimeter $\sigma_{W_0W_1}$, and the variance of the perimeter $\sigma_{W_1W_1}$ [208]:

$$\sigma_{W_0W_0} = 4abe^{-2ab\gamma} \sum_{k=1}^{\infty} \frac{(ab\gamma)^k}{k!(k+1)^2}, \tag{2.49}$$

$$\sigma_{W_0W_1} = 2ab(a+b)\gamma e^{-2ab\gamma} - 4(a+b)e^{-2ab\gamma} \sum_{k=2}^{\infty} \frac{(ab\gamma)^k}{k!} \frac{k+2}{k(k+1)}, \tag{2.50}$$

$$\begin{aligned}\sigma_{W_1W_1} = {} & 16(a+b)^2\gamma e^{-2ab\gamma} \left(\sum_{k=2}^{\infty} \frac{(ab\gamma)^k}{k!} \frac{1}{k} - \sum_{k=1}^{\infty} \frac{(ab\gamma)^k}{k!} \frac{1}{k+1} \right) \\ & + 8e^{-2ab\gamma} \sum_{k=1}^{\infty} \frac{(ab\gamma)^k}{k!} + 8(a^2+b^2)\gamma e^{-2ab\gamma} \sum_{k=0}^{\infty} \frac{(ab\gamma)^k}{k!} \frac{1}{k+2}.\end{aligned} \tag{2.51}$$

To compare these formulas against simulation results, I performed between $N = 5000$ and 150,000 simulations (depending on the computational cost) of Boolean models with rectangles for each different set of parameters: at varying number densities γ, with aspect ratio 1 or 1/2, and either aligning the rectangles w.r.t. the observation window ($\alpha = \infty$) or orienting them randomly ($\alpha = 0$). The linear system size L is chosen to be 20 times the large side length of a rectangle. In contrast to the derivation of the analytic formulas, I apply periodic boundary

[36] The results in Ref. [210] are even more general, but here I am only interested in the asymptotic covariances of the Minkowski functionals.

conditions. To estimate the covariance, I simulated more than 1,400,000 samples of Boolean models including about 350,000,000 rectangles in total.

For each sample $i \in \{1, \dots N\}$, I determine the Minkowski functionals W_μ^i ($\mu = 0, 1, 2$). The sample covariance then provides an estimate of the covariance between the Minkowski functionals:

$$s_{W_\mu W_\nu} = \frac{1}{N-1} \sum_{i=1}^{N} (W_\mu^i - \hat{W}_\mu)(W_\nu^i - \hat{W}_\nu)$$

using the sample mean $\hat{W}_\mu := \frac{1}{N} \sum_{i=1}^{N} W_\mu^i$ as an estimator of the expectation. It is then divided by the size of the observation window in accordance with the definition of the asymptotic covariance in Eq. (2.48). I finally use bootstrapping (with 1000 bootstrap samples) to estimate the mean and the error of this estimator.

Figure 2.22 compares Eq. (2.49)–(2.51) against simulation results (without loss of generality, I choose the area $a \cdot b$ of a single grain to be unity). They are in excellent agreement. The variances and covariances of the Minkowski functionals exhibit a complex behavior as functions of the number density γ similar to the Boolean model with discs in Ref. [210]. The variances of area and Euler characteristic appear to have only one local maximum, but the variance of the perimeter also has at least one local minimum. As expected, the three Minkowski functionals are positively correlated at low intensities γ, but at high intensities the area is anti-correlated to both the Euler characteristic and the perimeter.

Compared to the Boolean model with discs [210], the randomly oriented squares and rectangles exhibit a qualitatively new behavior. In the covariance between the perimeter and the Euler characteristic $\sigma_{W_1 W_2}$ two additional zero-crossings appear. There is a regime in the intensity γ (around the first local minimum) for which the randomly oriented squares and rectangles are anti-correlated, while the aligned grains are positively correlated like the discs in Ref. [210], which is probably related to the fact that rotated rectangles can more easily form clusters with holes than aligned rectangles or discs. The zero-crossing of the expectation of the Euler characteristic χ for the randomly oriented rectangles is within this regime. For the aligned rectangles, the zero-crossing of the mean value of χ is at the end of this regime.

The question remains whether the variances and covariances exhibit universal behavior like the first moments. Equations 2.49 and 2.50 show that at least for aligned rectangles the variance of the area $\sigma_{W_0 W_0}$, as well as the covariance between area and perimeter divided by the perimeter of a single grain $\sigma_{W_0 W_1}/(2a + 2b)$, are indeed independent of the aspect ratio. The simulation results from Fig. 2.22 might suggest that this could also be valid for the isotropic orientation distribution. However, the variance $\sigma_{W_0 W_0}$ and the rescaled covariance $\sigma_{W_0 W_1}/(2a + 2b)$ do

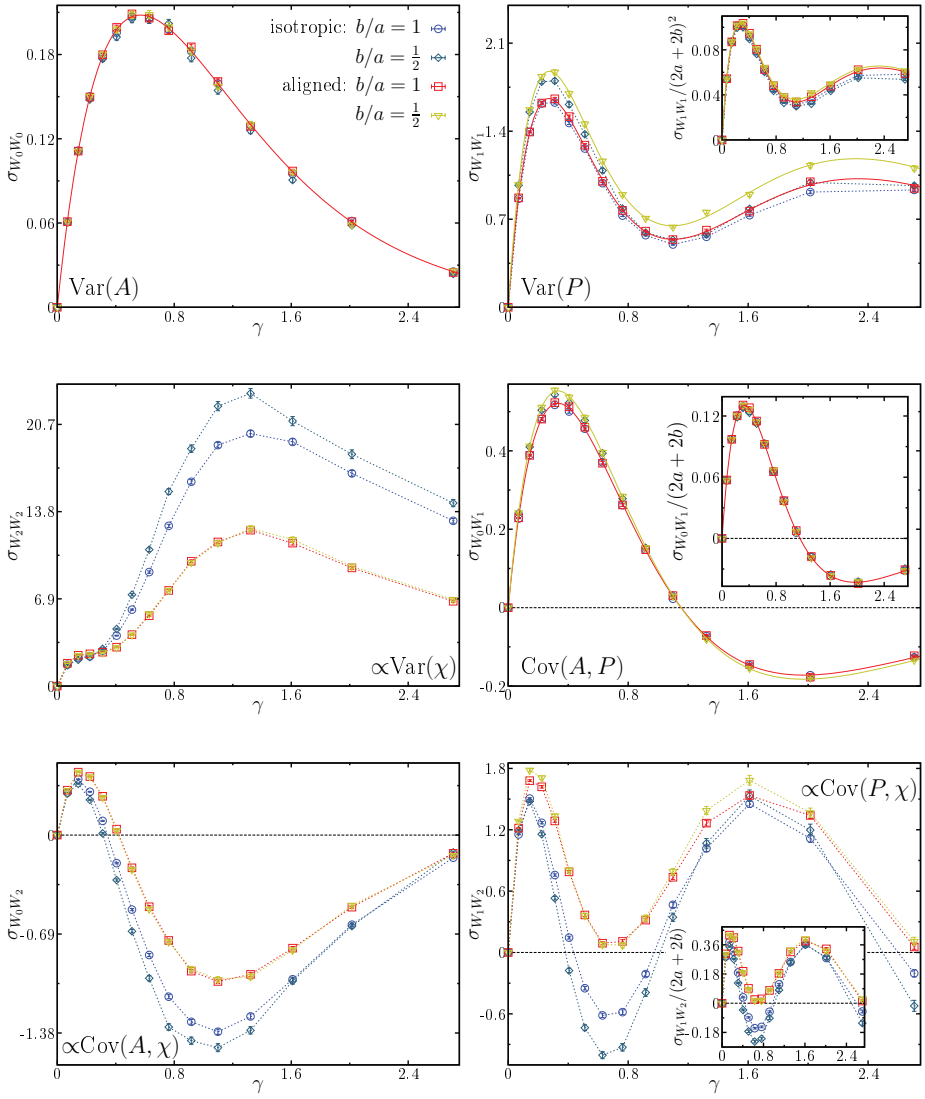

Figure 2.22: Variances and covariances of the Minkowski functionals W_0 (area A), W_1 (perimeter P), and W_2 (proportional to the Euler characteristic χ) of stationary Boolean models as a function of the number density γ. Depicted are both numerical estimates in finite observation windows with periodic boundary conditions (points with dashed lines as guides to the eye) and analytic curves (solid lines) of the asymptotic covariances, see Eqs. (2.49)–(2.51). Four different Boolean models are simulated: both for squares ($b/a = 1$) and rectangles ($b/a = 1/2$) either an isotropic orientation distribution is used or the grains are aligned (with the x-direction). In the insets, the covariances and the variance of the perimeter of the Boolean model are rescaled by the perimeter of a single grain. The unit of area is the size of a single grain.

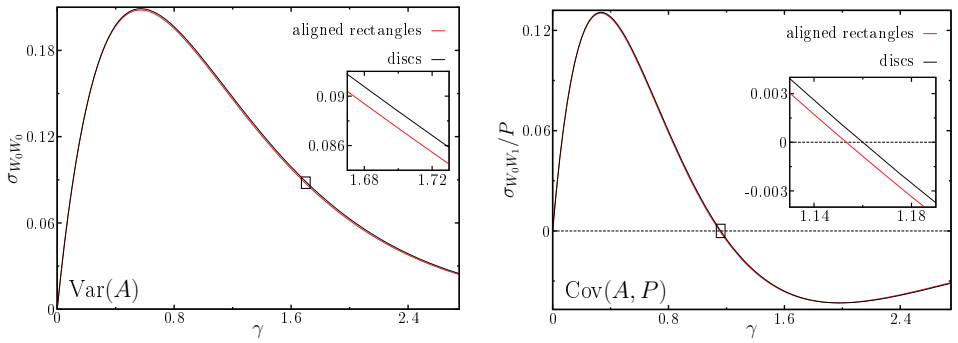

Figure 2.23: Asymptotic variances and covariances: (a) asymptotic variance of the area, (b) asymptotic covariance of area and perimeter divided by the perimeter of a single grain. They are shown both for Boolean models with aligned rectangles, see Eqs. (2.49) and (2.50), and for overlapping discs, see Ref. [210]. Note that the curves for the rectangles are independent of the aspect ratio of the rectangle. The insets are close-up views that point out that the covariances for rectangles and Boolean models differ, i.e., are not universal. For details, see Fig. 2.22.

depend on the grain distribution. I evaluate Eqs. (2.49) and (2.50) numerically and compare the covariances to those of the Boolean model with discs from Ref. [210]. Figure 2.23 shows that there is a weak but distinct difference in the analytic curves for the two different models.

The variance of the perimeter depends more clearly on the grain distribution. Even if it is rescaled by the perimeter of a single grain and even for aligned grains, the variance distinctly depends on the aspect ratio of the rectangles (except for small intensities γ). In the case of anisotropic orientation distributions, the numerical results cannot provide a final answer for the variance and covariances of the Euler characteristic, but for isotropic orientation distribution they are clearly nonuniversal.

Concluding, the first moments partially exhibit universal behavior in that the mean area or rescaled perimeter are independent of the grain distribution. In contrast to this, the variance-covariance structure exhibits a nonuniversal behavior. In some special cases, the covariances might be independent of the grain shape. In general, the second moments depend on the grain distribution, e.g., the orientation distribution, although maybe only weakly.

2.5.5 Universal probability density functions

If the probability distributions of the Minkowski functionals are rescaled by their variances, do they also depend on the grain distribution or are they universal? In

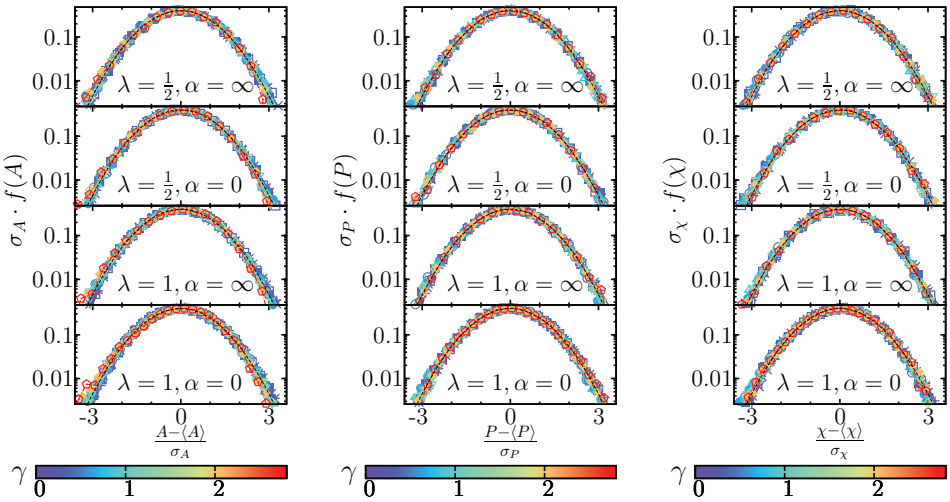

Figure 2.24: Rescaled empirical probability distributions of the Minkowski functionals of Boolean models with different aspect ratios λ, aligned rectangles ($\alpha = \infty$) or random orientations ($\alpha = 0$), and varying number densities γ: for all these different models, the distributions collapse already for the relatively small system size to the same universal qualitative behavior, which is in very good agreement with a normal distribution (dashed black line).

other words, is the qualitative behavior universal? Hug et al. [210] could indeed prove that the Minkowski functionals, when suitably normalized, satisfy a central limit theorem. They showed that the cumulative distribution functions of the rescaled Minkowski functionals converge in the limit of an infinite system size to the cumulative distribution function of a normal distribution. This theorem applies to all Minkowski functionals and very general Boolean models.

Here, I determine the Empirical Probability Density Function (EPDF) of the Minkowski functionals in a finite observation window for the differently anisotropic Boolean models with rectangles discussed above[37] Figure 2.24 plots the rescaled EPDFs of the Minkowski functionals of Boolean models with different aspect ratios λ, aligned rectangles ($\alpha = \infty$) or random orientations ($\alpha = 0$), and varying number densities γ, for which I use the same data as for the different models discussed above in Section 2.5.4.

[37] The EPDF is a histogram that is weighted by the bin width and total number of samples. Its information content is (up to binning) basically equivalent to the empirical cumulative distribution function. However, it is more convenient to compare the plot of the EPDF to the density of the normal distribution than to compare the corresponding cumulative distribution functions. Note that strictly speaking, the Minkowski functionals of the Boolean models simulated here do not have probability density functions because Dirac δ-peaks may appear. These peaks are not resolved in the EPDF in Fig. 2.24.

Already for these relatively small simulation boxes, where the linear system size L is 20 times the large side length of a rectangle, the rescaled distributions are for all Minkowski functionals, for all intensities, and for all of the simulated models in good agreement with the density of a normal distribution. In other words, even in small observation windows, the probability density functions of Minkowski functionals of Boolean models can well be approximated by Gaussian distributions. As expected, also a local version of the central limit theorem, i.e., a theorem for the probability density functions, seems to hold.

Combining this universal behavior of the rescaled probability density functions with the explicit results for the variances discussed in Section 2.5.4 can be used for sensitive hypothesis tests. Such a test could use the Minkowski functionals to decide for a given grain distribution whether or not a random two-phase medium can be modeled by overlapping grains. The joint distribution of the Minkowski functionals allows for a simultaneous characterization of the structure by several geometric functionals. This could lead to more sensitive tests, which take correlations between the MRJ into account. For a different random field with a Poisson distributed number of counts in a binned gamma-ray sky map, such a sensitive morphometric data analysis is described, tested, applied, and discussed in detail in Chapter 6. The same concepts could be applied to the Boolean model.

In Fig. 2.24, there are only small deviations from a normal distribution (relative to the error bars). The systematic deviations, e.g., due to the finite observation window size, seem to be rather small. In order to determine these deviations, a very high numerical accuracy is needed. For Boolean models consisting of rectangles with aspect ratio $1/2$, I simulate $3 \cdot 10^6$ samples for each an isotropic orientation distribution and perfect alignment (with the x-axis). For these simulations, I apply minus-sampling boundary conditions. To minimize the high computational costs, a relatively low number density γ is chosen for these simulations. It corresponds to an expected occupied area fraction $\phi = 1/15$; the linear size of the simulation box is still $L = 20a$. The resulting EPDFs are plotted in Fig. 2.25.

As expected, the high statistics reveal for the small system size a significant deviation from the normal distribution. Interestingly, all curves for the three Minkowski functionals and for the different Boolean models still collapse within error bars to a single master curve, at least for relatively small intensity.

The inset of Fig. 2.25 shows that the non-rescaled probability distributions differ distinctly for the Boolean models with either aligned or randomly oriented rectangles. In contrast to this, the normalized probability distributions collapse for both models within error bars to a single curve that agrees very well with the distribution of the number of grains hitting the observation window. Note that no fit parameter is involved, but the number of grains follows a Poisson distribution

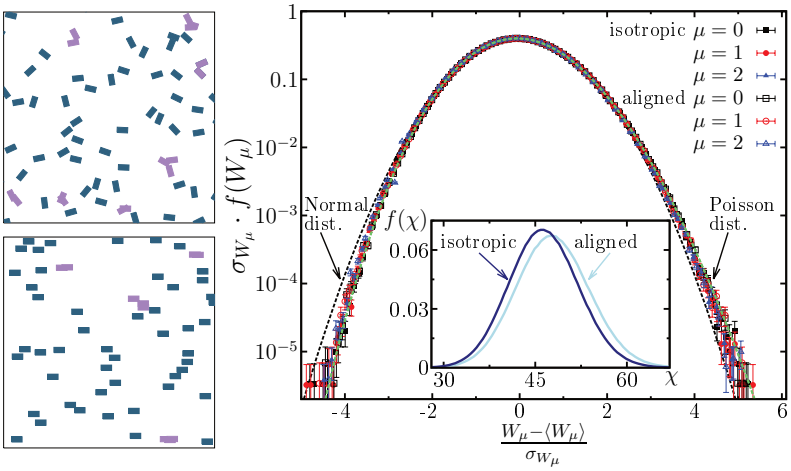

Figure 2.25: Rescaled Empirical Probability Density Function (EPDF) of the Minkowski functionals W_μ of Boolean models with either aligned or randomly oriented rectangles. The dashed black line depicts a normal distribution. On the left-hand side, two samples of the unit square of the Boolean models with either an isotropic orientation distribution or aligned rectangles are depicted; clusters of rectangles are colored purple. The inset shows the nonrescaled EPDF of the Euler characteristic comparing aligned to randomly oriented rectangles. Within error bars, all curves agree well with a master curve, which corresponds to a Poisson distribution (green dashed line) with a mean value equal to the expected number of particles hitting the unit square (≈ 60).

where the mean is equal to the product of the intensity and the mean area of the Minkowski sum of the observation window and a single grain[38]. Probably,

[38] Given a rectangle with p the larger and q the smaller semiaxis and an angle $\psi \in [-\frac{\pi}{2}, \frac{\pi}{2})$ between the main axes of the grain and the x-axis, then the area of the Minkowski sum with a square with side length L is

$$A_h(\psi) := \left[L + 2d\cos\left(|\psi| - \arctan\frac{q}{p}\right)\right]\left[L + 2d\sin\left(|\psi| + \arctan\frac{q}{p}\right)\right] - 4d^2\sin|\psi|\cos\psi$$

with $d := \sqrt{p^2 + q^2}$. The orientation ψ of the grain follows the orientation distribution $f(\psi)$. Therefore, the mean area $\bar{A}_h$ of the Minkowski sum is

$$\bar{A}_h := \int_{-\frac{\pi}{2}}^{\frac{\pi}{2}} \mathrm{d}\psi\, f(\psi) \cdot a(\psi)\ .$$

For aligned rectangles, $\bar{A}_h = L^2 + 4pq + 2L(p+q)$, and for an isotropic orientation distribution, $\bar{A}_h = L^2 + 4pq + \frac{8}{\pi}L(p+q)$. Note that $\bar{A}_h$ slightly depends on the orientation distribution. Therefore, the mean number of grains hitting the observation window is slightly different for aligned or randomly orientated rectangles. However, in Fig. 2.25 for rectangles with aspect ratio $1/2$ and a linear size of the simulation box $L = 20a$, the mean value only varies between 59.4 and 60.5, respectively. This difference is too small to be seen in Fig. 2.25.

the collapse could be explained at this relatively small intensity by the strong correlation between the Minkowski functionals and the number of grains hitting the simulation box.

2.5.6 Analytic bounds via concentration inequalities

As mentioned in the previous section, the analytic knowledge of the variances and covariances of the Minkowski functionals combined with the central limit theorem allows to define rigorous hypothesis tests for specific Boolean models. Such a test can then detect for large observation windows geometries that are unlikely in the assumed Boolean model.

For small observation windows, the probability distribution deviates distinctly from a normal distribution. However, similar rigorous tests can still be defined using analytic bounds on the complementary cumulative distribution function of, e.g., the area or perimeter. Such bounds were derived by Fabian Gieringer in his PhD thesis supervised by Günter Last [153]. Another advantage of this approach is that already a very limited knowledge about the parameters of the Boolean model is sufficient to calculate these bounds. An upper bound on the probability that the area A exceeds the expectation $\mathbb{E}[A]$ by more than r is given by the following concentration inequality:

$$P(A - \mathbb{E}[A] \geq r) \leq e^{\frac{\mathbb{E}[A]}{W_0}\left[\frac{r}{\mathbb{E}[A]} - \left(1+\frac{r}{\mathbb{E}[A]}\right)\log\left(1+\frac{r}{\mathbb{E}[A]}\right)\right]} \qquad r \geq 0\,, \tag{2.52}$$

where W_0 is the area of a single grain. Note that this bound does not depend on the orientation distribution of the grains.

Using the samples from Fig. 2.25, Figure 2.26 compares these analytic bounds to the Empirical Complementary Cumulative Distribution Function (ECCDF) for the Boolean models at an expected occupied area fraction $\phi = 1/15$ with three million samples for either aligned or randomly oriented rectangles. For the specific model studied here, the bounds are up to two orders of magnitude larger than the empirical estimate. However, for smaller observation windows and models with stronger fluctuations this difference can become distinctly smaller. For completeness, the probabilities for deviations from the expectation are also shown for the other Minkowski functionals, perimeter and Euler characteristic. Note the difference between the ECCDFs of the Euler characteristic for either aligned or randomly oriented rectangles, which was also discussed in the previous section.

Figure 2.27 compares the bounds to the ECCDF for larger expected areas $\mathbb{E}[A] = 2/15 \ldots 14/15$, i.e., for larger number densities γ. The same data is used as in Fig. 2.24. Comparing the bounds for different values of $\mathbb{E}[A]$ at the same values of r, we see that in contrast to the ECCDFs the bounds increase with increasing $\mathbb{E}[A]$. So, for large number densities, the bounds differ more from the ECCDFs.

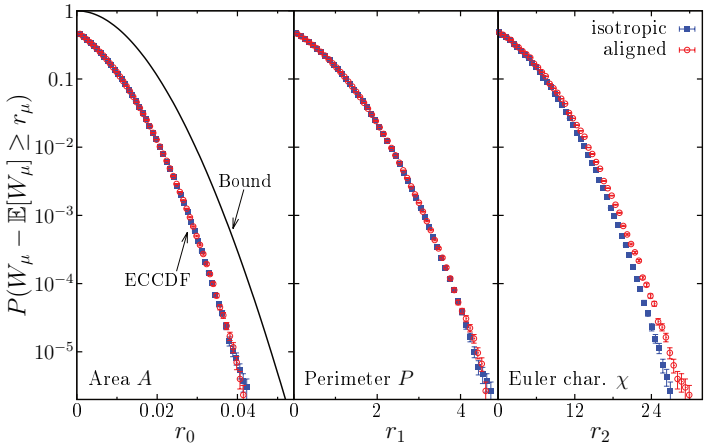

Figure 2.26: Empirical Complementary Cumulative Distribution Functions (ECCDF) of the Minkowski functionals of Boolean models in the unit square with either isotropically distributed or aligned grains; for details, see Fig. 2.25. The ECCDFs of the area (left-hand side) are compared to the upper bound (solid line) from inequality (2.52). The ECCDFs for perimeter and Euler characteristic are also depicted (center and right-hand side).

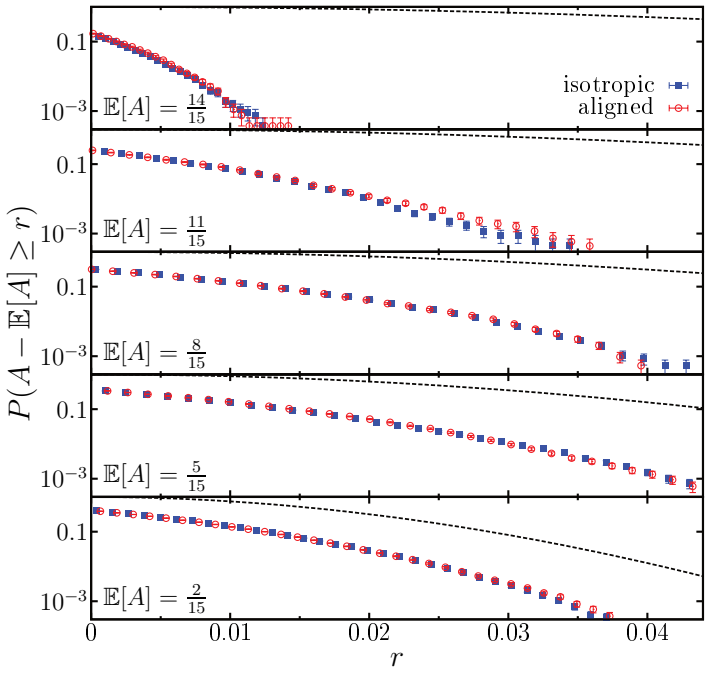

Figure 2.27: ECCDFs of the area of Boolean models in the unit square, see Figs. 2.25 and 2.26, for different expected occupied area fractions $\langle A \rangle = 2/15 \ldots 14/15$, i.e., at different number densities γ. The area of a single grain is $1/800$. The ECCDFs are compared to the upper bound (dashed line) from inequality (2.52).

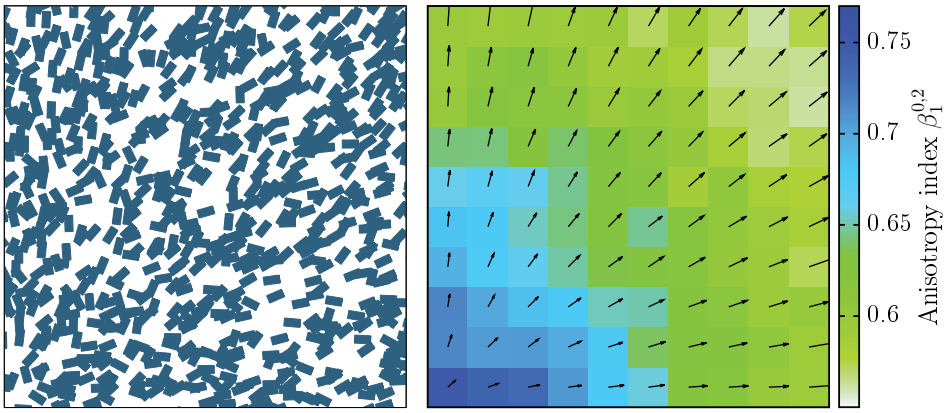

Figure 2.28: Inhomogeneous anisotropy: On the left-hand side, a sample of a model for porous media is depicted, overlapping rectangles that are randomly distributed in space. Their orientation distribution has a preferred direction that can vary for different locations: in the bottom-left corner of the sample, the system is nearly isotropic, in the top-left corner, the rectangles are strongly biased towards the vertical direction, and in the top-right corner of the sample, they are biased towards the diagonal of the simulation box. On the right-hand side, a Minkowski map determines by restricting the analysis to 10×10 scan windows the local degree of anisotropy $\beta_1^{0,2}$, which varies from almost isotropic (blue) to strongly anisotropic (green) as well as the varying preferred orientation (arrows). The Minkowski map is averaged over 100 samples.

2.5.7 Outlook: inhomogeneous Boolean models

For the Boolean model, all calculations have so far assumed stationarity, in other words, that the system is homogeneous. However, the calculations can easily be generalized also to inhomogeneous random fields. The Minkowski functionals and tensors are global characteristics, i.e., they average over the whole observation window. To quantify local structure, Schröder-Turk *et al.* [406] defined Minkowski maps: the Minkowski analysis is restricted to a small scan window; for each position of the scan window, the Minkowski tensor is evaluated and the shape index of interest is assigned to the position; by iterating over the whole image, the inhomogeneous anisotropy can be characterized.

Using Minkowski maps, the numerical techniques discussed above can also be applied to inhomogeneous Boolean models. As an example, a Boolean model with spatially varying orientation distribution is considered. Both the anisotropy parameter α and the preferred orientation θ are functions of the position $\mathbf{x}$: $\alpha(\mathbf{x}) = 1 + \alpha_0 \cdot \|\mathbf{x}\|^2$ with $\alpha_0 = 5 \cdot 10^{-6}$, and $\theta(\mathbf{x}) = \arctan(x_1/x_0)$. The expected occupied area fraction is $\phi \equiv 0.5$, the aspect ratio is $1/2$. The Minkowski map in Fig. 2.28, which is averaged over 100 samples, characterizes both the spatially varying preferred orientation and strength of the anisotropy.

2.6 Minkowski tensor densities of Gaussian random fields

Besides the Boolean model, the Gaussian random field is an important random field both in stochastic geometry and in applications, as discussed in Section 2.1.2.

In contrast to the Boolean model, the Gaussian random field g does not only take on binary values. It can be interpreted as a gray-scale image $g \in \mathbb{R}$. In order to apply the Minkowski analysis, the smooth field has to be turned into a black and white (b/w) image: the excursion set K is the set of all points $\mathbf{r}$ for which the functional value $g(\mathbf{r})$, i.e., the realization of the random field at this point, is larger or equal to a given threshold ρ [8]

$$K_\rho := \{\mathbf{r} \in \mathbb{R}^d \mid g(\mathbf{r}) \geq \rho\} \, .$$

Figure 2.29 depicts a sample of a Gaussian random wave model and a corresponding excursion set. The geometric properties, here the Minkowski tensor densities, of the excursion set are then studied as a function of the threshold ρ.

In this section, I characterize the anisotropy of stationary Gaussian random fields. There are intensive ongoing efforts to characterize the shape of Gaussian random fields and their excursion sets [e.g. 70, 77, 116, 274, 486], explicitly many results on the moments and distributions of Minkowski functionals could already be derived [e.g. 8–10, 131, 288, 455, 457]. I cannot give a full account of the literature on Minkowski functionals of Gaussian random fields. However, I want to shortly discuss the expectations of the Minkowski functionals and the second moment of the Euler characteristic of level sets of (sufficiently smooth) anisotropic Gaussian random fields, before I go on to characterize the anisotropy by calculating the mean values of the Minkowski tensors[39].

2.6.1 Global and local averages

Here, I express for general smooth stationary random fields f the global average of Minkowski tensors by a local average of the functional value $f(\mathbf{0})$ and the gradient $\nabla f(\mathbf{0})$ at the origin $\mathbf{0}$.

This is well known, e.g., for the density of the area of the excursion set K of a stationary random field, i.e., the volume/area fraction ϕ. It is simply given by the probability that the random field f is above the threshold ρ. For an observation

[39] The calculations in this section have been derived in collaboration with Klaus Mecke and Max Hörmann in whose Bachelor thesis the calculations are carried out in detail [199]. Figures 2.29–2.34 which I produced are also shown in Max Hörmann's Bachelor thesis [199].

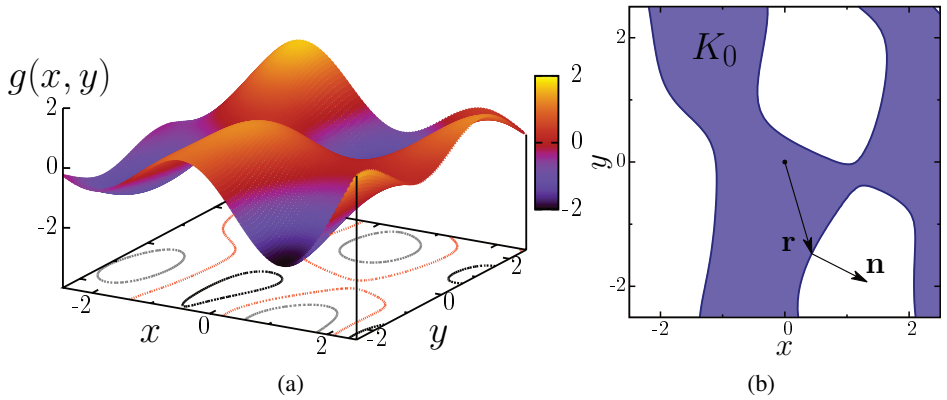

(a) (b)

Figure 2.29: Anisotropic Gaussian random fields: (a) sample of a Gaussian random wave model, see Section 2.1.2, showing both $g(\mathbf{r})$ with $\mathbf{r} = (x, y)$ and level sets for thresholds $\rho = -1, 0, 1$; (b) the corresponding excursion set K_0 for the threshold $\rho = 0$, where also a normal vector $\mathbf{n}$ on the boundary at position $\mathbf{r}$ is shown.

window O rescaled by a factor r the expected occupied area fraction is given by

$$\begin{aligned}\phi &= \lim_{r\to\infty} \frac{1}{A(rO)} \int \mathcal{D}f \int_K \mathrm{d}^d\,\mathbf{r} = \lim_{r\to\infty} \frac{1}{A(rO)} \int \mathcal{D}f \int_{rO} \mathrm{d}^d\mathbf{r}\; \Theta(f(\mathbf{r}) - \rho) \\ &= \lim_{r\to\infty} \frac{1}{A(rO)} \int_{rO} \mathrm{d}^d\mathbf{r} \int \mathcal{D}f\; \Theta(f(\mathbf{r}) - \rho)\;.\end{aligned}$$

By using the stationarity of the Gaussian random field g, ϕ is explicitly given by

$$\begin{aligned}\phi &= \lim_{r\to\infty} \frac{1}{A(rO)} \int_{rO} \mathrm{d}^d\mathbf{r}\; \frac{1}{2} \operatorname{erfc}\left[\frac{\rho}{\sqrt{2\mathrm{Var}[g]}}\right] \\ &= \lim_{r\to\infty} \frac{A(rO)}{A(rO)} \frac{1}{2} \operatorname{erfc}\left[\frac{\rho}{\sqrt{2\mathrm{Var}[g]}}\right] = \frac{1}{2} \operatorname{erfc}\left[\frac{\rho}{\sqrt{2\mathrm{Var}[g]}}\right]\end{aligned} \tag{2.53}$$

with $\operatorname{erfc}[x] = {}^2/\sqrt{\pi} \int_x^\infty dt\, \mathrm{e}^{-t^2}$.

From this calculation immediately follows that for the stationary random field f in an observation window O the volume tensors $W_0^{a,0}$ do not provide any additional information about the random field, but only about the observation window

$$\langle W_0^{a,0} \rangle = \int_{rO} \mathrm{d}^d\mathbf{r}\, \mathbf{r}^a \int \mathcal{D}f\; \Theta(f(\mathbf{r}) - \rho)\;. \tag{2.54}$$

In contrast to these translation-covariant tensors, the translation-invariant interfacial Minkowski tensor densities can indeed characterize the anisotropy of the

Gaussian random field. Similar to the Minkowski tensor densities of the Boolean model, I can express for rather general, sufficiently smooth random fields the global averages of both the Minkowski functionals [e.g. 8] and these interfacial Minkowski tensors by local averages. Therefore, I use the coarea formula [e.g. 488], where I neglect boundary contributions in the limit of an infinite observation window size.

If the Minkowski tensors $W_\nu^{0,s}$ can be represented by

$$W_\nu^{0,s} = \int_{\partial K} \mathrm{d}^{d-1}\mathbf{r}\, \mathbf{n}^s H_\nu(\mathbf{r}) \,,$$

a Minkowski tensor density $\langle w_\nu^{0,s} \rangle$, which combines spatial and probabilistic averaging, can be defined like for the Boolean model in Eq. (2.36).

For a sufficiently smooth random field f, a (suitably rescaled) spatial average $w_\nu^{0,s}$ of the Minkowski tensor of the excursion set K_ρ of a single realization of the random field f is defined and given by

$$\begin{aligned} w_\nu^{0,s} &:= \lim_{r\to\infty} \frac{1}{A(rO)} \int_{\partial K_\rho} \mathrm{d}^{d-1}\mathbf{r}\, \mathbf{n}^s H_\nu(\mathbf{r}) = \lim_{r\to\infty} \frac{1}{A(rO)} \int_{f^{-1}(\rho)} \mathrm{d}^{d-1}\mathbf{r}\, \mathbf{n}^s H_\nu(\mathbf{r}) \\ &= \lim_{r\to\infty} \frac{1}{A(rO)} \int_{rO} \mathrm{d}^d\mathbf{r}\, \|\nabla f(\mathbf{r})\| \delta(f(\mathbf{r}) - \rho) \mathbf{n}^s H_\nu(\mathbf{r}) \,. \end{aligned} \tag{2.55}$$

Combining the probabilistic average with this spatial average then leads to the definition of the Minkowski tensor densities $\langle w_\nu^{0,s} \rangle$ of the excursion set, for which I can express the global average by a local average,

$$\begin{aligned} \Rightarrow \langle w_\nu^{0,s} \rangle &:= \lim_{r\to\infty} \frac{1}{A(rO)} \int \mathcal{D}f \int_{rO} \mathrm{d}^d\mathbf{r}\, \|\nabla f(\mathbf{r})\| \delta(f(\mathbf{r}) - \rho) \mathbf{n}^s H_\nu(\mathbf{r}) \\ &= \lim_{r\to\infty} \frac{1}{A(rO)} \int_{rO} \mathrm{d}^d\mathbf{r} \int \mathcal{D}f\, \|\nabla f(\mathbf{r})\| \delta(f(\mathbf{r}) - \rho) \mathbf{n}^s H_\nu(\mathbf{r}) \\ &= \langle \|\nabla f(\mathbf{0})\|\, \delta(f(\mathbf{0}) - \rho)\, \mathbf{n}_\mathbf{0}^s\, H_\nu(\mathbf{0}) \rangle \,, \end{aligned} \tag{2.56}$$

using the stationarity in the last step, $\mathbf{n_0}$ denotes the normal vector at the origin.

2.6.2 Distribution of the gradient

To evaluate the average in Eq. (2.56) for the Gaussian random field g, the joint probability density of the derivatives of the Gaussian random fields is needed. Hörmann [199] discusses in detail the joint distributions of derivatives of arbitrary order. Because I concentrate in this thesis only on the interfacial Minkowski tensor

densities $\langle w_1^{0,s} \rangle$, I here only need the joint distribution of the gradient $\nabla g(\mathbf{0})$ and the functional value $g(\mathbf{0})$.

The probability density function f_g that the functional value at the origin of a Gaussian random field takes on the value g_0 is by definition a Gaussian distribution

$$f_g(g_0) = \frac{1}{\sqrt{2\pi \mathrm{Var}(g)}} \mathrm{e}^{-\frac{g_0^2}{2\mathrm{Var}(g)}} . \tag{2.57}$$

The variance follows, e.g., from the Fourier transform of the covariance function

$$\mathrm{Var}(g) = \int_{\mathbb{R}^d} \mathrm{d}^d \mathbf{q} \, \frac{\tilde{\sigma}^2(\mathbf{q})}{(2\pi)^d} .$$

For example for the Gaussian random wave model from Section 2.1.2, I have chosen the parameters such that $\mathrm{Var}(g) = 1$.

For the gradient, the probability distributions can, e.g., be derived from Eq. (2.2) via replacing the derivative by its Fourier transform, i.e., instead of the complicated derivatives we can simply calculate with products of wave vectors. By also using that the Gaussian random field is real valued, a lengthy calculation [199] finally yields the well-known result that the derivatives of a Gaussian random field are themselves Gaussian distributed; for example, Chung [101] explains this finding by that a linear operation of a Gaussian random field is again a Gaussian random field,

$$f_{\nabla g}(\mathbf{g_0'}) = \frac{1}{\sqrt{(2\pi)^d \det[\mathrm{Cov}(\nabla g)]}} \cdot \mathrm{e}^{-\frac{1}{2} \cdot \mathbf{g_0'}^t \mathrm{Cov}^{-1}(\nabla g) \mathbf{g_0'}} . \tag{2.58}$$

The entries in the covariance matrix $\mathrm{Cov}(\nabla g)$ of the gradient of the Gaussian random field at the origin are equal to the corresponding derivatives of the covariance of the Gaussian random field [8], or using the Fourier transformation

$$\mathrm{Cov}(\nabla g) = \int_{\mathbb{R}^d} \mathrm{d}^d q \, \frac{\tilde{\sigma}^2(\mathbf{q})}{(2\pi)^d} \cdot \mathbf{q} \otimes \mathbf{q} . \tag{2.59}$$

Moreover, it is well known that a homogeneous random field and its first order partial derivatives are uncorrelated [486], which implies in the case of a Gaussian random field that they are even stochastically independent [274]. In other words, the joint probability distribution of the functional value of a Gaussian random field and its first derivatives at the origin is simply a product of the distribution of the functional value $f_g(g_0)$ and the distribution of the gradient $f_{\nabla g}(\mathbf{g_0'})$

$$f_{g,\nabla g}(g_0, \mathbf{g_0'}) = f_g(g_0) \cdot f_{\nabla g}(\mathbf{g_0'}) .$$

For the Gaussian random wave model from Section 2.1.2, the eigenvalues λ_1 and λ_2 of the covariance matrix $\mathrm{Cov}(\nabla g)$ of the gradient of g follow straightforwardly from Eq. (2.59), see Ref. [199],

$$\lambda_1 = \frac{1+\alpha}{2+\alpha} \quad \text{and} \quad \lambda_2 = \frac{1}{2+\alpha} \,,$$

and depend as expected on the anisotropy of the model. In the limit of infinity α, the wave vectors all point in the same direction and the wavefronts are all parallel to each other. The model degenerates into an effectively one-dimensional random field, which is trivially repeated in the perpendicular direction; accordingly, $\lambda_1 \xrightarrow{\alpha\to\infty} \mathrm{Var}(g) = 1$ and $\lambda_2 \xrightarrow{\alpha\to\infty} 0$, and in the isotropic case ($\alpha = 0$), $\lambda_1 = \lambda_2 = 1/2$.

2.6.3 Minkowski functional densities

The Minkowski functional densities can easily be derived for anisotropic sufficiently smooth Gaussian random fields from Eq. (2.56) using Eqs. (2.57) and (2.58). The area density is already given in Eq. (2.53).

As mentioned above there are already many results on Minkowski functionals of Gaussian random fields [e.g. 8, 10, 288, 457]. However, as an introduction to the more complicated calculations for the Minkowski tensors, I want to shortly discuss the density of $\langle w_1 \rangle$, i.e., in two dimensions the perimeter and in three dimensions the surface area, for anisotropic Gaussian random fields. According to Eq. (2.56), it is given by

$$\begin{aligned}
\langle w_1 \rangle &= \langle \|\nabla g(\mathbf{0})\| \, \delta(g(\mathbf{0}) - \rho) \rangle \\
&= \int_{\mathbb{R}} \mathrm{d}(g(\mathbf{0})) \; \delta(g(\mathbf{0}) - \rho) \, f_g(g(\mathbf{0})) \int_{\mathbb{R}^d} \mathrm{d}^d(\nabla g(\mathbf{0})) \; \|\nabla g(\mathbf{0})\| \cdot f_{\nabla g}(\nabla g(\mathbf{0})) \\
&= f_g(\rho) \int_{\mathbb{R}^d} \mathrm{d}^d(\nabla g(\mathbf{0})) \; \|\nabla g(\mathbf{0})\| \cdot f_{\nabla g}(\nabla g(\mathbf{0})) \,,
\end{aligned}$$

with $f_g(\rho)$, and $f_{\nabla g}(\nabla g(\mathbf{0}))$ from Eqs. (2.57) and (2.58). If the integral is expressed in spherical coordinates, the integration of the absolute value of the gradient can be carried out. Only the integration of the direction $\mathbf{u} \in \mathbb{S}^{d-1}$ of the gradient remains

$$\langle w_1 \rangle = \frac{2^{\frac{d-1}{2}} \cdot \Gamma(\frac{d+1}{2}) \cdot f_g(\rho)}{(2\pi)^{d/2} \sqrt{\det[\mathrm{Cov}(\nabla g)]}} \cdot \int_{\mathbb{S}^{d-1}} \mathrm{d}\mathbf{u} \; \frac{1}{(\mathbf{u}^t \mathrm{Cov}^{-1}(\nabla g)\mathbf{u})^{\frac{d+1}{2}}} \,.$$

For example, in two dimensions the density is

$$\langle w_1 \rangle = \frac{f_g(\rho)}{2\sqrt{2\pi \cdot \lambda_1 \lambda_2}} \cdot \int_0^{2\pi} \mathrm{d}\omega \; \frac{1}{(\mathbf{u}^t \mathrm{Cov}^{-1}(\nabla g)\mathbf{u})^{\frac{3}{2}}} \,, \tag{2.60}$$

with $\mathbf{u} = (\cos(\omega), \sin(\omega))$ and $\det[\mathrm{Cov}(\nabla g)] = \lambda_1 \lambda_2$. Because the covariance matrix $\mathrm{Cov}(\nabla g)$ is positive definite[40] and symmetric, a rotation represented by the rotation matrix Q can diagonalize the covariance matrix

$$\mathrm{Cov}(\nabla g) = Q \begin{pmatrix} \lambda_1 & 0 \\ 0 & \lambda_2 \end{pmatrix} Q^t \,, \tag{2.61}$$

and the integral in Eq. (2.60) can w.l.o.g. be written as

$$\langle w_1 \rangle = \frac{f_g(\rho)}{2\sqrt{2\pi \cdot \lambda_1 \lambda_2}} \cdot \int_0^{2\pi} \mathrm{d}\omega \; \frac{1}{(\cos^2(\omega)/\lambda_1 + \sin^2(\omega)/\lambda_2)^{\frac{3}{2}}} \,,$$

which can be expressed by $E[k] = \int_0^{\pi/2} \mathrm{d}\omega \; \sqrt{1 - k \sin^2 \omega}$, the complete elliptic integral of the second kind,

$$\langle w_1 \rangle = \sqrt{\frac{2}{\pi}} \cdot f_g(\rho) \cdot \sqrt{\lambda_1} \cdot E[1 - \frac{\lambda_2}{\lambda_1}] \,. \tag{2.62}$$

The mean density for differently anisotropic Gaussian random fields differ by a prefactor from the isotropic model, the functional dependence on the threshold is proportional to a Gaussian function; see Fig. 2.30.

For the Euler characteristic, we have obtained a simplified integral expression for its second moment; the calculations were mainly carried out by Max Hörmann [199]. The final expression can easily be computed numerically. With the second moment of the Euler characteristic, its whole distribution is determined, because Estrade and León [131] could prove a central limit theorem for the Euler characteristic.

2.6.4 Minkowski tensor densities

In order to calculate the Minkowski tensor densities from Eq. (2.56), we also need the distribution of the normal vectors on the excursion set, or more precisely of the tensor product of the normal vectors.

It is well known that the gradient $\nabla f(\mathbf{r})$ of a function f is at the position $\mathbf{r}$ perpendicular to the level set $\rho = f(\mathbf{r})$ and pointing in direction of increasing functional values, in other words it is always antiparallel to the normal vector $\mathbf{n}$ on the excursion set. The normal vector is therefore simply given by

$$\mathbf{n} = -\frac{\nabla f(\mathbf{r})}{\|\nabla f(\mathbf{r})\|} \,, \tag{2.63}$$

[40] The extreme case of a quasi-one-dimensional Gaussian random field for $\alpha = \infty$ is discussed in Section 2.6.4.

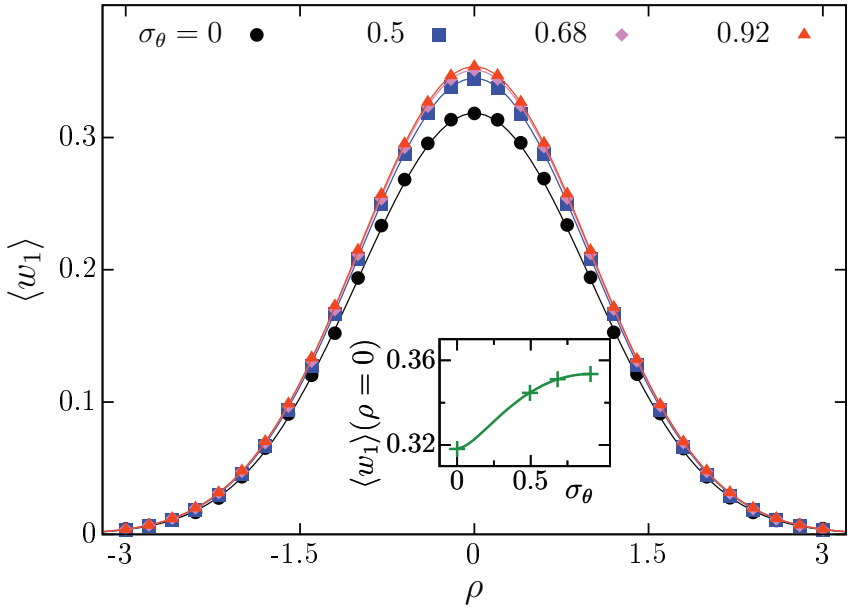

Figure 2.30: The perimeter density $\langle w_1 \rangle$ of the excursion set of a Gaussian random field as a function of the threshold ρ for differently anisotropic Gaussian random wave models: σ_θ is the standard deviation of the orientation distribution of the wave vectors; $\sigma_\theta = \pi/\sqrt{12} \approx 0.91$ corresponds to an isotropic Gaussian random field and $\sigma_\theta = 0$ to a perfectly anisotropic random field, i.e., a quasi-one-dimensional model where all random waves have the same wave vector. The points show numerical estimates, the lines represent the analytic curves from Eq. (2.62). They are in excellent agreement. The inset shows the change of the perimeter density at threshold $\rho = 0$ as a function of the anisotropy parameter σ_θ.

and the probability distribution of the gradient is already given in Eq. (2.58).

Equation 2.56 can then be evaluated straightforwardly for the interfacial Minkowski tensor densities $\langle w_1^{0,s} \rangle$ of the excursion set of a Gaussian random field g in any dimension d,

$$\begin{aligned}
\langle w_1^{0,s} \rangle &= \langle \|\nabla g(\mathbf{0})\| \, \delta(g(\mathbf{0}) - \rho) \, \mathbf{n}_\mathbf{0}^s \rangle \\
&= \int_{\mathbb{R}} \mathrm{d}(g(\mathbf{0})) \; \delta(g(\mathbf{0}) - \rho) \, f_g(g(\mathbf{0})) \\
&\qquad \cdot \int_{\mathbb{R}^d} \mathrm{d}^d(\nabla g(\mathbf{0})) \; \|\nabla g(\mathbf{0})\| \, \mathbf{n}_\mathbf{0}^s \cdot f_{\nabla g}(\nabla g(\mathbf{0})) \\
&= f_g(\rho) \int_{\mathbb{R}^d} \mathrm{d}^d(\nabla g(\mathbf{0})) \; \frac{(-1)^s \cdot (\nabla g(\mathbf{0}))^s}{\|\nabla g(\mathbf{0})\|^{s-1}} \cdot f_{\nabla g}(\nabla g(\mathbf{0})) \; .
\end{aligned} \tag{2.64}$$

From this integral expression can be seen that all Minkowski tensor densities of

odd rank vanish

$$\langle w_1^{0,2s-1} \rangle \equiv 0 \,, \tag{2.65}$$

because the absolute value $\|\nabla g(\mathbf{0})\|$ and the probability distribution of the gradient are symmetric $f_{\nabla g}(\nabla g(\mathbf{0})) = f_{\nabla g}(-\nabla g(\mathbf{0}))$, in contrast to $(\nabla g(\mathbf{0}))^s$. In the following, I therefore only consider even rank s.

Then, the remaining integral in Eq. (2.64)

$$\langle w_1^{0,s} \rangle = \frac{f_g(\rho)}{(2\pi)^{d/2}\sqrt{\det[\mathrm{Cov}(\nabla g)]}} \cdot \int_{\mathbb{R}^d} \mathrm{d}^d(\nabla g(\mathbf{0})) \, \frac{(\nabla g(\mathbf{0}))^s}{\|\nabla g(\mathbf{0})\|^{s-1}} \cdot \mathrm{e}^{-\frac{1}{2}(\nabla g(\mathbf{0}))^t \mathrm{Cov}^{-1}(\nabla g)(\nabla g(\mathbf{0}))},$$

can be expressed in spherical coordinates, and the integration of the absolute value of the gradient can be carried out. Only the integration of the direction $\mathbf{u} \in \mathbb{S}^{d-1}$ of the gradient remains

$$\langle w_1^{0,s} \rangle = \frac{2^{\frac{d-1}{2}} \cdot \Gamma(\frac{d+1}{2}) \cdot f_g(\rho)}{(2\pi)^{d/2}\sqrt{\det[\mathrm{Cov}(\nabla g)]}} \cdot \int_{\mathbb{S}^{d-1}} \mathrm{d}\mathbf{u} \, \frac{\mathbf{u}^s}{(\mathbf{u}^t \mathrm{Cov}^{-1}(\nabla g)\mathbf{u})^{\frac{d+1}{2}}} \,. \tag{2.66}$$

For example, in two dimensions the Minkowski tensors densities are

$$\langle w_1^{0,s} \rangle = \frac{f_g(\rho)}{2\sqrt{2\pi \cdot \lambda_1\lambda_2}} \cdot \int_0^{2\pi} \mathrm{d}\omega \, \frac{\mathbf{u}^s}{(\mathbf{u}^t \mathrm{Cov}^{-1}(\nabla g)\mathbf{u})^{\frac{3}{2}}} \,,$$

with $\mathbf{u} = (\cos(\omega), \sin(\omega))$ and $\det[\mathrm{Cov}(\nabla g)] = \lambda_1\lambda_2$. Note that for any rank s of the Minkowski tensor, the density is only a function of the covariance matrix of the gradient, which become important in Section 2.6.6.

Analogous to the discussion in Section 2.6.3: because the covariance matrix $\mathrm{Cov}(\nabla g)$ is positive definite[41] and symmetric, a rotation represented by the rotation matrix Q can diagonalize the covariance matrix, see Eq. (2.61). Thus simplifying the calculation, the second-rank tensor can be calculated explicitly

$$\langle w_1^{0,2} \rangle = \sqrt{\frac{2}{\pi}} \cdot f_g(\rho) \cdot \frac{\sqrt{\lambda_1\lambda_2}}{\lambda_2 - \lambda_1} \, Q \, \mathrm{diag}\begin{pmatrix} \sqrt{\lambda_1}(K[1-\frac{\lambda_1}{\lambda_2}] - E[1-\frac{\lambda_1}{\lambda_2}]) \\ \sqrt{\lambda_2}(E[1-\frac{\lambda_2}{\lambda_1}] - K[1-\frac{\lambda_2}{\lambda_1}]) \end{pmatrix} Q^t \tag{2.67}$$

where $K[k]$ or $E[k]$ are the complete elliptic integral of the first or second kind, respectively.

[41] The extreme case of a quasi-one-dimensional Gaussian random field for $\alpha = \infty$ is discussed below.

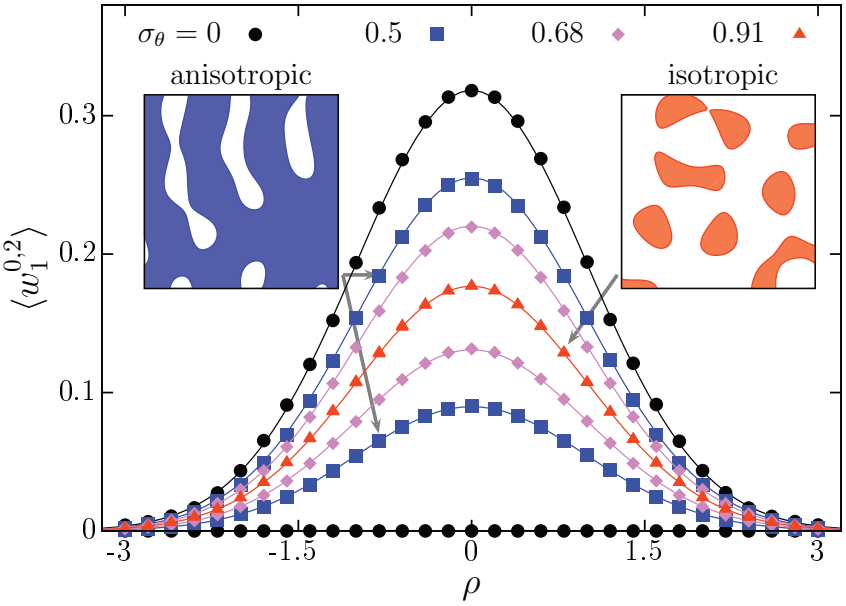

Figure 2.31: The eigenvalues of the Minkowski tensor $W_1^{0,2}$ of a Gaussian random field as a function of the threshold ρ for differently anisotropic Gaussian random wave models. For details, see Fig. 2.30.

The only dependence on the threshold ρ is given by $f_g(\rho)$; in other words, the eigenvalues of the Minkowski tensor density as a function of the threshold are Gaussian shaped like for the perimeter density $\langle w_1 \rangle$, see Eq. (2.62), which is expected because the sum of the eigenvalues of $W_1^{0,2}$, i.e., the trace of the tensor, is well known to be equal to the perimeter W_1.

However, independent of the threshold density the eigenvalues of the Minkowski tensor density $\langle w_1^{0,2} \rangle$ deviate and thus quantify the anisotropy of the Gaussian random field. They are plotted for differently anisotropic Gaussian random wave models in Fig. 2.31. For the isotropic system, the eigenvalues coincide $\langle w_1^{0,2} \rangle_{xx} = \langle w_1^{0,2} \rangle_{yy} = \frac{1}{2} \langle w_1 \rangle$. However, with increasing anisotropy of the orientation distribution of the wave vectors, the eigenvalue corresponding to the x-direction increases while the eigenvalue corresponding to the y-direction decreases. As discussed above, in the limit of aligned wave vectors $\alpha \to \infty$, the Gaussian random field becomes quasi-one-dimensional. In this limit, the perpendicular component $\langle w_1^{0,2} \rangle_{yy}$ of the Minkowski tensor density in Eq. (2.67) vanishes, see Ref. [199],

$$\langle w_1^{0,2} \rangle_{yy} \leq f_g(\rho) \cdot \sqrt{\frac{\pi}{2}} \cdot \sqrt{\lambda_2} \xrightarrow{\alpha \to \infty} 0 \,.$$

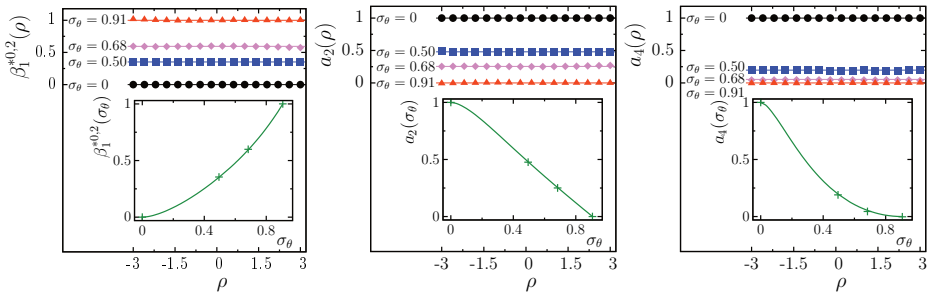

Figure 2.32: Anisotropy indices for Gaussian random fields, i.e., scalar measures derived from the interfacial Minkowski tensors, which quantify the strength of the anisotropy: (a) the ratio of the eigenvalues of the Minkowski tensor density $\langle w_1^{0,2} \rangle$; (b) and (c) the ratio of the absolute value of the irreducible representations $\mathcal{G}_k$ of rank 2 and rank 0 or rank 4 and rank 0, respectively, see Eq. (2.31). All three indices quantify the inherent anisotropy of the Gaussian random field, in that they are independent of the threshold ρ; the insets show these anisotropy parameters as a function of the anisotropy parameter σ_θ of the Gaussian random wave models. For details, see Fig. 2.30. The fourth rank tensor $W_1^{0,4}$ contains nonredundant anisotropy information compared to the second-rank tensor.

Assuming a diagonal covariance matrix of the gradient, also the fourth rank tensor can be calculated straightforwardly in the Cartesian representation, see Ref. [199],

$$\begin{aligned}
\langle w_1^{0,4} \rangle_{xxxx} &= \sqrt{\frac{2}{\pi}} \cdot f_g(\rho) \cdot \frac{\sqrt{\lambda_2} \cdot ((\lambda_1 + \lambda_2) E[1 - \tfrac{\lambda_1}{\lambda_2}] - 2\lambda_1 K[1 - \tfrac{\lambda_1}{\lambda_2}]) \cdot \lambda_1}{(\lambda_1 - \lambda_2)^2} \,, \\
\langle w_1^{0,4} \rangle_{yyyy} &= \langle w_1^{0,4} \rangle_{xxxx} \cdot \frac{\lambda_2}{\lambda_1} \,, \\
\langle w_1^{0,4} \rangle_{xxyy} &= \langle w_1^{0,2} \rangle_{xx} - \langle w_1^{0,4} \rangle_{xxxx} \,, \\
\langle w_1^{0,4} \rangle_{xyyy} &= \langle w_1^{0,4} \rangle_{xxxy} = 0 \,.
\end{aligned} \tag{2.68}$$

However, to extract the anisotropy information, the irreducible representation from Section 2.4.2 is needed.

2.6.5 Anisotropy indices of rank two and four

As discussed in Section 2.4.2, the irreducible representation w.r.t. SO(2) provides scalar anisotropy indices a_s, which characterize the degree of anisotropy w.r.t. the interfacial Minkowski tensors $W_1^{0,s}$. Inserting Eqs. (2.67) and (2.68) in Eqs. (2.32) or (2.33), lengthy but explicitly expressions can be given the Gaussian random

wave model. They extend the concept of the ratio of the eigenvalues $\beta_1^{0,2}$ of the second-rank tensor to arbitrary rank tensors.

These scalar anisotropy indices quantify the inherent anisotropy of the Gaussian random field, in that they are independent of the threshold ρ. They are plotted in Fig. 2.32, where instead of the standard $\beta_1^{0,2}$, the average ratio of the eigenvalues, I here use a slightly modified definition $\beta_1^{*0,2}$, the ratio of the eigenvalues of the Minkowski tensor density. The latter can easily be calculated from Eq. (2.67)

$$\beta_1^{*0,2} = \sqrt{\frac{\lambda_1}{\lambda_2}} \cdot \frac{K[1-\frac{\lambda_1}{\lambda_2}] - E[1-\frac{\lambda_1}{\lambda_2}]}{E[1-\frac{\lambda_2}{\lambda_1}] - K[1-\frac{\lambda_2}{\lambda_1}]} , \tag{2.69}$$

which is only a function of the ratio of the eigenvalues of the covariance matrix of the gradient.

Figure 2.32 shows that $a_4 > 0$. The fourth rank tensor $W_1^{0,4}$ contains nonredundant anisotropy information, in that it is not contained in the second-rank tensor $W_1^{0,2}$.

2.6.6 Extended Gaussian image density

Nevertheless, it is sufficient to only determine the second-rank Minkowski tensor to derive all higher-rank tensors of a Gaussian random field, which might at first sound counter-intuitively.

As discussed in Section 2.4.2, the extended Gaussian image $E(\omega)$, which is proportional to the distribution of the normal vectors in direction ω, contains the information of all Minkowski tensors $W_1^{0,s}$ of arbitrary rank s and in this sense provides a complete description of the anisotropy w.r.t. the interface.

Because of the normalization of the extended Gaussian image, it also needs to be rescaled by the size of the observation window before considering the limit of infinite system size. In this limit, I define for a homogeneous random field f the spatial average of the extended Gaussian image

$$e(\mathbf{u}) := \lim_{r\to\infty} \frac{1}{A(rO)} E(\mathbf{u}) = \lim_{r\to\infty} \frac{1}{A(rO)} \int_{\partial K_\rho} \mathrm{d}\mathbf{r}\, \delta(\mathbf{n}(\mathbf{r}) - \mathbf{u}) ,$$

where I again identify the direction $\mathbf{u} \in \mathbb{S}^1$ by the angle ω between the x-axis and the vector $\mathbf{u}$.

Following Eq. (2.55), the spatial average of the extended Gaussian image can

be rewritten for a sufficiently smooth, homogeneous random field f

$$\begin{aligned} e(\mathbf{u}) &= \lim_{r\to\infty} \frac{1}{A(rO)} \int_{f^{-1}(\rho)} \mathrm{d}\mathbf{r}\, \delta(\mathbf{n}(\mathbf{r}) - \mathbf{u}) \\ &= \lim_{r\to\infty} \frac{1}{A(rO)} \int_{rO} \mathrm{d}^d\mathbf{r}\, \|\nabla f(\mathbf{r})\| \delta(f(\mathbf{r}) - \rho)\, \delta(\mathbf{n}(\mathbf{r}) - \mathbf{u}) \ . \end{aligned}$$

The extended Gaussian image density $\langle e(\mathbf{u})\rangle$ is then defined by combining the probabilistic average with this spatial average, and I can again express the global average by a local average

$$\begin{aligned} \langle e(\mathbf{u})\rangle &:= \lim_{r\to\infty} \frac{1}{A(rO)} \int \mathcal{D}f \int_{rO} \mathrm{d}^d\mathbf{r}\, \|\nabla f(\mathbf{r})\| \delta(f(\mathbf{r}) - \rho)\, \delta(\mathbf{n}(\mathbf{r}) - \mathbf{u}) \\ &= \lim_{r\to\infty} \frac{1}{A(rO)} \int_{rO} \mathrm{d}^d\mathbf{r} \int \mathcal{D}f\ \|\nabla f(\mathbf{r})\| \delta(f(\mathbf{r}) - \rho)\, \delta(\mathbf{n}(\mathbf{r}) - \mathbf{u}) \\ &= \langle \|\nabla f(\mathbf{0})\|\, \delta(f(\mathbf{0}) - \rho)\, \delta(\mathbf{n_0} - \mathbf{u})\rangle \ . \end{aligned} \tag{2.70}$$

If the random field is a Gaussian random field g, this density can be calculated explicitly following the same line of argument as in Section 2.6.4.

$$\begin{aligned} \langle e(\mathbf{u})\rangle &= \langle \|\nabla g(\mathbf{0})\|\, \delta(g(\mathbf{0}) - \rho)\, \delta(\mathbf{n_0} - \mathbf{u})\rangle \\ &= \int_{\mathbb{R}} \mathrm{d}(g(\mathbf{0}))\ \delta(g(\mathbf{0}) - \rho) \cdot f_g(g(\mathbf{0})) \\ &\qquad \cdot \int_{\mathbb{R}^d} \mathrm{d}^d(\nabla g(\mathbf{0}))\ \|\nabla g(\mathbf{0})\|\, \delta(\mathbf{n_0} - \mathbf{u}) \cdot f_{\nabla g}(\nabla g(\mathbf{0})) \\ &= f_g(\rho) \cdot \int_{\mathbb{R}^d} \mathrm{d}^d(\nabla g(\mathbf{0}))\ \|\nabla g(\mathbf{0})\|\, \delta(\mathbf{n_0} - \mathbf{u}) \cdot f_{\nabla g}(\nabla g(\mathbf{0})) \ . \end{aligned}$$

Again the integral is separated into an integration of directions of the gradient $\nabla g(\mathbf{0})$, or equivalently[42] of the normal vector $\mathbf{n_0}$, and the absolute value of the gradient $\ell := \|\nabla g(\mathbf{0})\|$. In contrast to the calculations for the Minkowski tensors, the integration of the direction is in any dimension trivial because of the δ-distribution

$$\begin{aligned} \langle e(\mathbf{u})\rangle &= f_g(\rho) \cdot \int_0^\infty \mathrm{d}\ell\ \ell^{d-1} \int_{\mathbb{S}^{d-1}} \mathrm{d}\mathbf{n_0}\ \ell\, \delta(\mathbf{n_0} - \mathbf{u}) \cdot f_{\nabla g}(\ell\mathbf{n_0}) \\ &= f_g(\rho) \cdot \int_0^\infty \mathrm{d}\ell\ \ell^d \cdot f_{\nabla g}(\ell\mathbf{u}) \ . \end{aligned}$$

Inserting the probability density function of the gradient from Eq. (2.58) yields the

[42] The probability distribution of the gradient is point symmetric w.r.t. the origin $f_{\nabla g}(\nabla g(\mathbf{0})) = f_{\nabla g}(-\nabla g(\mathbf{0}))$.

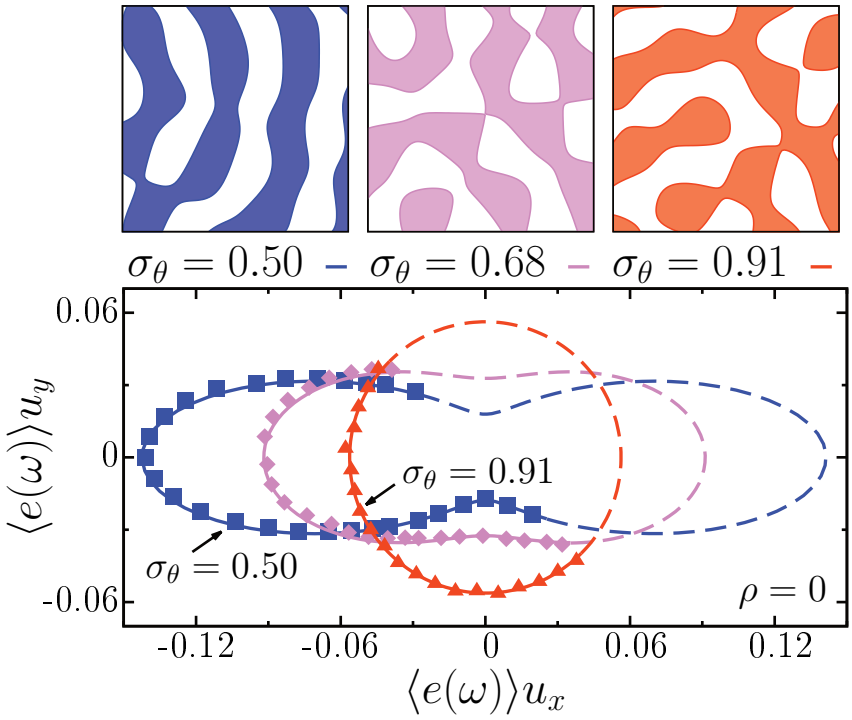

Figure 2.33: The extended Gaussian image density $e(\omega)$ for differently anisotropic Gaussian random wave models; for details, see Fig. 2.30. For the isotropic system, the polar plot is a circle; for the anisotropic systems, it gets dumbbell-shaped. The solid lines show the analytic curves, see Eq. (2.71); they are compared to the direct numerical estimates of $e(\omega)$ represented by the marks. The dashed lines correspond to estimates of the extended Gaussian image density based only on the measurement of $\langle w_1^{0,2}\rangle$ and the method of moments, see Fig. 2.34. This estimate is in excellent agreement with the analytic curves; note that the polar plot of $e(\omega)$ is in this case point symmetric w.r.t. the origin.

explicit expression for the extended Gaussian image density in any dimension d

$$\langle e(\mathbf{u})\rangle = \frac{2^{\frac{d-1}{2}} \cdot \Gamma(\frac{d+1}{2}) \cdot f_g(\rho)}{(2\pi)^{d/2}\sqrt{\det[\mathrm{Cov}(\nabla g)]}} \cdot \frac{1}{(\mathbf{u}^t \mathrm{Cov}^{-1}(\nabla g)\mathbf{u})^{\frac{d+1}{2}}} \,. \tag{2.71}$$

Because the averaging and the limit are linear operations, Equation (2.29) directly translates to the densities [199], and the Minkowski tensors densities $\langle w_1^{0,s}\rangle$ of arbitrary rank simply follow from the extended Gaussian image density by

$$\langle w_1^{0,s}\rangle = \int_{\mathbb{S}^{d-1}} \mathrm{d}\mathbf{u}\; \mathbf{u}^s \langle e(\mathbf{u})\rangle \,, \tag{2.72}$$

which is in agreement with Eq. (2.66).

The extended Gaussian image density $\langle e(\mathbf{u})\rangle$ is plotted in Fig. 2.33 for differently anisotropic Gaussian random wave models of which samples are depicted above the plot. For the isotropic system, the polar plot is a circle, but for the anisotropic systems, it gets dumbbell-shaped which indicates that more normal vectors are pointing in x- than in y-direction.

From the shape of the extended Gaussian image, we can once more deduce that the higher-rank tensors contain nontrivial higher-rank anisotropy information, i.e., not contained in the second-rank tensor density $\langle w_1^{0,2}\rangle$. However, $\langle g(\mathbf{u})\rangle$ is determined, i.e., parameterized, only by the covariance matrix of the gradient of the Gaussian random field $\mathrm{Cov}(\nabla g)$ and the variance $\mathrm{Var}(g)$ of the functional value at the origin, which can w.l.o.g. be set to unity by the choice of units.

The deeper geometrical reason is that the extended Gaussian image depends only on the distributions of the functional value and the gradient of the Gaussian random field, which are stochastically independent of each other. Because the random field is homogeneous, $\langle e(\mathbf{u})\rangle$ even depends on the distributions at the origin only. The distribution of the derivatives of a Gaussian random field are Gaussian themselves, and thus completely defined by their covariance matrix, because the mean value vanishes. The Minkowski tensors do therefore not depend on the whole correlation function of the Gaussian random field, but only on the variance of the functional value at the origin and the covariance of the gradient at the origin.

The covariance matrix of the gradient of the Gaussian random field $\mathrm{Cov}(\nabla g)$ can be estimated if only $\langle w_1^{0,2}\rangle$ at a single threshold, e.g., $\rho = 0$, is known by using the method of moments; in other words, by solving Eq. (2.67) for $\mathrm{Cov}(\nabla g)$ given an estimate of $\langle w_1^{0,2}\rangle$. Equation (2.67) cannot be solved for λ_1 and λ_2 analytically, but numerically in a robust way.

The eigenvectors of $\langle w_1^{0,2}\rangle$ determine the rotation matrix Q. The eigenvalues of the covariance matrix λ_1 and λ_2 follow from the eigenvalues of $\langle w_1^{0,2}\rangle$. The ratio of the latter is $\beta_1^{*0,2}$ a strictly monotonic function of λ_2/λ_1, which is explicitly given in Eq. (2.69) and plotted in Fig. 2.34. Given an estimate of $\beta_1^{*0,2}$, Equation (2.69) can be inverted numerically providing a method of moments estimate of λ_2/λ_1, see Fig. 2.34.

The absolute values of λ_2 and λ_1 then follow from the sum of the eigenvalues of $\langle w_1^{0,2}\rangle$, i.e., its trace which is equal to $\langle w_1\rangle$ from Eq. (2.62). At threshold $\rho = 0$, the perimeter density is according to Eq. (2.62)

$$\langle w_1\rangle = \frac{1}{\pi}\cdot\sqrt{\frac{\lambda_1}{\mathrm{Var}(g)}}\cdot E[1-\frac{\lambda_2}{\lambda_1}] = \frac{1}{\pi}\cdot\sqrt{\lambda_1}\cdot E[1-\frac{\lambda_2}{\lambda_1}]\,, \qquad (2.73)$$

where w.l.o.g. $\mathrm{Var}(g) = 1$ or in other words λ_1 is measured in units of $\mathrm{Var}(g)$, note that $\langle e(\mathbf{u})\rangle$ is independent of the unit of the functional values of g.

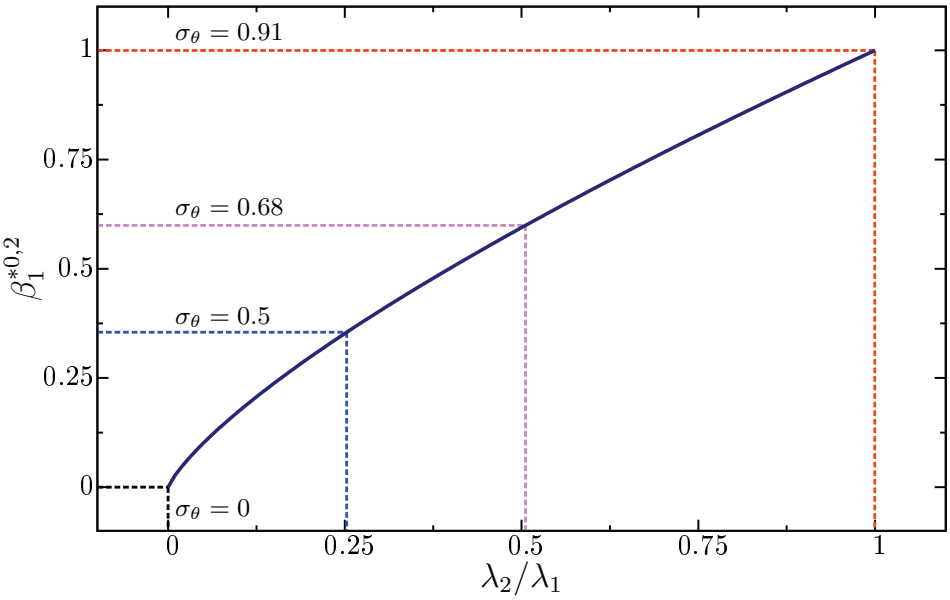

Figure 2.34: Estimation of the ratio of eigenvalues λ_1 and λ_2 of the covariance matrix of the gradient of the Gaussian random field via the method of moments given the measured ratio $\beta_1^{*0,2}$ of the eigenvalues of the Minkowski tensor density $\langle w_1^{0,2} \rangle$: the solid line shows the analytic curve from Eq. (2.69); the dashed lines show the estimates of $\beta_1^{*0,2}$ measured in simulations of differently anisotropic Gaussian random fields, the corresponding ratios λ_2/λ_1 are numerically determined.

From the estimate of the ratio λ_2/λ_1 from Fig. 2.34 and the measured $\langle w_1 \rangle$, which is equal to the trace of $\langle w_1^{0,2} \rangle$, follows the estimate of the eigenvalues of the covariance matrix of the gradient by solving Eq. (2.73) for λ_1; the other eigenvalue then simply follows from the estimate of the ratio λ_2/λ_1.

In conclusion, given an estimate of the Minkowski tensor density $\langle w_1^{0,2} \rangle$ at a single threshold, I can estimate the covariance matrix of the gradient of the Gaussian random field $\mathrm{Cov}(\nabla g)$, and thus the extended Gaussian image density $\langle e(\mathbf{u}) \rangle$ using Eq. (2.71). The dashed lines in Fig. 2.33 show this estimate of $\langle e(\mathbf{u}) \rangle$ based only on the measured $\langle w_1^{0,2} \rangle$. This estimate is robust and accurate, e.g., with much smaller statistical errors than the points representing the direct estimate of $\langle e(\mathbf{u}) \rangle$.

Surprisingly, although the Minkowski tensors of higher rank contain additional anisotropy information about the Gaussian random field, they can be determined using only the second-rank tensor $W_1^{0,2}$ if we know that the random field is indeed Gaussian. This is because although the extended Gaussian image density $\langle e(\mathbf{u}) \rangle$ contains for a Gaussian random field more anisotropy information than $\langle w_1^{0,2} \rangle$

alone, we know its functional form and can thus determine the complete anisotropy information by only measuring the second-rank tensor. Such a probably counter-intuitive finding allows for a profound insight into the shape of the excursion sets of anisotropic Gaussian random fields.

A simple geometrical analogon, which may help for a more intuitive understanding of this surprising relationship among the Minkowski tensors, is a rectangle: although the higher-rank tensors do contain nonredundant anisotropy information about its shape, the second-rank tensor is enough to estimate the aspect ratio and the perimeter of the rectangle. If we know that the object is a rectangle, this completely determines its shape and thus are all higher-rank tensors. In other words, because the shape can be parametrized and these parameters can be estimated from a second-rank tensor, the latter completely determines the geometry of the object.

Because the complete anisotropy information of a Gaussian random field can be deduced from a second-rank tensor alone, mean values of higher-rank tensors do not improve the estimation of parameters of a Gaussian random field. However, measuring the higher-rank tensors can be used for a test of non-Gaussianity in anisotropic random fields.

If the second-rank tensor density $\langle w_1^{0,2} \rangle$ is measured, the higher-rank tensor densities, e.g., $\langle w_1^{0,4} \rangle$, of a Gaussian random field can be predicted. If the measured $\langle w_1^{0,4} \rangle$ deviates statistically significantly, the random field is non-Gaussian.

In three dimensions, the translation invariant Minkowski tensor $W_2^{0,2}$ and the corresponding density can also be interpreted as moment tensors of a distribution of normal vectors, a curvature weighted extended Gaussian image. Following the same line of argument as here for $W_1^{0,2}$ in two dimensions, similar results can be achieved, see Ref. [199] for the analytic calculations.

2.7 Gray-scale Minkowski tensors

The Minkowski functionals and tensors are only defined on binary images. In many applications this is a natural assumption, e.g., the porous medium is divided into a solid and a void phase. However, many imaging techniques blur the data and provide gray-scale values instead of Boolean variables. Sometimes the physical system is initially defined by a density like for the pasta matter. Often a gray-scale image is first turned into a black and white image, usually via thresholding, e.g., in Sections 2.6, 5.3, or 6.1.2. The Minkowski tensors are then evaluated as a function of the threshold ρ. Sometimes an analysis of the dependence on the threshold can yield new structural insights into the material, e.g., see Section 5.3.

However, in many cases, the threshold dependence is physically irrelevant and can lead to unwanted ambiguities. For example, for computer tomography data this

standard segmentation algorithm is often not reliable, first, because of noise and other artifacts, but especially because of the so-called partial volume effect [205]. In these cases, a definition of Minkowski tensors of gray-scale data, which in the limit of a b/w image leads to the standard definition of a Minkowski tensor would be highly desirable.

Here, I show how the Minkowski tensors can naturally be extended to gray-scale images[43] in any dimension and with robust estimators also for voxelated data.

Starting from their definition by the extended Gaussian image or surface area measure, as described in Section 2.4.2 for the planar case, the surface tensor $W_1^{0,s}$ can be expressed as an integral measure of the normal distribution:

$$\begin{aligned} W_1^{0,s} &= \int_{\partial K} \mathrm{d}^{d-1}\mathbf{r}\; \mathbf{n}^s(\mathbf{r}) \\ &= \int_{\partial K} \mathrm{d}^{d-1}\mathbf{r} \int_{\mathbb{S}^{d-1}} \mathrm{d}\mathbf{u}\, \delta(\mathbf{n}(\mathbf{r}) - \mathbf{u})\, \mathbf{u}^s \\ &= \int_{\mathbb{S}^{d-1}} \mathrm{d}\mathbf{u}\, \mathbf{u}^s \int_{\partial K} \mathrm{d}^{d-1}\mathbf{r}\, \delta(\mathbf{n}(\mathbf{r}) - \mathbf{u}) \end{aligned}$$

for a domain K with boundary ∂K and normal vector $\mathbf{n}$ at $\mathbf{r}$. The latter integral

$$E(\mathbf{u}) := \int_{\partial K} \mathrm{d}^{d-1}\mathbf{r}\, \delta(\mathbf{n}(\mathbf{r}) - \mathbf{u}) \tag{2.74}$$

is called the extended Gaussian image of K [200, 450], and the Minkowski tensor $W_1^{0,2}$ can, as described in Section 2.4.2 for the planar case, then simply be interpreted as the covariance matrix of the extended Gaussian image

$$W_1^{0,s} = \int_{\mathbb{S}^{d-1}} \mathrm{d}\mathbf{u}\, \mathbf{u}^s\, E(\mathbf{u})\ . \tag{2.75}$$

In a gray-scale image D the domain K and thus also the normal vectors in Eq. (2.74) are not defined, but the latter can naturally be replaced by the direction of the gradient if the contribution to the integral is weighted by the norm of the gradient (a steep decrease should be contribute more to the "boundary" of the porous medium than only a slight variation) [327, 450]

$$E_g(\mathbf{u}) := \int_F \mathrm{d}^d\mathbf{r}\, \|\nabla D\|\, \delta\left(\frac{\nabla D}{\|\nabla D\|} - \mathbf{u}\right) \tag{2.76}$$

with F the whole field of view and D the gray-scale values defined on F. For voxelated images, Canny's edge detector [92] allows for robust estimates of the

[43] The concept follows the generalization of a MIL tensor to gray-scale images in Ref. [327].

gradient of D and thus of $E_g(\mathbf{n})$, which are appropriate for micro-computed tomography [327].

In the limit for which the gray-scale values D approach a b/w image, i.e., the characteristic function of a body K, the gradient of D only contributes at the boundary of K where $\nabla D/\|\nabla D\|$ approximates the normal vector. Using the coarea formula [e.g. 488], Equation (2.76) can be shown to converge to Eq. (2.74) for sufficiently smooth K.

Replacing E by the gray-scale extension E_g in Eq. (2.75) provides an extended interfacial Minkowski tensor $G_1^{0,s}$ for gray-scale images

$$\begin{aligned} G_1^{0,s} &= \int_{\mathbb{S}^{d-1}} \mathrm{d}\mathbf{u}\, \mathbf{u}^s\, E_g(\mathbf{u}) \\ &= \int_F \mathrm{d}^d\mathbf{r}\, \|\nabla D\| \int_{\mathbb{S}^{d-1}} \mathrm{d}\mathbf{u}\, \mathbf{u}^s\, \delta\Big(\frac{\nabla D}{\|\nabla D\|} - \mathbf{u}\Big) \\ &= \int_F \mathrm{d}^d\mathbf{r}\, \|\nabla D\| \left(\frac{\nabla D}{\|\nabla D\|}\right)^s . \end{aligned} \tag{2.77}$$

The volume tensors could be extended by weighting with the gray-scale value

$$G_0^{a,0} = \int_F \mathrm{d}^2\mathbf{r}\, \mathbf{r}^a D\ . \tag{2.78}$$

The new measures $G_\nu^{a,b}$ quantify the structure of gray-scale images directly; of course a suitable normalization can additionally be introduced.

As an example, I consider a rectangle $K = [-p,p] \times [-q,q]$ which is blurred by a Gaussian shaped point-spread function with standard deviation σ both in x- and y-direction. The resulting gray-scale image is

$$D(x,y) = \frac{1}{4}\left[\mathrm{erf}\left(\frac{x+p}{\sqrt{2}\sigma}\right) - \mathrm{erf}\left(\frac{x-p}{\sqrt{2}\sigma}\right)\right] \cdot \left[\mathrm{erf}\left(\frac{y+q}{\sqrt{2}\sigma}\right) - \mathrm{erf}\left(\frac{y-q}{\sqrt{2}\sigma}\right)\right] .$$

where $\mathrm{erf}(z) = \frac{2}{\sqrt{\pi}} \int_0^z \mathrm{e}^{-t^2}\, \mathrm{d}t$ is the error function.

Figure 2.35 shows the original and blurred rectangle for $p = 2$, $q = 1$, and $\sigma = 0.2$, which corresponds to strong blurring. The original Minkowski tensor of the rectangle is

$$W_1^{0,2} = \begin{pmatrix} 4 & 0 \\ 0 & 8 \end{pmatrix} .$$

However, because of the strong blurring the Minkowski tensors of the excursion sets strongly depend on the threshold ρ; for $\rho \in [0.01, 0.99]$ the ratio $\beta_1^{0,2}$ of the

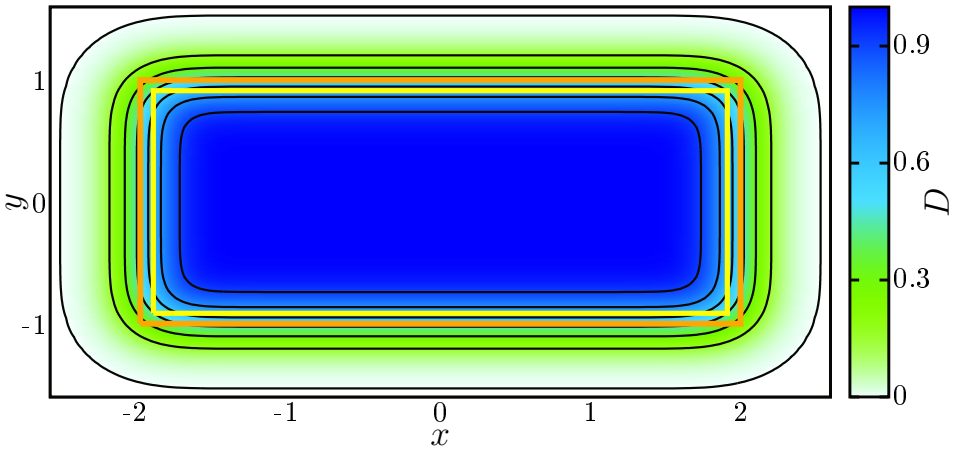

Figure 2.35: Rectangle (orange solid line) blurred by a Gaussian point-spread function resulting in a gray-scale image $D(x, y)$. The black lines depict the excursion sets for different thresholds $\rho \in (0, 1)$. The anisotropy of the excursion sets strongly depends on this threshold ρ. The yellow solid line depicts a rectangle with the same eigenvalues as the gray-scale Minkowski tensor $G_1^{0,2}$.

eigenvalues takes on values between 0.3 and 0.55; for $\rho \in [0.2, 0.8]$ the anisotropy index $\beta_1^{0,2}$ is between 0.44 and 0.52.

Numerically evaluating Eq. (2.77) provides

$$G_1^{0,2} \approx \begin{pmatrix} 3.652 & 0 \\ 0 & 7.652 \end{pmatrix}, \tag{2.79}$$

which corresponds to a ratio 0.4773 of the eigenvalues. The gray-scale Minkowski tensor avoids the ambiguity of different values at different thresholds and is in good agreement with the Minkowski tensor of the original rectangle.

2.8 Conclusions

For the well-defined models of random spatial structures discussed in this chapter, the shape can be studied rigorously [448]. I here analyze the geometry and topology of anisotropic models, the Boolean model and the Gaussian random field, aiming especially for a sensitive anisotropy characterization.

Orientation-dependent mean intercept length analyses are common tools to quantify anisotropy in porous bone materials [107, 347, 512], despite several weaknesses of this spatial structure measure [327]. Here, I have provided clarification on the interpretation or the morphological information content of these measures, by exploiting an analytic formula derived for an important model for anisotropic microstructures, namely the anisotropic Boolean model; see Eq. (2.19).

I find that the orientation and intensity dependence of the MIL separates into two factors; see Eqs. (2.20) and (2.26). The latter is only a function of the porosity and independent of the specific Boolean model. The orientation dependent factor $\bar{L}^{(1)}[\mathbf{u}]$ from Eq. (2.20) determines the shape of the MIL figure. Interestingly, the average length of an intercept with a typical grain does not enter the expression of $\bar{L}^{(1)}[\mathbf{u}]$. Instead, it is a function only of the volume and the average size of the projection of a single grain. I have expressed the global MIL by only local single grain characteristics. The whole anisotropy information of the MIL figure is thus contained in the average size of the projection of a single grain.

In contrast to the common assumption, I find that the MIL figure is in general not an ellipse for anisotropic heterogeneous media; see Eq. (2.23) and Figs. 2.3, 2.9(b), and 2.14. The assumption of Eq. (2.5) is not full-filled, and the thus defined MIL tensor is not a tensor. The deviations are substantial enough to adversely affect numerical anisotropy analyses, strongly depending on the fitting procedure. I explicitly show here for a realistic model of porous media how the MIL figure can be very different from an ellipse. Note that also in experimental measurements of the MIL of trabecular bone statistically significant deviations from an ellipsoid have been reported [240].

I also discuss further inherent disadvantages of the MIL analysis, like their sensitivity to noise, but their insensitivity to anisotropy, in the sense that there are systems both with obvious volume or even interfacial anisotropy, which appear perfectly isotropic w.r.t. the MIL figure; see Figs. 2.14 and 2.12. Moreover, from a practical point of view, standard implementations of the MIL analysis are very time-consuming and sensitive to noise [327].

These drawbacks can be corrected for by the family of Minkowski tensors. I show that, on the one hand, only a seemingly small change is needed for the covariance tensor of the MIL figure to be a linear combination of Minkowski tensors. However this step from the inverse of the number of intersections to the number of intersections has, on the other hand, great implications from both a practical and a fundamental point of view. For the Minkowski tensors are additive, continuous for convex distortions, and can be defined as volume and surface integrals; they are therefore robust against noise and there are fast linear-time algorithms. Free software is available; see Section 2.4.3. I discuss the irreducible representation of Minkowski tensors in two dimensions, the circular Minkowski tensors, see Eqs. (2.30), (2.34), and (2.35), from which scalar anisotropy indices can be defined for arbitrary rank, see Eqs. (2.31), (2.32), and (2.33).

The Minkowski tensors are more sensitive than the MIL analysis and detect the anisotropy in the systems that appeared to be isotropic w.r.t. the latter; see Figs. 2.14 and 2.15. In particular, the Minkowski tensors allow for a comprehensive and

systematic analysis of different types of anisotropy w.r.t. the volume, the surface, or the curvature. I show how the Minkowski tensors quantify anisotropy in systems that appear perfectly isotropic w.r.t. the common MIL analysis, even for interfacial anisotropy for which the MIL analysis has been designed, see Figs. 2.12, 2.15 and 2.14.

Explicit formulas are provided for the Minkowski tensor densities of general anisotropic Boolean models, see Eq. (2.39), and for our parametric Boolean model, see Eq. (2.40). The analytic curves are compared against simulation results, see Figs. 2.16–2.18 and 2.20 and 2.21. Similar to the MIL, the global averages of the Minkowski tensor densities can be expressed by single grain characteristics.

A measurement of the global average provides access to the average shape of a single grain. If a porous medium is, e.g., built up by the successive addition of inclusions, this knowledge about the shape of a typical inclusion can allow for a better understanding of the formation of the porous medium. Moreover, it allows to adjust the Boolean model to the experiment, e.g. trabecular bone, by choosing an appropriate grain distribution.

An unbiased estimator of model parameters using the measurement of a Minkowski tensor of a sample of a Boolean model is developed and tested, see Eqs. (2.44) and (2.45) and Fig. 2.19. I study the variances and covariances of the Minkowski functionals of the Boolean models with rectangles that are either aligned or that follow an isotropic orientation distributions. I find nonuniversal behavior in the covariances even if the first moments exhibit universal behavior, see Eqs. (2.49) and (2.50) and Fig. 2.22. Moreover, I study the empirical probability density functions of the Minkowski functionals for these Boolean models. The Minkowski functionals, when suitably normalized, satisfy a central limit theorem [210]. In my simulation study, I find that already for relatively small observation windows the empirical probability density functions of the rescaled Minkowski functionals are well approximated by Gaussian distributions, see Fig. 2.24.

By combining the central limit theorem for the Minkowski functionals of the Boolean model and the results for their variances, a very accurate approximation of the probability distribution of the Minkowski functionals of Boolean models—even for finite observation windows—can be derived. This allows to develop null hypothesis tests using the Minkowski functionals to decide for a given grain distribution whether or not a random two-phase medium can be modeled by overlapping grains. At small intensities, high statistics can be collected. Small, systematic deviations appear, as expected, because of the finite simulation box, see Fig. 2.25. However, the rescaled empirical probability density functions of the different Minkowski functionals for the four simulated Boolean model collapse within error bars to a master curve that is in very good agreement with a Poisson

distribution with a mean value equal to the expected number of grains hitting the observation window.

I calculate the expectations of the Minkowski tensors of anisotropic Gaussian random fields. For general homogeneous random fields, the volume Minkowski tensors $W_0^{a,0}$ do not contain additional geometrical information compared to the volume fraction, see Eq. (2.54), in contrast to the translation invariant Minkowski tensor densities. For sufficiently smooth homogeneous random fields, the global average of the latter can be expressed by a local average, see Eq. (2.56).

Because the gradient of a Gaussian random field is again Gaussian distributed, see Eq. (2.58), and statistically independent of the functional value, the density of the first order Minkowski functional for differently anisotropic Gaussian random fields as functions of the threshold are always proportional to Gaussian distributions, but the prefactors change, see Eq. (2.62) and Fig. 2.30.

To calculate the Minkowski tensors of the excursion set, I need to consider the normal vectors, which are by definition antiparallel to the gradient, see Eq. (2.63). Because the distribution of the gradient is point symmetric w.r.t. the origin, the interfacial Minkowski tensor densities of odd rank vanish on average, see Eq. (2.65). I then provide integral formulas for the average interface Minkowski tensor densities of arbitrary rank and in arbitrary dimension, see Eq. (2.66), and explicit formulas for the second and fourth rank tensors in two dimensions, see Eqs. (2.67) and (2.68) and Fig. 2.31.

Both the ratio of the eigenvalues and the ratios of the irreducible representation, i.e., the scalar anisotropy indices, are independent of the threshold, e.g., see Eq. (2.69). The higher-rank tensors do contain nonredundant anisotropy information, see Fig. 2.32.

However, by expressing the global average of the extended Gaussian image density of a homogeneous random field by a local average, see Eq. (2.70), and deriving an explicit formula for homogeneous Gaussian random fields, see Eq. (2.71), I find that the extended Gaussian image density does not depend on the complete covariance function of the Gaussian random field, but only on the covariance matrix of the gradient at the origin. Therefore, if the random field is indeed Gaussian, the extended Gaussian image density can be estimated robustly and accurately using only the average second-rank tensor density, see Figs. 2.33 and 2.34. Consequently, all average interfacial Minkowski tensors of arbitrary rank which can be derived from the extended Gaussian image density are determined by the second-rank tensor, see Eq. (2.72). The fact that the average higher-rank tensors do contain additional information, but for a homogeneous Gaussian random field nevertheless follow from the second-rank tensor can be used for a test of non-Gaussianity in anisotropic random fields.

Finally, I show how the Minkowski functionals can be generalized to gray-scale images, see Eq. (2.77). I apply it to a Gaussian blurred rectangle, see Fig. 2.35 and Eq. (2.79), which is a proof-of-principle that the generalization of the Minkowski tensors can reconstruct the anisotropy of a blurred image.

Chapter 3

Anisotropic continuum percolation[1]

The overlapping grains in the Boolean model form clusters of connected components. Starting from a dilute arrangement of grains, the mean size of these clusters grows with increasing occupied area fraction. However, these clusters are almost surely[2] bounded for occupied area fractions below a critical area fraction, the so-called percolation threshold, above which there is almost surely exactly one unbounded cluster that spans the whole system, the percolating or open cluster. This geometric phase transition and the universal scaling of geometrical properties is an intensively studied example of continuum percolation [313].

Dating back to works by Flory [144] and Stockmayer [445] and later by Broadbent and Hammersley [85], percolation theory describes in general the critical behavior of connected clusters, either on lattices or in the continuum [165, 441]. Being a rather fundamental concept, it can be applied to very different physical systems and complex networks, e.g., for flow through porous media, elasticity or conductivity of heterogeneous materials, gelation and polymerization, hopping conductivity, galaxy formation, or immunological systems [84, 394, 417, 460, 522], but also financial markets, social networks of customers, forest fires, or epidemics [60, 284, 326, 339, 433, 442, 443].

I am here interested in the interplay of geometry and topology in continuum percolation analyzed by Minkowski functionals. More precisely, I study anisotropic continuum percolation, which means the percolation in Boolean models with

[1] The results in this chapter were derived in collaboration with Klaus Mecke, in Section 3.1 also with Christian Scholz, and in Section 3.2 also with Gerd E. Schröder-Turk. Results of Section 3.1 have been published in Ref. [403].

[2] In probability theory, almost surely refers to an event that happens with probability one.

an orientation bias. While the value of the percolation threshold depends on the anisotropy of the system, even the most anisotropic model simultaneously percolates in all directions, i.e., the percolation threshold is isotropic. While predicting the percolation threshold is important for applications, the isotropic percolation in all directions is a more fundamental insight that is linked to the uniqueness of the percolating cluster.

For such a complex geometric problem, analytic results are hard to derive for non-trivial Boolean models. Precise numerical estimates need complex and time-consuming calculations. However, the expected values of the Euler characteristic, a topology index, are explicitly given and discussed in Chapter 2, which provides heuristic bounds on the percolation threshold.

Both the universal behavior, e.g., scaling exponents near the percolation threshold, and the nonuniversal behavior, e.g., the location of the percolation threshold or the behavior away from the critical region, are investigated in this chapter.

For the Boolean model in two dimensions, there are actually two different percolation transitions at the percolation threshold[3]: an unbounded cluster of connected grains appears, but the unbounded void cluster vanishes, in other words, the unoccupied regions decompose into finite islands. Here, I consider both transitions, the latter is in the following called void percolation.

Flow through the void region is only possible if there is a percolating void cluster. Because of the percolation being a phase transition, scaling laws can be found for both the permeability and a topology index like the Euler characteristic [402]. I investigate the scaling of the Euler characteristic of the open void cluster in extensive simulations for the isotropic Boolean model in Section 3.1.

The anisotropic continuum percolation is then studied in Section 3.2. Not only are many materials anisotropic, both man-made and natural, but anisotropic percolation exhibits an interesting qualitatively different behavior in finite samples or in the idealized infinite limit. Although there is no phase transition in a finite system, an effective percolation threshold can be defined for the ensemble, which is anisotropic. In other words, the system is more likely to percolate in the preferred direction than in the perpendicular direction. However, this difference vanishes in the thermodynamic limit as described above.

Finally, in Section 3.3, I discuss explicit formulas for approximating the percolation thresholds, both using empirical parameters and purely geometric formulas using both the mean values and the covariances of the Minkowski functionals. I then compare these different approximations to the numerical estimates of percolation threshold.

[3] In higher dimension, the grain and void phase can percolate at the same occupied volume fraction.

3.1 Universal scaling in topology and transport

Flow of liquids through porous medium is important in a great variety of physical or biological systems as well as engineering problems ranging from blood perfusion over filtration or ground water pollution to oil or gas reservoirs [7, 58, 105, 393]. Although some analytic results exist [58, 510], rigorous bounds could be derived [460], and efficient models and morphological descriptors were introduced [34, 35], the complex connection between the microstructure of the heterogeneous material and its transport properties is still not fully understood.

For laminar flow the flow rate Q can be related to the applied pressure difference ΔP across one dimension by a proportionality constant, which is given by the area A of the cross section of the material, the viscosity η of the fluid, and the so-called permeability k

$$Q = -\frac{k \cdot A}{\eta} \Delta P \,,$$

which was found empirically by Darcy [110] and could later be confirmed by homogenization theory [510]. A low permeability indicates the difficulty for fluids to flow through the porous medium. Because of the complex microstructure exact results for the permeability are difficult to derive for random porous media. Typically, relations between the geometry and the flow are looked for to predict the permeability, e.g., in model systems like the Boolean model [34, 270, 306]. The permeability of fluid flow through the void phase of a Boolean model must, e.g., somehow depend on the area fraction φ of the void phase[4].

Scholz et al. [402] experimentally found a relation between the permeability in the void phase of Boolean models and the topology of the percolating void cluster, which is the unbounded, or percolating, cluster of the void phase. In other words, a connected domain not covered by grains which spans the whole system; holes within a cluster of grains are therefore not part of the open void cluster[5], see Fig. 3.1. Its Euler characteristic χ_o rescaled by the number of grains N is proposed to describe the permeability k via

$$k = c l_c^2 \left(\frac{1 - \chi_o}{N} \right)^{\alpha} \,,$$

[4] Because the void phase is the complement of the grain phase, the corresponding area fractions are trivially related by $\varphi = 1 - \phi$.

[5] In a finite sample, a percolating cluster is defined as a cluster connecting opposite edges of the simulation box. Holes in clusters of grains that are connected to the boundary, but not directly to the open void cluster are not part of the open void cluster.

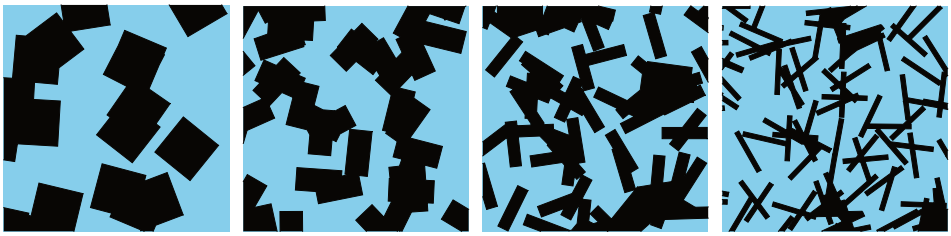

Figure 3.1: Samples of the open void cluster in Boolean models with randomly oriented overlapping squares (left-hand side) or rectangles with aspect ratios 1/2, 1/4, or 1/10 (from left to right). The open void cluster is the percolating void cluster, i.e., the connected component of the void phase that spans the whole system. Holes in clusters of grains that are connected to the boundary, but not directly to the open void cluster are not part of the open void cluster.

where l_c is the critical pore diameter [235], c a constant which depends on the local pore geometry, and $\alpha = 1.27 \pm 0.09$ a fit parameter.

In contrast to the Euler characteristic of the entire void phase which can be derived analytically as shown in Chapter 2, the Euler characteristic of the void cluster χ_o can only be estimated numerically[6], because an explicit formula would include an exact knowledge of the percolation threshold.

If there are no grains at all, $\chi_o = 1$, and in the dilute limit, i.e., if there are N particles in a finite sample and the overlap of the particles can be neglected, $\chi_o = 1 - N$, because there are N holes. Therefore,

$$\frac{1 - \chi_o}{N} \xrightarrow{\varphi \to 1} 1 \, .$$

If the porosity approaches the percolation threshold, this rescaled percolation threshold also vanishes in the thermodynamic limit, i.e., in the limit of infinite system size

$$\frac{1 - \chi_o}{N} \xrightarrow{\varphi \to \varphi_c} O(\frac{1}{N}) \to 0 \, .$$

If there is no percolating cluster, then $\chi_o = 0$. However, I here only analyze samples that are percolating in the void phase; in other words, I characterize the structure of the open void cluster conditional on its existence.

I investigate in a detailed simulation study the scaling of the topology of the void percolating cluster and whether χ_o also exhibits a critical behavior. The extensive simulations allow for both small statistical errors and reduced systematic errors because of large system sizes, and pixelation errors are avoided. Most importantly, they allow to access the behavior of the system close to the percolation

[6] In finite samples, open boundary conditions are assumed, i.e., a surrounding void phase.

threshold, which is otherwise very difficult to investigate in experiments measuring the vanishing flow rate at a huge system size.

I simulate isotropic Boolean models with rectangles of different aspect ratios (1, $1/2$, $1/4$, or $1/10$) following the procedure from Section 2.3.2 with minus-sampling boundary conditions for the positions of the rectangles, i.e., rectangles with centers outside of the simulation box but intersecting the simulation box are taken into account [448]. The porosity, i.e., the area fraction of the void phase, varies from the percolation threshold to the dilute limit, i.e., a vanishing number of expected grains per unit square. The calculations are repeated for different system sizes. The percolation thresholds φ_c are taken from Refs. [271, 513].

The number of simulated samples varies with the size of the simulation box and with the aspect ratio of the rectangles, i.e., with the number of grains in each sample. For squares with side length a in a simulation box with linear system size $L = 10a$, I simulate 1000 percolating samples at each void area fraction, i.e., 13,000 in total[7], which corresponds to about $2 \cdot 10^6$ squares. For rectangles with aspect ratio $b/a = 1/10$ in a simulation box with linear system size $L = 100a$, I simulate only 5 percolating samples at each void area fraction, i.e., 65 in total[8], but this corresponds to even more than 10^7 rectangles. For all aspect ratios, system sizes, and void area fractions, I simulate in total 35,750 samples containing $6 \cdot 10^7$ grains.

Figure 3.2 shows the rescaled Euler characteristic as a function of the rescaled porosities for differently large samples of Boolean models with rectangles with varying aspect ratio. The curves for isotropic Boolean models with rectangles of different aspect ratios b/a exhibit slight systematic deviations at the smallest system size, but for larger window sizes this difference seems to vanish and a universal scaling is found, in that for both squares and stick-like rectangles (see Fig. 3.1) the rescaled Euler characteristic as a function of the rescaled porosities collapse to the same master curve. Surprisingly, this scaling holds over the whole range of possible porosities even far away from the percolation threshold.

There are two different scaling regimes for χ_o. At low grain densities, i.e., large φ, the rescaled Euler characteristic and the rescaled area fraction are proportional to each other. Close to the percolation threshold, I find a critical behavior with a very small critical exponent. Further detailed simulation studies and an extrapolation to infinite system sizes are needed for reliable numerical estimates. Moreover, the difficult question remains whether in the limit of an infinite system size the curves truly collapse or whether small deviations between the curves persist. Then a different scaling close to and far from the percolation threshold might be required.

[7] For these results, I also needed to simulate about 6000 nonpercolating samples.
[8] For these results, I only needed to simulate a single nonpercolating sample.

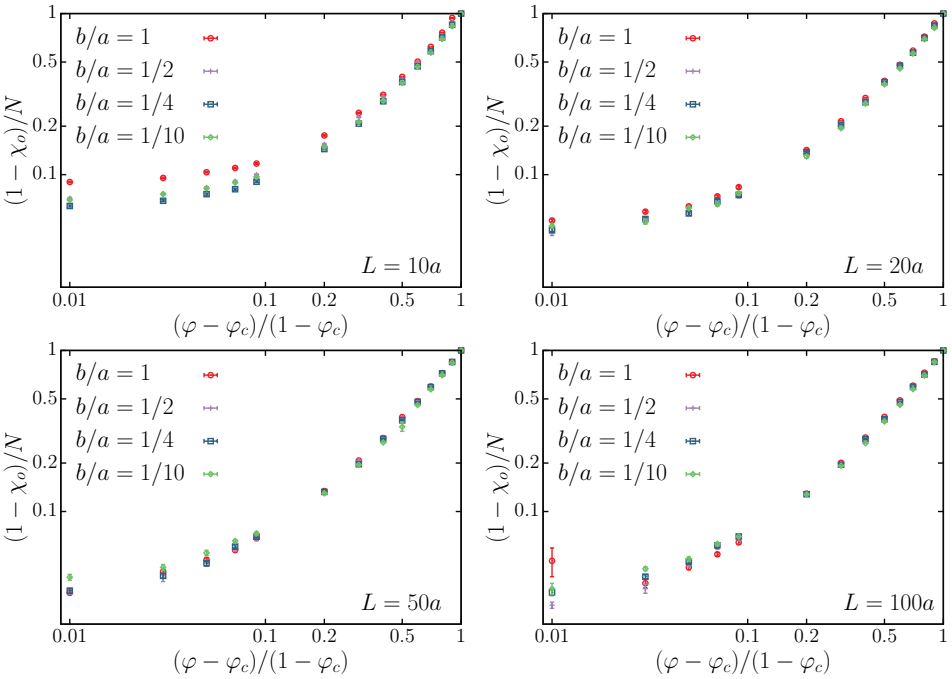

Figure 3.2: Universal scaling of the Euler characteristic χ_o of the open void cluster as a function of the rescaled porosity φ, i.e., the area fraction of the void phase for different linear system sizes L in units of the long side length of a rectangle a. The curves for isotropic Boolean models with rectangles of different aspect ratios b/a show slight systematic deviations at the smallest system size, but for larger window sizes this difference seems to vanish and a universal scaling is found over the whole range of possible porosities, in that for both squares and stick-like rectangles (see Fig. 3.1) the rescaled Euler characteristic as a function of the rescaled porosities collapse to the same master curve.

Here, the findings support the use of $(1-\chi_o)/N$ as a universally scaling quantity as suggested by Scholz et al. [402] and the result might help understanding and predicting the permeability of porous media via the connection of topology and geometry.

3.2 Anisotropic percolation and isotropic threshold

After investigating the void percolation in the section above, grain percolation is studied in the next two sections. An infinite two-dimensional system is a special case where void and grain percolation can be viewed as complement phenomena: the system is either percolating in the void or in the grain phase. Therefore, the percolation thresholds that are estimated or approximated by explicit formulas in

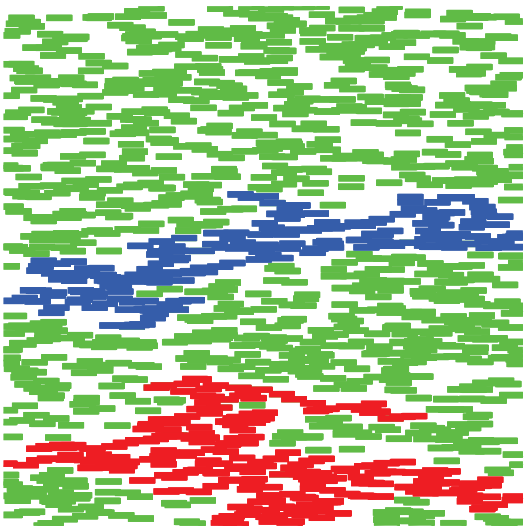

Figure 3.3: Finite sample of a Boolean model of aligned rectangles with aspect ratio 1/4. In a finite sample, a percolating cluster is defined as a cluster of rectangles that connects opposite sides of the sample, in other words, which spans the system in x- or in y-direction, i.e., horizontal or vertical direction, respectively. There are two percolating clusters in x-direction (colored blue and red). These two cluster are not connected to each other. There is no connected path spanning the system vertically, in other words, there is no percolation in y-direction. In contrast to an infinite system, we find in this finite sample neither grain nor void percolation in y-direction.

the next two sections are also valid for void percolation. In a finite sample, there is no phase transition and the percolating cluster is defined as a cluster that connects opposite sides of the sample, in other words, which spans the system in x- or in y-direction. In contrast to the infinite system, a such defined finite void and grain percolation are not complements to each other. Figure 3.3 shows a finite sample in which both the grain and the void phase percolate in horizontal but not in vertical direction.

After analyzing isotropic Boolean models in the section above, in the next two sections I investigate percolation in anisotropic systems, both for finite simulation boxes and in the limit of infinite system size. Anisotropic continuum percolation exhibits a qualitatively new behavior. I am especially interested in the connection of geometry and topology, or more precisely, how does the anisotropy of the Boolean model influence percolation, which is a topological property.

There have already been numerous studies of anisotropic continuum percolation[9], some using analytic calculations [e.g. 126] others are based on Monte Carlo simulations [e.g. 50, 81] or experiments [e.g. 51]. For Boolean models an increasing anisotropy typically also increases the percolation threshold of the grain phase [53, 98], and the percolation threshold in anisotropic percolation is found to be isotropic [81].

If the grains are added sequentially, a finite anisotropic sample percolates more likely first in x- and then in y-direction than vice versa. In other words, the occupied volume fraction at which the probability that the system percolates in x-

[9] There are also detailed studies of anisotropic lattice percolation [e.g. 216, 298, 379].

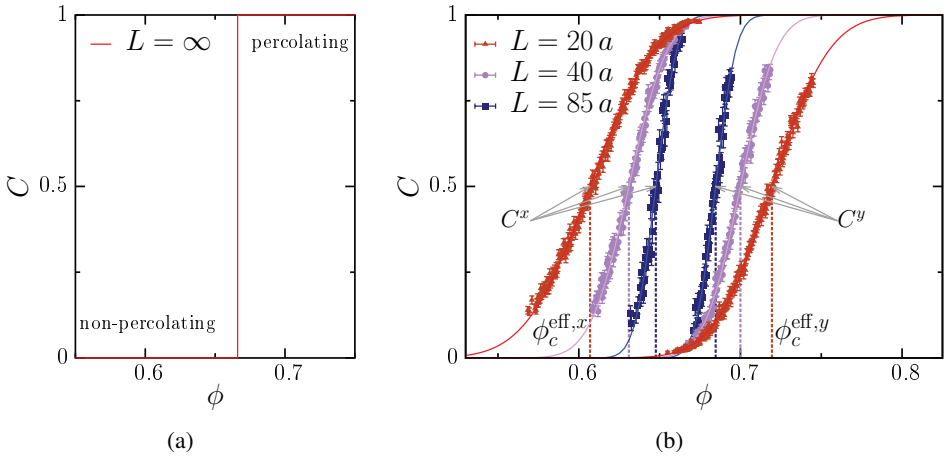

Figure 3.4: Connectivity C as a function of the occupied area fraction ϕ for Boolean models: (a) for infinite system size the connectivity is zero for $\phi < \phi_c$ and one for $\phi > \phi_c$; (b) for finite anisotropic systems the connectivity is a smooth function taking values $0 < C < 1$ and is different for percolation in x- and in y-direction. I show here numerical estimates of C for a Boolean model of aligned rectangles with aspect ratio $1/4$ for different system sizes L in units of the long side length of the rectangle. To each curve an error function is fitted according to Eq. (3.2).

direction with a given probability is lower than the corresponding volume fraction in y-direction. However, this difference vanishes in the limit of an infinite system size, no matter how anisotropic the system may be. Here, I also find empirically this isotropic percolation threshold by extrapolation using finite size scaling. Moreover, I present a heuristic argument how this is related to the uniqueness of the percolating cluster.

I study percolation in the parametric models from Section 2.1.1 to provide an overview of Boolean models with a varying anisotropy. I discuss the explicit dependence of the value of the threshold on the anisotropy of the system, and in the following section I derive and compare different explicit approximations of the percolation thresholds, and I discuss candidates for improved bounds.

3.2.1 Connectivity and effective percolation thresholds

Percolation is a geometric phase transition, see Fig. 3.4(a): above the critical occupied area fraction ϕ_c there is a percolating cluster with probability one, and below this threshold there is almost surely no percolation of the grains[10]. In other

[10] As noted above, in two dimensions, the void percolation is complementary, it percolates if the grain phase does not percolate and vice versa.

words, the probability that there is a percolating cluster, the so-called connectivity C, as a function of the occupied area fraction ϕ is a step function[11].

However, there is no phase transition in a finite system, but depending on statistical fluctuations there is or is not a system spanning cluster. For all occupied area fractions $0 < \phi < 1$ there is a finite probability that there is a percolating cluster, i.e., the connectivity is expected to be a smooth $0 < C < 1$.

I simulate the Boolean model following the procedure from Section 2.3.2 for varying area fractions and determine the connectivity[12], which is estimated by the fraction of samples that contain a percolating cluster. Figure 3.4(b) indeed shows the smooth increase of the connectivity with increasing occupied area fraction ϕ.

The figure shows the results for a Boolean model of aligned rectangles with aspect ratio 1/4. I distinguish the connectivity in x- and y-direction: the connectivities C^x and C^y are the probabilities, that there is a cluster that spans the system in x- or in y-direction, respectively. Because the rectangles are aligned in x-direction, see Fig. 3.3, the system is close to the percolation transition more likely to percolate horizontally than vertically. Because the particles are elongated in x-direction, more particles are needed for vertical than for horizontal percolation[13], and a fluctuation that spans the system horizontally is more likely than vertically. Even for relatively large system sizes, there are occupied volume fractions at which the system most likely percolates in x- but not in y-direction.

Since there is no phase transition in a finite system, the percolation threshold ϕ_c is not defined. Instead an effective percolation threshold[14] ϕ_c^{eff} must be defined. A simple and intuitive definition is

$$C(\phi_c^{\text{eff}}) = \frac{1}{2}\,. \tag{3.1}$$

A trivial estimate inverting the estimated connectivity as a function of the occupied area fraction would not be robust against statistical fluctuations. A robust estimate has been defined by Rintoul and Torquato [384]. The derivative of the connectivity $\mathrm{d}C/\mathrm{d}\phi$ as a function of the occupied area fraction ϕ is the probability that the system starts to percolate at ϕ[15]. Because of the phase transition, the behavior of the

[11] Here, I do not discuss the connectivity exactly at the percolation threshold ϕ_c.

[12] I have also simulated pixelated Boolean models, but there are strong pixelation errors, because even a fine pixelation can significantly alter the topology, by connecting or disconnecting clusters.

[13] In the case of aligned rectangles, this can be illustrated by a dilation in y-direction in order to derive a sample of Boolean model with aligned squares. This model is isotropic. However, because of the dilation the whole sample is then larger in y- than in x-direction and for a cluster spanning the system vertically more particles are needed than for a horizontally percolating cluster.

[14] Other names are apparent or average percolation threshold.

[15] Another possibility to define an effective percolation threshold is $\phi_c^{\text{eff}} := \int_0^1 \mathrm{d}\phi\, \phi \cdot \mathrm{d}C/\mathrm{d}\phi$ [441].

system is close to the percolation threshold and for large systems dominated by the universal scaling. If the derivative of the connectivity $\mathrm{d}C/\mathrm{d}\phi$ is approximated by a Gaussian distribution, the connectivity can be approximated by an error function with both an offset and a prefactor $1/2$:

$$C(\phi) \approx \frac{1}{2} + \frac{1}{2} \operatorname{erf}\left(\frac{\phi - \phi_c^{\mathrm{eff}}}{\Delta}\right) . \tag{3.2}$$

Fitting this rescaled error-function to the connectivity as a function of ϕ, where Δ and ϕ_c^{eff} are the fit parameters, see Fig. 3.4(b), thus provides a numerically robust estimate of the effective percolation threshold ϕ_c^{eff}. In the limit of infinite system size, the error function converges to a step function and $\phi_c^{\mathrm{eff}} \to \phi_c$.

The only difference of this approach to my simulation is that the latter uses the intensity γ as an input. In a finite system, there are statistical fluctuations in the occupied area fraction ϕ. Systematic errors can be avoided by replacing the volume fractions in Eq. (3.2) by the corresponding intensities.

The definition of the effective percolation threshold via Eq. (3.2) has the advantage that it can be easily interpreted and implemented. However, there are two major disadvantages: first, unnecessary samples are simulated especially at high thresholds, which are computationally expensive to simulate because of the large number of grains; second, the precision is limited by unknown systematic errors. Although the error function is a good approximation of the connectivity as a function of the occupied area fraction, high precision estimates of the connectivity reveal in finite systems statistically significant deviations from an error function. Therefore, although the statistical errors in my simulation are of the order $O(10^{-4})$, there are also systematic errors up to $O(10^{-3})$, see Table 3.1. There are more efficient algorithms using inhomogeneous Boolean models for more precise estimates of the percolation threshold of homogeneous models [e.g. 278, 373, 374]. In future research, these algorithms could be generalized to anisotropic systems.

In Fig. 3.4(b), an error function is fitted to each curve, and the resulting estimates of the effective percolation thresholds are visualized. The effective percolation thresholds in x-direction are distinctly smaller than in y-direction for all simulated systems sizes L.

However, the difference in the effective percolation thresholds depends on the size of the system. Figure 3.4(b) shows the connectivity and effective percolation thresholds for differently large simulation boxes. The difference between horizontal and vertical direction decreases with increasing system size. For small systems, a more or less straight connection from the left to the right-hand side is possible. The larger the system, the more unlikely is a straight connection from the left to the right-hand side and the more important are vertical connections of clusters. The

effective percolation threshold in x-direction increases and decreases in y-direction. However, even for quite large systems a significant difference remains.

3.2.2 Isotropic percolation threshold

Because percolation is a phase transition, the scaling of the effective percolation thresholds with the system size is universal for large system sizes[16] [150, 493]:

$$\phi_c^{\text{eff}} - \phi_c \propto L^{-1/\nu}$$

with the universal critical exponent $\nu = 4/3$ [441]. Note that the proportionality constant is nonuniversal and varies for the effective percolation thresholds $\phi_c^{\text{eff},x}$ in x- and $\phi_c^{\text{eff},y}$ in y-direction.

Therefore, I a priori distinguish in the limit of infinite system size the percolation thresholds in x- or in y-direction. In other words, I estimate the thresholds in x- or in y-direction separately:

$$\begin{aligned} \phi_c^{\text{eff},x} &= \phi_c^x + m^x L^{-1/\nu} \text{ and} \\ \phi_c^{\text{eff},y} &= \phi_c^y + m^y L^{-1/\nu} \ . \end{aligned} \tag{3.3}$$

However, as discussed above, I expect that the percolation threshold of Boolean models is actually isotropic, i.e., $\phi_c^x \equiv \phi_c^y$, even for the most anisotropic systems.

Considering the extreme case of aligned rectangles motivates this assumption: a Boolean model with aligned squares can be transformed by a dilation into a Boolean model consisting of aligned rectangles of arbitrary aspect ratios, but neither the area fraction nor the topology of the model change. Therefore, the percolation threshold for aligned rectangles must be independent of the aspect ratio. Moreover, because the model can either be dilated in x- or y-direction, the percolation threshold must be isotropic in this case[17].

A plausibility argument for the isotropic percolation threshold is that percolation in x-direction is almost surely not possible along a straight line but only along a winded path, which requires that also grains with different y-coordinates are connected.

However, there is a more fundamental reason, why I expect that this conjecture holds for any Boolean model: the uniqueness of the percolating cluster. Meester and Roy [312] could prove for Boolean models of spheres with varying size that there can be at most one unbounded component, but the results can be generalized to grains with very general shape, see also Ref. [313]. Either with probability one

[16] It does not depend on the grain distribution, actually it is even the same for continuum percolation and lattice percolation.

[17] Balberg and Binenbaum [50] provide a similar argument for anisotropic stick percolation.

Figure 3.5: If an anisotropic two-phase medium percolated in x- but not in y-direction (indicated by the red line), there would be a finite probability that there are two percolating clusters (dark blue and cyan), which are not connected to each other.

or zero there is either exactly one or none percolating cluster, in other words, the percolating cluster is almost surely unique[18].

The following heuristic argument suggests how the isotropy of the percolation threshold follows from this of the percolating cluster. It conjectures that if the unbounded cluster spanned the system only in x- but not in y-direction, there would be a finite probability for two percolating clusters which are not connected to each other, see Fig. 3.5. Assume that the percolating (dark blue) cluster is bounded in y-direction, that is, the cluster lies completely below some bound (maximum of red line). Because of the statistical homogeneity of the system, the probability that there is another percolating (cyan) cluster in the domain above the bound should be nonzero, which would lead to a contradiction of the uniqueness of the unbounded cluster. From this heuristic argument, I expect that in a statistically homogeneous system where there is almost surely at most one unique unbounded component, this percolating cluster must be unbounded both in x- and in y-direction, i.e., the percolation thresholds must coincide:

$$\phi_c^x \equiv \phi_c^y \ .$$

I simulate Boolean models of rectangles with aspect ratios $b/a \in \{1, 3/4, 1/2, 1/4\}$ and anisotropy parameter $\alpha \in \{0, 1, 3, 15, \infty\}$ varying from perfectly isotropic orientation distributions to perfect alignment. For each system, I determine the connectivity C as a function of the intensity for differently large simulation boxes with linear system sizes $L \in \{40a, 50a, 60a, 70a, 75a, 80a, 85a, 95a\}$, where as

[18] Similar proofs could be derived for other percolation models [e.g. 25, 90].

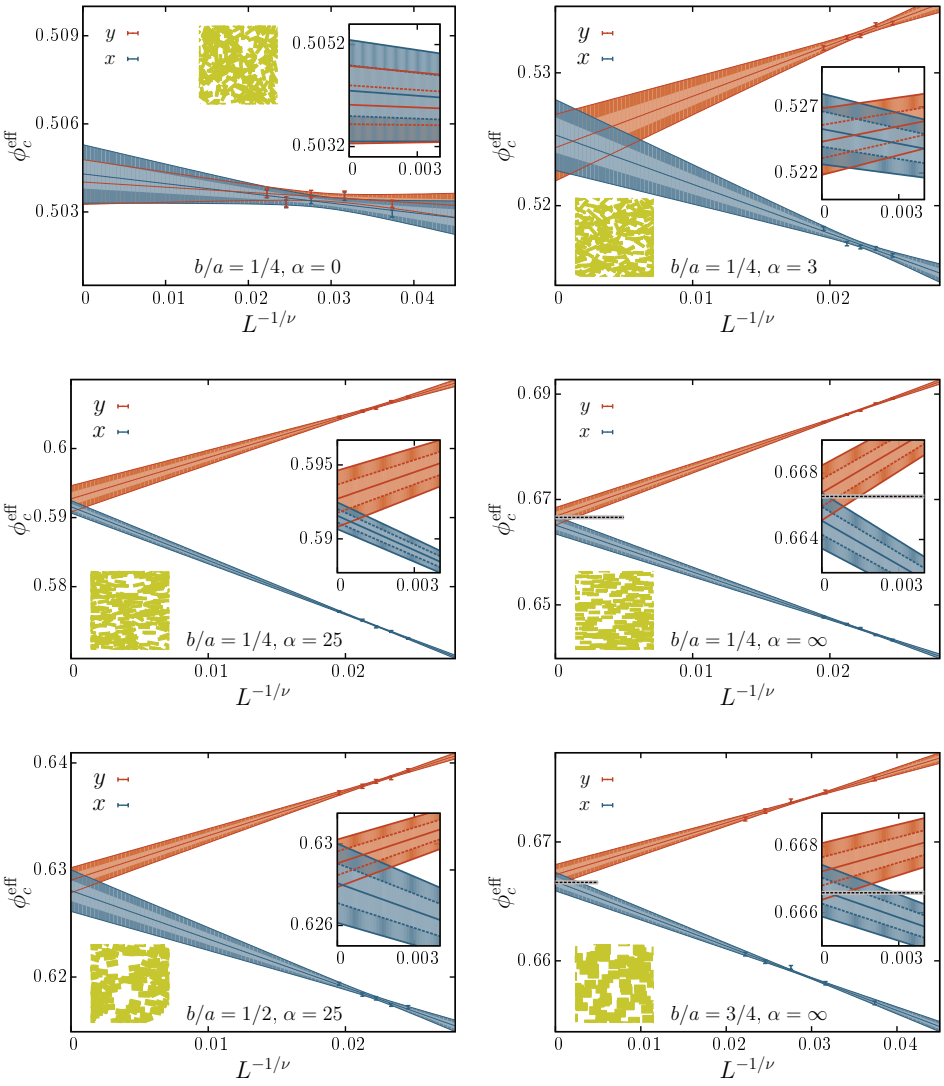

Figure 3.6: Finite size scaling of the effective percolation thresholds that are extrapolated separately for x- and the y-direction, see Eq. 3.3. The unit of length for the linear system size L is the long semiaxis of the rectangle. Each plot analyzes a different Boolean model of rectangles with aspect ratio b/a and orientation-bias α varying from perfect isotropy (0) to alignment (∞), see Eq. (2.1) and Fig. 2.2; in each plot a sample of the corresponding Boolean model is depicted. Except for the isotropic system (top left), the effective percolation thresholds in x-direction are significantly below those in y-direction. However, the extrapolated percolation thresholds are isotropic within statistical significance (the color bands represent the bands of one and two standard deviations). The dotted black line and gray band represent the estimate and the error bar of the percolation threshold of aligned squares from Ref. [47].

Anisotropy	α	Aspect ratio b/a	Percolation thresholds ϕ_c^x	ϕ_c^y	ϕ_c
isotropic	0	1/4	0.5043(3)	0.5040(3)	0.5042(2)
		1/2	0.5915(4)	0.5918(4)	0.5916(3)
		3/4	0.6208(4)	0.6202(4)	0.6205(3)
		1	0.6264(4)	0.6261(4)	0.6262(3)
	1	1/4	0.5102(3)	0.5098(3)	0.5100(2)
		1/2	0.5948(4)	0.5948(3)	0.5948(2)
		3/4	0.6213(4)	0.6211(4)	0.6212(3)
		1	0.6267(4)	0.6265(4)	0.6266(3)
	3	1/4	0.5253(8)	0.5244(9)	0.5249(6)
		1/2	0.6001(7)	0.6006(8)	0.6003(5)
		3/4	0.6219(4)	0.6224(4)	0.6222(3)
		1	0.6262(4)	0.6266(4)	0.6264(3)
	25	1/4	0.5916(7)	0.5927(8)	0.5921(5)
		1/2	0.6281(8)	0.6290(9)	0.6285(6)
		3/4	0.6376(4)	0.6386(4)	0.6380(3)
		1	0.6393(4)	0.6396(4)	0.6395(3)
aligned	∞	1/4	0.665(1)	0.6668(8)	0.6661(6)
		1/2	0.6674(9)	0.6656(8)	0.6664(6)
		3/4	0.6667(4)	0.6672(4)	0.6670(3)
		1	0.6668(4)	0.6674(4)	0.6671(3)

Table 3.1: Percolation thresholds of Boolean models with rectangles following orientation distributions proportional to $\cos^{\alpha}(\theta)$, see Eq. (2.1). The percolation thresholds ϕ_c^x and ϕ_c^y are estimated by extrapolating $\phi_c^{\mathrm{eff},x}$ and $\phi_c^{\mathrm{eff},y}$ to an infinite system size, see Eq. (3.3) and Fig. 3.6. The statistical errors are denoted in brackets, but slight deviations from the finite size scaling can lead to systematic errors up to $O(10^{-3})$. Within these errors, the isotropic percolation threshold is confirmed. So, $\phi_c^{\mathrm{eff},x}$ and $\phi_c^{\mathrm{eff},y}$ are also extrapolated to the same isotropic threshold ϕ_c, see Eq. (3.4).

discussed above the more anisotropic a Boolean model the larger the simulation boxes must be, so that the connectivity is accurately described by an error function and that the finite size scaling can be applied. For each system, I fit error functions[19] separately to the both the connectivity in x- and in y-direction. I thus estimate the effective percolation thresholds $\phi_c^{\mathrm{eff},x}$ and $\phi_c^{\mathrm{eff},y}$.

I then extrapolate the effective percolation thresholds to the limit of infinite system size using Eq. (3.3) with fit parameters ϕ_c^x and m^x or ϕ_c^y and m^y. Figure 3.6 shows for six of these Boolean models the effective percolation thresholds $\phi_c^{\mathrm{eff},x}$

[19] For each system the fit is applied to the five largest system sizes which are simulated for the according Boolean model.

and $\phi_c^{\text{eff},y}$ as a function of the rescaled system size as well as the extrapolation and the corresponding bands of one or two standard deviations. All final estimates of the percolation thresholds $\phi_c^{x,y}$ are listed in Table 3.1. Within statistical significance, the isotropic percolation threshold is confirmed.

Similar findings of isotropic percolation thresholds in anisotropic percolation can, e.g., be found in Refs. [50, 81]. Balberg and Binenbaum [50] also provide a renormalization-group argument why in an anisotropic square lattice an isotropic percolation threshold is expected.

3.2.3 Threshold estimates for differently anisotropic models

Because the percolation threshold is by plausibility argument and empirical findings confirmed to be isotropic, the finite size scaling from Eq. 3.3 can be replaced by

$$\begin{aligned} \phi_c^{\text{eff},x} &= \phi_c + m^x \, L^{-1/\nu} \text{ and} \\ \phi_c^{\text{eff},y} &= \phi_c + m^y \, L^{-1/\nu} \, , \end{aligned} \tag{3.4}$$

where the percolation threshold in the infinite system ϕ_c is isotropic. It is because of the nonuniversal prefactors m^x and m^y that the effective percolation thresholds differ in x- and y-direction.

I can now extrapolate simultaneously the effective percolation thresholds $\phi_c^{\text{eff},x}$ and $\phi_c^{\text{eff},y}$ with the constraint $\phi_c^x \equiv \phi_c^y$. I neglect the correlation of $\phi_{c,i}^{\text{eff},x}$ and $\phi_{c,i}^{\text{eff},y}$ in the simulation[20] and use the likelihood function

$$\mathcal{L} = \prod_{L_i} \text{Prob}\left[\phi_{c,i}^{\text{eff},x} | \phi_c, m^x\right] \cdot \text{Prob}\left[\phi_{c,i}^{\text{eff},y} | \phi_c, m^y\right]$$

with

$$\text{Prob}\left[\phi_{c,i}^{\text{eff},z} | \phi_c, m^z\right] = \frac{1}{\sqrt{2\pi}\sigma_{z,i}} \mathrm{e}^{-\frac{\left(\phi_{c,i}^{\text{eff},z} - \phi_c - m^z \cdot L_i^{-1/\nu}\right)^2}{2\sigma_{z,i}^2}} \, ,$$

where for each system size L_i the error of the effective percolation thresholds $\phi_{c,i}^{\text{eff},x}$ and $\phi_{c,i}^{\text{eff},y}$ are given by $\sigma_{x,i}$ and $\sigma_{y,i}$, respectively. The log-likelihood function can be written as

$$\log \mathcal{L} = \text{const.} - \frac{\chi_x^2}{2} - \frac{\chi_y^2}{2}$$

[20] Note that the effective percolation thresholds in x- and in y-directions may be strongly correlated, but the correlation cannot be considered in this analysis.

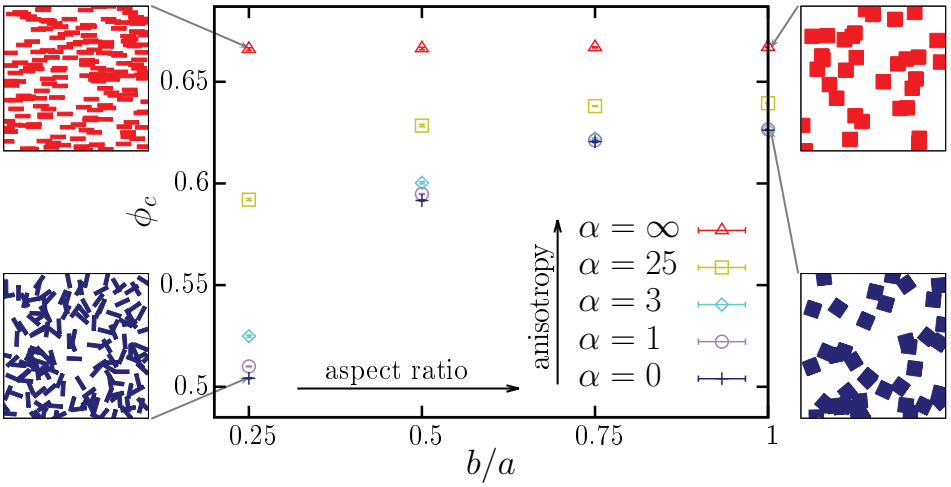

Figure 3.7: Isotropic percolation thresholds ϕ_c of Boolean models with differently anisotropic orientation distributions ($\alpha = 0$ randomly oriented and $\alpha = \infty$ aligned rectangles) as a function of their aspect ratio b/a. For details, see Table 3.1. On the left-hand and right-hand side are samples depicted of rectangles or squares, respectively, which are aligned (top) or randomly oriented (bottom).

with

$$\chi_x^2 + \chi_y^2 = \left(\begin{pmatrix} \phi_c^{\mathrm{eff},x} \\ \phi_c^{\mathrm{eff},y} \end{pmatrix} - F(L^{-1/\nu}) \right)^t \mathbf{Cov}^{-1} \left(\begin{pmatrix} \phi_c^{\mathrm{eff},x} \\ \phi_c^{\mathrm{eff},y} \end{pmatrix} - F(L^{-1/\nu}) \right)$$

and

$$F(L^{-1/\nu}) = \begin{pmatrix} 1 & L^{-1/\nu} & 0 \\ 1 & 0 & L^{-1/\nu} \end{pmatrix} \cdot \begin{pmatrix} \phi_c \\ m^x \\ m^y \end{pmatrix}, \tag{3.5}$$

where the covariance matrix **Cov** is assumed to be diagonal

$$\mathbf{Cov} = \mathrm{diag}(\sigma_{x,1}^2, \ldots, \sigma_{x,i}^2, \ldots, \sigma_{y,1}^2, \ldots \sigma_{y,i}^2, \ldots) \; .$$

Therefore, the maximum likelihood estimation equals a minimum least square fit with block matrices. The final results for the isotropic percolation thresholds ϕ_c are listed in Table 3.1 and plotted in Fig. 3.7.

3.3 Percolation threshold approximations

Numerical estimates of the percolation threshold are computationally very expensive. However, applications might need the threshold for some specific model

parameters for which no simulation results are yet available. Of great importance would, therefore, be the possibility to predict the percolation threshold without the need for expensive simulations, i.e., to find an explicit formula approximating the percolation threshold. Such an explicit formula should be well defined, accurate, and easy computable [338]. An example is the scaling relation for varying dimensions from Ref. [463], which is based on a lower bound [461] and a conjecture that no convex shape provides higher thresholds than the hyperspheres.

A common approximation is the excluded area approximation (or excluded volume in three dimensions) [7, 48, 49, 52, 53, 98, 336, 496]. It tries to predict percolation thresholds based on simulation results of similar models by approximating the dependence of the critical intensity on the model parameters by the change in the excluded area. The excluded area for convex objects can be expressed explicitly by a mixed intrinsic volume. Here, I compare the approximation of the excluded area to the percolation thresholds for the differently anisotropic models discussed above.

In contrast to the excluded area approximation which uses an empirical parameter, Mecke and Wagner [311] suggested a purely geometrical approximation based on the zero of the mean Euler characteristic as a function of the intensity or occupied area fraction. As discussed above, explicit formulas for the mean Euler characteristic are known for Boolean models and no simulations are needed for a reliable estimate of the percolation threshold. At least for the parametric Boolean models studied here, the approximation is a lower bound. Moreover, I find that the trend, i.e., the qualitative behavior, is very well described by the zero of the Euler characteristic. For not too small aspect ratios it allows for a very precise estimation of the percolation threshold of a Boolean model with anisotropic orientation distribution if the percolation threshold of a model with different grain shape but the same orientation distribution is known. In other words, this result allows for a very precise approximation if an empirical parameter is used like for the excluded area approximation.

The percolation threshold can also be approximated without using an empirical parameter by the extremal points of the variance-covariance structure of the Minkowski functionals. Here, I discuss candidates for close upper bounds on the percolation thresholds.

3.3.1 Excluded area approximation

The excluded area in two dimensions or the excluded volume in three dimensions is defined for two particles K and Q as the area or volume of the region of all center positions of the second particle Q for which Q intersects K [355]. In other words, the second particle Q cannot enter this area or volume without intersecting

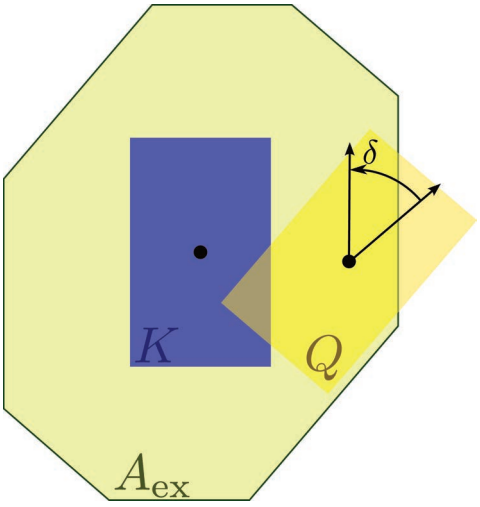

Figure 3.8: The excluded area $A_{ex}(K,Q)$ of the two rectangles K and Q is the area of the green octagon: if the center of Q is within this region, K and Q intersect. $A_{ex}(K,Q) = (a^2 + b^2)\sin|\delta| + 2ab\,(\cos|\delta| + 1)$, where δ is the angle between the two rectangles, each with side lengths a and b.

K, see Fig. 3.8 for the excluded area of two rectangles. The excluded area A_{ex} of two convex grains K and Q can explicitly be expressed using the mixed functional $V^0_{1,1}$ [400], as mentioned in Section 2.5.3,

$$A_{ex}(K,Q) = V^0{}_{1,1}(K,Q) + A(K) + A(Q)$$

Averaging with the orientation distribution $\mathcal{P}(\theta)$ yields the averaged excluded area for single grains[21]

$$\langle A_{ex}\rangle = \iint_{-\frac{\pi}{2}}^{\frac{\pi}{2}} \mathrm{d}\theta_i \mathrm{d}\theta_j\, \mathcal{P}(\theta_i)\cdot\mathcal{P}(\theta_j)\cdot A_{ex}(\vartheta(\theta_i)K, \vartheta(\theta_j)Q)\,, \tag{3.6}$$

where $\vartheta(\theta)$ denotes a rotation by the angle θ. For the isotropic orientation distribution $\mathcal{P}(\theta) \equiv$ const., the average mixed intrinsic volume separates, i.e., is proportional to the product of the perimeters of the grains. Therefore, the excluded area in two dimensions[22] can, as already known [80], be expressed by the areas A and the perimeters P of the single grains

$$\langle A_{ex}\rangle = \frac{1}{2\pi}P(K)\cdot P(Q) + A(K) + A(Q)\,.$$

Equation (2.47) provides the explicit formula for the mixed intrinsic volume of two rectangles. The excluded area of two rectangles R with orientations θ_i and θ_j

[21] I use a different notation to Ref. [52], in which the same quantity is denoted by $\langle A\rangle$, but $\langle A_{ex}\rangle$ is the total excluded area.

[22] For arbitrary dimensions, a general formula for the exclusion volume of identical randomly oriented convex particles is given is given in Ref. [463].

and side lengths a and b is therefore given by

$$A_{\mathrm{ex}}(\vartheta(\theta_i)R, \vartheta(\theta_j)R) = (a^2 + b^2)\sin|\theta_i - \theta_j| + 2ab\left(\cos|\theta_i - \theta_j| + 1\right) \quad (3.7)$$

Following a similar argument for lattice percolation [398], Balberg et al. [52] proposed that the so-called total excluded area, which is the product of critical intensity γ_c and the average excluded area $\langle A_{\mathrm{ex}}\rangle$, is an invariant quantity for similar systems. They also discussed that the total excluded area is equivalent to the average number of bonds per object at the critical intensity B_c, because the average number of bonds of a grain is equal to the average number of intersecting grains and thus equal to the average number of particles within the excluded area

$$B_c = \gamma_c \cdot \langle A_{\mathrm{ex}}\rangle \,. \quad (3.8)$$

This equality has also been confirmed numerically [e.g. 52, 53, 496].

The average number of bonds per object B_c is not a universal constant but depends, e.g., on the grain shape and orientation distribution. However, it varies to reasonable approximation only slightly for similar systems [e.g. 47, 52]. If the average number of bonds per object at the critical intensity B_c is empirically known, e.g., for a Boolean model of squares, and assumed to be the same for similar systems, e.g., Boolean models with rectangles following the same orientation distribution, the critical intensity of these similar models can be approximated by

$$\gamma_c = \frac{B_c}{\langle A_{\mathrm{ex}}\rangle} \,, \quad (3.9)$$

where the excluded area $\langle A_{\mathrm{ex}}\rangle$ is a geometric quantity, e.g., given above in Eq. (3.6).

In numerous simulation studies, the assumption of a system invariant total excluded area is shown to be a useful approximation [7, 98, 336] for which the critical intensity scales correctly with the particle size [496] and which approximates the functional dependence of the percolation threshold on the anisotropy of the model [52, 53].

In a recent publication, Chatterjee [98] calculated the excluded area for overlapping rectangles with anisotropic orientation distribution[23]. The approximation is compared to Monte Carlo simulations of isotropic models. For increasing anisotropy, an increase of the percolation threshold is predicted, which I confirm above.

Here, I compare the excluded area approximation to the Monte Carlo estimates of the anisotropic parametric Boolean model providing an overview of differently anisotropic models. At the critical intensity, the average number of bonds B_c

[23] Following Balberg et al. [52], the orientations are random within the interval $[-\alpha, \alpha]$.

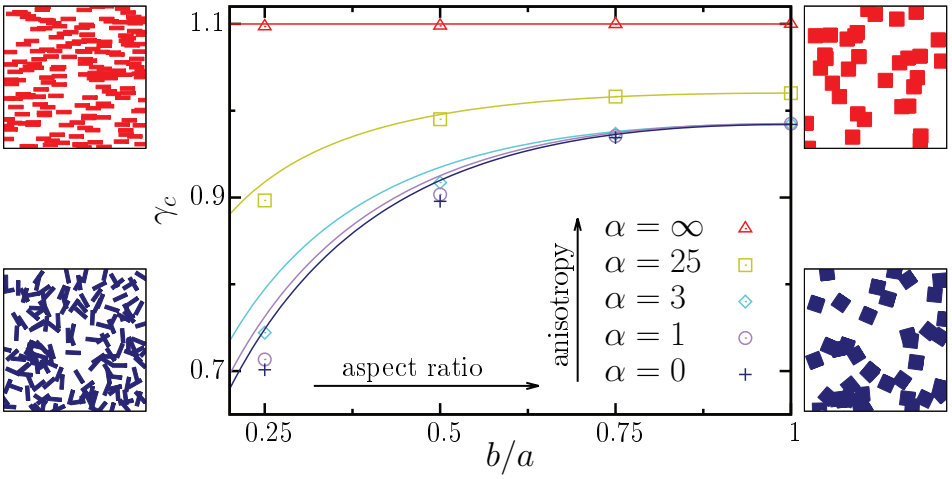

Figure 3.9: The critical intensities γ_c of the differently anisotropic Boolean models as a function of the aspect ratio b/a of the rectangles are approximated by the excluded area approximation, i.e., by Eq. (3.9) assuming a constant average number of bonds per object B_c for the same orientation distribution, and calculating the average excluded area by Eqs. (3.6) and (3.7). The estimates of B_c are derived from the percolation thresholds of squares for different anisotropy parameters α from Table 3.1 using Eq. (3.10). In other words, the critical intensities γ_c of the squares are used as empirical parameters, so that the functional dependence of γ_c on the aspect ratio can be approximated. At the left- and right-hand side samples of the Boolean models are depicted. For details, see Fig. 3.7.

for Boolean models can be derived from the percolation threshold ϕ_c. First, the critical intensity is calculated by solving $\phi_c = 1 - \mathrm{e}^{-\gamma_c A}$ (see Section 2.1.1). From Eq. (3.8) then follows

$$B_c = \frac{\langle A_{\mathrm{ex}} \rangle}{A} \ln \frac{1}{1 - \phi_c} , \tag{3.10}$$

where A is the area of a single grain. I have thus estimated B_c for overlapping squares with different orientation distributions using the percolation thresholds ϕ_c from Table 3.1. Using Eq. (3.9), I approximate the critical intensities of the overlapping rectangles and compare this excluded area approximation in Fig. 3.9 to the more precise critical intensities from Table 3.1.

For aligned rectangles, the independence of the percolation thresholds from the aspect ratio is correctly reproduced, because the excluded area of aligned rectangles $A_{\mathrm{ex}}(R, R) = 4ab$ is proportional to the area of a single grain, which is chosen to be unity. For the other Boolean models with preferred orientations or randomly oriented rectangles, the excluded area approximation seems to be a close upper bound for the rectangles if the empirical parameters of a square following the same orientation distribution are used. However, there are significant deviations from

the prediction, e.g., of the percolation threshold of randomly orientated rectangles with aspect ratio 1/4.

3.3.2 Euler characteristic approximation

Mecke and Wagner [311] suggested a purely geometrical approximation: the zero of the mean Euler characteristic as a function of the intensity or occupied area fraction. They were motivated by the idea that a vanishing Euler characteristic implies a balance between clusters and holes and by the finding that for the square-lattice and in general self-dual matching lattices the zero of the Euler characteristic and the critical point coincide exactly [451]. They compared the critical intensity γ_c to the zero of the Euler characteristic γ_0, for example, for overlapping discs and spheres, and suggested that γ_0 could be a close bound for γ_c.

Mecke and Seyfried [309] found in Monte Carlo simulations of a large class of discretized Boolean models a good qualitative agreement, in that the dependence on the shape of the constituents is captured well, but they found also quantitative deviations. Neher et al. [338] analyzed two-dimensional lattice graphs, for which the Euler characteristic provides a good approximation of the critical point. The criterion has, e.g., been applied to acid-etched titanium surfaces to be used for medical implants [388].

Be reminded, that the mean Euler characteristic of a Boolean model as a function of the occupied area fraction (or the intensity) is known explicitly and discussed in Sections 2.5.1 and 2.5.3. The criterion is thus easily applicable to a great variety of continuum percolation models.

I calculate the approximation and compare it to the percolation thresholds for the Boolean models with varying anisotropy studied above. I want to investigate how well the dependence of the threshold on the grain shape and orientation distribution is captured by the zero of the Euler characteristic, either γ_0 or ϕ_0, i.e., as a function of the intensity or of the occupied area fraction, respectively.

The Euler characteristic of a planar Boolean model[24] is given in Eq. (2.38). and more explicitly for the parametric model in Eq. (2.46), where the mixed intrinsic volume $V^0{}_{1,1}(R, \vartheta(\theta)R)$ of two rectangles rotated by an angle θ to each other is given in Eq. (2.47) and its average w.r.t. the orientation distribution of the grains is

$$\bar{V}^0_{1,1}(R,R) = \iint_{-\frac{\pi}{2}}^{\frac{\pi}{2}} \mathrm{d}\theta_i \mathrm{d}\theta_j \, \mathcal{P}(\theta_i) \cdot \mathcal{P}(\theta_j) \cdot V^0{}_{1,1}(\vartheta(\theta_i)R, \vartheta(\theta_j)R) \, .$$

[24] For arbitrary dimensions see Ref. [507].

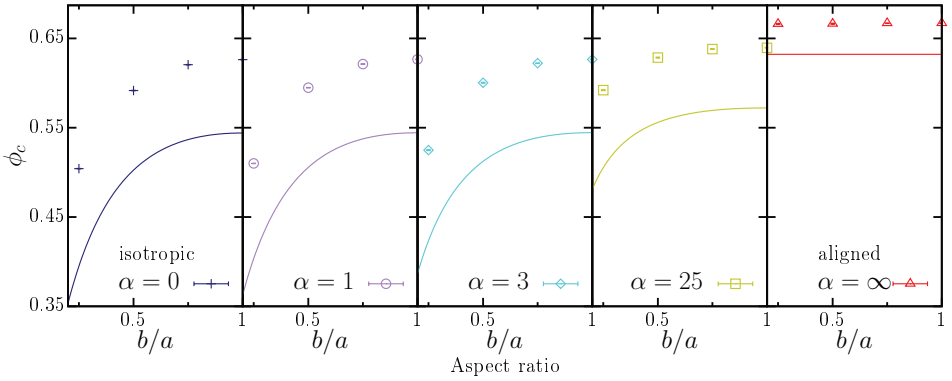

Figure 3.10: The percolation threshold ϕ_c (marks) is approximated by the zero of the Euler characteristic (lines) for Boolean models with rectangles. The single plots show the percolation thresholds as a function of the aspect ratio for differently anisotropic orientation distributions from randomly oriented (far left) to aligned (far right) rectangles. The zero of the Euler characteristic is a lower bound on the percolation threshold. Although there is a significant offset, the qualitative behavior, i.e., the dependence on anisotropy and grain shape, is described quite accurately.

The zero of the Euler characteristic then follows from

$$\begin{aligned} & \chi(\gamma_0) = 0 \\ \Leftrightarrow \quad & 1 - \frac{\bar{V}^0_{1,1}(R,R)}{2}\gamma_0 = 0 \\ \Leftrightarrow \quad & \gamma_0 = \frac{2}{\bar{V}^0_{1,1}(R,R)} \,. \end{aligned}$$

Note the similarity to the excluded area approximation in Eq. (3.9). As mentioned above, the mixed intrinsic volumes for rectangles can for randomly oriented squares by expressed by the perimeter of a single grain:

$$\gamma_0 = \frac{4\pi}{P^2} \,,$$

where P is the perimeter of the grain. The occupied area fraction at which the mean Euler characteristic changes its sign is then given by

$$\phi_0 = 1 - \mathrm{e}^{-\gamma_0 W_0} \,, \tag{3.11}$$

where W_0 is the area of a single grain.

Figure 3.10 compares the zero of the mean Euler characteristic ϕ_0 from Eq. (3.11) to the estimates of the isotropic percolation thresholds ϕ_c from Table 3.1. For these Boolean models, I can confirm that the zero of the Euler characteristic is

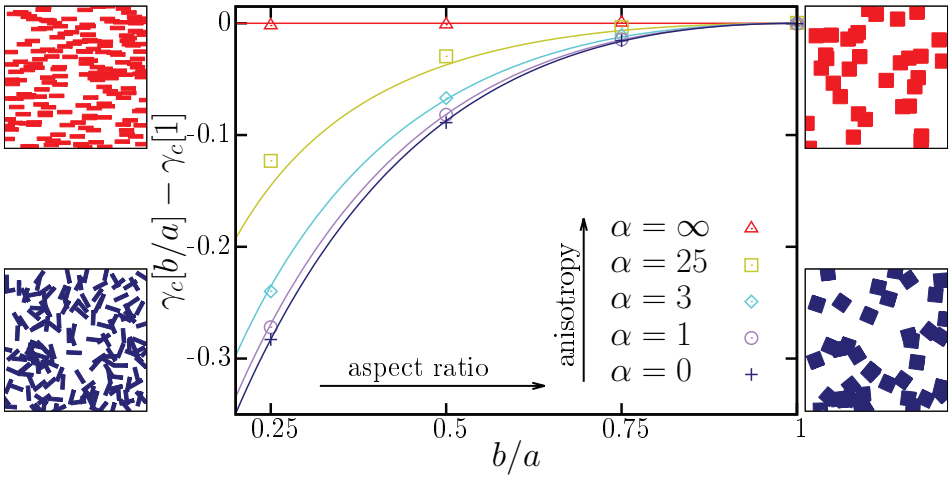

Figure 3.11: The change in the critical intensity γ_c (marks) for different aspect ratios b/a is well described by the change in the zero of the Euler characteristic γ_0 (lines); not only in the trivial case of aligned rectangles (red, see also samples depicted at the top of the right- and left-hand side), but a remarkably good approximation is provided for randomly oriented rectangles with aspect ratios $b/a > 1/4$ (blue, see also samples depicted at the bottom of the right- and left-hand side). For details, see Fig. 3.7 and Table 3.1.

a lower bound on ϕ_c. There is a significant quantitative deviation, but similar to the findings for discretized Boolean models [309], I find that the qualitative behavior of ϕ_c, i.e., the dependence on anisotropy and grain shape, is well described by ϕ_0.

To further investigate this accurate qualitative description, I plot the difference of the critical intensity of rectangles to the critical intensity of squares with the same orientation distribution in Fig. 3.11 and compare it to the difference of the corresponding zeros of the Euler characteristic. For the Boolean models studied here, I find a remarkable agreement. Only for an intermediate regime of strongly preferred orientation, but no perfect alignment ($\alpha = 25$), I find small statistically significant deviations. However, an excellent agreement of the difference in the critical intensities to the difference of the zeros of the Euler characteristic not only for the special case of perfect alignment but also for randomly oriented rectangles. If the critical intensity of squares is used as an empirical parameter, similar to the excluded area approximation, the zero of the Euler characteristic allows at least for these Boolean models a more precise prediction of the percolation threshold than the excluded area approximation, compare to Fig. 3.9.

Like the critical average number of bonds B_c, the offset between the critical intensity γ_c and the zero γ_0 of the Euler characteristic depends on the shape of

the grains; it is different for randomly oriented squares (0.196880(14)[25]) and discs (0.128085(2)[26]). Assuming a constant offset to the number of grains per area of a single grain would lead to a nonphysical behavior in the limit of vanishing aspect ratios: for grains with unit area both the critical intensity and the zero of the Euler characteristic trivially vanish in the limit of extreme anisotropy, i.e., for sticks, because of the choice of units. For example, for randomly oriented sticks of length unity, the zero of the Euler characteristic ($\gamma_0 = \pi$) is as expected a lower bound on the critical intensity ($\gamma_c = 5.6372858(6)$ [272]).

3.3.3 Second-moment approximations

Besides the mean values also the second moments of the Minkowski functionals can eventually yield approximations of the percolation threshold. Although the integral formulas are more intricate than for the first moments, they are analytically known [210], as discussed in Section 2.5.4.

An interesting different example is cell percolation in planar Poisson Voronoi tessellations: Voronoi cells of a Poisson point process are colored black with some probability p, and a percolating cluster is an unbounded and connected collection of black cells. The critical probability of this model of continuum percolation is $p_c = 1/2$ [76]. Last and Ochsenreither [261] have proved that this coincides exactly with the global maximum of the asymptotic variance of the Euler characteristic.

Hug et al. [210] provide besides the integral expressions for the asymptotic variance-covariance structure of the Minkowski functionals of general Boolean models also explicit results for Boolean models with discs. When these results are compared to the percolation threshold of overlapping discs, both the local minimum of the variance of the perimeter and the local minimum of the covariance of area and Euler characteristic are good approximations of the percolation threshold, e.g., the local minimum of the asymptotic covariance $\sigma_{0,2}$ is found at $\gamma \approx 1.15$ compared to the critical intensity $\gamma_c \approx 1.13$ [374], where the unit of area is again defined by the grain.

Here, I compare for four different Boolean models with rectangles the extremal points of the variance-covariance structure of the Minkowski functionals to the percolation threshold. I investigate whether the second moments could allow for accurate predictions of the thresholds without the need for empirical parameters, especially testing whether the local minima of $\sigma_{0,2}$ or $\sigma_{1,1}$ are close to the percolation threshold for anisotropic models.

The numerical estimates and analytic curves of the asymptotic covariances $\sigma_{W_\mu W_\mu}$ from Fig. 2.22 are again plotted in Figs. 3.12 and 3.13, but in contrast to

[25] Using the critical intensity from Ref. [271]
[26] Using the critical intensity from Refs. [375, 513].

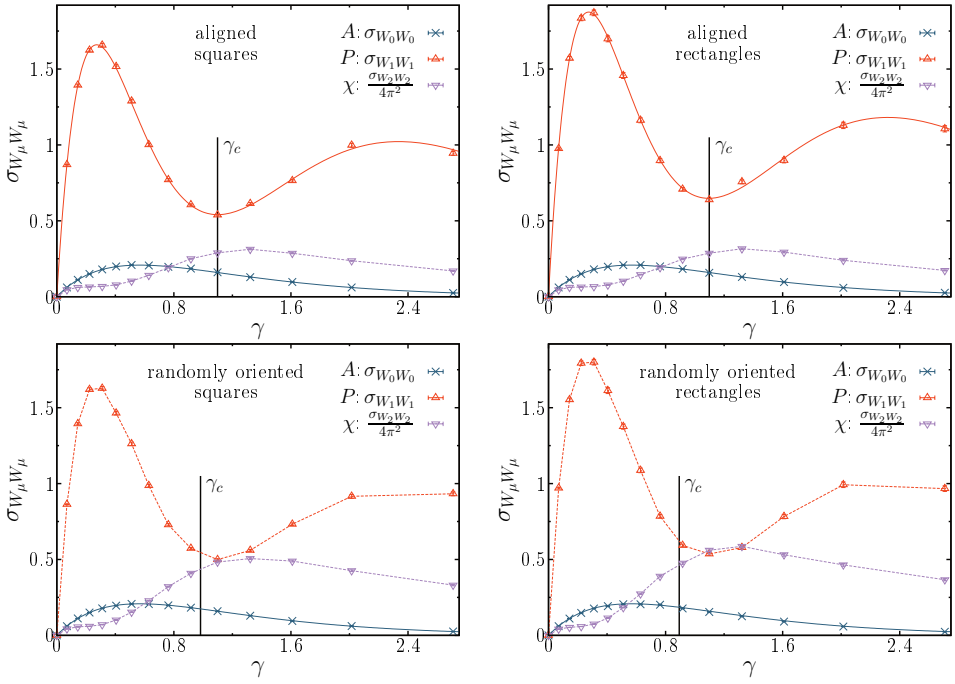

Figure 3.12: Asymptotic variances $\sigma_{W_\mu W_\mu}$ of the Minkowski functionals as functions of the intensity γ of the Boolean models with squares (left) or rectangles with aspect ration $1/2$ (right), the rectangles are either perfectly aligned (top) or follow an isotropic orientation distribution (bottom). The marks represent numerical estimates from simulations, the solid lines represent the analytic curves, and the dashed lines are guides to the eye. For details, see Fig. 2.22. The critical intensity γ_c is indicated by the black vertical line, the estimate for the aligned squares is taken from Ref. [463] and for the isotropic squares and rectangles from Refs. [47] or [271], respectively.

Fig. 2.22, a single plot shows the different asymptotic variances or covariances for a single type of Boolean model, i.e., either with squares or rectangles with aspect ratio $1/2$ which are either perfectly aligned or follow an isotropic orientation distribution. For these four Boolean models very accurate estimates of the percolation thresholds can be found in literature [513]. I use these precise estimates with at least four significant number of digits because I indeed find some remarkable agreement between the extremal points and the percolation threshold.

Like for the overlapping discs, a local minimum point of the variance of the perimeter is an excellent approximation of the percolation threshold for aligned squares or rectangles with aspect ratio $1/2$. The critical intensity of aligned squares is $\gamma_c = 1.0982(3)$ [463], the local minimum point of the asymptotic variance of the perimeter is $\gamma_m[b/a = 1] \approx 1.0994$, which is derived by numerically minimizing $\sigma_{W_1W_1}$ from Eq. (2.51) using Ref. [225]. While it is a remarkably

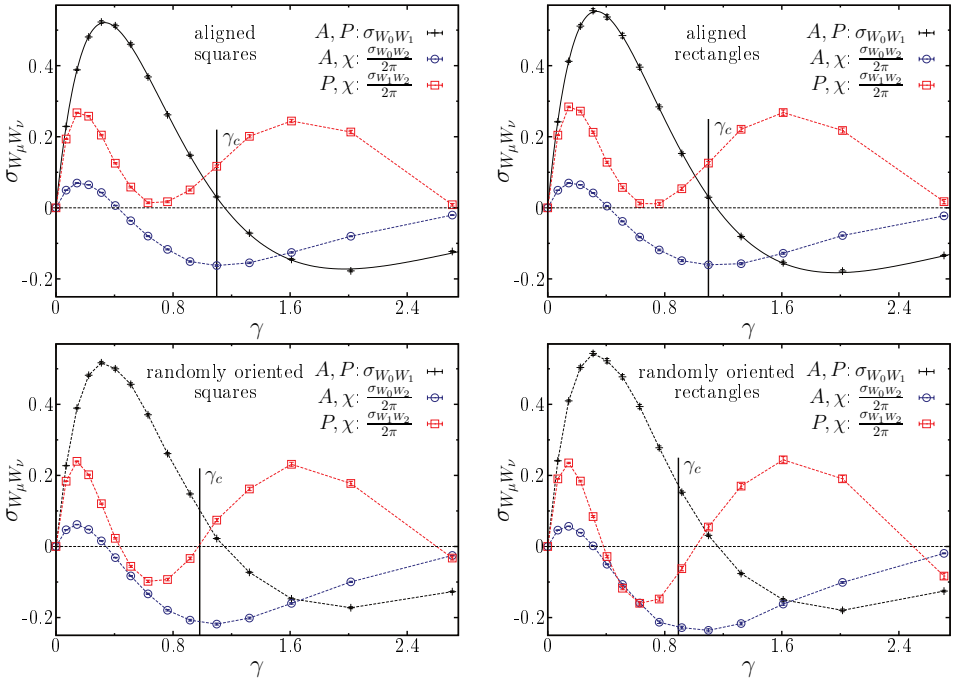

Figure 3.13: Asymptotic covariances $\sigma_{W_\mu W_\nu}$ of the Minkowski functionals as functions of the intensity γ of the Boolean models with squares (left) or rectangles with aspect ration $1/2$ (right), the rectangles are either perfectly aligned (top) or follow an isotropic orientation distribution (bottom). For details, see Fig. 3.12.

good approximation, there is a statistically significant difference. Moreover, while the critical intensity must not depend on the aspect ratio of the aligned rectangles, see Section 3.2, the local minimum point of the asymptotic variance of the perimeter slightly depends on the aspect ratio; for aspect ratio $1/2$ the local minimum point is at $\gamma_m[b/a = 1/2] \approx 1.0952$ and for aspect ratio $1/10$ it is $\gamma_m[b/a = 1/10] \approx 1.0727$. The local minimum point of the variance is also neither an upper nor a lower bound for the percolation threshold. For aligned rectangles, the minimum points can be below the critical intensity. However, the minimum points are above the critical intensities for aligned squares or for the randomly oriented squares and rectangles, see Figure 3.12.

A probably better candidate for an approximation of the percolation threshold could be the local minimum point of the covariance of area and Euler characteristic. Figure 3.13 shows that it is a very good approximation for aligned squares and rectangles with aspect ratio $1/2$ and a close upper bound if the grains are randomly oriented.

Only for one of the Boolean models, a vanishing correlation can serve as a good approximation of the percolation threshold: for randomly oriented squares the first zero of the covariance of perimeter and Euler characteristic ($\propto \sigma_{W_1 W_2}$) seems to be in good agreement with the critical intensity, see Fig. 3.13. However, for randomly oriented rectangles there is a distinct difference. Moreover, for aligned squares or rectangles, as well as for overlapping discs, this zero crossing from negative to positive correlation does not exist.

These results could be important for applications because I here discuss and suggest candidates for accurate approximations of the percolation thresholds without using any empirical parameters. Moreover, the results can also lead to more fundamental questions: Why is there such a good agreement between some of the extremum points and the percolation threshold? Is it a coincidence or is there a connection between local fluctuations and the global topology?

3.4 Conclusions

The Minkowski functionals help to study the relation between geometry, e.g., quantified by area or perimeter, and topology, e.g., quantified by the Euler characteristic. They can provide new insights into percolation as a topological phase transition. First, I study in extensive simulations of isotropic Boolean models a universal scaling of the Euler characteristic of the percolating void cluster, see Fig. 3.1, away from the critical behavior, see Fig. 3.2. Possible candidates for relations to dynamic properties, like permeability, conductivity, elasticity, etc., are discussed.

Then, anisotropic Boolean models are studied as a benchmark example of anisotropic continuum percolation. In a finite observation window, an anisotropic system is more likely to percolate earlier in the preferred direction than in the perpendicular direction, see Fig. 3.3. This anisotropic percolation in finite samples is demonstrated by determining the effective percolation thresholds, see Eqs. (3.1) and (3.2), by a fit of an error function to the connectivity, see Fig. 3.4. However, if the percolation thresholds are extrapolated to infinite system sizes, this difference vanishes and even the most anisotropic model simultaneously percolates in all directions. The percolation threshold is isotropic, see Fig. 3.6 and Table 3.1, which is related to the uniqueness of the percolating cluster, i.e., the fact that there is at most one percolating cluster, see Fig. 3.5. I then estimate the isotropic percolation thresholds for differently anisotropic Boolean models by a simultaneous fit of the finite size scaling in x- and y-direction, see Eqs. (3.4)–(3.5), Table 3.1, and Fig. 3.7. The value of the percolation threshold depends on the orientation distribution.

I discuss explicit formulas for approximations of the percolation threshold, either using an empirical parameter in the well-known excluded area approximation

or using the zero of the Euler characteristic in a purely geometric approach. If the percolation thresholds of squares with different orientation distributions are used as empirical parameters, the excluded area approximation is in relatively good agreement with the percolation thresholds of the rectangles, see Figs. 3.9. The zero of the Euler characteristic as a function of the intensity is for the Boolean models studied here empirically confirmed to serve as a simple and explicit lower bound on the percolation threshold without using any empirical parameters, see Fig. 3.10. If an empirical parameter is used similar to the excluded area approximation, an improved approximation for the models studied here can be derived from the zero of the Euler characteristic, see Fig. 3.11.

Possible approximations of the percolation threshold based on the second moments of the Minkowski functionals are tested for four differently anisotropic Boolean models. The extremum points of the asymptotic variances and covariances of the Minkowski functionals are compared to the critical intensities, and some are found to be in surprisingly good agreement, see Figs. 3.12 and 3.13. The minimum point of the covariance of area and Euler characteristic is suggested as a candidate for an approximation of the critical intensity without using any empirical parameters.

More examples and further research are needed to test this suggestion. Moreover, it might be interesting to study whether the agreement between the extremum points and critical intensities is merely a coincidence or probably might help find a connection between local fluctuations and global topology.

Chapter 4

Minkowski correlation functions of random tessellations[1]

In the last chapter, I have discussed how the local single grain orientation distribution influences the global percolation property. In contrast to this, I here demonstrate for quite different cellular systems how the local structure can be rather insensitive to global structure information. The local structure analysis based on single cell characteristics is extended by introducing global correlation functions of Minkowski functionals, which find for tessellations with qualitatively very similar local structure a distinctly different global structure. The sensitivity of these Minkowski correlation functions is also demonstrated by showing that they can distinguish systems with equal standard two-point correlation functions.

The Boolean model consists of overlapping spheres, i.e., the underlying point process is simply an uncorrelated point process. However, there is a rich variety in physics and mathematics of interacting particle processes, which exhibit global correlations. One of the most common model systems for crystals, colloids, liquids, glasses, heterogeneous materials, foams, and biological systems is that of hard, i.e., impenetrable, spheres [95, 152, 154, 180, 250, 287, 314, 393, 460, 527]. Among them an especially intricate global structure has been found in the most random among the set of all jammed, i.e., mechanically stable, packings; it is therefore called the maximally random jammed (MRJ) state [119, 471]. This state is disordered hyperuniform [467], i.e., at short distances the system is disordered like a liquid, but at large length scales it is homogeneous like a crystal, see Section 4.1.

[1] The results in this chapter were derived in collaboration with Klaus Mecke and Salvatore Torquato. Large parts of this chapter are direct quotes from our publication Ref. [244], from which some of the figures in this chapter and the table are reproduced; copyright by the American Physical Society.

A point process, like these overlapping or hard sphere particle processes, is intuitively related to a tessellation via the Voronoi diagram, which assigns to each particle a cell containing all points closer to this particle than to any other particle. The local structure of the packing can be analyzed by characterizing the shape of a single cell.

I characterize the structure of MRJ sphere packings by computing the Minkowski functionals (volume, surface area, and integrated mean curvature) of their associated Voronoi cells. The probability distribution functions of these functionals of Voronoi cells in MRJ sphere packings are qualitatively similar to those of an equilibrium hard-sphere liquid and partly even to the uncorrelated Poisson point process, implying that such local statistics are relatively structurally insensitive in the sense that they are insensitive to global structural information, see Section 4.2.

To improve upon this, I introduce in Section 4.3 descriptors that incorporate nonlocal information via the correlation functions of the Minkowski functionals of two cells at a given distance as well as certain cell-cell probability density functions. I evaluate these higher-order functions for our MRJ packings as well as equilibrium hard spheres and the Poisson point process in Sections 4.4 and 4.5. I find strong anticorrelations in the Voronoi volumes for the hyperuniform MRJ packings, consistent with previous findings for other pair correlations [119], indicating that large-scale volume fluctuations are suppressed by accompanying large Voronoi cells with small cells, and vice versa. In contrast to the aforementioned local Voronoi statistics, the correlation functions of the Voronoi cells qualitatively distinguish the structure of MRJ sphere packings (prototypical glasses) from that of not only the Poisson point process but also the correlated equilibrium hard-sphere liquids. I also analyze cross-correlations of different Minkowski functionals of cells at a given distance and find surprising relations among them which can be related to vanishing correlations of deviations from the expected values.

In Section 4.6, I show that the Minkowski correlation functions contain more information than the corresponding standard pair-correlation functions. Point patterns with exactly the same pair-correlation function are clearly distinguished by the Minkowski correlation function, which is shown for models of galaxy distributions.

4.1 Ordered and disordered hard-sphere packings

Packings of frictionless monodisperse hard spheres in three dimensions serve as a simple, yet effective tool for modeling the complex behavior of such diverse many-particle systems as crystals, colloids, liquids, glasses, heterogeneous materials, foams, and biological systems [95, 152, 154, 180, 250, 287, 314, 393, 460, 527].

Among the rich multitude of states they are known to exhibit, considerable interest has been given towards sphere packings that are jammed (i.e., mechanically stable), including maximally dense packings, low-density crystals, and amorphous packings [39, 40, 139, 177, 188, 234, 352, 469, 470, 522].

In order to characterize the properties of sphere packings, one may employ a geometric-structure approach in which configurations are considered independently of both their frequency of occurrence and the algorithm by which they are created [470]. For example, the simplest characteristic of a sphere packing is its packing fraction ϕ, i.e., the fraction of space occupied by the spheres. Other useful characteristics of the structure include its pair-correlation function [40, 103, 114, 223, 359, 423, 462, 468, 506], the pore-size distribution [119, 460], and structure factor [71, 180, 253, 428, 468].

It is also valuable to quantify the degree of ordering in a packing, especially those that are jammed (defined more precisely below). To this end, a variety of scalar order metrics ψ have been suggested [470, 471] in which $\psi = 0$ is defined as the most disordered state (i.e. the Poisson point process) and $\psi = 1$ is the most ordered state. Using the geometric-structure approach, one may therefore construct an "order map" in the ϕ-ψ plane [470], where the jammed packings form a subset in this map. The boundaries of the jammed region are optimal in some sense, including, for example, the densest packings (the face-centered-cubic crystal and its stacking variants with $\phi_{\max} = \pi/\sqrt{18} \approx 0.74$ [177]) and the least dense jammed packings (conjectured to be the "tunneled crystals" with $\phi_{\min} = 2\phi_{\max}/3$ [469]).

Among the set of all isotropic and statistically homogeneous jammed sphere packings, the maximally random jammed (MRJ) state is that which minimizes some order metric ψ. This definition makes mathematically precise the familiar notion of random closed packing (RCP) in that it can be unambiguously identified for a particular choice of order metric. A variety of sensible, positively correlated order metrics produce an MRJ state with the same packing fraction 0.64[2] [231], which agrees roughly with the commonly suggested packing fraction of RCP in three dimensions [470]. However, it must be stressed that density alone is not sufficient to characterize a packing; in fact, packings with a large range of ψ may be observed at this packing fraction [223, 231].

In order to study the MRJ state, a precise definition of jamming is needed. Therefore, rigorous hierarchical jamming categories have been defined [466, 472]: A packing is *locally jammed* if no particle can move while the positions of the other particles are fixed; it is *collectively jammed* if no subset of particles can move without deforming the system boundary; and if also a deformation of the system boundary is not possible without increasing its volume, the packing is *strictly*

[2] Note that there are many other more ordered packings with the same packing fraction.

jammed, i.e., it is stable against both uniform compression and shear deformations[3]. Strictly jammed MRJ sphere packings often contain a small fraction of rattlers (unjammed particles), but the remainder of the packing, i.e., the mechanically rigid backbone, is strictly jammed [41].

Determining the contact network of a packing is a subtle problem requiring high numerical fidelity. The Torquato-Jiao (TJ) sphere packing algorithm [462] meets this challenge by efficiently producing highly disordered, strictly jammed packings with unsurpassed numerical fidelity as well as ordered packings [290, 462]. The algorithm achieves this by solving a sequence of linear programs which iteratively densify a collection of spheres in a deformable periodic cell subject to locally linearized nonoverlap constraints. The resulting packings are, by definition, strictly jammed and they are with high probability exactly isostatic (meaning that they possess the minimum number of contacts required for jamming) [41, 121]. The TJ packing protocol is intrinsically capable of producing MRJ states with very high fidelity [41, 462]. The MRJ state can be regarded as a prototypical glass because it is maximally disordered (according to a variety of order metrics) while having infinite elastic moduli [470]. Atkinson et al. [41] recently carried out a detailed characterization of the rattler population in these MRJ sphere packings. They found a rattler fraction of 1.5 % (substantially lower than other packing protocols, such as the well-known Lubachevsky-Stillinger packing algorithm [279]) and that the rattlers were highly spatially correlated, implying that they have a significant influence on the structure of the packing [119]. Moreover, as in previous studies [121], it was shown [41] that the backbone of the MRJ state is isostatic. I include rattlers in my analysis unless stated otherwise.

MRJ packings have been characterized using a variety of statistical descriptors, including the radial pair-correlation function $g_2(r)$ ($\rho^2 g_2$ is the probability density for finding two sphere centers separated by a radial distance r, where ρ is the number density, i.e., the number of particles per unit volume) [462], the bond-orientational order metric Q_6 and the translational order metric T^* [41, 231], the cumulative pore-size distribution $F(\delta)$ [119], and the statistics of rattlers [41]. In addition, MRJ sphere packings exhibit disordered hyperuniformity [119], meaning that they are locally disordered, but possess a hidden order on large length scales such that infinite-wavelength density fluctuations of MRJ packings vanish, i.e., the structure factor vanishes at the origin[4]: $\lim_{\boldsymbol{k}\to\boldsymbol{0}} S(\boldsymbol{k}) = 0$ [467]. Disordered hyperuniformity can be seen as an "inverted critical phenomenon" with a direct

[3] The jamming category of a finite system depends on the boundary conditions; see Refs. [466] and [472]

[4] This determines the asymptotic behavior of the total correlation function and the number variance or density fluctuations within a spherical observation window as a function of the radius of an observation window [119].

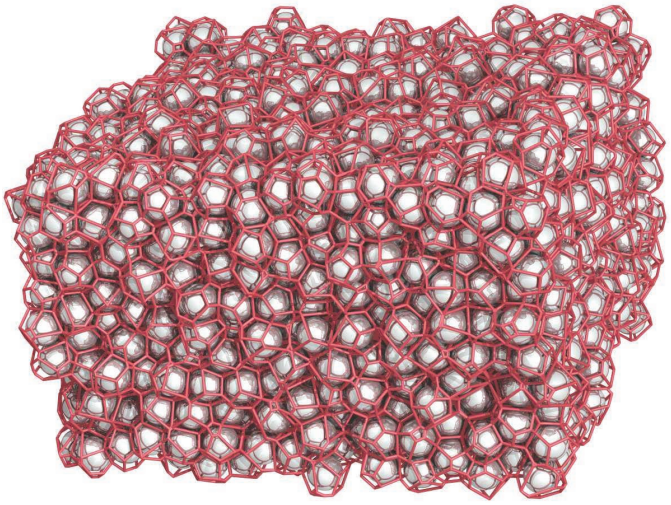

Figure 4.1: Maximally random jammed (MRJ) sphere packing and its Voronoi diagram. Among all jammed sphere packings (roughly speaking, the mechanically stable packings), the MRJ state is the most disordered one.

correlation function $c(r)$ that is long ranged [198, 467]. In this chapter, I characterize the MRJ sphere packings generated in Ref. [41] using Voronoi statistics, including certain types of correlation functions. I compare these computations to corresponding calculations for both a Poisson distribution of points and equilibrium hard-sphere liquids (for which sphere configurations are provided by Steven Atkinson).

Many studies for disordered sphere packings have been devoted to computing the volume distribution of the Voronoi cells [e.g., 38, 39, 137, 139, 233, 234, 268, 407, 440, 526]; see Fig. 4.1 for a MRJ sphere packing and its Voronoi diagram[5]. However, such statistics are incomplete in that they only quantify local structural information. For example, with appropriately rescaled variables, I show that the distributions of the Voronoi volumes, surface areas, and integrated mean curvatures for the MRJ sphere packings are qualitatively similar to the distributions for an equilibrium hard-sphere liquid and partly even for the spatially uncorrelated Poisson point process.

To quantify nonlocal structural information, I formulate and compute correlation functions of the volume of Voronoi cells at a given distance and cell-cell probability density functions of finding a given sized Voronoi cell at a given distance of a sphere with another sized Voronoi cell. Because the volume is only one of a large class of versatile shape measures, namely, the Minkowski functionals [305, 307, 400, 408], I devise and compute the correlation functions of all of the

[5] For each sphere, a Voronoi cell is assigned which contains all points closer to this sphere than to any other sphere in the packing.

Table 4.1: Mean $\langle W_\mu \rangle$, standard deviation σ_{W_μ}, and correlation coefficients $\rho_{\mu,\nu}$ of the Minkowski functionals W_μ of single Voronoi cells in the Poisson point process, in a system of hard spheres in equilibrium at a packing fraction $\phi = 0.48$, and in the MRJ state. The unit of length is $\lambda = 1/\rho^{1/3}$, i.e., the number density ρ is set to unity.

		$\langle W_\mu \rangle$	σ_{W_μ}	$\rho_{\mu,1}$	$\rho_{\mu,2}$
			Poisson		
Volume	W_0	1.0005(3)	0.4230(2)	0.98161(3)	0.94486(8)
Surface area	W_1	5.823(1)	1.4798(7)		0.98701(2)
Integ. mean curv.	W_2	9.1623(8)	1.0941(5)		
			Equilibrium		
Volume	W_0	1.00000(7)	0.07434(5)	0.97700(5)	0.9282(2)
Surface area	W_1	5.4488(3)	0.2681(2)		0.98136(5)
Integ. mean curv.	W_2	8.6477(2)	0.2163(2)		
			MRJ		
Volume	W_0	1.00000(3)	0.04335(2)	0.96976(4)	0.9035(1)
Surface area	W_1	5.4043(1)	0.1695(8)		0.97248(5)
Integ. mean curv.	W_2	8.5894(1)	0.1470(7)		

Minkowski functionals[6]. Besides characterizing MRJ packings in this way, I also carry out analogous calculations for the Poisson point process and the equilibrium hard-sphere liquid for purposes of comparison. I show that these Minkowski correlation functions contain visibly more information than the corresponding standard pair-correlation functions, even in the case of the Poisson point process.

4.2 Local distributions of Minkowski functionals and tensors

While there are many detailed studies of the volume distribution in disordered sphere packings [e.g., 38, 39, 137, 139, 233, 234, 268, 407, 440, 526], I here analyze in a logarithmic plot the volume distributions of true MRJ packings as describe above and extend the analysis to all three (nontrivial) Minkowski functionals: the volume, the surface area, and the integrated mean curvature. I use voro++ [390, 391] to construct the Voronoi diagram of Poisson point patterns (about 1000 patterns, each with 2000 points), equilibrium hard-sphere packings [180, 460] at a packing fraction $\phi = 0.48$, which is slightly below the freezing

[6] As mentioned above, the Euler characteristic χ, which is proportional to $W_3 = 4\pi\chi$, is a topological constant. For a single Voronoi cell, it is therefore always trivially equal to one.

transition (100 packings, each with 10000 spheres), and MRJ sphere packings produced by the TJ algorithm [41, 462] (about 1000 packings, each with 2000 spheres). For the hard-sphere packings, the sphere configurations are from Steven Atkinson. The program KARAMBOLA [318, 410] then computes the Minkowski functionals of each cell.

I first determine the distributions of the three Minkowski functionals (W_0, volume; W_1, surface area; and W_2, integrated mean curvature) of the single Voronoi cells. Table 4.1 provides the estimates of the mean values, the standard deviations, and the correlation coefficients $\rho_{\mu,\nu} = \frac{\langle W_\mu W_\nu\rangle - \langle W_\mu\rangle\langle W_\nu\rangle}{\sigma_{W_\mu}\sigma_{W_\nu}}$ of the three different Minkowski functionals. As a unit of length, I use $\lambda = 1/\rho^{1/3}$ with ρ the number density, i.e., I compare the Poisson point process, the equilibrium hard-sphere liquid, and the MRJ state at the same number density $\rho = 1$ (the unit volume contains one particle on average)[7]. Because the number density is set to unity, the mean cell volume is also one. The average surface area and integrated mean curvature of a Voronoi cell in the MRJ state or in the equilibrium ensemble are slightly larger than those of a Poisson Voronoi cell because the latter is less regular, i.e., more aspherical. The Voronoi volume fluctuations and the standard deviations of the other Minkowski functionals are much stronger in the irregular Poisson point process than in the hard-sphere packings, where the MRJ state has significantly smaller Voronoi volume fluctuations than the equilibrium hard-sphere liquid. The Minkowski functionals of a single Voronoi cell, e.g., its volume and its surface area, are strongly correlated, i.e., the correlation coefficients $\rho_{\mu,\nu}$ are at least 0.9. The numerical estimates for the Poisson Voronoi tessellation are in agreement with the analytic values and numerical estimates in Ref. [100] and references therein.

The high fidelity of the MRJ sphere packings produced by the TJ algorithm allows one to study the relation between the number of contacts of a sphere and the Minkowski functionals of its Voronoi cell. As expected, small cells have a higher number of contacts on average because a high local packing fraction[8] implies that there are many close neighbors. In units of λ, the mean Voronoi volume of a rattler, i.e., an unjammed particle, is 1.04 and that of a particle with 11 contacts is 0.88. The mean surface area of the Voronoi cells of rattlers and backbone spheres with up to 11 contacts varies from 5.50 to 4.92, respectively, and the average integrated mean curvature varies from 8.65 to 8.17, respectively. However, because of the small difference between near contacts and true contacts, the distributions of the Minkowski functionals for rattlers are only slightly shifted compared to the distributions of a typical cell. There are, for example, very small cells containing

[7] Because the packing fraction of the equilibrium hard-sphere liquid is lower than for the MRJ state, the corresponding diameters of the spheres differ.

[8] The local packing fraction is the volume of the sphere divided by the volume of the Voronoi cell.

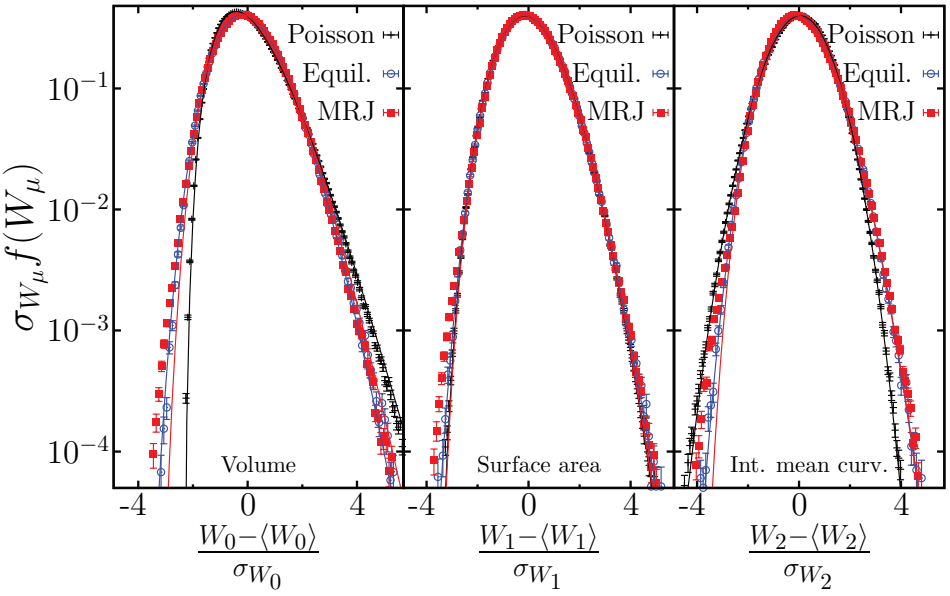

Figure 4.2: Distributions of the single Minkowski functionals W_μ of a three-dimensional Voronoi cell in a Poisson point process, an equilibrium hard-sphere system at a packing fraction $\phi = 0.48$, and an MRJ sphere packing: $\mu = 0$ volume (left), $\mu = 1$ surface area (center), and $\mu = 2$ integrated mean curvature (right). The distributions are rescaled—like in Ref. [440]—by their mean value $\langle W_\mu \rangle$ and their standard deviation σ_{W_μ} (see Table 4.1). The lines in the plot of the volume distributions are γ distributions; generalized γ distributions are fitted to the distributions of the surface area and the integrated mean curvature.

rattlers, which is consistent with previous findings [41].

Starr et al. [440] and, similarly, Aste et al. [39] showed that by shifting the volume distribution by its mean value and rescaling with its standard deviation, the volume distributions of many different sphere packings collapse. Figure 4.2 shows the rescaled distributions of the Minkowski functionals for the Poisson point process, the equilibrium hard-sphere liquid, and the MRJ packing. As expected, the volume distributions of the equilibrium hard-sphere packings and the MRJ packings are qualitatively very similar, while the distribution of the Poisson point process deviates. The same is true for the distribution of the mean curvatures. The distributions of the surface area for both the MRJ and the equilibrium hard-sphere packings are not only qualitatively similar to each other but also to the uncorrelated Poisson point process. So, besides the quantitative difference in the mean values and the standard deviations of the Minkowski functionals, the distributions of the Minkowski functionals of single Voronoi volumes are qualitatively similar for the equilibrium hard-sphere liquid and the MRJ state as well as even partially for the

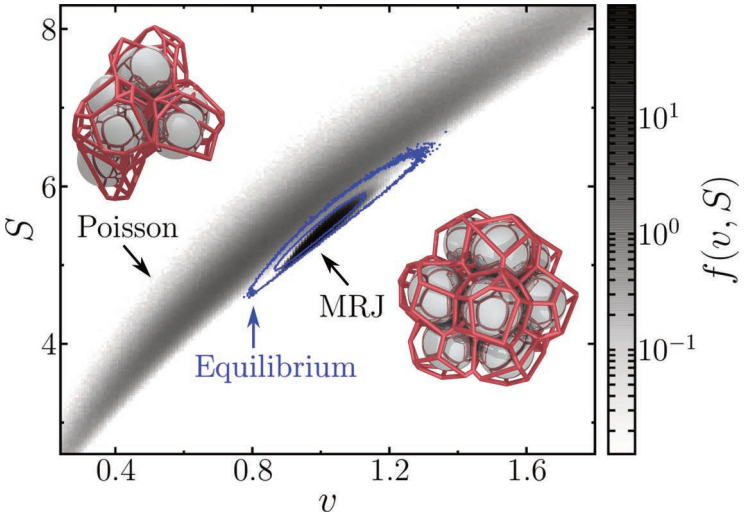

Figure 4.3: Joint distribution of volume v and surface area S of a single three-dimensional Voronoi cell in a logarithmic scale for a Poisson point process and a MRJ sphere packing; the joint distribution for the equilibrium hard-sphere liquid is represented by the blue contour plot. The unit of length is $\lambda = 1/\rho^{1/3}$, where ρ is the number density. Samples of a MRJ sphere packing and an overlapping sphere packing, where the sphere centers follow a Poisson point process, are depicted together with their Voronoi diagrams.

Poisson point process. The distribution of the Minkowski functionals of a single cell only incorporates local information and is rather insensitive to global structural features such as hyperuniformity of the MRJ state [119, 198].

Figure 4.3 shows the joint probability distribution of the volume and the surface area of a single Voronoi cell in a Poisson point process, an equilibrium hard-sphere liquid, and a MRJ sphere packing. The joint probability distributions for the equilibrium hard-sphere liquid and the MRJ state are also relatively similar.

Both for the Poisson point process [369] and for many different numerical and experimental sphere packings [39], the volume distribution follows well a γ distribution. More precisely, the volume distributions are well approximated by shifted γ distributions,

$$f(v) = \frac{1}{\Gamma(k)\theta^k}(v - v_{\min})^{k-1} \mathrm{e}^{-(v-v_{\min})/\theta}$$

where the parameters $k = (\langle v\rangle - v_{\min})^2/\sigma_v^2$ and $\theta = \sigma_v^2/(\langle v\rangle - v_{\min})$ are determined by the mean value $\langle v\rangle$ and standard deviation σ_v of the volume distribution [39]. The volume of a Voronoi cell of a hard-sphere packing must be greater than the volume $v_{\min}$ of a dodecahedron with the sphere touching all of its faces [39, 463]. I also find, for the volume distributions for the Poisson point process and the

equilibrium hard-sphere liquid, an excellent agreement with γ distributions: the parameters k of the γ distributions are $k = 5.6$ for the Poisson point process, $k = 24.3$ for the equilibrium hard-sphere liquid, and $k = 13.3$ for the MRJ sphere packings. However, for the MRJ sphere packings there is a slight but statistically significant deviation for very small cells for which the frequency of occurrence is too high.

The surface area and the integrated mean curvature distributions are well approximated by generalized γ distributions, which was already found for the Poisson point process by Refs. [233, 267]. The generalized γ distributions is defined as

$$\gamma_q(x) := \frac{q(x - x_{\min})^{q(k-1)} \mathrm{e}^{-((x-x_{\min})/\theta)^q}}{\Gamma(k - 1 + 1/q)\theta^{1+q(k-1)}}$$

where the parameter θ is fixed by the mean value of the surface area or of the integrated mean curvature, and the parameters k and q are fit parameters. The minimum surface area and integrated mean curvature is assumed to be that of a dodecahedron. Note that Lazar et al. [267] showed with very high statistics, using 250,000,000 cells, that the Voronoi volume distribution of a Poisson point process also deviates statistically significantly from a two-parameter γ distribution, but is very well described by the generalized γ distribution.

However, the distributions for the MRJ sphere packings deviate slightly but statistically significantly from a generalized γ distribution for cells with small surface area or small integrated mean curvature, respectively. The reduced χ squared of the fits to the surface area distributions and integrated mean curvature distributions are for the equilibrium hard-sphere packings 0.94 or 0.96, respectively, and for the Poisson point process 2.40 or 2.43, respectively, but for the MRJ sphere packings, they are 23.2 or 25.7, respectively.

A possible refinement of the local analysis is to quantify the anisotropy of a single cell by the Minkowski tensors, which allows, e.g., to detect phase transitions and the onset of crystallinity in jammed packings [232–234, 320]. Here, I have collected data for a variety of different tessellation models.

I analyze the Voronoi diagrams of very different particle processes ranging from the uncorrelated Poisson point process, over the equilibrium hard-sphere liquid to hard-sphere crystals; the data for the Minkowski functionals and tensors of the equilibrium hard-sphere liquids are from Markus Spanner and Fabian Schaller, see also Refs. [233, 410]; the crystal sphere packings are provided by Richard Schielein, for more details see Ref. [411].

The model of "random sequential addition" (RSA), also called "random sequential adsorption", yields packings of hard spheres. Intuitively speaking, spheres are subsequently placed into space (uniformly distributed). However, a sphere

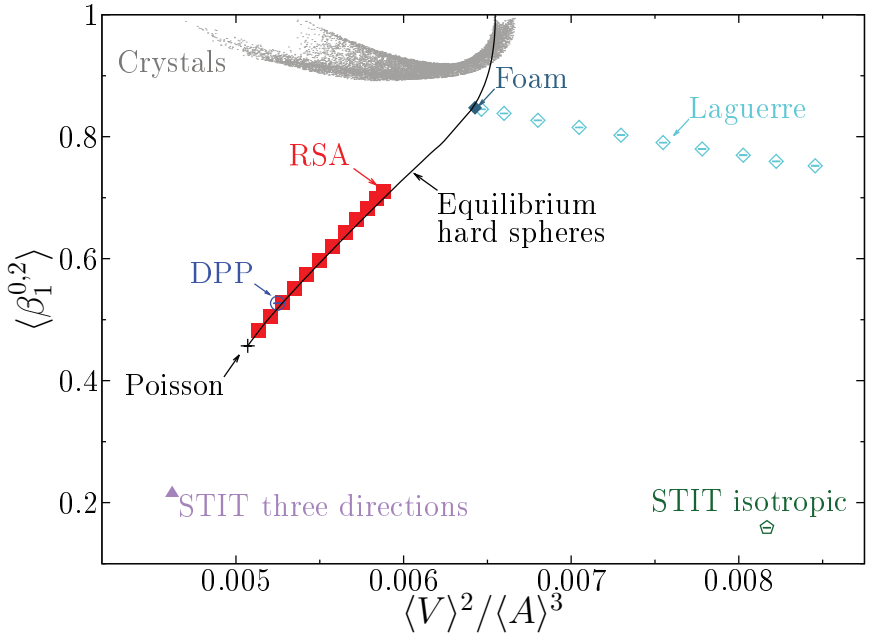

Figure 4.4: Map of local anisotropy with the mean anisotropy index $\beta_1^{0,2}$ and the ratio of mean volume to the power of two over the mean surface area to the power of three, which are plotted for various tessellations ranging from the uncorrelated Poisson point process to crystals. The map of anisotropy reveals structural differences between the models, but also how they are related to each other. Including or based on data from Andy Kraynik (foam), Markus Spanner and Fabian Schaller (equilibrium hard spheres), Richard Schielein (crystals), and Claudia Redenbach (Laguerre and STIT tessellations).

is only accepted if there is no overlap with spheres that have already been accepted [460]. It is nearly identical to the in mathematics literature well-known Matérn III process [324]. Note, that I am here not only referring to the saturation limit, that is, the packing where no additional sphere can be accepted (which corresponds to a packing fraction of about $0.384131(\pm 2 \cdot 10^{-6})$ [523]). Instead, I consider packings for which a target packing fraction (below the saturation limit) is chosen and spheres are added until this global packing fraction is reached.

The determinantal point process (DPP), which is used to model fermions in quantum mechanics [68] or transmitters in wireless networks [115], is a purely repulsive particle process with soft repulsive particles, i.e., although unlikely the particles can get arbitrarily close in contrast to the hard-sphere packings; it is defined via a given kernel which determines the n-point correlation functions [283]; I simulate the DPP with a software package provided by Ege Rubak [265] written for SPATSTAT [46] which is a package for the statistics software R.

The monodisperse foam simulated by Andy Kraynik is a realistic model for dry[9] soap froth, minimizing the surface area and balancing the mechanical forces [250, 251]. The random Laguerre tessellations with varying volume distributions are intended as a mathematical model for foam structures [264]; they are simulated by Claudia Redenbach.

Another class of random tessellations are the so-called STIT tessellations (stable against iteration) [100, 331]. Starting from a given cell, e.g., the simulation box, a random exponentially distributed lifetime is assigned to the cell. After this time, the cell is divided by a random plane. The two new cells again have random lifetimes that are exponentially distributed and independent from each other. This cell division process is iterated until after some fixed time the process is stopped. Different STIT models can be constructed from different orientation distributions of the random planes: here, isotropic refers to an "isotropic" distribution, and "three directions" refers to only three equally probably and mutually orthogonal directions where the single cells are cuboids, see Fig. 1.4(d). Because of the intersection of a hyperplane with a single cell, the resulting cells are not face-to-face in contrast to the Voronoi diagrams. The STIT tessellations are simulated by Claudia Redenbach.

From these data sets for all of these tessellation models, I then construct a map of anisotropy, see Fig. 4.4. Each tessellation is represented by its mean anisotropy index $\beta_1^{0,2}$ and its mean volume normalized by its mean area, which is basically the surface area of a cell with unit volume but chosen to be scale-free, because some of these models are scale-free.

The map of anisotropy provides a reference for the tessellation models and characterizes their anisotropy, which can help choosing the appropriate model for applications. The map reveals structural differences between the models, but also how they are related to each other: The STIT tessellations constructed by random planes have on average the most anisotropic cells of all models studied here. The Poisson point process is also very irregular, and its Voronoi cells are therefore rather anisotropic. A dilute hard-sphere liquid or RSA packings are nearly indistinguishable from a Poisson point process in this analysis, and they have indeed a very similar structure because an overlap is very unlikely.

The denser the hard-sphere liquid gets, the more regular and isotropic become the cells. Upon reaching the densest global packing fraction $\phi_{\max} = \pi/\sqrt{18} \approx 0.74$ [177], the spheres form a face-centered-cubic crystal or one of its stacking variants and the cells are perfectly isotropic. Also the other crystals have as expected isotropic or only slightly anisotropic cells.

The anisotropy of the RSA or DPP Voronoi cells is very similar to that of a hard-sphere liquid, the same is true for the Laguerre tessellation in the monodisperse

[9] Foam in the limit of vanishing liquid content.

limit. On the one hand the similarity arises from a similar Voronoi structure of these repulsive particle processes, on the other hand the local analysis based only on the mean anisotropy is not sensitive enough to distinguish the fine structural differences of these packings. This also applies to the foam data, for which the simulation starts from the Voronoi diagram of a random jammed hard-sphere packing, derived by the so-called Lubachevsky-Stillinger packing algorithm [279], then the soap froth is equilibrated by Kenneth Brakke's Surface Evolver [83]. Therefore, the shape of a foam cell or a Voronoi cell in an equilibrium hard-sphere liquid are to some extend similar, but of course also distinctly different, e.g., the faces of a foam cell are curved [249]. A more refined local Minkowski analysis can identify the structural differences for the above mentioned similar packings.

However, not even a complete shape characterization can uniquely identify a tessellation by only the local shape of the single cells. Counter examples are the STIT tessellations compared to Poisson hyperplane tessellations [100]. The latter are constructed by placing uncorrelated hyperplanes randomly in space, for example, random lines in two dimensions. They intersect and form cells that are by definition always face-to-face with their neighbors. Therefore, a Poisson hyperplane tessellation has an obviously different global structure compared to a STIT tessellation with the same orientation distribution of the hyperplanes. However, it has been rigorously proven, that cells in a STIT or in a corresponding Poisson hyperplane tessellation have the same shape distribution[10] [331]. Therefore, the full probability distributions of all Minkowski functionals and tensors are exactly the same, although these two packings have an obviously different global structure.

4.3 Global correlation functions and probability density functions of Minkowski functionals

In order to quantify the global structure of the Voronoi diagram, correlation functions of the Minkowski functionals of cells at a distance r and cell-cell probability density functions are introduced and defined here.

4.3.1 Correlation functions of Minkowski functionals

I define the volume-volume correlation function $C_{00}(\mathbf{r}_1, \mathbf{r}_2)$ of the Voronoi cells of an arbitrary point process as the correlation between the volume of two Voronoi

[10] To be more precise the cell interiors have the same distribution; the face-to-face property at the boundary is as explained different.

cells given that the corresponding centers are at the positions $\mathbf{r}_1$ and $\mathbf{r}_2$:

$$C_{00}(\mathbf{r}_1, \mathbf{r}_2) := \frac{\langle v(\mathbf{r}_1) v(\mathbf{r}_2) \rangle - \langle v(\mathbf{r}_1) \rangle \langle v(\mathbf{r}_2) \rangle}{\sigma_{v(\mathbf{r}_1|\mathbf{r}_2)} \sigma_{v(\mathbf{r}_2|\mathbf{r}_1)}} \tag{4.1}$$

where $\langle . \rangle$ denotes the ensemble average given two points at $\mathbf{r}_1$ and $\mathbf{r}_2$; and $\sigma_{v(\mathbf{r}_i|\mathbf{r}_j)}$ is the standard deviation of the volume v of the Voronoi cell at $\mathbf{r}_i$ given that there is another point at $\mathbf{r}_j$. Note that because of this condition, both the mean value and the standard deviation of a single Voronoi volume are functions of the positions $\mathbf{r}_1$ and $\mathbf{r}_2$: e.g., knowing that there is a point in close proximity, very large volumes are less likely and the mean volume decreases. For a statistically homogeneous and isotropic point process, the volume-volume correlation is simply a radial function, which I denote by $C_{00}(r)$, where $r = \|\mathbf{r}_2 - \mathbf{r}_1\|$. The correlation function $C_{00}(r) \in [-1, 1]$ measures the correlations, both positive and negative (anticorrelations), between Voronoi volumes of cells given that their centers are at a distance r.

The Voronoi tessellation assigns to each point a volume of its corresponding Voronoi cell. This is a special case of a marked point process where the constructed mark assigned to each point is determined by the positions of the points in the neighborhood. In this sense, the volume-volume correlation function can be seen as a special type of a marked correlation function [100, 217, 307].

The volume-volume correlation function does not, in general, converge to perfect correlation for vanishing radial distance $\lim_{r\to 0} C_{00}(r) < 1$ because for all $r > 0$ the correlation function $C_{00}(r)$ provides the correlation of the Voronoi volumes of two different cells with volumes $v(0)$ and $v(r)$. Because the cell is perfectly correlated with itself, i.e., $C_{00}(0) = 1$, the correlation function $C_{00}(r)$ is discontinuous at the origin. If there is no long-range order, the correlation function tends to zero for infinite radial distance $\lim_{r\to\infty} C_{00}(r) = 0$.

The correlation functions of the other Minkowski functionals are defined analogously to Eq. (4.1), replacing volume ($\mu = 0$) by surface area ($\mu = 1$) or integrated mean curvature ($\mu = 2$):

$$C_{\mu\mu}(\mathbf{r}_1, \mathbf{r}_2) := \frac{\langle W_\mu(\mathbf{r}_1) W_\mu(\mathbf{r}_2) \rangle - \langle W_\mu(\mathbf{r}_1) \rangle \langle W_\mu(\mathbf{r}_2) \rangle}{\sigma_{W_\mu(\mathbf{r}_1|\mathbf{r}_2)} \sigma_{W_\mu(\mathbf{r}_2|\mathbf{r}_1)}} \tag{4.2}$$

with $\sigma_{W_\mu(\mathbf{r}_i|\mathbf{r}_j)}$ the standard deviation of the Minkowski functional W_μ of the Voronoi cell at $\mathbf{r}_i$ given that there is another point at $\mathbf{r}_j$. For a statistically homogeneous and isotropic point process, the correlation function of the Minkowski functionals is again a radial function, which I denote by $C_{\mu\mu}(r)$. In general, $C_{\mu\mu}(r)$ is discontinuous for $r \to 0$, as noted above for the volume-volume correlation function.

In Section 4.4, I calculate the volume-volume correlation function analytically for the one-dimensional Poisson point process and numerically estimate the correlation functions $C_{\mu\mu}$ for the three-dimensional Poisson point process, the equilibrium hard-sphere liquid, and MRJ sphere packings.

A different type of correlation function, a pointwise Voronoi correlation function, assigns to arbitrary points the volumes of the Voronoi cells in which they lie [526]. Correlations between Voronoi volumes have also already been studied by finding a nonlinear scaling in the aggregate Voronoi volume fluctuations as a function of the sample size [38].

4.3.2 Cell-cell probability density functions

The volume-volume correlation function $C_{00}(\mathbf{r}_2, \mathbf{r}_1)$ is defined conditionally on the fact that the centers of the two cells are at $\mathbf{r}_1$ and $\mathbf{r}_2$. The full two-point information about the Voronoi volumes is given by the cell-cell probability density function $p(\mathbf{r}_2, v, \mathbf{r}_1, v^*)$ of finding two points in the point process at two arbitrary positions $\mathbf{r}_2$ and $\mathbf{r}_1$ with associated Voronoi volumes v and v^*, respectively. It quantifies, for example, how likely it is to find near a point with a small Voronoi cell another point with either a large or another small Voronoi cell. Integrating over the volumes yields the standard pair-correlation function,

$$g_2(\mathbf{r}_2, \mathbf{r}_1) = \iint \mathrm{d}v\, \mathrm{d}v^* \, \frac{p(\mathbf{r}_2, v, \mathbf{r}_1, v^*)}{\rho(\mathbf{r}_2)\rho(\mathbf{r}_1)} \, .$$

This relation clearly indicates that the Minkowski probability density function $p(\mathbf{r}_2, v, \mathbf{r}_1, v^*)$ contains more information than $g_2(\mathbf{r}_2, \mathbf{r}_1)$. Moreover, the volume-volume correlation function $C_{00}(\mathbf{r}_2, \mathbf{r}_1)$ from Section 4.3.1 follows from calculating the moments $\langle v v^* \rangle$, $\langle v \rangle$, and $\langle v^* \rangle$ of $\frac{p(\mathbf{r}_2, v, \mathbf{r}_1, v^*)}{\rho(\mathbf{r}_2)\rho(\mathbf{r}_1) g_2(\mathbf{r}_2, \mathbf{r}_1)}$ and the corresponding standard deviations σ_v and σ_{v^*}.

For a statistically homogeneous and isotropic point process, the cell-cell probability density function is a radial function, i.e., it only depends on the radial distance $r = \|\mathbf{r}_2 - \mathbf{r}_1\|$: $p(r, v, v^*)$ is the probability density of finding two points with Voronoi volumes v and v^* at a radial distance r. If there is no long-range order, the cell-cell probability density function $p(r, v, v^*)$ converges for large radii $r \to \infty$ to $\rho^2 f(v) f(v^*)$, with ρ the number density and $f(v)$ the distribution of the Voronoi volume v of a single cell (see Section 4.2).

For a better visualization and comparison of different volumes, I divide the cell-cell probability density function by its long-range value; the cell-cell pair-correlation function is defined as

$$g_{vv}(\mathbf{r}_2, v, \mathbf{r}_1, v^*) := \frac{p(\mathbf{r}_2, v, \mathbf{r}_1, v^*)}{\rho(\mathbf{r}_2) f(v) \rho(\mathbf{r}_1) f(v^*)}$$

and, for a homogeneous and isotropic system,

$$g_{vv}(r, v, v^*) := \frac{p(r, v, v^*)}{\rho^2 f(v) f(v^*)} \,. \tag{4.3}$$

If $g_{vv}(r, v, v^*) > 1$, it is more likely to find a pair of Voronoi cells with volumes v and v^* at a distance r than to find them at a large distance, i.e., uncorrelated. If $g_{vv}(r, v, v^*) < 1$, the occurrence of a point in the point process with a Voronoi volume v at a distance r of another Voronoi center with a Voronoi volume v^* is suppressed. Analogous cell-cell pair-correlation functions can be defined for the other Minkowski functionals.

In Section 4.4.1, I calculate the cell-cell probability density function analytically for the one-dimensional Poisson point process. In Section 4.5, I determine the cell-cell pair correlation function numerically for the three-dimensional Poisson point process, the equilibrium hard-sphere liquid, and MRJ sphere packings.

4.4 Correlation functions of Minkowski functionals

In order to sample the correlation functions of the Minkowski functionals, the distances of all pairs of particles[11] are computed and assigned to a bin. For each radial distance, i.e., for each bin, the correlation coefficient of the Minkowski functionals of the two Voronoi cells is determined.

Figures 4.6 and 4.7 compare the correlation functions of the Minkowski functionals for the Poisson point process, equilibrium hard-sphere liquids, and MRJ sphere packings. It is seen that these Minkowski correlation functions contain visibly more information than the corresponding standard pair-correlation functions, even in the case of the Poisson point process.

4.4.1 One-dimensional Poisson point process

As an introductory example of the global Voronoi statistics introduced in this thesis, I analytically calculate the correlation functions of the Voronoi cells in the one-dimensional Poisson point process. Therefore, I use the probability density functions $H_p(n_l)$ and $H_p(n_r)$ of the nearest neighbor on the left-hand side at a distance n_l or on the right-hand side at a distance n_r, respectively.

Two points x_1 and x_2 at a distance r are given. Without loss of generality, I assume in the following $x_1 = 0$ and $x_2 = r$. The nearest-neighbor probability density functions of x_1 are $H_p(n_l) = \rho \mathrm{e}^{-\rho n_l}$ and $H_p(n_r) = \rho \mathrm{e}^{-\rho n_r} \theta(r - n_r) +$

[11] The distance of two particles is their minimum image separation distance if periodic boundary conditions are applied.

$e^{-\rho r}\delta(r - n_r)$, where $\theta(x)$ is the Heaviside step function and $\delta(x)$ is the Dirac δ-distribution. For x_2, the distributions for the right- and the left-hand side simply exchange. The probability distribution $f(v^*|r)$ of the volume v^* of the cell corresponding to $x_1 = 0$ is given by the average of $\delta(\frac{n_r+n_l}{2} - v^*)$:

$$f(v^*|r) = \begin{cases} 4v^*\rho^2 e^{-2v^*\rho} & \text{if } v^* < \frac{r}{2} \\ 2\rho(r\rho+1)e^{-2v^*\rho} & \text{if } v^* \geq \frac{r}{2}\,. \end{cases} \tag{4.4}$$

Given a volume v^* of the cell corresponding to x_1: If $v^* < r/2$, there is at least one additional point y between x_1 and x_2. Its distance z to x_2 is uniformly distributed between $r - 2v^*$ and r. With $h(z|r, v^*)$ denoting the probability density function of this distance, the conditional probability distribution of the volume v of the cell corresponding to x_2 is given by

$$f(v|r, v^*) = \int_0^r \mathrm{d}z\, h(z|r, v^*) \cdot f(v|z) \tag{4.5}$$

with $f(v|z)$ from Eq. (4.4). A case-by-case analysis for differently large v compared to r and v^* is needed. If $v < \frac{r}{2} - v^*$,

$$f(v|r, v^*) = 4v\rho^2 e^{-2v\rho}\,. \tag{4.6}$$

If $\frac{r}{2} - v^* < v < \frac{r}{2}$, then

$$\begin{aligned} f(v|r, v^*) =& \frac{\rho e^{-2v\rho}}{2v^*}\left[4v(r-v)\rho - (r-2v^*)^2\rho\right. \\ &\left. +4(v+v^*) - 2r\right]\,. \end{aligned}$$

If $v > \frac{r}{2}$, then

$$f(v|r, v^*) = 2\rho e^{-2v\rho}\left[1 + \rho(r - v^*)\right]\,.$$

If $v^* > r/2$, there is at least one additional point y between x_1 and x_2 with probability $r\rho/(r\rho+1)$ and with probability $1/(r\rho+1)$ the points x_1 and x_2 are nearest neighbors. In the first case, the conditional probability distribution of the volume v is given by Eq. (4.5), but the distance z is now uniformly distributed between 0 and r. If $v < \frac{r}{2}$, then

$$f(v|r, v^*) = \frac{4v\rho e^{-2v\rho}}{r}((r-v)\rho + 1)\,.$$

If $v > \frac{r}{2}$, then

$$f(v|r, v^*) = \rho e^{-2v\rho}(r\rho + 2)\,.$$

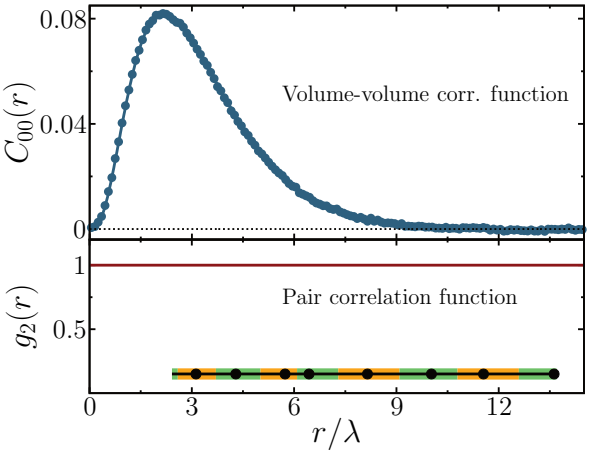

Figure 4.5: Correlation functions for the one-dimensional Poisson point process: pair-correlation function $g_2(r)$ (bottom); volume-volume correlation function $C_{00}(r)$ (top). The distance r is scaled (in this one-dimensional example) by the inverse of the number density $\lambda = 1/\rho$. An example of a one-dimensional Voronoi diagram of a Poisson point process is depicted.

In the second case, where there is no point between x_1 and x_2, the volume v is at least $r/2$ and completely determined by the nearest neighbor of x_2 on the right-hand side,

$$f(v|r, v^*) = 2\rho \mathrm{e}^{r\rho} \mathrm{e}^{-2v\rho} .$$

The cell-cell probability density function $p(r, v, v^*)$ from Section 4.3.2 is then given by

$$p(r, v, v^*) = \rho^2 \cdot f(v^*|r) \cdot f(v|r, v^*) . \tag{4.7}$$

From Eqs. (4.4) and (4.6) follows the asymptotic behavior of $p(r, v, v^*) \xrightarrow{r\to\infty} \rho^2 f(v) f(v^*)$.

As described in Section 4.3.2, the volume-volume correlation function C_{00} from Section 4.3.1 follows straightforwardly,

$$C_{00}(r) := \frac{r^2\rho^2 - 2r\rho + 2 - 2\mathrm{e}^{-r\rho}}{4 - 4r\rho\mathrm{e}^{-r\rho} - 2\mathrm{e}^{-2r\rho}} \cdot \mathrm{e}^{-r\rho} . \tag{4.8}$$

Figure 4.5 depicts the volume-volume correlation function $C_{00}(r)$ of the one-dimensional Poisson point process; both the analytic result and simulation data are shown.

As discussed in Section 4.4.2 for the three-dimensional Poisson point process, the Voronoi neighbors are correlated by construction. Although very large Voronoi cells are rather unlikely, their next-neighbor correlation leads to a large correlation length in $C_{00}(r)$. In contrast to the three-dimensional case, the Voronoi neighbors are uncorrelated if the distance of their centers vanishes because in one dimension

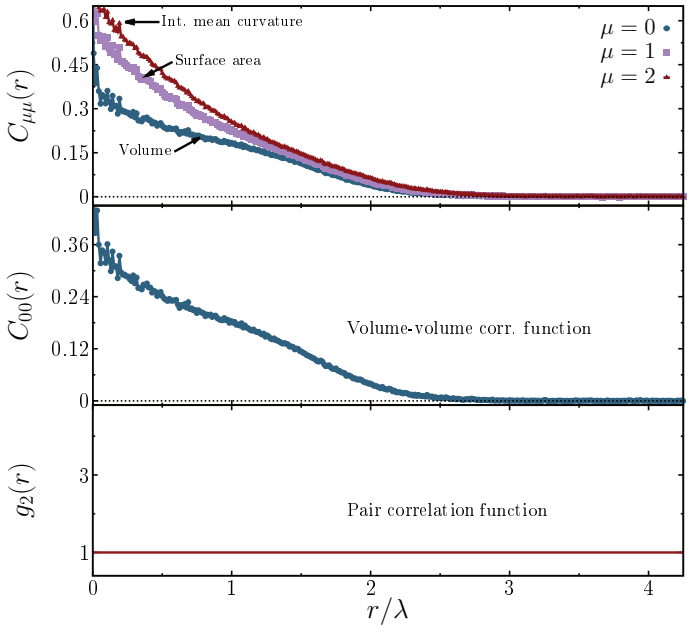

Figure 4.6: Correlation functions for a three-dimensional *Poisson point process*: pair-correlation function $g_2(r)$ (bottom); volume-volume correlation function $C_{00}(r)$ (center), which is the correlation function of the volumes of two Voronoi cells given that their centers are at a distance r; the mark correlation functions of the three different Minkowski functionals (top): $\mu = 0$ volume, $\mu = 1$ surface area, and $\mu = 2$ integrated mean curvature. The radial distance r is normalized by $\lambda = 1/\rho^{1/3}$, where ρ is the number density.

these Voronoi cells become independent. They only depend on either the nearest neighbor on the left- or on the right-hand side of $x_1 = x_2$, which are independent of each other. For large radii, the correlation vanishes exponentially, as expected, because there is no long-range order in the Voronoi diagram.

4.4.2 Three-dimensional Poisson point process

It is evident that in the infinite-system limit, the pair-correlation function $g_2(r)$ is a constant (unity) for the Poisson point process, i.e., the points are completely uncorrelated. Because a Voronoi cell is determined by the neighbors of its center, the volumes are obviously correlated; see Fig. 4.6. There are large Voronoi volume fluctuations for the Poisson point process. Very large cells lead to a strong correlation of the Voronoi volumes even for distances up to four times the mean nearest-neighbor distance. This is to be contrasted with the standard pair-correlation function $g_2(r)$, which is trivially unity for all radial distances.

Figure 4.6 compares the correlation functions $C_{\mu\mu}(r)$ for all Minkowski func-

tionals $\mu = 0, 1, 2$. All functionals have approximately the same correlation length. For $r \to 0$, the surface areas are more strongly correlated than the volumes because at small radial distances, the cells most likely share a face.

4.4.3 Equilibrium hard-sphere liquid

Figure 4.7(a) shows the pair-correlation function and the correlation functions of the Minkowski functionals for equilibrium hard-sphere liquid configurations at a packing fraction $\phi = 0.48$. Because the hard spheres are impenetrable, the correlation functions of the Minkowski functionals are only defined for radial distances larger or equal to the diameter D of a sphere; in this case, $D \approx 0.97\,\lambda$.

There is a strong correlation of the Voronoi volumes of spheres that are in near contact because the Voronoi neighbors are correlated by construction of the Voronoi diagram. However, the maximum correlation is reached for noncontacting spheres at $r \approx 1.3\,\lambda$; a large cell has many neighbors and a Voronoi neighbor with a sphere not in contact is, on average, larger than another neighbor cell with a contacting sphere.

Between $1.8\,\lambda$ and $2.4\,\lambda$, there is a double peak of anticorrelation and, for larger radial distances, there is an oscillating anticorrelation and correlation similar to the pair correlation function g_2, but nearly inverted. The correlation length of the Voronoi volumes in the hard-sphere liquid is larger than in the uncorrelated Poisson point process, where the correlation was only due to the large Voronoi volume fluctuations.

At the top of Fig. 4.7(a), the correlation functions of the other Minkowski functionals are compared. Similar to the Poisson case, the integrated mean curvature is more strongly correlated at contact $r = D$ than the surface area which, in turn, is more strongly correlated than the volume. There is no double anticorrelation peak in the integrated mean curvature. For large radii, the correlation functions are shifted against each other despite the strong correlation of the different functionals for a single Voronoi cell. The surface area and the integrated mean curvature are slightly less (anti)correlated.

4.4.4 MRJ sphere packings

The pair-correlation function $g_2(r)$ and the correlation functions of the Minkowski functionals of the MRJ sphere packings are shown in Fig. 4.7(b). The diameter of the spheres in the MRJ sphere packings is $D \approx 1.07\lambda$. The most striking differences in the pair correlation of the jammed packings to the equilibrium packings are the two discontinuities at $r = \sqrt{3}D$ and $r = 2D$, the split-second peak, which corresponds to configurations of two edge-sharing equilateral and

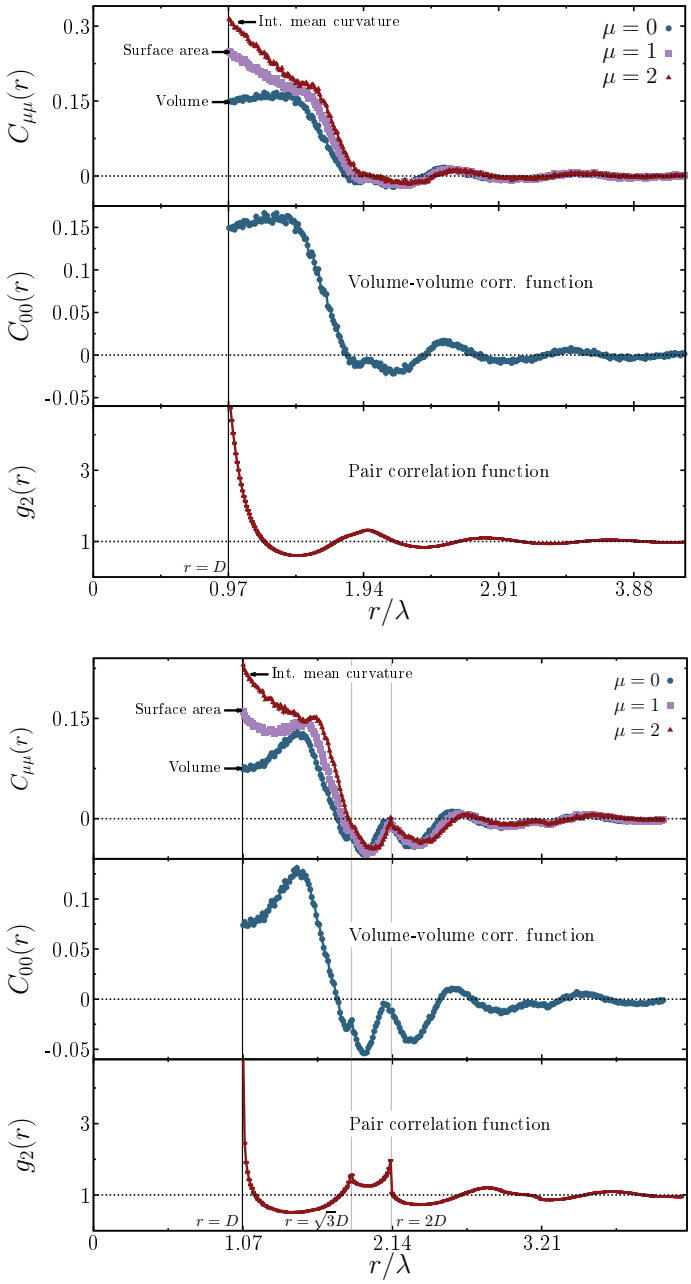

Figure 4.7: Correlation functions for *equilibrium hard spheres* with diameter D at a packing fraction $\phi = 0.48$ (top) and *MRJ sphere packings* of spheres with diameter D with an average packing fraction $\phi \approx 0.64$ (bottom); the pair-correlation function $g_2(r)$ is in agreement with previous results for MRJ sphere packings [41]. For details, see Fig. 4.6.

coplanar triangles ($r = \sqrt{3}D$) or a linear chain of three particles ($r = 2D$), respectively [120]. There is also a significant (seemingly nonanalytic) feature of the volume-volume correlation function $C_{00}(r)$ at $r = \sqrt{3}D$: a dip in the anticorrelation. However, at $r = 2D$, the feature is statistically insignificant. At least two double anticorrelation peaks are clearly resolved.

The most important qualitative differences in the volume-volume correlation function are the much stronger anticorrelations in the MRJ packings compared to the equilibrium packings. The correlation with the nearest neighbors is weaker, and the first anticorrelation double peak is more than twice as strong as for the equilibrium hard-sphere packings. The MRJ sphere packings are hyperuniform [119, 198], i.e., large-scale density fluctuations are suppressed. Therefore, strong Voronoi volume anticorrelations are necessary such that Voronoi cells with a high local packing fraction are accompanied by cells with rather low packing fractions, and vice versa.

Another difference between MRJ and equilibrium packings is a stronger shift of the correlation functions of the other Minkowski functionals. For the MRJ packings, there are radial distances, e.g., $r = 2.51\,\lambda$, at which the integrated mean curvatures are anti-correlated [$C_{22}(2.51\,\lambda) < 0$] but the volumes are correlated [$C_{00}(2.51\,\lambda) > 0$], and vice versa.

So, in contrast to the local Voronoi analysis, the global Voronoi analysis of the MRJ packing reveals qualitative structural differences to the equilibrium hard-sphere liquid.

4.4.5 Mixed correlation functions

The above defined Minkowski correlation functions $C_{\mu\mu}$ consider the correlation between a Minkowski functionals W_μ of a cell to the same Minkowski functional W_μ of another cell. This concept can be generalized even further by considering the correlation of a Minkowski functionals W_μ of a cell to a different Minkowski functional W_ν of another cell, e.g., the correlation of volume of the first cell to the surface area of a cell at distance r.

The mixed Minkowski correlation functions $C_{\mu\nu}(\mathbf{r}_1, \mathbf{r}_2)$ are defined for an arbitrary point process as the correlation between the Minkowski functional W_μ of a Voronoi cells with its center at the position $\mathbf{r}_1$ and the Minkowski functional W_ν of a Voronoi cell with its center at the positions $\mathbf{r}_2$:

$$C_{\mu\nu}(\mathbf{r}_1, \mathbf{r}_2) := \frac{\langle W_\mu(\mathbf{r}_1) W_\nu(\mathbf{r}_2)\rangle - \langle W_\mu(\mathbf{r}_1)\rangle\langle W_\nu(\mathbf{r}_2)\rangle}{\sigma_{W_\mu(\mathbf{r}_1|\mathbf{r}_2)}\sigma_{W_\nu(\mathbf{r}_2|\mathbf{r}_1)}} \tag{4.9}$$

with $\sigma_{W_\mu(\mathbf{r}_1|\mathbf{r}_2)}$ or $\sigma_{W_\nu(\mathbf{r}_2|\mathbf{r}_1)}$ the standard deviations of the Minkowski functionals W_μ or W_ν of the Voronoi cells at $\mathbf{r}_1$ or $\mathbf{r}_2$ given that there is another point at the

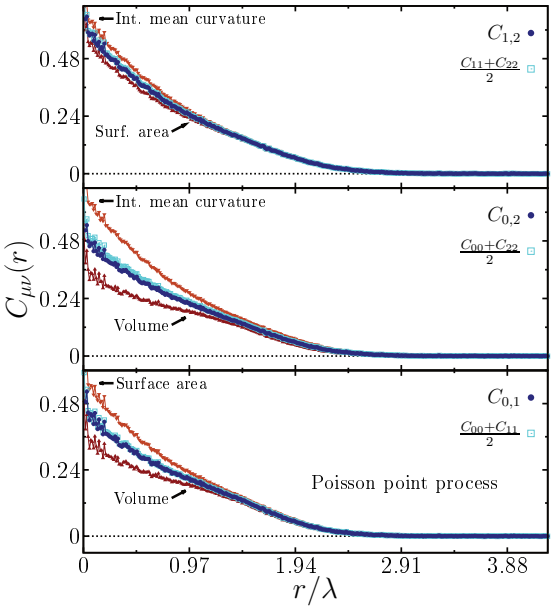

Figure 4.8: Mixed correlation functions $C_{\mu\nu}(r)$ (dark blue curve) for a three-dimensional Poisson point process, i.e., the correlation of the Minkowski functionals W_μ and W_ν of two Voronoi cells at a distance r. They are in a remarkably good agreement with the arithmetic mean (cyan curve) of the corresponding correlation functions $C_{\mu\mu}$ and $C_{\nu\nu}$, which are depicted in red or orange, respectively. For details, see Fig. 4.6.

position $\mathbf{r}_2$ or $\mathbf{r}_1$, respectively. For a statistically homogeneous and isotropic point process, the correlation function of the Minkowski functionals is again a radial function, which I denote by $C_{\mu\nu}(r)$. As noted above for the Minkowski correlation functions $C_{\mu\mu}(r)$, $C_{\mu\nu}(r)$ is discontinuous for $r \to 0$.

For the models studied in this chapter both in three and two dimensions, I have determined the mixed correlation functions, see Figs. 4.8–4.10, where the sampling of the mixed correlation functions is exactly the same as discussed in Section 4.4. In all cases, I found that the correlation of the two different Minkowski functionals is to a good approximation given by the arithmetic mean of the correlation functions of the single Minkowski functionals:

$$C_{\mu\nu}(\mathbf{r}_1,\mathbf{r}_2) \approx \frac{C_{\mu\mu}(\mathbf{r}_1,\mathbf{r}_2) + C_{\nu\nu}(\mathbf{r}_1,\mathbf{r}_2)}{2} , \tag{4.10}$$

which is in the following shown to be equivalent to a nearly vanishing correlation. Therefore, I define rescaled Minkowski functionals

$$\widetilde{W}_\mu(\mathbf{r}_1,\mathbf{r}_2) := \frac{W_\mu(\mathbf{r}_1) - \langle W_\mu(\mathbf{r}_1)\rangle}{\sigma_{W_\mu(\mathbf{r}_1|\mathbf{r}_2)}} . \tag{4.11}$$

For convenience, I write in the following $\widetilde{W}_\mu(\mathbf{r}_1) := \widetilde{W}_\mu(\mathbf{r}_1,\mathbf{r}_2)$ and $\widetilde{W}_\mu(\mathbf{r}_2) := \widetilde{W}_\mu(\mathbf{r}_2,\mathbf{r}_1)$. The mixed correlation function can be expressed by these rescaled

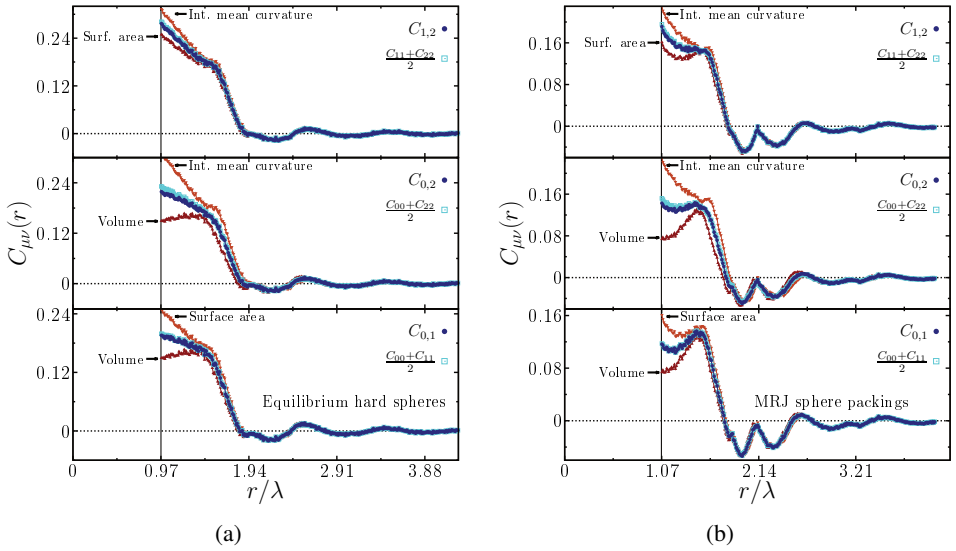

Figure 4.9: Mixed correlation functions $C_{\mu\nu}(r)$ for (a) equilibrium hard spheres at a packing fraction $\phi = 0.48$ and for (b) MRJ sphere packings with an average packing fraction $\phi \approx 0.64$. For details, see Fig. 4.8.

functionals

$$C_{\mu\nu}(\mathbf{r}_1, \mathbf{r}_2) = \langle \widetilde{W}_\mu(\mathbf{r}_1) \widetilde{W}_\nu(\mathbf{r}_2) \rangle \, .$$

For a correlation function which is symmetric in the positions $\mathbf{r}_1$ and $\mathbf{r}_2$, i.e., which fulfill[12] $C_{\mu\nu}(\mathbf{r}_1, \mathbf{r}_2) = C_{\mu\nu}(\mathbf{r}_2, \mathbf{r}_1)$, the approximation in Eq. (4.10) is equivalent to a vanishing correlation of the difference of the rescaled Minkowski functionals:

$$\begin{aligned}
& \langle (\widetilde{W}_\mu(\mathbf{r}_1) - \widetilde{W}_\nu(\mathbf{r}_1))(\widetilde{W}_\mu(\mathbf{r}_2) - \widetilde{W}_\nu(\mathbf{r}_2)) \rangle = 0 \\
\Leftrightarrow \quad & \langle \widetilde{W}_\mu(\mathbf{r}_1) \widetilde{W}_\nu(\mathbf{r}_2) \rangle + \langle \widetilde{W}_\mu(\mathbf{r}_2) \widetilde{W}_\nu(\mathbf{r}_1) \rangle = \langle \widetilde{W}_\mu(\mathbf{r}_1) \widetilde{W}_\mu(\mathbf{r}_2) \rangle + \langle \widetilde{W}_\nu(\mathbf{r}_1) \widetilde{W}_\nu(\mathbf{r}_2) \rangle \\
\Leftrightarrow \quad & 2\langle \widetilde{W}_\mu(\mathbf{r}_1) \widetilde{W}_\nu(\mathbf{r}_2) \rangle = \langle \widetilde{W}_\mu(\mathbf{r}_1) \widetilde{W}_\mu(\mathbf{r}_2) \rangle + \langle \widetilde{W}_\nu(\mathbf{r}_1) \widetilde{W}_\nu(\mathbf{r}_2) \rangle \\
\Leftrightarrow \quad & C_{\mu\nu}(\mathbf{r}_1, \mathbf{r}_2) = \frac{C_{\mu\mu}(\mathbf{r}_1, \mathbf{r}_2) + C_{\nu\nu}(\mathbf{r}_1, \mathbf{r}_2)}{2} \, . \qquad (4.12)
\end{aligned}$$

For example, if for a homogeneous and isotropic point process the mixed correlation of volume and surface area is to a good approximation given by the arithmetic mean of the volume-volume correlation function and the surface area-surface area correlation function

$$C_{01}(r) \approx \frac{C_{00}(r) + C_{11}(r)}{2} \, ,$$

[12] This is, e.g., the case for a correlation function of a homogeneous and isotropic point process.

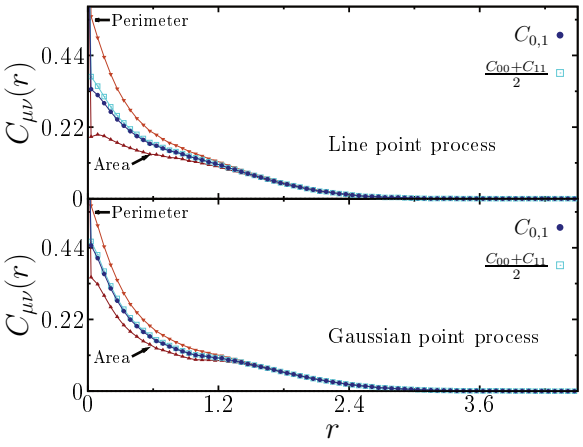

Figure 4.10: Mixed correlation functions $C_{01}(r)$ (dark blue) in two dimensions for the Gaussian point process and line point process from Section 4.6. For the Gauss point process, $C_{\mu\nu}$ is in very good agreement with the arithmetic mean (cyan) of the area-area C_{00} (red) and perimeter-perimeter C_{11} (orange) correlation functions. For the line point process there is a small deviation for vanishing radial distance.

then the correlation of the difference of rescaled volume and surface area nearly vanishes

$$\langle(\widetilde{V}(0)-\widetilde{S}(0))(\widetilde{V}(r)-\widetilde{S}(r))\rangle \approx 0\ . \tag{4.13}$$

This correlation is depicted for the three-dimensional particle processes in Fig. 4.11. Indeed the correlation is much smaller than the correlation functions $C_{\mu\nu}(r)$.

The correlation of only the volume of the cell at the origin to the difference of the cell at a distance r, i.e., $\langle\widetilde{V}(0)(\widetilde{V}(r)-\widetilde{S}(r))\rangle = C_{00}(r)-C_{01}(r)$, is by an order of magnitude larger, see Fig. 4.12. So, there is a correlation between the geometry of one cell and the deviation of area and surface area of the other cell. However, there is a strong correlation between the volume of a single cell and its surface area ($\rho_{0,1} > 0.96$, see Table 4.1). Therefore, it appears reasonable to assume that the correlation of only the surface area of the cell at the origin to the difference of the cell at a distance r is approximately the same:

$$\langle\widetilde{S}(0)(\widetilde{V}(r)-\widetilde{S}(r))\rangle \approx \langle\widetilde{V}(0)(\widetilde{V}(r)-\widetilde{S}(r))\rangle\ ,$$

which is empirically confirmed in Fig. 4.12. Therefore, $C_{01}(r)-C_{11}(r) \approx C_{00}(r)-C_{01}(r) \Leftrightarrow C_{01}(r) \approx [C_{00}(r)+C_{11}(r)]/2$. However, although small, the correlation $\langle(\widetilde{W}_\mu(\mathbf{r}_1)-\widetilde{W}_\nu(\mathbf{r}_1))(\widetilde{W}_\mu(\mathbf{r}_2)-\widetilde{W}_\nu(\mathbf{r}_2))\rangle$ contains interesting global structural information: despite the strong correlation of volume and surface area of a single cell, relative fluctuation between volume and surface area appear; how are such fluctuations related between cells at a distance r? Interestingly, the smallest correlation appears in the MRJ packings, see Fig. 4.11, but they exhibit the strongest anticorrelation, which appear to be again linked to the hyperuniformity as discussed above.

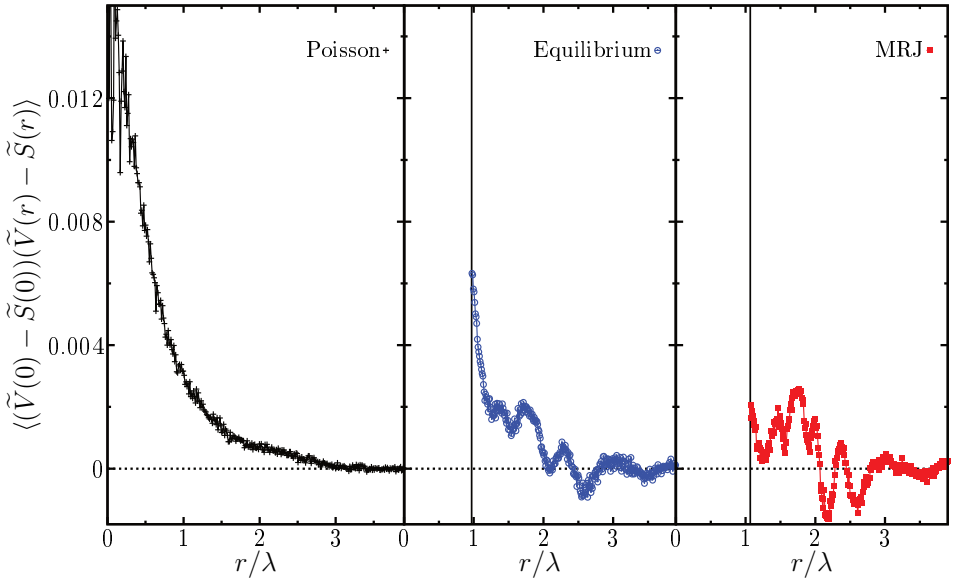

Figure 4.11: Nearly vanishing correlation of the differences of the rescaled volume $\widetilde{V}$ and surface area $\widetilde{S}$ of two Voronoi cells at a distance r, see Eqs. (4.11) and (4.13). The MRJ packings exhibit both the smallest correlation and strongest anticorrelation.

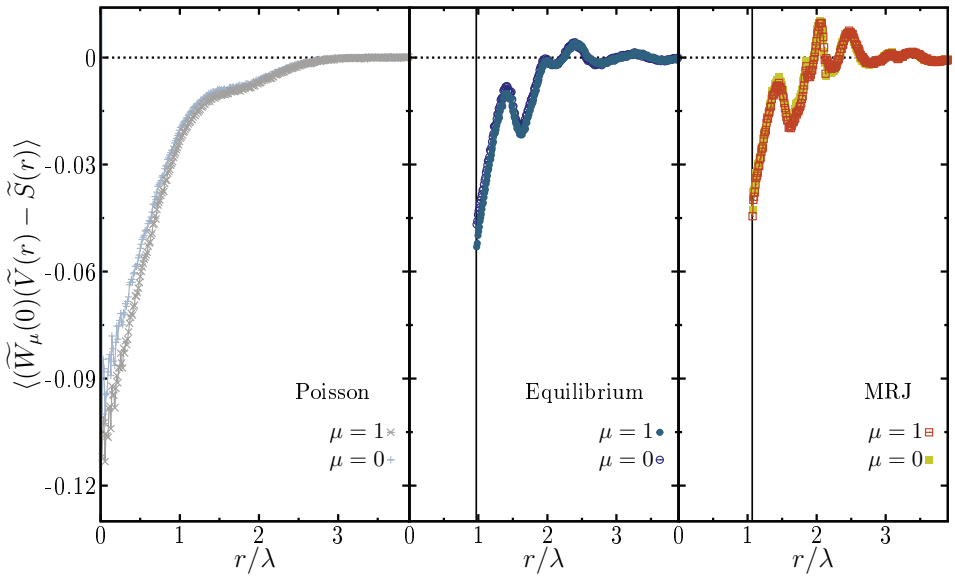

Figure 4.12: Correlation of either the rescaled volume ($\mu = 0$) or the rescaled surface area ($\mu = 1$) of a cell at the origin to the difference of rescaled volume $\widetilde{V}(r)$ and rescaled surface area $\widetilde{S}(r)$ of a cell at a distance r.

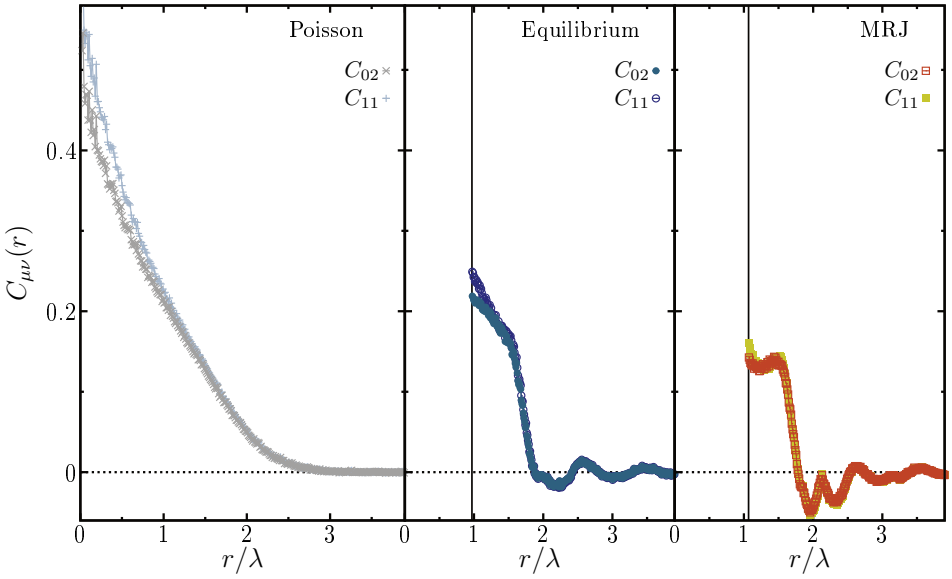

Figure 4.13: The surface area-surface area correlation function $C_{11}(r)$ is approximately equal to the volume-integrated mean curvature correlation function $C_{02}(r)$ for the Voronoi cells of a Poisson point process, equilibrium hard spheres at a packing fraction $\phi = 0.48$, and of MRJ sphere packings.

Additionally to Eq. (4.10), I find the unexpected approximation that the surface area-surface area correlation function $C_{11}(r)$ is approximately equal to the volume-integrated mean curvature correlation function $C_{02}(r)$, see Fig. 4.13. I have yet not well-understood why this is the case.

The interesting question remains whether these findings are special features of the Voronoi tessellation or in general valid for random tessellations. To answer this question the Minkowski correlation functions or other tessellation models like the Poisson hyperplane tessellations or STIT tessellations need to be determined in future research.

4.5 Cell-cell probability density functions

The sampling of the cell-cell probability density function $p(r, v, v^*)$ is very similar to that of the pair-correlation function g_2 (see, e.g., Ref. [460]); only an additional binning with respect to the Voronoi volumes is needed. Figures 4.14–4.15 show the cell-cell pair-correlation function $g_{vv} = p(r, v, v^*)/(\rho^2 f(v) f(v^*))$ for exemplary large or small cell volumes v, v^* in the three-dimensional Poisson point process, in an ensemble of equilibrium hard spheres, or in the MRJ sphere packings. As examples of large or small cells, the volumes were chosen such that their probability

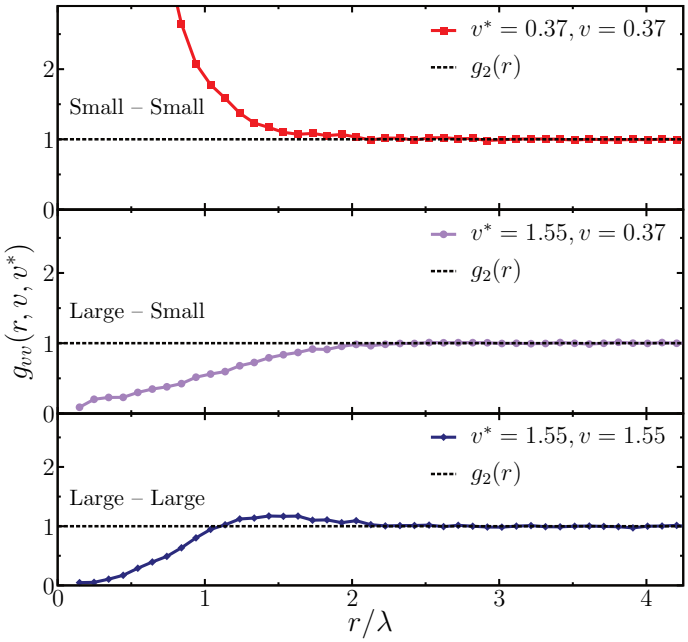

Figure 4.14: The cell-cell pair-correlation function $g_{vv}(r, v, v^*)$ for a three-dimensional *Poisson point process* for either two large cells (bottom), a large and a small cell (center), or two small cells (top). As examples of large or small cells, the volumes were chosen such that their probability density is equal to $1/3$ of the maximum of the volume distribution; see Table 4.1 and Fig. 4.2. The curves are compared to the standard pair-correlation function $g_2(r)$ (dashed black line), which is trivially unity for the uncorrelated Poisson point process. The radial distance r is normalized by $\lambda = 1/\rho^{1/3}$, where ρ is the number density.

density is equal to $1/3$ of the maximum of the volume distribution; see Table 4.1 and Fig. 4.2.

For the Poisson point process, the small cells are strongly correlated at short distances because, by construction, there must be points at close distances, and the neighbor cells of a small Voronoi cell are more likely to be small as well. However, the probability of finding a point with either a corresponding large or a small cell at a short radial distance of the center of a large cell is strongly suppressed because it is unlikely for the center of a large cell to have close neighbors. At intermediate distances, two large cells are correlated, as expected, because of the Voronoi construction.

In the equilibrium hard-sphere liquid, the large cells at near contact are less correlated than the small cells. However, at slightly larger distances, where g_2 shows anticorrelation and the small cells are even more strongly anti-correlated, the large cells are positively correlated. For distances larger than twice the diameter,

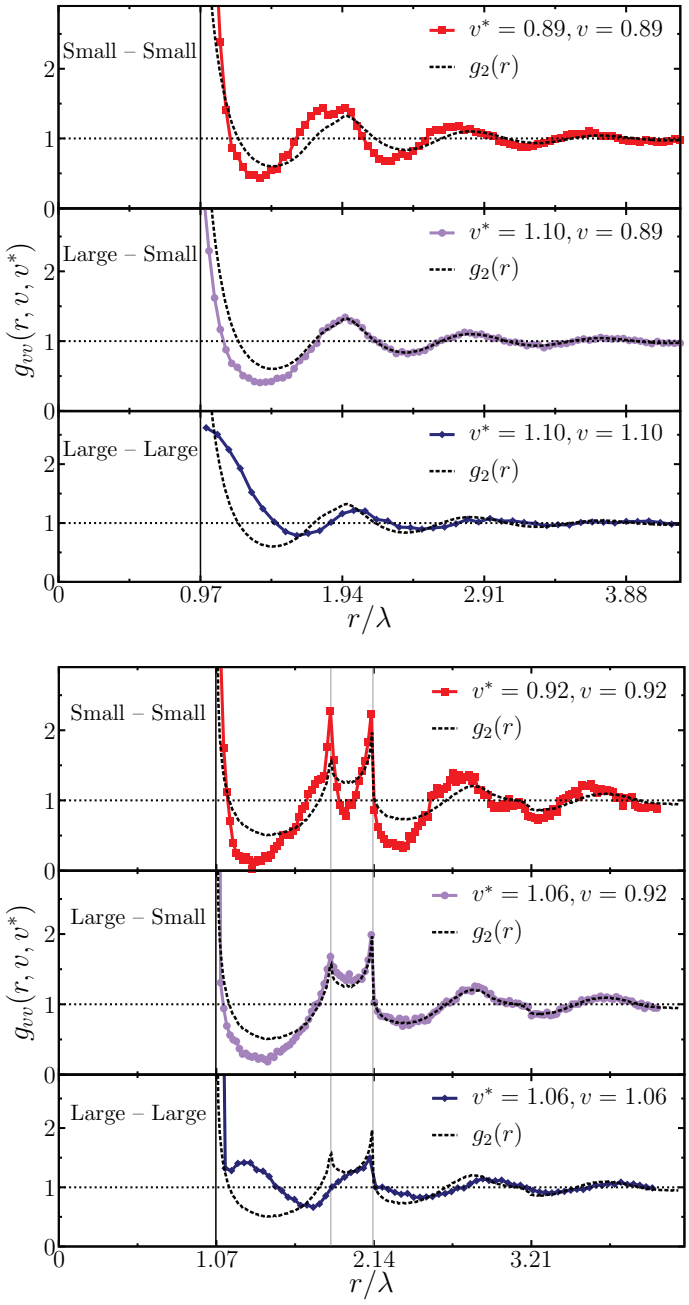

Figure 4.15: The cell-cell pair-correlation function $g_{vv}(r, v, v^*)$ for *equilibrium hard spheres* at a global packing fraction $\phi = 0.48$ (top), and *MRJ sphere packings*; the average packing fraction is $\phi \approx 0.64$ (bottom). For details, see Fig. 4.14.

the cell-cell pair-correlation function for a large and a small cell is equal to the standard pair-correlation function within statistical significance. However, both the cell-cell pair-correlation functions of finding two short or of finding two large cells at large radial distance r are shifted compared to the standard pair-correlation function.

These features can also be found in the MRJ sphere packings. Moreover, the anticorrelations of two small cells are much stronger. The split-second peak even separates in two stronger peaks with anticorrelation in between, where the standard pair-correlation function shows positive correlation. In contrast to this, the peak at $r = \sqrt{3}D$ completely vanishes for two large cells $g_{vv}(\sqrt{3}D, 1.06, 1.06) = 1$, and the peak at $r = 2D$ is significantly weaker.

4.6 n-point information in Minkowski correlation functions

n-point correlation functions are needed in material science for improved bounds on the effective elastic constants, diffusion constants, and permeabilities of heterogeneous materials [460, 465], in medical image processing [329], and especially in astronomy: to quantify the clustering of galaxies [511] or to analyze the large-scale structure of the universe [362], thereby testing, e.g., the assumption of hierarchical structure formation [452] or constraining the galaxy-mass bias, i.e., the relationship between visible and dark matter distributions [302]. Quantum fluctuations during inflation could explain Gaussian initial conditions, in this case, the stochastic process would be fully characterized by its two-point correlation function. To test the assumption of such Gaussian primordial fluctuations n-point information for $n > 2$ is needed [419].

However, the standard pair correlation function is by definition limited to two-point information, and multipoint correlation functions get quickly both analytically and numerically intractable. The brute-force approach to calculate an n-point correlation function scales with the number of data points M like $O(M^n)$. This can be critical for even modest-sized data sets. Although complex algorithms have been developed to improve upon this scaling, they typically still allow only for estimates of the three- or four-point correlation functions [289, 325, 524, 525].

In contrast to this, the Minkowski functionals contain multipoint information [282, 308] and can provide a more efficient and robust access to higher n-information, which is complementary to the conventional approach, which is restricted to lower-order correlation functions. Therefore, the Minkowski functionals are used to test for non-Gaussian features [127, 151, 308, 399].

While the Minkowski functionals only provide local or globally averaged

information, the Minkowski correlation functions defined here overcome this limitation and allow for a global Minkowski cell shape characterization. These correlation functions are more sensitive than the standard pair correlation function, in that they contain visibly more information: although the $C_{\mu\nu}(\mathbf{r})$ are functions only of the radial distance, they contain multipoint information. I show here that the Minkowski correlation functions can clearly distinguish point patterns with exactly the same standard pair correlation function.

4.6.1 Clustering planar point processes

In a simulation study, I compare two point processes discussed by Martin Kerscher [237] in a study of point processes modeling the distribution of galaxies[13]: the first model is the so-called line-segment process, a similar model has been introduced to model the galaxy distribution [91]; this is compared to a Gauss-Poisson process, i.e., a point process fully characterized by its second-order characteristics.

In the line-segment process, lines with a fixed length l (here $l = 1$) and a random orientation are placed uncorrelated within the observation window, i.e., their centers follow from a Poisson point process with mean value ρ_s (here $\rho = 201$). The actual points in the line-segment process are then randomly distributed on these lines; the number of points on each line is itself a random Poisson variable. If the number density of the points in the line-segment process is denoted by ρ (here $\rho = 200$), the mean number of points on a single line is given by ρ/ρ_s. A sample is depicted in Fig. 4.16; here, periodic boundary conditions are applied. The pair correlation function is given by [237, 448]

$$g_2(r) = \begin{cases} 1 + \frac{1}{\pi l \rho_s}\left(\frac{1}{r} - \frac{1}{l}\right) & \text{for } r < l \\ 1 & \text{else.} \end{cases} \tag{4.14}$$

Qualitatively similar to the observed pair correlation function of the galaxy distribution, the pair correlation diverges for $r \to 0$, $g_2(r) \propto r^{-1}$ [237].

In contrast to the line-segment process, which contains nontrivial higher-order correlations, the Gauss-Poisson point process is fully characterized by its number density and pair correlation function[14]. It can be constructed as a special Poisson cluster process: the uncorrelated cluster centers, the so-called parent points, are Poisson distributed with intensity ρ_P; in a Gauss-Poisson point process the clusters consist with probability q_1 only of the parent point $\mathbf{x}$ and with probability $q_2 = 1 - q_1$ a single child point $\mathbf{y}$ is assigned where a Probability Density Function (PDF)

[13] Here, I use same parameters and nearly the same notation as in Ref. [237].

[14] In this sense, the Gauss-Poisson process is the point process counterpart of the Gaussian random field [237].

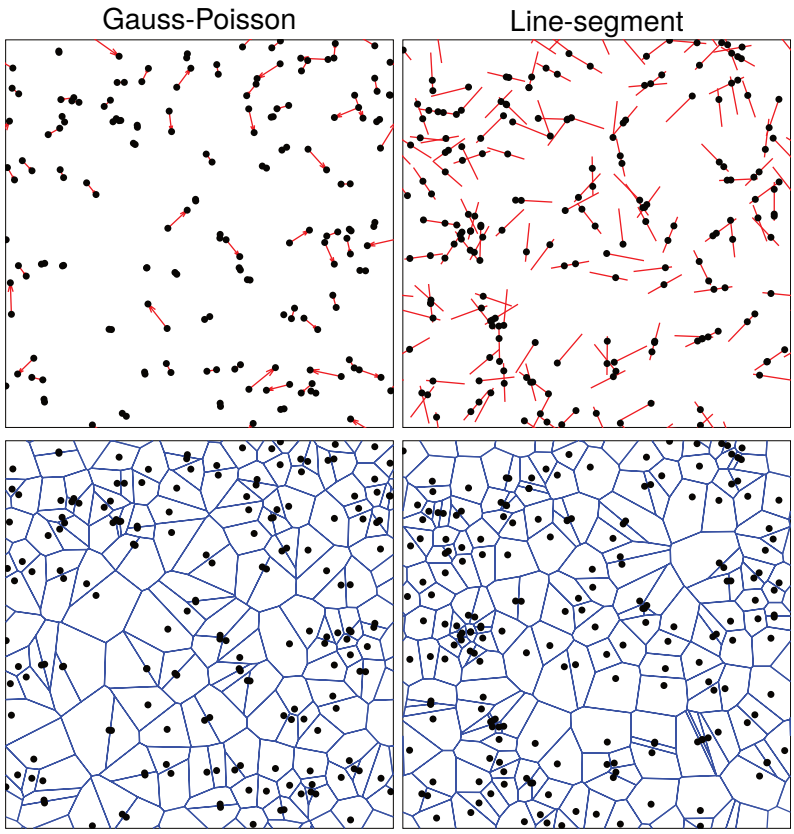

Figure 4.16: Samples of the Gauss-Poisson point process (left) and the line-segment process (right). At the top, the final point patterns are depicted, and the algorithm is indicated: for the Gauss-Poisson point process the red arrows point from the parent point to its child, and for the line-segment process the initial random lines are depicted. At the bottom, the corresponding Voronoi diagrams are depicted.

$s(|\mathbf{x}-\mathbf{y}|)$ determines the radial distance to its parent point. In other words, the cluster consists of either one or two points. Therefore, the pair correlation function can easily be controlled by adjusting the PDF[15] $s(r) \propto (g_2(r)-1)$ if the correlation function $(g_2(r)-1)$ can be normalized by $c := \int_0^\infty \mathrm{d}r\, 2\pi r(g_2(r)-1)$ to be a proper PDF and if $\rho c \leq 1$, which is reformulation of the constraint of at maximum two points per cluster. The intensity of the parent point, i.e., the expected number of parent points per unit square, is given by $\rho_P = \rho(1-\rho\cdot c/2)$ and the probability

[15] Poisson cluster process with on average more than two points in a cluster, e.g., a Neyman-Scott process, have a more complicated relation between the radial distribution function s and the pair correlation function $g_2(r)$ [217].

for a child point $q_2 = (\rho c)/(2 - \rho c)$ [237]. Therefore, a Gauss-Poisson process can be defined with exactly the same two-point characteristics as a line-segment process with $\rho < \rho_s$. A simulated sample is depicted in Fig. 4.16. A structural difference between the two point processes in Fig. 4.16 is hardly visible to the unaided eye.

I have simulated 50,000 samples of each of these two processes with analytically the same number density and pair correlation function. Their higher-order correlation functions, however, differ from each other. This equality is also tested numerically. The mean number density is estimated to be $\langle \lambda \rangle = 199.92 \pm 0.09$ or 200.14 ± 0.09 in the Gauss-Poisson point or the line-segment process, respectively. The pair correlation function is shown at the bottom of Fig. 4.17: the black line represents the analytic curve and the orange circles, and blue squares depict the numerical estimates for the Gauss-Poisson or line-segment process, respectively; they are in perfect agreement. The standard pair correlation function cannot distinguish the two processes.

4.6.2 Distinguishing point patterns by their global structure

In order to apply the Minkowski analysis, I construct the Voronoi diagrams, see Fig. 4.16, determine the area of each cell, and determine the Minkowski correlation function $C_{00}(r)$, i.e., the correlation coefficient of the cell areas given to points of the process at a radial distance r, see Eq. (4.1). The result is shown at the top of Fig. 4.17: the circles and squares represent numerical estimates with error bars smaller than point size and the lines are also numerical estimates, but using a finer binning of the radial distances.

The very accurate estimate rules out any deviations because of statistical fluctuations. The Minkowski correlation function $C_{00}(r)$ detects a distinctly different structure for the Gauss-Poisson compared to the line-segment process. At short radial distances, the cells in the Gauss-Poisson process are significantly more correlated than those in the line-segment process. This could be in agreement with larger voids in the line-segment than in the Gauss-Poisson process found in Ref. [237]. There is also a regime (with r about the length of the line segments) where the cells in the line-segment process are stronger correlated than those in the Gauss-Poisson process. This changes again at intermediate distances. In the limit of large r, the correlations vanish, because there is no long range order. This relative change in correlation strength might indicate competing length scales in the two models. However, the full cell-cell probability distribution from Eq. (4.3) is needed[16] for a thorough structural explanation and further insights. This analysis

[16] In two dimensions, the volume must be replaced by the area.

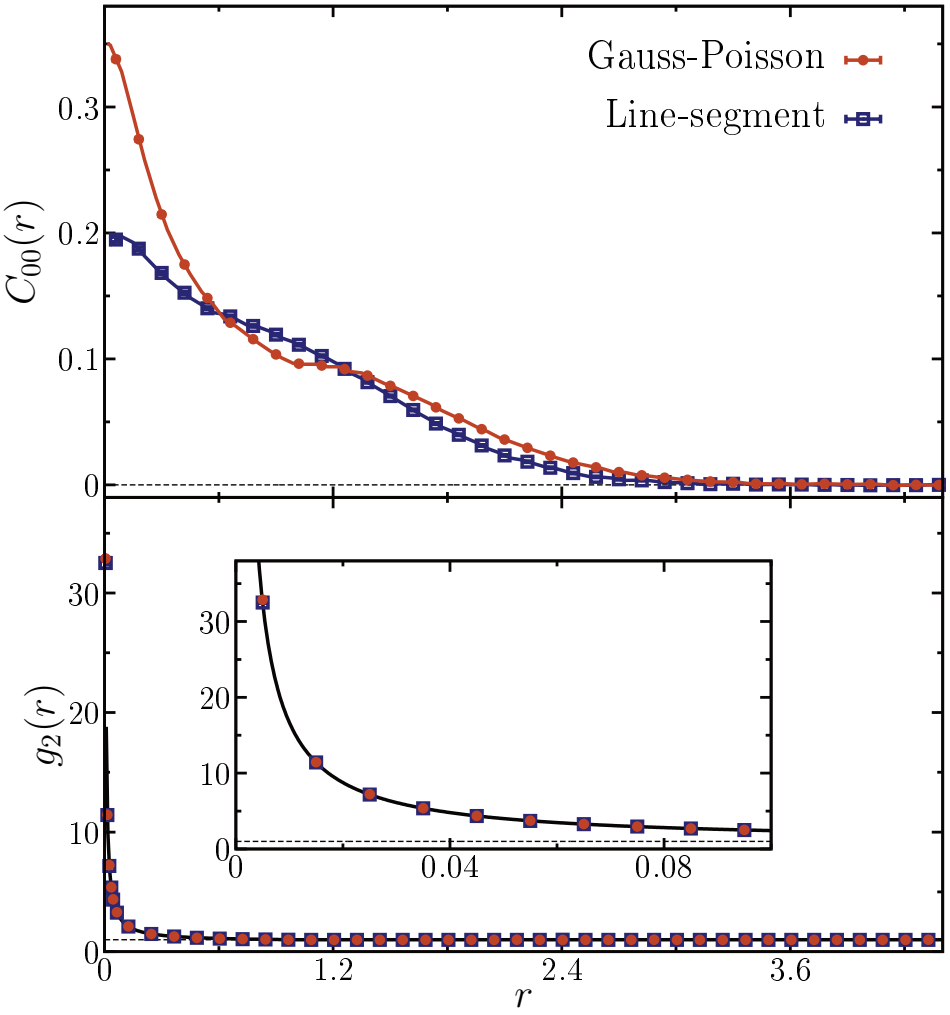

Figure 4.17: Minkowski correlation functions contain multipoint information and can distinguish point processes with identical pair correlation function. The correlation functions of the Gauss-Poisson point process are compared to those of the line-segment point process at number density $\gamma = 2$ and a line segment with length unity, see also Fig. 4.16. At the bottom, the standard pair correlation functions g_2 are shown to be identical for the two different processes; the black line depicts the analytic curve—see Eq. (4.14); the orange circles and blue squares are numerical estimates of g_2 of the Gauss-Poisson or the line-segment process, respectively, based on 50,000 simulations for each system; the inset is a close up of small radial distances. At the top, accurate numerical estimates of the Minkowski correlation functions $C_{00}(r)$ of the cell areas are plotted, see Eq. (4.1): the correlation of the areas given two particles at a distance r is distinctly different for the Gauss-Poisson point process or the line-segment point process; at very short distances the cells in the first process are stronger correlated than those of the latter, but this changes twice at intermediate distances.

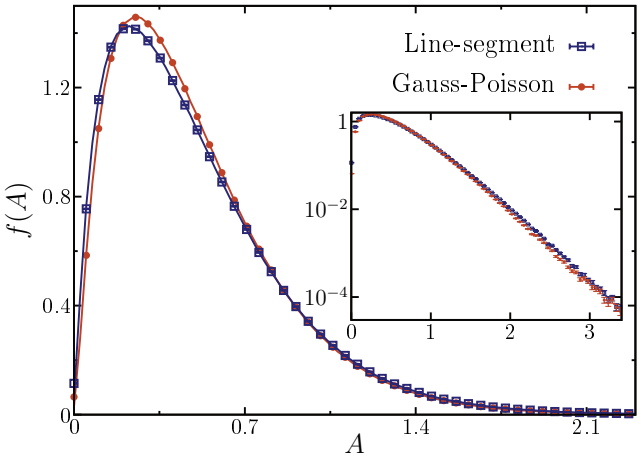

Figure 4.18: Empirical probability distributions of the area A of the Voronoi cells in either a Gauss-Poisson point process or a line-segment point process at number density $\gamma = 2$. There is a small but significant difference between the two distributions. The inset shows the same distribution in a logarithmic scale.

shows that although the Minkowski correlation functions only depend on the radial distance, they contain higher-order correlation information via the Minkowski functionals of the Voronoi cells. In this sense, they are supreme to the standard pair correlation function and allow for a complementary approach than the conventional estimation of n-point correlation functions, which are restricted to small n.

Note that because of the very high statistics with about 10,000,000 cells in each process, also a small difference in the local distribution of the cell areas can be resolved. Figure 4.18 plots the empirical probability distributions of the cell areas for both processes. Like at the top of Fig. 4.17, the circles and squares represent numerical estimates with error bars smaller than point size, and the lines show numerical estimates using a very fine binning of the cell areas. Although the distributions are very similar, there is a small but significant deviation: in the line segment process small cells are slightly more likely as well as very large cells (their frequencies are depicted in the inset in logarithmic scale). The latter finding is in accordance with the above-mentioned previous finding of larger voids in the line-segment process in Ref. [237].

For the other nontrivial Minkowski functional in two dimensions, the perimeter P, there are similar findings as for the cell areas, but a much weaker difference in the correlation function $C_{11}(r)$ and a hardly detectable deviation in the local distribution $f(P)$.

Because the Minkowski functionals contain information from n-point correlation functions with $n > 2$, both the local distribution and the Minkowski correlation functions can detect the structural differences in the Gauss-Poisson point process from the line-segment process with the same second-order characteristics. However, there are more distinct differences in the global correlation functions. This powerful new shape characteristic could also be interesting to study other

point processes with or without higher-order correlation functions. For example, the determinantal point processes (DPP) from Section 4.2 which have nontrivial higher-order correlation functions. It could be compared to another (maximally uncorrelated) repulsive point pattern with the same pair correlation function but no nontrivial higher-order correlations, e.g., produced by a dependent Poisson thinning. A random order of arrival is assigned to the points in a Poisson point process, and for each point there is a rejection probability depending on the radial distance to the other accepted points, which have arrived earlier.

The pair correlation of this thinned Poisson point process can be adjusted to that of the DPP, by choosing the thinning probability accordingly. However, to detect the differences in the multipoint correlations of these two point processes very high statistics are needed. This is because on the one hand, the higher-order correlations are short-ranged, but on the other hand the process is repulsive and short radial distances are suppressed.

For the hard-sphere packings from Section 4.1 in three dimensions or maximally random jammed hard discs packings in two dimensions recently found in Ref. [42] a point process with the same pair correlation function can neither be constructed via a weakly clustering Gauss-Poisson point process nor with a purely repulsive Poisson thinning. Instead, a reconstruction algorithm can be applied (similar to simulating a Gibbs process [217]), which converges a random point pattern to a configuration with the same chosen characteristics as a given sample: starting from a binomial point process, i.e., uncorrelated points, but a fixed number of particles, an energy is introduced which measures the difference of the current pair correlation function to the target characteristic, e.g., the integral over the square of the difference. Then, a simulated annealing algorithm is applied where in each step a particle is randomly moved, the new energy calculated, and the move accepted or rejected according to the Metropolis-Hastings algorithm [217, 370, 476].

Finally, it would be interesting to compare the Minkowski correlation functions to other measures for higher order correlations, like void or nearest neighbor distribution functions used in Ref. [237].

4.7 Conclusions

I have characterized the structure of the uncorrelated Poisson point process, equilibrium hard-sphere liquids, and MRJ sphere packings by computing the Minkowski functionals, i.e., the volume, the surface area, and the integrated mean curvature, of the associated Voronoi cells. The local analysis, i.e., the probability distribution of the Minkowski functionals of a single Voronoi cell, provides qualitatively similar results for the equilibrium hard-sphere liquid and the MRJ packings and partly even

for the uncorrelated Poisson point process. In order to study the global structure of the Voronoi cells, I have improved upon this analysis by introducing the correlation functions $C_{\mu\mu}(r)$ of the Minkowski functionals and the cell-cell probability density function $p(r, v, v^*)$. The correlation function $C_{\mu\mu}(r)$ measures the correlation of the Minkowski functionals W_μ of two Voronoi cells given that the corresponding centers are at a distance r. The cell-cell probability density function $p(r, v, v^*)$ also incorporates the probability that there are two particles at a distance r. For an easier interpretation and better visualization, I have defined the dimensionless cell-cell pair-correlation function $g_{vv} = p(r, v, v^*)/(\rho^2 f(v) f(v^*))$, where $f(v)$ is the probability of the Voronoi volume v. The generalization of the pair-correlation to the cell-cell pair correlations provides powerful theoretical and computational tools to characterize the complex local geometries that arise in jammed disordered sphere packings.

Because the faces of a Voronoi cell are bisections between a point in the point process (whether a packing or not) and its neighbors and, moreover, because Voronoi neighbors share a face and edges, the Minkowski functionals of neighboring Voronoi cells are correlated by construction. This leads to a large correlation length for the Voronoi cells in a Poisson point process because of large Voronoi volume fluctuations. In the equilibrium hard-sphere liquid and MRJ sphere packings, there are correlations and anticorrelations. In contrast to the qualitatively similar local Voronoi structure, the global Voronoi structure of the MRJ hard-sphere packings is qualitatively quite different from that of an equilibrium hard-sphere liquid. I find strong Voronoi volume anticorrelations, which is consistent with previous findings that MRJ sphere packings are hyperuniform [119, 198], i.e., large-scale density fluctuations are suppressed.

MRJ sphere packings are prototypical glasses in that they have no long-range order, but they are perfectly rigid, i.e., the elastic moduli are unbounded [291, 470, 472]. The global analysis introduced here reveals the difference in the structure of the Voronoi cells of the MRJ state and those of a hard-sphere liquid, which further indicates that the structure of a glass is not that of a "frozen liquid" [198, 291, 474].

An already known distinct structural difference between the hyperuniform MRJ sphere packings and equilibrium hard-sphere liquids is that while in the equilibrium packing the total pair-correlation function $h(r) = g_2(r) - 1$ is exponentially damped, the total correlation function of the MRJ state has a negative algebraic power-law tail [119, 198, 291]. It is an interesting question as to whether the asymptotic behaviors of the correlation function of the Minkowski functionals $C_{\mu\mu}(r)$ or the radial cell-cell correlation functions $g_{vv}(r, v, v^*)$ are different for the MRJ state and the hard-sphere liquid. However, a direct observation of the power-law tail has, so far, not been possible [119, 198, 291]; much larger systems are needed but are not

available at the moment. Still, the global characteristics $C_{\mu\mu}(r)$ and $g_{\nu\nu}(r, v, v^*)$ introduced here allow for an investigation of the underlying geometrical reasons for the negative algebraic tail in the total pair-correlation function: the suppressed clustering of regions with low and high local packing fractions [198]. Moreover, they also allow for a quantification of the global structure of other cellular structures, e.g., foams, where the centers of mass of the single cells can be used as centers of the cells instead of the Voronoi centers used here.

For the mixed correlation functions, i.e., cross-correlation of Minkowski functionals of different cells, see Eq. (4.9), I find that they can be approximated by the arithmetic mean of the single Minkowski functional correlation functions, e.g., the volume-perimeter correlation function by the volume-volume and the perimeter-perimeter correlation functions, see Eq. (4.10) and Figs. 4.8–4.10. I can relate this approximation to a nearly vanishing correlation of the difference of rescaled Minkowski functionals, see Eq. (4.12) and Fig. 4.11.

Moreover, I show that the Minkowski correlation functions contain visibly more information than the standard two-point correlation function because Minkowski functionals contain higher n-point information. Comparing a model for the distribution of galaxies to a simple clustering process with the same pair-correlation function, the Minkowski correlation functions reveal the different global structure, see Fig. 4.17. Also the local structure, i.e., the empirical distribution functions of the Minkowski functionals of a single cell, is slightly, but statistically significantly different, see Fig. 4.18.

A frequently discussed question is whether or not there are local icosahedral configurations in jammed packings [40, 103, 138, 234, 253], i.e., a central sphere with 12 spheres in contact where the centers of the touching spheres form a regular icosahedron. The Voronoi cell of the central sphere in such an icosahedron is a regular dodecahedron, which has the maximum possible local packing fraction ($\approx$ 0.76). There is growing evidence that there are no regular icosahedral arrangements in hard-sphere packings, e.g., see Refs. [40, 120, 232]. Indeed, I find in the MRJ sphere packings no regular and hardly any nearly regular dodecahedral Voronoi cells. All spheres out of more than two million have less than 12 contacts. There are local packing fractions up to 0.75, but only 4.2×10^{-5} of all cells have a local packing fraction greater than 0.74.

In a preliminary approach to look for possibly strongly distorted dodecahedral Voronoi cells in the MRJ sphere packings, I examined the topology of the Voronoi polyhedra, i.e., the number of faces and the corresponding types of polygons, following Refs. [56, 138, 266]. In a compact notation, the topology of a polyhedron is given by the so-called p vector $(n_3\ n_4\ n_5\ n_6)$, where n_3 is the number of triangles, n_4 of quadrilaterals, n_5 of pentagons, and n_6 of hexagons. The dodecahedron is

formed by 12 pentagons, i.e., its topology is denoted by (0 0 12 0). Although these polyhedron characteristics are discontinuous and inadequately metric for definite conclusions [140], they can provide a first insight into whether there could be a significant number of distorted dodecahedra. In the MRJ sphere packings, 1.1 % of all cells have the topology of a dodecahedron (0 0 12 0)[17]. The average local packing fraction of those distorted dodecahedra is 0.69 and is thus significantly greater than the total mean local packing fraction, which is 0.64. However, only 0.4 % of the distorted dodecahedra have a local packing fraction greater than 0.74. The distorted dodecahedra also have a higher average number of contacts, ≈ 7, compared to the typical cell, ≈ 6, but as stated above there is not a single sphere with 12 contacts in this high-quality MRJ data. There are 25 other topologies in the Voronoi diagram of the MRJ sphere packings that occur more frequently than the dodecahedron. With 5.2 % of all cells, the most likely topology is (0 3 6 5). However, by adding one or two faces, the dodecahedron can transform to the following polyhedra [138]: 1.1 % of all cells in the MRJ sphere packings are (1 0 9 3), 3.1 % are (0 1 10 2), and 4.4 % are (0 2 8 4). The latter is the second most common type in the MRJ sphere packings. So, while I find no regular icosahedral configurations in the MRJ sphere packings, the preliminary topological analysis indicates that more detailed studies of probably strongly distorted icosahedra could be interesting. For example, also in metallic glasses, significant numbers of distorted icosahedra have been found [192, 269].

[17] In the equilibrium hard-sphere liquid, 0.45 % of all cells are distorted dodecahedra; in a Poisson Voronoi tessellation, the fraction is less than 2×10^{-5}.

Chapter 5

Shape indices for nuclear matter[1]

Intricate spatial structures appear even at the smallest length scales: in nuclear matter. Near equilibrium density (a density of nucleons $\rho_0 \approx 0.16\,\mathrm{fm}^{-3}$ corresponding to $\approx 2.7 \cdot 10^{14}\,\mathrm{g/cm}^3$ [412]), nuclear matter is a homogeneous quantum liquid, somewhat trivial from a structure perspective. However, an exciting world of various geometrical profiles develops at slightly lower densities, where the nuclear matter unfolds into a rich variety of spatially structured phases; it forms rods, slabs, tubes, or bubbles [187, 358, 377, 503]. Most of these phases can be considered as manifestations of liquid crystals [365] and the geometrical analogy to spaghetti, lasagna, etc., has led to these being summarized under the notion of a nuclear "pasta." Although this nuclear matter is not observable in laboratories on Earth, it plays a crucial role in astrophysical scenarios such as neutron stars or core-collapse supernovae [72, 147]. The application of Minkowski functionals and tensors to nuclear physics again demonstrates their versatility.

The Minkowski functionals characterize the shape of these structures and allow for a complete classification of the states found in dynamical simulations. After a short introduction to pasta matter in Section 5.1, the simulation procedure is outlined in Section 5.2, the static and time-dependent Hartree-Fock approach is briefly reviewed, and the emerging pasta shapes are presented. They are analyzed

[1] This work was achieved in collaboration with Klaus Mecke, Gerd E. Schröder-Turk, Kei Iida, Paul-Gerhard Reinhard, Joachim A. Maruhn, and Bastian Schütrumpf, who simulated the pasta matter using both static and dynamic Hartree-Fock calculations in periodic lattices. Together, we then performed a detailed morphometric analysis based on the Minkowski functionals and tensors. Large parts of this chapter are direct quotes from our publications Refs. [246, 412–416], where my collaborators are the main authors of the parts describing their simulations, the nuclear physics background, and its implications for astronomy as well as the appearance of gyroids in different fields of physics. Some of the figures in this chapter and the tables are reproduced from Refs. [413, 416]; copyright by the American Physical Society.

by the Minkowski functionals and tensors in Section 5.3. In Section 5.4, the pasta shapes in the small simulation boxes are classified by the signs of integrated mean curvature and Euler characteristic, a map of pasta shapes for varying temperature and mean density is constructed, and thermal fluctuations in the density profiles are investigated and their connection with melting of the inhomogeneous structures is discussed.

Moreover, with the help of the Minkowski functionals, we find in Section 5.5 an especially interesting and intricate paste shape: the single gyroid network structure, which is a well-known configuration in nanostructured soft-matter systems. We find the gyroid both as a cooled static solution and in the course of the dynamical simulations, where the single gyroid structures forms spontaneously. In contrast to the nanostructured soft-matter gyroids, the lattice spacing of the pasta gyroid is $a = 22\,\mathrm{fm}$, which is thus the smallest gyroid found in dynamical simulations. However, the pasta gyroid is found to be an isomeric state. The very small energy differences to the ground state indicate its relevance for structures in nuclear pasta. The analysis of the complex pasta shapes also introduces the Minkowski tensors to nuclear physics, where we use them to detect and characterize anisotropic deformations of the pasta shapes, especially of the gyroid.

5.1 Nuclear pasta

Core-collapse supernovae, see Refs. [72, 147] for a review, play a key role in many astrophysical phenomena, such as acceleration of cosmic rays, formation of neutron stars and black holes, or the synthesis of heavy nuclei. Hydrodynamics simulation studies of stellar collapse and subsequent explosion have led to an improved understanding of the mechanism of such supernovae, especially with respect to dimensionality and neutrino transport, rotation, magnetic fields, and the effects of general relativity [89]. Nevertheless, many aspects of the mechanism still needs clarification [147]. For such clarification, the properties of matter that constitutes the supernova cores such as the equation of state, the nuclei present, and the neutrino opacity are indispensable. This matter, which is believed to be charge-neutral and mostly beta-equilibrated while having a degenerate gas of electron neutrinos trapped inside, is often referred to as supernova matter. In early studies of supernova matter below normal nuclear density and at temperatures of order or lower than 10 MeV, nuclei in equilibrium were shown to be relatively neutron-rich by using a liquid-drop model [254], a Thomas-Fermi theory [351], and a Hartree-Fock (HF) theory [78].

At densities just below normal nuclear density, nearly spherical nuclei arranged in a Coulomb lattice and embedded in a roughly uniform neutralizing background

of electrons are so closely packed that the total surface area becomes very large. Then, the system tends to lower the total surface area by elongating the nuclei and forming nuclear rods [96, 366]. It was predicted from seminal liquid-drop calculations [187, 377] that with further increase in density, the shapes of inhomogeneous nuclear matter change from rods to slabs, tubes, and bubbles until the system melts into uniform matter. These exotic nuclear configurations are often denoted as pasta nuclei, which arise from a subtle competition between the surface and Coulomb energies. The pasta nuclei are manifestations of liquid-gas mixed phases of nuclear matter, among which the phases with rods, slabs, and tubes can be regarded as liquid crystals [365].

In the conventional liquid-drop approach [377, 503], pasta nuclei have been studied by assuming a geometrical shape of nuclear matter and using the Wigner-Seitz approximation. For more realistic description of pasta nuclei, multidimensional calculations without any assumption of the geometrical shape were performed in the Thomas-Fermi approach [260, 514], the Hartree-Fock approach [78, 156, 285, 340], and the Quantum Molecular Dynamics (QMD) approach [296, 435]. In these calculations, the shapes assumed in the Wigner-Seitz approximation were reproduced, while some cases did indicate the presence of more complex structures.

Astrophysically, the possible influence of pasta nuclei on the neutrino opacity may affect supernova explosions and subsequent protoneutron star cooling. The cross section for the neutrino-nucleus scattering depends on the structure of inhomogeneous nuclear matter [201, 202, 434]. In fact, the neutrino scattering processes are no longer coherent in the directions in which nonspherical nuclei are elongated. This is a great contrast to the case of roughly spherical nuclei of which the finiteness in any direction leads to constructive interference in the scattering.

Recently, first Time-Dependent Hartree-Fock (TDHF) have come up which describe pasta nuclei in supernova matter [421, 422]. In contrast to static calculations, which concentrate on the one configuration at minimal energy, the TDHF approach allows nucleons to explore multiple low-lying configurations in the energy landscape mapped by the time evolution of the mean field. Bastian Schütrumpf and his colleagues have performed such dynamic calculations at finite temperature, which are expected to give a realistic description of supernova matter as long as two-nucleon collisions can be ignored. As we shall see, the resultant map of pasta shapes is basically consistent with the phase diagrams obtained from the QMD calculations [435].

The TDHF simulations produce a great variety of involved, three-dimensional structures. One needs tools to characterize a given configuration in terms of a few key numbers. This is simple for single finite nuclei where the radius and a couple of deformation parameters serve very well. However, we encounter here

compounds where much less is known ahead of time. For example, we do not even know the number of subunits or their connectivity.

The Minkowski functionals provide the optimal technique to quantify pasta matter and so classify the different possible shapes. Similar approaches had already been exploited, e.g., in Refs. [435, 504, 505]. Here, this is continued, and the studies are improved and deepened along this line.

5.2 Numerical simulation scheme

Bastian Schütrumpf and his colleagues simulated the pasta shapes using both the static and the time-dependent Hartree-Fock (TDHF) calculations [412]. In the following, a summary describing their simulations is presented for a better understanding of the pasta shapes and the numerical data.

Static HF solutions are computed by accelerated gradient iteration [380] while time stepping is done with Taylor expansion of the mean-field time-evolution operator, for technical details see Ref. [294]. The Coulomb solver with periodic boundary conditions is used. Charge neutrality is enforced by assuming a compensating homogeneous cloud of negative charges. This approximation ignores electron screening. Its effect on matter under astrophysical conditions has been much discussed in the past [26, 123, 297, 502]. Although screening lengths vary widely and reach occasionally the order of structure size, the net effect of electron screening is found to be small [297, 502], thus excusing the homogeneous electron approximation for this exploration.

TDHF is a self-consistent mean field theory, which was originally proposed by Dirac in 1930 [118]. In general, the TDHF equations are derived from a time-dependent variational principle with the variational space restricted to one single, time dependent Slater determinant. In nuclear applications, TDHF usually employs an effective interaction as, e.g., the Skyrme force, for a review see Ref. [65]. The treatment becomes then practically identical to a time-dependent density functional theory in local density approximation as it is widely used in electronic systems, see e.g. [166]. Computational limitations restricted earlier TDHF calculations in system size or symmetry [111, 337]. With the advance of computational power, it is now possible to perform full three-dimensional calculations without any symmetry restrictions even for a large number of wave functions. This led to a revival of nuclear TDHF studies in various dynamical regimes as, e.g., collective vibrations [295, 429], large amplitude motion in fusion and nuclear reactions [480, 481], or, similar as done by Bastian Schütrumpf, for simulations of stellar matter [421, 422].

The calculations are performed on an equidistant grid in three-dimensional

coordinate space in a finite simulation box using periodic boundary conditions. Box size and lattice spacing are adjusted to give the desired conditions of matter. We consider grid spacings of $0.875\,\text{fm} \leq \Delta r \leq 1.125\,\text{fm}$ with $N_x = N_y = N_z$ grid points ranging from 16 to 24. This spans periodic simulation boxes in the range $a = 15$–$26\,\text{fm}$. While we found no sensitivity on the grid spacing [2], the dependence on the box size is studied in detail for the more intricate (primitive and gyroid) structures in Section 5.5.

The Coulomb problem is solved with assumed global neutrality which means that the proton charges are compensated by a homogeneous negatively charged background that is supposed to simulate the electron gas around. This amounts to use the Coulomb solver with periodic boundary conditions and to skip the singular zero momentum component of the Coulomb field in Fourier space. The kinetic energy operator is evaluated in Fourier space and time evolution is performed using a Taylor expansion of the mean-field propagator. For the present calculations, the Skyrme parametrization SLy6 is chosen which was developed with an emphasis on describing neutron-rich matter [94]. The code for these calculations goes back to Ref. [482] and has been used since in many applications to nuclear resonances, e.g. [381] and heavy-ion dynamics, e.g. [276].

Initialization

We here consider matter with a proton fraction of $X_p = 1/3$. In order to produce not too high excitations, the calculations are initialized by distributing a number N_α of α particles (i.e., Helium nuclei consisting of two protons and two neutrons) randomly over the grid keeping a minimal distance between each α core to avoid perturbations by the overlap. To that end, ground state wave functions for the α particles are produced before in a stationary HF calculation. The number N_α is varied to produce systems with different densities.

In the dynamic simulation, the temperature T is controlled by the initialization temperature T_{init}. We utilize two different ways of initialization, a more energetic and a less energetic one. For the more energetic in the first part, the α cores are distributed in momentum space following a Maxwell-Boltzmann distribution with a given initialization temperature T_{init} and further neutron states are introduced as plane wave states using a Fermi distribution with the same temperature to describe free background neutrons. For the less energetic initialization for the more complicated networks, see Section 5.5, the additional neutrons are added as plane waves filling the states with lowest kinetic energy; the α-particles were taken at rest and the minimal distance between them was larger such that the distribution

[2] The experience from nuclear TDHF calculations is that the variation up to 1.1 fm produces only minor quantitative changes in the percent level.

was more homogeneous (yet still random) and less energetic. Nonetheless, this initialization scheme produces systems at rather large excitation energies with temperature $T \approx 7\,\mathrm{MeV}$. Note that always both spin up and spin down states are occupied simultaneously to avoid a large spin excitation. Finally, before starting the TDHF calculation, these wave functions are orthonormalized.

The time evolution is assumed to be sufficiently chaotic such that robust final states properties are reached which depend only on temperature and average density, although there are some regions where two states compete and the final outcome depends also on the initialization. The average density is tuned by the number of particles and the temperature by T_{init} in the sampling of α particles and neutrons. Even systems with $T_{\mathrm{init}} = 0$ store a considerable amount of excitation stemming from the interaction energy of the α particles and the neutron gas.

This randomized setup leads usually to a system without strong a priori symmetry assumptions. However, a general problem with the analysis of sub-structures of infinite systems in a finite simulation box is that the imposed periodic boundary conditions have an impact on the structures due to possible symmetry violation by the box and subsequent spatial mismatch [30, 193, 354]. A study within classical molecular dynamics without Coulomb interactions implies that this may be particularly critical for extended, inhomogeneous structures [323]. Spurious shell effects may further blur the analysis in a quantum-mechanical framework [340].

However, the numerical expense of fully quantum-dynamical simulations sets limits on the affordable box sizes. To get some idea of the size dependence, the box is, as mentioned above, in the second part varied in the rather broad range of 15–26 fm. This average smooths some artifacts and thus allows for an even more rigorous structure identification, and larger calculations would run on a very long timescale.

Temperature

The excitation state of matter is characterized by its actual temperature T. It is, however, difficult to measure temperature in the quantum simulation of a microcanonical ensemble as generated by the present TDHF calculations. As a rough measure, we estimate T by the excitation energy E^* through the Fermi gas relation $E^* = (\pi^2 A)(2\varepsilon_{\mathrm{F}})\,T^2$ where A is the total number of nucleons and ε_{F} the Fermi energy of the system [37]. The excitation energy E^* is defined as the difference of the actual energy E to the ground state energy E_0. The latter is computed by solving the static HF problem for the given density. This amounts to

$$T = \frac{1}{\pi}\sqrt{2\varepsilon_{\mathrm{F}}\,\frac{E^*}{N}}\,.$$

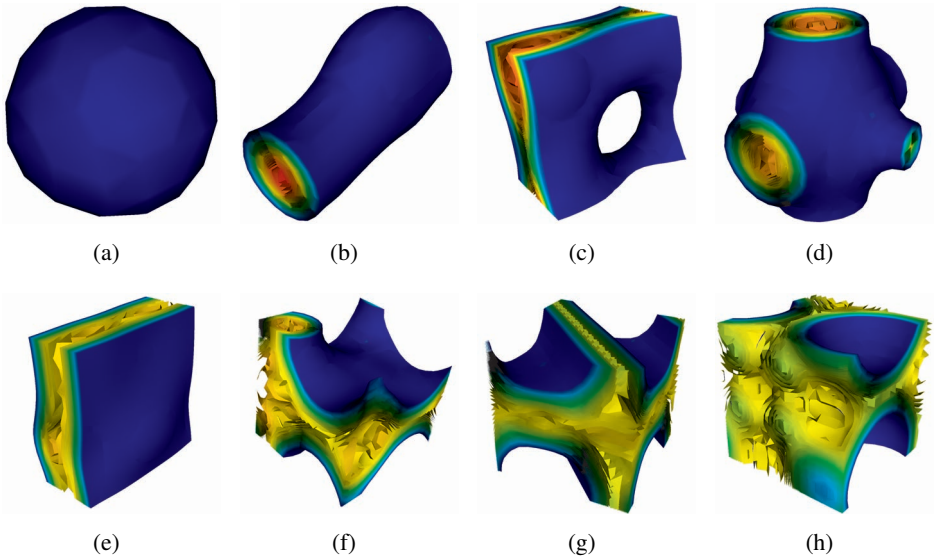

Figure 5.1: Typical shapes of pasta structures at the lowest temperatures, which continue to evolve with time but do not change their morphological character anymore; the bubble shape illustrations show gas phase, which is indicated by the color scale—from $0.06\,\mathrm{fm}^{-3}$ (blue) to $0.16\,\mathrm{fm}^{-3}$ (orange): (a) spherical, (b) rod, (c) rod(2), (d) rod(3), which is topologically identical to a domain bounded by a special minimal surface, called Schwarz primitive, (e) slab, (f) rod(2) bubble, (g) rod bubble, (h) spherical bubble.

This excitation temperature T is to be distinguished from the "initial temperature" T_{init} which we use to boost stochastically the initial ensemble of α particles and the background neutrons. Calculating the excitation temperature T for the different values of the initial temperature T_{init}, we find empirically $T \approx 7\,\mathrm{MeV} + \sqrt{T_{\mathrm{init}}(T_{\mathrm{init}} + 100\,\mathrm{MeV})}/6$. This is taken henceforth for a rough calibration of T.

Pasta shapes

Each setup is evolved in time for $1500\,\mathrm{fm/c}$. After that time, shapes do not change significantly. The system goes over into a pasta state where some type of equilibrium is achieved. Depending on the temperature differently strong fluctuations can be observed.

In Fig. 5.1 many different pasta shapes are classified. Among the structures found are rod and slab structures, which have been discovered, e.g., by QMD calculations [435]. Rod(2) corresponds to rods forming a two-dimensional layer. The shape rod(3) describes three rods in x-, y- and z-direction that cross in one

point; its boundary is topologically identical to a P-surface; see Section 5.5. Similar shapes were discovered in [358, 421] and the rod(3) structure was also found in [340].

5.3 Shape characterization

Using the Minkowski functionals and tensors, the geometry and topology of these pasta shapes can be quantified and then classified. The TDHF results for pasta matter are given as gray-scale data with a density ρ_i assigned to each voxel i, i.e., a grid point. In order to compute the Minkowski functionals of a domain K, the density field is turned into binary data via standard thresholding [304, 406, 408]. A threshold density ρ_{th} is introduced. Each voxel i with $\rho_i \geq \rho_{th}$ is set to black, but if $\rho_i < \rho_{th}$, white is assigned. In other words, an isodensity surface divides the space into a liquid phase (solid), and a gas phase (void). The Minkowski functionals of the union of all black voxels, interpreted as a polygon K, can then quantify the shape of the pasta matter in dependence of the threshold density ρ_{th}. Beforehand however, the marching cube algorithm [277] is applied, which provides a smoothed polygonal representation in order to reduce voxelization errors. The Minkowski functionals of the polygon are evaluated using the linear-time algorithm from Refs. [408, 410].

In the following, we analyze the Euler characteristic χ of the whole liquid nuclear matter phase, not only the Euler index χ_S of its bounding surface, which is often used for minimal surfaces and which is for a three-dimensional solid body twice as large $\chi_S = 2\chi$. Note that the Euler characteristic χ_S of an orientable surface is related to its genus g via $\chi_S = 2 - 2g$.

The threshold density can take on values $\rho_{th} \in [0, \rho_{\max}]$. But for small thresholds $\rho_{th} \approx 0$ and for high thresholds $\rho_{th} \approx \rho_{\max}$, the Minkowski functionals exhibit erratic behavior because of quantum fluctuations; thus, the structure values for these thresholds are ignored [318, 408]. The regimes of the physical values for the threshold density which yield reliably stable values of the Minkowski functionals for pasta configurations with the lowest value of temperature are roughly $\rho_{th} \in [0.03\,\mathrm{fm}^{-3}, 0.08\,\mathrm{fm}^{-3}]$. For lower threshold densities, only few dots are recognized as "white" (below threshold density) due to quantum fluctuations in the gas phase. At higher densities mainly quantum fluctuations of the liquid phase are observed. Figure 5.2 shows the Minkowski functionals W_ν and the anisotropy index $\beta_1^{0,2}$ as a function of the threshold density ρ_{th} for the pasta shapes spherical, rod, slab, rod(2), and spherical bubble. The boundary of rod(3) is, as mentioned above, topologically identical to a P-surface and discussed in Section 5.5, where it is compared to the gyroid structure.

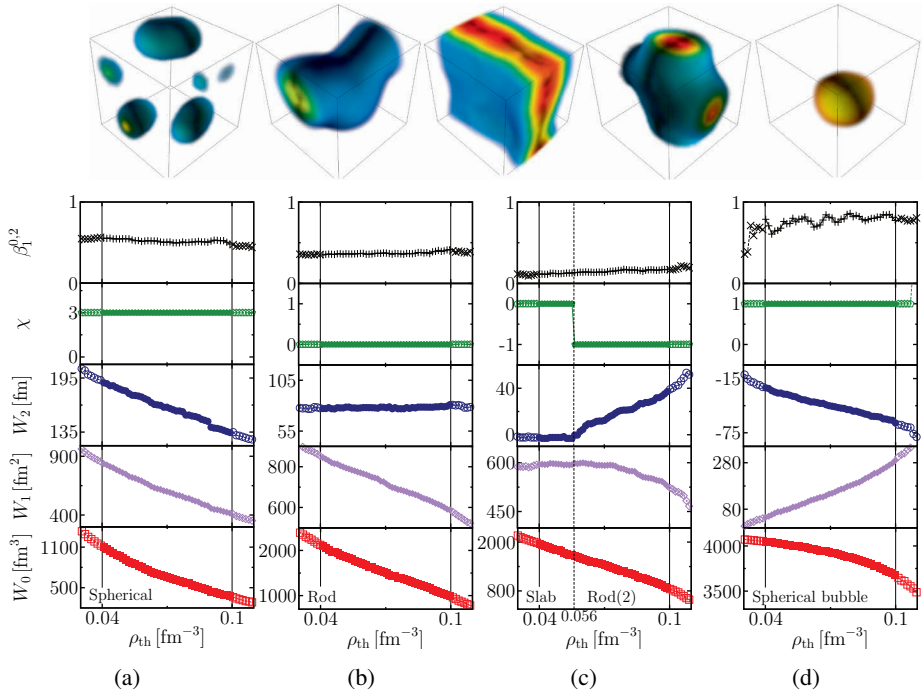

Figure 5.2: Minkowski functionals W_ν and anisotropy index $\beta_1^{0,2}$ as a function of the threshold density ρ_{th} of pasta shapes: spherical, rod, a hybrid of slab and rod(2), and spherical bubble; depicted on the top are (non-hybrid) examples of these shapes; for the primitive, i.e., rod(3), and gyroid structures, see Fig. 5.11. The solid lines indicate the central regime of threshold densities for which the Minkowski functionals are stable; for smaller or larger threshold densities the Minkowski functionals are affected by quantum fluctuations.

For all pasta shapes the volume must decrease with increasing threshold density ρ_{th} because pixels can only turn from black to white. However, the sign of the derivatives varies, they are related to the other Minkowski functionals via the Steiner formula [448] for the Minkowski functionals of a parallel body, which can be expressed by polynomials in the distance r of the surfaces. For sufficiently small Δ_{th}, the isodensity surface at a threshold density $\rho_{th} + \Delta_{th}$ is a parallel surface to the pasta shape at a threshold density ρ_{th}. Note that here only polygonal approximations of the surfaces are available.

This can best be observed for the integrated mean curvature and the Euler characteristic. First, if the latter is positive, the integrated mean curvature is decreasing, e.g., both for the spherical shape and the spherical bubble. Second, if the Euler characteristic is zero, the integrated mean curvature is a constant

independent of the threshold ρ_{th}, e.g., for the rod or the slab shape[3]. Finally, if the Euler characteristic is negative, the integrated mean curvature is increasing, e.g., rod(2), rod(2) bubble, and rod(3) consist of channels and tunnels, which corresponds to a negative Euler characteristic $\chi < 0$ [214].

The slab bubble and rod(3) bubble phases are equivalent to the slab or rod(3) phase, respectively, i.e., they are symmetric in gas and liquid phase. However, the spherical, rod, and rod(2) are, although obviously related, different to the corresponding bubble phases, i.e., their complement shapes. In Fig. 5.2, only the Minkowski functionals of the spherical bubble phase are depicted, but Fig. 5.3 compares the integrated mean curvature and Euler characteristic of all pasta shapes from Fig. 5.1. For the spherical, rod, and rod(2) pasta shapes the surface area decreases with increasing threshold density, as expected, and increases for the corresponding bubble phase. Besides the different trend in the surface area, the integrated mean curvature changes sign for the bubble phases, because both principal curvatures change their sign. Therefore, the Euler characteristic remains in each case the same for the bubble and non-bubble phases. However, in the example of the spherical pasta shape shown in Fig. 5.2, the nuclear matter is separated in three disjoint clusters and thus $\chi = 3$ instead of $\chi = 1$ like in the spherical bubble pasta shape. The three clusters in the simulation box with periodic boundary conditions are depicted in the image at the top of Fig. 5.2.

The name "spherical" is only related to the topology of the single pasta clusters. The anisotropy index reveals that they are actually strongly anisotropic. Of course, the rod, slab, and rod(3) shapes are even more anisotropic than the spherical shape. For the rod shape, the two eigenvalues corresponding to the normals perpendicular to the axis of the distorted cylinder are obviously much larger than the one corresponding to the normal vector along the axis; like for a prolate spheroid. For the slab and rod(2) shapes, one eigenvalue is, as expected, much larger than the other two; like for an oblate spheroid. The same is valid for the corresponding bubble phases.

There are purely slab phases and also purely rod(2) phases. Depicted here is, however, and interesting hybrid finding. At low threshold densities, the pasta matter is in the slab phase. However, within this sheet there is a region of nuclear density still above the gas density but smaller, less that 0.056 fm. Therefore, at higher threshold densities the pasta shape turns into a mesh with Euler characteristic $\chi = -1$ and positive integrated mean curvature. The two phases are coexisting, and one pasta shape is very slowly changing into the other, i.e., the hole in the

[3] The Euler characteristic is zero if one of the principal curvatures vanishes on average. In the rod shape, this is the curvature in direction of the axis of the cylinder and in the slab phase both principal curvatures are zero.

mesh phase is closing by condensation of nucleons, or a new hole is evaporating in the slab. Especially at higher temperatures and mean densities these mixtures of phases can appear (cf. [422]). A unique assignment to a single pasta phase can either be choosing the pasta phase with the bigger range in ρ_{th} or by choosing a specific isodensity surface: the Gibbs dividing surface, a standard tool of solid state physics. It is chosen such that the liquid phase volume V_b contains all the matter in a liquid phase with constant density ρ_0. This means that $V_b \rho_0 = N_{\mathrm{tot}}$ where N_{tot} is the total number of particles in the box. For ρ_0 we take the maximum density of the individual states. The fraction u of the liquid volume is

$$u = \frac{V_b}{V} = \frac{\rho}{\rho_0} \ , \ \rho = \frac{N_{\mathrm{tot}}}{V}$$

where ρ is the mean density and V the volume of the whole numerical box. Note, however, that in most cases the topology of the pasta shape is independent of the chosen threshold density (within the physically reasonable regime).

We have also performed Minkowski analyses of only either the proton or the neutron density to check if their distributions within the simulation box, i.e., pasta shapes, are the same or different from those of the combined density of protons and neutrons. In other words, besides the total nuclear density field ρ_i, we also consider the density of only the protons ρ_i^p or only the neutrons ρ_i^n. For all pasta shapes, the Minkowski functionals as a function of the threshold of either the proton, neutron, or total densities were only shifted w.r.t. each other because of the different average nuclear density (the proton fraction is $X_p = 1/3$). The pasta shapes of either only protons agree with those of only neutrons or of the total density.

5.4 Classification and map of pasta shapes and fluctuations

Comparing in Fig. 5.3 the values of the integrated mean curvature and the Euler characteristic for all shapes as a function of threshold density, we see that we can uniquely classify these different shapes in simple fashion: only their signs are needed; see Table 5.1. This was also found in Ref. [435]. However, it is a bit more demanding to discriminate the rod(3) shape. We need the full trend of the mean curvature to classify the rod(3) shape correctly.

As mentioned above, both the slab and the rod(3) shapes are symmetric in gas and liquid phase. The shape of the liquid phase at low thresholds corresponds to the gas phase at high thresholds. Thus, the integral mean curvature as a function of the threshold ρ_{th} is point symmetric w.r.t. a mid value for the threshold density.

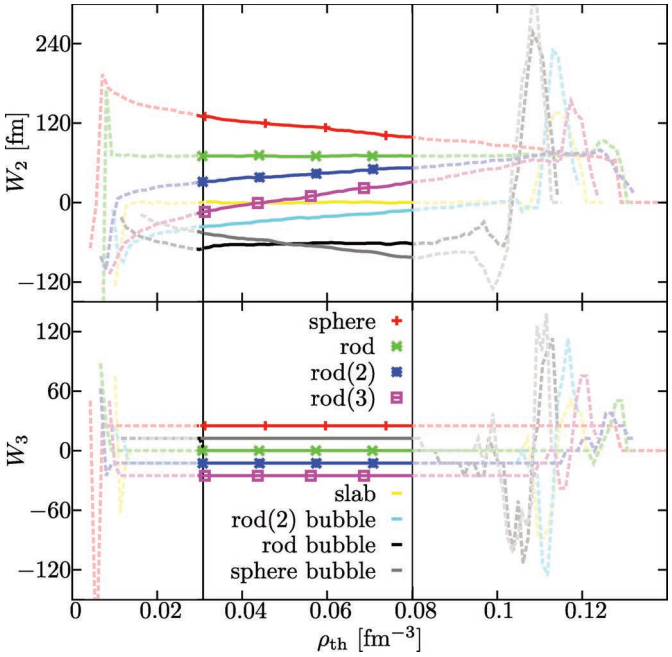

Figure 5.3: The Minkowski functionals W_2, integral mean curvature, and W_3, proportional to the Euler characteristic, as functions of the threshold density ρ_{th} for the pasta shapes shown in Fig. 5.1.

This is trivially true for the slab with $W_2 \approx 0$ but holds also for the nonzero mean curvature of rod(3).

Bastian Schütrumpf constructed a map of pasta shapes, see Fig. 5.4; it shows for which density and temperature the different shapes appear. Note that two calculations were performed for each point in the map. Because of the random initial conditions the final shapes may differ although the same values for temperature and mean density are assumed. The hatched areas with a mixture of colors indicate the different final states reached in these cases. At higher densities, bubble structures can be seen (the gas phase has a pasta like shape). Many shapes can coexist here in one point of the map.

At mid densities, it seems to highly depend on the initial condition whether slab or rod(3) shape is formed. For both shapes, the gas phase has the same shapes as

Table 5.1: Signs of the integral mean curvature W_2 and Euler characteristic $\chi \propto W_3$ for the pasta shapes shown in Fig. 5.1.

shape	sph	rod	rod(2)	rod(3)	slab	rod(2) b	rod b	sph b
W_2	> 0	> 0	> 0	- to +	≈ 0	< 0	< 0	< 0
W_3	> 0	$= 0$	< 0	< 0	$= 0$	< 0	$= 0$	> 0

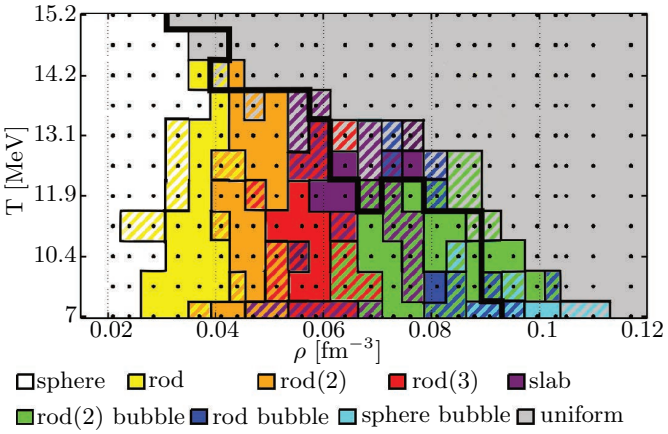

Figure 5.4: Map of pasta shapes achieved in a TDHF calculation starting from a gas of α particles with neutron background for various real temperatures and mean densities. The proton fraction is 1/3. Each dot represents two calculations. The solid black line indicates a phase separation line. Image produced by Bastian Schütrumpf.

the corresponding liquid phase. So gas and liquid phase symmetrically complement each other. Hence, both shapes are possible for this region.

Here, the simulated matter is restricted to be periodic by 16 fm in each direction with 16 grid points in each direction. In these smaller systems, the more involved gyroid structure is not appearing. Later in Section 5.5, the box sizes are varied in the range 15–26 fm and the number of grid points $N_x = N_y = N_z$ range from 16 to 24, as mentioned above to investigate more intricate pasta shapes. The calculations in larger simulation boxes indeed find other periodic network-like structures with negatively curved interfaces like the rod(3) structure, but they are metastable. To distinguish these complicated isomeric states from the rod(3) phase, the sign of the Euler characteristic is no longer sufficient, but its absolute value is needed as a topology index, see Section 5.5.3 and Fig. 5.8.

To analyze the fraction of liquid and gas phase and the transition to uniform matter, Bastian Schütrumpf plotted the threshold density profiles for various calculations in Fig. 5.5. For the lowest temperature and low mean density, there is a big peak at small densities and a long tail to high densities. With increasing mean density a peak at high density develops. At the densities where rod(3) and slab shapes appear ($5 \cdot 10^{-2}\,\mathrm{fm}^{-3} < \rho < 7 \cdot 10^{-2}\,\mathrm{fm}^{-3}$) the peaks for low and high densities have nearly the same width and height. At higher mean densities the peak for low densities disappears, and only a tail remains.

With increasing temperature the double peak structure vanishes and finally a single peak around the mean density is forming which moves successively to central density with ever higher T. Consider, e.g., the case of the mean density of $6.4 \cdot 10^{-2}\,\mathrm{fm}^{-3}$ in Fig. 5.5: We can observe a double peak structure for the lowest temperature $T = 7\,\mathrm{MeV}$. For $T = 11.2\,\mathrm{MeV}$ we can separate the two phases at a mid value of the peak and still observe pasta structure. For higher temperatures, no

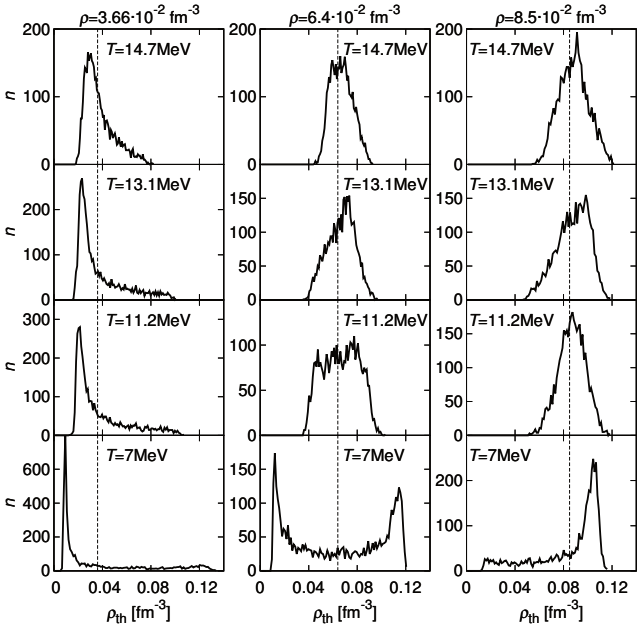

Figure 5.5: Threshold density profiles for calculations varying in density ρ and temperature T. On each single plot, the number of grid points n corresponding to a certain density value is plotted. The dashed lines show the mean density. Image produced by Bastian Schütrumpf.

pasta structure can be observed. Only fluctuations around the mean value plotted as a dashed line remain, so that it is considered as uniform matter.

As the pasta structures vanish with higher density, the variance from the mean value of the calculation of these plots decreases. Going through the systematics of the results, Bastian Schütrumpf found as a reasonable value for a limit of the variance to observe pasta structures $2 \cdot 10^{-4}$ fm^{-6}. The phase separation line computed with this observable is displayed in Fig. 5.4 as a bold line.

Comparing these results to Ref. [358], the transition density to uniform matter at $T = 7$ MeV with $9.5 \cdot 10^{-2}$ fm^{-3} is in good agreement, but at $T = 10$ MeV we get a higher value of about $9.0 \cdot 10^{-2}$ fm^{-3} compared to $7.7 \cdot 10^{-2}$ fm^{-3} in Ref. [358].

5.5 The single gyroid network phase

To further investigate the role of periodic network-like structures with negatively curved interfaces, like the rod(3) structure, in nuclear pasta structures in periodic lattices, we have looked for and identified for the first time the single gyroid network structure; both as a cooled static solution and forming spontaneously in the course of the dynamical simulations.

The gyroid is a particularly intricate structure amongst the pasta phases. It is a triply-periodic geometry consisting of two inter-grown network domains

separated by a periodic manifold-like surface which is (at least on average) saddle-shaped and with negative Gaussian curvature (cf. Fig. 5.10). In soft-matter systems, these periodic saddle-shaped surfaces have been found in solid biological systems [148, 317, 342, 371, 397, 409, 515], in the so-called "core-shell" gyroid phase of di-block copolymers [176] and in inverse bicontinuous phases in lipid-water systems [259]. Gyroid-like geometries can also be expected in nuclear pasta, due to a balance between the nuclear and Coulomb forces [332, 333].

As partly mentioned above, the possible occurrence of periodic bicontinuous structures was found by stationary Hartree-Fock calculations [155, 156, 285, 300, 340, 358, 366], later on in dynamical simulations of supernova matter using time-dependent Hartree-Fock (TDHF) calculations for supernova matter [421, 422] and also in a quantum molecular dynamics approach [435].

Gyroids have been examined so far only within a liquid-drop model [332, 333] where double gyroids were found to be energetically close to the ground state. (Note the important difference between single and double gyroid geometries.) If realized in supernova matter, the network-like percolating nature of the gyroid could greatly affect neutrino transport during the collapse of a massive star's core and the subsequent core bounce.

5.5.1 Constant mean-curvature (CMC) surfaces

We are here interested in what is called *hyperbolic* surfaces, where the interface is saddle-shaped and has Gaussian curvature $K \leq 0$ (κ_1 and κ_2 with different sign). Such interfaces can form the continuous bounding surfaces of *periodic* labyrinth-like domains; they now have a firm place in the taxonomy of soft-matter nanostructures [213]. More specifically, we search within the class of constant-mean-curvature surfaces (CMC) which have constant H. They provide structures with the same topology and symmetries, yet with variable volume fractions $u(H)$ [31, 167, 168]. Gyroids belong to the CMC and require, in particular, that $\chi = -4$.

In soft-matter systems, these periodic saddle-shaped surfaces occur in two forms, called "single" or "double". The *double gyroid* (DG) is a structure composed of two inter-grown nonoverlapping network domains, bounded by two CMC gyroid surfaces with mean curvatures $\pm H$ separated by the so-called matrix phase. The *single gyroid* (SG, or simply G) is composed of two domains, one solid and one void of volume fractions u and $(1 - u)$, with a gyroid CMC surface as the interface between them; single gyroids have been identified so far only in solid biological systems [148, 317, 342, 371, 397, 409, 515]. We concentrate in the following on the "single" structures because double structures have not been found to be stable for the assumed parameters in this work. However, the gyroid is not the only

Table 5.2: Surface area A_P and mean curvature H_P of the exact CMC and pasta primitive surfaces for different mean densities ρ and corresponding volume fractions u. For the pasta shapes, the average mean curvature is given. The values t_P are the threshold values for the nodal representations of P in Eq. (5.2) with volume fractions u. The unit of length is the lattice constant.

ρ[fm^{-3}]	u	A_P		H_P		t_P
		CMC	pasta	CMC	pasta	
0.0326	0.22					0.99
0.0434	0.29	2.11		1.22		0.75
0.0543	0.37	2.26	2.46	0.66	0.60	0.46
0.0651	0.45	2.33	2.51	0.24	0.23	0.18
0.0715	0.50	2.35		0.0		0.0
0.0759	0.53	2.34	2.54	-0.13	-0.17	-0.09
0.0868	0.61	2.29	2.44	-0.55	-0.55	-0.39
0.0977	0.70	2.15		-1.08		-0.69

CMC structure meeting all of the above criteria. They come along with the related primitive (P) and diamond (D) structures, all three of which are distinguished by their structural uniformity or homogeneity [215]. While any negatively curved interface necessarily exhibits spatial variations of the pointwise Gaussian curvature K, see Ref. [132], for a discussion) and the pointwise domain width or thickness d, the P, D and G surfaces appear to be optimal structures with minimal variations of K [145], and the G surface is the optimal structure with minimal variations of domain width d [404, 405]. This homogeneity is likely to explain the ubiquity of these three structures in soft-matter systems, particularly that of the gyroid.

The close relationship between the P-, D- and G-surface is also visible from the fact that they can be connected by the Bonnet transformation [213] which leaves all metric and curvature properties unchanged and which relates the corresponding unit cell box lengths as $a_P/a_G = 0.81$ and $a_D/a_G = 1.27$. (These ratios correspond to the oriented space groups for the single structures with symmetry groups $Pm\bar{3}m$, $Fd\bar{3}m$, and $I4_132$ for the P, D, and G structures.) While it is not a physical transformation (as intermediate structures are self-intersecting and not embedded), the specific "Bonnet ratio" of lattice parameters as given above is often observed in lipid systems that form two of the P, D and G mesophases [57]. This Bonnet ratio can also help to relate and characterize structures. The D surfaces are not found to be stable and thus ignored here.

Tables 5.2 and 5.3 show values for surface area A, volume fraction u and mean curvature H for the G and P surface, which might especially prove useful for further liquid drop calculations. One can represent the various surfaces by the

Table 5.3: Surface area A_G and mean curvature H_G of the exact CMC and pasta gyroid surfaces for different mean densities ρ and corresponding volume fractions u. For the pasta shapes, the average mean curvature is given. The values t_G are the threshold values for the nodal representations of G in Eq. (5.3) with volume fractions u. The unit of length is the lattice constant.

ρ[fm^{-3}]	u	A_G		H_G		t_G
		CMC	pasta	CMC	pasta	
0.0326	0.22	2.61	2.84	1.96	1.85	0.86
0.0434	0.29	2.83	3.01	1.31	1.31	0.66
0.0543	0.37	3.00	3.25	0.74	0.75	0.41
0.0651	0.45	3.08	3.34	0.28	0.26	0.16
0.0715	0.50	3.09		0.0		0.0
0.0759	0.53	3.09	3.35	-0.15	-0.24	-0.08
0.0868	0.61	3.02	3.30	-0.62	-0.72	-0.34
0.0977	0.70	2.87	3.10	-1.19	-1.32	-0.60

simple *nodal* approximation [401] in terms of "potential" functions $\phi_i(x, y, z)$ with $i \in \{\mathrm{S}, \mathrm{P}, \mathrm{G}\}$. For structures scaled to lattice parameters $a = 2\pi$ one uses

$$\phi_S/\phi_0 = \cos x \,, \tag{5.1}$$

$$\phi_P/\phi_0 = \cos x + \cos y + \cos z \,, \tag{5.2}$$

$$\phi_G/\phi_0 = \cos x \sin y + \cos y \sin z + \cos z \sin x \,, \tag{5.3}$$

where ϕ_0 is some constant potential value. The slab (S) is generated by the potential from Eq. (5.1) producing parallel sheets of matter, also called "lasagna". The P surface, which is generated by the potential from Eq. (5.2), consists of a simple cubic lattice of rods in three orthogonal directions that have common crossing points. The G surface is produced by Eq. (5.3). The minimal surfaces are approximated by $\phi_i(x, y, z) = 0$ and the CMC surfaces by $\phi_i(x, y, z)/\phi_0 = \pm t$ (where t is the threshold value for the nodal representation, see Tables 5.2 and 5.3). For the volume fractions considered here, the differences between the nodal approximations and the exact CMC surfaces are negligible compared to the spatial resolution of the computational grid.

5.5.2 Stationary structures

The search for locally stable CMC configurations is done by biased initialization. First, Bastian Schütrumpf initializes the system with plane waves up to the wanted amount of protons and neutrons. For the first 1000 static iterations, he imprints a bias by adding an external guiding potential ϕ_i according to Eqs. (5.1)–(5.3)

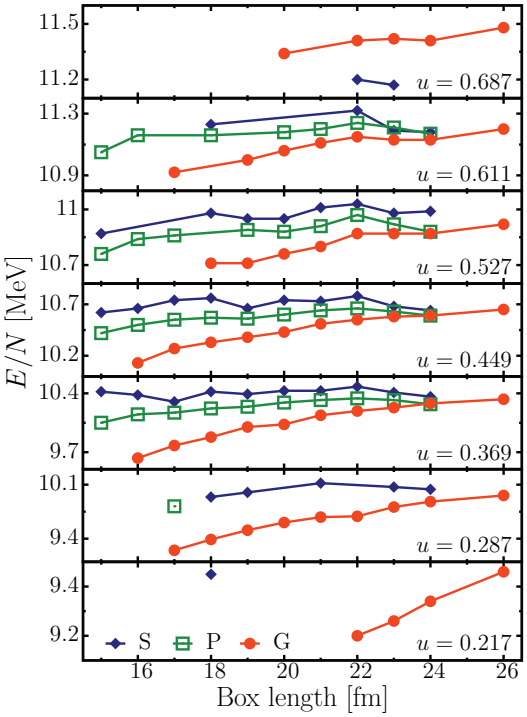

Figure 5.6: Binding energies per nucleon E/N for the metastable ground states for different volume fractions. G (gyroid, circles), P (primitive, squares), and S (slab, diamonds) denotes the initial guiding potentials. The states shown in this plot remained topologically stable for the 9000 iterations. Higher values of E/N correspond to more tightly bound and hence more favorable solutions.

with $\phi_0 = 10\,\mathrm{MeV}$. After these first 1000 iterations, he switches off the guiding potential and continues with 9000 further pure HF iterations. The system is then driving to a local minimum, not necessarily the ground state. If the stationary state thus found stays close to the intended structure, we consider this structure as (meta)stable.

The static HF calculations are repeated under various conditions of density and box size up to $a = 26\,\mathrm{fm}$. He found stable S, P and G structures, the latter both of the "single" type. The resulting energies are summarized in Fig. 5.6. The gyroid is stable for $a \geq 22\,\mathrm{fm}$ in the widest range of volume fractions compared to P and S. Binding energies of P and G exhibit a clear scaling with box length. For P, the binding energy has a maximum at $a \approx 22\,\mathrm{fm}$. Under the assumption that an effective description of the pasta Hamiltonian by curvature terms is possible, we expect that the G has a maximum binding energy at $a \approx 27\,\mathrm{fm}$ due to the Bonnet transformation. The binding energies for P at $a = 22\,\mathrm{fm}$ and G at $a = 26\,\mathrm{fm}$ are lower (and hence less favorable) than those for S, except for $u = 0.687$, but at this high volume fraction the rod(2) bubble shape (not shown here) has larger binding energies than both G and S. Note that the DG, whose energy was calculated in the liquid drop model [332, 333], is unstable in the TDHF simulations. Tables 5.2

and 5.3 show that the surface area A and the mean curvature H of the pasta G and P surfaces agree with the exact values, within the rough voxelization of the TDHF calculations. As an additional estimate of the error due to the voxelization of the gyroid, I discretize a gyroid with 20^3 voxels, like above, but shift[4] the voxels in x-, y-, and z-direction before applying the marching cube algorithm. There can be relative errors in volume and area up to a few percent. Because of the partially vanishing integrated mean curvature its relative error is not well defined; the absolute error is comparable to that of the area and perimeter. The integer Euler characteristic is very stable.

Using the Minkowski tensor anisotropy analysis, we find a slight but systematic deviation of G and P obtained in TDHF simulations from the nodal models: an anisotropic deformation of the interface surface. While the nodal surface models have cubic symmetry, the directional distribution of interfaces in TDHF simulations are slightly biased towards an axis, exposing more interfacial area in this direction that in the two perpendicular ones. The anisotropy index $\beta_1^{0,2}$ evaluated for a Marching cubes representation of the Gibbs dividing surface interface, adopts values not below 0.75 for G and values between 0.4 and 1 for P structures. The voxelization error of this anisotropy measure, estimated as described above, can only explain anisotropy indices larger than 0.9. Therefore, both the pasta gyroid and primitive structures are significantly anisotropic.

5.5.3 Dynamical stability

To look for dynamical formation and stability of the structures, Bastian Schütrumpf performed TDHF simulations with rather large excitation energies ($T \approx 7\,\mathrm{MeV}$). The mean density was fixed to $\rho = 0.06\,\mathrm{fm}^{-3}$. The box length was varied here in the range $a = 20$–$24\,\mathrm{fm}$. For each a, ten simulations were performed running over $1000\,\mathrm{fm/c}$. The final structure emerges typically after $400\,\mathrm{fm/c}$ and then stays stable, of course, as a fluctuating state.

A rich variety of complex pasta shapes emerges spontaneously, see Fig. 5.7, for which we quantify the connectedness by the Euler characteristic. Figure 5.8 shows the histograms of the Euler characteristic χ for all box lengths. All structures have negative Euler characteristic, implying that these are labyrinth-like structures; three examples of these complex networks of nuclear matter are depicted in Fig. 5.9. In the histogram of the Euler characteristic, $\chi = -2$ indicates P, $\chi = -3$ corresponds to mixed structures not discussed here, and $\chi = -4$ is a necessary condition for a gyroid. I finally identify a gyroid by trying to draw the gyroid nodal network through the void. We have indeed successfully found spontaneous formation of the

[4] The shifts are, of course, smaller than the size of a single voxel.

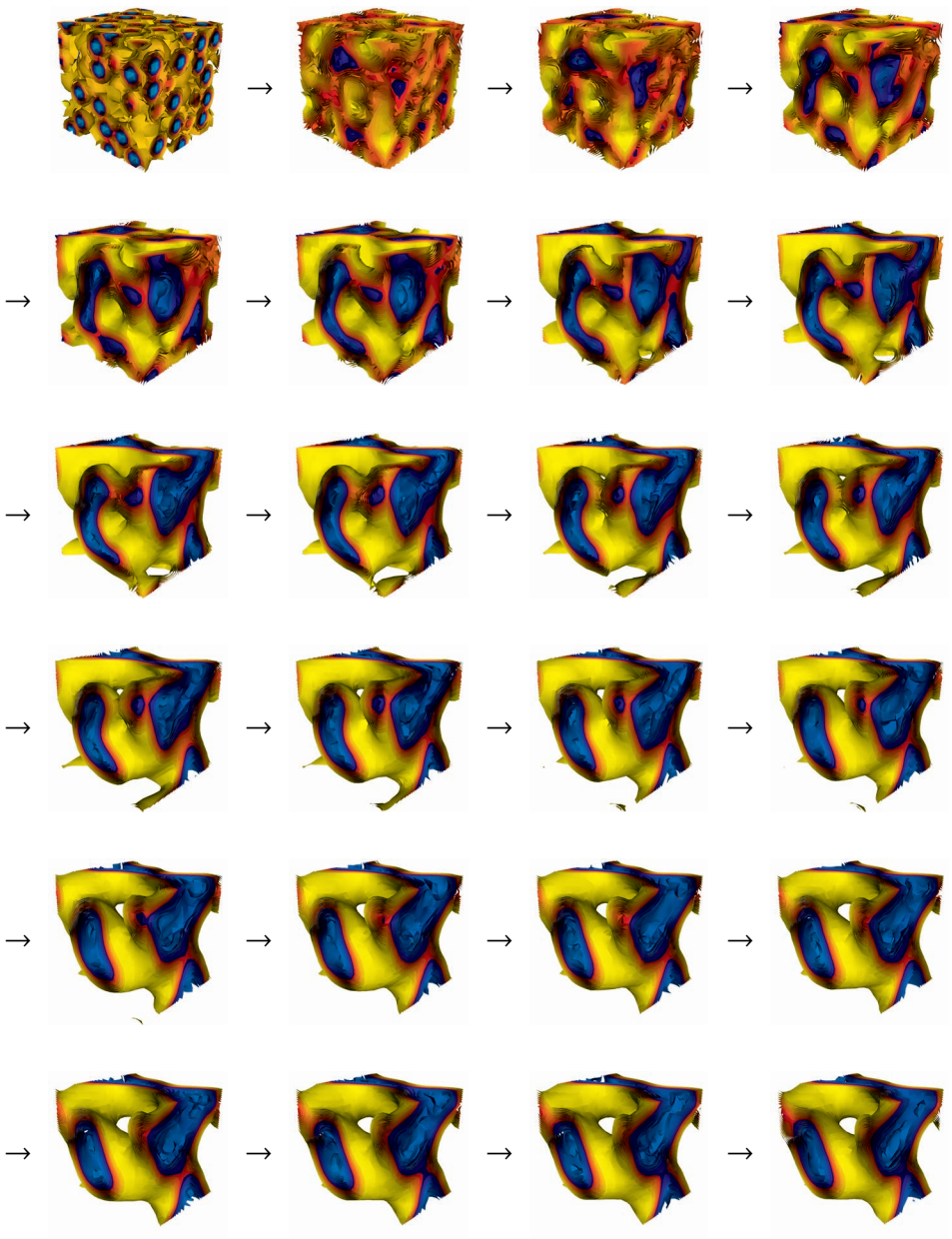

Figure 5.7: Spontaneous formation of a complex three-dimensional labyrinthine pasta shape, which is later identified as a gyroid network (bottom right), in the TDHF calculations, starting from homogeneously and randomly distributed α particles and neutrons (top left).

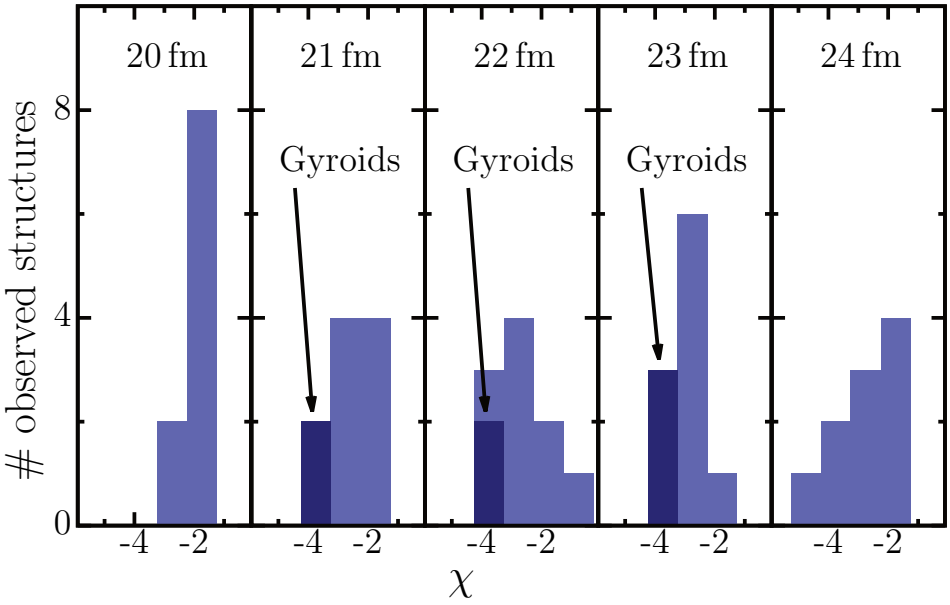

Figure 5.8: Histograms of the resulting Euler characteristic χ for different box lengths 20–24 fm of the dynamic, randomly initialized calculations. The shaded area marks the identified gyroid structures.

single gyroid structure, see Fig. 5.7. Figure 5.10 provides a graphical demonstration of this occurrence of a meta-stable gyroid phase in nuclear pasta. It shows the Gibbs diving surface and draws the liquid phase as filled, the gas phase as void (although in practice filled with some neutron dust). The network-like domain on the left-hand side of the figure represents the liquid (or high density) domain in full TDHF and subsequent SHF calculations whose shape and topology match closely those of one of the gyroid network domains (shown on the left-hand side of the figure). The remaining void space (the gas phase) forms a complementary network-like domain with the same topology, albeit of different volume fraction.

In Fig. 5.8, I have explicitly marked the gyroid structures by shaded areas. The figure demonstrates that a great variety of CMC structures can emerge spontaneously in a finite temperature calculation. Note in particular the repeated appearance of the involved, labyrinth-like single gyroid which thus demonstrates that it can be stable even under the extreme conditions of high temperature. As quantum shell effects disappear at temperatures $T > 2\,\mathrm{MeV}$ [82], we also can conclude that the appearance of a G structure is not determined by shell effects (may they be physical or spurious ones [340]). As expected, there is no chiral-asymmetry, i.e., we have both found left- to right-handed networks of the nuclear

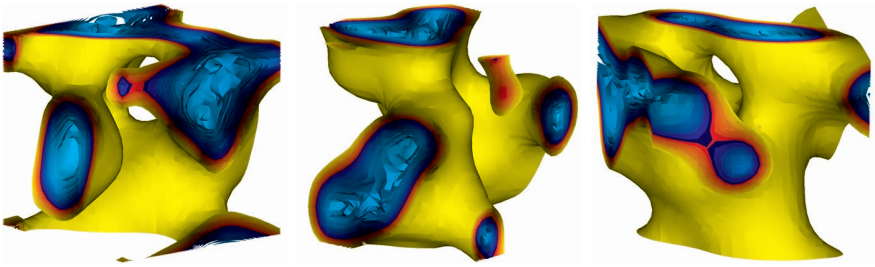

(a) (b) (c)

Figure 5.9: Dynamically formed intricate nuclear pasta labyrinths. Three independent TDHF simulations in a simulation box with (a) 22 fm box length or (b–c) 24 fm box length (different colors represent different isodensity surfaces).

liquid. Note that ten random samples per box do not provide sufficient statistics to compare quantitatively the abundances of the structures. The figure merely indicates their possible appearance even under these highly excited conditions.

Figure 5.11 shows a detailed Minkowski analysis of both a primitive and a gyroid structure. While the area is, as expected, decreasing, the area has a maximum at vanishing integrated mean curvature, because the minimal P- or G-surfaces with zero integrated mean curvature have the maximal area among the related CMC surfaces. Because of the negative Euler characteristic and the Steiner formula, the integrated mean curvature increases. For both the primitive and the gyroid structures it changes sign as a function of the threshold density ρ_{th}. Therefore, the classification scheme from Table 5.1 must be extended. To distinguish the P- from the G-surface the absolute value of the Euler characteristic has to be taken into account: $\chi(P) = -2$ and $\chi(G) = -4$. Like in the static simulations, both the primitive and the gyroid structure are strongly anisotropic; the latter is even more anisotropic. The anisotropy index is independent of the threshold density, which is another hint that this is an inherent feature of these pasta shapes. However, the directions of the eigenvectors seem to be isotropically distributed; see Fig. 5.11 (c). There is no systematically preferred orientation.

The dynamical simulations thus have delivered a couple of (highly excited) G structures. It is interesting to recover stationary G structures by starting with static HF from the dynamical states. To that end, we take the final states of a TDHF simulation as the initial states for an SHF ground state iteration. Doing this for the dynamical G configurations, three cases out of seven remain gyroidal. The binding energies of the cooled gyroidal structure are close to those from purely static calculations. For example, for $a = 22$ fm we find $E/N = 10.357$ MeV from cooling the dynamical state versus $E/N = 10.377$ MeV from purely static HF.

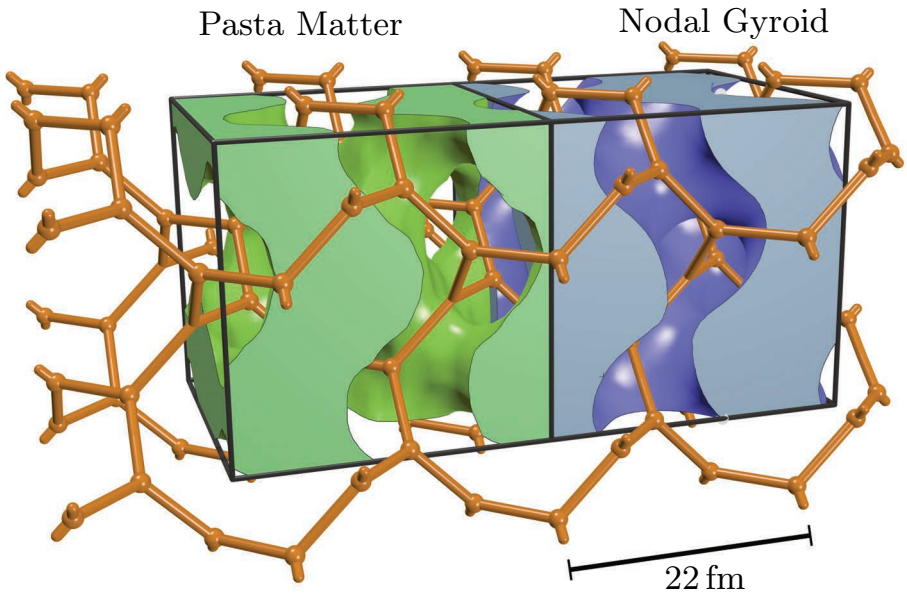

Figure 5.10: Gyroidal pasta shape: the green structure on the left-hand side represents the density distribution of the gyroidal state of nuclear pasta matter computed with TDHF for an average density of $0.06\,\mathrm{fm}^{-3}$ and a box length of $a = 22\,\mathrm{fm}$. Shown is the Gibbs dividing surface with a corresponding threshold density. The solid volume represents densities above this value, and the void represents densities below this value. The blue structure on the right-hand side shows the nodal approximation (5.3) of a single gyroid CMC surface at the same volume fraction. Also shown by orange bars is a gyroid network in the void phase of both the pasta shape and the nodal approximation, showing that they are indeed homotopic. The black frames are guides to the eye, of size $1.25\,a$, the cubic lattice parameter.

However, the "cooled" dynamical G is more anisotropic while its scalar Minkowski converge to those of the statically calculated G. The binding energy thus depends primarily on the scalar measures like surface area, curvature, and bulk volume and is rather insensitive to the deformation. We thus are probably dealing with a variety of isomeric G configurations. This is another interesting detail calling for further investigations.

5.6 Conclusions

We have investigated the appearance of nonhomogeneous structures in nuclear matter under astrophysical conditions, i.e., matter at sub-nuclear densities, tuning different average densities and temperatures, and paying particular attention to structures with network-like geometry and topology, amongst them as a particularly

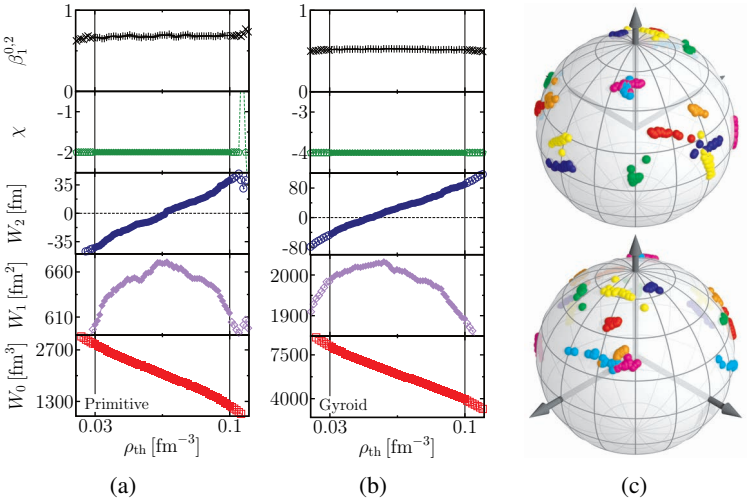

Figure 5.11: Minkowski functionals and anisotropy index of (a) the primitive and (b) the gyroid structure. For details, see Fig. 5.2. On the right-hand side (c), the directions of the eigenvectors of the Minkowski tensor $W_1^{0,2}$ of dynamical simulations of the gyroid structure are plotted as points on the unit sphere; top and bottom correspond to two different views on the same three-dimensional plot. Each color represents a different sample, for each sample all three eigenvectors are shown at different thresholds.

appealing shape is the single gyroid. To that end, Bastian Schütrumpf and his colleagues used static optimization as well as dynamical simulations within a self-consistent nuclear mean-field model (Skyrme-Hartree-Fock). In the TDHF simulations, the initial states evolve to a topologically stable state of pasta matter within about 1000 fm/c. This allows us to deduce a map of pasta shapes in the plane of temperature and density, see Fig. 5.4.

I characterize these rather involved three-dimensional structures by the Minkowski functionals, see Fig. 5.2. To the smooth density distributions, which cover continuously all values between zero and maximum density, a 0 to 1 step function is applied by setting a threshold density. The Minkowski functionals are considered as a function of this threshold density. Thus, we can classify the various shapes in the small simulation boxes in terms of a few key numbers, see Table 5.1. This allows, e.g., to discriminate reliably the different rod structures or to work out the smooth transition to uniform matter at high temperature. By taking the variance of the density profile as a complementing further observable, we can define a phase border between uniform matter and pasta shapes. The Minkowski functionals as functions of the threshold density also revealed hybrid pasta shapes, i.e., different topologies at different threshold densities, which hints towards a transition between

these phases, see Fig. 5.2(c). The Minkowski tensors have been introduced to nuclear physics as powerful measures of anisotropy revealing, e.g., significant distortions in the primitive and gyroid structures.

The Euler characteristic reveals a rich variety of labyrinthine pasta networks, see Figs. 5.8 and 5.9, and, moreover, allows to find pasta gyroids. To uniquely identify a gyroid, an additional subsequent graphical analysis has been performed. We have shown that single gyroid (G) structures indeed emerge in static and dynamical simulations, see Fig. 5.10. We have looked at further CMC surfaces and find close competition with the primitive (P) surface and the slab (S) while the diamond seems to play no role. The static calculations by the nuclear physicists reveal that G and P are mostly metastable while S usually provides the ground state, however, with only slightly larger binding energies, see Fig. 5.6. G and P, being triply periodic saddle surfaces, have maxima for the binding energies as a function of box length, for P at $a \approx 22\,\mathrm{fm}$ and for G predicted at $a \approx 27\,\mathrm{fm}$, assuming that the Bonnet transformation is applicable in this system. Dynamical simulations at high excitation energy produce several cases where these structures appear again. This indicates that these network-like geometries are rather robust in nuclear matter. We also find some static G structures with deformations that may be due to the fact that the surface energy is rather small under the given conditions, thus easily allowing deformed G isomers, see Fig. 5.11.

The large expense of these microscopic calculations limits presently the size of the affordable numerical box. This inhibits so far an unambiguous assessment by studying the trends with box sizes in larger ranges. The present results are, however, strong indicators for the appearance of CMC and particularly G structures that call for further studies.

It is especially interesting to study the neutrino cross section for the pasta shapes identified here through the Minkowski measures and to check whether the shapes are associated with corresponding typical patterns in the cross sections.

Chapter 6

Minkowski sky maps in gamma-ray astronomy[1]

Here, I turn from such small length scales as presented in the last chapter to the largest length scale in this thesis. I use the Minkowski functionals for a morphometric data analysis of gamma-ray sky maps. By characterizing the shape of a noisy sky-map more information can be taken out of the same data without assuming prior knowledge about the source, and formerly undetected sources are eventually detected by a refined structure characterization.

As shown throughout this thesis, the Minkowski functionals can efficiently, comprehensively, and robustly quantify the complex shape provided by spatial data [288, 406, 408, 410]. They allow for a powerful data analysis and a sensitive hypothesis test. Because of their versatility, they cannot only check for specific structures or arrangements but can detect any structural deviation from the expected background. In other words, they serve as unbiased detectors of source structure or in general of inhomogeneities in background noise and can extract the essential features.

The methods and concepts in this chapter are in principle applicable to any random field and any spatial data to detect inhomogeneities or other structural deviations. It could, for example, be interesting for medical data sets, e.g., in tumor recognition[2] [33, 315, 316], for geospatial data and raster data in earth

[1] This work was achieved in collaboration with Klaus Mecke, Christian Stegmann, Daniel Göring (see Ref. [161]), Bruno Ebner, and Norbert Henze. Parts of this chapter are direct quotes from our publications Refs. [162] and [245]. Some of the figures in this chapter and a table are reproduced from these references with permission ©ESO and AIP Publishing LLC.

[2] For example, Canuto et al. [93] and Larkin et al. [257] use Minkowski functionals to analyze inhomogeneities in magnetic resonance images to detect responses to treatments of tumors.

science [446], in image and video analysis, where a fast analysis for the detection of objects is needed [79, 236, 372, 520], or in the related field of pattern recognition [219, 456], see also Section 6.1.1. However, the technique is especially interesting for very high energy (VHE) gamma-ray astronomy, where faint extended signals are overlaid by strong background noise [88]. Especially, for short observation times and low statistics, i.e., when an increase in sensitivity is most needed, the advantage of additional, structural information should be most effective: the excess in the number of counts might not be significant because of the strong fluctuations of a Poisson distribution relative to the small mean value. However, the improbable spatial arrangement of the fluctuations can eventually lead to the detection of the source.

Daniel Göring and Christian Stegmann from the Erlangen Center for Astroparticle Physics (ECAP) and the High Energy Stereoscopic System (H.E.S.S.), Klaus Mecke, and I have developed a morphometric analysis which detects structural deviations from a uniform background noise [160–162, 243, 245]. The method was introduced in Ref. [160] and extended in Ref. [243]. However, because some details in the definition had to be modified and slightly corrected in a joint work of Ref. [161] and this thesis, Sections 6.1.1–6.2 provide an introduction to this reviewed morphometric analysis. Parts of this chapter have also already been published in Ref. [162]. Then, I discuss important properties and the behavior of the structure characterization and the morphometric analysis: the application of the marching square algorithm, and in Section 6.3, I provide a conservative yet tight estimate of the trial factor, which is needed because of the repeated hypothesis tests at different thresholds. In Section 6.4, the correction of detector effects is improved by introducing a local trial factor that can lead to a significant increase in sensitivity of the morphometric analysis if applied to real data.

The most intricate problem is a precise estimate of the joint probability distribution of the Minkowski functionals of a random field, which is a complex problem [448] and unsolved for many random fields. The calculation is based on the number of possible configurations which vary from $O(10^1)$ to $O(10^{64})$ for a 15×15 b/w image. My approach can in principle be used for more general random black and white pixelated images to efficiently calculate these probability distributions. Here, I use it to derive an accurate estimate of the structure of a discrete Poisson random field. I combine analytic knowledge of the structure distributions with a very efficient algorithm from statistical physics for estimating density of states, the so-called Wang-Landau algorithm, see Section 6.5.

This combination of analytic knowledge and numeric estimates allows to analyze larger scan windows up to 15×15 pixels that contains complex structural information in contrast to the so far accessible 7×7 windows. By that, I can finally

show the increase in sensitivity via structure quantification, see Section 6.6. By analyzing the same data simultaneously by all three Minkowski functionals instead of a simple structure characterization, the compatibility with the background structure can drop by 14 orders of magnitude, i.e., the probability to find such a fluctuation in the background is 10^{-19} instead of 10^{-5}. Formerly undetected sources can thus eventually be detected, which depends of course on the shape of the source whether there is a structural deviation or not.

I introduce a new test statistic in Section 6.7 which combines different thresholds leading, e.g., to a better detection of diffuse radiation. The morphometric analysis is then compared in Section 6.8 to a standard null hypothesis test in gamma-ray astronomy. The comparison depends both on the shape of the source and on the experimental details. An advantage of the morphometric analysis is that it is rather independent of the size of the scan window. Moreover, I discuss an example for which there is no significant excess in the total number of counts, but the source can still be detected because of the additional structural information. In Section 6.9, I analyze with a Minkowski sky map the extended VHE gamma-ray source RX J1713.7−3946 and the galactic center ridge observed by the H.E.S.S. experiment.

After the analysis of the probability distribution with high precision for high significance, I present in Section 6.10 now also in collaboration with Bruno Ebner and Norbert Henze from Karlsruhe a broader applicable approach combining analytic calculations of the covariances and empirical cumulative distributions, which can also be applied for very large windows and in principle to other applications with a less precise knowledge of the background structure, but it can still sensitively detect inhomogeneities in cases where there is no excess of the total number of counts.

6.1 Structure characterization

The aim is to develop a novel approach to spatial data analysis, especially in VHE gamma-ray astronomy, where extended sources are detected via morphometric measures.

6.1.1 Morphological data analysis in astronomy

Early studies in VHE gamma-ray astronomy focused on the study of point sources. For this purpose, highly efficient analysis techniques were established, such as the quantification of the significance of a photon count excess using a likelihood ratio method [273]. However, the increasing number of large extended sources [e.g.

18, 20] and first detection of diffuse VHE emissions [17] emphasize the need for new approaches that might be more suitable for extended structures.

While this additional information is negligible for point sources, it might provide a means to detect and study faint extended sources, which are too weak to be seen when looking at the number of excess photons only. However, note that because of the large point spread function in VHE gamma-ray astronomy even strong point sources are extended (Gaussian-shaped) sources and additional structural information may be available. An analysis based exclusively on the number of excess counts above the expected background level discards all information about the shape of the region where the excess is observed. Furthermore, it does not use the information of possible correlations of nearby excess regions.

A well-known approach to include all available information in an analysis is the full likelihood fit of a model to the measured data, as used by high-energy gamma-ray telescopes like EGRET [301] or Fermi/LAT [43]. While likelihood analyses are very powerful, they require extended a priori knowledge to build a proper model for the background and potential sources. The quality of a likelihood analysis is strongly influenced by the quality of the chosen models.

The morphometric analysis presented here incorporates the additional structural information of extended sources into an analysis without the need for prior knowledge about the source. In contrast to the full likelihood fit of a model, the morphometric analysis detects any significant structural deviation by comparing the structure of the counts map to that of the expected background, where a counts map is a binned sky map where to each bin the number of events k detected within this bin is assigned. To achieve this, a reliable and powerful technique for quantifying structures of gamma-ray counts maps is needed which is provided by the Minkowski functionals. They were already successfully applied in astronomy [e.g. 308]. They were used to investigate point processes in cosmology and the large-scale structure of the universe [104, 238, 239] and as probes of non-Gaussianity in the cosmic microwave background [127, 151, 399].

6.1.2 Shape of counts maps

This section describes the structure characterization of a gamma-ray counts map. While similar methods may be used to quantify the shape of extended gamma-ray sources, such an analysis is not performed in this thesis. Here, the shape of the counts map itself is characterized and compared to the structure of the background model in order to look for structural deviations.

The counts map is turned into a black-and-white (b/w) image via thresholding like the Gaussian random fields in Section 2.6 or the pasta matter in Section 5.3. It is, as stated above, a common procedure for the structure characterization of gray-

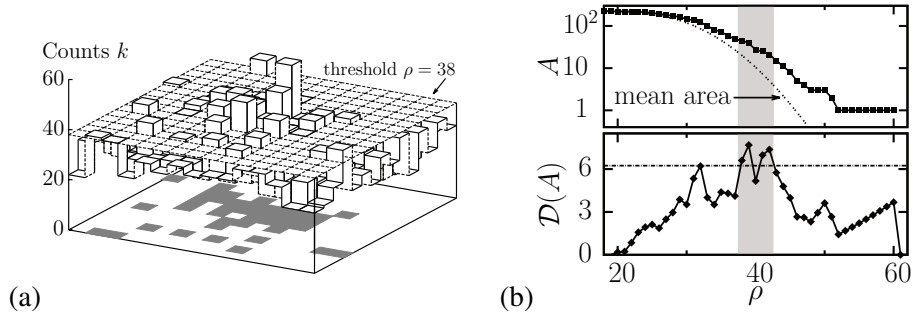

Figure 6.1: Structure characterization of a counts map: (a) The counts map is turned into a b/w image via thresholding. For each pixel the count of events k is compared to the threshold ρ: if $k \geq \rho$, the bin is set to black, otherwise to white. (b) Top: The Minkowski functionals characterize the shape as a function of the threshold—here w.r.t. the area of the black bins. Bottom: The deviation strength $\mathcal{D}$, defined in Eqs. (6.2) and (6.3), quantifies the difference to the expected background structure. Because $\mathcal{D}(\rho) > 6.2$ for thresholds ρ in the highlighted range, the null hypothesis that the events follow a uniform Poisson distribution is rejected.

scale images [8, 304, 305, 448]. For each threshold value ρ, all pixels with counts $k \geq \rho$ are set to black, the others remain white, see Fig. 6.1 (a). The structure of each b/w image is then quantified by the Minkowski functionals, e.g., in Fig. 6.1 (b) by the area. The area as a function of the threshold contains the knowledge about the number of counts. However, it does not supply any information about their arrangement, for which additional information is provided by the perimeter and the Euler characteristic.

Minkowski functionals The Minkowski functionals are useful shape measures for this data analysis, because of their additivity and continuity, they are robust against noise and have short computation times. There are several linear time algorithms for calculating the area, perimeter, and Euler characteristic [e.g. 288, 406] and for 3 D data [e.g. 36, 408, 410]. The straightforward and efficient linear time algorithm used here is based on Table 6.1[3]. The image is decomposed into 2×2 neighborhoods. The value of the Minkowski functionals is assigned to each of the 16 possible configurations. Because of their additivity, the sum of the local contributions yields their global value. The unit of length is defined as the edge-length of a single pixel, thus the area of a pixel is one. To avoid multiple countings when iterating over the whole image, only that part may contribute

[3] In Ref. [243], I provide look-up tables for the translational invariant Minkowski functionals and tensor $W_1^{0,2}$ for a 2 D black and white (b/w) image where the marching square algorithm has been applied. Further look-up tables are provided in Appendix B for motion covariant Minkowski tensors with the marching square algorithm being applied.

Table 6.1: Look-up table for Minkowski functionals: the functional values of area A, perimeter P, and Euler characteristic χ are assigned to each 2×2 neighborhood of the image. The unit of length is the edge-length of a pixel. Similar data can be found in [304] and [288].

Conf.		A	P	χ	Conf.		A	P	χ
1		0	0	0	9		1/4	1	1/4
2		1/4	1	1/4	10		1/2	2	-1/2
3		1/4	1	1/4	11		1/2	1	0
4		1/2	1	0	12		3/4	1	-1/4
5		1/4	1	1/4	13		1/2	1	0
6		1/2	1	0	14		3/4	1	-1/4
7		1/2	2	-1/2	15		3/4	1	-1/4
8		3/4	1	-1/4	16		1	0	0

which is unique to a 2×2 neighborhood, i.e., each quarter of the four pixels next to the center. For example, a single black pixel has area and Euler characteristic one and perimeter four. However, when iterating over the image, it appears in four different 2×2 neighborhoods, namely configurations two, three, five, and nine. Thus, Table 6.1 assigns to each of them area and Euler characteristic one fourth and perimeter one. The white pixel in configuration 15 can be interpreted as part of a hole; it contributes negatively to the Euler characteristic. In configurations seven and ten in Table 6.1 the black pixels sharing only a vertex are chosen to be connected. If they were disconnected, the weights for the Euler characteristic would be positive. The choice is arbitrary, as long as the probability distribution for the Euler characteristic is calculated consistently, because this is about identifying structural deviations from the background structure and not about the reconstruction of an original structure as stated above[4]. However, connecting the black pixels helps to distinguish a single cluster of black pixels from two domains distant from each other.

The choice of bin size is free, because a uniform Poisson field remains a homogeneous Poisson field for any choice of the bin size or point spread function; the null hypothesis is unchanged. However, to quantify features arising from a source and not merely random noise, the bin size should be adjusted to the point spread function.

Boundary conditions The boundary conditions can in general have a severe impact on the reconstruction of the unpixelated image and the estimate of, e.g., the

[4] For the same reason, the application of the marching square algorithm yields no significant increase in the sensitivity, which is shown in Section 6.2.3.

mean of the Minkowski functionals. Examples of boundary conditions are white, black, periodic, symmetric, or minus sampling. However, for the morphometric analysis this influence is limited as long as the analysis is consistent w.r.t. the boundary conditions, i.e., the correct boundary condition is used to determine the probability distribution of the Minkowski functional.

A detailed analysis in joint work with Daniel Göring showed that there are no significant systematic differences in the deviation strength; meaning that although the mean Minkowski functionals vary, the significance of the structural deviations is on average nearly unchanged [161]: although there might be slight differences in single realizations, we found no systematic bias between different boundary conditions.

However, there is a significant effect if minus-sampling boundary conditions are applied: in contrast to the area, the perimeter and the Euler characteristic take the boundary pixels into account. Thus, they access more data than the area. For sliding observation windows in an extended source, this can lead to huge differences in the sensitivity of the three functionals, mainly because of the better statistics and not because of the morphometric idea to gain an increase in sensitivity by characterizing the structure. In order to prove that an increase in sensitivity is due to the latter, open (white) or closed (black) boundary conditions have to be applied.

In Section 6.5, it is shown that for determining the probability distribution of the Minkowski functionals, the so-called density of states (DoS), i.e., the number of configurations for given area A, perimeter P, and Euler characteristic χ is needed. If the DoS for open boundary conditions is known, also the DoS for closed boundary conditions can easily be derived simply by inverting the whole image. If black and white pixels are interchanged, the perimeter P does not change, the area A is mapped to $N^2 - A$, and the Euler characteristic χ to $1 - \chi$. However, the definition of the Euler characteristic changes: for the white boundary conditions two black pixels only sharing a vertex are connected; if the images are inverted, the white pixels are connected instead.

The white boundary conditions help to identify large black clusters, i.e., regions of excess, and are thus preferable in the gamma-ray astronomy, where sources are to be detected against a constant background noise. In the following, white boundary conditions are applied except it is stated otherwise.

Pattern recognition In the sense of identifying structural features and comparing the match with expected features, the morphometric analysis is similar to statistical pattern recognition techniques [219, 456]. However, our approach is fundamentally different in that the Minkowski functionals allow for a simple, yet concise and

versatile structure characterization for very general random fields, in contrast to the feature extraction in pattern recognition which typically uses a variety of specialized or application-dependent features [171, 219]. Moreover, we are not applying one of the common machine learning algorithms [292] but determine the joint probability distribution of our geometric measures. Most importantly, our morphometric analysis uses a null hypothesis test, i.e., no prior knowledge about the source is needed, and the method is sensitive to any structural deviation from the background. We either accept the null hypothesis that there are only background sources or we reject it but do not choose an alternative theory. In contrast to that the pattern recognition divides the data into at least two classes and chooses between these [128].

6.2 Source detection

With the structure characterized by the Minkowski functionals, a null hypothesis test has to be defined to detect significant structural deviations from the expected background structure: both a global and a local test.

6.2.1 Global null hypothesis test

Structural deviations from the background structure are to be detected. Therefore, the characteristic structure of a background measurement has to be known. Because the Minkowski functionals quantify the shape, the probability distribution $\mathcal{P}$ of their functional values $X \subset \{A, P, \chi\}$ for a counts map of a background measurement is needed. The first step is to choose a suitable background model.

In general, determining $\mathcal{P}(X)$ is the most complex task in the morphometric analysis. A reasonable model for background counts in VHE gamma-ray astronomy is the assumption of homogeneously and isotropically Poisson-distributed counts in each bin of a sky map with equal area bins. This is because most background events in ground-based VHE gamma-ray astronomy are caused by VHE hadrons. These hadrons loose their direction correlations in interstellar magnetic fields and arrive at the Earth as a uniform flux of VHE particles from every direction. For a real measurement, the homogeneous and isotropic background is distorted by detector effects and nonuniform exposure of the sky. As I show in Section 6.4, the data can be corrected for these effects, i.e., the typical structure of a background measurement can be derived from the structure of a pure homogeneous and isotropic Poisson background.

The likelihood for the area A of the black pixels is a suitable introductory example; the probability distribution for each threshold ρ is given by the binomial

distribution

$$\mathcal{P}(A) = \mathrm{Binom}(A, p_\rho, N^2)\,,$$

where A is the number of black pixels, N^2 the number of pixels in an $N \times N$ sky map, and p_ρ the probability that a pixel is black, i.e., there are more counts or their number is equal to the threshold ρ. Assuming a Poisson background with an expected number of counts per bin of λ, p_ρ is given by

$$p_\rho = \sum_{i=\rho}^{\infty} \frac{\lambda^i}{i!} e^{-\lambda}\,. \tag{6.1}$$

The probability distributions $\mathcal{P}(A)$, $\mathcal{P}(P)$, and $\mathcal{P}(\chi)$ of the area, perimeter, and Euler characteristic, respectively, are plotted in Fig. 6.2 (a-c) for different probabilities p_ρ that the number of counts in a pixel is above the threshold ρ. For small N, these distributions can be found by evaluating all possible b/w images and inferring the distribution by counting equivalent pixel configurations.

Gamma-ray sources can be detected by looking for structures, which are very unlikely to be found if the hypothesis of a pure background measurement was true, i.e., assuming that there are only background events within the observation window. A probability measure that a given counts map with a structural characteristic X is compatible with this hypothesis may be defined as follows: The compatibility

$$C(X) = \sum_{\mathcal{P}(X_i) \leq \mathcal{P}(X)} \mathcal{P}(X_i) \tag{6.2}$$

is the probability that a less likely structure appears. Figure 6.2 (d) shows the compatibility $C(\chi)$ for the Euler characteristic from Fig. 6.2 (c).

The compatibility is defined following the scheme given in Ref. [341] to construct a most efficient hypothesis test. The form used here may be derived from the general scheme given in the paper by setting the supremum of alternative hypotheses to 1, i.e., imposing no constraints on alternative hypotheses. The hypothesis of a pure background measurement is rejected if the compatibility is lower than $0.6 \cdot 10^{-6}$. This hypothesis criterion is adjusted to the commonly used $5\,\sigma$ deviation; a normally distributed random variable deviates from the expected value by at least $5\,\sigma$ with a probability of approximately $0.6 \cdot 10^{-6}$.

Instead of dealing with tiny compatibilities, it is often more convenient to use the logarithm of this likelihood value or to define the deviation strength

$$\mathcal{D} := -\log_{10}(C)\,. \tag{6.3}$$

The null hypothesis is rejected if the deviation strength is larger than 6.2. Figure 6.1 shows for the introductory example the deviation strength w.r.t. the area as a

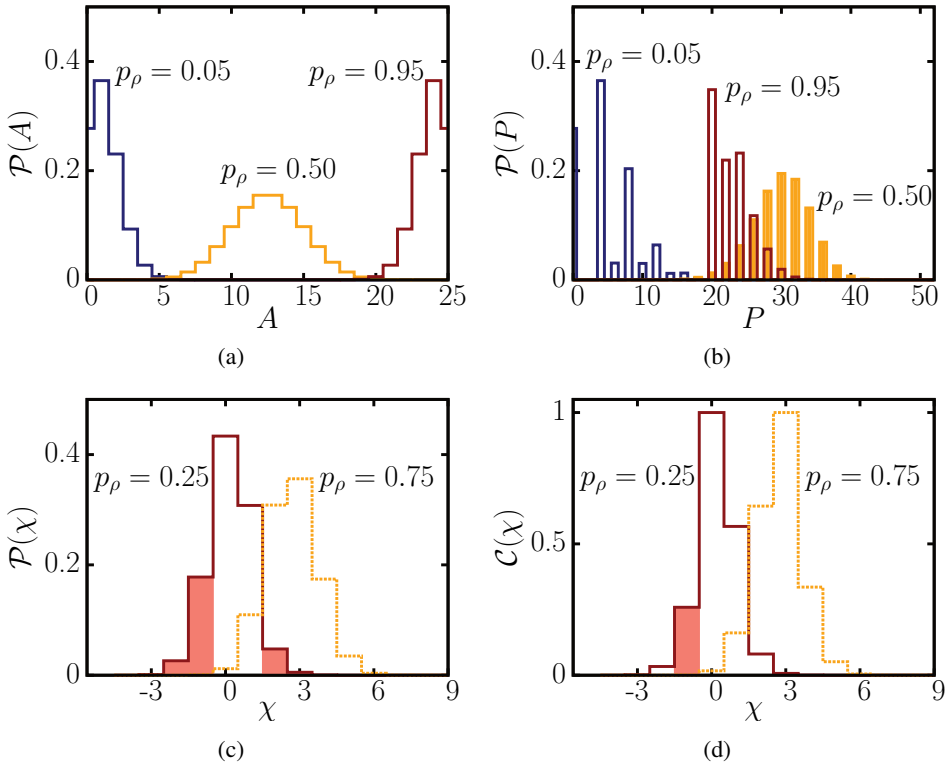

Figure 6.2: Structure of background noise for a 5×5 bin field at different thresholds ρ resulting in different probabilities $p_\rho = \sum_{i=\rho}^{\infty} \lambda^i \, e^{-\lambda} / i!$ for a black pixel. Probability distributions $\mathcal{P}$ of (a) area A; (b) perimeter P; (c) Euler characteristic χ. (d) Compatibility C of Euler characteristic χ, with $C(\chi = -1)$ the sum of all probabilities $\mathcal{P} \leq \mathcal{P}(\chi = -1)$, which is visualized by the equally large colored regions beneath the graphs in (c) and (d)—mind the different scales.

function of the threshold. A more formal definition of the morphometric analysis is given in Appendix A. The conversion between compatibility C and standard deviation σ is given by $C(\sigma) = \mathrm{erfc}\left(\sigma / \sqrt{2}\right)$, where

$$\mathrm{erfc}(x) = \frac{2}{\sqrt{\pi}} \int_x^\infty \exp(-t^2) \, \mathrm{d}t$$

is the error function.

Figure 6.3 depicts exemplary structure analyses of both a rather extended and of a more pointlike source, but their total flux is equal. The figure investigates simulated data of Poisson-distributed random number of counts. The deviation strength $\mathcal{D}$ is plotted over the threshold ρ. Because for both sources there are

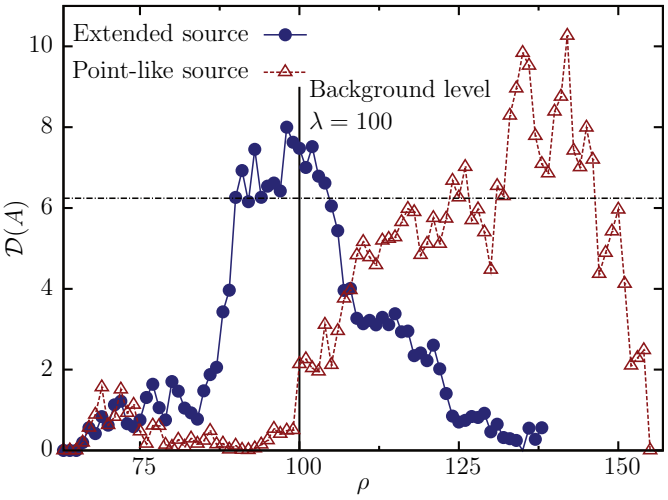

Figure 6.3: Deviation strength $\mathcal{D}(A)$ for structure quantification via area A as a function of the threshold ρ for an extended and for a point source of equal flux within an observation window of 100×100 bins.

thresholds for which the deviation strength is greater than 6.2, the null hypothesis of a pure background measurement can be rejected in either case. The results differ for the two sources and reveals basic information about the extension of the sources. The pointlike source cannot be detected at thresholds near the background level λ and is only apparent for high thresholds, i.e., only bins with high counts contribute to the detection. For the extended source only counts in the order of the magnitude of the background fluctuations are present in the sky map. However, as the number of bins with slightly increased counts exceeds the typical background predictions, the hypothesis is nevertheless rejected. The repeated null hypothesis tests at different thresholds can be taken into account by introducing a trial factor, see Section 6.3.

6.2.2 Local Minkowski sky maps

So far, it is possible to scan the entire field of view (FoV) of an observation for additional structures w.r.t. the expected background. To localize the deviations and thus locate gamma-ray sources and gain insight into their extension and structure, more information is needed. Owing to their motion invariance, the scalar Minkowski functionals cannot be used directly to localize structures.

Instead of analyzing the entire FoV with the methods introduced so far, a small sliding window may be used. This window can be moved across the FoV to study the local structure of the sky map in the sliding window. With this approach one can construct Minkowski sky maps from the counts maps that are just as useful as significance maps constructed using the approach from Ref. [273], but which provide the additional sensitivity from the structural information used to determine

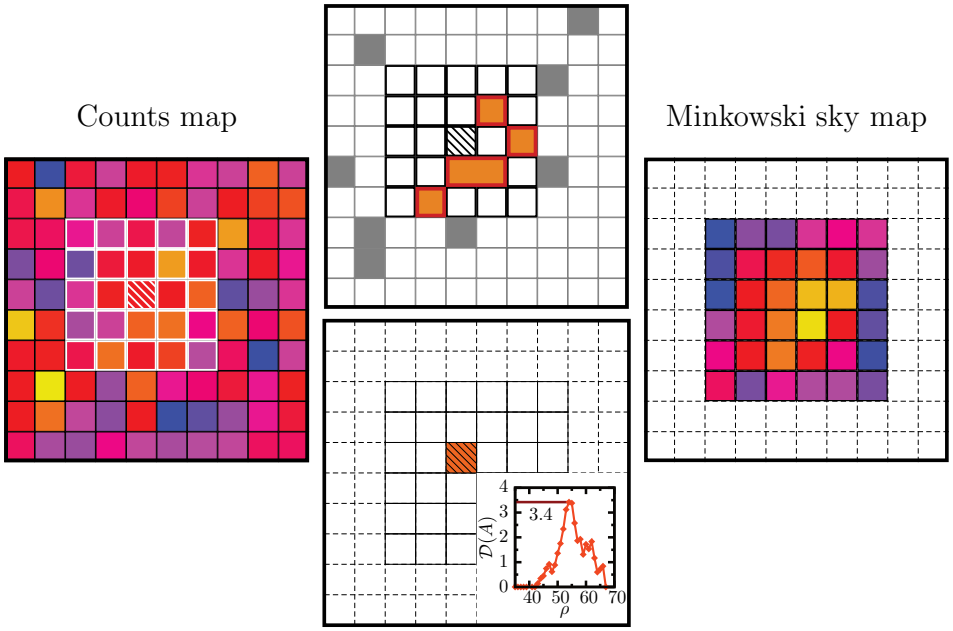

Figure 6.4: Computation of a Minkowski sky map: analyzing a given counts map (left), for each pixel the local structure within the sliding window is characterized (center, top) and the maximum deviation strength for all thresholds is assigned to it in the Minkowski sky map (center, bottom); iterating through all pixels provides the Minkowski sky map (right).

the deviation strength.

Figure 6.4 depicts the concept of a *Minkowski sky map*. For each of the inner pixels of the counts map the local structure is to be characterized (depicted on the left). Therefore, the Minkowski functionals of a sliding window with $N \times N$ pixels are evaluated (illustrated in the top picture in the middle of Fig. 6.4). The maximum deviation strength for all thresholds ρ is assigned to the pixel at the center of the sliding window (plotted in the bottom picture in the middle). Iterating over all inner pixels for which the sliding window is completely within the counts map provides the Minkowski sky map.

The information content and intuitive interpretation of such Minkowski sky maps can be enhanced by adding a sign to the deviation strength of the different pixels. By choosing the sign to be negative if $A < N^2 p$, i.e., if there are fewer black pixels than expected, and positive otherwise, the sign of a pixel shows if the local deviation is caused by an overestimation of the background or by additional flux from potential gamma-ray sources. Minkowski sky maps detect local structural deviations and depict them in an illustrative and quantitative image, depicting the lack of trust in the hypothesis that there are only background fluctuations. Although

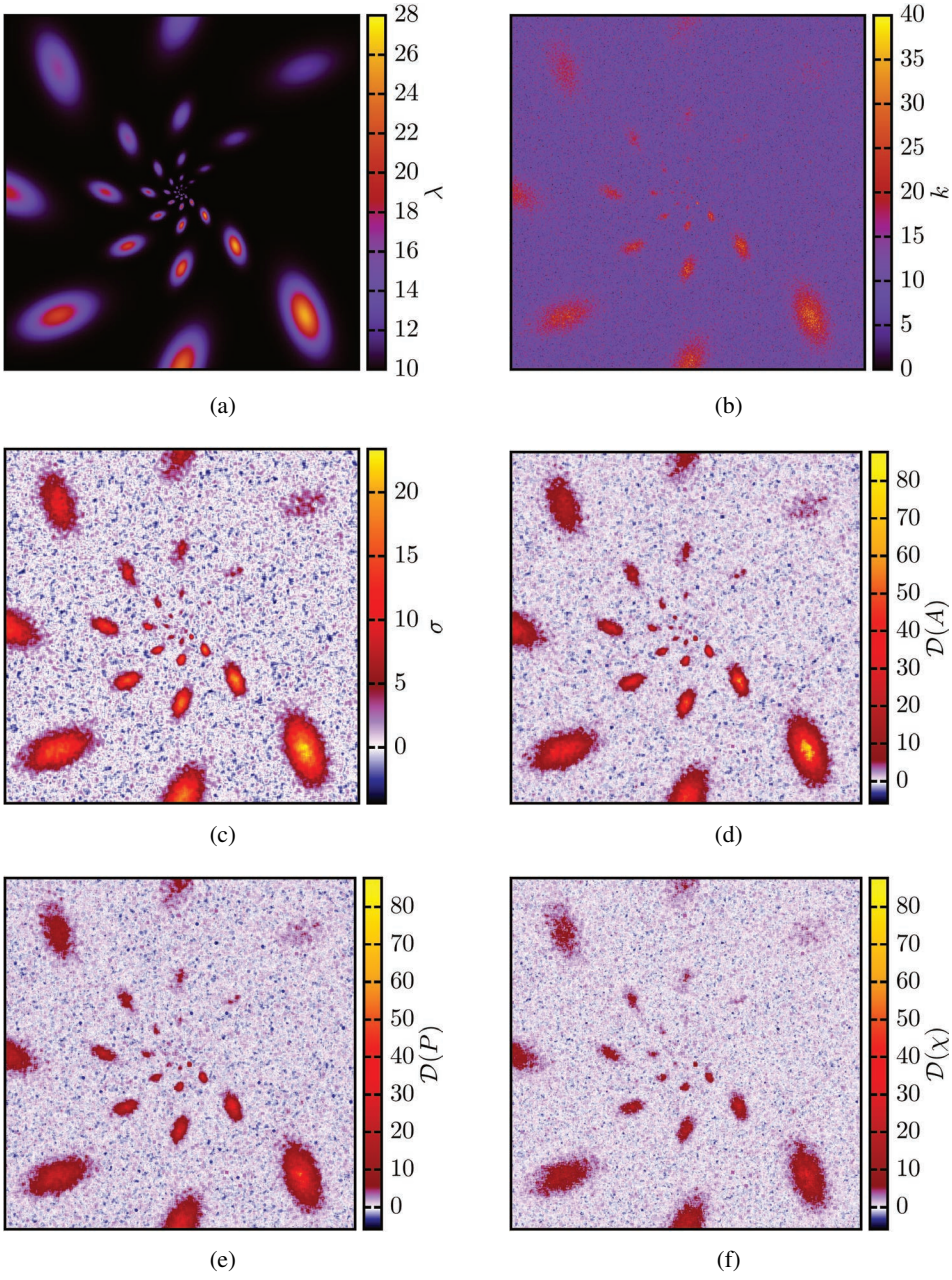

Figure 6.5: Structure analysis of simulated sky maps. (a) Given intensity profile. (b) Simulated counts map. (c) Significance map, evaluated with standard techniques, weighting the count excess. (d) Minkowski sky map; the structure is characterized with the area A, (e) the perimeter P, and (f) the Euler characteristic χ.

the null hypothesis is tested locally, the background assumption is a global null hypothesis, i.e., the expected number of counts per bin λ is chosen globally[5]. If λ is chosen locally for every sliding window, structures larger than the sliding window may result in an increased λ and in no deviation at all if the local structure is homogeneous and isotropic within the sliding window.

It is now possible to detect, localize, and study the shape of gamma-ray sources using the morphometric analysis with Minkowski sky maps. Figure 6.5 depicts an analysis of exemplary simulated data. Figure (a) shows the given intensity profile of the test pattern sources, the expected number of counts per bin caused by the chosen sources. The test pattern consists of Gaussian-shaped extended sources with a ratio of the semi-major axes of 2. The peak intensities of the sources along a central ray from the image center are equal. The sizes of sources with the same distance from the center are equal, and the peak intensities are increasing in counter-clockwise direction. Figure 6.5 (b) is the simulated counts map, which is then analyzed in (c–f). In Figure (c) the standard analysis technique of Li and Ma [273] as used by the H.E.S.S. experiment [cf. 16] is applied to the counts map (b) for comparison; for more details see Section 6.8. Figures (d–f) are the Minkowski sky maps with a sliding window size 5×5; the structure is quantified by either the area A, the perimeter P, or the Euler characteristic χ. The same 5×5 window is used as *on*-region for the significance determination using Ref. [273].

The first apparent result drawn from Fig. 6.5 is that the single functionals and the standard analysis are similarly sensitive to sources; area, perimeter, and Euler characteristic are comparably competitive in finding gamma-ray signals.

6.2.3 Marching square algorithm and pixelation

The structure characterization described in Section 6.1.2 uses a simple pixelation of the excursion set of which the Minkowski functionals are then calculated. A bit more complex reconstruction of the unpixelated excursion set is provided by the marching square algorithm, which assigns polygons with probably diagonal faces[6] to each 2×2 neighborhood [288]. In this case, the look-up table needs to be adjusted for the calculation of the Minkowski functionals[7], which can be found in Ref. [243], and the probability distributions of the Minkowski functionals must be

[5] Although the background intensity must be estimated and chosen globally, detector effects can be corrected locally, which can lead to a significant increase in sensitivity as I show in Section 6.4.

[6] Diagonal faces are for example needed for an improved estimate of the Minkowski tensors, otherwise there would be only four possible directions of the normal vectors on the boundary [243].

[7] In Ref. [243], I provided also a look-up table for the translational invariant Minkowski tensor $W_1^{0,2}$. In Appendix B, I also present look-up tables for motion covariant Minkowski tensors.

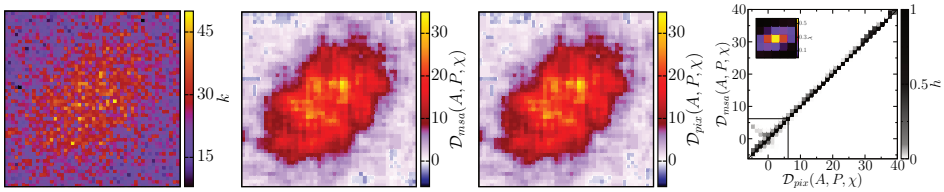

Figure 6.6: Influence of the marching square algorithm on the analysis of an exemplary source: (a) counts map; (b) Minkowski sky map with 5×5 scan window analyzing a pixelated b/w image or (c) a polygon from the marching square algorithm; (d) joint frequency $h := \text{Freq}\left(\mathcal{D}_{msa}(A,P,\chi)|\mathcal{D}_{pix}(A,P,\chi)\right)$ of the deviation strength using the marching square algorithm and the deviation strength analyzing pixelated images for an exemplary source (intensity profile in inset) in a 5×5 observation window.

calculated consistently[8].

Figures 6.6 (a)–(c) compare the analysis of an exemplary simulated source both with the pixelated and with the marching square analysis for a 5×5 sliding window. There is no difference in the deviation strength. Also the systematic analysis of the conditional frequency in Fig. 6.6 (d) shows that at least for small window sizes the two methods provide nearly the same result. So, the prospects of finding a significant effect for larger windows is also low, but the effort would increase tremendously compared to pixelated images. So, from now on I only consider pixelated b/w images. The simple pixelation is actually a fast and efficient tool for the morphometric analysis.

In Fig. 6.6, I already use the joint structure characteristic by area A, perimeter P, and Euler characteristic χ. A more detailed discussion of the calculation of the probability distributions and a comparison of the joint characteristic by all three functionals to that of only the area is given in detail in Sections 6.5 and 6.6.

6.3 Trial correction

The maximum of the deviation strength $\mathcal{D}$ as a function of the threshold ρ is used for the final hypothesis test. Therefore, a trial correction is needed to avoid overestimating the significance of the detected deviations, because of the repeated trials at different thresholds. Taking the maximum of the deviation strengths[9] over

[8] In agreement with Ref. [243], I use in this subsection minus-sampling boundary conditions, which means that the outermost rows and columns are used as boundary conditions.

[9] The trial correction is prior to the assignment of a sign for the illustration of the Minkowski sky, so only the magnitude of the deviation strength is considered $\mathcal{D} > 0$.

all thresholds corresponds to repeated null hypothesis tests for the different b/w images. Each b/w image can be seen as a single trial, but the more trials, the higher the probability for a significant random fluctuation. Because the different b/w images are constructed from the same count map, they are obviously closely correlated, which reduces the trial effect. Deriving the exact distribution of maximum deviation strengths is, however, not analytically solvable. A 15×15 count map with not more than 100 counts in each bin has 10^{450} possible configurations.

However, by assuming that the different b/w images are independent of each other, a conservative estimate of the trial correction can be derived: given n_t independent trials, the probability to find a compatibility lower than α is for each single b/w image α; the probability to find no such deviation in any of the n_t independent trials is $(1-\alpha)^{n_t}$. Thus, the probability to find at least one trial with a compatibility lower than α is given by

$$\alpha_{n_t} = 1 - (1-\alpha)^{n_t} .$$

For $\alpha \ll 1 : \ \alpha_{n_t} = n_t\alpha + O(\alpha^2)$, i.e., the influence of the repeated trials can simply be taken into account by multiplying the compatibility with a constant, the so-called trial factor n_t. The deviation strength is corrected by

$$\mathcal{D}_{n_t} = -\log_{10}\left(1 - (1 - 10^{-\mathcal{D}})^{n_t}\right), \tag{6.4}$$

which is for a large deviation strength ($\mathcal{D} > 3$) well approximated by a constant offset: $\mathcal{D}_{n_t} \approx \mathcal{D} - \log_{10}(n_t)$.

Setting n_t equal to the number of different thresholds provides a simple and conservative estimate. Figure 6.7(a) shows the Empirical Probability Density Function (EPDF) of the maximum of the deviation strength for different intensities and differently large observation windows derived from 10^8 Poisson fields for each system. Even a constant upper bound on the number of thresholds $n_t = 200$ provides a close upper bound for the trial correction. Therefore, in this thesis with intensities well below $\lambda = 200$, the maximum of the deviation strength $\mathcal{D}$ over all thresholds is corrected for this trial effect by mapping to $\mathcal{D}_{n_t} = -\log_{10}\left(1 - (1 - 10^{-\mathcal{D}})^{n_t}\right)$ in Eq. (6.4) with $n_t = 200$. The EPDF of this trial corrected deviation strength is plotted in Fig. 6.7(b). It is compared to the probability density function of the deviation strength $\mathcal{D}(\rho)$ of a single trial at threshold ρ, i.e., the actual claim of significance. Only in the case of nearly perfect agreement with the background structure, i.e., for $\mathcal{D}_t < 0.05$ (see inset), the empirical distribution has a strong peak. For all deviation strengths of interest, the estimate of $\mathcal{D}_t$ is conservative yet relatively close to the optimum (dashed line).

Note that the fluctuations of the distribution at relatively small deviation strengths are no statistical fluctuations but are reproducible features of the actual distribution which is very irregular because of the finite system size.

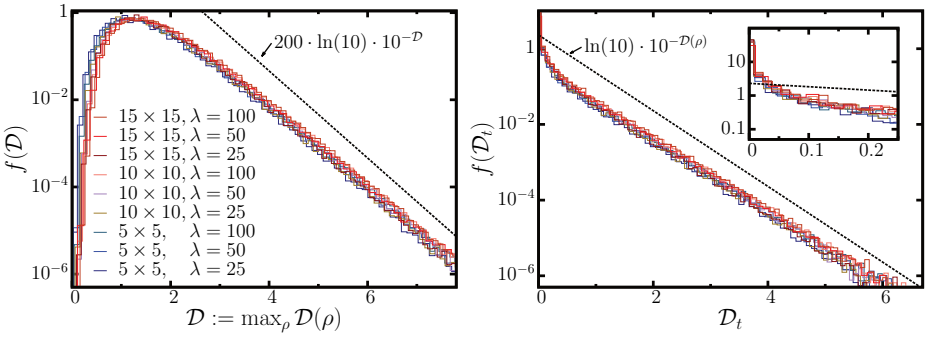

Figure 6.7: Trial correction: (a) Empirical Probability Density Function (EPDF) of the maximum of the deviation strength for pure Poisson background signals at different intensities λ and in differently sized observation windows. The dashed line shows an upper bound for the distribution of the deviation strength; for large $\mathcal{D}$ this corresponds to the distribution of the maximum of 200 trials, which is in this thesis an upper bound on the number of thresholds; (b) EPDF of the trial corrected deviation strength $\mathcal{D}_t$ using Eq. (6.4) with $n_t = 200$. The dashed line shows the probability density function of the deviation strength $\mathcal{D}(\rho)$ of a single trial at threshold ρ. Inset: close up of the peak at $\mathcal{D}_t \to 0$.

If the deviation from the background structure is quantified only by the area or also by the perimeter and by the Euler characteristic, the trial factor can slightly change, because the probability that there is a deviation in at least one of the Minkowski functionals is slightly larger than the probability that there is a deviation only in the area. Therefore, the above simulations of the distribution of the deviation strengths are evaluated w.r.t. all Minkowski functionals[10], to make sure that the trial correction is indeed conservative.

In order to compare the joint deviation strength, i.e., w.r.t. all Minkowski functionals, to the simple deviation strength w.r.t. only the area, I also numerically determine the distribution of the simple deviation strength and compare whether there is a significant difference in the trial factors. Figure 6.8 shows both the distributions of the trial-corrected simple and joint deviation strengths. The binned distribution of the simple deviation strength, as depicted in Fig. 6.8, is very irregular; be reminded that these are not statistical fluctuations, but reproducible features of the complex distribution function, which is even more irregular than

[10] While for a 5×5 observation window, the joint probability distribution of the Minkowski functionals can be calculated by simple iteration over all possible b/w images. For the larger windows, e.g., 15×15, a much more intricate derivation is needed which can distinguish states with $O(10^{64})$ realizations from those with only a unique representation; as mentioned above, this problem is solved in Section 6.5.

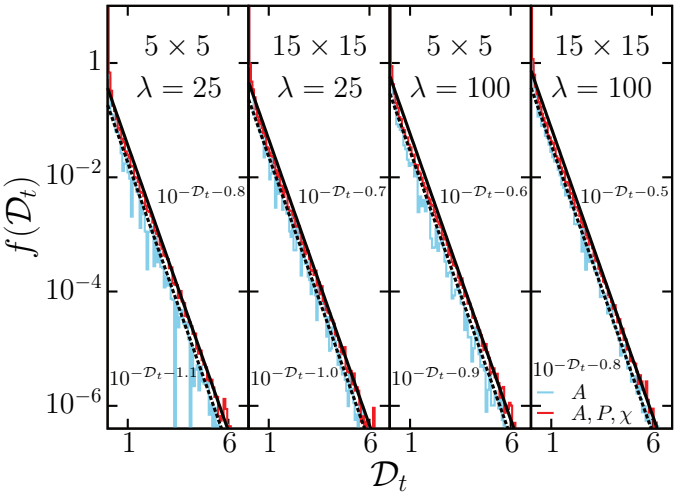

Figure 6.8: Comparison of the simple and joint deviation strength: empirical probability density f of the trial corrected deviation strength $\mathcal{D}_t$ w.r.t. only the area (A) or all three Minkowski functionals (A, P, χ), respectively. For the different system sizes and background intensities λ, the distributions are approximated by shifted exponential distributions $\ln(10)10^{-\mathcal{D}_t-c}$.

the distribution of the joint deviation strength, because of the significantly smaller number of macrostates. For different system sizes and background intensities, the distributions are approximated by shifted exponential distributions $\ln(10)10^{-\mathcal{D}_t-c}$, where $c = \mathcal{O}(1)$ measures how conservative the above described trial correction is. The difference in c for the simple and for joint deviation strength is only about 0.3, which is neglected in the following. This small systematic uncertainty must, strictly speaking, be taken into account if the joint and the simple deviation strength are compared in Section 6.6. However, the increase in the deviation strength because of the joint structure characterization of all Minkowski functionals is much larger, and the smaller offset 0.3 is negligible.

For convenience and because all results in the following are trial corrected and there is no ambiguity, I drop the subscript t, which indicates the trial correction, i.e., $\mathcal{D}$ is used from now on instead of $\mathcal{D}_t$.

In Section 6.7 however, I define a new test statistic that includes the sum of the deviation strengths of all thresholds. For this test statistic, no analytic derivation of the cumulative distribution function is possible, so I determine the empirical cumulative distribution function and no trial correction is needed. Note that this approach also accurately assesses the nonsignificant fluctuations.

6.4 Detector acceptance correction

An analysis of real data must also take the spatially varying detector acceptance into account. After modeling the camera acceptance, the effect must be corrected for to regain an isotropic and homogeneous structure for background measurements.

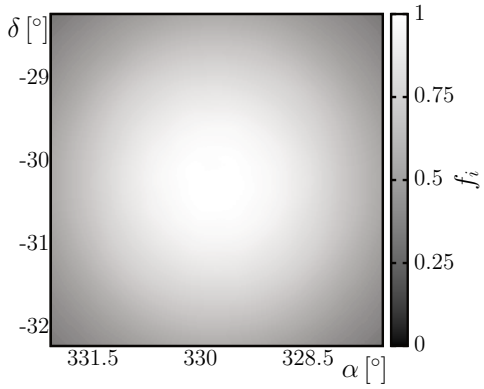

Figure 6.9: Exemplary acceptance map of a H.E.S.S. VHE gamma-ray observation; from observations of the source PKS 2155−304 [3, 14, 15, 19, 21–23]; the data is kindly provided by the H.E.S.S. collaboration.

For each bin i only a fraction f_i of the signals are expected to be detected; see Fig. 6.9. If each bin is simply weighted with $1/f_i$, fractional photon counts occur that destroy the Poisson structure of the sky map.

6.4.1 Monte Carlo observations

The null hypothesis, that is, that for an ideal camera acceptance there is only background noise with intensity λ, allows an acceptance correction, which preserves the Poisson structure. Because only the fraction f_i of the events in bin i are detected, the actual background intensity $\lambda_i = f_i \cdot \lambda$ varies with each bin. Following the null hypothesis, that the number of counts is a Poisson-distributed random variable with mean value λ_i, the original random process with mean value λ can be regained if a new Poisson-distributed random variable (a Monte Carlo observation) with mean value $\lambda_i^+ = (1 - f_i) \cdot \lambda$ is added, which was derived in Ref. [160].

In the center of the field of view, where $f_i \approx 1$, the number of counts remains effectively unchanged. For $f_i \ll 1$, the additionally created pseudo-photon counts may cover features, but they never introduce additional structural deviations from the homogeneous isotropic Poisson field because they fulfill the given null hypothesis by construction. Covering regions of low acceptance with a layer of pseudo-events corresponds to the fact that the instrument is less sensitive to signals in these regions than in regions with high acceptance.

6.4.2 Postselection

If there is a strong pointlike source within the field of view, it needs to be subtracted from the data in order to detect diffuse gamma-ray signals, i.e., broad sources in the same field of view [17]. For the morphometric analysis, a naive multiplication with a factor is not appropriate, because instead of a homogeneous Poisson field this

would produce fractal counts. Therefore, I introduced in Ref. [243] a postselection, which is based on a new null hypothesis that there is no additional source, i.e., that there is only a uniform Poisson noise with intensity λ in each bin and the predicted pointlike source with an intensity Λ_i in some bins i. On average, the number of counts must be reduced by a factor of $\lambda/(\lambda + \Lambda_i)$. However, the reduction must maintain the integer number of counts. This is achieved by a Monte Carlo postselection of the signals: only n of the k measured signals is kept, where n follows a Binomial distribution with probability $\lambda/(\lambda+\Lambda_i)$. I showed in Ref. [243] that the resulting random field is indeed a homogeneous Poisson field with intensity λ where the estimate is conservative and thus stable against errors in the model of the pointlike source.

6.4.3 Combined postselection and MC observations

The detector acceptance correction by adding Monte Carlo signals to gain a homogeneous Poisson field can be very conservative, especially in regions of very low acceptance $f_i \ll 1$, see Fig. 6.9. An additional Poisson random number suppresses the detection of a significant excess or structural deviation in the actual counts.

To improve upon this, Reference [161] combined the Monte Carlo observations and the postselection: the signals are not on average filled up to the original expected intensity λ, but to a chosen level $f \cdot \lambda$, where f is in-between the maximum and minimum acceptance. For bins with $f_i < f$ MC observations are added to the data set, on average $(f - f_i)\lambda$ events are added, and for bins with $f_i > f$ the signals are reduced via the postselection as described above, on average f/f_i signals are kept. By setting f to the corresponding value f_j in the region of interest, a nearly optimal detector acceptance correction can be achieved for a limited region with $f_i \approx f_j$. However, for the rest of the observation window the estimate is still very conservative.

6.4.4 Local detector acceptance correction

The sensitivity of the morphometric analysis can be tremendously increased by changing from a global detector acceptance correction as described above to a local detector acceptance correction. Instead of correcting the detector acceptance globally and prior to the construction of the Minkowski sky map, it is performed separately and independently for each position of the sliding window: given the acceptance f_i of the central bin of a sliding window, the target intensity is chosen to be $f_i \cdot \lambda$ and the original observed counts map is corrected by the combined postselection and MC observation. Thus, for each sliding window an optimal acceptance correction is performed. Additionally, this slightly decreases

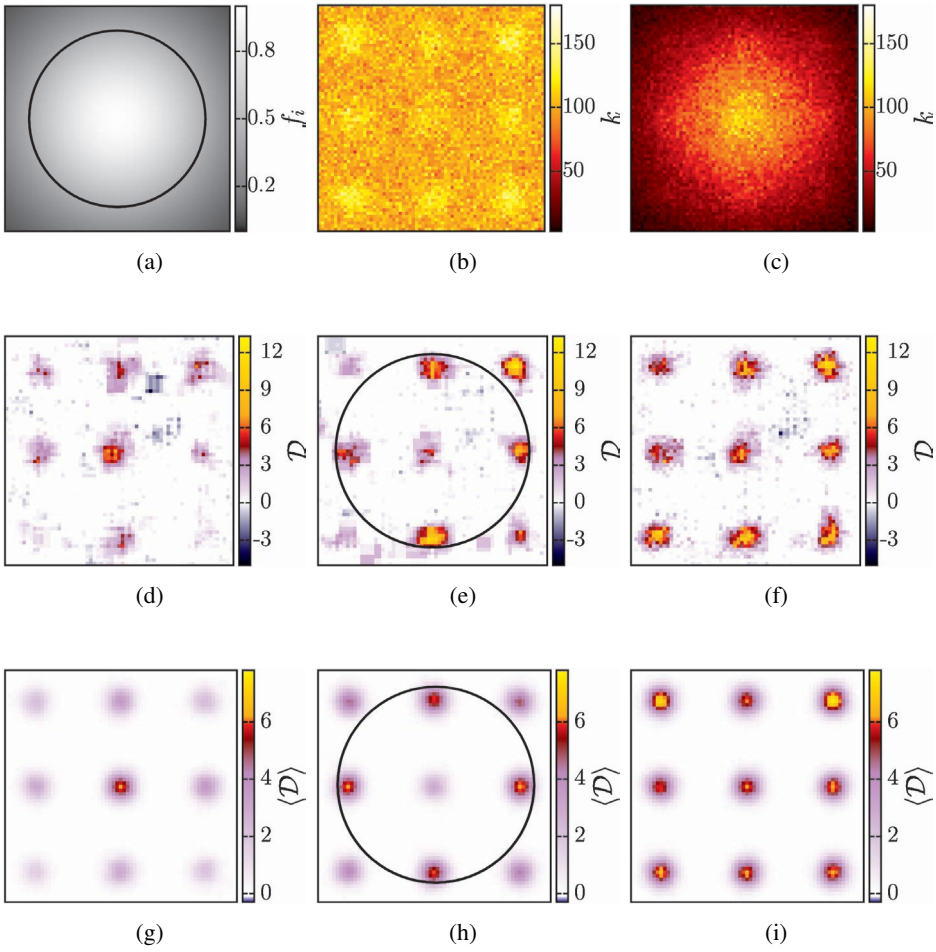

Figure 6.10: Detector acceptance correction: (a) acceptance map f_i; (b) unreduced simulated count map; (c) counts are randomly reduced according to acceptance map; (d–f) Minkowski sky maps analyzing the count map depicted in (c) for which the acceptance is corrected (d) globally via Poisson filling, (e) globally via both Poisson filling and postselection with the target intensity $\lambda/2$ (the corresponding region is indicated by a black circle), and (f) locally; (g–i) for each pixel an average over 100 Minkowski sky maps is shown where the acceptance is corrected (g) globally via Poisson filling, (h) globally via both Poisson filling and postselection with the target intensity $f_i = 0.5$, and (i) locally. Only if the acceptance is corrected locally, can in this example a single Minkowski sky map detect all sources at any distance to the center.

the correlation between the deviation strength of overlapping observation windows, because the random variables of the postselection and MC observation, i.e., the added or subtracted counts, are different.

The huge gain in sensitivity is demonstrated for simulated data in Fig. 6.10. The detector acceptance is approximated in this simulation by a Gaussian with $f_i = 1$ in the center of the sky map and the line of half-maximum indicated as a black line in (a). First, a count map is simulated at a homogeneous Poisson background with intensity 100 and with nine differently strong sources at different distances to the center, see Fig. 6.10 (b). Then, for each pixel only a fraction f_i of the counts are accepted according to (a). The resulting count map is depicted in (c). Figures 6.10 (d–f) are Minkowski sky maps based on the area, the perimeter, and the Euler characteristic analyzing the count map in figure (c). The sliding window size is 6×6. Because the reduction and Poisson filling at very low intensities can strongly fluctuate, 100 Minkowski sky maps are averaged in each pixel in Figs. 6.10 (g–i).

If the whole count map is corrected for a homogeneous Poisson field with background intensity λ by filling with Poisson counts, see Figs. 6.10 (d,g), only the central source is detected. The other source signals are overwhelmed by the additional simulated Poisson signals. If a target intensity $\lambda' = \lambda/2$ is chosen and a homogeneous Poisson field is regained under the null hypothesis via both Monte Carlo observations and postselection, see Figs. 6.10 (e,h), only the sources in the region of the target intensity can be detected; if there is slight offset, the sources are hardly detected. The sources in the corners can only be detected in single samples where the source signals are by chance very strong. Also the source in the center, where there is originally a perfect detector acceptance, is no longer detected. However, if the detector effects are corrected locally, see Figs. 6.10 (f,i), the improved background correction allows to detect all sources at any distance to the center in a single Minkowski sky map.

Because for each pixel in the Minkowski sky map the hypothesis test is performed for a different background intensity, the probability that a pixel is black at a given threshold varies for all sliding windows. Therefore, the probability distribution of the Minkowski functionals has to be determined separately for each sliding window. Therefore, the computation time strongly increases compared to the former detector acceptance corrections with a global background intensity. However, if there are strong detector effects and the analysis is supposed to detect more than just an expected pointlike source at a known position, the local detector correction introduced here can provide a tremendous increase in sensitivity that justifies this additional computational effort.

6.5 Structure probability distributions

The most difficult part of the morphometric analysis is to determine the joint probability distribution of the Minkowski functionals. Often in stochastic geometry, only first and second moments of distributions are determined because the analytic calculation, as well as a precise numerical estimate of the probability distribution, is a very complex problem [8, 448].

For the homogeneous Poisson field, this task can be reformulated as a question for the "Density of States" (DoS) Ω which is defined as the number of different b/w images ("microstates") with the same Minkowski functionals ("macrostate"). The probability $\mathcal{P}(A, P, \chi)$ to find a configuration with area A, perimeter P and Euler characteristic χ is then given by

$$\mathcal{P}(A, P, \chi) = \Omega(A, P, \chi) \cdot p_\rho^A \cdot (1 - p_\rho)^{N^2 - A}, \tag{6.5}$$

with $p_\rho = \sum_{i=\rho}^{\infty} \frac{\lambda^i}{i!} e^{-\lambda}$ being the probability that a pixel is black. In contrast to the probability distribution, the density of states is independent of the probability p_ρ that a pixel is black, i.e., of the intensity λ and the threshold ρ. Thus, if the density of states is known, the probability distribution can easily be calculated for any observed values of the Minkowski functionals.

For small window sizes up to 6×6, this problem can be solved by simply computing the Minkowski functionals of all possible b/w images. However, the total number of microstates increases super-exponentially $\sum_{A,P,\chi} \Omega = 2^{N^2}$; for 6×6 the total number of states is already $\sum_{A,P,\chi} \Omega = 68.719.476.736$.

Using combinatorial techniques from the theory of partition numbers, an algorithm can be constructed whose complexity only increases sub-exponentially in the number of bins [161]. However, the need of memory very quickly outgrows today's available hardware. The density of states can be determined only for up to a 7×7 observation window.

However, it is crucial to use larger observation windows, because only those can incorporate considerable structural information leading to a significantly more sensitive hypothesis test. Already for small sliding windows, there is a slight increase in sensitivity if the source has strong structural features within the sliding window, e.g., a strong intensity gradient like a Gaussian peak with an extension smaller than the window. However, only hints towards a strong sensitivity increase could be found. All attempts to determine the DoS of larger windows failed.

The DoS for larger systems cannot be determined analytically, but only numerically. However, a simple Monte Carlo simulation, which estimates the DoS of a macrostate by the frequency of its appearance in a simple sampling of the space of microstates, is not sufficient. Although a configuration might be entropically

suppressed in the simple sampling, i.e., it might be a very unlikely configuration of the excursion set of a Poisson background noise, it might be likely to appear in the presence of a source. If such a yet unknown macrostate is detected, it will result in an infinite deviation strength because the numerical estimate of the compatibility is zero. The missing configurations thus produce unacceptable artifacts in the Minkowski sky map and the null hypothesis is no longer well-defined[11].

An intelligent algorithm is needed, which is, e.g., able to give for a 15×15 observation window a reliable estimate for both macrostates with a DoS $O(10^{64})$ and for those with a DoS of $O(1)$. We had the idea to, therefore, use the so-called Wang-Landau algorithm developed in condensed matter physics for studying phase transitions and critical phenomena [499, 500].

It uses a non-Markovian random walk to efficiently sample the DoS; by continuously adjusting the density of states a locally flat histogram is achieved. More precisely, it samples the space of microstates according to a probability distribution that is inverse to the DoS. Thus, each macrostate is encountered equally often, which is called flat histogram sampling. The a priori unknown DoS is estimated by gradually improving an initial estimate, which is why the algorithm is non-Markovian. The initial estimate can, for example, be a constant for all macrostates, which corresponds to no initial information.

Using the Wang-Landau algorithm in this thesis finally allows to determine the joint probability distribution of the Minkowski functionals for a Poisson field up to a 15×15 observation window with a very high precision, which is well suited for very accurate hypothesis tests in gamma-ray astronomy.

6.5.1 Wang-Landau algorithm combined with analytic DoS

The Wang-Landau algorithm uses a random walk through the space of macrostates, the so-called energy space, where the microstates are, e.g., black and white images. The energy space is scanned by randomly changing the microstate, e.g., randomly changing the pixels from black to white and vice versa [255, 475]. In each step,

[11] Only if an accurate estimation of the probability distribution of the Minkowski functionals at a single threshold is known and the deviation strength is thus well-defined, a simple Monte Carlo simulation can be used to determine the trial factor, see Section 6.3. However, in Section 6.10, another test statistic is defined based on the covariance of the Minkowski functionals of a Poisson random field. It is well-defined for all possible values of the Minkowski functionals because it only measures the deviation of the measured to the expected Minkowski functionals, which is then weighted by the covariance. In this case, a simple Monte Carlo simulation can be used to determine the quantiles, but on modern computers this is limited to a deviation strength of about nine.

the numerical estimate of the density of states $\hat{\Omega}$ is adjusted[12]: if the resulting macrostate is (A, P, χ), then $\hat{\Omega}(A, P, \chi) \to f \cdot \hat{\Omega}(A, P, \chi)$. A finite modification factor f introduces a systematic error and has to decrease during the simulation. Steps to macrostates with a smaller density of states are always accepted, but changes which result in a macrostate with a larger density of states are only accepted with a probability that is proportional to the ratio of the density of states:

$$\text{Prob}_{\text{accept}}\left[(A_1, P_1, \chi_1) \to (A_2, P_2, \chi_2)\right] = \min\left\{1, \frac{\hat{\Omega}\left(A_1, P_1, \chi_1\right)}{\hat{\Omega}\left(A_2, P_2, \chi_2\right)}\right\} .$$

Thus, a flat histogram in the energy space, i.e., the number of visits of macrostate, is achieved. If the histogram is sufficiently flat, e.g., if the minimum value is at least 80 % of the average, the modification factor is replaced by its square root.

For the morphometric analysis, I replaced the energy by a macrostate characterized by the area A, the perimeter P, and the Euler characteristic χ. However, the simple implementation where each step changes the color of a random pixel is too inefficient for finding the DoS of all three Minkowski functionals A, P, and χ. The configuration space is too large and converges too slowly on modern hardware, e.g., for a 15×15 b/w image there are about a million macrostates, i.e., possible values of area, perimeter, and Euler characteristic[13]. Moreover, the probability distribution is not normalized, which could lead to an unknown systematic error.

I achieved the important breakthrough by incorporating the analytically known number of configurations with a given area A, the binomial coefficient $\binom{N^2}{A}$: instead of randomly choosing a pixel and changing its color, the number of black pixels, i.e., the area A, is fixed and a random black pixel is chosen and randomly shifted to a formerly white pixel; the black pixels perform random jumps. Note that the scanning of the energy space is still ergodic although each simulation is restricted to a subset because the calculations are repeated for every possible value of the area $0 \le A \le N^2$. Because of this separation of the energy space into disjoint subsets, the DoS has to be determined only w.r.t. the perimeter and the Euler characteristic. For example for a 15×15 window, the number of macrostates given the number of black pixels remains below 10^4, two orders of magnitude smaller than the number of all macrostates defined by area A, perimeter P, and Euler characteristic χ. Moreover, less memory is needed, and further optimizations are possible which further decrease the computation time by at least one order of magnitude. Depending on the number of black pixels, a single simulation needs

[12] Thus, detailed balance is not fulfilled, i.e., the probability of changing from state i to state j and is different to changing from j to i. Solutions to this problem exist, but the violation of detailed balance is of no relevance in this application.

[13] Compare to the number of possible values of the area alone: 225.

from a few minutes to about two days on a single core of Intel Xeon E3-1280 processor (3.5 GHz). The separate simulation for different areas A also allows for a trivial and thus perfect parallelization. Very importantly, the probability distribution is now perfectly normalized: following from Eq. (6.5)

$$\begin{aligned}\sum_{A,P,\chi} \mathcal{P}(A,P,\chi) &= \sum_{A=0}^{N^2} p_\rho^A \cdot (1-p_\rho)^{N^2-A} \sum_{P,\chi} \Omega(A,P,\chi) \\ &= \sum_{A=0}^{N^2} p_\rho^A \cdot (1-p_\rho)^{N^2-A} \cdot \binom{N^2}{A} = 1\end{aligned} \tag{6.6}$$

because I use $\sum_{P,\chi} \Omega(A,P,\chi) = \binom{N^2}{A}$ as a normalization of the DoS for a given area A. Moreover, for either small or larger values of the area A, the DoS can be determined analytically, which is, e.g., very important for pointlike sources, which result in a few black pixels at high thresholds. Using this trick, I determined the DoS for scan windows up to 20×20, i.e., for systems with up to 10^{120} microstates. However, for this thesis 15×15 windows are sufficient. The method is applicable to any boundary condition. Here, the calculations are carried out for open boundary conditions.

6.5.2 Saturation of error

Belardinelli and Pereyra showed that the original algorithm does not converge, but the systematic error saturates [62–64]. They show that is could be corrected for in an optimal way by choosing the modification proportional to the inverse of time. However, in this thesis it is sufficient to use the standard algorithm, but instead of taking the square root if a flat histogram is reached, f is only replaced by $f^{0.7}$. With these parameters, the systematic error then remains well below the statistical one. Figure 6.11 shows estimates $\hat{\Omega}$ of the DoS as a function of the modification factor f for several macrostates for different window sizes and number of black pixels; in each case 20 independent estimates are shown. The insets show the onset of the saturation of error at $f < 10^{-7}$. So, the simulation is stopped if the modification factor drops below 10^{-7} before the error saturates. For the smaller systems, the outcome is compared to the analytic result (dashed lines). Averaging over several independent simulations leads to reliable estimates of the DoS.

The final numerical estimates of the DoS $\hat{\Omega}$ are averaged over eight independent simulations for each number of black pixels. The relative statistical error of $\hat{\Omega}$ is $O(10^{-3})$. The compatibility is the sum of probabilities of many macrostates, see Eq. (6.2); therefore, the relative error of the deviation strength is even some orders

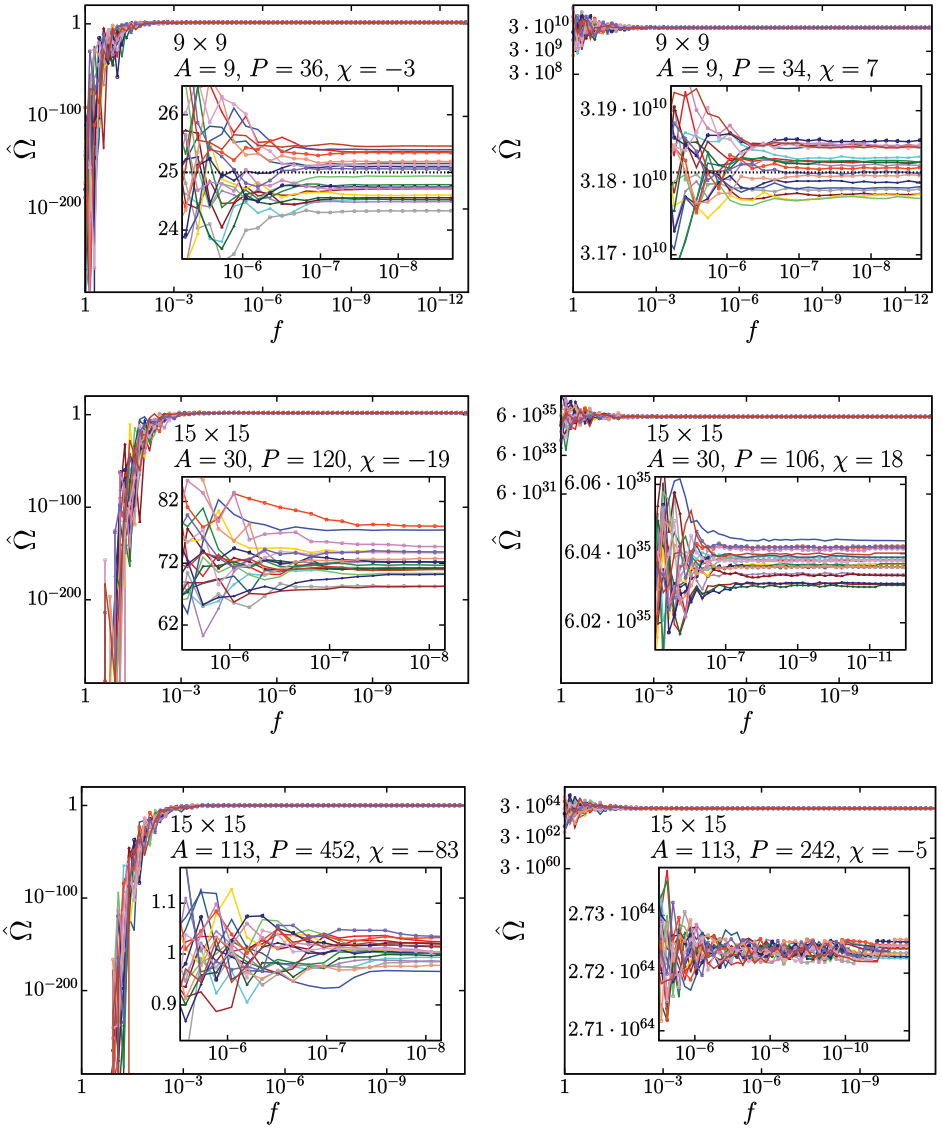

Figure 6.11: Saturation of error for the Wang-Landau sampling: numerical estimate $\hat{\Omega}$ of the DoS as a function of the modification factor f that decreases when the histogram of the macrostates gets sufficiently flat. Each subfigure shows the estimates of 20 independent simulations for a different macrostate; these macrostates were chosen because they have minimum or maximum $\hat{\Omega}$ for the given window size and number of black pixels. The dashed lines in the top figures are the analytic DoS.

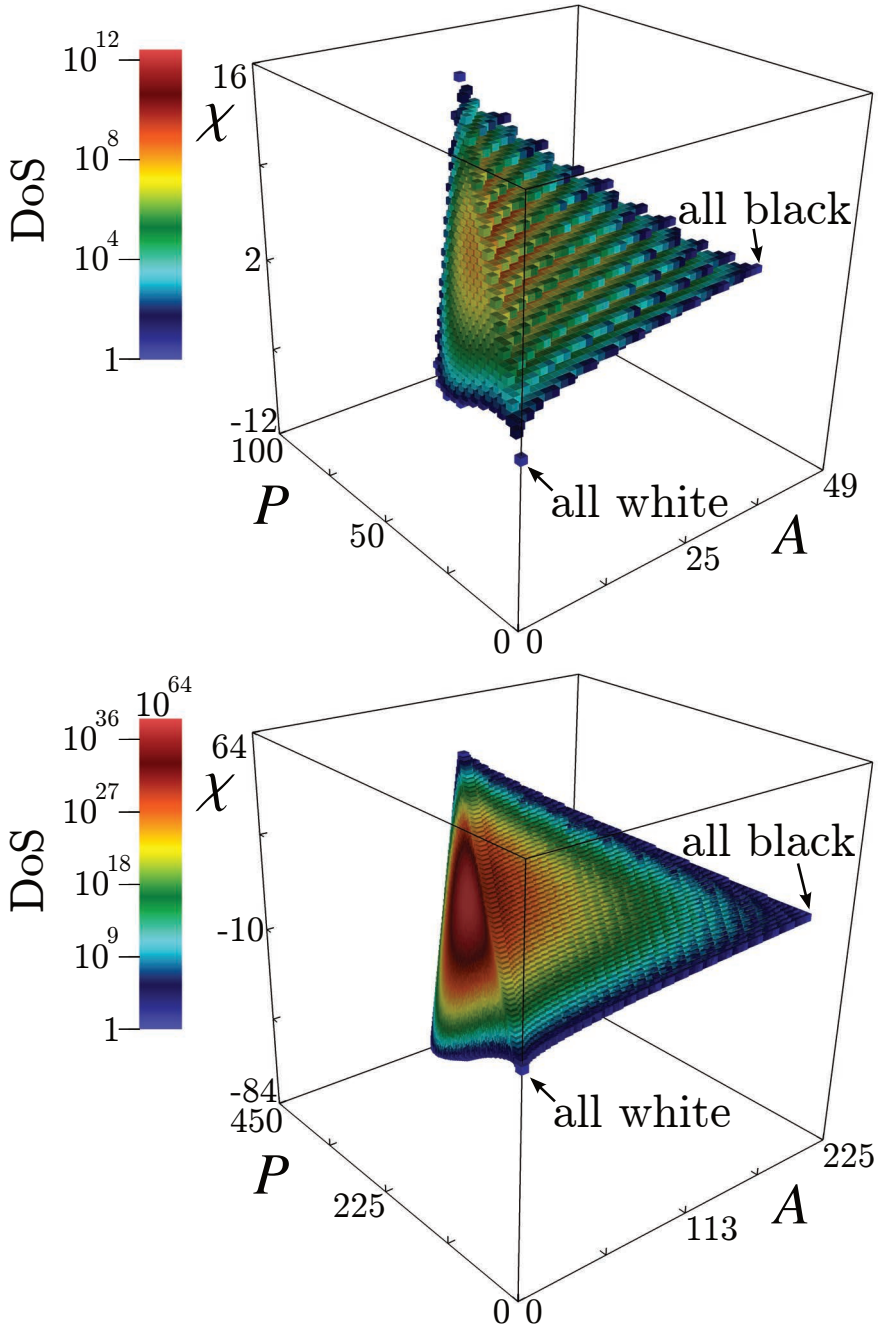

Figure 6.12: Density of states (DoS): the number of b/w images for a given area A, perimeter P, and Euler characteristic χ with open boundary conditions: at the top, for a 7×7 window; at the bottom, for a 15×15 window. For the latter, the color code saturates at 10^{36}. The unit of area is a pixel.

of magnitude smaller. The trial factor simulations in Fig. 6.7 in Section 6.3 finally show the reliability of the numerical estimate of the DoS.

6.5.3 The density of states for large observation windows

I accurately estimated the DoS of area A, perimeter P, and Euler characteristic χ for all window sizes between 5×5 to 15×15. For the smaller systems, the calculation was carried out analytically via the above-described brute force approach, for larger systems the DoS was estimated using the Wang-Landau method. The whole computation time for all systems was about 2.3 years on a single core of an Intel Xeon E3-1280 processor (3.5 GHz).

Figure 6.12 shows the DoS for a 7×7 or a 15×15 observation window, respectively. Each voxel represents a macrostate, and the color code plots the DoS. Note that this plot visualizes the complete structure of a Poisson random field w.r.t. the Minkowski functionals. The DoS reveals interesting bounds on the possible values of area, perimeter, and Euler characteristic, which would be interesting for a further analysis of the geometrical properties of a Poisson random field. There are also complex features like steps and discrete jumps between allowed macrostates; note that these are no artifacts but appear due to the finite system size. Most interesting for the morphometric analysis, the DoS seems to converge fast to an asymptotic distribution that might be estimated from the known distributions. This would allow for a global analysis of the joint deviation strength for whole observation windows or even a galactic scan. At least, this could be used as an initial estimate of the DoS for the Wang-Landau algorithm which would lead to a very fast convergence even for huge system sizes.

6.6 Sensitivity increase via structure characterization

Although the morphometric analysis is a promising and innovative spatial data analysis and has many advantages mentioned above, no strong sensitivity increase could be proven in former attempts to arise because of an improved structure characterization, i.e., a more sensitive test by all three Minkowski functionals instead of only one functional which then detects formerly undetected sources. Here, I finally show that by succeeding to determine the DoS of larger scan windows I can indeed gain a distinct sensitivity increase via the joint structure characterization of all three Minkowski functionals.

The deviation strength $\mathcal{D}(A)$ w.r.t. only the area is the following called “simple deviation strength”, while the deviation strength $\mathcal{D}(A, P, \chi)$ w.r.t. the complete characterization via all three Minkowski functionals is called “joint deviation strength”.

6.6.1 Examples of Minkowski sky maps

In order to compare the simple to the joint deviation strength, I define a test pattern including sources of different sizes and different integrated fluxes and thus simulate count maps, see Fig. 6.13(a).

The count map is both analyzed by a Minkowski sky map of the simple and the joint deviation strength, see Figs. 6.13(b) and 6.13(c), respectively. Note that the sources are much weaker than in the test pattern in Fig. 6.5. This is because the 15×15 sliding window uses more statistics than the small 5×5 sliding windows. Therefore, weaker sources can be detected against strong background noise[14].

Similar to Section 6.4.4, also the average over 100 Minkowski sky map analyzing different simulations is plotted for a more systematic comparison, i.e., to prove that the better sensitivity is not a coincidence, but a true gain in sensitivity, Figs. 6.13(d) and 6.13(e).

The simple deviation strength is on average only significant for the strongest sources or in single simulations if there is an exceptionally strong fluctuation. However, using all Minkowski functionals to characterize the structure of the counts maps, i.e., extracting more information from the same data, all sources are detected. The very faint sources are, of course, in single simulations sometimes detected or not depending on statistical fluctuations. This finally confirms the initial idea to improve the sensitivity via structure characterization.

Moreover, another strength of the morphometric analysis is visible in Fig. 6.13: many, very differently large extended sources can be detected with the same scan window size in contrast to the standard counting method. This is discussed in more detail in Section 6.8.

Although larger windows than 15×15 are impractical, I carried out a very time-consuming calculation of the DoS of a 20×20 scan window to compare the results to those for a 15×15 window. Indeed, the sensitivity increase gets even stronger, but the gain is not enough considering the computational effort that would be necessary. Also, the blurring effects of the Minkowski sky map because of the large window size become too strong and no longer allow for a visualization of the source. Therefore, in this first part of the chapter the maximum windows size is 15×15. However, in Sections 6.10, I show that using a different approach, which is based on the covariances of the Minkowski functionals and empirical cumulative distribution functions, allows for extending the analysis to scan windows up to 100×100. This limits, however, the maximum deviation strength that can be evaluated to about nine.

[14] This is also why a new test pattern had to be defined, because using a 15×15 sliding window for the old test pattern in Section 6.2.2 leads to a compatibility below the numerical precision of the program. Therefore, a new test pattern is defined.

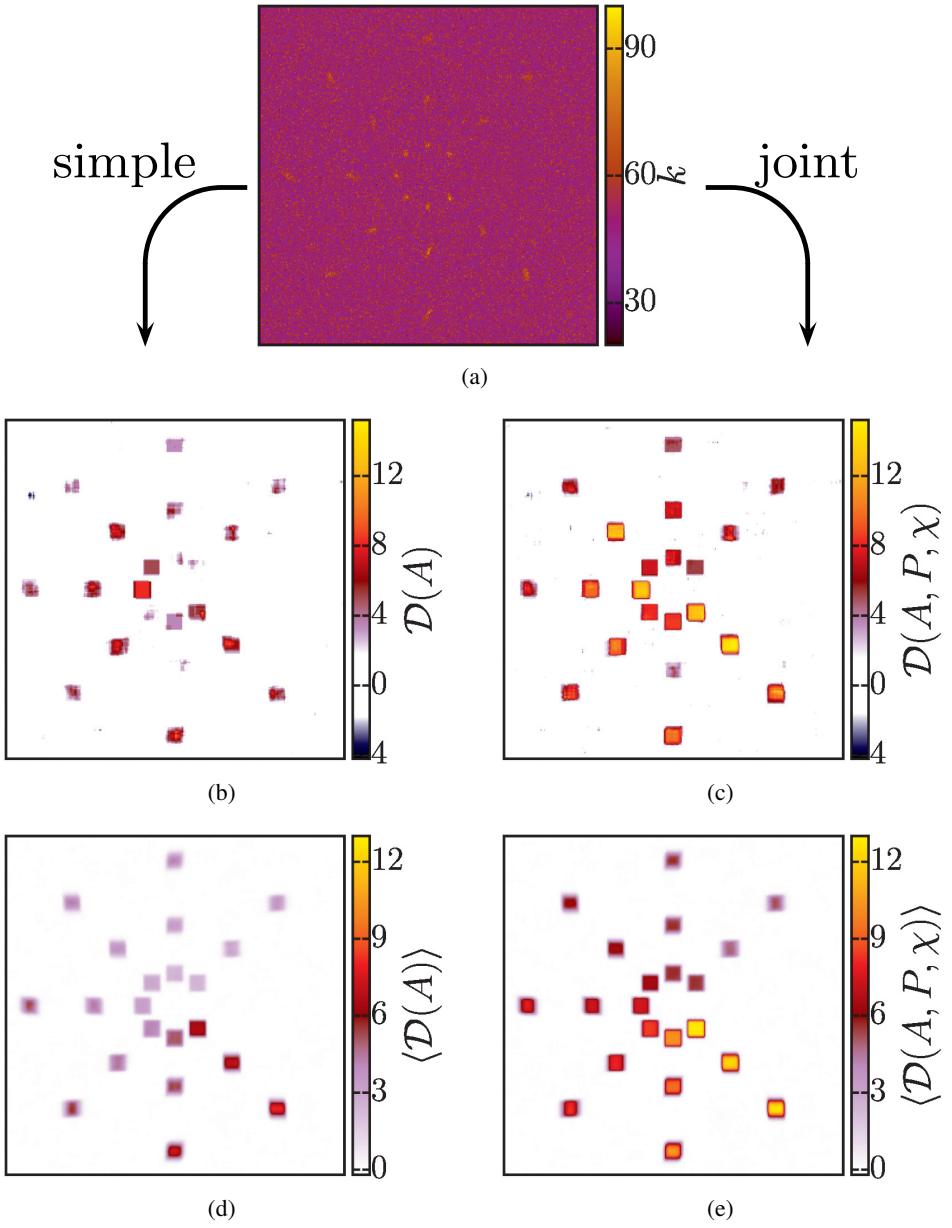

Figure 6.13: Strong sensitivity increase via joint structure characterization: (a) simulated counts map including sources of different sizes and different integrated fluxes; the same count map is first analyzed by (b) a Minkowski sky map using the simple deviation strength, i.e., only area, then, using (c) the joint deviation strength, i.e., all Minkowski functionals; formerly undetected sources are now detected. For a more systematic comparison also averages of 100 Minkowski sky maps w.r.t. (d) only the area and (e) all three Minkowski functionals are shown.

6.6.2 Systematic analysis of increase in sensitivity

The test pattern in Fig. 6.13 demonstrates that using the joint structure characterization allows for detecting formerly undetected sources by taking additional morphometric information into account. However, this can only be if there actually is an additional nontrivial shape information, i.e., if the shape of the source is structured on the length scale of the sliding window.

If any morphometric approach is to analysis a completely uniform source, i.e., a Poisson random field with a different intensity $\lambda' > \lambda$, the result must be less significant than for a simple method based only the total number of counts; simply because the additional structural information is in perfect accordance with the background model and the only difference is a different total number of counts.

In Fig. 6.13, the simple and joint deviation strengths are systematically compared to each other for differently shaped sources: a true point source which is smaller than a pixel, a uniform offset in the background intensity, and a Gaussian shaped source. Between 0.75 and 7.5 million counts maps (15×15) are simulated using the same intensity profile but different integrated fluxes. For each count map, both the simple and the joint deviation strength are determined. Given a simple deviation strength $\mathcal{D}(A)$, the conditional frequency $f[\mathcal{D}(A, P, \chi)|\mathcal{D}(A)]$ of the joint deviation strength $\mathcal{D}(A, P, \chi)$ is determined, i.e., for all cells with a simple deviation strength $\mathcal{D}(A)$ the empirical probability density function of the joint deviation strength $\mathcal{D}(A, P, \chi)$ is computed. The result is plotted using a color scale in Fig. 6.13. The black diagonal line indicates identical simple and joint deviation strength. The vertical and horizontal black lines depict the null hypothesis criterion for the simple or joint deviation strength, respectively.

Not even the strongest true point source in these simulations would have been detected by a simple counting method because the source signals are suppressed by the large additional background. In contrast to this, even the simple deviation strength uses additional information the dependence on the threshold ρ and can thus, e.g., detect a single pixel with an exceptional high number of counts because of a very unlikely black pixel at very high thresholds. This advantage in being more independent on the system size is discussed in more detail below in Section 6.8.

However, comparing $\mathcal{D}(A)$ to $\mathcal{D}(A, P, \chi)$, there is no additional information in the perimeter P or Euler characteristic χ: If there is only a single black pixel at high thresholds, the only possible values for P and χ are 4 or 1, respectively. Therefore, are the simple and joint deviation strengths are exactly identical.

For the uniform source, the additional information (P, χ) must, as stated above, lead to a decrease of the deviation strength. Interestingly, this decrease turns out to be rather small even in the extreme case of a constant offset. The decrease of the deviation strength could even be an advantage in that the joint deviation strength is

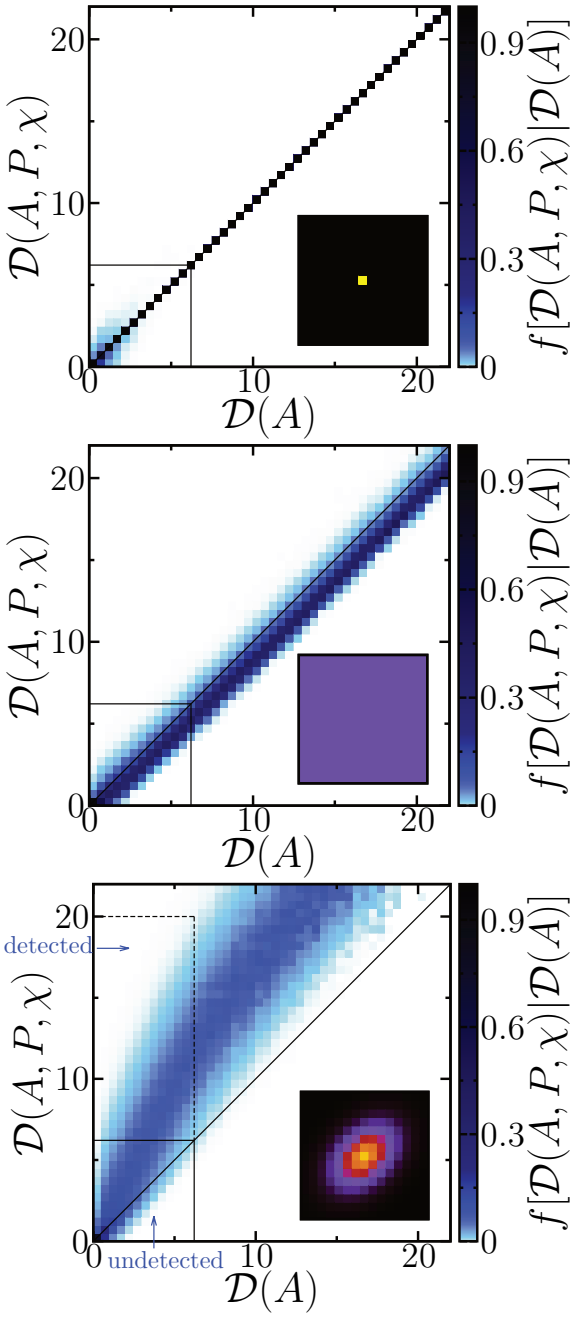

Figure 6.14: Shape dependence of sensitivity increase: systematic comparison between simple and joint deviation strength, which shows the frequency f of the joint deviation strength $\mathcal{D}(A,P,\chi)$ given a simple deviation strength $\mathcal{D}(A)$ for the same counts map; for a true point source smaller than a pixel (top), a uniform offset compared to the background intensity (center), an extended source with a nontrivial shape within the scan window (bottom), i.e., a strong gradient in the intensity. In the insets, the intensity profiles of the sources are depicted.

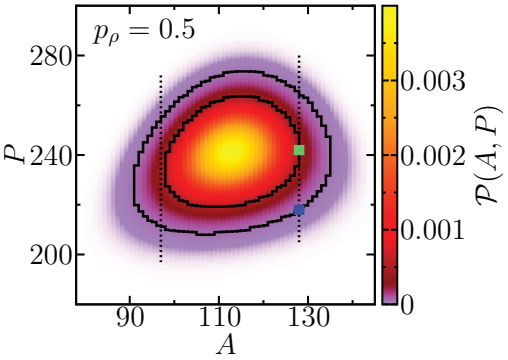

Figure 6.15: Probability distribution $\mathcal{P}$ of area A and perimeter P of a 15×15 b/w image with probability $p_\rho = 0.5$ for a pixel being black. Because of the white boundary conditions the perimeter can only take on even values; for an odd value of P the probability is zero. For an easier visualization the bin length in P is two.

slightly less sensitive to errors in the estimation of the background intensity and a source would still be detected because of the strong deviation in the area A.

For the structured source, there is a tremendous increase in sensitivity for the joint deviation strength compared to the simple one. For all counts maps for which the corresponding values of the deviation strengths are within the dashed box, the source is not detected if only the area characterizes the structure, but it is detected by the joint deviation strength, i.e., if all Minkowski functionals characterize the shape of the counts map. For the same counts map for which the simple deviation strength based only on the area is below 5, i.e., the compatibility is more than 10^{-5}, the joint deviation strength reaches values nearly 20, i.e., with compatibilities less than 10^{-19}. In other words, if the structure is characterized not only by the area but by all Minkowski functionals, the compatibility with the background structure can drop by 14 orders of magnitude. There is no significant excess in the total number of counts but in the structure of the counts map. Only by taking this morphometric information into account, a formerly undetected source can now be detected using the same data.

A more formal explanation of this intuitive understanding can be given with the aid of Fig. 6.15. Given a measured area, e.g., $A = 128$, the compatibility $C(A)$ w.r.t. only the area is the sum over all probabilities left of the left dotted line and right of the right dotted line, i.e., all macrostates with an area less likely than the given area $A = 128$.

In the example of a uniform offset in the background intensity, the structure, quantified by the perimeter P, is in agreement with the background structure and the perimeter most likely takes on a "typical" value, i.e., a very likely perimeter for a given area A, e.g., the green square represents $P = 242$. The compatibility $C(A,P)$ is then the sum over all probabilities outside the inner contour line, which results in $C(A,P) > C(A)$. However, in the example of a structured source the perimeter P might take on an unlikely value for the perimeter, e.g., the blue square represents

$P = 218$. The compatibility $C(A, P)$ is now the sum over all probabilities outside the outer contour line and thus, $C(A, P) < C(A)$. A structural deviation from the background structure leads to a more significant result of the morphometric analysis compared to simple counting methods. For two different b/w images with the same compatibility with the background w.r.t. the area, the additional information of the perimeter specifies whether the b/w image is indeed compatible to the background structure or not.

6.7 Combining different thresholds

So far, only the deviation strength of a single threshold is directly used for the null hypothesis test. The deviation strengths at other thresholds are used only indirectly by the fact that they are smaller than the maximum. However, Figure 6.3 shows that the deviation strength as a function of the thresholds contains a lot of information, e.g., even to some degree the extension of the source. Taking this information into account could yield a profound additional insight in the spatial data. However, it is currently out of reach to determine the probability distribution of the deviation strength as a function of the threshold.

Nevertheless, the most important information is whether the maximal deviation strength is only a fluctuation at a single threshold or whether there are strong structural deviations over a large range of thresholds like in Fig. 6.3. This can be quantified by replacing the maximum of the deviation strength by the sum of all thresholds[15],

$$\mathcal{S} := \sum_{\rho=0}^{\infty} \mathcal{D}(\rho)\,, \tag{6.7}$$

which is well defined, i.e., $\mathcal{S} < \infty$, because for every counts map there is a maximum count $k_{\max}$; thus, for $\rho > k_{\max}$ the b/w image is completely white. For a large enough threshold $\rho_l \gg 1$, this becomes the most likely configuration, because if $p \to 0$, $\mathcal{P}(A = 0) = (1 - p)^{N^2} \to 1$. For $\rho > \rho_l$, the compatibility is one and the deviation strength zero; the series, defined in Eq. (6.7), is actually a finite sum.

The sum $\mathcal{S}$ is a new test statistic instead of the maximum deviation strength $\mathcal{D}$ before. The distribution of this new test statistic can impossibly be calculated analytically, but efficient and tight approximations might be achievable, although out of the scope of this thesis. Here, the cumulative distribution is determined numerically, and the sensitivity gain is shown for simulated data.

[15] In the notation of Appendix A, the infinity norm l_∞ is replaced by the 1-norm l_1.

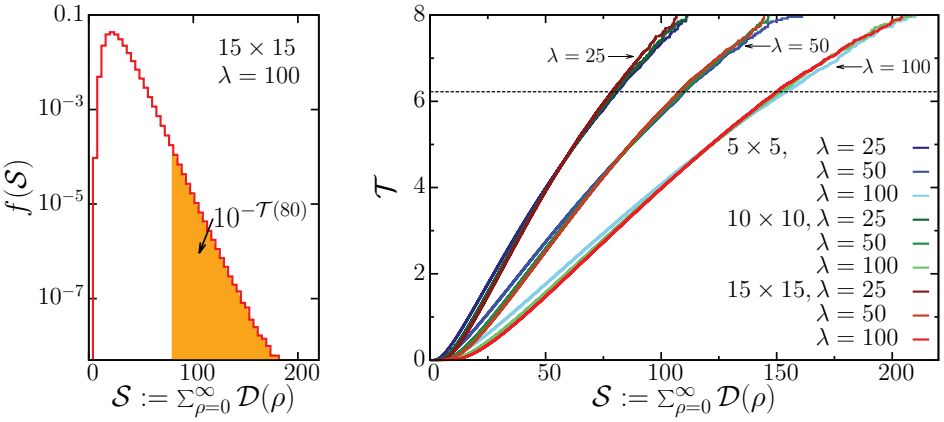

Figure 6.16: Sum of deviation strengths $\mathcal{D}(\rho)$ over all thresholds ρ: (a) empirical probability density function $f(\mathcal{S})$ and (b) the new test statistic $\mathcal{T}$, which is the negative decadic logarithm of the empirical complementary cumulative distribution function for different system sizes and background intensities λ; the dashed line indicates the hypothesis criterion, which is adjusted to the common 5σ criterion.

6.7.1 Empirical cumulative distributions

I simulate 10^9 counts maps and for each calculate $\mathcal{S} := \sum_{\rho=0}^{\infty} \mathcal{D}(\rho)$, from which I derive the Empirical Probability Density Functions (EPDF) for different window sizes and background intensities. Figure 6.16 shows the EPDF $f(\mathcal{S})$ for a 15×15 Poisson counts map with intensity $\lambda = 100$.

The new test statistic is defined as the empirical complementary cumulative distribution function (ECCDF), i.e., given a measured sum of deviation strength $\mathcal{S}$, the probability to find a larger value $\mathcal{S}' > \mathcal{S}$. This definition follows, as that for the compatibility C in Section 6.2.1, the scheme given in Ref. [341] to construct a most efficient hypothesis test.

For convenience, again the negative decadic logarithm is used instead,

$$\mathcal{T}(\mathcal{S}) = -\log_{10} \int_{\mathcal{S}}^{\infty} \mathrm{d}s \, f(\mathcal{S}) \,, \tag{6.8}$$

and the null hypothesis is rejected if $\mathcal{T} > 6.2$, which corresponds to the common 5σ criterion. Figure 6.16 plots Eq. (6.8) for different system sizes and background intensities, based on 10^9 simulated count maps for each system.

As expected, the test statistic strongly depends on the background intensity λ because the number of thresholds with nonzero deviation strength varies. Interestingly, the dependence on the system size is rather weak.

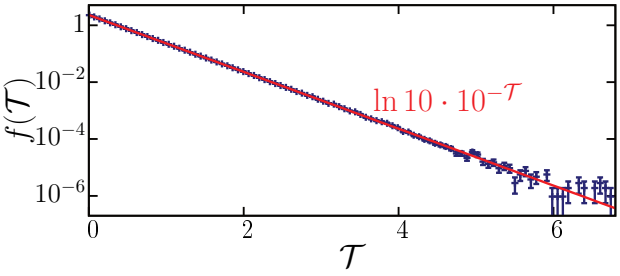

Figure 6.17: Empirical probability density function of the test statistic $\mathcal{T}$ from Eq. (6.8) for a 15×15 count map with a background intensity $\lambda = 50$; it is in very good agreement with the target probability distribution from Eq. (6.9).

The new test statistic is chosen such that in simulations of the background model its EPDF is the same as for the deviation strength $\mathcal{D}$ at a single threshold,

$$f(\mathcal{T}) = \ln 10 \cdot 10^{-\mathcal{T}} \,, \tag{6.9}$$

see Fig. 6.17.

6.7.2 Sensitivity increase for diffuse radiation

Especially for broad sources, which exhibit structural deviations at a large range of thresholds, see e.g. Fig. 6.3, the new test statistic $\mathcal{T}$ can lead to an additional increase in sensitivity.

Figure 6.18 exemplarily shows this increase for simulated diffusion radiation. The new testing procedure is more sensitive because it includes the information that there are also strong structural deviations at other thresholds than the maximum deviation strength.

6.8 Comparison to a standard counting method

The standard null hypothesis test in gamma-ray astronomy was introduced in 1983 by Li and Ma [273]: it compares the number of signals N_{on} in the so-called "on-region", i.e., in the vicinity of an expected source, to the number of background signals detected in an N_{off} "off-region", i.e., a region in the sky without sources. The method simply counts the number of photons. Given an exposure ratio α, the significance σ is

$$\sigma = \sqrt{2N_{on} \ln\left[\frac{1+\alpha}{\alpha}\left(\frac{N_{on}}{N_{on}+N_{off}}\right)\right] + 2N_{off} \ln\left[(1+\alpha)\left(\frac{N_{off}}{N_{on}+N_{off}}\right)\right]} \,.$$

The significance can be expressed in terms of a deviation strength, see Section 6.2.1,

$$\mathcal{D}(\sigma) = -\log_{10}\left(\operatorname{erfc}\left(\frac{\sigma}{\sqrt{2}}\right)\right) \tag{6.10}$$

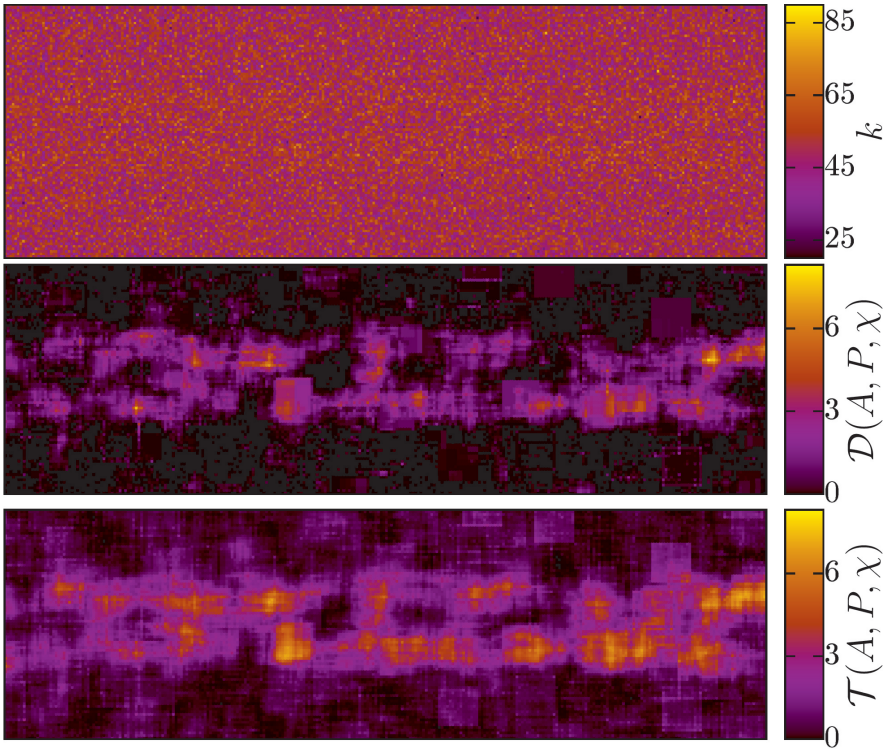

Figure 6.18: Diffuse radiation along the horizontal axis is added to a homogeneous background noise with intensity $\lambda = 50$, which leads to an excess in the number of counts k (top). The Minkowski sky map based on the maximum of the deviation strength $\mathcal{D}$ w.r.t. all Minkowski functionals detects the structural deviations of this very broad source (center), but the new test statistic that sums over all thresholds leads to a significant increase in sensitivity (bottom).

where $\operatorname{erfc}(x) = \frac{2}{\sqrt{\pi}} \int_x^\infty \exp(-t^2)\, \mathrm{d}t$ is the error function. This standard counting method allows for a simple and fast null hypothesis test. However, the analysis only uses the total number of counts in the observation window.

Our morphometric analysis follows a completely new ansatz based on structure characterization, which can not only detect an excess of counts but is able to detect any structural deviation from the background noise. For example, in Section 6.10.3 I detect structural deviations in count maps where the number of expected counts is in perfect agreement with the background intensity.

6.8.1 Dependence on experimental details

Therefore, there is no direct and straightforward comparison that one of the methods is always more sensitive than the other. A comparison of the advantages and

different possibilities of the two methods is complicated and depends on the experimental details and the source shape. The standard counting method is more likely to detect sources if there is no interesting structure to be quantified within the scan window. The additional structural information is in agreement with the background noise, as discussed in Section 6.6.2. The morphometric analysis based on all Minkowski functionals is, in this case, less likely to detect a source compared to an analysis that only takes the total number of counts into account. However, if there is a distinct structural difference from the background noise, the morphometric analysis has the advantage of being able to use this additional information.

Whether or not there is an increase in sensitivity compared to the counting method by Li and Ma also very much depends on the experimental details, e.g., the bin size, as shortly discussed in Ref. [161]. In contrast to the total number of counts, our morphometric analysis strongly depends on the choice of the bin size. If the bins are too large, interesting source structure might be hidden because it is contained in a single bin. However, if the bin size is too small, the sky map does not only get very noisy but we can also loose structural information. In the extreme case that in the black and white image all black pixels are separated from each other by white pixels, the translation invariant Minkowski functionals can no longer distinguish different configurations, but only the total number of black bins. Therefore, the bin size needs to be chosen reasonably taking the size of the scan window, the point spread function of the telescope, the quality of the data, and the source shape into account, see Ref. [161].

As mentioned above, the morphometric analysis can detect sources even if there is no excess in the signals compared to the background intensity, see Section 6.6.2. Therefore, I expect the morphometric analysis to be robust against overestimates of the background intensity λ. However, a more thorough analysis of such effects for real data is beyond the scope of this thesis. Ideally, it would need extensive simulations to determine the empirical cumulative distribution function with a priori unknown λ, but instead using an efficient estimation of the background intensity, as described in Ref. [161]. A main advantage of the morphometric analysis compared to the counting method could eventually be that it avoids observations of off-region because a less precise estimate of the background intensity is sufficient.

The method by Li and Ma compares the number of counts in the source region and in regions with only background signals. Obviously, it strongly depends on how accurate the estimate of the background intensity is. Here, I compare the morphometric analysis to the significance of the Li and Ma test for the extreme and most sensitive case of an infinitely long observation of the off-region[16] $N_{off} \to \infty$

[16] An infinite observation time corresponds to using the exact background intensity.

while $\alpha = \lambda_{tot}/N_{off} \to 0$. In this limit,

$$\sigma = \sqrt{2}\left\{N_{on}\ln\left[\frac{N_{on}}{\lambda_{tot}}\right] + \lambda_{tot} - N_{on}\right\}^{1/2} . \tag{6.11}$$

For a final comparison of both methods, their dependencies on these experimental details must be accurately studied, which is beyond the scope of this thesis. Here, I discuss the advantages of the refined morphometric analysis and compare it to the counting method in two examples, where the morphometric analysis detects sources in contrast to the standard method by Li and Ma. These examples show the potential of the morphometric ansatz. However, the choice of the optimal method strongly depends on the details of the data which is to be analyzed, and it also depends on the information or features that are to be extracted.

6.8.2 Scan window size dependence and low statistics

Besides the above mentioned robustness against overestimated background intensities or the ability to even detect inhomogeneities with no excess in the total number of counts, another important advantage of the morphometric analysis is that it depends much less on the choice of the size of the scan window. Even sources with extensions much smaller than the scan window size are detected in the morphometric analysis, although there is no significant change in the total number of counts.

Figure 6.14 shows how even a point source, i.e., a single pixel with increased intensity, can sensitively be detected, because at high threshold even a single black pixel is very unlikely, which is independent of counts in other pixels possibly in agreement with the null hypothesis. The morphometric analysis can detect sources of very different extensions with the same scan window size.

In contrast to this, the standard counting method cannot detect a source if there are at the same time too many pixels with only background signals in the same scan window. If there are many pixels within the scan window which contain only background signals, the source signals can be suppressed. The small excess in the total number of counts is no longer significant. This effect can be reduced if the size of the scan window is adjusted to the extension of the source. However, such an adaption can possibly lead to a biased choice of the parameter or an unknown trial factor if the analysis is repeated with different window size.

In Fig. 6.19, the test pattern from Fig. 6.13 with differently large sources is analyzed using the same scan window size as the morphometric analysis, see Figs. 6.13(b)–6.13(e). The large outer sources are of the same size as the scan window; they are detected with a similar significance as by the morphometric analysis. However, the smaller inner sources are not statistically significantly detected,

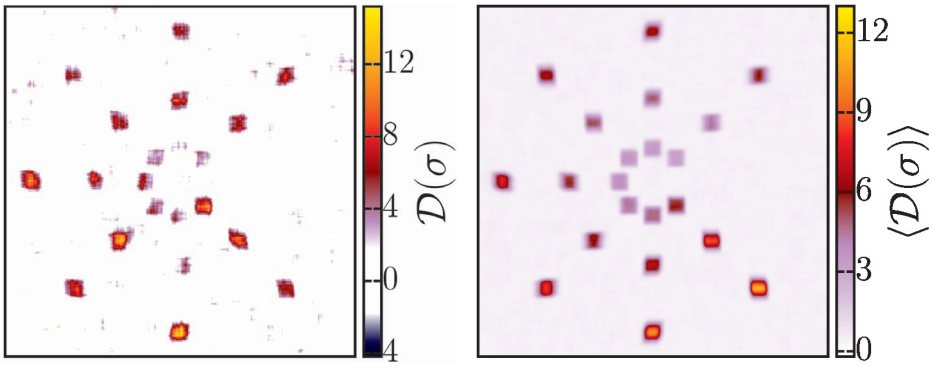

(a) (b)

Figure 6.19: For the test pattern in Fig. 6.13, the excess in the total number of counts is determined; the deviation strength in the total number of counts is derived from the significance of the excess according to Eqs. (6.10) and (6.11): (a) a single sky map is shown like in Figs. 6.13(b) or 6.13(c), (b) an average of 100 Minkowski sky maps like in Figs. 6.13(d) or 6.13(e); for a direct comparison, the same color scales are used. For the chosen 15×15 scan window, the outer sources are detected with a similar significance as in Fig. 6.13. However, in order to detect the inner sources, the scan window size must be adjusted.

because there are too many background signals in the same scan window. If the scan window size is adjusted, these sources can be detected highly significantly. However, the problem of a possibly biased choice of parameters, as well as an unknown trial factor, remains.

The most important advantage of the morphometric analysis is, of course, that it incorporates additional structural information. Especially, if only low statistics are available, an increase in the sensitivity by quantifying the structure of the counts map is probably most needed. For example, a slight excess in the total number of counts might not be significant because of the strong fluctuations of a Poisson distribution relative to the small mean value. Interestingly, especially in such a case the significance in the structural deviation is relatively strong compared to the significance in the number of counts. For example, for a Poisson random field with a low intensity the clustering of a given number of black pixels is equally likely or unlikely as in a field with high intensity. The excess in the number of counts might not be significant, but the improbable arrangement of the black pixels can lead to the detection of the source. So, the advantage of additional structural information should be most effective when it is most needed.

Figure 6.20 shows such an example of a weak and hardly detectable source where only low statistics are available. Although hardly visible by eye in the count map, there are strong intensity gradients. The source resembles a dotted pattern; it

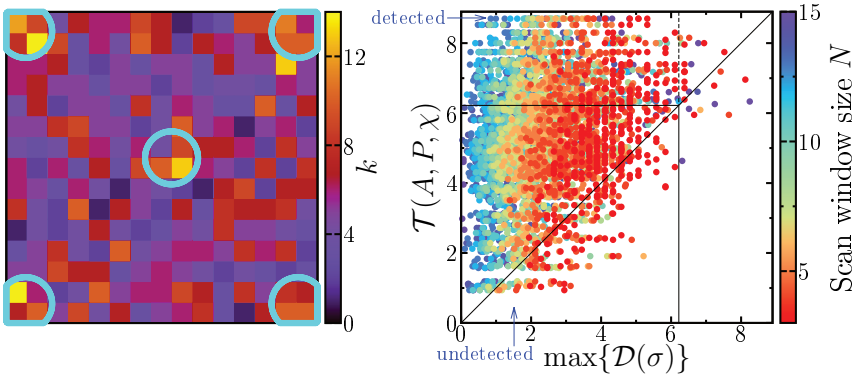

Figure 6.20: A source like a dotted pattern where only low statistics are available: (a) the source consists of several pointlike sources (marked by circles) hardly visible by eye in the counts map; (b) comparison of the deviation strength $\mathcal{T}(A,P,\chi)$ of the morphometric analysis to $\mathcal{D}(\sigma)$ of the standard counting method from Eqs. (6.10) and Eq. (6.11). 400 samples are simulated. For each sample, the morphometric analysis is applied to the whole 15×15 counts map. For the same sample, it is compared to $\mathcal{D}(\sigma)$, which is evaluated for all scan window sizes between 15×15 (blue points) and 3×3 (red points) where the maximum of all iterations over the counts map is used. Although the trial factors for $\max\{\mathcal{D}(\sigma)\}$ are ignored, the morphometric analysis is for the vast majority of samples more sensitive $\mathcal{T}(A,P,\chi) > \max\{\mathcal{D}(\sigma)\}$. Although there might be no significant excess in the total number of counts, the source can be detected simply by taking more information out of the same data.

consists of several nearly pointlike sources that are marked in the count map on the left-hand side. Because of the strong intensity gradients and thus the significant structural deviation from the background noise, the morphometric analysis can take advantage of the additional geometrical information.

Because of the low statistics, there are strong statistical fluctuations in the single sky maps. For a more systematic analysis, I simulate 400 samples and compare the deviation strength $\mathcal{T}(A,P,\chi)$ of the morphometric analysis to $\mathcal{D}(\sigma)$ of the standard counting method from Eqs. (6.10) and (6.11), see the right-hand side of Fig. 6.20.

The morphometric analysis analyzes the whole 15×15 count map. However, it is not only compared to $\mathcal{D}(\sigma)$ of the standard counting method using the same scan window size (blue points), rather for all scan windows down to very small sizes 3×3 (red points). Thus, the effect of windows size dependence in the standard counting method can be taken into account. For scan windows smaller than the total size of the counts map, I iterate the scan window over the count map and compare the maximum of all deviation strengths $\mathcal{D}(\sigma)$ to $\mathcal{T}(A,P,\chi)$.

Although the thus necessary trial factors for $\max\{\mathcal{D}(\sigma)\}$ are ignored, which in some cases would reduce the deviation strength by more the 1.4, the morphometric

analysis is for the vast majority of samples more sensitive than the counting method $\mathcal{T}(A,P,\chi) > \max\{\mathcal{D}(\sigma)\}$. While there are only about 5 out of 400 samples with $\max\{\mathcal{D}(\sigma)\} > 6.22$, there are many samples where the source is not detected by $\max\{\mathcal{D}(\sigma)\}$ but by $\mathcal{T}(A,P,\chi)$. In other words, although there might be no significant excess in the total number of counts, the source can still be detected by taking more information out of the same data. In general, a comparison of the morphometric analysis and the standard method by Li and Ma depends on both the experimental details and the structure of the source. For this example, the morphometric analysis is more sensitive.

6.9 Experimental data from H.E.S.S. sky maps

With the methods discussed so far, we can analyze experimental data of ground-based VHE gamma-ray telescopes such as the H.E.S.S. experiment. The morphometric analysis is especially targeted at extended structures. Therefore, I have chosen for an exemplary analysis first the supernova remnant RX J1713.7−3946 [18] and second an extended band of gamma-ray emission in the galactic center ridge [17].

6.9.1 The supernova remnant RX J1713.7−3946

RX J1713.7−3946 has one of the largest angular diameters of the sources seen with H.E.S.S. and its shape has already been studied in detail and is well known [18], which makes it a suitable benchmark for more detailed analyses.

The data set used for analysis corresponds to the data used in [18] but instead of the Hillas-based event reconstruction discussed there, the advanced event reconstruction based on a likelihood-model fit presented in Ref. [113] was used to compute the list of reconstructed events from the recorded camera images. These reconstructed events were used to fill the binned counts map, which is the main input of the morphometric analysis. The second input needed is an acceptance map describing the spatial sensitivity of the given observations, which is used to perform the acceptance correction discussed above. This map was created using standard H.E.S.S. analysis tools. In particular, the so-called 2 D acceptance model discussed in Ref. [112] was used. The overall background level λ was determined from the counts map by excluding all regions containing known sources of VHE gamma rays and computing the mean number of counts in the remaining bins normalized by the corresponding acceptance.

Figure 6.21 shows the resulting Minkowski sky maps of a morphometric analysis based on the area A, the perimeter P, and the Euler characteristic χ. The underlying counts and acceptance maps used for this analysis were created using square

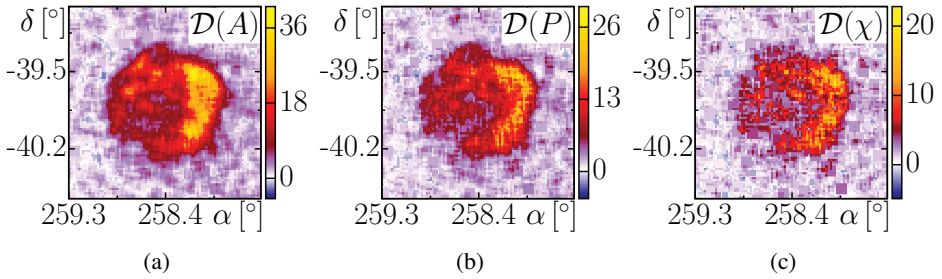

Figure 6.21: Minkowski sky maps of RX J1713.7−3946. The morphometric analysis is based on (a) area A, (b) perimeter P, and (c) Euler characteristic χ.

bins of 0.02 ° width. The resulting sky maps clearly show RX J1713.7−3946 and agree well with the results of the standard H.E.S.S. analysis given in Ref. [18]. This demonstrates the feasibility of an analysis based on the structure of the measured counts map. For more such examples of H.E.S.S. sky maps analyzed by the morphometric analysis see Ref. [161].

An increase in sensitivity of such a well-observed and extremely significant source is not necessary. Instead, a weak source with shorter observation times would be more interesting because even a slight increase in sensitivity can lead to the detection of a formerly undetected source. However, I do not want to actually claim additional significance in real data or even the detection of a source, which would need the approval of the whole H.E.S.S. group, which would be beyond the scope of this thesis. In order to both analyze a weak source and not claim new significance, I analyze the well-studied source RX J1713.7−3946 but artificially reduce the quality of the original count map. An increase in sensitivity would not lead to an actual claim of new significance or even to physically new insights. However, it can serve as a proof of principle, showing how my refined analysis improves the morphometric analysis and thus increases its sensitivity.

The H.E.S.S. count map in Fig. 6.22(a), which is analyzed in Fig. 6.21, can reveal fine details of the gamma-ray source. I reduce this high quality by postselection and Monte Carlo observations as described in Section 6.4. First, I simulate a shorter observation time by homogeneously applying the postselection from Section 6.4.2: in each bin I keep on average only a fraction $f = 0.11$ of the counts. Then, I also add a strong simulated noise to data: Poisson distributed Monte Carlo observations such that the final expected background intensity is $\lambda = 5$[17]. In the

[17] This manipulation of the data increases some of the difficulties of a comparison to the standard counting method of Li and Ma mentioned above in Section 6.8. A detailed comparison is beyond the scope of this thesis, and I do not apply the standard counting method of Li and Ma [273] here.

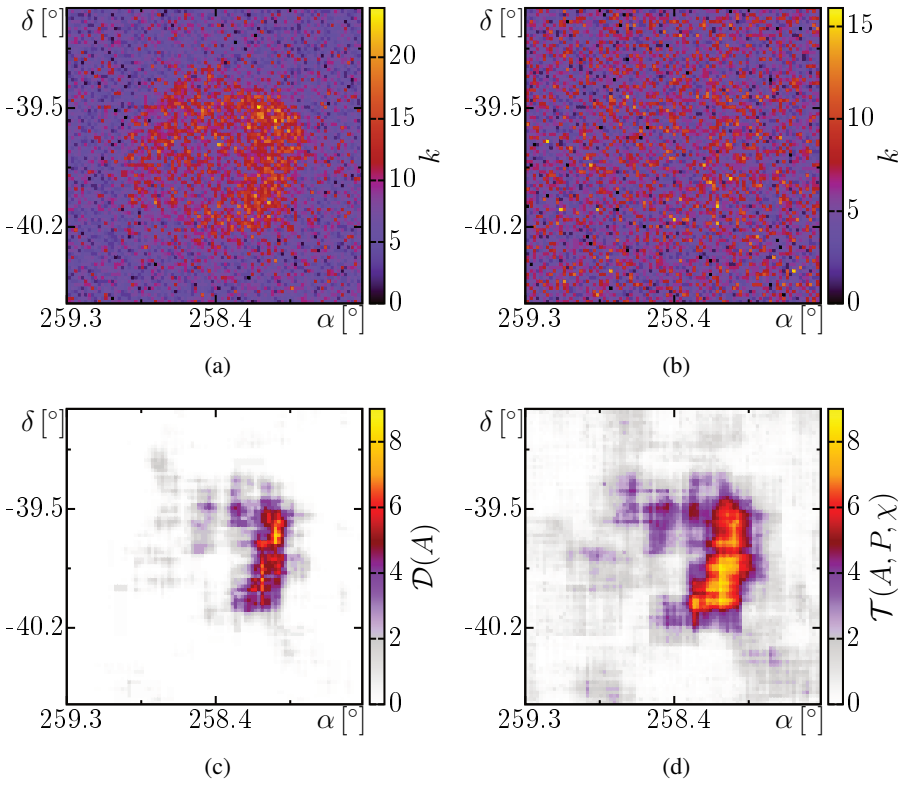

Figure 6.22: Sky maps of RX J1713.7−3946: (a) H.E.S.S. counts map with highly significant source detection, (b) source signals are suppressed by postselection and additional Monte Carlo noise to the count map, (c) the former test statistic $\mathcal{D}(A)$ can hardly detect the source, but (d) the refined analysis of this thesis leads to a strong increase in sensitivity for $\mathcal{T}(A,P,\chi)$, the source is clearly detected.

resulting count map in Fig. 6.22(b), the supernova remnant source is because of this reduced observation time and additional noise so weak that it is hardly visible by eye in the count map. The source can only be detected in large scan windows, which are studied in this thesis.

First, the maximum of the deviation strength w.r.t. only the area, $\mathcal{D}(A)$, is determined for this count map[18], see Fig. 6.22(c), which was possible before this thesis for a 15×15 scan window. Then, I determine the here defined test statistic $\mathcal{T}(A,P,\chi)$ which combines the deviation strengths at different thresholds and simultaneously characterizes the shape of the count map by all three Minkowski functionals also using a 15×15 scan window, see Fig. 6.22(d). These improvements

[18] $\mathcal{D}(A)$ is trial corrected according to Section 6.3.

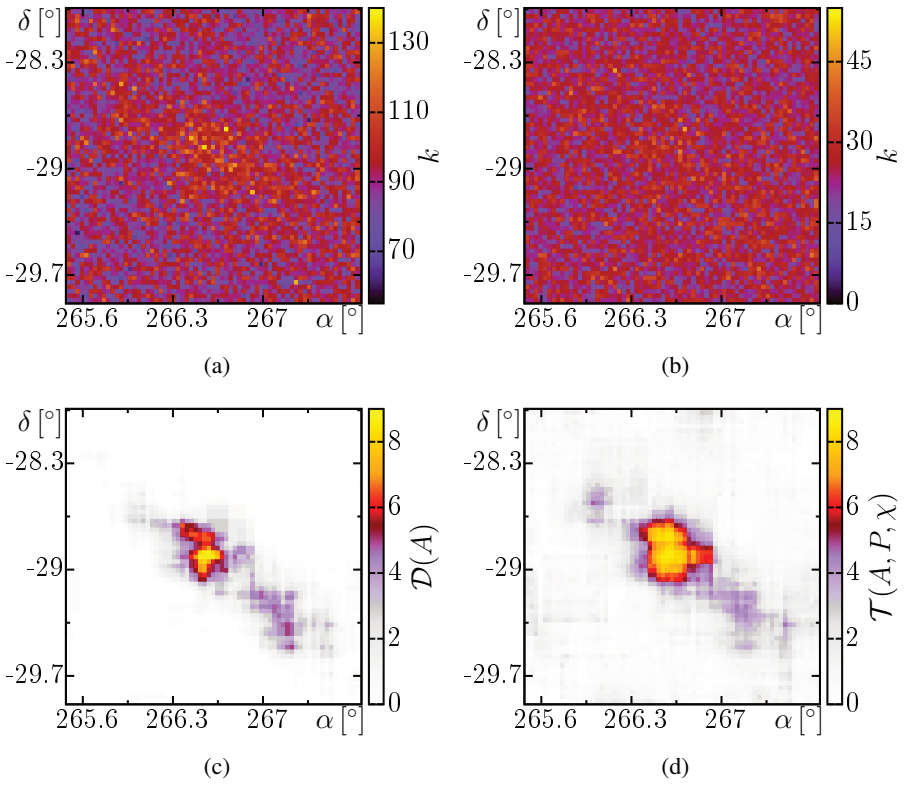

Figure 6.23: Sky maps of the diffusion of the galactic center ridge: (a) H.E.S.S. count map with highly significant source detection, (b) source signals in the count map are suppressed by postselection, (c) for the latter count map the basic test statistic $\mathcal{D}(A)$ detects the source only in the most significant, central region, (d) the refined analysis of this thesis leads to a strong increase in sensitivity for $\mathcal{T}(A,P,\chi)$.

lead to a strong increase in sensitivity even in the logarithmic scales of $\mathcal{D}(A)$ and $\mathcal{T}(A,P,\chi)$. The original shape of the supernova remnant is also better visible.

6.9.2 The galactic center ridge

The H.E.S.S. collaboration has in detailed studied in the galactic center ridge besides two pointlike sources, HESS J1745−290 [12] and G0.9 + 0.1 [13], an extended band of VHE gamma-ray emission, which are spatially correlated with molecular gas clouds [17].

In Ref. [243], I have analyzed the H.E.S.S. sky map of the galactic center ridge with our morphometric analysis. I have subtracted the two well-known pointlike

sources and analyzed the highly significant extended region of gamma-ray emission, see Fig. 6.23(a); for more details on the H.E.S.S. data and acceptance correction see also Ref. [160]. Similar to the supernova remnant RX J1713.7−3946, I artificially reduce the quality of the count map by postselection, reducing the background intensity from about 91 to 25, see Fig. 6.23(b). Because of this simulated shorter observation time, the extended band is hardly visible by eye.

Again, the source can only be detected in large scan windows. Using 15×15 scan windows, the maximum of the deviation strength w.r.t. only the area, $\mathcal{D}(A)$, can detect the emission close to the center, see Fig. 6.23(c). However, using the here defined test statistic $\mathcal{T}(A, P, \chi)$ again leads to a strong increase in sensitivity, see Fig. 6.23(d).

6.10 Covariance approach

Window sizes of up to 20×20 are the maximum for which the DoS can be determined with sufficient numerical accuracy using the Wang-Landau method with modern technology. This is sufficient for most applications to gamma-ray astronomy. However, there might be other applications where much larger window sizes are necessary.

Moreover, in other applications a suitable model for the background might be missing or because of experimental inaccuracy only the mean values and the covariances of the Minkowski functionals of the background model is known.

For these cases, we have developed in cooperation with Bruno Ebner and Norbert Henze from the Karlsruhe Institute of Technology a new test statistic following the idea of the morphometric data analysis. The structure is also quantified by the Minkowski functionals, but the new test statistic is a deviation from the expected functional values weighted by the covariance matrix of the background model.

We calculated for the Poisson point process the covariance matrix for arbitrary window size analytically. For other processes or random fields, it might be necessary to determine the covariances numerically or derive them empirically.

6.10.1 Variances and covariances of Minkowski functionals

In our null hypothesis, we again assume that there are only Poisson distributed background signals. More precisely, the null hypothesis is that the point pattern formed by the detected signals forms a Poisson point process, i.e., the events are independently and randomly distributed within the observation window, with a given mean number of points per unit area γ. In the binned image with linear bin size b_l, the equivalent null hypothesis is that the number of counts in each

bin follows a Poisson distribution with mean value $\lambda = \gamma \cdot b_l^2$ and is statistically independent of the other bins.

This null hypothesis is tested for some given count map by comparing its structure to the shape that is expected under the null hypothesis. In other words, the main idea remains the same: to look for any significant structural deviation from the expected background structure without any prior knowledge about potential sources. In this sense, we again use the Minkowski functionals as unbiased shape descriptors. However, the test statistic and thus the required precision in the knowledge of the background structure changes.

Therefore, we need the expectations, variances, and covariances of the Minkowski functionals under this null hypothesis. We derive explicit analytically expressions for an $m \times m$ b/w image, where the m^2 pixels are independently colored black with probability p_ρ or otherwise white[19]. If the pixel $(i, j) \in \{1, \ldots, m\}^2$ is black, we denote this by $b_{i,j} = 1$, otherwise $b_{i,j} = 0$.

For a more convenient scaling of the covariance with the linear system size m of the observation window, the unit of length is changed: the count map is without loss of generality chosen to represent the unit square $[0, 1]^2$; additionally, we define a scaled Euler characteristic $\chi_m := \chi/m$. For these rescaled Minkowski functionals, we provide explicit formulas by using the look-up table from Table 6.1: for the area

$$A_m := \frac{1}{m^2} \sum_{i,j=1}^{m} b_{i,j}$$

and the perimeter

$$P_m := \frac{1}{m} \sum_{i,j=1}^{m} \psi(b_{i,j}),$$

where for $i, j \in \{1, \ldots, m\}$

$$\psi(b_{i,j}) := \begin{cases} 0, & \text{if } b_{i,j} = 0, \\ 4 - (b_{i-1,j} + b_{i+1,j} + b_{i,j-1} + b_{i,j+1}), & \text{if } b_{i,j} = 1. \end{cases}$$

Finally, we study the rescaled Euler characteristic

$$\chi_m := \frac{1}{m} \sum_{i,j=0}^{m} W_{i,j},$$

[19] Be reminded, that this b/w images is constructed from the Poisson random field, i.e., a background counts map with independent m^2 pixels for which the number of counts $k_{i,j}$ in pixel $(i, j) \in \{1, \ldots, m\}^2$ is Poisson distributed. For a threshold ρ, the probability that the number of counts $k_{i,j}$ are larger or equal than ρ is p_ρ from Eq. (6.1), in other words, the probability that a pixel is colored black.

where, putting $S_{i,j} := b_{i,j} + b_{i+1,j} + b_{i,j+1} + b_{i+1,j+1}$,

$$W_{i,j} := \begin{cases} 1/4, & \text{if } S_{i,j} = 1, \\ -1/4, & \text{if } S_{i,j} = 3, \\ -1/2, & \text{if } S_{i,j} = 2 \text{ and } b_{i,j}b_{i+1,j+1} = 1 \text{ or } b_{i+1,j}b_{i,j+1} = 1, \\ 0, & \text{otherwise .} \end{cases}$$

The labels $b_{i,j}$ are Bernoulli random variables which are independently and identically distributed; from lengthy calculations [129], we derive the expectations, variances, and covariances of the Minkowski functionals. For the area, we get

$$\mathbb{E}(A_m) = \frac{1}{m^2} \sum_{i,j=1}^{m} \mathbb{E}(b_{i,j}) = p_\rho =: \mu_A(p_\rho). \tag{6.12}$$

Because

$$\mathbb{E}(\psi(b_{i,j})) = \begin{cases} p_\rho(4 - 4p_\rho), & i,j \in \{2,\ldots,m-1\}, \\ p_\rho(4 - 3p_\rho), & i \in \{1,m\}, j \in \{2,\ldots,m-1\}, \\ p_\rho(4 - 3p_\rho), & j \in \{1,m\}, i \in \{2,\ldots,m-1\}, \\ p_\rho(4 - 2p_\rho), & i,j \in \{1,m\}, \end{cases}$$

the expected perimeter is given by

$$\begin{aligned} \mathbb{E}(P_m) &= \frac{1}{m} \sum_{i,j=1}^{m} \mathbb{E}(\psi(b_{i,j})) \\ &= 4p_\rho(m - (m-1)p_\rho) =: \mu_P(p_\rho), \end{aligned}$$

and for the expected (scaled) Euler characteristic we have

$$\begin{aligned} \mathbb{E}(\chi_m) &= \frac{1}{m} \sum_{i,j=0}^{m} \mathbb{E}(W_{ij}) \\ &= \frac{1}{m} \left(p_\rho + 2(m-1)p_\rho(1-p_\rho) + (m-1)^2 p_\rho(1-p_\rho)(p_\rho^2 - 3p_\rho + 1) \right) \\ &=: \mu_\chi(p_\rho). \end{aligned}$$

Thus, under the null hypothesis that the number of counts are independently Poisson distributed, the mean values of the Minkowski functionals of the excursion sets are a function of the probability p_ρ depending on the threshold ρ and on m and we denote the three-dimensional mean vector by

$$\mu^\rho := \begin{pmatrix} \mu_A(p_\rho) \\ \mu_P(p_\rho) \\ \mu_\chi(p_\rho) \end{pmatrix}.$$

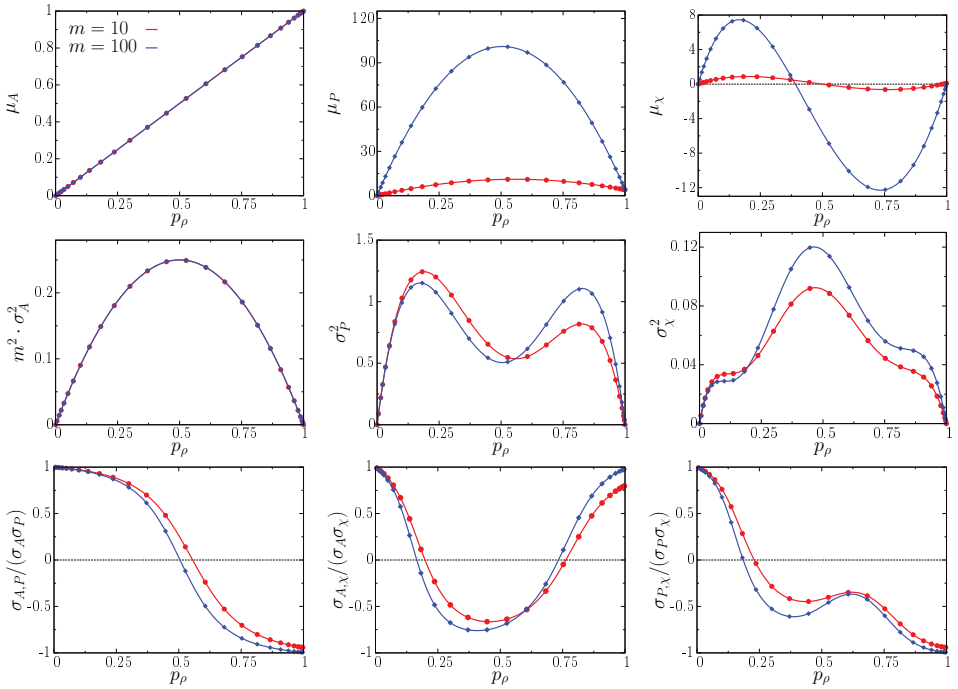

Figure 6.24: Expectations, variances, and correlations of the Minkowski functionals of a Poisson random field, i.e., a background count map. The system size m indicates if a 10×10 (red) or a 100×100 (blue) count map is considered. The background intensity is $\lambda = 25$. The points represent numerical estimates derived from 10,000,000 samples; they are in perfect agreement with the analytic curves from Eqs. (6.12)–(6.13). Because of the white boundary conditions, the curves are not symmetric w.r.t. the probability $p_\rho = 0.5$ that a pixel is black.

Moreover, the variances of the rescaled Minkowski functionals are given by

$$\begin{aligned}
\sigma_A^2 &= \frac{1}{m^2} p_\rho (1-p_\rho), \\
\sigma_P^2 &= \frac{8}{m^2} p_\rho (1-p_\rho) \left((7m^2 - 13m + 4) p_\rho^2 - 7m(m-1) p_\rho + 2m^2 \right), \\
\sigma_\chi^2 &= \frac{1}{m^2} p_\rho (1-p_\rho) \Big(\left(9m^2 - 30m + 25\right) p_\rho^6 - \left(59m^2 - 194m + 159\right) p_\rho^5 \\
&\quad + \left(137m^2 - 434m + 341\right) p_\rho^4 - \left(139m^2 - 406m - 291\right) p_\rho^3 \\
&\quad + \left(64m^2 - 158m + 94\right) p_\rho^2 - \left(12m^2 - 18m + 6\right) p_\rho + m^2 \Big),
\end{aligned}$$

and the covariances $\sigma_{W_\mu, W_\nu} := \mathrm{Cov}(W_\mu, W_\nu)$ are

$$\sigma_{A,P} = \frac{1}{m^3} p_\rho (1-p_\rho) \left(4m^2 (1 - 2p_\rho) + 8m p_\rho \right),$$

$$\begin{aligned}\sigma_{A,\chi} &= \frac{1}{m^3} p_\rho (1-p_\rho) \left(4(m-1)^2 p_\rho^3 + 12(m-1)^2 p_\rho^2 \right. \\ &\qquad \left. -4(m-1)(2m-1)p_\rho + m^2\right), \\ \sigma_{P,\chi} &= \frac{4}{m^2} p_\rho (1-p_\rho) \left(\left(6m^2 - 16m + 10\right) p_\rho^4 - \left(22m^2 - 56m + 34\right) p_\rho^3 \right. \\ &\qquad \left. + \left(23m^2 - 49m + 24\right) p_\rho^2 - \left(9m^2 - 13m + 4\right) p_\rho + m^2\right). \end{aligned} \tag{6.13}$$

All covariances between Minkowski functionals are summarized by the symmetric 3×3-matrix

$$\Sigma_{\rho,m,\lambda} := \begin{pmatrix} \sigma_A^2 & \sigma_{A,P} & \sigma_{A,\chi} \\ \sigma_{A,P} & \sigma_P^2 & \sigma_{P,\chi} \\ \sigma_{A,\chi} & \sigma_{P,\chi} & \sigma_\chi^2 \end{pmatrix}.$$

The index indicates the dependence of the covariances on the threshold ρ, the intensity λ of the Poisson distribution and on the linear system size m. For mA_m and the other functionals and $m \to \infty$, the asymptotic covariance matrix Σ is well-defined and explicitly given as well as its inverse Σ^{-1}.

These calculations are supported by simulations, in that they are plotted and compared against numerical estimates in Fig. 6.24. Some features can easily be understood: for example, that area and perimeter are correlated at small p_ρ, but anticorrelated at high p_ρ, which is because in the first case an additional black pixel most likely also increases the perimeter, but in the latter case an additional black pixel most likely closes a gap and thus decrease the perimeter. However, there is also a very complex behavior without an intuitive explanation, e.g., the local maximum in the correlation of perimeter and Euler characteristic.

6.10.2 Testing procedure

Now that we have calculated the expectations, variances, and covariances of the Minkowski functionals under our null hypothesis, i.e., for excursion sets of maps with independently Poisson distributions of number of counts, we can define the null hypothesis test. As stated above, the main idea is to test the hypothesis by looking for significant structural deviations from the expectation of the Minkowski functionals for each threshold ρ.

Given the measured Minkowski functionals A_m, P_m, and χ_m, their deviation from the mean values μ_A, μ_P, and μ_χ is weighted by the standard deviation or to be more precise by the square root of the inverse of the covariance matrix; then the absolute value is a scalar measure of the relative structural deviation. The test

statistic is finally defined as the sum over all thresholds,

$$T(A_m, P_m, \chi_m) := \sum_{\rho \in \mathbb{N}_0} \left\| \Sigma^{-\frac{1}{2}}_{\rho,m,\lambda} \left(\begin{pmatrix} A_m \\ P_m \\ \chi_m \end{pmatrix} - \mu^\rho \right) \right\|, \tag{6.14}$$

where $\| \cdot \|$ denotes the Euclidean norm. If the test statistic is only defined w.r.t. the area, it is simply given by

$$T(A_m) := \sum_{\rho \in \mathbb{N}_0} \left| \frac{A_m - \mu_A}{\sigma_A} \right|. \tag{6.15}$$

The stronger the structural deviation of the count map from the background shape, the larger these test statistics can get. For the hypothesis test, I then determine the empirical cumulative distribution function of these test statistics for a homogeneous Poisson background a various intensities λ. The advantage of this approach is that it is well-defined for all possible (or even impossible) values of the Minkowski functionals, and a simple Monte Carlo simulation can be applied, because even if a specific configuration appears in the data that has not been found in the simulation of the background, the test statistic provides reasonable results, i.e., deviation strengths that appear for similar structural deviations. Of course, this also means that it is less sensitive to specific uncommon configurations.

Because a less precise knowledge of the background structure is sufficient, I am able to analyze extremely large observation windows, here, up to 100×100. In a simple Monte Carlo simulation, I simulate N =10,000,000 samples for each 10×10, 50×50, and 100×100 count maps with homogeneous background intensities $\lambda = 10, 20, 50, 100, 200$ from which I derive the empirical cumulative distribution functions

$$\hat{F}_{A,P,\chi}(T) := \frac{1}{N} \sum_{i=1}^{N} \mathbf{1}_{\{T_i(A_m, P_m, \chi_m) \leq T\}}, \tag{6.16}$$

or if the test statistic is only defined w.r.t. the area

$$\hat{F}_A(T) := \frac{1}{N} \sum_{i=1}^{N} \mathbf{1}_{\{T_i(A_m) \leq T\}}, \tag{6.17}$$

where $\mathbf{1}_{\{T_i \leq T\}}$ is the indicator function. Figure 6.25 shows the empirical cumulative distribution functions for the different count map sizes and background intensities.

Given a significance level α, I estimate the $(1-\alpha)$-quantile $Q_{1-\alpha}$ from the null hypothesis that the number of counts in each bin is a Poisson random variable with

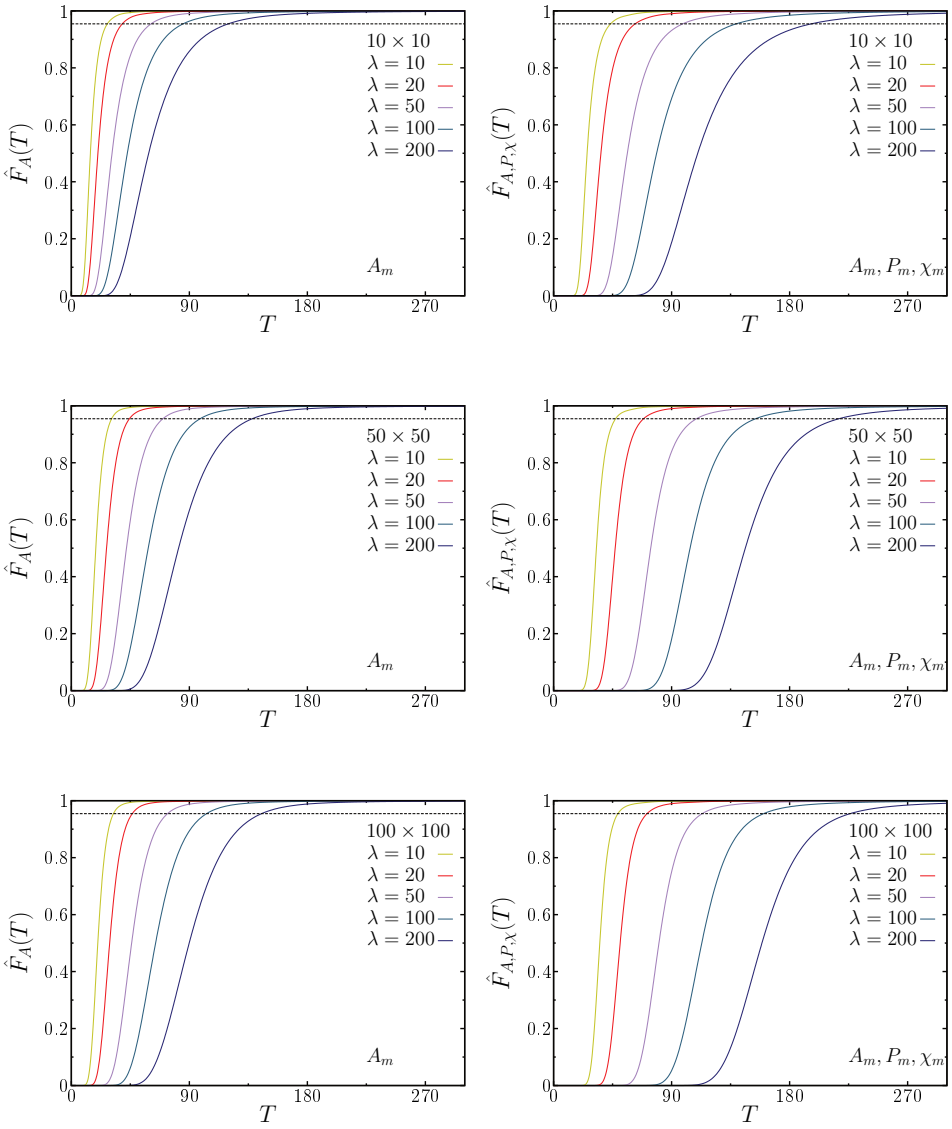

Figure 6.25: Empirical cumulative distribution functions $\hat{F}$ of the test statistic T w.r.t. either only the area (left) or w.r.t. all three Minkowski functionals (right), see Eqs. (6.14)–(6.17), based on 10,000,000 samples for each choice of number of pixels (10×10, 50×50, or 100×100) and mean number of events per pixel λ. The dashed line represents the hypothesis criterion: for a significance level $\alpha = 1 - \mathrm{erf}(\sqrt{2}) \approx 0.0455$, the $(1-\alpha)$-quantile $Q_{1-\alpha}$ is determined; the null hypothesis is rejected if $T > Q_{1-\alpha}$.

mean value λ. This null hypothesis is rejected if $T > Q_{1-\alpha}$, i.e., if the measured test statistic detects a structural deviation too unlikely for a statistical fluctuation (within the given significance α). Of course, I need to distinguish the quantiles for the test statistics either w.r.t. only the area or w.r.t. all three Minkowski functionals: the null hypothesis criteria are

$$T(A_m) > Q^A_{1-\alpha} \text{ or } T(A_m, P_m, \chi_m) > Q^{A,P,\chi}_{1-\alpha} \ , \tag{6.18}$$

respectively.

Given enough samples, i.e., small enough statistical errors, any desired significance level α can be chosen. While in the Sections 6.2.1 or 6.7.1 a very small significance $\alpha = 6.3 \cdot 10^{-7}$ is considered, I want to show here that the new morphometric approach can lead also to a sensitivity increase in less significant fluctuations. In reminiscence of the 2σ criterion for a normal distributed random variable, I here choose $\alpha = 1 - \text{erf}(\sqrt{2}) \approx 0.0455$. For example for a 100×100 count map with a background intensity $\lambda = 50$, the quantiles are $Q^A_{1-\alpha} = 74.89$ or $Q^{A,P,\chi}_{1-\alpha} = 114.84$. These parameters are used in the following section to test the sensitivity .

6.10.3 Sensitive test for inhomogeneities

I have found that the morphometric analysis based on the covariance structure is especially sensitive in detecting inhomogeneities when there is no excess in the expected total number of counts, but the background intensity fluctuates around the expected homogeneous background.

As an example, I simulate a doubly stochastic Poisson process, also called Cox process [100]. It is a generalization of an inhomogeneous Poisson process where the intensity $\lambda(x, y)$ is spatially varying, in other words, a nonconstant function on the observation window. In the Cox processes, this intensity $\lambda(x, y)$ is itself a random field. Therefore, the name "doubly stochastic Poisson process", because it can be seen as a two-stage random process: first, a random field is sampled, then an inhomogeneous Poisson point process is drawn from this distribution [217].

Here, I simulate $\lambda(x, y)$ as a Gaussian random field[20] with mean value $\lambda = 50$. More specifically, I simulate an isotropic Gaussian random wave model where the wave vectors have a constant absolute value $\|\mathbf{k}\| = 10$, see Section 2.1.2. I then simulate the number of counts, i.e., the Poisson random variables with a different mean value for each pixel. Figure 6.26 shows the intensity profiles and samples of

[20] Strictly speaking, I need to ensure that the intensity profile is always strictly positive, but with an amplitude of the fluctuations much smaller than the mean intensity, this does not in the least affect the system.

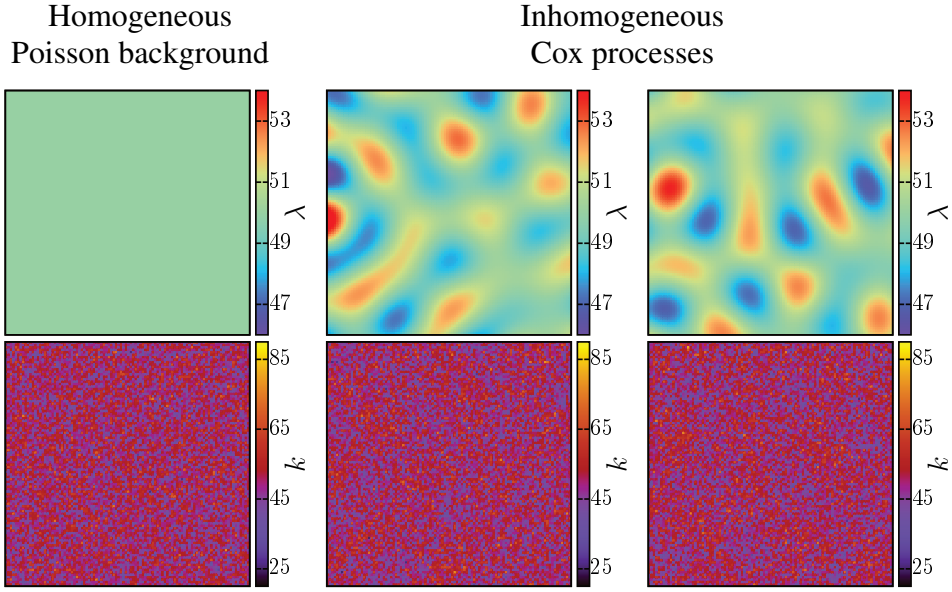

Figure 6.26: Intensity distributions (top) and count maps (bottom) of either a homogeneous Poisson background (left) or of inhomogeneous Cox processes (center and right). The intensity distributions of the latter are Gaussian random fields. Below the maps, the acceptance or rejection of the null hypothesis by the different tests are denoted: σ_{LiMa} the significance of the excess of counts, see Eq. (6.11), $T(A_m)$ the morphometric test statistic w.r.t. only the area, see Eq. (6.15), $T(A_m, P_m, \chi_m)$ the morphometric test statistic w.r.t. area, perimeter, and Euler characteristic, see Eq. (6.14). Without a comparison to the intensity profile, the inhomogeneities are hardly visible by eye. Nevertheless, the joint structure characterization by all three Minkowski functionals allows our morphometric analysis to reject the homogeneous null hypothesis tests reliably.

count maps for a homogeneous background and two different samples of the Cox process.

I then test the null hypothesis of a homogeneous Poisson background noise with the above mentioned testing procedure based on only the area $T(A_m)$ or based on all three Minkowski functionals $T(A_m, P_m, \chi_m)$. I also apply the standard null hypothesis test in gamma-ray astronomy by Li and Ma [273], although it is important to note that the test is not designed for such a scenario. It can only detect the inhomogeneities if there is an excess of counts compared to the expected background. In the Cox process, there can be locally an excess of counts, but this is on average compensated by regions with fewer counts as expected; the expected total number of counts is equivalent to the null hypothesis test. Therefore, applying

						
Amplitude	0	0.8	1.1	1.2	1.3	1.8
σ_{LiMa}	0.046(1)	0.054(1)	0.060(2)	0.062(2)	0.063(3)	0.086(2)
T_{A_m}	0.047(1)	0.092(2)	0.200(2)	0.270(2)	0.352(5)	0.815(3)
T_{A_m,P_m,χ_m}	0.045(1)	0.149(2)	0.453(4)	0.593(3)	0.715(4)	0.980(1)

Table 6.2: Rejection rates of the null hypothesis tests for simulated Cox processes with varying inhomogeneities: to a constant background intensity $\lambda = 50$ a Gaussian random field is added; the strength of the inhomogeneity is quantified by the amplitude of the fluctuations. The systems vary from a homogeneous Poisson point process (left-hand side) to a distinctly inhomogeneous Cox process (right-hand side). Samples are depicted above the corresponding columns. Three different null hypothesis tests each with a 2σ significance level are compared: based on the significance σ_{LiMa} of the excess of counts, see Eq. (6.11) or the morphometric test statistics $T_{A_m} := T(A_m)$ or $T_{A,P,\chi;m} := T(A_m, P_m, \chi_m)$ w.r.t. either only the area, see Eq. (6.15), or w.r.t. all three Minkowski functionals, see Eq. (6.14), respectively. The excess of counts is not designed to detect inhomogeneities, but only fluctuations in the total number of counts. However, our morphometric test statistic can detect these structural deviations. Especially, the combination of all three Minkowski functionals significantly increases the sensitivity.

the null hypothesis test merely reveals that there is indeed no significant change in the total number of counts.

This is not the usual case in gamma-ray astronomy, where an accurate estimate of the background intensity must be derived from observations of off-regions without any source. Then, a source can only lead to additional counts not to fewer counts than expected. Therefore, the discussion in this section might be more interesting for other applications with both negative and positive fluctuations of the intensity. However, for example, for very extended sources or diffuse radiation an independent estimate of the background intensity might be difficult; then, these results could be interesting because our method could detect such a diffuse radiation even if the background intensity is overestimated because of the diffuse radiation.

The samples in Fig. 6.26 are accepted by the null hypothesis test by Li and Ma [273], but while our morphometric analysis accepts the sample consisting only of a homogeneous background it can detect the inhomogeneous samples of the Cox processes even if there is no excess in the number of counts. These samples already indicate the advantage of extending the analysis from only one functional to all three Minkowski functionals, by which not only one of the inhomogeneous samples, but both of them are rejected.

This increase in sensitivity is analyzed more systematically in Table 6.26, where the rejection rates are determined for differently strong fluctuations of the

intensity field, which is quantified by their different amplitudes. More precisely, the intensity is given by a constant background intensity plus a Gaussian random field with zero mean value. The amplitude is a prefactor multiplied to the Gaussian random wave model in Eq. (2.3).

I simulate for each amplitude 20,000 samples of the Cox process; I apply the null hypothesis tests to each sample and check whether they accept or reject the assumption of a homogeneous background for a significance level $\alpha = 1 - \mathrm{erf}(\sqrt{2}) \approx 0.0455$. The rejection rate is then estimated by the fraction of rejected samples.

As mentioned above, the null hypothesis test by Li and Ma [273] is not designed to and cannot detect the inhomogeneities without an excess of the expected total number of counts. The null hypothesis is mostly accepted for the inhomogeneous count maps, and the rejection rate only increases very slightly because the fluctuations of the total number of counts in the Cox process is slightly different from those of the homogeneous background noise.

In contrast to this, the morphometric analysis can detect the structural difference and can reject the null hypothesis, even if only the area is used as a shape descriptor. Although the area cannot access the arrangement of black pixels, the test statistic $T(A_m)$ can still detect the inhomogeneities because it is evaluated for all thresholds. The locally varying intensity can reduce the number of black pixels at some threshold and increase them at other thresholds.

The true potential of the new methods unfolds if all Minkowski functionals are included, the perimeter and the Euler characteristic. The refined structure characterization distinctly increases the sensitivity of the method and the inhomogeneities can be reliably detected, i.e., the null hypothesis is rejected.

In the case of very weak fluctuations (amplitude = 0.8), the combined analysis by all Minkowski functionals rejects about 15% of the simulated count maps, while the null hypothesis test w.r.t. only the area can only reject about 9% of the samples. This difference increases with increasing strength of the fluctuations, for an amplitude of 1.3 the joint characterization by all Minkowski functionals can reject more than twice as many samples than the simple analysis by only the area. For very strong inhomogeneities (amplitude = 1.3), both test statistics can reliable reject the null hypothesis with rejection rates of 98% or 82%, respectively.

In further research, our morphometric analysis should be compared to other tests for inhomogeneities [e.g. 367]. Moreover, we are currently working on the asymptotic theory for infinite number of total counts, where we aim to rigorously prove the consistency of this null hypothesis test, i.e., that deviations from the background are almost surely detected, if there are infinitely many observations.

6.11 Conclusion

Our morphometric analysis is a novel approach to data analysis in VHE gamma-ray astronomy. In contrast to the commonly applied hypothesis test by Ref. [273] to detect a significant excess of gamma-ray counts on top of the expected background, it allows us to incorporate additional morphometric information into the analysis of gamma-ray counts maps. Still, the underlying model depends only on λ, the expected background level of a given measurement, and there is no need for a priori modeling of potential sources, as opposed to an analysis based on a likelihood fit of a comprehensive model to the data, as commonly used in satellite-based gamma-ray experiments, for instance, Fermi/LAT [43].

The morphometric analysis is based on the characterization of the typical structure of a pure homogeneously and isotropically Poisson-distributed background counts map. This typical structure is determined using the Minkowski functionals. Significant deviations from the typical background structure in measured gamma-ray counts maps can be used to detect gamma-ray sources, and Minkowski sky maps can visualize the gamma-ray sources, see Figs. 6.4 and 6.5. I derive an accurate estimate of the distribution of the background structure, which is simultaneously characterized by all Minkowski functionals. Such a refined structure characterization can eventually detect formerly undetected sources.

First, the morphometric analysis is refined in detailed simulation studies. At least for small window sizes, applying a marching square algorithm instead of using a pixelated representation of the count map has no measurable effect, see Fig. 6.6 Because of the repeated null hypothesis tests at different thresholds, a trial correction is needed. I show that assuming independent trials at different thresholds provides a conservative yet close estimate for trial correction, see Fig. 6.7. A local detector acceptance correction can increase the sensitivity of the morphometric analysis in the application to real data significantly, see Fig. 6.10.

The main difficulty is to derive a detailed knowledge about the background fluctuations, in other words, a precise estimate of the joint distribution of area, perimeter, and Euler characteristic. This problem can easily be reformulated in finding the density of states, i.e., the number of b/w images with given values of the Minkowski functionals, see Eq. (6.5). However, the total number of configurations of a 15×15 b/w image is $O(10^{67})$ and the density of states for different macrostates can vary from $O(10^{1})$ to $O(10^{64})$. For accurate estimates of the density of states even for large observation windows up to 15×15, I combine analytic knowledge of the structure distributions with a highly efficient algorithm from statistical physics for estimating densities of states. It is called the Wang-Landau algorithm. With this accurate estimate, see Figs. 6.11 and 6.12, I can perform a null hypothesis test using the joint structure characterization for observation windows larger than 7×7.

Comparing the simple to the joint structure characterization, I can indeed demonstrate a significant increase in sensitivity, see Fig. 6.13. For the same counts map for which the simple deviation strength based only on the area is below 5, i.e., the compatibility is more than 10^{-5}, the joint deviation strength can reach values of nearly 20, i.e., compatibilities less than 10^{-19}, see Fig. 6.14. The compatibility with the background structure drops by 14 orders of magnitude and formerly undetected sources can be detected simply by applying a refined morphometric analysis. Of course, the increase in sensitivity depends on the shape of the source, see Fig. 6.15.

I introduce a new test statistic combining different thresholds, see Eq. (6.8). Instead of the maximum of the deviation strength, I use the sum of the deviation strengths over all thresholds, see Eq. (6.7), and determine the empirical complementary cumulative distribution function, see Fig. 6.16. The combination of the structural information at different thresholds improves especially the detection of diffuse radiation and extended sources, see Fig. 6.18. A comparison of the morphometric analysis to the standard null hypothesis test by Li and Ma in gamma-ray astronomy, see Eqs. (6.10) and (6.11), depends both on the shape of the source and on the experimental details, like the binning or the accuracy of the estimate of the background intensity. The morphometric analysis follows a very different ansatz. Besides the advantage of including additional structural information, it depends less on the size of the scan window and can detect both rather extended and pointlike sources using the same scan window size, compare Figs. 6.13 and 6.19. Moreover, the advantage of additional structural information should be most effective for short observation times and low statistics. Figure 6.20 shows an example for which there is no significant excess in the total number of counts, but the source can still be detected because of the additional structural information.

Figures 6.21–6.23 show Minkowski sky maps of observations by the H.E.S.S. experiment of the gamma-ray source RX J1713.7−3946 and how the improvements of this thesis increase the sensitivity of the morphometric analysis.

Moreover, I discuss an alternative testing procedure which requires less knowledge about the background structure, namely the covariance structure and the empirical cumulative distribution function of the new test statistic, see Eqs. (6.12)–(6.17) and Figs. 6.24 and 6.25, but can still sensitively detect inhomogeneities in cases where there is no excess of the total number of counts, see Fig. 6.26 and Table 6.2.

6.12 Outlook

The morphometric analysis is here shown to be an innovative and efficient spatial data analysis. Via such a structure characterization, more information can be taken

from the same data and the sensitivity increases. Of course, there are even further possibilities to extend the analysis. For example, the method can naturally be extended to any spatial dimension if the structure of the d dimensional b/w image is characterized by the $(d + 1)$ Minkowski functionals. If in other systems different physical properties should be tested, the morphometric analysis can simply be adjusted to other structure measures; see Section 6.12.1.

We have developed the morphometric analysis for analyzing counts map in gamma-ray astronomy, where the counts in different pixels are uncorrelated because they result from different events (showers) clearly separated in time. So, above the morphometric analysis distinguishes homogeneous from inhomogeneous Poisson random fields. However, because we only formulate a null hypothesis and test against any structural deviation. The method can also be used to detect any other deviation from the Poisson assumption, e.g., correlations between the counts in different pixels; see Section 6.12.2.

Note also, that the concept of the morphometric analysis can immediately be extended to other random fields, e.g., the Boolean models or the Gaussian random field. Of course, the probability distributions of the Minkowski functionals need to be determined and probably only numerical estimates are possible.

6.12.1 Other shape descriptors

The above-defined analysis is very general, and indeed any useful shape descriptor can be used. The Minkowski functionals are very versatile tools and can comprehensively quantify the structure of very different random fields. However, if for a certain system another shape index is physically better motivated, it can replace the Minkowski functionals, but the basic idea remains unchanged. Only the probability distribution, i.e., the DoS has to be determined following Section 6.5 using the Wang-Landau algorithm.

The Minkowski functionals already incorporate all additive and conditional continuous scalar geometrical information, and I have already introduced the Minkowski tensors in the morphometric analysis in Ref. [243]. Other shape descriptors like the mean width (which is in two dimensions the perimeter of the convex hull for any compact set) or the convexity number [448] or Betti numbers [387] are directly applicable to the method describe above.

Even functions can be used as shape characteristics; an interesting example might be the cluster function that is the probability of finding two points at a given distance in the same cluster. Only one additional step is needed: the correlation function must be mapped to a scalar. A good choice would be the integral over the absolute value of the difference to the mean value (i.e., expected) correlation function of a Poisson random field; this is well defined if there are no long-range

correlations, because then all correlation functions converge sufficiently fast to the same constant and thus, the difference to zero.

6.12.2 Correlations between pixels

The morphometric analysis is able to detect any structural deviation from a homogeneous Poisson random field. Above, I discuss in detail the detection of inhomogeneities and different background intensities. However, the method is also able to detect if the measured count map is actually not even an inhomogeneous Poisson random field, but if there are correlations between the pixels. There might be no deviation in the number of counts (globally or even locally), but a strong deviation in the structure quantified by the Minkowski functionals.

Although we have developed the morphometric analysis for analyzing counts map with uncorrelated pixels, its use might even be more efficient for other applications with correlations between the counts in different pixels, e.g., in detectors where an event is simultaneously triggered in neighboring pixels.

Chapter 7

Summary

On nearly all length scales, random or disordered spatial structures appear in very different shapes which can determine the physical properties. By combining the knowledge of different fields, I have demonstrated in my thesis how a refined morphometric analysis using Minkowski functionals and tensors allows for a sensitive, robust, and comprehensive structure characterization.

I show the versatility of this approach by applying it to a great variety of very different random spatial systems: physical systems on length scales ranging from nuclear matter to gamma-ray astronomy which are also very different w.r.t. their shape including random fields, particle packings, and cellular systems. Therefore, I determine mean values, higher moments, and probability distributions in both analytic and numeric calculations, and I analyze sky maps from the H.E.S.S. experiment in Chapter 6.

I extend and refine the Minkowski morphometric analysis, e.g., by introducing the Minkowski correlation functions in Chapter 4. I apply the Minkowski functionals and tensors to both common models of porous media (see Chapter 2) and exotic or recently found states of matter, like pasta shapes or disordered hyperuniform sphere packings.

I show how an intuitive and comprehensive shape analysis can help to understand the complex geometry of these systems, which is often a good road to understanding their physics: for example, I find a scaling law for continuum percolation that might help to identify possible candidates for relations to dynamic properties (see Chapter 3), in contrast to a local analysis I find signatures of hyperuniformity in the global structure of the Voronoi diagram (see Chapter 4), I identify the smallest gyroid structure found in dynamical simulations (see Chapter 5), and I show how to detect gamma-ray sources via deviations from the background structure (see Chapter 6).

For the models of porous media, I provide a thorough structure characterization, which is, e.g., important for hypothesis tests or to adjust the model to physical systems, e.g., see Section 2.5.3, or predict their behavior,e.g., see Section 3.3. Moreover, the analysis of these models yields a better understanding of their structure, e.g., that the mean anisotropy of the level sets of a Gaussian random field quantified by interfacial Minkowski tensors can be parameterized by a second-rank tensor, see Section 2.6.6, or to understand the isotropic percolation threshold in anisotropic continuum percolation, see Section 3.2.

In this thesis, a special emphasis is on anisotropy characterization. I compare the common mean intercept (MIL) analysis to the Minkowski tensors and discuss the advantages of the latter over the first. The Minkowski tensors allow for a systematic anisotropy analysis and sensitively quantify anisotropy in systems which appear perfectly anisotropic w.r.t. the MIL analysis, see Sections 2.3.5 and 2.4.3. Besides the detailed analysis of the geometry and topology of the anisotropic Boolean models and level sets of Gaussian random fields, see Sections 2.5 and 2.6, anisotropy also is studied in the tessellation models, for which I construct a map of anisotropy, see Section 4.2, and the Minkowski tensors are used to analyze anisotropic deformations of the pasta shapes, which introduces the Minkowski tensors to nuclear physics, see Section 5.5.

Another key aspect is to not only consider mean values, but also estimate higher moments or even the full probability distribution of Minkowski functionals and show what can be learned from their fluctuations. I discuss in Sections 2.5.4 and 2.5.5 the second moments and the probability density functions of the Minkowski functionals of anisotropic Boolean models. While the variances and covariances exhibit in general a nonuniversal behavior, the probability distributions exhibit a universal qualitative behavior, in that the Minkowski functionals, when suitably normalized, satisfy a central limit theorem [210]. In a simulation study, I find that their rescaled empirical probability density functions collapse to a master curve even for relatively small observation windows. I estimate the probability to find a percolating cluster in a finite observation window, see Section 3.2.1. In Section 4.2, I determine the joint distributions of Minkowski functionals of single cells in random tessellations, and in Sections 4.3–4.6 I define and calculate Minkowski correlation functions and cell-cell probability density functions. For the intricate labyrinthine pasta shapes, I present the distribution of the Euler characteristic, see Section 5.5.3. Finally, I derive accurate estimates of the joint distribution of Minkowski functionals of gamma-ray background, i.e., Poisson random fields, I verify the distribution of the test statistic, see Sections 6.3 and 6.5, and analytically calculate the covariance structure of the Minkowski functionals of a Poisson random field, see Section 6.10.

Among the important achievements of this thesis are, for example, the following results:

1. I provide a detailed shape description of anisotropic Boolean models and the Gaussian random field.

2. I discuss simple and explicit approximations of the isotropic percolation threshold in anisotropic continuum percolation.

3. I introduce global Minkowski correlation functions and show how their sensitivity provides deeper insights to the global structure of tessellations. They can show how systems with the same local structure can exhibit a distinctly different global structure.

4. I identify among the complex pasta shapes the smallest gyroid structure found in dynamical simulations.

5. I achieve to extend the morphometric analysis in gamma-ray astronomy to larger scan windows and show how the refined structure characterization can lead to an increase in sensitivity. Formerly undetected sources can eventually be found in the same data by including structure information.

The powerful Minkowski analysis is demonstrated to offer deep insights into the geometry and physics of these systems. It is provided as a tool for even many more possible applications to random spatial structures in physics.

Appendix A

Formal definition of the morphometric analysis

The counts map can be interpreted as a random vector $\mathbf{n} \in \mathbb{N}_0^{N^2}$ drawn from the probability distribution $\prod_{i=1}^{N^2} \text{Poisson}(n_i, \lambda)$. X is defined as a map of the counts map and the threshold ρ to a macrostate, i.e., a three-dimensional vector containing area A, perimeter P, and Euler characteristic χ:

$$\begin{aligned} X: \quad & \mathbb{N}_0^{N^2} \times \mathbb{N} \to \mathbb{R}^3 \\ & (\mathbf{n}, \rho) \mapsto (A, P, \chi)\,. \end{aligned}$$

If the density of states Ω, which is the number of configurations of black and white pixels (microstate) with the same macrostate (A, P, χ), is given,

$$\begin{aligned} \Omega: \quad & \mathbb{R}^3 \to \mathbb{N}_0 \\ & (A, P, \chi) \mapsto \Omega(A, P, \chi)\,, \end{aligned}$$

then the probability distribution $\mathcal{P}$ of the macrostates is given by

$$\begin{aligned} \mathcal{P}: \quad & \mathbb{R}^3 \to [0, 1] \\ & (A, P, \chi) \mapsto \Omega(A, P, \chi) \cdot p_\rho^A \cdot (1 - p_\rho)^{N^2 - A}\,, \end{aligned}$$

with p_ρ the probability that a pixel is black, i.e., that $n_i > \rho$,

$$p_\rho := \sum_{i=\rho}^{\infty} \frac{\lambda^i}{i!} e^{-\lambda}\,.$$

The compatibility C maps the bin field and the threshold ρ to a real value:

$$\begin{aligned} C: \quad & \mathbb{N}_0^{N^2} \times \mathbb{N} \to \mathbb{R} \\ & (\mathbf{n}, \rho) \mapsto \sum_{\mathcal{P}(X_i) \leq \mathcal{P}(X(\mathbf{n},\rho))} \mathcal{P}(X_i)\,, \end{aligned}$$

summing over the probabilities for all macrostates that are less likely. The deviation strength $\mathcal{D}$ is simply

$$\begin{aligned} \mathcal{D}: \quad & \mathbb{N}_0^{N^2} \times \mathbb{N} \to \mathbb{R} \\ & (\mathbf{n}, \rho) \mapsto -\log_{10}\left(C(\mathbf{n}, \rho)\right)\,. \end{aligned}$$

The morphometric analysis can be summarized as a mapping $\mathcal{M}$ of a count map to the space of null sequences $c_0 \subset \mathbb{R}^{\mathbb{N}}$:

$$\begin{aligned} \mathcal{M}: \quad & \mathbb{N}_0^{N^2} \to c_0 \\ & \mathbf{n} \mapsto (\mathcal{D}(\mathbf{n}, i))_{i \in \mathbb{N}}\,. \end{aligned}$$

For constructing the Minkowski sky map, the maximum of this null sequence is assigned to each pixel, which is simply the infinity norm,

$$\begin{aligned} l_\infty: \quad & c_0 \to \mathbb{R} \\ & (\mathcal{D}(\mathbf{n}, i))_{i \in \mathbb{N}} \mapsto \max_{i \in \mathbb{N}} \{\mathcal{D}(\mathbf{n}, i)\}\,. \end{aligned}$$

Appendix B

Look-up tables for Minkowski tensors

In Ref. [243], I provided look-up tables for the translational invariant Minkowski functionals and the Minkowski tensor $W_1^{0,2}$ of a 2 D black and white (b/w) image where the marching square algorithm has been applied. Here, I supplement this by the translational invariant Minkowski tensors $W_1^{0,s}$ of arbitrary rank and the translational covariant tensors $W_2^{r,0}$. The values from the look-up tables from Ref. [243] are also repeated for completeness.

For convenience, the normalization of the Minkowski functionals and tensors are here chosen to be

$$W_1^{0,s} = \int_{\partial M} \mathrm{d}l\, \mathbf{n}^s,$$
$$W_2^{r,0} = \int_{\partial M} \mathrm{d}l\, \mathbf{x}^r \frac{\kappa}{2\pi}\,.$$

The unit of length is a pixel.

In the look-up tables for the covariant tensors, the center of the 2×2 neighborhood, i.e., the common vertex of all four pixels, is used as a point of reference, i.e., the look-up table lists the functional values $W_\nu^{r,s}(M_i)$ of the ith marching square polygon within the 2×2 neighborhood w.r.t. this center. The whole domain M within the observation window is the union of the Minkowski sums with the vector t_i between the center of the 2×2 neighborhood and the point of reference of the whole observation window: $M = \bigcup_i (M_i \uplus t_i)$. The Minkowski tensor of

the observation window is

$$W_\nu^{r,s}(M) = \sum_i \sum_{c=0}^{r} \binom{r}{c} t_i^c \otimes W_\nu^{r-c,s}(M_i)$$

with $\otimes$ the symmetric tensor product, see Ref. [406].

In this thesis, look-up tables for the tensors $W_2^{r,0}$ are given. The local contribution can be taken from Tables B.11–B.18, the displacement t is calculated, and the contribution to the Minkowski tensor is given by

$$W_2^{r,0}(M_i \uplus t_i) = \sum_{c=0}^{r} \binom{r}{c} t_i^c \otimes W_2^{r-c,0}(M_i) \ .$$

For example,

$$W_2^{1,0}(M_i \uplus t_i) = W_2^{1,0}(M_i) + W_2(M_i) \cdot t_i$$
$$W_2^{2,0}(M_i \uplus t_i) = W_2^{2,0}(M_i) + W_2^{1,0}(M_i) \otimes t_i + t_i \otimes W_2^{1,0}(M_i) + W_2(M_i) \cdot t_i \otimes t_i$$

Note that if the image is pixelated, i.e., the marching square algorithm does not introduce diagonal boundary segments, the look-up table for the Minkowski tensors $W_2^{r,0}$ is very simple, because the only point with nonvanishing curvature is at $x = y = 0$:

$$W_2^{r,0} \equiv 0, \qquad \forall r > 0 \ .$$

Then, the Minkowski tensor of the observation window is simply given by

$$W_2^{r,0}(M) = \sum_i W_2(M_i) \cdot t_i^r \ .$$

If the points with nonvanishing curvature lie on the boundary of the 2×2 neighborhood, the opening angle of a wedge and thus the curvature at this point is unknown in a single step of the iteration. However, if the endpoints of the boundary within a 2×2 neighborhood are approximated via an infinitesimal line perpendicular to the boundary of the 2×2 neighborhood, the points with nonvanishing curvature are again within the neighborhood and a contribution to $W_2^{r,0}$ can be assigned to each patch. The look-up table for the Minkowski tensors are given in Tables B.1–B.9 or Tables B.10–B.18 for translational invariant or covariant Minkowski tensors, respectively.

The here chosen algorithm connects two black pixels in a 2×2 neighborhood that are connected only via one vertex, i.e., with two adjacent white pixels. Look-up tables for algorithms disconnecting these or disconnecting them with some

probability can very easily be produced from the tables given here by summing the contributions of configurations with only one black pixel, i.e., of numbers two and four or one and eight, respectively.

The look-up tables presented here can be used for different boundary conditions. The nine tables per Minkowski functional or tensor are for direct application to minus-sampling boundary conditions. If the center of a pixel in the 2×2 neighborhood belongs to an outermost row or column of the observation window, the corresponding pixel does not contribute to the Minkowski functionals or tensors, i.e., if a line and thus the wedges are within an outermost row or column, they do not contribute.

Config.	Nr.	Area A	Perimeter P	Euler χ	Minkowski Tensor $(W_1^{0,2})_{xx}$	$(W_1^{0,2})_{xy}$	$(W_1^{0,2})_{yy}$	$(W_1^{0,s})_{\underbrace{x\ldots x}_{n}\underbrace{y\ldots y}_{m}}$
	0	0	0	0	0	0	0	0
	1	1/8	$\sqrt{2}/2$	1/4	$\sqrt{2}/4$	$-\sqrt{2}/4$	$\sqrt{2}/4$	$(-1)^n/(2\sqrt{2}^{s-1})$
	2	1/8	$\sqrt{2}/2$	1/4	$\sqrt{2}/4$	$\sqrt{2}/4$	$\sqrt{2}/4$	$1/(2\sqrt{2}^{s-1})$
	3	1/2	1	0	0	0	1	δ_{n0}
	4	1/8	$\sqrt{2}/2$	1/4	$\sqrt{2}/4$	$\sqrt{2}/4$	$\sqrt{2}/4$	$(-1)^s/(2\sqrt{2}^{s-1})$
	5	1/2	1	0	1	0	0	$(-1)^n\delta_{m0}$
	6	3/4	$\sqrt{2}$	-1/2	$\sqrt{2}/2$	$-\sqrt{2}/2$	$\sqrt{2}/2$	$[(-1)^n+(-1)^m]/(2\sqrt{2}^{s-1})$
	7	7/8	$\sqrt{2}/2$	-1/4	$\sqrt{2}/4$	$-\sqrt{2}/4$	$\sqrt{2}/4$	$(-1)^n/(2\sqrt{2}^{s-1})$
	8	1/8	$\sqrt{2}/2$	1/4	$\sqrt{2}/4$	$-\sqrt{2}/4$	$\sqrt{2}/4$	$(-1)^m/(2\sqrt{2}^{s-1})$
	9	3/4	$\sqrt{2}$	-1/2	$\sqrt{2}/2$	$\sqrt{2}/2$	$\sqrt{2}/2$	$[1+(-1)^s]/(2\sqrt{2}^{s-1})$
	10	1/2	1	0	1	0	0	δ_{m0}
	11	7/8	$\sqrt{2}/2$	-1/4	$\sqrt{2}/4$	$\sqrt{2}/4$	$\sqrt{2}/4$	$1/(2\sqrt{2}^{s-1})$
	12	1/2	1	0	0	0	1	$(-1)^m\delta_{n0}$
	13	7/8	$\sqrt{2}/2$	-1/4	$\sqrt{2}/4$	$\sqrt{2}/4$	$\sqrt{2}/4$	$(-1)^s/(2\sqrt{2}^{s-1})$
	14	7/8	$\sqrt{2}/2$	-1/4	$\sqrt{2}/4$	$-\sqrt{2}/4$	$\sqrt{2}/4$	$(-1)^m/(2\sqrt{2}^{s-1})$
	15	1	0	0	0	0	0	0

Table B.1: Translational invariant Minkowski functionals and tensors of a 2×2 neighborhood in the interior of the observation window; the values for the Minkowski functionals and the tensor $W_1^{0,2}$ are taken from Ref. [243].

Config.	Nr.	Area A	Perimeter P	Euler χ	Minkowski Tensor $(W_1^{0,2})_{xx}$	$(W_1^{0,2})_{xy}$	$(W_1^{0,2})_{yy}$	$(W_1^{0,s})_{\underbrace{x\ldots x}_{n}\underbrace{y\ldots y}_{m}}$
	0	0	0	0	0	0	0	0
	1	1/8	$\sqrt{2}/2$	1/4	$\sqrt{2}/4$	$-\sqrt{2}/4$	$\sqrt{2}/4$	$(-1)^n/(2\sqrt{2}^{s-1})$
	2	1/8	$\sqrt{2}/2$	1/4	$\sqrt{2}/4$	$\sqrt{2}/4$	$\sqrt{2}/4$	$1/(2\sqrt{2}^{s-1})$
	3	1/2	1	0	0	0	1	δ_{n0}
	4	0	0	0	0	0	0	0
	5	1/4	1/2	0	1/2	0	0	$(-1)^n\delta_{m0}/2$
	6	3/8	$\sqrt{2}/2$	-1/4	$\sqrt{2}/4$	$-\sqrt{2}/4$	$\sqrt{2}/4$	$(-1)^m/(2\sqrt{2}^{s-1})$
	7	1/2	0	-1/8	0	0	0	0
	8	0	0	0	0	0	0	0
	9	3/8	$\sqrt{2}/2$	-1/4	$\sqrt{2}/4$	$\sqrt{2}/4$	$\sqrt{2}/4$	$(-1)^s/(2\sqrt{2}^{s-1})$
	10	1/4	1/2	0	1/2	0	0	$\delta_{m0}/2$
	11	1/2	0	-1/8	0	0	0	0
	12	0	0	0	0	0	0	0
	13	3/8	$\sqrt{2}/2$	-1/8	$\sqrt{2}/4$	$\sqrt{2}/4$	$\sqrt{2}/4$	$(-1)^s/(2\sqrt{2}^{s-1})$
	14	3/8	$\sqrt{2}/2$	-1/8	$\sqrt{2}/4$	$-\sqrt{2}/4$	$\sqrt{2}/4$	$(-1)^m/(2\sqrt{2}^{s-1})$
	15	1/2	0	0	0	0	0	0

Table B.2: Translational invariant Minkowski functionals and tensors of a 2×2 neighborhood in the top row of the observation window; the values for the Minkowski functionals and the tensor $W_1^{0,2}$ are taken from Ref. [243].

Config.	Nr.	Area A	Perimeter P	Euler χ	Minkowski Tensor $(W_1^{0,2})_{xx}$	$(W_1^{0,2})_{xy}$	$(W_1^{0,2})_{yy}$	$(W_1^{0,s})_{\overbrace{x\ldots x}^{n}\overbrace{y\ldots y}^{m}}$
	0	0	0	0	0	0	0	0
	1	1/8	$\sqrt{2}/2$	1/4	$\sqrt{2}/4$	$-\sqrt{2}/4$	$\sqrt{2}/4$	$(-1)^n/(2\sqrt{2}^{s-1})$
	2	0	0	0	0	0	0	0
	3	1/4	1/2	0	0	0	1/2	$\delta_{n0}/2$
	4	1/8	$\sqrt{2}/2$	1/4	$\sqrt{2}/4$	$\sqrt{2}/4$	$\sqrt{2}/4$	$(-1)^s/(2\sqrt{2}^{s-1})$
	5	1/2	1	0	1	0	0	$(-1)^n\delta_{m0}$
	6	3/8	$\sqrt{2}/2$	-1/4	$\sqrt{2}/4$	$-\sqrt{2}/4$	$\sqrt{2}/4$	$(-1)^m/(2\sqrt{2}^{s-1})$
	7	1/2	0	-1/8	0	0	0	0
	8	0	0	0	0	0	0	0
	9	3/8	$\sqrt{2}/2$	-1/4	$\sqrt{2}/4$	$\sqrt{2}/4$	$\sqrt{2}/4$	$1/(2\sqrt{2}^{s-1})$
	10	0	0	0	0	0	0	0
	11	3/8	$\sqrt{2}/2$	-1/8	$\sqrt{2}/4$	$\sqrt{2}/4$	$\sqrt{2}/4$	$1/(2\sqrt{2}^{s-1})$
	12	1/4	1/2	0	0	0	1/2	$(-1)^m\delta_{n0}/2$
	13	1/2	0	-1/8	0	0	0	0
	14	3/8	$\sqrt{2}/2$	-1/8	$\sqrt{2}/4$	$-\sqrt{2}/4$	$\sqrt{2}/4$	$(-1)^m/(2\sqrt{2}^{s-1})$
	15	1/2	0	0	0	0	0	0

Table B.3: Translational invariant Minkowski functionals and tensors of a 2×2 neighborhood in the far-left column of the observation window; the values for the Minkowski functionals and the tensor $W_1^{0,2}$ are taken from Ref. [243].

Config.	Area	Perimeter	Euler	Minkowski Tensor				
Nr.	A	P	χ	$(W_1^{0,2})_{xx}$	$(W_1^{0,2})_{xy}$	$(W_1^{0,2})_{yy}$	$(W_1^{0,s})$	$\overbrace{x\ldots x}^{n}\overbrace{y\ldots y}^{m}$
0	0	0	0	0	0	0	0	0
1	0	0	0	0	0	0	0	0
2	1/8	$\sqrt{2}/2$	1/4	$\sqrt{2}/4$	$\sqrt{2}/4$	$\sqrt{2}/4$	$1/(2\sqrt{2}^{s-1})$	
3	1/4	1/2	0	0	0	1/2	$\delta_{n0}/2$	
4	0	0	0	0	0	0	0	0
5	0	0	0	0	0	0	0	0
6	3/8	$\sqrt{2}/2$	-1/4	$\sqrt{2}/4$	$-\sqrt{2}/4$	$\sqrt{2}/4$	$(-1)^n/(2\sqrt{2}^{s-1})$	
7	3/8	$\sqrt{2}/2$	-1/8	$\sqrt{2}/4$	$-\sqrt{2}/4$	$\sqrt{2}/4$	$(-1)^n/(2\sqrt{2}^{s-1})$	
8	1/8	$\sqrt{2}/2$	1/4	$\sqrt{2}/4$	$-\sqrt{2}/4$	$\sqrt{2}/4$	$(-1)^m/(2\sqrt{2}^{s-1})$	
9	3/8	$\sqrt{2}/2$	-1/4	$\sqrt{2}/4$	$\sqrt{2}/4$	$\sqrt{2}/4$	$(-1)^s/(2\sqrt{2}^{s-1})$	
10	1/2	1	0	1	0	0	δ_{m0}	
11	1/2	0	-1/8	0	0	0	0	
12	1/4	1/2	0	0	0	1/2	$(-1)^m\delta_{n0}/2$	
13	3/8	$\sqrt{2}/2$	-1/8	$\sqrt{2}/4$	$\sqrt{2}/4$	$\sqrt{2}/4$	$(-1)^s/(2\sqrt{2}^{s-1})$	
14	1/2	0	-1/8	0	0	0	0	
15	1/2	0	0	0	0	0	0	

Table B.4: Translational invariant Minkowski functionals and tensors of a 2×2 neighborhood in the far-right column of the observation window; the values for the Minkowski functionals and the tensor $W_1^{0,2}$ are taken from Ref. [243].

Config.	Nr.	Area	Perimeter	Euler	Minkowski Tensor				
		A	P	χ	$(W_1^{0,2})_{xx}$	$(W_1^{0,2})_{xy}$	$(W_1^{0,2})_{yy}$	$(W_1^{0,s})$	$\underbrace{x\ldots x}_{n}\underbrace{y\ldots y}_{m}$
	0	0	0	0	0	0	0		0
	1	0	0	0	0	0	0		0
	2	0	0	0	0	0	0		0
	3	0	0	0	0	0	0		0
	4	1/8	$\sqrt{2}/2$	1/4	$\sqrt{2}/4$	$\sqrt{2}/4$	$\sqrt{2}/4$	$(-1)^s/(2\sqrt{2}^{s-1})$	
	5	1/4	1/2	0	1/2	0	0	$(-1)^n\delta_{m0}/2$	
	6	3/8	$\sqrt{2}/2$	-1/4	$\sqrt{2}/4$	$-\sqrt{2}/4$	$\sqrt{2}/4$	$(-1)^n/(2\sqrt{2}^{s-1})$	
	7	3/8	$\sqrt{2}/2$	-1/8	$\sqrt{2}/4$	$-\sqrt{2}/4$	$\sqrt{2}/4$	$(-1)^n/(2\sqrt{2}^{s-1})$	
	8	1/8	$\sqrt{2}/2$	1/4	$\sqrt{2}/4$	$-\sqrt{2}/4$	$\sqrt{2}/4$	$(-1)^m/(2\sqrt{2}^{s-1})$	
	9	3/8	$\sqrt{2}/2$	-1/4	$\sqrt{2}/4$	$\sqrt{2}/4$	$\sqrt{2}/4$	$1/(2\sqrt{2}^{s-1})$	
	10	1/4	1/2	0	1/2	0	0	$\delta_{m0}/2$	
	11	3/8	$\sqrt{2}/2$	-1/8	$\sqrt{2}/4$	$\sqrt{2}/4$	$\sqrt{2}/4$	$1/(2\sqrt{2}^{s-1})$	
	12	1/2	1	0	0	0	1	$(-1)^m\delta_{n0}$	
	13	1/2	0	-1/8	0	0	0	0	
	14	1/2	0	-1/8	0	0	0	0	
	15	1/2	0	0	0	0	0	0	

Table B.5: Translational invariant Minkowski functionals and tensors of a 2×2 neighborhood in the bottom row of the observation window; the values for the Minkowski functionals and the tensor $W_1^{0,2}$ are taken from Ref. [243].

Config. Nr.	Area A	Perimeter P	Euler χ	Minkowski Tensor $(W_1^{0,2})_{xx}$	$(W_1^{0,2})_{xy}$	$(W_1^{0,2})_{yy}$	$(W_1^{0,s})_{\overbrace{x\ldots x}^{n}\overbrace{y\ldots y}^{m}}$
0	0	0	0	0	0	0	0
1	1/8	$\sqrt{2}/2$	1/4	$\sqrt{2}/4$	$-\sqrt{2}/4$	$\sqrt{2}/4$	$(-1)^n/(2\sqrt{2}^{s-1})$
2	0	0	0	0	0	0	0
3	1/4	1/2	0	0	0	1/2	$\delta_{n0}/2$
4	0	0	0	0	0	0	0
5	1/4	1/2	0	1/2	0	0	$(-1)^n\delta_{m0}/2$
6	1/8	$\sqrt{2}/2$	0	$\sqrt{2}/4$	$-\sqrt{2}/4$	$\sqrt{2}/4$	$(-1)^m/(2\sqrt{2}^{s-1})$
7	1/4	0	0	0	0	0	0
8	0	0	0	0	0	0	0
9	1/4	0	-1/4	0	0	0	0
10	0	0	0	0	0	0	0
11	1/4	0	-1/8	0	0	0	0
12	0	0	0	0	0	0	0
13	1/4	0	-1/8	0	0	0	0
14	1/8	$\sqrt{2}/2$	0	$\sqrt{2}/4$	$-\sqrt{2}/4$	$\sqrt{2}/4$	$(-1)^m/(2\sqrt{2}^{s-1})$
15	1/4	0	0	0	0	0	0

Table B.6: Translational invariant Minkowski functionals and tensors of a 2×2 neighborhood in the top left corner of the observation window; the values for the Minkowski functionals and the tensor $W_1^{0,2}$ are taken from Ref. [243].

Config.	Nr.	Area	Perimeter	Euler	Minkowski Tensor				
		A	P	χ	$(W_1^{0,2})_{xx}$	$(W_1^{0,2})_{xy}$	$(W_1^{0,2})_{yy}$	$(W_1^{0,s})$	$\underbrace{x\ldots x}_{n}\underbrace{y\ldots y}_{m}$
	0	0	0	0	0	0	0		0
	1	0	0	0	0	0	0		0
	2	1/8	$\sqrt{2}/2$	1/4	$\sqrt{2}/4$	$\sqrt{2}/4$	$\sqrt{2}/4$		$1/(2\sqrt{2}^{s-1})$
	3	1/4	1/2	0	0	0	1/2		$\delta_{n0}/2$
	4	0	0	0	0	0	0		0
	5	0	0	0	0	0	0		0
	6	1/4	0	-1/4	0	0	0		0
	7	1/4	0	-1/8	0	0	0		0
	8	0	0	0	0	0	0		0
	9	1/8	$\sqrt{2}/2$	0	$\sqrt{2}/4$	$\sqrt{2}/4$	$\sqrt{2}/4$		$(-1)^s/(2\sqrt{2}^{s-1})$
	10	1/4	1/2	0	1/2	0	0		$\delta_{m0}/2$
	11	1/4	0	0	0	0	0		0
	12	0	0	0	0	0	0		0
	13	1/8	$\sqrt{2}/2$	0	$\sqrt{2}/4$	$\sqrt{2}/4$	$\sqrt{2}/4$		$(-1)^s/(2\sqrt{2}^{s-1})$
	14	1/4	0	-1/8	0	0	0		0
	15	1/4	0	0	0	0	0		0

Table B.7: Translational invariant Minkowski functionals and tensors of a 2×2 neighborhood in the top right corner of the observation window; the values for the Minkowski functionals and the tensor $W_1^{0,2}$ are taken from Ref. [243].

Config. Nr.	Area A	Perimeter P	Euler χ	Minkowski Tensor $(W_1^{0,2})_{xx}$	$(W_1^{0,2})_{xy}$	$(W_1^{0,2})_{yy}$	$(W_1^{0,s})_{\overbrace{x\ldots x}^{n}\overbrace{y\ldots y}^{m}}$
0	0	0	0	0	0	0	0
1	0	0	0	0	0	0	0
2	0	0	0	0	0	0	0
3	0	0	0	0	0	0	0
4	1/8	$\sqrt{2}/2$	1/4	$\sqrt{2}/4$	$\sqrt{2}/4$	$\sqrt{2}/4$	$(-1)^s/(2\sqrt{2}^{s-1})$
5	1/4	1/2	0	1/2	0	0	$(-1)^n\delta_{m0}/2$
6	1/4	0	-1/4	0	0	0	0
7	1/4	0	-1/8	0	0	0	0
8	0	0	0	0	0	0	0
9	1/8	$\sqrt{2}/2$	0	$\sqrt{2}/4$	$\sqrt{2}/4$	$\sqrt{2}/4$	$1/(2\sqrt{2}^{s-1})$
10	0	0	0	0	0	0	0
11	1/8	$\sqrt{2}/2$	0	$\sqrt{2}/4$	$\sqrt{2}/4$	$\sqrt{2}/4$	$1/(2\sqrt{2}^{s-1})$
12	1/4	1/2	0	0	0	1/2	$(-1)^m\delta_{n0}/2$
13	1/4	0	0	0	0	0	0
14	1/4	0	-1/8	0	0	0	0
15	1/4	0	0	0	0	0	0

Table B.8: Translational invariant Minkowski functionals and tensors of a 2×2 neighborhood in the bottom left corner of the observation window; the values for the Minkowski functionals and the tensor $W_1^{0,2}$ are taken from Ref. [243].

Config.	Nr.	Area	Perimeter	Euler	Minkowski Tensor				
		A	P	χ	$(W_1^{0,2})_{xx}$	$(W_1^{0,2})_{xy}$	$(W_1^{0,2})_{yy}$	$(W_1^{0,s})$	$\underbrace{x\ldots x}_{n}\underbrace{y\ldots y}_{m}$
	0	0	0	0	0	0	0		0
	1	0	0	0	0	0	0		0
	2	0	0	0	0	0	0		0
	3	0	0	0	0	0	0		0
	4	0	0	0	0	0	0		0
	5	0	0	0	0	0	0		0
	6	1/8	$\sqrt{2}/2$	0	$\sqrt{2}/4$	$-\sqrt{2}/4$	$\sqrt{2}/4$	$(-1)^n/(2\sqrt{2}^{s-1})$	
	7	1/8	$\sqrt{2}/2$	0	$\sqrt{2}/4$	$-\sqrt{2}/4$	$\sqrt{2}/4$	$(-1)^n/(2\sqrt{2}^{s-1})$	
	8	1/8	$\sqrt{2}/2$	1/4	$\sqrt{2}/4$	$-\sqrt{2}/4$	$\sqrt{2}/4$	$(-1)^m/(2\sqrt{2}^{s-1})$	
	9	1/4	0	-1/4	0	0	0		0
	10	1/4	1/2	0	1/2	0	0		$\delta_{m0}/2$
	11	1/4	0	-1/8	0	0	0		0
	12	1/4	1/2	0	0	0	1/2		$(-1)^m\delta_{n0}/2$
	13	1/4	0	-1/8	0	0	0		0
	14	1/4	0	0	0	0	0		0
	15	1/4	0	0	0	0	0		0

Table B.9: Translational invariant Minkowski functionals and tensors of a 2×2 neighborhood in the bottom right corner of the observation window; the values for the Minkowski functionals and the tensor $W_1^{0,2}$ are taken from Ref. [243].

Config. Nr.	Minkowski Vector $(W_2^{1,0})_x$	Minkowski Vector $(W_2^{1,0})_y$	Minkowski Tensors $(W_2^{2,0})_{xx}$	Minkowski Tensors $(W_2^{r,0})_{\overbrace{x\ldots x}^{n}\overbrace{y\ldots y}^{m}}$
0	0	0	0	0
1	1/16	-1/16	1/32	$[\delta_{n0}\cdot(-1)^m+\delta_{m0}]/(8\cdot 2^r)$
2	-1/16	-1/16	1/32	$[\delta_{n0}\cdot(-1)^m+\delta_{m0}\cdot(-1)^n]/(8\cdot 2^r)$
3	0	0	0	0
4	1/16	1/16	1/32	$[\delta_{n0}+\delta_{m0}]/(8\cdot 2^r)$
5	0	0	0	0
6	0	0	-1/16	$(-1)\cdot[\delta_{n0}\cdot(1+(-1)^m)+\delta_{m0}\cdot(1+(-1)^n)]/(8\cdot 2^r)$
7	1/16	-1/16	-1/32	$(-1)\cdot[\delta_{n0}+\delta_{m0}\cdot(-1)^n]/(8\cdot 2^r)$
8	-1/16	1/16	1/32	$[\delta_{n0}+\delta_{m0}\cdot(-1)^n]/(8\cdot 2^r)$
9	0	0	-1/16	$(-1)\cdot[\delta_{n0}\cdot(1+(-1)^m)+\delta_{m0}\cdot(1+(-1)^n)]/(8\cdot 2^r)$
10	0	0	0	0
11	-1/16	-1/16	-1/32	$(-1)\cdot[\delta_{n0}+\delta_{m0}]/(8\cdot 2^r)$
12	0	0	0	0
13	1/16	1/16	-1/32	$(-1)\cdot[\delta_{n0}\cdot(-1)^m+\delta_{m0}\cdot(-1)^n]/(8\cdot 2^r)$
14	-1/16	1/16	-1/32	$(-1)\cdot[\delta_{n0}\cdot(-1)^m+\delta_{m0}]/(8\cdot 2^r)$
15	0	0	0	0

Table B.10: Minkowski functionals and tensors of a 2×2 neighborhood in the interior of the observation window; $(W_2^{2,0})_{yy}\equiv(W_2^{2,0})_{xx}$ and $(W_2^{2,0})_{xy}\equiv 0$.

Config. Nr.	Minkowski Vector $(W_2^{1,0})_x$	Minkowski Vector $(W_2^{1,0})_y$	Minkowski Tensors $(W_2^{2,0})_{xx}$	Minkowski Tensors $(W_2^{r,0})_{\underbrace{x\ldots x}_{n}\underbrace{y\ldots y}_{m}}$
0	0	0	0	0
1	1/16	-1/16	1/32	$[\delta_{n0}\cdot(-1)^m+\delta_{m0}]/(8\cdot 2^r)$
2	-1/16	-1/16	1/32	$[\delta_{n0}\cdot(-1)^m+\delta_{m0}\cdot(-1)^n]/(8\cdot 2^r)$
3	0	0	0	0
4	0	0	0	0
5	0	0	0	0
6	-1/16	1/16	-1/32	$(-1)\cdot[\delta_{n0}\cdot(-1)^m+\delta_{m0}]/(8\cdot 2^r)$
7	0	0	0	0
8	0	0	0	0
9	1/16	1/16	-1/32	$(-1)\cdot[\delta_{n0}\cdot(-1)^m+\delta_{m0}\cdot(-1)^n]/(8\cdot 2^r)$
10	0	0	0	0
11	0	0	0	0
12	0	0	0	0
13	1/16	1/16	-1/32	$(-1)\cdot[\delta_{n0}\cdot(-1)^m+\delta_{m0}\cdot(-1)^n]/(8\cdot 2^r)$
14	-1/16	1/16	-1/32	$(-1)\cdot[\delta_{n0}\cdot(-1)^m+\delta_{m0}]/(8\cdot 2^r)$
15	0	0	0	0

Table B.11: Minkowski functionals and tensors of a 2×2 neighborhood in the top row of the observation window; $(W_2^{2,0})_{yy}\equiv(W_2^{2,0})_{xx}$ and $(W_2^{2,0})_{xy}\equiv 0$.

Config. Nr.	Minkowski Vector $(W_2^{1,0})_x$	$(W_2^{1,0})_y$	Minkowski Tensors $(W_2^{2,0})_{xx}$	$(W_2^{r,0})_{\underbrace{x\ldots x}_{n}\underbrace{y\ldots y}_{m}}$
0	0	0	0	0
1	1/16	-1/16	1/32	$[\delta_{n0}\cdot(-1)^m+\delta_{m0}]/(8\cdot 2^r)$
2	0	0	0	0
3	0	0	0	0
4	1/16	1/16	1/32	$[\delta_{n0}+\delta_{m0}]/(8\cdot 2^r)$
5	0	0	0	0
6	-1/16	1/16	-1/32	$(-1)\cdot[\delta_{n0}\cdot(-1)^m+\delta_{m0}]/(8\cdot 2^r)$
7	0	0	0	0
8	0	0	0	0
9	-1/16	-1/16	-1/32	$(-1)\cdot[\delta_{n0}+\delta_{m0}]/(8\cdot 2^r)$
10	0	0	0	0
11	-1/16	-1/16	-1/32	$(-1)\cdot[\delta_{n0}+\delta_{m0}]/(8\cdot 2^r)$
12	0	0	0	0
13	0	0	0	0
14	-1/16	1/16	-1/32	$(-1)\cdot[\delta_{n0}\cdot(-1)^m+\delta_{m0}]/(8\cdot 2^r)$
15	0	0	0	0

Table B.12: Minkowski functionals and tensors of a 2×2 neighborhood in the far-left column of the observation window; $(W_2^{2,0})_{yy}\equiv(W_2^{2,0})_{xx}$ and $(W_2^{2,0})_{xy}\equiv 0$.

Config.	Nr.	Minkowski Vector		Minkowski Tensors		
		$(W_2^{1,0})_x$	$(W_2^{1,0})_y$	$(W_2^{2,0})_{xx}$	$(W_2^{r,0})$ $\underbrace{x\ldots x}_{n}\underbrace{y\ldots y}_{m}$	
	0	0	0	0	0	
	1	0	0	0	0	
	2	-1/16	-1/16	1/32	$[\delta_{n0}\cdot(-1)^m+\delta_{m0}\cdot(-1)^n]/(8\cdot 2^r)$	
	3	0	0	0	0	
	4	0	0	0	0	
	5	0	0	0	0	
	6	1/16	-1/16	-1/32	$(-1)\cdot[\delta_{n0}+\delta_{m0}\cdot(-1)^n]/(8\cdot 2^r)$	
	7	1/16	-1/16	-1/32	$(-1)\cdot[\delta_{n0}+\delta_{m0}\cdot(-1)^n]/(8\cdot 2^r)$	
	8	-1/16	1/16	1/32	$[\delta_{n0}+\delta_{m0}\cdot(-1)^n]/(8\cdot 2^r)$	
	9	1/16	1/16	-1/32	$(-1)\cdot[\delta_{n0}\cdot(-1)^m+\delta_{m0}\cdot(-1)^n]/(8\cdot 2^r)$	
	10	0	0	0	0	
	11	0	0	0	0	
	12	0	0	0	0	
	13	1/16	1/16	-1/32	$(-1)\cdot[\delta_{n0}\cdot(-1)^m+\delta_{m0}\cdot(-1)^n]/(8\cdot 2^r)$	
	14	0	0	0	0	
	15	0	0	0	0	

Table B.13: Minkowski functionals and tensors of a 2×2 neighborhood in the far-right column of the observation window; $(W_2^{2,0})_{yy}\equiv(W_2^{2,0})_{xx}$ and $(W_2^{2,0})_{xy}\equiv 0$.

Config.	Nr.	Minkowski Vector $(W_2^{1,0})_x$	Minkowski Vector $(W_2^{1,0})_y$	Minkowski Tensors $(W_2^{2,0})_{xx}$	Minkowski Tensors $(W_2^{r,0})_{\underbrace{x\ldots x}_{n}\underbrace{y\ldots y}_{m}}$
	0	0	0	0	0
	1	0	0	0	0
	2	0	0	0	0
	3	0	0	0	0
	4	1/16	1/16	1/32	$[\delta_{n0} + \delta_{m0}]/(8 \cdot 2^r)$
	5	0	0	0	0
	6	1/16	-1/16	-1/32	$(-1) \cdot [\delta_{n0} + \delta_{m0} \cdot (-1)^n]/(8 \cdot 2^r)$
	7	1/16	-1/16	-1/32	$(-1) \cdot [\delta_{n0} + \delta_{m0} \cdot (-1)^n]/(8 \cdot 2^r)$
	8	-1/16	1/16	1/32	$[\delta_{n0} + \delta_{m0} \cdot (-1)^n]/(8 \cdot 2^r)$
	9	-1/16	-1/16	-1/32	$(-1) \cdot [\delta_{n0} + \delta_{m0}]/(8 \cdot 2^r)$
	10	0	0	0	0
	11	-1/16	-1/16	-1/32	$(-1) \cdot [\delta_{n0} + \delta_{m0}]/(8 \cdot 2^r)$
	12	0	0	0	0
	13	0	0	0	0
	14	0	0	0	0
	15	0	0	0	0

Table B.14: Minkowski functionals and tensors of a 2×2 neighborhood in the bottom row of the observation window; $(W_2^{2,0})_{yy} \equiv (W_2^{2,0})_{xx}$ and $(W_2^{2,0})_{xy} \equiv 0$.

Config.	Nr.	Minkowski Vector		Minkowski Tensors		
		$(W_2^{1,0})_x$	$(W_2^{1,0})_y$	$(W_2^{2,0})_{xx}$	$(W_2^{r,0})_{\underbrace{x\ldots x}_{n}\underbrace{y\ldots y}_{m}}$	
	0	0	0	0	0	
	1	1/16	-1/16	1/32	$[\delta_{n0}\cdot(-1)^m+\delta_{m0}]/(8\cdot 2^r)$	
	2	0	0	0	0	
	3	0	0	0	0	
	4	0	0	0	0	
	5	0	0	0	0	
	6	-1/16	1/16	-1/32	$(-1)\cdot[\delta_{n0}\cdot(-1)^m+\delta_{m0}]/(8\cdot 2^r)$	
	7	0	0	0	0	
	8	0	0	0	0	
	9	0	0	0	0	
	10	0	0	0	0	
	11	0	0	0	0	
	12	0	0	0	0	
	13	0	0	0	0	
	14	-1/16	1/16	-1/32	$(-1)\cdot[\delta_{n0}\cdot(-1)^m+\delta_{m0}]/(8\cdot 2^r)$	
	15	0	0	0	0	

Table B.15: Minkowski functionals and tensors of a 2×2 neighborhood in the top left corner of the observation window; $(W_2^{2,0})_{yy} \equiv (W_2^{2,0})_{xx}$ and $(W_2^{2,0})_{xy} \equiv 0$.

Config. Nr.	Minkowski Vector $(W_2^{1,0})_x$	Minkowski Vector $(W_2^{1,0})_y$	Minkowski Tensors $(W_2^{2,0})_{xx}$	Minkowski Tensors $(W_2^{r,0})_{\underbrace{x\ldots x}_{n}\underbrace{y\ldots y}_{m}}$
0	0	0	0	0
1	0	0	0	0
2	-1/16	-1/16	1/32	$[\delta_{n0}\cdot(-1)^m + \delta_{m0}\cdot(-1)^n]/(8\cdot 2^r)$
3	0	0	0	0
4	0	0	0	0
5	0	0	0	0
6	0	0	0	0
7	0	0	0	0
8	0	0	0	0
9	1/16	1/16	-1/32	$(-1)\cdot[\delta_{n0}\cdot(-1)^m + \delta_{m0}\cdot(-1)^n]/(8\cdot 2^r)$
10	0	0	0	0
11	0	0	0	0
12	0	0	0	0
13	1/16	1/16	-1/32	$(-1)\cdot[\delta_{n0}\cdot(-1)^m + \delta_{m0}\cdot(-1)^n]/(8\cdot 2^r)$
14	0	0	0	0
15	0	0	0	0

Table B.16: Minkowski functionals and tensors of a 2×2 neighborhood in the top right corner of the observation window; $(W_2^{2,0})_{yy} \equiv (W_2^{2,0})_{xx}$ and $(W_2^{2,0})_{xy} \equiv 0$.

Config.	Nr.	Minkowski Vector		Minkowski Tensors		
		$(W_2^{1,0})_x$	$(W_2^{1,0})_y$	$(W_2^{2,0})_{xx}$	$(W_2^{r,0})$ $\overbrace{x\ldots x}^{n}\overbrace{y\ldots y}^{m}$	
	0	0	0	0	0	
	1	0	0	0	0	
	2	0	0	0	0	
	3	0	0	0	0	
	4	1/16	1/16	1/32	$[\delta_{n0} + \delta_{m0}]/(8 \cdot 2^r)$	
	5	0	0	0	0	
	6	0	0	0	0	
	7	0	0	0	0	
	8	0	0	0	0	
	9	-1/16	-1/16	-1/32	$(-1) \cdot [\delta_{n0} + \delta_{m0}]/(8 \cdot 2^r)$	
	10	0	0	0	0	
	11	-1/16	-1/16	-1/32	$(-1) \cdot [\delta_{n0} + \delta_{m0}]/(8 \cdot 2^r)$	
	12	0	0	0	0	
	13	0	0	0	0	
	14	0	0	0	0	
	15	0	0	0	0	

Table B.17: Minkowski functionals and tensors of a 2×2 neighborhood in the bottom left corner of the observation window; $(W_2^{2,0})_{yy} \equiv (W_2^{2,0})_{xx}$ and $(W_2^{2,0})_{xy} \equiv 0$.

Config. Nr.	Minkowski Vector $(W_2^{1,0})_x$	Minkowski Vector $(W_2^{1,0})_y$	Minkowski Tensors $(W_2^{2,0})_{xx}$	Minkowski Tensors $(W_2^{r,0})\ \underbrace{x\ldots x}_{n}\underbrace{y\ldots y}_{m}$
0	0	0	0	0
1	0	0	0	0
2	0	0	0	0
3	0	0	0	0
4	0	0	0	0
5	0	0	0	0
6	1/16	-1/16	-1/32	$(-1)\cdot[\delta_{n0}+\delta_{m0}\cdot(-1)^n]/(8\cdot 2^r)$
7	1/16	-1/16	-1/32	$(-1)\cdot[\delta_{n0}+\delta_{m0}\cdot(-1)^n]/(8\cdot 2^r)$
8	-1/16	1/16	1/32	$[\delta_{n0}+\delta_{m0}\cdot(-1)^n]/(8\cdot 2^r)$
9	0	0	0	0
10	0	0	0	0
11	0	0	0	0
12	0	0	0	0
13	0	0	0	0
14	0	0	0	0
15	0	0	0	0

Table B.18: Minkowski functionals and tensors of a 2×2 neighborhood in the bottom right corner of the observation window; $(W_2^{2,0})_{yy} \equiv (W_2^{2,0})_{xx}$ and $(W_2^{2,0})_{xy} \equiv 0$.

Bibliography

[1] CGAL, Computational Geometry Algorithms Library, http://www.cgal.org.

[2] Image sources for Fig. 1.1: cosmic microwave background: image credit NASA/ WMAP Science Team [334]; distribution of galaxies: image credit M. Blanton and the Sloan Digital Sky Survey [281]; galaxy cluster: image credit NASA, ESA, and J. Lotz, M. Mountain, A. Koekemoer, and the HFF Team (STScI) [335]; geostatistics: image courtesy of Stanford Project on Deep-water Depositional Systems (SPODDS), Stanford [438]; foam: image courtesy of Feitosa group, James Madison University, and Durian group, University of Pennsylvania [135]; trabecular bone: image courtesy of Hansma lab, USCB [183]; chocolate muffin: image reproduced from Ref. [275] with permission from Elsevier; composite materials: image reproduced from Ref. [106] used under license Creative Commons attribution-type BY-NC [109]; red blood cells: image credit Janice Carr, CDC [220]; synthetic lava: image reproduced from Ref. [263] with permission from Elsevier; atomic cluster: image reproduced from Ref. [431], contribution of the National Institute of Standards and Technology; nuclear pasta: data from Bastian Schuetrumpf, see Fig. 1.8 and Chapter 5.

[3] A. Abramowski et al. (H.E.S.S. Collaboration). VHE γ-ray emission of PKS 2155-304: spectral and temporal variability. *Astron. Astrophys.*, 520: A83, 2010.

[4] K. N. Abazajian et al. The Seventh Data Release of the Sloan Digital Sky Survey. *Astrophys. J. Suppl. S.*, 182(2):543, 2009.

[5] G. O. Abell, H. G. Corwin, Jr., and R. P. Olowin. A catalog of rich clusters of galaxies. *Astrophys. J. Suppl. S.*, 70:1, 1989.

[6] B. S. Acharya et al. Introducing the CTA concept. *Astropart. Phys.*, 43(0):3, 2013.

[7] P. M. Adler, J.-F. Thovert, and V. V. Mourzenko. *Fractured Porous Media*. Oxford University Press, Oxford, 2012.

[8] R. J. Adler. *The Geometry of Random Fields*. Classics in Applied Mathematics. SIAM, Philadelphia, 1981.

[9] R. J. Adler and A. M. Hasofer. Level Crossings for Random Fields. *Ann. Probab.*, 4(1):1, 1976.

[10] R. J. Adler and J. E. Taylor. *Random fields and geometry*. Springer Science & Business Media, New York, 2009.

[11] J. M. Aguilera and P. J. Lillford. *Food Materials Science: Principles and Practice*. Food Engineering Series. Springer, New York, 2007.

[12] F. Aharonian et al. Very high energy gamma rays from the direction of Sagittarius A*. *Astron. Astrophys.*, 425(1):L13, 2004.

[13] F. Aharonian et al. Very high energy gamma rays from the composite SNR G 0.9+0.1. *Astron. Astrophys.*, 432(2):L25, 2005.

[14] F. Aharonian et al. H.E.S.S. observations of PKS 2155-304. *Astron. Astrophys.*, 430(3):865, 2005.

[15] F. Aharonian et al. Multi-wavelength observations of PKS 2155-304 with H.E.S.S. *Astron. Astrophys.*, 442(3):895, 2005.

[16] F. Aharonian et al. Observations of the Crab nebula with H.E.S.S. *Astron. Astrophys.*, 457(3):899, 2006.

[17] F. Aharonian et al. Discovery of Very-High-Energy Gamma-Rays from the Galactic Centre Ridge. *Nature*, 439:695, 2006.

[18] F. Aharonian et al. A detailed spectral and morphological study of the gamma-ray supernova remnant RX J1713.7-3946 with HESS. *Astron. Astrophys.*, 449(1):223, 2006.

[19] F. Aharonian et al. An Exceptional Very High Energy Gamma-Ray Flare of PKS 2155-304. *Astrophys. J. Lett.*, 664(2):L71, 2007.

[20] F. Aharonian et al. H.E.S.S. Observations of the Supernova Remnant RX J0852.0—4622: Shell-Type Morphology and Spectrum of a Widely Extended Very High Energy Gamma-Ray Source. *Astrophys. J.*, 661(1):236, 2007.

[21] F. Aharonian et al. Simultaneous multiwavelength observations of the second exceptional γ-ray flare of PKS 2155-304 in July 2006. *Astron. Astrophys.*, 502(3):749, 2009.

[22] F. Aharonian et al. Simultaneous Observations of PKS 2155-304 with H.E.S.S., Fermi, RXTE, and Atom: Spectral Energy Distributions and Variability in a Low State. *Astrophys. J. Lett.*, 696(2):L150, 2009.

[23] F. Aharonian et al. A multiwavelength view of the flaring state of PKS 2155-304 in 2006. *Astron. Astrophys.*, 539:A149, 2012.

[24] A. Aharony and D. Stauffer. *Introduction To Percolation Theory*. Taylor & Francis, London, 2003.

[25] M. Aizenman, H. Kesten, and C. M. Newman. Uniqueness of the infinite cluster and continuity of connectivity functions for short and long range percolation. *Comm. Math. Phys.*, 111(4):505, 1987.

[26] P. N. Alcain, P. A. Giménez Molinelli, J. I. Nichols, and C. O. Dorso. Effect of Coulomb screening length on nuclear "pasta" simulations. *Phys. Rev. C*, 89:055801, 2014.

[27] S. Alesker. Continuous rotation invariant valuations on convex sets. *Ann. Math.*, 149(3):977, 1999.

[28] S. Alesker. Description of continuous isometry covariant valuations on convex sets. *Geometriae dedicata*, 74(3):241, 1999.

[29] S. Alesker, A. Bernig, and F. E. Schuster. Harmonic Analysis of Translation Invariant Valuations. *Geometric and Functional Analysis*, 21(4):751, 2011.

[30] M. P. Allen and D. J. Tildesley. *Computer Simulation of Liquids*. Oxford University Press, New York, 1987.

[31] D. M. Anderson, H. T. Davis, J. C. C. Nitsche, and L. E. Scriven. Periodic Surfaces of Prescribed Mean Curvature. In J. Meunier, D. Langevin, and N. Boccara, editors, *Physics of Amphiphilic Layers*, volume 21 of *Springer Proceedings in Physics*, page 130. Springer, Berlin, Heidelberg, 1987.

[32] L. Apostol, V. Boudousq, O. Basset, C. Odet, S. Yot, J. Tabary, J.-M. Dinten, E. Boller, P.-O. Kotzki, and F. Peyrin. Relevance of 2D radiographic texture analysis for the assessment of 3D bone micro-architecture. *Med. Phys.*, 33 (9):3546, 2006.

[33] F. Arfelli et al. Mammography with Synchrotron Radiation: Phase-Detection Techniques. *Radiology*, 215(1):286, 2000.

[34] C. H. Arns, M. A. Knackstedt, and K. R. Mecke. Reconstructing Complex Materials via Effective Grain Shapes. *Phys. Rev. Lett.*, 91:215506, 2003.

[35] C. H. Arns, M. A. Knackstedt, and K. R. Mecke. Boolean reconstructions of complex materials: Integral geometric approach. *Phys. Rev. E*, 80:051303, 2009.

[36] C. H. Arns, M. A. Knackstedt, and K. Mecke. 3d structural analysis: sensitivity of Minkowski functionals. *J. Microsc.*, 240(3):181, 2010.

[37] N. W. Ashcroft and N. D. Mermin. *Solid State Physics*. Brooks Cole, 1976.

[38] T. Aste and T. Di Matteo. Correlations and aggregate statistics in granular packs. *Eur. Phys. J. E*, 22(3):235, 2007.

[39] T. Aste and T. Di Matteo. Emergence of Gamma distributions in granular materials and packing models. *Phys. Rev. E*, 77:021309, 2008.

[40] T. Aste, M. Saadatfar, and T. J. Senden. Geometrical structure of disordered sphere packings. *Phys. Rev. E*, 71:061302, 2005.

[41] S. Atkinson, F. H. Stillinger, and S. Torquato. Detailed characterization of rattlers in exactly isostatic, strictly jammed sphere packings. *Phys. Rev. E*, 88:062208, 2013.

[42] S. Atkinson, F. H. Stillinger, and S. Torquato. Existence of isostatic, maximally random jammed monodisperse hard-disk packings. *P. Natl. Acad. Sci. USA*, 111(52):18436, 2014.

[43] W. B. Atwood et al. The Large Area Telescope on the Fermi Gamma-Ray Space Telescope Mission. *Astrophys. J.*, 697:1071, 2009.

[44] J. Auneau-Cognacq, J. Ziegel, and E. B. Vedel Jensen. Rotational integral geometry of tensor valuations. *Adv. Appl. Math.*, 50(3):429, 2013.

[45] A. Bäcker and R. Schubert. Autocorrelation function of eigenstates in chaotic and mixed systems. *J. Phys. A: Math. Gen.*, 35(3):539, 2002.

[46] A. Baddeley and R. Turner. spatstat: An R Package for Analyzing Spatial Point Patterns. *J. Stat. Softw.*, 12(6):1, 2005.

[47] D. R. Baker, G. Paul, S. Sreenivasan, and H. E. Stanley. Continuum percolation threshold for interpenetrating squares and cubes. *Phys. Rev. E*, 66: 046136, 2002.

[48] I. Balberg. Universal percolation-threshold limits in the continuum. *Phys. Rev. B*, 31:4053, 1985.

[49] I. Balberg. Recent developments in continuum percolation. *Philosophical Magazine Part B*, 56(6):991, 1987.

[50] I. Balberg and N. Binenbaum. Computer study of the percolation threshold in a two-dimensional anisotropic system of conducting sticks. *Phys. Rev. B*, 28:3799, 1983.

[51] I. Balberg, N. Binenbaum, and S. Bozowski. Anisotropic percolation in carbon black-polyvinylchloride composites. *Solid State Communications*, 47(12):989, 1983.

[52] I. Balberg, C. H. Anderson, S. Alexander, and N. Wagner. Excluded volume and its relation to the onset of percolation. *Phys. Rev. B*, 30:3933, 1984.

[53] I. Balberg, N. Binenbaum, and N. Wagner. Percolation Thresholds in the Three-Dimensional Sticks System. *Phys. Rev. Lett.*, 52:1465, 1984.

[54] M. Barbosa, R. Natoli, K. Valter, J. Provis, and T. Maddess. Integral-geometry characterization of photobiomodulation effects on retinal vessel morphology. *Biomed. Opt. Express*, 5(7):2317, 2014.

[55] J. M. Bardeen, P. J. Steinhardt, and M. S. Turner. Spontaneous creation of almost scale-free density perturbations in an inflationary universe. *Phys. Rev. D*, 28:679, 1983.

[56] D. Barnette. On p-vectors of 3-polytopes. *J. Comb. Theory*, 7(2):99, 1969.

[57] P. Barois, S. T. Hyde, B. Ninham, and T. Dowling. Observation of two phases within the cubic phase region of a ternary surfactant solution. *Langmuir*, 6: 1136, 1990.

[58] J. Bear. *Dynamics of Fluids in Porous Media*. Dover Civil and Mechanical Engineering. Dover Publications, New York, 2013.

[59] J. Becker, G. Grun, R. Seemann, H. Mantz, K. Jacobs, K. R. Mecke, and R. Blossey. Complex dewetting scenarios captured by thin-film models. *Nat. Mater.*, 2:59, 2003.

[60] T. Beer and I. G. Enting. Fire spread and percolation modelling. *Mathematical and Computer Modelling*, 13(11):77, 1990.

[61] C. Beisbart, M. S. Barbosa, H. Wagner, and L. d. F. Costa. Extended morphometric analysis of neuronal cells with Minkowski valuations. *Eur. Phys. J. B*, 52(4):531, 2006.

[62] R. E. Belardinelli and V. D. Pereyra. Wang-Landau algorithm: A theoretical analysis of the saturation of the error. *J. Chem. Phys.*, 127(18):184105, 2007.

[63] R. E. Belardinelli and V. D. Pereyra. Fast algorithm to calculate density of states. *Phys. Rev. E*, 75:046701, 2007.

[64] R. E. Belardinelli, S. Manzi, and V. D. Pereyra. Analysis of the convergence of the $1/t$ and Wang-Landau algorithms in the calculation of multidimensional integrals. *Phys. Rev. E*, 78:067701, 2008.

[65] M. Bender, P.-H. Heenen, and P.-G. Reinhard. Self-consistent mean-field models for nuclear structure. *Rev. Mod. Phys.*, 75:121, 2003.

[66] M. P. Bendsøe and O. Sigmund. Material interpolation schemes in topology optimization. *Archive of Applied Mechanics*, 69(9–10):635, 1999.

[67] C. L. Bennett et al. Nine-year Wilkinson Microwave Anisotropy Probe (WMAP) Observations: Final Maps and Results. *Astrophys. J. Suppl. S.*, 208:20, 2013.

[68] R. Berman. Determinantal Point Processes and Fermions on Complex Manifolds: Large Deviations and Bosonization. *Commun. Math. Phys.*, 327 (1):1, 2014.

[69] M. V. Berry. Regular and irregular semiclassical wavefunctions. *J. Phys. A: Math. Gen.*, 10(12):2083, 1977.

[70] M. V. Berry and M. R. Dennis. Phase singularities in isotropic random waves. *P. Roy. Soc. A-Math. Phy.*, 456(2001):2059, 2000.

[71] L. Berthier, P. Chaudhuri, C. Coulais, O. Dauchot, and P. Sollich. Suppressed Compressibility at Large Scale in Jammed Packings of Size-Disperse Spheres. *Phys. Rev. Lett.*, 106:120601, 2011.

[72] H. A. Bethe. Supernova mechanisms. *Rev. Mod. Phys.*, 62:801, 1990.

[73] U. Bindrich and D. Stoyan. Stereology for pores in wheat bread: statistical analyses for the Boolean model by serial sections. *J. Microsc.*, 162(2):231, 1991.

[74] H. Boehm, C. Raeth, R. Monetti, D. Newitt, S. Majumdar, E. Rummeny, G. Morfill, and T. Link. Nicht-lineare Texturmaße basierend auf den Minkowski-Funktionalen in 3D: Vorhersage der Bruchlast trabekulärer Knochenpräparate durch Strukturanalyse hochauflösender MR-Aufnahmen. In T. Tolxdorff, J. Braun, H. Handels, A. Horsch, and H.-P. Meinzer, editors, *Bildverarbeitung für die Medizin 2004*, Informatik aktuell, page 140. Springer, Berlin, Heidelberg, 2004.

[75] H. F. Boehm, T. Link, R. Monetti, D. Mueller, E. Rummeny, D. Newitt, S. Majumdar, and C. W. Raeth. Application of the Minkowski Functionals in 3D to High Resolution MR Images of Trabecular Bone for the Prediction of the Biomechanical Strength. *Microsc. Microanal.*, 10:716, 2004.

[76] B. Bollobás and O. Riordan. The critical probability for random Voronoi percolation in the plane is 1/2. *Probab. Theory Rel.*, 136(3):417, 2006.

[77] A. Bonami and A. Estrade. Anisotropic Analysis of Some Gaussian Models. *J. Fourier Anal. Appl.*, 9(3):215, 2003.

[78] P. Bonche and D. Vautherin. A mean-field calculation of the equation of state of supernova matter. *Nucl. Phys. A*, 372(3):496, 1981.

[79] M. Borg, D. Thirde, J. Ferryman, F. Fusier, V. Valentin, F. Bremond, and M. Thonnat. Video surveillance for aircraft activity monitoring. In *Advanced Video and Signal Based Surveillance, 2005. AVSS 2005. IEEE Conference on*, page 16, 2005.

[80] T. Boublík. Two-dimensional convex particle liquid. *Mol. Phys.*, 29(2):421, 1975.

[81] W. J. Boudville and T. C. McGill. Finite-size effects in two-dimensional continuum percolation. *Phys. Rev. B*, 39:369, 1989.

[82] M. Brack and P. Quentin. The Strutinskij method and its foundation from the Hartree-Fock-Bogolyubov approximation at finite temperature. *Nucl. Phys. A*, 361:35, 1981.

[83] K. A. Brakke. The Surface Evolver. *Exp. Math.*, 1(2):141, 1992.

[84] C. J. Brinker and G. W. Scherer. *Sol-Gel Science: The Physics and Chemistry of Sol-Gel Processing*. Academic Press, Elsevier, Boston, 2013.

[85] S. R. Broadbent and J. M. Hammersley. Percolation processes. *Mathematical Proceedings of the Cambridge Philosophical Society*, 53:629, 1957.

[86] R. W. Brown, Y.-C. N. Cheng, E. M. Haacke, M. R. Thompson, and R. Venkatesan. *Magnetic Resonance Imaging: Physical Principles and Sequence Design*. John Wiley & Sons, Inc., Hoboken, NJ, 2nd edition, 2014.

[87] F. Bruckmann, F. Gruber, N. Cundy, A. Schäfer, and T. Lippert. Topology of dynamical lattice configurations including results from dynamical overlap fermions. *Phys. Lett. B*, 707(2):278, 2012.

[88] J. Buckley, K. Byrum, B. Dingus, A. Falcone, P. Kaaret, H. Krawzcynski, M. Pohl, V. Vassiliev, and D. A. Williams. The Status and future of ground-based TeV gamma-ray astronomy. A White Paper prepared for the Division of Astrophysics of the American Physical Society. *ArXiv e-prints*, 2008. arXiv:0810.0444.

[89] A. Burrows. Perspectives on Core-Collapse Supernova Theory. *ArXiv e-prints*, 2012.

[90] R. M. Burton and R. W. J. Meester. Long range percolation in stationary point processes. *Random Struct. Algor.*, 4(2):177, 1993.

[91] O. Buryak and A. Doroshkevich. Correlation function as a measure of the structure. *Astron. Astrophys.*, 306:1, 1996.

[92] J. Canny. A Computational Approach to Edge Detection. *IEEE T. Pattern Anal.*, PAMI-8(6):679, 1986.

[93] H. C. Canuto, C. McLachlan, M. I. Kettunen, M. Velic, A. S. Krishnan, A. A. Neves, M. de Backer, D.-E. Hu, M. P. Hobson, and K. M. Brindle. Characterization of image heterogeneity using 2D Minkowski functionals increases the sensitivity of detection of a targeted MRI contrast agent. *Magn. Reson. Med.*, 61(5):1218, 2009.

[94] E. Chabanat, P. Bonche, P. Haensel, J. Meyer, and R. Schaeffer. A Skyrme parametrization from subnuclear to neutron star densities Part II. Nuclei far from stabilities. *Nucl. Phys. A*, 635(1–2):231, 1998.

[95] P. M. Chaikin and T. C. Lubensky. *Principles of Condensed Matter Physics*. Cambridge University Press, Cambridge, 2000.

[96] N. Chamel and P. Haensel. Physics of Neutron Star Crusts. *Living Rev. Relativ.*, 11(10), 2008.

[97] C. Chappard, A. Basillais, L. Benhamou, A. Bonassie, B. Brunet-Imbault, N. Bonnet, and F. Peyrin. Comparison of synchrotron radiation and conventional x-ray microcomputed tomography for assessing trabecular bone microarchitecture of human femoral heads. *Med. Phys.*, 33(9):3568, 2006.

[98] A. P. Chatterjee. Percolation Thresholds and Excluded Area for Penetrable Rectangles in Two Dimensions. *J. Stat. Phys.*, 158(1):248, 2015.

[99] H. Childs et al. VisIt: An End-User Tool For Visualizing and Analyzing Very Large Data. In *High Performance Visualization—Enabling Extreme-Scale Scientific Insight*, page 357. 2012.

[100] S. N. Chiu, D. Stoyan, W. S. Kendall, and J. Mecke. *Stochastic Geometry and Its Applications*. Wiley, New York, 2013.

[101] M. K. Chung. Random Fields Theory, 2012. [from http://pages.stat.wisc.edu/~mchung/teaching/768/reading/lecture08-fields.pdf; accessed: 2015 June 12].

[102] T. E. Ciarelli, D. P. Fyhrie, M. B. Schaffler, and S. A. Goldstein. Variations in Three-Dimensional Cancellous Bone Architecture of the Proximal Femur in Female Hip Fractures and in Controls. *J. Bone Miner. Res.*, 15(1):32, 2000.

[103] A. S. Clarke and H. Jónsson. Structural changes accompanying densification of random hard-sphere packings. *Phys. Rev. E*, 47:3975, 1993.

[104] S. Colombi, D. Pogosyan, and T. Souradeep. Tree Structure of a Percolating Universe. *Phys. Rev. Lett.*, 85:5515, 2000.

[105] Committee on Chemical Engineering Frontiers: Research Needs and Opportunities, National Research Council. *Frontiers in Chemical Engineering: Research Needs and Opportunities*. The National Academies Press, 1988.

[106] A. C. B. d. Costa, A. G. P. d. Silva, and U. U. Gomes. Analysis of the structure of a hard metal: a simple method of relating properties to stereological structures. *Mat. Res.*, 8(2):131, 2005.

[107] S. C. Cowin and S. B. Doty. *Tissue mechanics*. Springer, New York, 2009.

[108] S. C. Cowin and M. M. Mehrabadi. Identification of the elastic symmetry of bone and other materials. *J. Biomech.*, 22(6):503, 1989.

[109] Creative Commons. Attribution-NonCommercial 4.0 International (CC BY-NC 4.0), 2015. [Online; `http://creativecommons.org/licenses/by-nc/4.0/legalcode`; accessed 22-August-2015].

[110] H. Darcy. *Les fontaines publiques de la ville de Dijon [The public fountains of the city of Dijon]*. Victor Dalmont, Paris, 1856.

[111] K. T. R. Davies, K. R. S. Devi, S. E. Koonin, and M. R. Strayer. TDHF Calculations of Heavy-Ion Collisions. In D. A. Bromley, editor, *Treatise on Heavy-Ion Physics, Vol. 3 Compound System Phenomena*, page 3. Plenum Press, New York, 1985.

[112] M. de Naurois. L'astronomie γ de trés haute énergie. Ouverture d'une nouvelle fenêtre astronomique sur l'Univers non thermique. Habilitation thesis, Université Paris VI, 2012.

[113] M. de Naurois and L. Rolland. A high performance likelihood reconstruction of γ-rays for imaging atmospheric Cherenkov telescopes. *Astropart. Phys.*, 32(5):231, 2009.

[114] G. W. Delaney, T. Di Matteo, and T. Aste. Combining tomographic imaging and DEM simulations to investigate the structure of experimental sphere packings. *Soft Matter*, 6:2992, 2010.

[115] N. Deng, W. Zhou, and M. Haenggi. The Ginibre Point Process as a Model for Wireless Networks With Repulsion. *IEEE T. Wirel. Commun.*, 14(1): 107, 2015.

[116] M. R. Dennis. Nodal densities of planar gaussian random waves. *Eur. Phys. J.-Spec. Top.*, 145(1):191, 2007.

[117] A. Derossi, T. De Pilli, and C. Severini. Statistical Description of Fat and Meat Phases of Sausages by the Use of Lineal-Path Distribution Function. *Food Biophys.*, 7(3):258, 2012.

[118] P. A. M. Dirac. Note on Exchange Phenomena in the Thomas Atom. *Math. Proc. Cambridge*, 26(03):376, 1930.

[119] A. Donev, F. H. Stillinger, and S. Torquato. Unexpected Density Fluctuations in Jammed Disordered Sphere Packings. *Phys. Rev. Lett.*, 95:090604, 2005.

[120] A. Donev, S. Torquato, and F. H. Stillinger. Pair correlation function characteristics of nearly jammed disordered and ordered hard-sphere packings. *Phys. Rev. E*, 71:011105, 2005.

[121] A. Donev, R. Connelly, F. H. Stillinger, and S. Torquato. Underconstrained jammed packings of nonspherical hard particles: Ellipses and ellipsoids. *Phys. Rev. E*, 75:051304, 2007.

[122] T. J. Donovan and Y. Danon. Application of Monte Carlo chord-length sampling algorithms to transport through a two-dimensional binary stochastic mixture. *Nucl. Sci. Eng.*, 143(3):226, 2003.

[123] C. O. Dorso, P. A. G. Molinelli, J. A. López, and E. Ramírez-Homs. Coulomb forces in neutron star crusts. *arXiv:1208.4841 [nucl-th]*, 2012.

[124] E. R. Dougherty and R. A. Lotufo. *Hands-on Morphological Image Processing*. Spie Press Series. Society of Photo Optical, Washington, 2003.

[125] G. Dougherty. *Medical Image Processing: Techniques and Applications*. Biological and Medical Physics, Biomedical Engineering. Springer, New York, 2011.

[126] A. Drory, I. Balberg, U. Alon, and B. Berkowitz. Analytic derivation of percolation thresholds in anisotropic systems of permeable objects. *Phys. Rev. A*, 43:6604, 1991.

[127] A. Ducout, F. R. Bouchet, S. Colombi, D. Pogosyan, and S. Prunet. Non-Gaussianity and Minkowski functionals: forecasts for Planck. *Mon. Not. R. Astron. Soc.*, 429(3):2104, 2013.

[128] R. O. Duda, P. E. Hart, and D. G. Stork. *Pattern Classification*. Wiley, New York, 2012.

[129] B. Ebner. *Private communication*, 2014-08.

[130] H. K. Eriksen, D. I. Novikov, P. B. Lilje, A. J. Banday, and K. M. Górski. Testing for Non-Gaussianity in the Wilkinson Microwave Anisotropy Probe Data: Minkowski Functionals and the Length of the Skeleton. *Astrophys. J.*, 612(1):64, 2004.

[131] A. Estrade and J. R. León. A central limit theorem for the Euler characteristic of a Gaussian excursion set. MAP5 2014-05, hal-00943054, 2015.

[132] M. E. Evans and G. E. Schröder-Turk. In a Material World. Hyperbolische Geometrie in biologischen Materialien. *Mitteilungen der Deutschen Mathematiker-Vereinigung*, 22(3):158, 2014.

[133] P. M. Falcone, A. Baiano, F. Zanini, L. Mancini, G. Tromba, D. Dreossi, F. Montanari, N. Scuor, and M. A. D. Nobile. Three-dimensional Quantitative Analysis of Bread Crumb by X-ray Microtomography. *J. Food Sci.*, 70 (4):E265, 2005.

[134] M. Fathy and M. Y. Siyal. An image detection technique based on morphological edge detection and background differencing for real-time traffic analysis. *Pattern Recogn. Lett.*, 16(12):1321, 1995.

[135] Feitosa group, James Madison University, and Durian group, University of Pennsylvania. Dry foam. [Online; `http://sites.jmu.edu/feitosa/research/`; accessed 22-August-2015].

[136] R. Filliger, O. Mermoud, D. Trivun, and P. Walther. 3D anisotropy measurement methodology for surface microstructures. *Surf. Interface Anal.*, 44 (13):1547, 2012.

[137] J. L. Finney. Random Packings and the Structure of Simple Liquids. I. The Geometry of Random Close Packing. *P. R. Soc. A Math. Phys.*, 319(1539): 479, 1970.

[138] J. L. Finney. Fine structure in randomly packed, dense clusters of hard spheres. *Mater. Sci. Eng.*, 23(2–3):199, 1976.

[139] J. L. Finney. Modelling the structures of amorphous metals and alloys. *Nature*, 266:309, 1977.

[140] J. L. Finney and J. Wallace. Interstice correlation functions; a new, sensitive characterisation of non-crystalline packed structures. *J. Non-Cryst. Solids*, 43(2):165, 1981.

[141] N. I. Fisher, T. L. Lewis, and B. J. Embleton. *Statistical analysis of spherical data*. Cambridge University Press, Cambridge, 1987.

[142] M. Florescu, S. Torquato, and P. J. Steinhardt. Designer disordered materials with large, complete photonic band gaps. *P. Natl. Acad. Sci.*, 106(49):20658, 2009.

[143] M. Florescu, P. J. Steinhardt, and S. Torquato. Optical cavities and waveguides in hyperuniform disordered photonic solids. *Phys. Rev. B*, 87:165116, 2013.

[144] P. J. Flory. Molecular Size Distribution in Three Dimensional Polymers. I. Gelation1. *J. Am. Chem. Soc.*, 63(11):3083, 1941.

[145] A. Fogden and S. T. Hyde. Continuous transformations of cubic minimal surfaces. *Eur. Phys. J B*, 7:91, 1999.

[146] I. Freund. Optical vortices in Gaussian random wave fields: statistical probability densities. *J. Opt. Soc. Am. A*, 11(5):1644, 1994.

[147] M. Fukugita and A. Suzuki, editors. *Physics and Astrophysics of Neutrinos*. Springer, Tokyo, Tokyo, 1994.

[148] J. W. Galusha, L. R. Richey, J. S. Gardner, J. N. Cha, and M. H. Bartl. Discovery of a diamond-based photonic crystal structure in beetle scales. *Phys. Rev. E*, 77(5):050904, 2008.

[149] E. J. Garboczi, D. P. Bentz, K. A. Snyder, N. Stutzmann, P. E. Martys, and C. Ferraris. Modeling and measuring the structure and properties of cement based materials: an electronic monograph, 2011.

[150] E. T. Gawlinski and H. E. Stanley. Continuum percolation in two dimensions: Monte Carlo tests of scaling and universality for non-interacting discs. *J. Phys. A-Math. Gen.*, 14(8):L291, 1981.

[151] C. Gay, C. Pichon, and D. Pogosyan. Non-Gaussian statistics of critical sets in 2D and 3D: Peaks, voids, saddles, genus, and skeleton. *Phys. Rev. D*, 85: 023011, 2012.

[152] J. L. Gevertz and S. Torquato. A Novel Three-Phase Model of Brain Tissue Microstructure. *PLoS Comput. Biol.*, 4(8):e1000152, 2008.

[153] F. Gieringer. *Konzentrationsungleichungen für Poisson- und Binomialfunktionale in der Stochastischen Geometrie*. PhD thesis, Karlsruhe Institut für Technologie, 2016.

[154] A. Gillman, K. Matouš, and S. Atkinson. Microstructure-statistics-property relations of anisotropic polydisperse particulate composites using tomography. *Phys. Rev. E*, 87:022208, 2013.

[155] P. Gögelein. Nuclear "pasta" phase in a triaxial relativistic mean field approach. *Prog. Part. Nuc. Phys.*, 59:206, 2007.

[156] P. Gögelein and H. Müther. Nuclear matter in the crust of neutron stars. *Phys. Rev. C*, 76:024312, 2007.

[157] J. W. Goodman. *Statistical Optics*. Wiley, New York, 1985.

[158] J. W. Goodman. *Speckle Phenomena in Optics: Theory and Applications*. Roberts & Company, Greenwood Village, 2007.

[159] D. Göring. Curvatures in the anisotropic Gaussian Random Field Model, 2007. Research report.

[160] D. Göring. Analysis of the Poisson Structure of H.E.S.S. Sky Maps with Minkowski Functionals. Master's thesis (Diplomarbeit), Universität Erlangen-Nürnberg, 2008.

[161] D. Göring. *Gamma-Ray Astronomy Data Analysis Framework based on the Quantification of Background Morphologies using Minkowski Tensors*. PhD thesis, Universität Erlangen-Nürnberg, 2012.

[162] D. Göring, M. A. Klatt, C. Stegmann, and K. Mecke. Morphometric analysis in gamma-ray astronomy using Minkowski functionals. *Astron. Astrophys.*, 555:A38, 2013.

[163] R. O. Gould and W. Borchardt-Ott. *Crystallography: An Introduction*. Springer, Berlin, Heidelberg, 2011.

[164] R. W. Goulet, S. A. Goldstein, M. J. Ciarelli, J. L. Kuhn, M. B. Brown, and L. A. Feldkamp. The relationship between the structural and orthogonal compressive properties of trabecular bone. *J. Biomech.*, 27(4):375, 1994.

[165] G. Grimmett. *Percolation*. Springer, New York, 2013.

[166] E. K. U. Gross, J. F. Dobson, and M. Petersilka. Density functional of Time-Dependent Phenomena. *Top. Curr. Chem.*, 181:81, 1996.

[167] K. Grosse-Brauckmann. On Gyroid Interfaces. *J. Coll. Interf. Sci.*, 187(2): 418, 1997.

[168] K. Grosse-Brauckmann. Gyroids of Constant Mean Curvature. *Exp. Math.*, 6(1):33, 1997.

[169] H. J. G. Gundersen, R. W. Boyce, J. R. Nyengaard, and A. Odgaard. The conneulor: unbiased estimation of connectivity using physical disectors under projection. *Bone*, 14(3):217, 1993.

[170] A. H. Guth and S.-Y. Pi. Quantum mechanics of the scalar field in the new inflationary universe. *Phys. Rev. D*, 32:1899, 1985.

[171] I. Guyon and A. Elisseeff. An Introduction to Feature Extraction. In I. Guyon, M. Nikravesh, S. Gunn, and L. Zadeh, editors, *Feature Extraction*, volume 207 of *Studies in Fuzziness and Soft Computing*, page 1. Springer, Berlin, Heidelberg, 2006.

[172] H. Hadwiger. Beweis eines Funktionalsatzes für konvexe Körper. *Abh. Math. Sem. Univ. Hamburg*, 17(1):69, 1951.

[173] H. Hadwiger. Additive Funktionale k-dimensionaler Eikörper, I. *Arch. Math.*, 3(6):470, 1952.

[174] H. Hadwiger. *Vorlesungen über Inhalt, Oberfläche und Isoperimetrie*. Springer, Berlin, 1957.

[175] H. Hadwiger and C. Meier. Studien zur vektoriellen Integralgeometrie. *Mathematische Nachrichten*, 56(1–6):261, 1973.

[176] D. A. Hajduk, P. E. Harper, S. M. Gruner, C. C. Honeker, G. Kim, E. L. Thomas, and L. J. Fetters. The Gyroid: A New Equilibrium Morphology in Weakly Segregated Diblock Copolymers. *Macromolecules*, 27(15):4063, 1994.

[177] T. C. Hales. A proof of the Kepler conjecture. *Ann. Math.*, 162:1065, 2005.

[178] P. Hall. *Introduction to the theory of coverage processes*. Wiley series in probability and mathematical statistics: Probability and mathematical statistics. Wiley, New York, 1988.

[179] J.-H. Han and D.-Y. Kim. Analysis of the proportionality constant correlating the mean intercept length to the average grain size. *Acta Metall. Mater.*, 43(8):3185, 1995.

[180] J. P. Hansen and I. R. McDonald. *Theory of Simple Liquids*. Elsevier Science, Amsterdam, 2006.

[181] H. Hansen-Goos and K. Mecke. Fundamental Measure Theory for Inhomogeneous Fluids of Nonspherical Hard Particles. *Phys. Rev. Lett.*, 102: 018302, 2009.

[182] H. Hansen-Goos and K. Mecke. Tensorial density functional theory for non-spherical hard-body fluids. *J. Phys.: Condens. Matter*, 22:364107, 2010.

[183] Hansma lab, USCB. Scanning electron micrograph of human bone. [Online; `http://hansmalab.physics.ucsb.edu/afmbone.html`; accessed 22-August-2015].

[184] Y. Harano, R. Roth, and M. Kinoshita. On the energetics of protein folding in aqueous solution. *Chem. Phys. Lett.*, 432:275, 2006.

[185] Y. Harano, R. Roth, Y. Sugita, M. Ikeguchi, and M. Kinoshita. Physical Basis for Characterizing Native Structure of Proteins. *Chem. Phys. Lett.*, 437:112, 2007.

[186] T. P. Harrigan and R. W. Mann. Characterization of microstructural anisotropy in orthotropic materials using a second rank tensor. *J. Mater. Sci.*, 19:761, 1984.

[187] M. Hashimoto, H. Seki, and M. Yamada. Shape of Nuclei in the Crust of Neutron Star. *Prog. Theor. Phys.*, 71(2):320, 1984.

[188] C. L. Henley. Sphere packings and local environments in Penrose tilings. *Phys. Rev. B*, 34:797, 1986.

[189] G. Hermann, W. Hofmann, and H. J. Völk. H.E.S.S.—High Energy Stereoscopic System: The New Window on the High-Energy Universe, 2004. Inauguration of the High Energy Stereoscopic System [Online; `http://www.mpi-hd.mpg.de/hfm/HESS/pages/about/download/HESS_broschuere_04_c.pdf`; accessed 15-April-2015].

[190] T. Hildebrand, A. Laib, R. Müller, J. Dequeker, and P. Rüegsegger. Direct Three-Dimensional Morphometric Analysis of Human Cancellous Bone: Microstructural Data from Spine, Femur, Iliac Crest, and Calcaneus. *J. Bone Miner. Res.*, 14(7):1167, 1999.

[191] A. M. Hillas. Evolution of ground-based gamma-ray astronomy from the early days to the Cherenkov Telescope Arrays. *Astropart. Phys.*, 43(0):19, 2013.

[192] A. Hirata, L. J. Kang, T. Fujita, B. Klumov, K. Matsue, M. Kotani, A. R. Yavari, and M. W. Chen. Geometric Frustration of Icosahedron in Metallic Glasses. *Science*, 341(6144):376, 2013.

[193] R. W. Hockney and J. W. Eastwood. *Computer Simulations Using Particles*. McGraw-Hill, New York, 1981.

[194] R. Hodgskinson and J. D. Currey. The effect of variation in structure on the Young's modulus of cancellous bone: a comparison of human and non-human material. *P. I. Mech. Eng. H*, 204(2):115, 1990.

[195] R. Hodgskinson and J. D. Currey. Effects of structural variation on Young's modulus of non-human cancellous bone. *P. I. Mech. Eng. H*, 204(1):43, 1990.

[196] J. Homminga, B. Van-Rietbergen, E.-M. Lochmüller, H. Weinans, F. Eckstein, and R. Huiskes. The osteoporotic vertebral structure is well adapted to the loads of daily life, but not to infrequent "error" loads. *Bone*, 34(3): 510, 2004.

[197] W. G. Hoover and F. H. Ree. Melting Transition and Communal Entropy for Hard Spheres. *J. Chem. Phys.*, 49(8):3609, 1968.

[198] A. B. Hopkins, F. H. Stillinger, and S. Torquato. Nonequilibrium static diverging length scales on approaching a prototypical model glassy state. *Phys. Rev. E*, 86:021505, 2012.

[199] M. Hörmann. Minkowski Tensors of Gaussian Fields. Bachelor's thesis, Universität Erlangen-Nürnberg, 2014.

[200] B. K. P. Horn. Extended Gaussian images. *Proc. IEEE*, 72(12):1671, 1984.

[201] C. J. Horowitz, M. A. Pérez-García, J. Carriere, D. K. Berry, and J. Piekarewicz. Nonuniform neutron-rich matter and coherent neutrino scattering. *Phys. Rev. C*, 70:065806, 2004.

[202] C. J. Horowitz, M. A. Pérez-García, and J. Piekarewicz. Neutrino-"pasta" scattering: The opacity of nonuniform neutron-rich matter. *Phys. Rev. C*, 69:045804, 2004.

[203] J. Hörrmann. *The method of densities for non-isotropic Boolean models*. KIT Scientific Publishing, Karlsruhe, 2015.

[204] J. Hörrmann, D. Hug, M. A. Klatt, and K. Mecke. Minkowski tensor density formulas for Boolean models. *Adv. Appl. Math.*, 55(0):48, 2014.

[205] A. N. Houston, W. Otten, P. C. Baveye, and S. Hapca. Adaptive-window indicator kriging: a thresholding method for computed tomography images of porous media. *Comput. Geosci.*, 54(0):239, 2013.

[206] J. Hsieh. *Computed Tomography: Principles, Design, Artifacts, and Recent Advances*. John Wiley & Sons, Inc., SPIE Press, Hoboken, NJ, Bellingham, Wash, 2nd edition, 2009.

[207] A. T. Huber and L. J. Gibson. Anisotropy of foams. *J. Mater. Sci.*, 23(8): 3031, 1988.

[208] D. Hug and M. Schulte. *Private communication*, 2015-05.

[209] D. Hug, G. Last, and W. Weil. Polynomial parallel volume, convexity and contact distributions of random sets. *Probab. Theory Relat. Fields*, 135(2): 169, 2006.

[210] D. Hug, G. Last, and M. Schulte. Second-order properties and central limit theorems for geometric functionals of Boolean models. *Ann. Appl. Probab.*, 26(1):73–135, 2016.

[211] A. Hunt, R. Ewing, and B. Ghanbarian. *Percolation Theory for Flow in Porous Media*. Lecture Notes in Physics. Springer, Cham, 3rd edition, 2014.

[212] A. G. Hunt. Basic transport properties in natural porous media: Continuum percolation theory and fractal model. *Complexity*, 10(3):22, 2005.

[213] S. Hyde, S. Andersson, K. Larsson, Z. Blum, T. Landh, S. Lidin, and B. Ninham. *The Language of Shape*. Elsevier Science B. V., Amsterdam, 1st edition, 1997.

[214] S. T. Hyde. The topology and geometry of infinite periodic surfaces. *Z. Kristallogr.*, 187(3–4):165, 1989.

[215] S. T. Hyde. Curvature and the global structure of interfaces in surfactant-water systems. In *Colloque de Physique C7-1990*, Supplément au Journal de Physique, page 209, 1990.

[216] H. Ikeda. Percolation in Anisotropic Systems: Real-Space Renormalization Group. *Prog. Theor. Phys.*, 61(3):842, 1979.

[217] J. Illian, P. A. Penttinen, H. Stoyan, and D. Stoyan. *Statistical Analysis and Modelling of Spatial Point Patterns*. Statistics in Practice. Wiley, Chichester, 2008.

[218] D. Inglis and S. Pietruszczak. Characterization of anisotropy in porous media by means of linear intercept measurements. *Int. J. Solids Struct.*, 40 (5):1243, 2003.

[219] A. K. Jain, R. P. W. Duin, and J. Mao. Statistical pattern recognition: a review. *IEEE T. Pattern Anal.*, 22(1):4, 2000.

[220] Janice Carr, CDC. Scanning electron micrograph of red blood cells—image id: 7315, 2005. [Online; `http://phil.cdc.gov/phil/home.asp`; accessed 22-August-2015].

[221] C. Jiang, M. L. Giger, M. R. Chinander, J. M. Martell, S. Kwak, and M. J. Favus. Characterization of bone quality using computer-extracted radiographic features. *Med. Phys.*, 26(6):872, 1999.

[222] Y. Jiao, F. H. Stillinger, and S. Torquato. A superior descriptor of random textures and its predictive capacity. *P. Natl. Acad. Sci. USA*, 106(42):17634, 2009.

[223] Y. Jiao, F. H. Stillinger, and S. Torquato. Nonuniversality of density and disorder in jammed sphere packings. *J. Appl. Phys.*, 109(1):013508, 2011.

[224] Y. Jiao, T. Lau, H. Hatzikirou, M. Meyer-Hermann, J. C. Corbo, and S. Torquato. Avian photoreceptor patterns represent a disordered hyperuniform solution to a multiscale packing problem. *Phys. Rev. E*, 89:022721, 2014.

[225] E. Jones et al. SciPy: Open source scientific tools for Python, 2001. [Online; `http://www.scipy.org/`; accessed 2015-05-21].

[226] J. Kabel, B. Van Rietbergen, A. Odgaard, and R. Huiskes. Constitutive relationships of fabric, density, and elastic properties in cancellous bone architecture. *Bone*, 25(4):481, 1999.

[227] M. Kachanov. Solids with cracks and non-spherical pores: proper parameters of defect density and effective elastic properties. *Int. J. Fracture*, 97(1–4):1, 1999.

[228] W.-A. Kahl, R. Hinkes, V. Feeser, and A. Holzheid. Microfabric and anisotropy of elastic waves in sandstone—An observation using high-resolution X-ray microtomography. *J. Struct. Geol.*, 49(0):35, 2013.

[229] K.-I. Kanatani. Distribution of directional data and fabric tensors. *Int. J. Eng. Sci.*, 22(2):149, 1984.

[230] K.-I. Kanatani. Stereological determination of structural anisotropy. *Int. J. Eng. Sci.*, 22(5):531, 1984.

[231] A. R. Kansal, S. Torquato, and F. H. Stillinger. Diversity of order and densities in jammed hard-particle packings. *Phys. Rev. E*, 66:041109, 2002.

[232] S. C. Kapfer. *Morphometry and Physics of Particulate and Porous Media*. PhD thesis, Friedrich-Alexander-Universität Erlangen-Nürnberg, 2011.

[233] S. C. Kapfer, W. Mickel, F. M. Schaller, M. Spanner, C. Goll, T. Nogawa, N. Ito, K. Mecke, and G. E. Schröder-Turk. Local anisotropy of fluids using Minkowski tensors. *J. Stat. Mech. Theory E.*, 2010(11):P11010, 2010.

[234] S. C. Kapfer, W. Mickel, K. Mecke, and G. E. Schröder-Turk. Jammed spheres: Minkowski tensors reveal onset of local crystallinity. *Phys. Rev. E*, 85:030301, 2012.

[235] A. J. Katz and A. H. Thompson. Quantitative prediction of permeability in porous rock. *Phys. Rev. B*, 34:8179, 1986.

[236] A. Kaup. *Private communication*, 2013-05.

[237] M. Kerscher. Constructing, characterizing, and simulating Gaussian and higher-order point distributions. *Phys. Rev. E*, 64:056109, 2001.

[238] M. Kerscher, K. Mecke, J. Schmalzing, C. Beisbart, T. Buchert, and H. Wagner. Morphological fluctuations of large-scale structure: The PSCz survey. *Astron. Astrophys.*, 373:1, 2001.

[239] M. Kerscher, K. Mecke, and P. Schücker. Non-Gaussian morphology on large scales: Minkowski functionals of the REFLEX cluster catalogue. *Astron. Astrophys.*, 377:1, 2001.

[240] R. A. Ketcham and T. M. Ryan. Quantification and visualization of anisotropy in trabecular bone. *J. Microsc.*, 213(2):158, 2004.

[241] R. P. King. Random geometrical models for porous media and other two-phase materials. *Chem. Eng. J. Bioch. Eng.*, 62(1):1, 1996.

[242] D. A. Klain and G.-C. Rota. *Introduction to Geometric Probability*. Cambridge University Press, Cambridge, 1997.

[243] M. A. Klatt. Morphometric analysis in gamma-ray astronomy. Master's thesis (Diplomarbeit), Universität Erlangen-Nürnberg, 2010.

[244] M. A. Klatt and S. Torquato. Characterization of maximally random jammed sphere packings: Voronoi correlation functions. *Phys. Rev. E*, 90:052120, 2014.

[245] M. A. Klatt, D. Göring, C. Stegmann, and K. Mecke. Shape analysis of counts maps. *AIP Conf. Proc.*, 1505(1):737, 2012.

[246] M. A. Klatt, T. Ichikawa, K. Iida, N. Itagaki, J. A. Maruhn, K. Matsuyanagi, K. Mecke, S. Ohkubo, P.-G. Reinhard, and B. Schuetrumpf. Exotic cluster structures in the mean-field theory. *J. Phys.: Conf. Ser.*, 445(1):012036, 2013.

[247] R. Kodama, R. Roth, Y. Harano, and M. Kinoshita. Morphometric approach to thermodynamic quantities of solvation of complex molecules: Extension to multicomponent solvent. *J. Chem. Phys.*, 135:045103, 2011.

[248] P.-M. König, R. Roth, and K. R. Mecke. Morphological Thermodynamics of Fluids: Shape Dependence of Free Energies. *Phys. Rev. Lett.*, 93:160601, 2004.

[249] A. M. Kraynik. The Structure of Random Foam. *Adv. Eng. Mater.*, 8(9):900, 2006.

[250] A. M. Kraynik, D. A. Reinelt, and F. van Swol. Structure of random monodisperse foam. *Phys. Rev. E*, 67:031403, 2003.

[251] A. M. Kraynik, D. A. Reinelt, and F. van Swol. Structure of Random Foam. *Phys. Rev. Lett.*, 93:208301, 2004.

[252] J. M. Kreider. Trabecular bone mechanical properties in patients with fragility fractures. *Clin. Orthop. Relat. R.*, 467(8):1955, 2009.

[253] R. Kurita and E. R. Weeks. Experimental study of random-close-packed colloidal particles. *Phys. Rev. E*, 82:011403, 2010.

[254] D. Q. Lamb, J. M. Lattimer, C. J. Pethick, and D. G. Ravenhall. Hot Dense Matter and Stellar Collapse. *Phys. Rev. Lett.*, 41:1623, 1978.

[255] D. P. Landau, S.-H. Tsai, and M. Exler. A new approach to Monte Carlo simulations in statistical physics: Wang-Landau sampling. *Am. J. Phys.*, 72 (10):1294, 2004.

[256] L. Landini and L. Verrazzani. Spectral characterization of tissues microstructure by ultrasounds: a stochastic approach. *Ultrasonics, Ferroelectrics, and Frequency Control, IEEE Transactions on*, 37(5):448, 1990.

[257] T. J. Larkin, H. C. Canuto, M. I. Kettunen, T. C. Booth, D.-E. Hu, A. S. Krishnan, S. E. Bohndiek, A. A. Neves, C. McLachlan, M. P. Hobson,

and K. M. Brindle. Analysis of image heterogeneity using 2D Minkowski functionals detects tumor responses to treatment. *Magn. Reson. Med.*, 71 (1):402, 2014.

[258] U. D. Larsen, O. Signund, and S. Bouwsta. Design and fabrication of compliant micromechanisms and structures with negative Poisson's ratio. *J. Microelectromechanical Systems*, 6(2):99, 1997.

[259] K. Larsson. Cubic lipid-water phases: structures and biomembranes aspects. *J. Phys. Chem.*, 93:7304, 1989.

[260] M. Lassaut, H. Flocard, P. Bonche, P. H. Heenen, and E. Suraud. Equation of state of hot dense matter. *Astron. Astrophys.*, 183:L3, 1987.

[261] G. Last and E. Ochsenreither. Percolation on stationary tessellations: models, mean values, and second-order structure. *J. Appl. Probab.*, 51A:311, 2014.

[262] P. Launeau and P.-Y. F. Robin. Fabric analysis using the intercept method. *Tectonophysics*, 267(1–4):91, 1996.

[263] P. Launeau, C. J. Archanjo, D. Picard, L. Arbaret, and P.-Y. Robin. Two-and three-dimensional shape fabric analysis by the intercept method in grey levels. *Tectonophysics*, 492(1):230, 2010.

[264] C. Lautensack. *Random Laguerre Tessellations*. PhD thesis, Universität Karlsruhe, 2007.

[265] F. Lavancier, J. Møller, and E. Rubak. Determinantal point process models and statistical inference. *J. Roy. Stat. Soc. B*, 77(4):853–877, 2015.

[266] E. A. Lazar, J. K. Mason, R. D. MacPherson, and D. J. Srolovitz. Complete Topology of Cells, Grains, and Bubbles in Three-Dimensional Microstructures. *Phys. Rev. Lett.*, 109:095505, 2012.

[267] E. A. Lazar, J. K. Mason, R. D. MacPherson, and D. J. Srolovitz. Statistical topology of three-dimensional Poisson-Voronoi cells and cell boundary networks. *Phys. Rev. E*, 88:063309, 2013.

[268] F. Lechenault, F. da Cruz, O. Dauchot, and E. Bertin. Free volume distributions and compactivity measurement in a bidimensional granular packing. *J. Stat. Mech.*, 2006(07):P07009, 2006.

[269] G. W. Lee, A. K. Gangopadhyay, K. F. Kelton, R. W. Hyers, T. J. Rathz, J. R. Rogers, and D. S. Robinson. Difference in Icosahedral Short-Range Order

in Early and Late Transition Metal Liquids. *Phys. Rev. Lett.*, 93:037802, 2004.

[270] P. Lehmann, M. Berchtold, B. Ahrenholz, J. Tölke, A. Kaestner, M. Krafczyk, H. Flühler, and H. R. Künsch. Impact of geometrical properties on permeability and fluid phase distribution in porous media. *Adv. Water Resour.*, 31(9):1188, 2008. Quantitative links between porous media structures and flow behavior across scales.

[271] J. Li and M. Östling. Percolation thresholds of two-dimensional continuum systems of rectangles. *Phys. Rev. E*, 88:012101, 2013.

[272] J. Li and S.-L. Zhang. Finite-size scaling in stick percolation. *Phys. Rev. E*, 80:040104, 2009.

[273] T.-P. Li and Y.-Q. Ma. Analysis methods for results in gamma-ray astronomy. *Astrophys. J.*, 272:317, 1983.

[274] M. A. Lifšic. *Gaussian Random Functions*. Mathematics and Its Applications. Kluwer, Dordrecht, 1995.

[275] K. S. Lim and M. Barigou. X-ray micro-computed tomography of cellular food products. *Food Res. Int.*, 37(10):1001, 2004.

[276] N. Loebl, A. S. Umar, J. A. Maruhn, P.-G. Reinhard, P. D. Stevenson, and V. E. Oberacker. Single-particle dissipation in a time-dependent Hartree-Fock approach studied from a phase-space perspective. *Phys. Rev. C*, 86: 024608, 2012.

[277] W. E. Lorensen and H. E. Cline. Marching cubes: A high resolution 3D surface construction algorithm. *SIGGRAPH Comput. Graph.*, 21(4):163, 1987.

[278] C. D. Lorenz and R. M. Ziff. Precise determination of the critical percolation threshold for the three-dimensional "Swiss cheese" model using a growth algorithm. *J. Chem. Phys.*, 114(8):3659, 2001.

[279] B. D. Lubachevsky and F. H. Stillinger. Geometric properties of random disk packings. *J. Stat. Phys.*, 60(5–6):561, 1990.

[280] G. M. Luo, A. M. Sadegh, and S. C. Cowin. The mean intercept length polygons for systems of planar nets. *J. Mater. Sci.*, 26:2389, 1991.

[281] M. Blanton and the Sloan Digital Sky Survey. SDSS Galaxy Map. [Online; `http://www.sdss3.org/science/gallery_sdss_pie2.php`; accessed 22-August-2015].

[282] M. Kerscher, K. Mecke, P. Schuecker, H. Böhringer, L. Guzzo, C. A. Collins, S. Schindler, S. De Grandi, and R. Cruddace. Non-Gaussian morphology on large scales: Minkowski functionals of the REFLEX cluster catalogue. *Astron. Astrophys.*, 377(1):1, 2001.

[283] O. Macchi. The coincidence approach to stochastic point processes. *Adv. Appl. Probab.*, 7:83, 1975.

[284] G. MacKay and N. Jan. Forest fires as critical phenomena. *J. Phys. A-Math. Gen.*, 17(14):L757, 1984.

[285] P. Magierski and P.-H. Heenen. Structure of the inner crust of neutron stars: Crystal lattice or disordered phase? *Phys. Rev. C*, 65:045804, 2002.

[286] W. Man, M. Florescu, K. Matsuyama, P. Yadak, G. Nahal, S. Hashemizad, E. Williamson, P. Steinhardt, S. Torquato, and P. Chaikin. Photonic band gap in isotropic hyperuniform disordered solids with low dielectric contrast. *Opt. Express*, 21(17):19972, 2013.

[287] V. N. Manoharan, M. T. Elsesser, and D. J. Pine. Dense Packing and Symmetry in Small Clusters of Microspheres. *Science*, 301(5632):483, 2003.

[288] H. Mantz, K. Jacobs, and K. Mecke. Utilising Minkowski Functionals for Image Analysis. *J. Stat. Mech.*, 12:P12015, 2008.

[289] W. B. March, K. Czechowski, M. Dukhan, T. Benson, D. Lee, A. J. Connolly, R. Vuduc, E. Chow, and A. G. Gray. Optimizing the Computation of N-point Correlations on Large-scale Astronomical Data. In *Proceedings of the International Conference on High Performance Computing, Networking, Storage and Analysis*, SC '12, page 74:1, Los Alamitos, CA, USA, 2012. IEEE Computer Society Press.

[290] É. Marcotte and S. Torquato. Efficient linear programming algorithm to generate the densest lattice sphere packings. *Phys. Rev. E*, 87:063303, 2013.

[291] É. Marcotte, F. H. Stillinger, and S. Torquato. Nonequilibrium static growing length scales in supercooled liquids on approaching the glass transition. *J. Chem. Phys.*, 138(12):12A508, 2013.

[292] S. Marsland. *Machine Learning: An Algorithmic Perspective*. Chapman & Hall/CRC machine learning & pattern recognition series. Taylor & Francis, Boca Raton, 2014.

[293] N. S. Martys, S. Torquato, and D. P. Bentz. Universal scaling of fluid permeability for sphere packings. *Phys. Rev. E*, 50:403, 1994.

[294] J. A. Maruhn, P.-G. Reinhard, P. D. Stevenson, and A. S. Umar. The TDHF Code Sky3D. *Comp. Phys. Comm.*, 185(7):2195, 2014.

[295] J. A. Maruhn et al. Dipole giant resonances in deformed heavy nuclei. *Phys. Rev. C*, 71:064328, 2005.

[296] T. Maruyama, K. Niita, K. Oyamatsu, T. Maruyama, S. Chiba, and A. Iwamoto. Quantum molecular dynamics approach to the nuclear matter below the saturation density. *Phys. Rev. C*, 57:655, 1998.

[297] T. Maruyama, T. Tatsumi, D. N. Voskresensky, T. Tanigawa, and S. Chiba. Nuclear "pasta" structures and the charge screening effect. *Phys. Rev. C*, 72: 015802, 2005.

[298] M. Masihi, P. R. King, and P. Nurafza. Effect of anisotropy on finite-size scaling in percolation theory. *Phys. Rev. E*, 74:042102, 2006.

[299] G. Matheron. *Random Sets and Integral Geometry*. J. Wiley & Sons, New York, 1975.

[300] M. Matsuzaki. Ordered bicontinuous double-diamond morphology in sub-saturation nuclear matter. *Phys. Rev. C*, 73:028801, 2006.

[301] J. R. Mattox et al. The Likelihood Analysis of EGRET Data. *Astrophys. J.*, 461:396, 1996.

[302] C. K. McBride, A. J. Connolly, J. P. Gardner, R. Scranton, R. Scoccimarro, A. A. Berlind, F. Marín, and D. P. Schneider. Three-point Correlation Functions of SDSS Galaxies: Constraining Galaxy-mass Bias. *Astrophys. J.*, 739(2):85, 2011.

[303] P. McMullen. Isometry covariant valuations on convex bodies. *Rend. Circ. Mat. Palermo (2) Suppl.*, 50:259, 1997.

[304] K. Mecke. Morphological characterization of patterns in reaction-diffusion systems. *Phys. Rev. E*, 53(5):4794, 1996.

[305] K. Mecke. Integral Geometry and Statistical Physics. *Int. J. Mod. Phys. B*, 12:861, 1998.

[306] K. Mecke and C. H. Arns. Fluids in porous media: a morphometric approach. *J. Phys.: Condensed Matter*, 17(9):S503, 2005.

[307] K. Mecke and D. Stoyan. *Statistical Physics and Spatial Statistics - The Art of Analyzing and Modeling Spatial Structures and Pattern Formation*, volume 554 of *Lecture Notes in Physics*. Springer, Berlin, 1st edition, 2000.

[308] K. Mecke, T. Buchert, and H. Wagner. Robust morphological measures for large-scale structure in the universe. *Astron. Astrophys.*, 288:697, 1994.

[309] K. R. Mecke and A. Seyfried. Strong dependence of percolation thresholds on polydispersity. *EPL – Europhys. Lett.*, 58(1):28, 2002.

[310] K. R. Mecke and D. Stoyan. Morphological Characterization of Point Patterns. *Biometrical J.*, 47(4):473, 2005.

[311] K. R. Mecke and H. Wagner. Euler characteristic and related measures for random geometric sets. *J. Stat. Phys.*, 64(3–4):843, 1991.

[312] R. Meester and R. Roy. Uniqueness of Unbounded Occupied and Vacant Components in Boolean Models. *Ann. Appl. Probab.*, 4(3):933, 1994.

[313] R. Meester and R. Roy. *Continuum Percolation*. Cambridge Tracts in Mathematics. Cambridge University Press, Cambridge, 1996.

[314] A. Mejdoubi and C. Brosseau. Numerical calculations of the intrinsic electrostatic resonances of artificial dielectric heterostructures. *J. Appl. Phys.*, 101(8):084109, 2007.

[315] T. Michel, F. Bayer, T. Weber, and G. Anton. *Private communication*, 2013-02.

[316] T. Michel et al. On a dark-field signal generated by micrometer-sized calcifications in phase-contrast mammography. *Phys. Med. Biol.*, 58(8): 2713, 2013.

[317] K. Michielsen and D. G. Stavenga. Gyroid cuticular structures in butterfly wing scales: biological photonic crystals. *J. R. Soc. Interface*, 5(18):85, 2008.

[318] W. Mickel, S. Münster, L. M. Jawerth, D. A. Vader, D. A. Weitz, A. P. Sheppard, K. Mecke, B. Fabry, and G. E. Schröder-Turk. Robust Pore Size Analysis of Filamentous Networks from Three-Dimensional Confocal Microscopy. *Biophys. J.*, 95(12):6072, 2008.

[319] W. Mickel, G. E. Schröder-Turk, and K. Mecke. Tensorial Minkowski functionals of triply periodic minimal surfaces. *Interface Focus*, 2(5):623, 2012.

[320] W. Mickel, S. C. Kapfer, G. E. Schröder-Turk, and K. Mecke. Shortcomings of the bond orientational order parameters for the analysis of disordered particulate matter. *J. Chem. Phys.*, 138(4):044501, 2013.

[321] I. S. Molchanov. Set-Valued Estimators for Mean Bodies Related to Boolean Models. *Statistics*, 28(1):43, 1996.

[322] I. S. Molchanov and D. Stoyan. Directional analysis of fibre processes related to Boolean models. *Metrika*, 41(1):183, 1994.

[323] P. A. G. Molinelli, J. I. Nichols, J. A. López, and C. O. Dorso. Simulations of cold nuclear matter at sub-saturation densities. *Nucl. Phys. A*, 923(0):31, 2014.

[324] J. Møller, M. L. Huber, and R. L. Wolpert. Perfect simulation and moment properties for the Matérn type III process. *Stoch. Proc. Appl.*, 120(11): 2142–2158, 2010.

[325] A. W. Moore, A. J. Connolly, C. Genovese, A. Gray, L. Grone, N. Kanidoris II, R. C. Nichol, J. Schneider, A. Szalay, I. Szapudi, and L. Wasserman. Fast Algorithms and Efficient Statistics: N-Point Correlation Functions. In A. Banday, S. Zaroubi, and M. Bartelmann, editors, *Mining the Sky*, ESO Astrophysics Symposia, page 71. Springer, Berlin, Heidelberg, 2001.

[326] C. Moore and M. E. J. Newman. Epidemics and percolation in small-world networks. *Phys. Rev. E*, 61:5678, 2000.

[327] R. Moreno, M. Borga, and O. Smedby. Generalizing the mean intercept length tensor for gray-level images. *Med. Phys.*, 39(7):4599, 2012.

[328] R. Moreno, M. Borga, and O. Smedby. Evaluation of the plate-rod model assumption of trabecular bone. In *Biomedical Imaging (ISBI), 2012 9th IEEE International Symposium on*, page 470, 2012.

[329] K. Mosaliganti, F. Janoos, O. Irfanoglu, R. Ridgway, R. Machiraju, K. Huang, J. Saltz, G. Leone, and M. Ostrowski. Tensor classification of N-point correlation function features for histology tissue segmentation. *Med. Image Anal.*, 13(1):156, 2008.

[330] S. Nachtrab, S. C. Kapfer, C. H. Arns, M. Madadi, K. Mecke, and G. E. Schröder-Turk. Morphology and Linear-Elastic Moduli of Random Network Solids. *Adv. Mater.*, 23(22–23):2633, 2011.

[331] W. Nagel and V. Weiss. Crack STIT tessellations: characterization of stationary random tessellations stable with respect to iteration. *Adv. in Appl. Probab.*, 37(4):859, 2005.

[332] K. Nakazato, K. Oyamatsu, and S. Yamada. Gyroid Phase in Nuclear Pasta. *Phys. Rev. Lett.*, 103:132501, 2009.

[333] K. Nakazato, K. Iida, and K. Oyamatsu. Curvature effect on nuclear "pasta": Is it helpful for gyroid appearance? *Phys. Rev. C*, 83:065811, 2011.

[334] NASA / WMAP Science Team. Nine Year Microwave Sky. [Online; `http://map.gsfc.nasa.gov/media/121238/index.html`; accessed 22-August-2015].

[335] NASA, ESA, and J. Lotz, M. Mountain, A. Koekemoer, and the HFF Team (STScI). Hubble Frontier Field Abell 2744. [Online; `http://hubblesite.org/gallery/album/pr2014001a/`; accessed 22-August-2015].

[336] Z. Néda, R. Florian, and Y. Brechet. Reconsideration of continuum percolation of isotropically oriented sticks in three dimensions. *Phys. Rev. E*, 59: 3717, 1999.

[337] J. W. Negele. The Mean-Field Theory of Nuclear Structure and Dynamics. *Rev. Mod. Phys.*, 54:913, 1982.

[338] R. A. Neher, K. Mecke, and H. Wagner. Topological estimation of percolation thresholds. *J. Stat. Mech.-Theory E.*, 2008(01):P01011, 2008.

[339] M. E. J. Newman, I. Jensen, and R. M. Ziff. Percolation and epidemics in a two-dimensional small world. *Phys. Rev. E*, 65:021904, 2002.

[340] W. G. Newton and J. R. Stone. Modeling nuclear "pasta" and the transition to uniform nuclear matter with the 3D Skyrme-Hartree-Fock method at finite temperature: Core-collapse supernovae. *Phys. Rev. C*, 79:055801, 2009.

[341] J. Neyman and E. S. Pearson. On the Problem of the Most Efficient Tests of Statistical Hypotheses. *Phil. Trans. R. Soc. London, Ser. A*, 231(694–706): 289, 1933.

[342] H.-U. Nissen. Crystal orientation and plate structure in echinoid skeletal units. *Science*, 166:1150, 1969.

[343] NRAO/AUI and N.E. Kassim, Naval Research Laboratory. Galactic Center Wide Field VLA Radio Image. [Online; `http://images.nrao.edu/326`; accessed 22-August-2015].

[344] M. Oda. Fabric tensor for discontinuous geological materials. *Soils Found.*, 22(4):96, 1982.

[345] M. Oda, K. Suzuki, and T. Maeshibu. Elastic compliance for rock-like materials with random cracks. *Soils Found.*, 24(3):27, 1984.

[346] M. Oda, S. Nemat-Nasser, and J. Konishi. Stress-induced anisotropy in granular masses. *Soils Found.*, 25(3):85, 1985.

[347] A. Odgaard. Three-dimensional methods for quantification of cancellous bone architecture. *Bone*, 20(4):315, 1997.

[348] A. Odgaard and H. J. G. Gundersen. Quantification of connectivity in cancellous bone, with special emphasis on 3-D reconstructions. *Bone*, 14 (2):173, 1993.

[349] A. Odgaard, E. B. Jensen, and H. J. G. Gundersen. Estimation of structural anisotropy based on volume orientation. A new concept. *J. Microsc.*, 157 (2):149, 1990.

[350] A. Odgaard, J. Kabel, B. van Rietbergen, M. Dalstra, and R. Huiskes. Fabric and elastic principal directions of cancellous bone are closely related. *J. Biomech.*, 30(5):487, 1997.

[351] R. Ogasawara and K. Sato. Nuclei in Neutrino-Degenerate Dense Matter. I. *Prog. Theor. Phys.*, 68(1):222, 1982.

[352] C. S. O'Hern, A. J. Liu, and S. R. Nagel. Effective Temperatures in Driven Systems: Static Versus Time-Dependent Relations. *Phys. Rev. Lett.*, 93: 165702, 2004.

[353] A. Okabe, B. Boots, K. Sugihara, and S. N. Chiu. *Spatial Tessellations: Concepts and Applications of Voronoi Diagrams*. Wiley Series in Probability and Statistics. Wiley, Chichester, 2009.

[354] M. Okamoto, T. Maruyama, K. Yabana, and T. Tatsumi. Three-dimensional structure of low-density nuclear matter. *Phys. Lett. B*, 713:284, 2012.

[355] L. Onsager. The effects of shape on the interaction of colloidal particles. *Ann. N. Y. Acad. Sci.*, 51(4):627, 1949.

[356] Q. Ouyang and H. Swinney. Transition to chemical turbulence. *Chaos*, 1: 411, 1991.

[357] S. W. Paddock. *Confocal Microscopy Methods and Protocols*, volume 122 of *Methods in Molecular Biology*. Humana Press, New Jersey, 1999.

[358] H. Pais and J. R. Stone. Exploring the Nuclear Pasta Phase in Core-Collapse Supernova Matter. *Phys. Rev. Lett.*, 109:151101, 2012.

[359] M. Palombo, A. Gabrielli, V. D. P. Servedio, G. Ruocco, and S. Capuani. Structural disorder and anomalous diffusion in random packing of spheres. *Sci. Rep.*, 3:2631, 2013.

[360] A. M. Parfitt, C. H. Mathews, A. R. Villanueva, M. Kleerekoper, B. Frame, and D. S. Rao. Relationships between surface, volume, and thickness of iliac trabecular bone in aging and in osteoporosis. Implications for the microanatomic and cellular mechanisms of bone loss. *J. Clin. Invest.*, (4): 1396, 1983.

[361] C. Park, J. Yoon, and E. L. Thomas. Enabling nanotechnology with self assembled block copolymer patterns. *Polymer*, 44(22):6725, 2003.

[362] P. J. E. Peebles. *The Large-scale Structure of the Universe*. Princeton series in physics. Princeton University Press, Princeton, 1980.

[363] P. J. E. Peebles. *Principles of Physical Cosmology*. Princeton series in physics. Princeton University Press, Princeton, 1993.

[364] C. W. Pernell, E. A. Foegeding, P. J. Luck, and J. P. Davis. Properties of whey and egg white protein foams. *Colloid Surface A*, 204(1):9, 2002.

[365] C. J. Pethick and A. Y. Potekhin. Liquid crystals in the mantles of neutron stars. *Phys. Lett. B*, 427(1–2):7, 1998.

[366] C. J. Pethick and D. G. Ravenhall. Matter at Large Neutron Excess and the Physics of Neutron-Star Crusts. *Ann. Rev. Nucl. Part. Sci*, 45(1):429, 1995.

[367] A. Petrie and T. R. Willemain. An empirical study of tests for uniformity in multidimensional data. *Comput. Stat. Data An.*, 64(0):253, 2013.

[368] L. Pietronero, A. Gabrielli, and F. S. Labini. Statistical Physics for cosmic structures. *Physica A*, 306(0):395, 2002. Invited Papers from the 21th IUPAP International Conference on Statistical Physics.

[369] E. Pineda, P. Bruna, and D. Crespo. Cell size distribution in random tessellations of space. *Phys. Rev. E*, 70:066119, 2004.

[370] A. Pommerening and D. Stoyan. Reconstructing spatial tree point patterns from nearest neighbour summary statistics measured in small subwindows. *Can. J. Forest Res.*, 38(5):1110, 2008.

[371] C. Pouya, D. G. Stavenga, and P. Vukusic. Discovery of ordered and quasi-ordered photonic crystal structures in the scales of the beetle Eupholus magnificus. *Opt. Express*, 19(12):11355, 2011.

[372] K. Quast and A. Kaup. Auto GMM-SAMT: An Automatic Object Tracking System for Video Surveillance in Traffic Scenarios. *EURASIP J. Image Video Process.*, 2011:14, 2011.

[373] J. Quintanilla and S. Torquato. Percolation for a model of statistically inhomogeneous random media. *J. Chem. Phys.*, 111:5947, 1999.

[374] J. Quintanilla, S. Torquato, and R. M. Ziff. Efficient measurement of the percolation threshold for fully penetrable discs. *J. Phys. A-Math. Gen.*, 33 (42):L399, 2000.

[375] J. A. Quintanilla and R. M. Ziff. Asymmetry in the percolation thresholds of fully penetrable disks with two different radii. *Phys. Rev. E*, 76:051115, 2007.

[376] C. Räth, R. Monetti, J. Bauer, I. Sidorenko, D. Müller, M. Matsuura, E. M. Lochmüller, P. Zysset, and F. Eckstein. Strength through structure: visualization and local assessment of the trabecular bone structure. *New J. Phys.*, 10(12):125010, 2008.

[377] D. G. Ravenhall, C. J. Pethick, and J. R. Wilson. Structure of Matter below Nuclear Saturation Density. *Phys. Rev. Lett.*, 50:2066, 1983.

[378] M. C. Rechtsman and S. Torquato. Effective dielectric tensor for electromagnetic wave propagation in random media. *J. Appl. Phys.*, 103(8):084901, 2008.

[379] S. Redner and H. E. Stanley. Anisotropic bond percolation. *J. Phys. A-Math. Gen.*, 12(8):1267, 1979.

[380] P.-G. Reinhard and R. Y. Cusson. A comparative study of Hartree-Fock iteration techniques. *Nucl. Phys. A*, 378:418, 1982.

[381] P.-G. Reinhard, L. Guo, and J. A. Maruhn. Nuclear giant resonances and linear response. *Eur. Phys. J. A*, 32:19, 2007.

[382] H. Reiss and A. D. Hammerich. Hard spheres: scaled particle theory and exact relations on the existence and structure of the fluid/solid phase transition. *J. Phys. Chem.*, 90(23):6252, 1986.

[383] J.-Y. Rho, L. Kuhn-Spearing, and P. Zioupos. Mechanical properties and the hierarchical structure of bone. *Med. Eng. Phys.*, 20(2):92, 1998.

[384] M. D. Rintoul and S. Torquato. Precise determination of the critical threshold and exponents in a three-dimensional continuum percolation model. *J. Phys. A-Math. Gen.*, 30(16):L585, 1997.

[385] A. P. Roberts and E. J. Garboczi. Elastic Properties of Model Porous Ceramics. *J. Am. Ceram. Soc.*, 83(12):3041, 2000.

[386] A. P. Roberts and S. Torquato. Chord-distribution functions of three-dimensional random media: approximate first-passage times of Gaussian processes. *Phys. Rev. E*, 59(5):4953, 1999.

[387] V. Robins. Computational Topology for Point Data: Betti Numbers of α-Shapes. In K. Mecke and D. Stoyan, editors, *Morphology of Condensed Matter*, volume 600 of *Lecture Notes in Physics*, page 261. Springer, Berlin, Heidelberg, 2002.

[388] M. A. Rodríguez-Valverde, P. J. Ramón-Torregrosa, and M. A. Cabrerizo-Vílchez. Estimation of percolation threshold of acid-etched titanium surfaces using Minkowski functionals. volume 3 of *Microscopy Book Series*, page 1978. Formatex (Badajoz, Spain), 2010. Microscopy: Science, Technology, Applications and Education.

[389] D. M. Roy and G. R. Gouda. Optimization of strength in cement pastes. *Cement and Concrete Research*, 5(2):153, 1975.

[390] C. H. Rycroft. VORO++: A three-dimensional Voronoi cell library in C++. *Chaos*, 19(4):041111, 2009.

[391] C. H. Rycroft, G. S. Grest, J. W. Landry, and M. Z. Bazant. Analysis of granular flow in a pebble-bed nuclear reactor. *Phys. Rev. E*, 74:021306, 2006.

[392] C. Ryu, K.-W. Kwon, A. L. S. Loke, H. Lee, T. Nogami, V. M. Dubin, R. A. Kavari, G. W. Ray, and S. S. Wong. Microstructure and reliability of copper interconnects. *Electron Devices, IEEE Transactions on*, 46(6):1113, 1999.

[393] M. Sahimi. *Flow and Transport in Porous Media and Fractured Rock: From Classical Methods to Modern Approaches*. Wiley, New York, 2011.

[394] M. Sahimi. *Applications of percolation theory*. CRC Press, Boca Raton, 2nd edition, 2013.

[395] E. A. Sander and V. H. Barocas. Comparison of 2D fiber network orientation measurement methods. *J. Biomed. Mater. Res. A*, 88(2):322, 2009.

[396] L. Santaló. *Integral Geometry and Geometric Probability*. Addison-Wesley, Reading, 1976.

[397] V. Saranathan, C. O. Osuji, S. G. J. Mochrie, H. Noh, S. Narayanan, A. Sandy, E. R. Dufresne, and R. O. Prum. Structure, function, and self-assembly of single network gyroid (I4132) photonic crystals in butterfly wing scales. *P. Natl. Acad. Sci.*, 107(26):11676, 2010.

[398] H. Scher and R. Zallen. Critical density in percolation processes. *J. Chem. Phys.*, 53(9):3759, 1970.

[399] J. Schmalzing, T. Buchert, A. L. Melott, V. Sahni, B. S. Sathyaprakash, and S. F. Shandarin. Disentangling the Cosmic Web. I. Morphology of Isodensity Contours. *Astrophys. J.*, 526(2):568, 1999.

[400] R. Schneider and W. Weil. *Stochastic and Integral Geometry (Probability and Its Applications)*. Springer, Berlin, 2008.

[401] H. G. Schnering and R. Nesper. Nodal surfaces of Fourier series: Fundamental invariants of structured matter. *Z. Phys. B*, 83(3):407, 1991.

[402] C. Scholz, F. Wirner, J. Götz, U. Rüde, G. E. Schröder-Turk, K. Mecke, and C. Bechinger. Permeability of Porous Materials Determined from the Euler Characteristic. *Phys. Rev. Lett.*, 109:264504, 2012.

[403] C. Scholz, F. Wirner, M. A. Klatt, D. Hirneise, G. E. Schröder-Turk, K. Mecke, and C. Bechinger. Direct relations between morphology and transport in Boolean models. *Phys. Rev. E*, 92(4), 2015.

[404] G. E. Schröder, S. J. Ramsden, A. G. Christy, and S. T. Hyde. Medial surfaces of hyperbolic structures. *Eur. Phys. J. B*, 35:551, 2003.

[405] G. E. Schröder-Turk, A. Fogden, and S. T. Hyde. Bicontinuous geometries and molecular self-assembly: Comparison of local curvature and global packing variations in genus-three cubic, tetragonal and rhombohedral surfaces. *Eur. Phys. J B*, 54:509, 2006.

[406] G. E. Schröder-Turk, S. Kapfer, B. Breidenbach, C. Beisbart, and K. Mecke. Tensorial Minkowski functionals and anisotropy measures for planar patterns. *J. Microsc.*, 238(1):57, 2010.

[407] G. E. Schröder-Turk, W. Mickel, M. Schröter, G. W. Delaney, M. Saadatfar, T. J. Senden, K. Mecke, and T. Aste. Disordered spherical bead packs are anisotropic. *Europhys. Lett.*, 90(3):34001, 2010.

[408] G. E. Schröder-Turk, W. Mickel, S. C. Kapfer, M. A. Klatt, F. M. Schaller, M. J. F. Hoffmann, N. Kleppmann, P. Armstrong, A. Inayat, D. Hug, M. Reichelsdorfer, W. Peukert, W. Schwieger, and K. Mecke. Minkowski Tensor Shape Analysis of Cellular, Granular and Porous Structures. *Adv. Mater.*, 23 (22–23):2535, 2011.

[409] G. E. Schröder-Turk, S. Wickham, H. Averdunk, M. C. J. Large, L. Poladian, F. Brink, J. D. Fitz Gerald, and S. T. Hyde. The chiral structure of porous chitin within the wing-scales of Callophrys rubi. *J. Struct. Biol.*, 174:290, 2011.

[410] G. E. Schröder-Turk, W. Mickel, S. C. Kapfer, F. M. Schaller, B. Breidenbach, D. Hug, and K. Mecke. Minkowski tensors of anisotropic spatial structure. *New J. Phys.*, 15(8):083028, 2013.

[411] G. E. Schröder-Turk, R. Schielein, S. C. Kapfer, F. M. Schaller, G. W. Delaney, T. Senden, M. Saadatfar, T. Aste, and K. Mecke. Minkowski tensors and local structure metrics: Amorphous and crystalline sphere packings. *AIP Conf. Proc.*, 1542(1):349, 2013.

[412] B. Schuetrumpf. *Time-Dependent Hartree-Fock Approach to Nuclear "Pasta"*. PhD thesis, Universität Frankfurt am Main, 2014.

[413] B. Schuetrumpf, M. A. Klatt, K. Iida, J. Maruhn, K. Mecke, and P.-G. Reinhard. Time-dependent Hartree-Fock approach to nuclear "pasta" at finite temperature. *Phys. Rev. C*, 87:055805, 2013.

[414] B. Schuetrumpf, M. A. Klatt, K. Iida, J. A. Maruhn, K. Mecke, and P.-G. Reinhard. Time-Dependent Hartree-Fock Approach to Nuclear Pasta at Finite Temperature. *J. Phys.: Conf. Ser.*, 426(1):012009, 2013.

[415] B. Schuetrumpf, M. A. Klatt, K. Iida, G. E. Schröder-Turk, J. A. Maruhn, K. Mecke, and P.-G. Reinhard. Minimal surfaces in nuclear pasta with the time-dependent Hartree-Fock approach. *Proceedings of Science*, Bormio2014:032, 2014.

[416] B. Schuetrumpf, M. A. Klatt, K. Iida, G. E. Schröder-Turk, J. A. Maruhn, K. Mecke, and P.-G. Reinhard. Appearance of the single gyroid network phase in "nuclear pasta" matter. *Phys. Rev. C*, 91:025801, 2015.

[417] L. S. Schulman and P. E. Seiden. Percolation and Galaxies. *Science*, 233 (4762):425, 1986.

[418] L. M. Schwartz, N. Martys, D. P. Bentz, E. J. Garboczi, and S. Torquato. Cross-property relations and permeability estimation in model porous media. *Phys. Rev. E*, 48:4584, 1993.

[419] R. Scoccimarro. The Bispectrum: From Theory to Observations. *Astrophys. J.*, 544(2):597, 2000.

[420] L. Scriven. Equilibrium bicontinuous structure. *Nature*, 263:123, 1976.

[421] F. Sébille, S. Figerou, and V. de la Mota. Self-consistent dynamical mean-field investigation of exotic structures in isospin-asymmetric nuclear matter. *Nucl. Phys. A*, 822(1–4):51, 2009.

[422] F. Sébille, V. de la Mota, and S. Figerou. Probing the microscopic nuclear matter self-organization processes in the neutron star crust. *Phys. Rev. C*, 84:055801, 2011.

[423] G. T. Seidler, G. Martinez, L. H. Seeley, K. H. Kim, E. A. Behne, S. Zaranek, B. D. Chapman, S. M. Heald, and D. L. Brewe. Granule-by-granule reconstruction of a sandpile from x-ray microtomography data. *Phys. Rev. E*, 62: 8175, 2000.

[424] B. Shafiro and M. Kachanov. Materials with fluid-filled pores of various shapes: effective elastic properties and fluid pressure polarization. *Int. J. Solids Struct.*, 34(27):3517, 1997.

[425] D. N. Shanbhag. On infinite server queues with batch arrivals. *J. Appl. Prob.*, 3(1):274, 1966.

[426] I. N. Sidorenko, J. Bauer, R. Monetti, D. Mueller, E. J. Rummeny, F. Eckstein, and C. W. Raeth. Comparison and combination of scaling index

method and Minkowski functionals in the analysis of high resolution magnetic resonance images of the distal radius in vitro, 2008.

[427] O. Sigmund and S. Torquato. Design of materials with extreme thermal expansion using a three-phase topology optimization method. *J. Mech. Phys. Solids*, 45(6):1037, 1997.

[428] L. E. Silbert and M. Silbert. Long-wavelength structural anomalies in jammed systems. *Phys. Rev. E*, 80:041304, 2009.

[429] C. Simenel and P. Chomaz. Nonlinear vibrations in nuclei. *Phys. Rev. C*, 68:024302, 2003.

[430] C. A. Simmons and J. A. Hipp. Method-Based Differences in the Automated Analysis of the Three-Dimensional Morphology of Trabecular Bone. *J. Bone Miner. Res.*, 12(6):942, 1997.

[431] J. S. Sims et al. Accelerating Scientific Discovery Through Computation and Visualization II. *J. Res. Natl. Inst. Stand. Technol.*, 107(3):223, 2002.

[432] G. F. Smoot et al. Structure in the COBE differential microwave radiometer first-year maps. *Astrophys. J. Lett.*, 396:L1, 1992.

[433] S. Solomon, G. Weisbuch, L. de Arcangelis, N. Jan, and D. Stauffer. Social percolation models. *Physica A*, 277(1–2):239, 2000.

[434] H. Sonoda, G. Watanabe, K. Sato, T. Takiwaki, K. Yasuoka, and T. Ebisuzaki. Impact of nuclear "pasta" on neutrino transport in collapsing stellar cores. *Phys. Rev. C*, 75:042801, 2007.

[435] H. Sonoda, G. Watanabe, K. Sato, K. Yasuoka, and T. Ebisuzaki. Phase diagram of nuclear "pasta" and its uncertainties in supernova cores. *Phys. Rev. C*, 77:035806, 2008.

[436] W. Stadje. The busy period of the queueing system M/G/∞. *J. Appl. Prob.*, 22:697, 1985.

[437] J. Stam. Diffraction Shaders. In *Proceedings of the 26th Annual Conference on Computer Graphics and Interactive Techniques*, SIGGRAPH '99, page 101, New York, NY, USA, 1999.

[438] Stanford Project on Deep-water Depositional Systems. P-Impedance horizon slice. [Online; `https://pangea.stanford.edu/researchgroups/spodds/research/geostatistics-and-rock-physics`; accessed 22-August-2015].

[439] H. E. Stanley. Application of fractal concepts to polymer statistics and to anomalous transport in randomly porous media. *J. Stat. Phys.*, 36(5–6):843, 1984.

[440] F. W. Starr, S. Sastry, J. F. Douglas, and S. C. Glotzer. What Do We Learn from the Local Geometry of Glass-Forming Liquids? *Phys. Rev. Lett.*, 89: 125501, 2002.

[441] D. Stauffer. *Introduction to percolation theory*. Taylor & Francis, 1985.

[442] D. Stauffer. Percolation Models Of Financial Market Dynamics. *Adv. Complex Syst.*, 04(01):19, 2001.

[443] D. Stauffer and D. Sornette. Self-organized percolation model for stock market fluctuations. *Physica A*, 271(3–4):496, 1999.

[444] P. J. Steinhardt, D. R. Nelson, and M. Ronchetti. Bond-orientational order in liquids and glasses. *Phys. Rev. B*, 28:784, 1983.

[445] W. H. Stockmayer. Theory of Molecular Size Distribution and Gel Formation in Branched Polymers II. General Cross Linking. *J. Chem. Phys.*, 12 (4):125, 1944.

[446] M. Stonebraker, J. Frew, K. Gardels, and J. Meredith. The SEQUOIA 2000 Storage Benchmark. *SIGMOD Rec.*, 22(2):2, 1993.

[447] D. Stoyan and K. Mecke. *The Boolean Model: from Matheron till Today, in: 'Space, Structure and Randomness' edited by Michel Bilodeau, Fernand Meyer and Michel Schmitt, pp. 151-182*. Springer, New York, 2005.

[448] D. Stoyan, W. Kendall, and J. Mecke. *Stochastic geometry and its applications*. John Wiley and Sons, 1987.

[449] K. Sukumaran, B. C. Pai, and M. Chakraborty. The effect of isothermal mechanical stirring on an Al-Si alloy in the semisolid condition. *Mat. Sci. Eng. A-Struct*, 369(1):275, 2004.

[450] C. Sun and J. Sherrah. 3D symmetry detection using the extended Gaussian image. *IEEE T. Pattern Anal.*, 19(2):164, 1997.

[451] M. F. Sykes and J. W. Essam. Exact Critical Percolation Probabilities for Site and Bond Problems in Two Dimensions. *J. Math. Phys.*, 5(8):1117, 1964.

[452] I. Szapudi, M. Postman, T. R. Lauer, and W. Oegerle. Observational Constraints on Higher Order Clustering up to $z \simeq 1$. *Astrophys. J.*, 548(1):114, 2001.

[453] L. Takács. On a Probability Problem Arising in the Theory of counters. *Proc. Cambridge Phil. Soc.*, 52:488, 1956.

[454] L. Takács. *Introduction to the Theory of Queues*. Oxford University Press, New York, 1962.

[455] J. E. Taylor and R. J. Adler. Euler Characteristics for Gaussian Fields on Manifolds. *Ann. Probab.*, 31(2):533, 2003.

[456] S. Theodoridis and K. Koutroumbas. *Pattern Recognition*. Academic Press, Boston, 4th edition, 2009.

[457] H. Tomita. Statistical Properties of Random Interface System. *Prog. Theor. Phys.*, 75(3):482, 1986.

[458] S. Torquato. Random Heterogeneous Media: Microstructure and Improved Bounds on Effective Properties. *Appl. Mech. Rev.*, 44(2):37, 1991.

[459] S. Torquato. Modeling of physical properties of composite materials. *Int. J. Solids Struct.*, 37(1–2):411, 2000.

[460] S. Torquato. *Random Heterogeneous Materials: Microstructure and Macroscopic Properties*. Interdisciplinary Applied Mathematics. Springer, New York, 2002.

[461] S. Torquato. Effect of dimensionality on the continuum percolation of overlapping hyperspheres and hypercubes. *J. Chem. Phys.*, 136(5):054106, 2012.

[462] S. Torquato and Y. Jiao. Robust algorithm to generate a diverse class of dense disordered and ordered sphere packings via linear programming. *Phys. Rev. E*, 82:061302, 2010.

[463] S. Torquato and Y. Jiao. Effect of dimensionality on the percolation threshold of overlapping nonspherical hyperparticles. *Phys. Rev. E*, 87:022111, 2013.

[464] S. Torquato and D. C. Pham. Optimal Bounds on the Trapping Constant and Permeability of Porous Media. *Phys. Rev. Lett.*, 92:255505, 2004.

[465] S. Torquato and G. Stell. Microstructure of two-phase random media. I. The n-point probability functions. *J. Chem. Phys.*, 77(4):2071, 1982.

[466] S. Torquato and F. H. Stillinger. Multiplicity of Generation, Selection, and Classification Procedures for Jammed Hard-Particle Packings. *J. Phys. Chem. B*, 105(47):11849, 2001.

[467] S. Torquato and F. H. Stillinger. Local density fluctuations, hyperuniformity, and order metrics. *Phys. Rev. E*, 68:041113, 2003.

[468] S. Torquato and F. H. Stillinger. New Conjectural Lower Bounds on the Optimal Density of Sphere Packings. *Exp. Math.*, 15(3):307, 2006.

[469] S. Torquato and F. H. Stillinger. Toward the jamming threshold of sphere packings: Tunneled crystals. *J. Appl. Phys.*, 102(9):093511, 2007.

[470] S. Torquato and F. H. Stillinger. Jammed hard-particle packings: From Kepler to Bernal and beyond. *Rev. Mod. Phys.*, 82:2633, 2010.

[471] S. Torquato, T. M. Truskett, and P. G. Debenedetti. Is Random Close Packing of Spheres Well Defined? *Phys. Rev. Lett.*, 84:2064, 2000.

[472] S. Torquato, A. Donev, and F. H. Stillinger. Breakdown of elasticity theory for jammed hard-particle packings: conical nonlinear constitutive theory. *Int. J. Solids Struct.*, 40(25):7143, 2003.

[473] C. Torrence and G. P. Compo. A Practical Guide to Wavelet Analysis. *Bull. Amer. Meteor. Soc.*, 79(1):61, 1998.

[474] T. M. Truskett, S. Torquato, and P. G. Debenedetti. Towards a quantification of disorder in materials: Distinguishing equilibrium and glassy sphere packings. *Phys. Rev. E*, 62:993, 2000.

[475] S.-H. Tsai, F. Wang, and D. P. Landau. Wang-Landau sampling of an asymmetric ising model: a study of the critical endpoint behavior. *Braz. J. Phys.*, 36:635, 2006.

[476] A. Tscheschel and D. Stoyan. Statistical reconstruction of random point patterns. *Comput. Stat. Data An.*, 51(2):859, 2006.

[477] C. H. Turner and S. C. Cowin. Dependence of elastic constants of an anisotropic porous material upon porosity and fabric. *J. Mater. Sci.*, 22(9): 3178, 1987.

[478] C. H. Turner, S. C. Cowin, J. Y. Rho, R. B. Ashman, and J. C. Rice. The fabric dependence of the orthotropic elastic constants of cancellous bone. *J. Biomech.*, 23(6):549, 1990.

[479] M. D. Turner, M. Saba, Q. Zhang, B. P. Cumming, G. E. Schroder-Turk, and M. Gu. Miniature chiral beamsplitter based on gyroid photonic crystals. *Nat. Photon.*, 7(10):801, 2013.

[480] A. S. Umar and V. E. Oberacker. Three Dimensional Unrestricted Time Dependent Hartree Fock Fusion Calculations Using the Full Skyrme Interaction. *Phys. Rev. C*, 73:054607, 2006.

[481] A. S. Umar and V. E. Oberacker. Heavy Ion Interaction Potential Deduced From Density Constrained Time Dependent Hartree Fock Calculation. *Phys. Rev. C*, 74:021601, 2006.

[482] A. S. Umar, M. R. Strayer, P.-G. Reinhard, K. T. R. Davies, and S.-J. Lee. Spin-orbit force in time-dependent Hartree-Fock calculations of heavy-ion collisions. *Phys. Rev. C*, 40:706, 1989.

[483] E. E. Underwood. *Quantitative stereology*. Addison-Wesley series in metallurgy and materials. Addison-Wesley, Reading, 1970.

[484] J. D. Urbina and K. Richter. Supporting random wave models: a quantum mechanical approach. *J. Phys. A: Math. Gen.*, 36(38):L495, 2003.

[485] G. R. Valenzuela. Theories for the interaction of electromagnetic and oceanic waves—A review. *Bound.-Lay. Meteorol.*, 13(1-4):61, 1978.

[486] E. Vanmarcke. *Random Fields: Analysis and Synthesis*. World Scientific, Singapore, 2010.

[487] B. Vasilić, C. S. Rajapakse, and F. W. Wehrli. Classification of trabeculae into three-dimensional rodlike and platelike structures via local inertial anisotropy. *Med. Phys.*, 36(7):3280, 2009.

[488] E. B. Vedel Jensen. *Local Stereology*. Advanced Series on Statistical Science & Applied Probability. World Scientific, Singapore, 1998.

[489] E. B. Vedel Jensen and A. Rasmusson. Rotational Integral Geometry and Local Stereology - with a View to Image Analysis. In V. Schmidt, editor, *Stochastic Geometry, Spatial Statistics and Random Fields*, volume 2120 of *Lecture Notes in Mathematics*, page 233. Springer International Publishing, 2015.

[490] E. B. Vedel Jensen and J. F. Ziegel. Local Stereology of Tensors of Convex Bodies. *Methodol. Comput. Appl.*, 16(2):263, 2014.

[491] L. Verde, L. Wang, A. F. Heavens, and M. Kamionkowski. Large-scale structure, the cosmic microwave background and primordial non-Gaussianity. *Mon. Not. R. Astron. Soc.*, 313(1):141, 2000.

[492] A. Vesterby. Star volume in bone research. A histomorphometric analysis of trabecular bone structure using vertical sections. *Anat. Rec.*, 235(2):325, 1993.

[493] T. Vicsek and J. Kertesz. Monte Carlo renormalisation-group approach to percolation on a continuum: test of universality. *J. Phys. A-Math. Gen.*, 14 (2):L31, 1981.

[494] P. Vielva, E. Martínez-González, R. B. Barreiro, J. L. Sanz, and L. Cayón. Detection of Non-Gaussianity in the Wilkinson Microwave Anisotropy Probe First-Year Data Using Spherical Wavelets. *Astrophys. J.*, 609(1):22, 2004.

[495] P. Vukusic and J. Sambles. Photonic structures in biology. *Nature*, 424:852, 2003.

[496] N. Wagner, I. Balberg, and D. Klein. Monte Carlo results for continuum percolation in low and high dimensions. *Phys. Rev. E*, 74:011127, 2006.

[497] M. J. Wald, B. Vasilic, P. K. Saha, and F. W. Wehrli. Spatial autocorrelation and mean intercept length analysis of trabecular bone anisotropy applied to in vivo magnetic resonance imaging. *Med. Phys.*, 34(3):1110, 2007.

[498] J. S. Walker. Fourier analysis and wavelet analysis. *Not. Am. Math. Soc.*, 44 (6):658, 1997.

[499] F. Wang and D. P. Landau. Determining the density of states for classical statistical models: A random walk algorithm to produce a flat histogram. *Phys. Rev. E*, 64:056101, 2001.

[500] F. Wang and D. P. Landau. Efficient, Multiple-Range Random Walk Algorithm to Calculate the Density of States. *Phys. Rev. Lett.*, 86:2050, 2001.

[501] H. Wang and S. M. Shaler. Computer-simulated three-dimensional microstructure of wood fibre composite materials. *J. Pulp Pap. Sci.*, 24(10): 314, 1998.

[502] G. Watanabe and K. Iida. Electron screening in the liquid-gas mixed phases of nuclear matter. *Phys. Rev. C*, 68:045801, 2003.

[503] G. Watanabe, K. Iida, and K. Sato. Effects of neutrino trapping on thermodynamic properties of nuclear "pasta". *Nucl. Phys. A*, 687(3–4):512, 2001. erratum ibid. 726, 357(E), 2003.

[504] G. Watanabe, K. Sato, K. Yasuoka, and T. Ebisuzaki. Structure of cold nuclear matter at subnuclear densities by quantum molecular dynamics. *Phys. Rev. C*, 68:035806, 2003.

[505] G. Watanabe, K. Sato, K. Yasuoka, and T. Ebisuzaki. Phases of hot nuclear matter at subnuclear densities. *Phys. Rev. C*, 69:055805, 2004.

[506] E. R. Weeks and D. A. Weitz. Properties of Cage Rearrangements Observed near the Colloidal Glass Transition. *Phys. Rev. Lett.*, 89:095704, 2002.

[507] W. Weil. Iterations of translative integral formulae and non-isotropic Poisson processes of particles. *Math. Z.*, 205(1):531, 1990.

[508] S. Weiner and H. D. Wagner. The Material Bone: Structure-Mechanical Function Relations. *Annu. Rev. Mater. Sci.*, 28(1):271, 1998.

[509] S. Weiner, W. Traub, and H. D. Wagner. Lamellar Bone: Structure-Function Relations. *J. Struct. Biol.*, 126(3):241, 1999.

[510] S. Whitaker. Flow in porous media I: A theoretical derivation of Darcy's law. *Transport in Porous Media*, 1(1):3, 1986.

[511] S. D. M. White. The hierarchy of correlation functions and its relation to other measures of galaxy clustering. *Mon. Not. R. Astron. Soc.*, 186:145, 1979.

[512] W. J. Whitehouse. The quantitative morphology of anisotropic trabecular bone. *J. Microsc.*, 101(2):153, 1974.

[513] Wikipedia. Percolation threshold—Wikipedia, The Free Encyclopedia, 2015. [Online; `http://en.wikipedia.org/w/index.php?title=Percolation_threshold&oldid=658789808`; accessed 21-May-2015].

[514] R. D. Williams and S. E. Koonin. Sub-saturation phases of nuclear matter. *Nucl. Phys.*, 435(3–4):844, 1985.

[515] B. D. Wilts, K. Michielsen, J. Kuipers, H. De Raedt, and D. G. Stavenga. Brilliant camouflage: photonic crystals in the diamond weevil, Entimus imperialis. *Proc. R. Soc. B*, 279(1738):2524, 2012.

[516] R. Wittmann, M. Marechal, and K. Mecke. Fundamental measure theory for smectic phases: Scaling behavior and higher order terms. *J. Chem. Phys.*, 141(6):064103, 2014.

[517] H. Wium, P. S. Pedersen, and K. B. Qvist. Effect of coagulation conditions on the microstructure and the large deformation properties of fat-free Feta cheese made from ultrafiltered milk. *Food Hydrocolloid*, 17(3):287, 2003.

[518] Y. Xiao. Sample Path Properties of Anisotropic Gaussian Random Fields. In D. Khoshnevisan and F. Rassoul-Agha, editors, *A Minicourse on Stochastic Partial Differential Equations*, volume 1962 of *Lecture Notes in Mathematics*, page 145. Springer, Berlin, Heidelberg, 2009.

[519] R. Xie, G. G. Long, S. J. Weigand, S. C. Moss, T. Carvalho, S. Roorda, M. Hejna, S. Torquato, and P. J. Steinhardt. Hyperuniformity in amorphous silicon based on the measurement of the infinite-wavelength limit of the structure factor. *Proc. Natl. Acad. Sci. USA*, 110(33):13250, 2013.

[520] A. Yilmaz, O. Javed, and M. Shah. Object tracking: A survey. *ACM Comput. Surv.*, 38(4), 2006.

[521] C. E. Zachary and S. Torquato. Improved reconstructions of random media using dilation and erosion processes. *Phys. Rev. E*, 84:056102, 2011.

[522] R. Zallen. *The Physics of Amorphous Solids*. Wiley Interscience, New York, 1998.

[523] G. Zhang and S. Torquato. Precise algorithm to generate random sequential addition of hard hyperspheres at saturation. *Phys. Rev. E*, 88:053312, 2013.

[524] L. L. Zhang and U.-L. Pen. Fast n-point correlation functions and three-point lensing application. *New Astronomy*, 10(7):569, 2005.

[525] X. Zhang and C. Yu. Fast n-point Correlation Function Approximation with Recursive Convolution for Scalar Fields. In *Cloud Computing Technology and Science (CloudCom), 2011 IEEE Third International Conference on*, page 634, 2011.

[526] S.-C. Zhao, S. Sidle, H. L. Swinney, and M. Schröter. Correlation between Voronoi volumes in disc packings. *Europhys. Lett.*, 97(3):34004, 2012.

[527] T. I. Zohdi. On the optical thickness of disordered particulate media. *Mech. Mater.*, 38(8–10):969, 2006.

[528] P. K. Zysset and A. Curnier. An alternative model for anisotropic elasticity based on fabric tensors. *Mech. Mater.*, 21(4):243, 1995.

Acknowledgments

I express my special thanks to my supervisor Klaus Mecke for continuous support, guidance, and advice. I am very grateful to him for giving me the possibility to work on this fascinating topic and write this thesis as well as for his inspiring questions, ideas, and suggestions. I thank him for showing me a wider view on the geometry of random and disordered structures, how a simple yet concise analysis can reveal deep insights, and the elegance of how a general concept is applicable to very different fields of research. Moreover, I am especially grateful for his encouragement and support to start collaborations with very different fields. I am very much obliged to him for making it possible that I could present my work at many international and interdisciplinary conferences that I could visit and work at Princeton University.

I also thank all of my collaborators for our productive and friendly collaborations: Bruno Ebner, Daniel Göring, Norbert Henze, Max Hörmann, Julia Hörrmann, Daniel Hug, Kei Iida, Günter Last, Joachim A. Maruhn, Paul-Gerhard Reinhard, Maria Schlecht, Christian Scholz, Matthias Schulte, Bastian Schütrumpf, Christian Stegmann, and Salvatore Torquato, whom I also thank for the warm welcome in Princeton. I especially thank Gerd Schröder-Turk for his support, advice, and encouragement as well as for our valuable discussions and his very helpful suggestions.

I thank all members of the "Theorie 1" in Erlangen. Although I cannot mention all by name, I thank everyone of them especially for many interesting discussions and helpful advice ranging over very different topics of physics and mathematics to programming. I also thank all members of the DFG-Forschergruppe "Geometry and Physics of Spatial Random Systems" for instructive discussions between physicists and mathematicians. I especially thank all proofreaders of my thesis. I thank the H.E.S.S. collaboration for kindly providing me data from their experiment. I also thank Claudia Redenbach, Andy Kraynik, Steven Atkinson, Richard Schielein, Fabian Schaller, and Markus Spanner for their data. For their support with the publication, the layout, and cover image, I thank Beate Gresser and Eva Volleth

from FAU University Press. I thank very much Margret Heinen-Krumreich for her help and kindness during my years in Erlangen.

For both their financial and conceptual support, I especially thank the "Studienstiftung des deutschen Volkes" for their scholarship. Moreover, I thank the "German Science Foundation (DFG)" for financial support and the DFG-Forschergruppe "Geometry and Physics of Spatial Random Systems" for the possibility to connect and collaborate across the boundaries of countries and disciplines. I am very much obliged to the "Elitenetwork of Bavaria" and their Elite Graduate Program "Physics with integrated Doctorate Program". I also thank the "Elitenetwork of Bavaria" and the "Foundation Lindau Nobel Prizewinners Meeting at Lake Constance" for giving me the unique possibility to attend the "65th Lindau Nobel Laureate Meeting" and to present my work there in two talks.

I am grateful for all the kindness and help by many friends and colleagues. I thank Anna, Karin and Martin Sokoll for their encouragement. I thank the parishes of St. Kunigund in Nürnberg and St. Paul in Princeton. I am very much obliged to Johannes Knauf for his advice and help since the beginning of my studies at the TU Kaiserslautern via distance learning up to my PhD thesis.

I especially thank my family for all of their encouragement, their help throughout the years. I am deeply grateful to my mother Gertrud and my father Wilfried, whose love and moral support are beyond description, and I am deeply obliged to my brother Matthias, who as a seven-year-old child taught me, his little brother, how to read and write. He thus laid the foundation for all of my following work. I thank my grandfather Gerhard Klatt. I thank each member of the Riedl family and the Eisenbarth family, Reinhildis Klatt and her family, and my uncle Josef Schmidt for their friendship. I thank my uncle Ludwig Schmidt for all of his support. I am especially obliged to my late grandmother Margarete Schmidt, who gave me more than I could ever give to her. Most importantly, I thank the Lord, to whom I commend all of my work.

From the large-scale structure of the universe to exotic states in nuclear matter: random or disordered spatial structures appear on nearly all length scales in very different physical, chemical, or biological systems. In systems with complex structure, there is often a close interconnection of physics and geometry, and physical insight is often best achieved by a rigorous characterization of the structure. This thesis demonstrates how a family of integral geometric shape descriptors, the so-called Minkowski functionals and tensors, provide an intuitive and versatile morphometric analysis. It sensitively and comprehensively describes the geometry in diverse systems on radically different length scales.

The morphometric analysis is refined and applied to mathematical models and simulations of physical systems as well as experimental data sets. For example, the structures appearing in models from stochastic geometry are examined with a particular emphasis on anisotropy. In one of these models, the Minkowski functionals help to better understand and predict a geometrical phase transition. Moreover, a structural characterization across length scales of a physical model, which consists of hard particles, reveals how systems with similar local configurations can nevertheless exhibit a distinctly different global structure. On extremely small length scales, the Minkowski functionals help to characterize complex shapes of exotic states of nuclear matter. Among a variety of these spontaneously forming so-called pasta shapes, a gyroid network is identified, which was, e.g., already found in the wing scales of a butterfly. In a morphometric data analysis, the Minkowski functionals quantify the shape of noise in sky maps from gamma-ray astronomy. Thus, additional geometric information can be extracted from the data without prior assumptions about potential sources. The latter can then be detected by a significant deviation of the structure of the observed sky map from the shape of the background noise. By an enhanced characterization of this background structure, formerly undetected sources can eventually be detected in the same data.

The Minkowski functionals and tensors allow for a better understanding of quite different mathematical models and physical systems as well as a sensitive analysis of experimental observations. Thereby, this morphometric analysis relates seemingly unrelated fields of research.

ISBN 978-3-944057-77-4

9 783944 057774

FAU UNIVERSITY PRESS 2016